

3 **MARINE GEOHAZARDS AND GEO-ENGINEERING**
4 **CONSTRAINTS ON THE GLACIATED EUROPEAN MARGINS**

5 Benjamin Bellwald (corresponding author), NGI, Oslo, Norway, benjamin.bellwald@ngi.no and University of Oslo, Oslo,
6 Norway

7 Bartosz Kurjanski, University of Aberdeen, Aberdeen, UK, bkurjanski@abdn.ac.uk

8 Gareth Carter, Arup, Edinburgh, UK, gareth.carter@arup.com

9 Gareth Wood, bp International, Sunbury on Thames, UK, gareth.wood@bp.com

10 Leah Arlott, RWE Renewables, Swindon, UK, leah.arlott@rwe.com

11 Andrea Plaza-Faverola, UiT The Arctic University of Norway, Tromsø, Norway, andrea.a.faverola@uit.no

12 Heather A. Stewart, Kelpie Geoscience Limited, Edinburgh, UK, hstewart@kelpiegeoscience.com

13 Berit Oline Hjelstuen, University of Bergen, Bergen, Norway, berit.hjelstuen@uib.no

14 Helge Løseth, Equinor ASA, Trondheim, Norway, heloe@equinor.com

15 Katrine Juul Andresen, Aarhus University, Aarhus, Denmark, katrine.andresen@geo.au.dk

16 Stefan Wenau, ATLAS MARIDAN ApS Germany, Bremen, Germany, stefan.wenau@atlasmaridan.com

17 Roger Birchall, SSE Renewables, Glasgow, UK, roger.birchall@sse.com

18 Claire McGhee, AtkinsRéalis, Glasgow, UK, claire.mcghee@atkinsrealis.com

19 Steven J. Gibbons, NGI, Oslo, Norway, steven.gibbons@ngi.no

20 Carl B. Harbitz, NGI, Oslo, Norway, carl.bonnevie.harbitz@ngi.no

21 Brian Carlton, NGI, Oslo, Norway, brian.carlton@ngi.no

22 Andrew M. W. Newton, Queen's University Belfast, Belfast, UK, a.newton@qub.ac.uk

23 Mads Huuse, The University of Manchester, Manchester, UK, mads.huuse@manchester.ac.uk

24 Dieter Issler, NGI, Oslo, Norway, dieter.issler@ngi.no

25 Finn Løvholt, NGI, Oslo, Norway, finn.lovholt@ngi.no

26 Carl Fredrik Forsberg, NGI, Oslo, Norway, carl.fredrik.forsberg@ngi.no

27 Mark Coughlan, University College Dublin, Dublin, Ireland, mark.coughlan@ucd.ie

28 Simona Caruso, bp International, Aberdeen, UK, simona.caruso@bp.com

29 Michael Long, University College Dublin, Dublin, Ireland, mike.long@ucd.ie and NGI, Oslo, Norway,
30 michael.long@ngi.no

31 David Tappin, BGS, Nottingham, UK, drta@bgs.ac.uk

32 Paul Dimmock, NGI, Perth, Australia, paul.dimmock@ngi.no

33 Rasmus Tofte Klinkvort, NGI, Oslo, Norway, rasmus.klinkvort@ngi.no

34 Maarten Vanneste, NGI, Oslo, Norway, maarten.vanneste@ngi.no

35
36 **This is a non-peer-reviewed preprint submitted to EarthArXiv.**

37 **The paper was submitted to Earth-Science Reviews.**

39 **MARINE GEOHAZARDS AND GEO-**
40 **ENGINEERING CONSTRAINTS ON THE**
41 **GLACIATED EUROPEAN MARGINS**

42 Benjamin Bellwald^{1,2}, Bartosz Kurjanski³, Gareth Carter^{4,5}, Gareth Wood⁶, Leah Arlott⁷, Andreia
43 Plaza-Faverola⁸, Heather A. Stewart⁹, Berit Oline Hjelstuen¹⁰, Helge Løseth¹¹, Katrine Juul
44 Andresen¹², Stefan Wenau¹³, Roger Birchall¹⁴, Claire McGhee¹⁵, Steven J. Gibbons¹, Carl B. Harbitz¹,
45 Brian Carlton¹, Andrew M. W. Newton¹⁶, Mads Huuse¹⁷, Dieter Issler¹, Finn Løvholt¹, Carl Fredrik
46 Forsberg¹, Mark Coughlan¹⁸, Simona Carusoack⁶, Michael Long^{1,18}, David Tappin¹⁹, Paul Dimmock²⁰,
47 Rasmus Tofte Klinkvort¹, Maarten Vanneste¹

48 ¹NGI, Sandakerveien 140, Oslo, Norway

49 ²University of Oslo, Oslo, Norway

50 ³University of Aberdeen, Aberdeen, UK

51 ⁴British Geological Survey, Lyell Centre, Research Avenue South, Edinburgh, UK

52 ⁵Arup, Edinburgh, UK

53 ⁶bp, ICBT, Chertsey Rd, Sunbury-on-Thames, UK

54 ⁷RWE Renewables, Swindon, UK

55 ⁸iC3 – Centre for ice, Cryosphere, Carbon and Climate, Department of Geosciences, UiT the Arctic
56 University of Norway, 9037 Tromsø, Norway

57 ⁹Kelpie Geoscience Limited, Murchison House, 10 Max Born Crescent, Edinburgh, UK

58 ¹⁰Department of Earth Science, University of Bergen, Bergen, Norway

59 ¹¹Equinor ASA, NO-7005 Trondheim, Norway

60 ¹²Department of Geoscience, Aarhus University, Høegh-Guldbergs Gade 2, 8000 Aarhus C, Denmark

61 ¹³ATLAS MARIDAN ApS Germany, Heerenholz 17, Bremen, Germany

62 ¹⁴SSE Renewables, Glasgow, UK

63 ¹⁵AtkinsRéalis, Glasgow, UK

64 ¹⁶Queen's University Belfast, Belfast, UK

65 ¹⁷University of Manchester, Manchester, UK

66 ¹⁸University College Dublin, Dublin, Ireland

67 ¹⁹British Geological Survey, Kingsley Dunham Centre, Keyworth, Nottingham, UK

68 ²⁰NGI, Perth, Australia

69 **Abstract**

70 The glaciated European continental margins (spanning 49-82°N and 16°W-36°E) are home to a thriving
71 offshore energy sector and densely inhabited coastal areas. These regions face numerous marine
72 geohazards and geo-engineering challenges due to complex subsurface conditions shaped by large-scale
73 geological and climate processes. The geological complexity of this area is among the highest globally,
74 featuring dynamic processes such as distinct ice-sheet oscillations and sea-level changes, which have
75 led to rapidly evolving paleo-geographic and depositional environments. Consequently, the soil
76 conditions are highly variable and heterogeneous, both vertically and laterally, requiring meticulous
77 evaluation for engineering projects, such as offshore wind developments.

78 This study reviews the marine geohazards and geo-engineering constraints along the glaciated European
79 margins, with a particular focus on the Quaternary period, during which the most significant
80 environmental changes occurred. We examine the implications of shallow subsurface deposits and
81 fluids on engineering foundations and hazards for offshore activities, including offshore wind energy,
82 carbon storage, hydrocarbon exploration, marine infrastructure, and marine ecosystems. Additionally,
83 we assess the risks of tsunamis and earthquakes related to the Quaternary evolution of the Northern
84 European margin. This array of hazards presents substantial risks and challenges to both coastal
85 communities and offshore industries.

86

87 **Keywords:** *Geohazards; Geo-engineering; Quaternary geology; Data integration; Glacial and marine*
88 *sediments; Shallow gas; Gas hydrates; Fluid flow; Strength variability; Boulder; Gravel; Weathered*
89 *bedrock; Peat; Glaciotectonic deformation; Glacigenic landforms; Ocean currents; Slope instabilities;*
90 *Glacio-isostatic adjustment; Seismicity; Tsunami*

91

92 **1. Introduction**

93 The Quaternary is the current and most recent period of Earth's geological history, spanning from 2.58
94 million years ago to the present day (Walker and Geissman, 2022). It is divided into two epochs: the
95 Pleistocene (2.58 million to 11.7 thousand years ago) and the Holocene (11.7 thousand years ago to
96 present; Walker and Geissman, 2022). The Pleistocene is characterized by repeated cycles of glaciation,
97 with ice sheets periodically advancing and retreating across much of North America, Europe, and Asia,
98 leaving a distinct imprint on the geomorphology, lithology, and stress history in the sedimentary
99 sequences (Svendsen et al., 2004; Batchelor et al., 2019; Newton et al., 2024a).

100 The Quaternary deposits along the glaciated European margins and the crustal response related to the
101 spatio-temporal loading and unloading of these deposits by large-scale Pleistocene ice sheets have
102 resulted in a variety of marine geohazards and geo-engineering constraints (Eyles, 2013). Broadly
103 speaking, geohazards have the potential to cause damage to health, environment, marine developments,
104 offshore infrastructure, and/or loss of life both in coastal communities and on offshore assets. Geo-
105 engineering constraints can have wide-ranging negative impacts on the development of offshore
106 projects, ranging from increased costs and timelines to making a project uneconomical or technically
107 infeasible (Bienen et al., 2015; Watts et al., 2021).

108 There are multiple definitions and interpretations of what constitutes a marine geohazard, especially in
109 the context of geo-engineering and geo-risk management activities (Table 1.1; e.g., Vanneste et al.,
110 2014; Giles, 2020a; IAEG, 2022; OSIG, 2022; Dimmock et al., 2023). In marine geoscience, a
111 geohazard is often regarded as an event that can occur naturally or can be triggered anthropogenically
112 (induced geohazard), with consequences for coastal communities. On the other hand, for offshore
113 industries, a marine geohazard includes any unforeseen natural geological conditions that have any
114 adverse effects on human life, operations (project timeline, budget, and safety), infrastructure, or
115 environment (ISO 19901-10; SUT, 2022). The definition formulated by Vanneste et al. (2014) states
116 that a marine geohazard is "a geological condition which represents – or has the potential to develop
117 further into – a situation leading to damage or uncontrolled risk". The definition of hazard (and
118 geohazard in this instance) can also be adapted from the occupational health and safety (OHS) approach.
119 For example, according to Standards Australia/Standards New Zealand a (geo)hazard is "a source or a
120 situation with a potential for harm in terms of human injury or ill-health, damage to property, damage
121 to the environment, or a combination of these" (Standards Australia, 2001). Another approach uses the
122 idea of energy release to define (geo)hazards. In this context, (geo)hazards are 'sources of potentially
123 damaging energy which either exist naturally or as a result of humankind's modification of the naturally
124 occurring world ... where damage (injury) is the result of an incident energy whose intensity at the point
125 of contact with the recipient exceeds the damage threshold of the recipient (Viner, 1991)'.

126 Dimmock et al. (2023) separates geohazards from geo-engineering constraints: Geohazards are defined
 127 as dynamic geo-events/processes that are a risk to the development and are addressed by project
 128 management frameworks whereas geo-engineering constraints are defined as existing, static ground
 129 features that pose an engineering challenge to the development and that are addressed by routine geo-
 130 engineering solutions.

131 **Table 1.1.** Selected definitions of geohazards.

| Organization | Geohazard Definition |
|---|--|
| British Geological Survey | Geohazards, such as volcanoes, earthquakes and landslides, are the natural geological processes that present a direct risk to people or an indirect risk by impacting development. |
| Dimmock et al. (2023) | It is proposed to restrict the term ‘geohazard’ to dynamic processes that impact the development. Another term ‘geo-engineering constraint’ is proposed to cover pre-existing features, static in nature, that require engineering consideration. |
| European Marine Board | A geohazard (or geological hazard) is a geological condition which represents - or has the potential to develop into - a situation leading to damage or uncontrolled risk. |
| Giles (2020a) | A geological hazard (geohazard) is the consequence of an adverse combination of geological processes and ground conditions, sometimes precipitated by anthropogenic activity. The term implies that the event is unexpected and likely to cause significant loss or harm. |
| International Association for Engineering Geology and the Environment (2022) | Geological and geomorphological processes or phenomena that can adversely impact a project. |
| International Ocean Discovery Program | Natural geological processes and phenomena, such as earthquakes, tsunamis, landslides, and volcanic eruptions, that pose significant risks to human life, infrastructure, and the environment. |
| ISO 19901-10 | A geological condition that has the potential to have adverse effects on persons, operations, infrastructure, or the environment. |
| National Oceanography Centre (Southampton) | Marine Geohazards are a range of underwater phenomena all of which can either directly or indirectly represent a threat to humans and the environment. These include underwater landslides, volcanic eruptions, turbidity currents and tsunamis. |
| Natural Resources Canada | Marine geohazards are geological conditions at the sea floor or within sub-bottom sediments that, if unrecognized, could result in dangerous or catastrophic events with attendant risks to life and/or infrastructure. Examples of such hazards include earthquakes and submarine landslides that can trigger tsunamis, iceberg scouring of the seabed, and gas migration or build-up that can lead to locally overpressurized sediments and potential terrain instability and/or blowouts. |
| Offshore Site Investigation and Geotechnics (2022) | A geological state, feature, or process that presents a risk to humans, property, or the environment. |
| United States Geological Survey | Marine geohazards, or ‘dangers in the deep’ include earthquakes, volcanic eruptions, submarine landslides, and tsunamis, as well as dissociation of gas hydrates—which can cause seafloor collapse—and oil spills or toxic seeps that affect deep sea life or change the physical characteristics of ocean environments. |
| Vanneste et al. (2014) | Geohazards are defined as a geological condition which represents – or has the potential to develop further into – a situation leading to damage or uncontrolled risk. |
| Viner (1991) | Geohazards are sources of potentially damaging energy which either exist naturally or as a result of humankind’s modification of the naturally occurring world ... where damage (injury) is the result of an incident energy whose intensity at the point of contact with the recipient exceeds the damage threshold of the recipient |

132

133 Risk is defined as the combination of likelihood (or frequency of occurrence) and the severity of
134 consequence of a process or constraint (i.e., hazard) impacting infrastructure and development. The
135 consequences of geohazards can be divided into the ones i) affecting life, health, and environment, ii)
136 causing material losses, and iii) disturbing global economy. For offshore industries and coastal
137 communities, the marine geohazard identification is the first step of risk assessment.

138 Induced (or operational) geohazards are manifested on a small, subregional to borehole scale. Often
139 associated with drilling and emplacement of subsea infrastructure on the seafloor, they are the main
140 focus of scientific drilling, energy-industry drilling, and offshore development activities (Shipp, 2017).
141 Prominent induced offshore geohazards along the glaciated European margins cover blowouts, loss of
142 well control, and loss of well stability. One of the best documented, and most tragic, induced geohazards
143 in our study area is the shallow gas blow-out at the West Vanguard platform on the mid-Norwegian
144 margin (Table 1.2; Figures 1.1c and 1.2). Although shallow gas is recognised as a potential geohazard,
145 and pre-drilling site surveys are mandatory, accidents can still occur such as the UK22/4b platform
146 blowout in 1990 (Table 1.2; Figure 1.1d).

147 Naturally occurring geohazards, often manifested on a larger regional scale, are historically more
148 frequently threatening larger areas than induced ones and preferentially affecting coastal communities.
149 A good example is the wave run-up and inundation associated with a rock-avalanche-triggered tsunami,
150 such as the Taffjord event in 1934 (Table 1.2; Figure 1.1a). The tsunami related to the Storegga landslide
151 around 8100 years ago might have impacted settlements located on the formerly terrestrially exposed
152 Doggerland (Hill et al., 2014) and classical coastlines (Walker et al., 2020). Several tsunamis also
153 occurred in lakes located on the glaciated European margins (e.g., Loen rock avalanche and tsunami in
154 1905 and 1936 with 61 and 74 fatalities; Grimstad and Nesdal, 1990; Waldmann et al., 2021), but these
155 events are not part of this paper. Slope instabilities along the coastlines, and in fjord systems, often
156 result in road closures (Figure 1.1b; NVE 2021; Lacasse et al., 2022), or, in worst case, in injury or loss
157 of life.

158 **Table 1.2.** Selected offshore accidents and natural disasters on the glaciated European margins related
159 to geohazards and engineering challenges since 1900 AD. Listed are only published and known events
160 in the marine realm, and thus the table is under-representative for the incidents that occurred along the
161 margin.

162

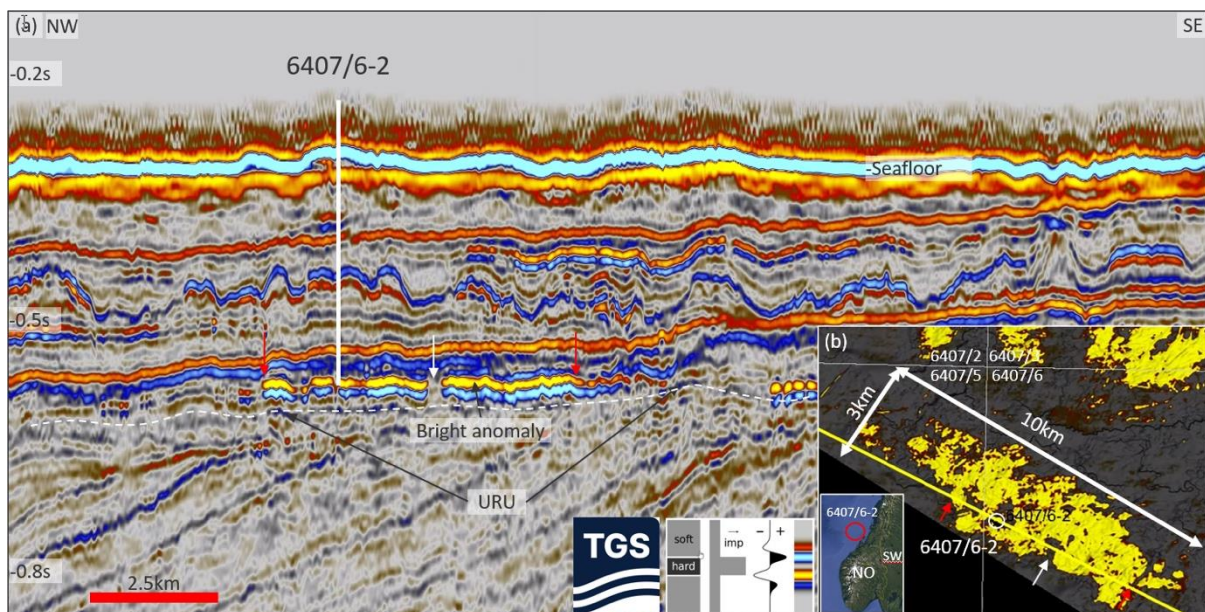
| Event | Area | Consequences | Cause | Reference |
|--|-------------------------|---------------------------|--|--|
| Tafjord tsunami, 1934 | Western Norwegian fjord | 40 fatalities | Tsunami triggered by rock avalanche | Harbitz et al., 1993; Braathen et al. 2004 |
| West Vanguard, 1985 | Mid-Norwegian margin | 1 fatality | Shallow gas blow-out | Vinnem and Røed, 2020 |
| High Seas Driller platform UK22/4b-4, 1990 | North Sea | 0 fatalities | Shallow gas blow-out | Leifer and Judd, 2015 |
| Horns Rev III OWF, Wind Turbine Foundation, 2019 | North Sea | 0 fatalities | Liquefaction, likely due to jack-up operations and low strength subsurface | Vattenfall, 2019 |
| Kråkneset quick clay landslide, Alta, 2020 | Northern Norway | 0 fatalities; road closed | Low initial slope stability and placement of fill, eventually triggered by unfavourable ground water pressure from snow melt | NVE, 2021; Lacasse et al., 2022 |



166 **Figure 1.1.** Historic accidents along the glaciated European margins. **a)** Tafjord rock avalanche and
 167 tsunami in 1934. Photo by Alfred Skar, Arbeiderbevegelsens arkiv og bibliotek. **b)** Quick clay landslide
 168 at Kråkneset in Alta in 2020. Photo by Anders Bjordal/NVE. **c)** Shallow gas blowout at West Vanguard
 169 platform in 1985. Photo by Øyvind Hagen/Equinor. **d)** MODU High Seas Driller – UK22-4b-4 Blowout
 170 – North Sea. Photo from <https://the-norwegian.com/north-sea-blowouts-and-fires-1964-2020/>.

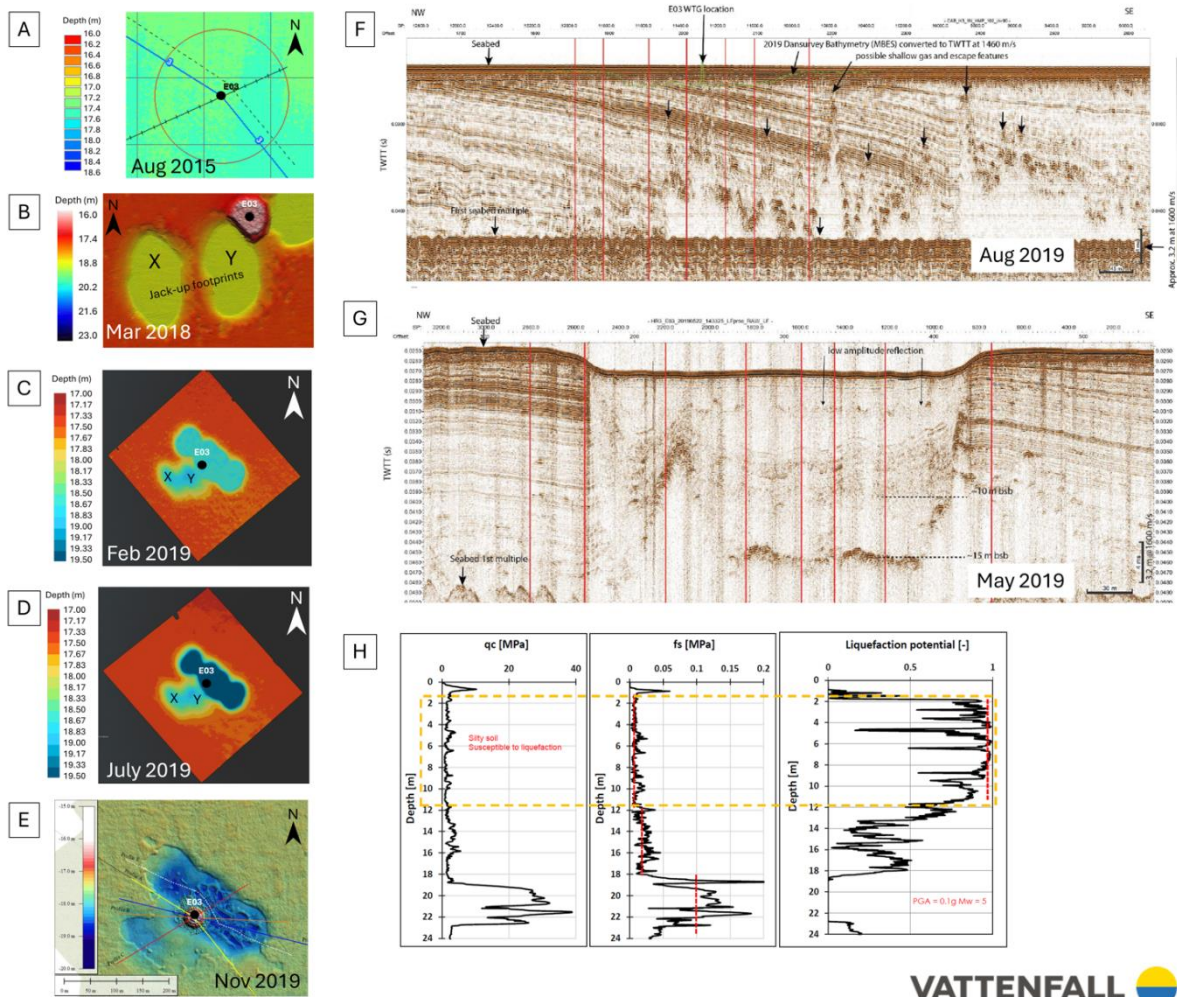
171 Glaciated margins are burdened with a complex set of geological conditions linked to of ice-sheet
 172 dynamic and resulting in a spatially and temporally heterogeneous glacial and interglacial sedimentary
 173 package further affected by sea-level oscillations, and glacio-isostatic rebound. These complex
 174 Quaternary conditions are encountered in the shallow subsurface directly at and under the seabed in a
 175 zone critical for engineering where all offshore infrastructure (e.g. offshore windfarms, pipelines, cables
 176 and O&G platforms) has been placed since the mid-20th century (Figures 1.2, 1.3, and 2.1). A variety
 177 of industries (offshore wind, carbon capture and storage, oil and gas, shipping traffic, fishing activities;
 178 Figure 1.4) compete for acreage within these areas (e.g., de Jonge-Anderson and Underhill, 2022; Paolo
 179 et al., 2024), which are also unique habitats for a variety of birds, fish and for marine mammals (e.g.,
 180 Virtanen et al., 2022; Danish Maritime Authority, 2023). The challenge for decision makers and
 181 authorities is to manage the multiple conflicts of interests and seek synergies and opportunities between
 182 the various industries, public safety, and the natural environment (Virtanen et al., 2022).

183 The aim of this paper is to review and systematise marine geohazards and geo-engineering constraints
 184 present on the formerly glaciated European margins. The study area includes the Barents Sea, the mid-
 185 Norwegian margin, the North Sea, the areas West of Shetland and the Outer Hebrides, the Baltic Sea
 186 including the Gulf of Bothnia, the Irish Sea, the Celtic Sea, and the Rockall Trough (Figure 2.1). We
 187 also discuss the impact of ice sheet loading on the regional tectonic stress history, and the effect it
 188 exerted on the mechanical properties of sediments and rocks. We summarize lithologies and landforms
 189 of the study area, as these give valuable insights into the extent and progressive decay of ice sheets, the
 190 existing fluid flow, and structural properties of the subsurface. Finally, we describe in depth geo-
 191 engineering constrains and geohazards specific to the study area and glacial and post glacial processes.
 192 We also discuss the implications of each hazard and constrain for offshore engineering undertakings.



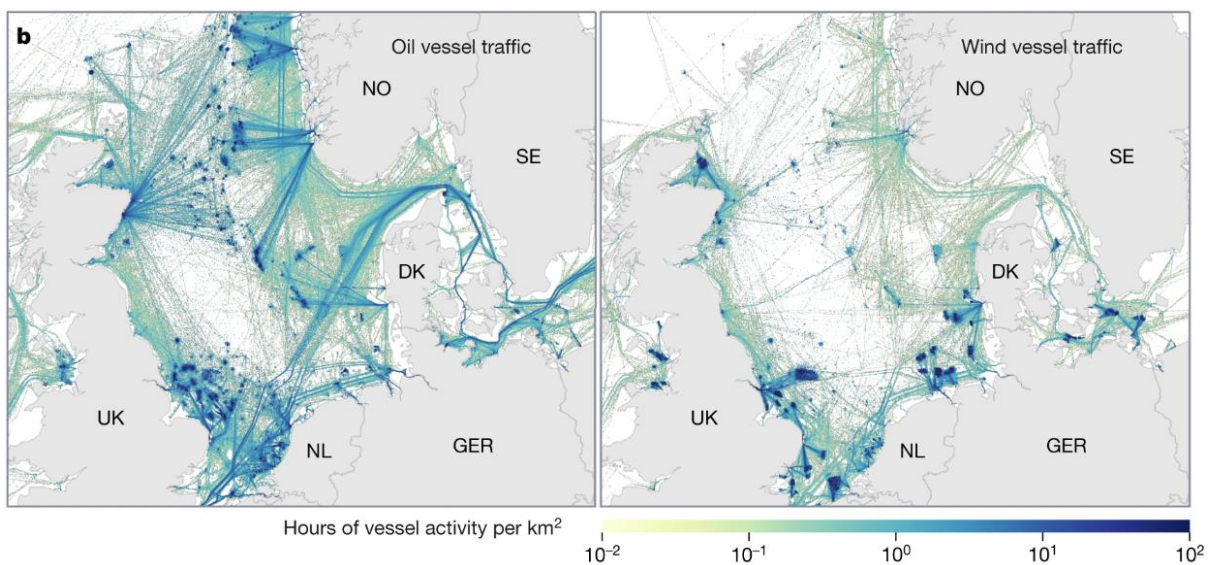
193

194 **Figure 1.2.** Location of the West Vanguard gas blow-out in well 6407/6-2 on Haltenbanken, mid-
 195 Norwegian shelf. **a)** Seismic profile across the West Vanguard gas field. The position of the well
 196 6407/6-2 is shown on a new seismic section (inline 24016 of the 3D: PGS 18M01). A bright anomaly
 197 is present immediately above the Upper Regional Unconformity (URU). **b)** Extent of the minimum
 198 amplitude anomaly extracted from the 3D seismic data (shown in yellow), covering an area of
 199 approximately 19 km² (3 km x 10 km). This bright low impedance anomaly is interpreted as a gas
 200 charged sand. The red and white arrows show the same position on seismic profile and map view. Data
 201 courtesy of TGS.



202
 203 **Figure 1.3.** Time series illustrations of multibeam echosounder data (MBES) (**a-e**), sub-bottom profiles
 204 (**f-g**) and CPT (**h**) before and after the liquefaction event at the E03 wind turbine foundation site in the
 205 Horns Rev III offshore wind farm, Danish North Sea. The site comprised a thick post-glacial silt unit
 206 with low strength and high liquefaction potential (**h**). The causes for the liquefaction remain uncertain
 207 but likely relate to multiple jack-up operations at the site, that involved jetting and soil displacement.
 208 Further triggers may relate to repeated storm events during spring 2019 and shallow gas in the silt
 209 (Vattenfall, 2019). **a)** MBES data from August 2015 prior to installation of scour protection. **b)** MBES
 210 data from March 2018 showing deep (1.4 m) jack-up footprints (X and Y) and damage to scour

211 protection. **c)** MBES data from February 2019 showing enlarged depressions around the E03 site. **d)**
 212 MBES data from July 2019 showing deepened depressions around the E03 site. Seabed lowering was
 213 reported to an approximate rate of 0.2-0.5 cm/day (~6-15 cm/month). **e)** MBES data from November
 214 2019 after remediation (initiated in August 2019) and reconstruction of scour protection. **f)** Sub-bottom
 215 profile from August 2015 across the E03 site showing a flat seafloor, gently dipping reflections within
 216 the post-glacial silt layer and shallow gas 3-9 m below the seabed. **g)** Sub-bottom profile from May
 217 2019 across the E03 site showing the ca. 2.5 m deep seafloor depression and the altered acoustic signal
 218 within the post-glacial silt unit down to a level of ca. 15 m below the seabed. **h)** D-CPT at site E03 from
 219 2015, showing a high calculated liquefaction potential within the uppermost ~11 m of the post-glacial
 220 silt unit. Data and figures provided by Vattenfall (Vattenfall, 2019).



221
 222 **Figure 1.4.** Examples of competing interests in the North Sea. Global Fishing Watch uses AI and
 223 satellite imagery to map vessel traffic and offshore infrastructure to provide an unprecedented view of
 224 previously unmapped industrial use of the ocean, as seen here in the North Sea). Figure from Paolo et
 225 al. (2024).

226 **2. Regional setting, glacial history, and paleogeography**

227 The intensification of the global glacial-interglacial cycle at the onset of the Quaternary (~2.58 Ma) was
 228 a critical tipping-point in Earth's recent climate history (e.g., Raymo et al., 2006; Westerhold et al.,
 229 2020). The increased severity of cold intervals at the Plio-Pleistocene boundary triggered the
 230 development of large-scale continental ice sheets in the Northern Hemisphere (Sejrup et al., 2005;
 231 Batchelor et al., 2019). The European continental margins throughout the Pleistocene have experienced
 232 multiple episodes of glaciation as and when the Eurasian Ice Sheets (EIS) advanced and covered vast
 233 areas of land and seabed (Lee et al., 2012). These episodes of glaciations are separated by interglacial
 234 periods during which the ice sheet is melted completely or significantly reduced in size. As a result, the
 235 European offshore basins and continental margins preserve the most comprehensive sedimentary record

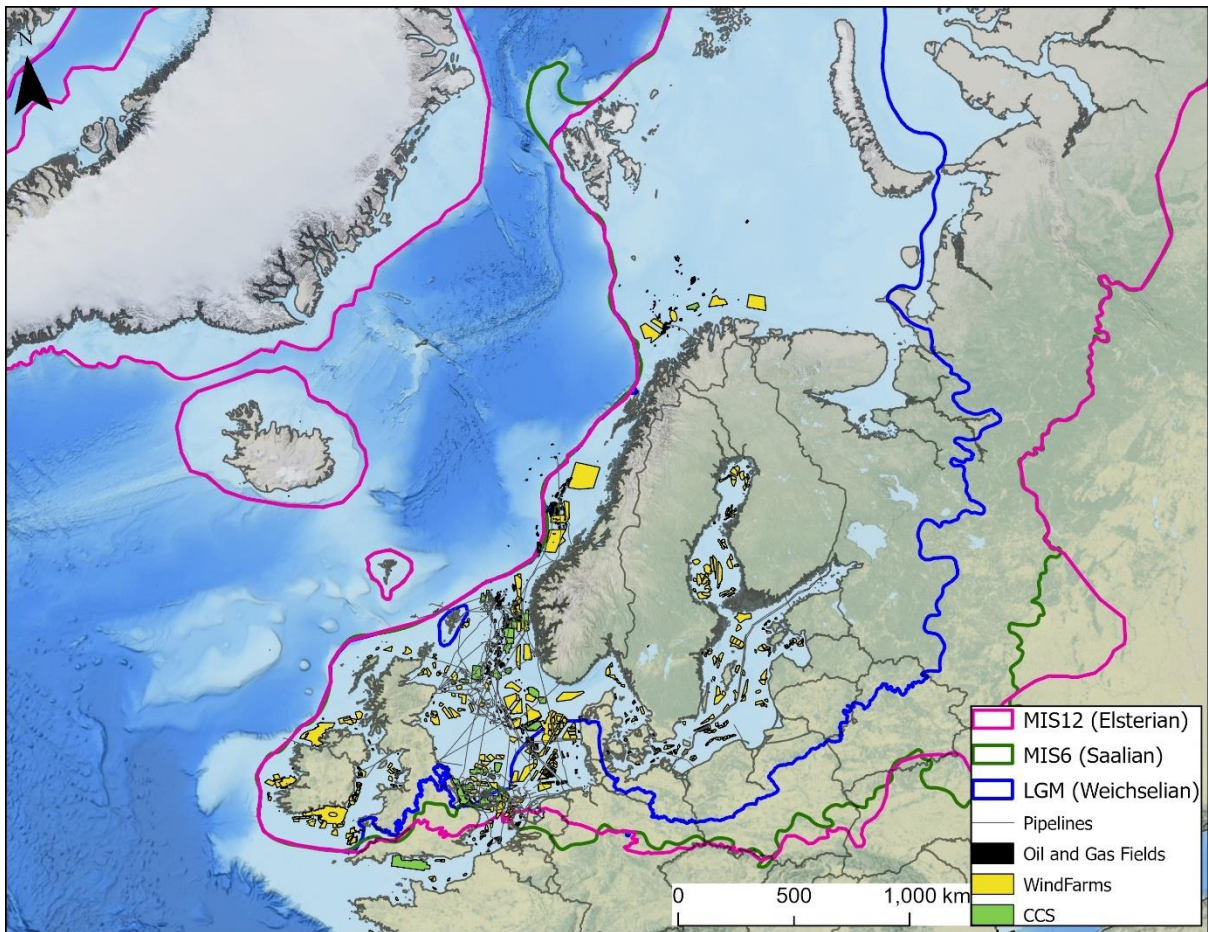
236 of the EIS and interglacial conditions, including the large river systems supplying sediments to those
237 basins (e.g., [Svendsen et al., 2004](#); [Sejrup et al., 2005](#); [Lee et al., 2012](#); [Hughes et al., 2016](#); [Batchelor
238 et al., 2019](#)). The EIS itself can be separated into the Kara-Svalbard–Barents Sea Ice Sheet (SBIS), the
239 Fennoscandian Ice Sheet (FIS), and the British–Irish Ice Sheet (BIIS; [Figure 2.1](#)) which nucleated and
240 evolved separately for large parts of their existence but also coalesced on multiple occasions forming a
241 continuous ice mass covering a large part of the continent and adjacent continental seas, but also
242 extended periodically all the way to the continental shelf break. These EIS ice domes were drained by
243 many, fast flowing ice streams which were time transgressive, and their flow was re-organized in
244 response to changes in ice sheet geometry.

245 The Quaternary glaciations strengthened further during the Mid-Pleistocene Transition (MPT ~1.3-0.7
246 Ma), with three major glaciations (Elsterian/Anglian, Saalian/Wolstonian, and Weichselian/Devensian)
247 recognised since 500 ka. These glaciations often left distinctive unconformities in the sedimentary
248 package, such as the Upper Regional Unconformity in the Barents Sea ([Bellwald et al., 2019c](#)). The
249 traditional view, whereby the Early Pleistocene is characterized by minor ice coverage with regional
250 shelf-edge glaciations, and the Middle- and Late Pleistocene glaciations were more extensive and
251 reached the shelf-edge, is being challenged by new landform and sedimentary records providing
252 evidence of widespread glaciations during the Early Pleistocene although there remain many questions
253 regarding Pleistocene glaciation both in Europe and globally (e.g., [Rea et al. 2018](#); [Newton et al., 2024a](#);
254 [Ottesen et al., 2024](#); [Lien et al., 2022](#); [Bellwald et al., 2024a](#), vs. [Sejrup et al., 2005](#); [Nygård et al.,
255 2005](#); [Knies et al., 2009](#)). Nevertheless, during the Pleistocene, glacial processes redistributed large
256 volumes of sediments from the hinterland across the continental shelves and onto the slopes, forming
257 prograding sequences and large trough mouth fans or filling offshore basins ([Vorren and Laberg, 1997](#);
258 [Lamb et al., 2017](#); [Rea et al., 2018](#); [Gales et al., 2019](#); [Hjelstuen et al., 2021](#)).

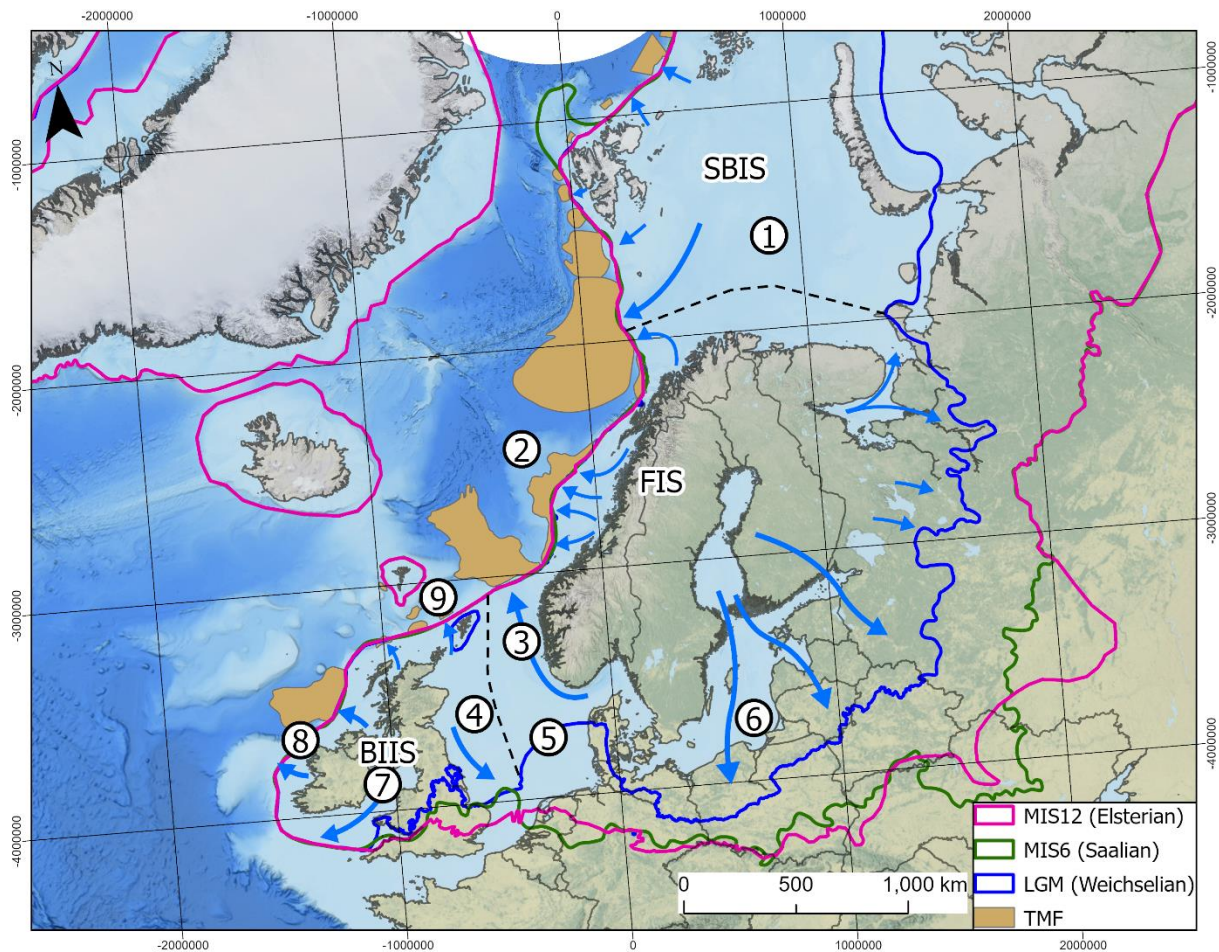
259 This complex mosaic of glacial and interglacial sediments recording multiple episodes of deposition,
260 incision, reworking and erosion is now occupied by numerous industries with competing interests and
261 is posed to play a key role in the process of energy transition. ([Figure 1.4](#)). The offshore areas, in
262 particular the shallower waters of the shelves with an active hydrocarbon exploration, have been the
263 focus of a large coverage of geophysical, geological, and geotechnical datasets. Industrial activity in
264 the harsher and more remote environments of the Arctic Barents Sea has so far been far lower than in
265 the North Sea.

266 There is ongoing work to better understand and correlate the onshore and offshore stratigraphical
267 schemes across the wider formerly glaciated European margins and link them to the deep-ocean oxygen
268 isotope record. However, correlation remains difficult and is largely inferred in areas where the units
269 lack good chronostratigraphic control ([Newton et al. 2024b](#)). Some direct links can be made in well-
270 dated sections of the offshore stratigraphy (e.g., [Rea et al., 2018](#)). Existing regional seismostratigraphic

271 frameworks (e.g., Faleide et al., 1996; Kuhlman and Wong, 2008; Rise et al., 2010; Stoker et al., 2011;
272 Rydningen et al., 2016; Ottesen et al. 2018; Løseth et al., 2022; Newton et al., 2024a) are presented
273 here to illustrate the Quaternary evolution of the glaciated European margins and are valuable for an
274 early assessment of the expected ground conditions but should be carefully evaluated against site-
275 specific datasets. Figure 2.1 illustrates the study area of this review and denotes specific regions that
276 are described in greater detail in terms of their Quaternary evolution and resulting region-specific
277 ground conditions.



278



279

280 **Figure 2.1.** The glaciated European margins. **a)** Offshore energy activities ongoing in the region. Shown
 281 are blocks for offshore wind and CCS, Oil and Gas discoveries, and pipelines. Ice-sheet extents from
 282 Batchelor et al. (2019). **b)** Study area showing the Weichselian, Saalian, and Elsterian ice sheet extents
 283 (after Batchelor et al., 2019), major drainage routes of the Eurasian Ice Sheet complex (as for Last
 284 Glacial Maximum), trough mouth fans (both after Patton et al., 2017; and references therein), and ice
 285 divides (Hughes et al., 2016). Numbers indicated different regions of the glaciated European margin:
 286 1: Barents Sea, 2: Mid-Norway, 3: Northern North Sea, 4: Central North Sea, 5: Southern North Sea, 6:
 287 Baltic Sea and Gulf of Bothnia, 7: Irish Sea and Celtic Sea, 8: Outer Hebrides and Rockall, 9: West of
 288 Shetland. BIIS: British-Irish Ice Sheet, FIS: Fennoscandian Ice Sheet; SBSIS: Svalbard-Barents Sea
 289 Ice Sheet (also named Kara-Barents Sea-Svalbard Ice Sheet).

290 2.1 Quaternary evolution

291 2.1.1 Barents Sea

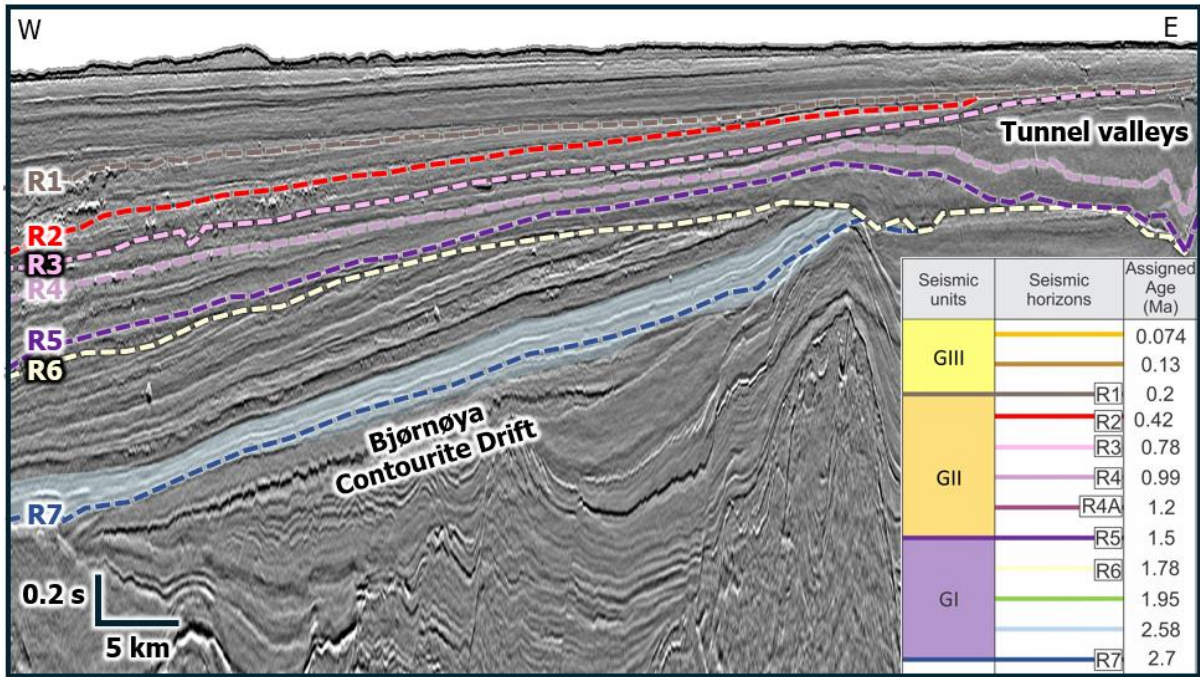
292 The Barents Sea (Figure 2.1) is a shallow epicontinental sea with an average water depth of 230 m and
 293 a maximum water depth of 500 m, and it is one of the widest continental shelves on Earth. In the
 294 Pliocene to Early Pleistocene, the Barents Sea was an exposed land area (Dimakis et al., 1998; Butt et
 295 al., 2000). The area experienced erosion depths that varied regionally from 10 to >1000 m, caused by
 296 repeated glaciations throughout the Pleistocene (Fjeldskaar and Amantov, 2018, Faleide et al., 1996).

297 Field data constrained ice-sheet models suggesting that sub-glacial erosion can account for up to ca.
298 200 m of bedrock excavation, accumulated through the last glacial cycle (for the last ca. 100 kyr; [Patton](#)
299 [et al., 2022](#)). These erosive episodes resulted in a glacial unconformity (Upper Regional Unconformity),
300 that divides Quaternary sediments (mainly subglacial till) from the underlying pre-Quaternary
301 sedimentary bedrock. Deep troughs such as Bjørnøyrenna formed during ice-streaming phases, and
302 some of the Earth's largest trough mouth fans are depocenters of these processes ([Figure 2.1](#); e.g., the
303 Bear Island Fan and Storfjorden Fan). The glacial processes shifted the shelf topography from a
304 terrestrial platform to the present shelf geometry ([Løseth, 2023](#)). The Quaternary sediments are 0 to 70
305 m in thickness on the shelf but can reach thicknesses of up to 4 kilometres on the slopes ([Figure 2.2](#);
306 [see also Figure 6.4](#); [Faleide et al., 1996](#); [Hjelstuen and Sejrup, 2021](#); [Alexandropoulou et al., 2021](#);
307 [Lasabuda et al., 2023](#); [Bellwald et al., 2024a](#)). The Quaternary stratigraphy around the modern shelf
308 break is dominated by turbidites, slide debrites, and subglacial till, and the Bjørnøya Contourite Drift
309 at the base ([Figure 2.2](#); [Rydningen et al., 2020](#)).

310 During the Last Glacial Maximum, the SBSIS extended all the way to the continental shelf break in the
311 north and west and was coalescent with the FIS in the south ([Svendsen et al., 2004](#); [Hughes et al., 2016](#)).
312 The Quaternary deposits of the shelf are mainly of Late Weichselian age ([Mangerud et al., 1998](#); [Laberg](#)
313 [et al., 2010](#)). The thick sequences on the slopes, in contrast, record the Quaternary processes since the
314 onset of the Pleistocene ([Figure 2.2](#); [Vorren et al., 1998](#); [Laberg et al., 2010](#); [2012](#); [Alexandropoulou et](#)
315 [al., 2021](#); [Bellwald et al., 2024a](#)). The last major deglaciation started at c. 18–16.9 ka (ka: thousands of
316 years before present) in the SW Barents Sea ([Rüther et al., 2011](#)), with the SBIS and FIS separating by
317 c. 16 ka ([Sejrup et al., 2022](#)). A complex assemblage of glaciogenic landforms and sediments is
318 preserved at the seabed, including multiple paleo-ice stream troughs, ice-marginal ridges, grounding
319 zone wedges, meltwater channels, and iceberg ploughmarks (e.g., [Winsborrow et al., 2010](#); [Newton and](#)
320 [Huuse, 2017](#)). Less than 2 m of Holocene sediments cover most of the Barents Sea, covering some of
321 the glacial landforms ([Elverhøi and Solheim, 1983](#)).

322 The modelled glacio-isostatic response is around 800 m for the last one million years but varies strongly
323 across the Barents Sea ([Fjeldskaar and Amantov, 2018](#)). The glacial history of the Barents Sea combined
324 with complex tectonics (i.e., marked by cycles of isostatic rebound and subsidence, erosion and
325 sedimentation, fault reactivation, and fracturing) has contributed to a highly dynamic fluid flow regime
326 ([Kishankov et al., 2022](#)). Vast hydrocarbon prone basins have been contributing fluids to the shallow
327 subsurface, sustaining widespread gas accumulations, seafloor seepage, and gas hydrate formation. The
328 gas hydrate stability zone (GHSZ) thickness across the Barents Sea can be up to ~400 m in troughs and
329 basins, while at shallow water depths (200–300 m) the upper tens of meters of the sedimentary column
330 are prone to complete gas hydrate dissociation in response to bottom water temperature variations
331 ([Vadakkepuliymbatta et al., 2017](#)). On the uppermost continental slopes, thick contourite drifts host
332 widespread gas hydrates and associated free gas accumulations within the uppermost 200 m bsf (e.g.,

333 [Hustoft et al., 2009](#)). Salt tectonics and volcanic sill intrusions also had impact on fluids and gas hydrate
 334 dynamics and Quaternary deformation in the western Barents Sea region (e.g., [Chand et al., 2008](#); see
 335 also [Figures 5.32 and 5.38](#)). Overpressure-prone contourites and beds underlying glacial debris
 336 flows are often associated with slope failure and mass transport events along the continental slopes of
 337 the Barents Sea and the west Svalbard margins (e.g., [Bellwald and Planke, 2019](#)).



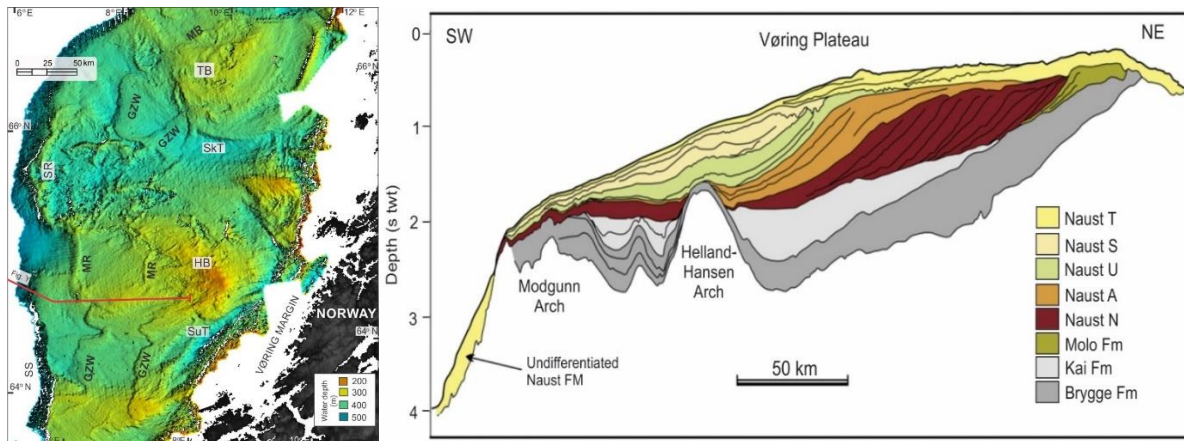
338
 339 **Figure 2.2.** Seismic stratigraphy of the SW Barents Sea margin. Chronostratigraphy from
 340 Alexandropoulou et al. (2021), and seismic profile modified after Bellwald et al. (2024a). Data courtesy
 341 of TGS.

342 2.1.2 Mid-Norway

343 The Mid-Norwegian margin ([Figures 2.1 and 2.3](#)) comprises three segments; the Møre, Vøring, and
 344 Lofoten-Vesterålen. The Møre margin is characterized by a narrow continental shelf, reaching
 345 approximately 40 km wide, and where the seabed of the upper continental slope is imprinted by the
 346 8200 ka BP Storegga Slide (e.g., [Haflidason et al., 2005](#)). A broad continental shelf region, where the
 347 present shelf edge is located about 200 km west of the Norwegian coast, characterizes the Vøring margin
 348 ([Figure 2.3](#)). The seabed in this region is dominated by prominent cross-shelf troughs, such as the
 349 Trænadjupet, Sklinnadjupet, and Suladjupet, that reach water depths of approximately 400 m, and
 350 shallow banks, such as the Haltenbanken and Trænabanken, characterized by water depths of around
 351 200 m ([Ottesen et al., 2005](#); [Rise et al., 2005](#)). The Lofoten-Vesterålen margin segment consists of an
 352 outer narrow part, the Lofoten and Vesterålen basements highs and the inner Vestfjorden and
 353 Andfjorden sedimentary basins. The continental slope is intersected by several canyons ([Figure 2.4](#);
 354 [Rise et al., 2013](#)).

355 Most of the Vestfjorden, Lofoten, and Vesterålen area (Figure 2.4) was a land area at the initiation of
356 the Pleistocene ice-age as recorded by the immediate pre-Quaternary Molo Formation interpreted as
357 a coastal shelf delta located west of Røst (Henriksen and Weimar 1996; Eidvin et al., 2007; Løseth et
358 al. 2017; Løseth 2021; 2023). Southward and northward-flowing ice streams in the Vestfjorden and
359 Andfjorden, respectively, eroded deep into the sediment succession and fed the prograding shelf in Mid
360 Norway and Troms regions (Figure 2.4) (Ottesen et al., 2005; Laberg et al., 2009). Westward-bound ice
361 flows from the Lofoten and Vesterålen basement highs reached the shelf edge where the associated
362 sediments mostly continued down the fifteen submarine canyons incised along the steeply dipping (5–
363 8°) continental slope, without building out a shelf edge (Figure 2.4; Rise et al., 2013). A mostly thin
364 layer of sediments from the last glaciation covers the URU, including thick recessional moraines in
365 Vestfjorden (Ottesen et al., 2005; Laberg et al., 2009). The strandflat in Lofoten and Vesterålen is
366 limited to the subcropping basement areas, is submerged in the south and, rises northwards to be
367 subaerially exposed. (Løseth, 2023).

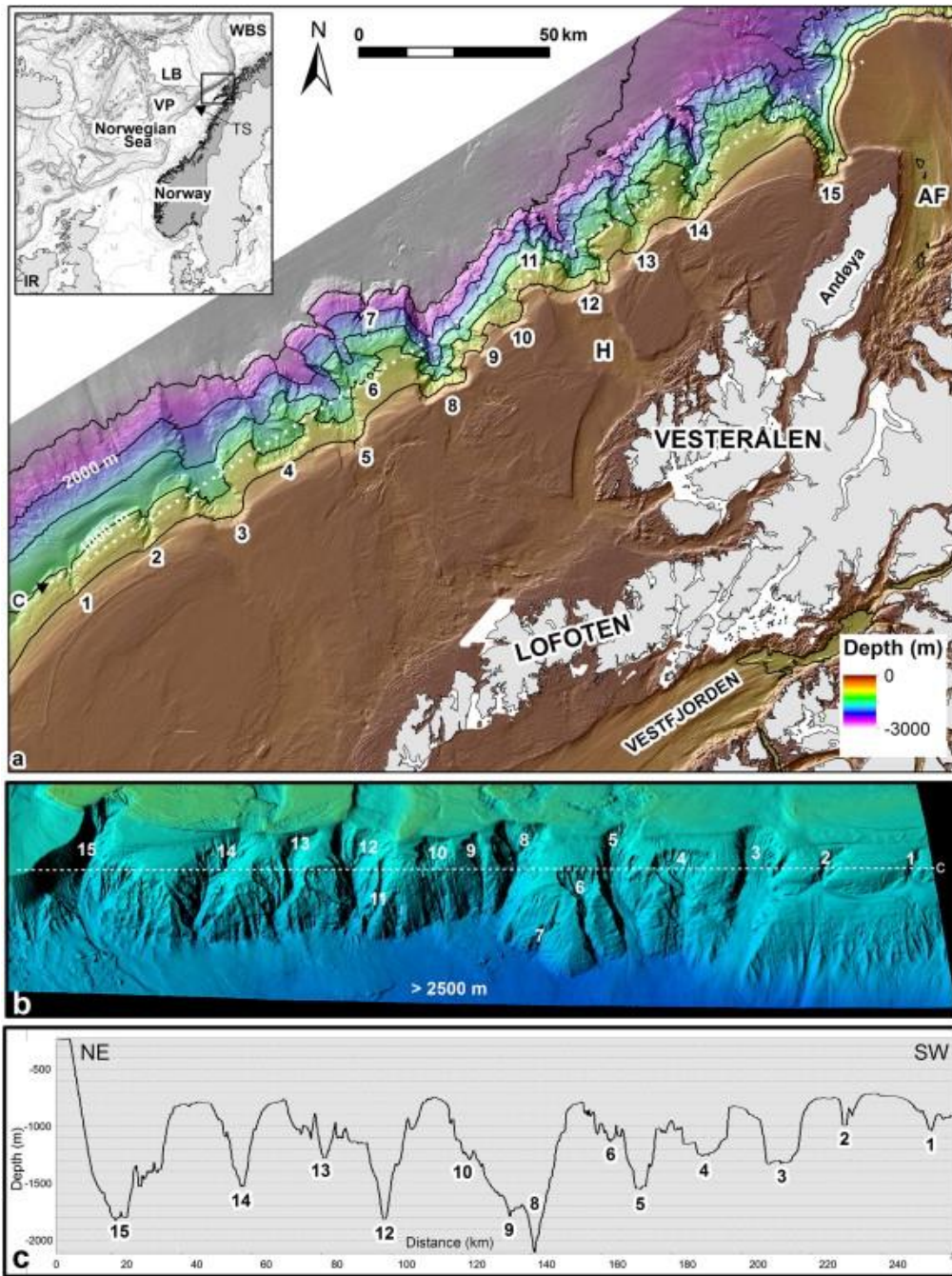
368 The present-day configuration of the Mid-Norwegian margin is intrinsically linked to the Quaternary
369 development of the region, when this margin was repetitively influenced by ice sheets that advanced to
370 the shelf edge (e.g., Sejrup et al., 2005; Montelli et al., 2017), causing huge quantities of sediments to
371 be transported to the continental shelves and slopes (e.g., Hjelstuen and Sejrup, 2021). During this
372 period, the prominent Naust Formation developed as a prograding wedge, up to 1200 m thick (Figure
373 2.3; Ottesen et al., 2009, Dowdeswell et al., 2010, Chand et al., 2011). The seabed of the Mid-
374 Norwegian continental shelf is dominated by a wide range of glacial landforms, including terminal
375 moraines and grounding zone wedges (e.g., Bachelor et al., 2023; Ottesen et al., 2022; Nygård et al.,
376 2004; Rydningen et al., 2015; Sejrup et al., 2022; Figure 2.3). The Mid-Norwegian margin was affected
377 by several sub-marine slide events during the Quaternary period (e.g., Solheim et al., 2005a) and
378 sediment remobilization related to ooze diapirism and overpressure release (e.g., Hjelstuen et al., 1997;
379 Riis et al., 2005; Bellwald et al., 2024b). Along the entire Mid-Norwegian margin, contourite deposits
380 are commonly identified (e.g., Laberg et al., 2016; Bellwald et al., 2022a), and such layers may
381 represent “weak layers” in the sediment stratigraphy that can behave similar to gas hydrates identified
382 on the southern Vøring Margin (Bünz and Mienert, 2004), representing a pre-conditioning factor of
383 sub-marine slides. Polygonal faults, frequently observed in pre-Quaternary sediments, penetrate locally
384 into the Quaternary sediment package and have been suggested to be important fluid flow pathways
385 with regards to pore-pressure build-up in the region (Solheim et al., 2005b) and so could also create
386 favourable pre-conditions of submarine landslides. Soft bright anomalies, interpreted as shallow gas,
387 are frequently observed in the Quaternary Naust Formation sediments (Figure 1.2).



388

389 **Figure 2.3.** Bathymetry and subsurface of the Vøring margin. **a)** Seabed imagery of the Vøring margin
 390 continental shelf, characterised by up to 400 m deep cross shelf troughs and shallow banks at a water
 391 depth of around 200 m. Terminal moraines (MR) and grounding zone wedges (GZW) are frequently
 392 identified. SkT: Sklinnadjupet Trough, SuT: Suladjupet Trough, TB: Træna Bank, HB: Halten Bank,
 393 SR: Skjold Ridge, SS: Storegga Slide. Figure modified from Nygård et al. (2004) and Hjelstuen and
 394 Sejrup (2023). **b)** Interpreted 2D multichannel seismic profile from the southern Vøring margin,
 395 showing the characteristics of the Quaternary prograding wedge, the Naust Formation, in this region.
 396 Figure modified from Rise et al. (2010).

397



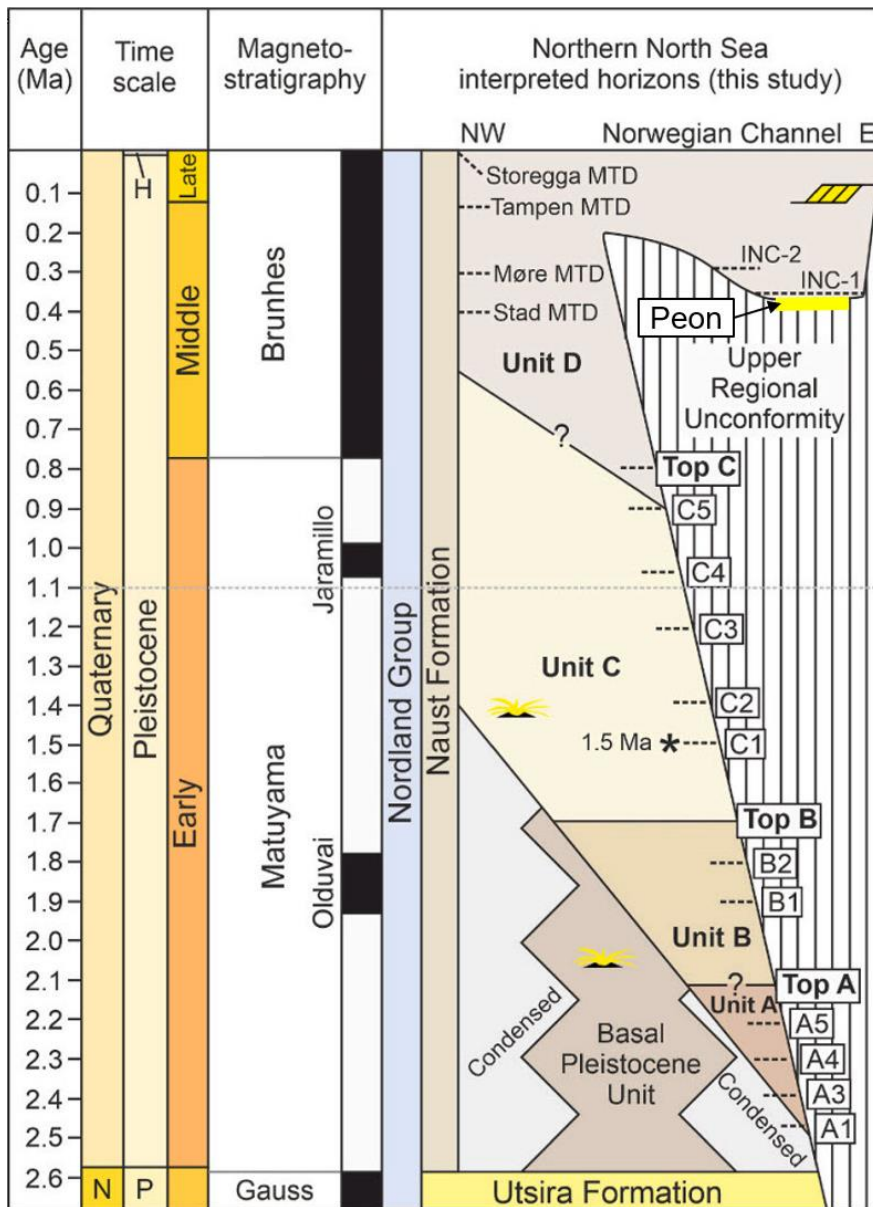
398

399 **Figure 2.4.** Canyons along the Lofoten-Vesterålen margin (from Rise et al., 2013). **a)** High-resolution
 400 bathymetric relief image of the Lofoten-Vesterålen margin. AF: Andfjorden; H: Hola cross-shelf
 401 trough; VP: Vøring Plateau; LB: Lofoten Basin; IR: Ireland; WBS: Western Barents Sea; TS: Headwall
 402 of Trænadjupet Slide. **b)** 3D view of canyons incised into the continental slope seen from the northwest.
 403 Canyons defined by Rise's criteria are annotated with numbers. Bleiksdjupet northwest of Andøya is
 404 canyon 15. **c)** Vertical profile along the slope. See a and b for location.

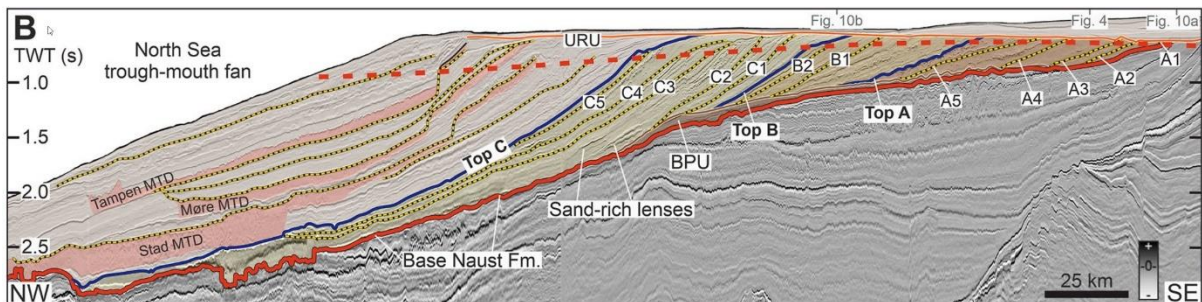
405 2.1.3 Northern North Sea

406 The Northern North Sea, from 60°N to 62°N, comprises of the western shallow sea area (<200 m deep)
 407 and the deep NNW-SSE striking Norwegian Channel with water depths up to 400 m. Regional 3D

408 broadband seismic data covering the entire northern North Sea reveal a detailed Pleistocene geological
409 history (Figure 2.5). It is suggested that the inception of the Pleistocene ice age came with locally
410 sourced ice entering the North Sea from the former Sognefjord valley, Western Norway (Løseth et al.
411 2020). Glacial shelf deposits built out on top of the Utsira East Formation in the N-S-elongated deep
412 marine North Sea Basin (Ottesen et al. 2018). The westward prograding shelf grew wider and their
413 buried shelf surfaces show evidence of glaciogenic debris flows (Løseth et al. 2020). At the same time,
414 an early Quaternary fluvial delta built out eastwards from the East Shetland Platform and the associated
415 deep marine deposits interfingered with the westward prograding glacial debris flows from Norway
416 (Løseth et al., 2022). At around 1.5 Ma, the deep marine strait filled up and the glacial shelves continued
417 to build NW-ward and SW-ward until the entire deep marine North Sea Basin was filled up northward
418 to 62°N at around 1.0 Ma (Ottesen et al. 2018; Løseth et al. 2022). The infill of the deep basin encouraged
419 the initiation of the northward flowing Norwegian Channel Ice Stream which delivered glacial
420 sediments to the North Sea TMF (King et al., 1996, Nygård et al. 2005; Løseth et al. 2022). The ice flow
421 in the Norwegian Channel eroded locally more than 500 m of sediments and the angular Upper Regional
422 Unconformity (URU) was formed (Sejrup et al. 1995; Ottesen et al., 2018; Baig et al. 2019; Løseth et
423 al., 2022). The delivery of large volumes of sediment in the North Sea TMF led to permanent isostatic
424 subsidence and tilting of the northern North Sea. This gave accommodation room for sediments to
425 deposit within the Norwegian Channel (Løseth et al. 2022). Strata above the URU have been tied from
426 the Norwegian Channel to the North Sea TMF (Løseth et al. 2022) and suggest that subglacial fluvial
427 sands, basal tills and marine clays were deposited within the Norwegian Channel during the last 0.35
428 Ma (Løseth et al. 2022), which is converse to previous studies (e.g., Sejrup et al., 1995). Some of these
429 sands, like the Peon glaciofluvial outwash fan (Ottesen et al., 2012; Mikalsen, 2015; Bellwald et al.,
430 2022b), were later charged with gas (Figure 2.6).

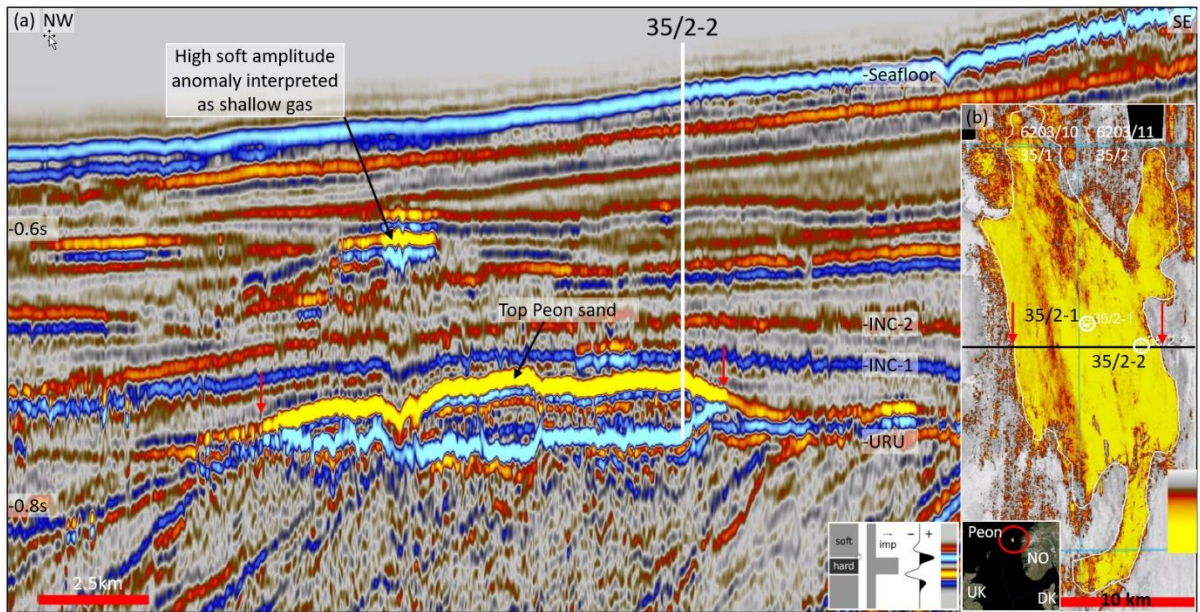


431



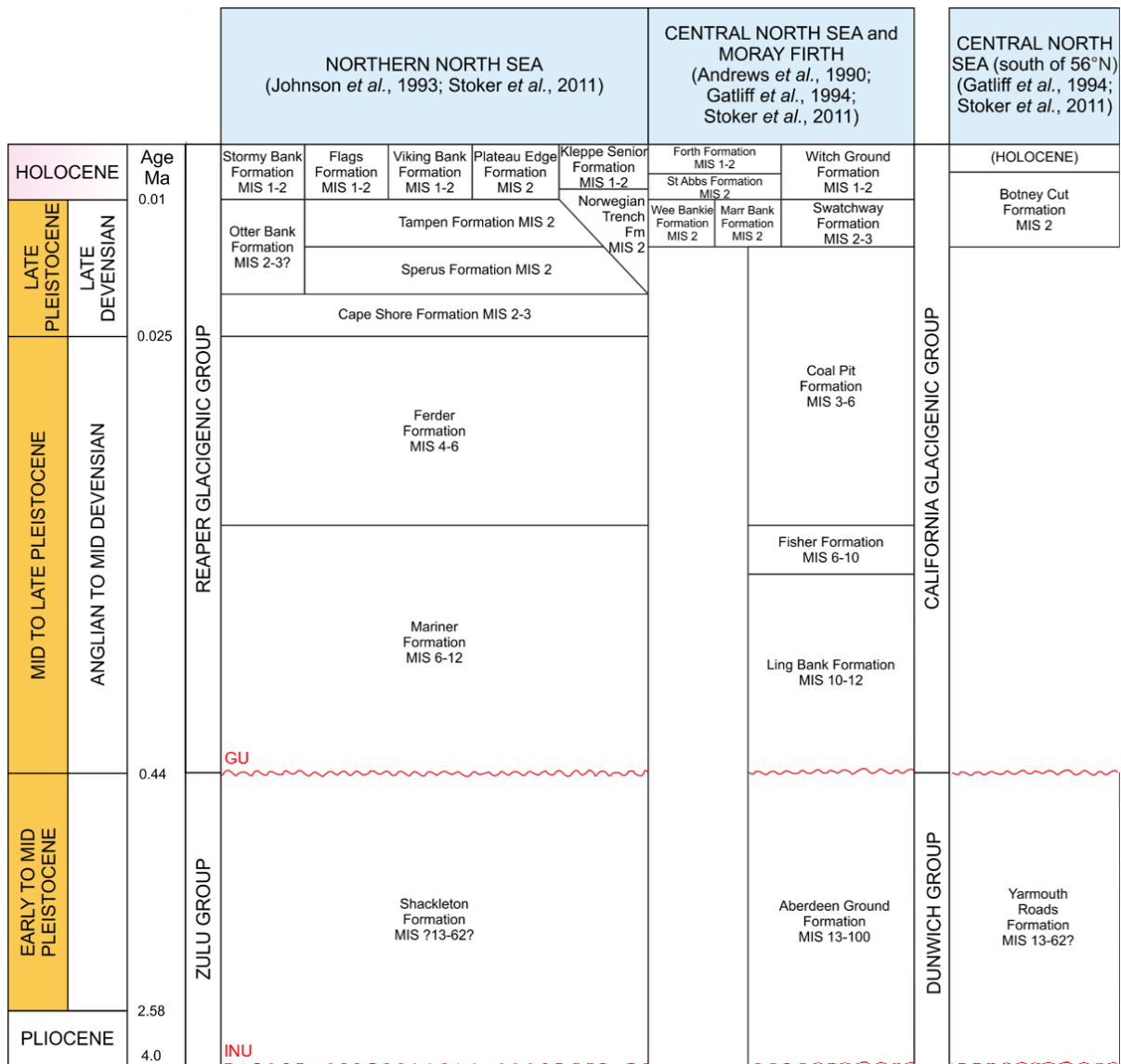
432

433 **Figure 2.5. a)** Stratigraphy of the Quaternary Naust Formation in the Northern North Sea from Løseth
 434 et al. (2022). The Upper Regional Unconformity was formed by fast ice sheet erosion that formed the
 435 Norwegian Channel from 0.8-0.35 Ma. **b)** A seismic section showing the Quaternary Naust Formation
 436 units in the Northern North Sea (Løseth et al. 2022).



437

438 **Figure 2.6.** Peon shallow gas discovery. Well 35/2-1 proved gas in the Quaternary Peon sand, located
 439 above the Upper Regional Unconformity (URU). **a)** Seismic section (inline 34410 of the CGG2018 3D)
 440 showing the gas filled sand as a high-amplitude, soft bright amplitude. **b)** Extent of the minimum
 441 amplitude anomaly at the top sand reflection extracted from 3D seismic data. The sand is covered by a
 442 till layer and a marine clay, which tops are termed Intra Norwegian Channel-1 (INC-1) (0.35 Ma) and
 443 Intra Norwegian Channel-2 (INC-2) (0.3Ma), respectively (Løseth et al. 2022). Red arrows show the
 444 extent of the gas anomaly on seismic and amplitude map. Data owner: Viridien.



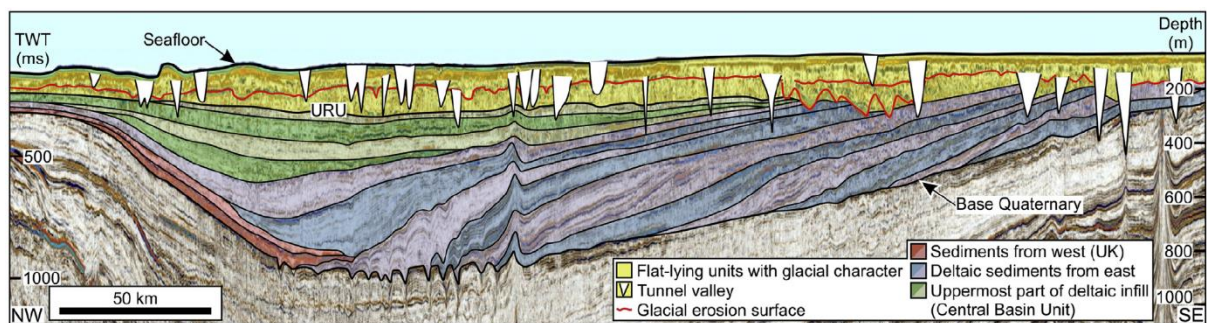
445
 446 **Figure 2.7.** Summary of the Quaternary stratigraphy in the Northern and Central North Sea. Note that
 447 recent studies in the region using 3D seismic datasets (e.g. [Ottesen et al., 2018](#); [Løseth et al., 2022](#))
 448 utilise an alternative regional stratigraphy ([Figure 2.5a](#)), correlated by [Newton et al. \(2024a\)](#). GU =
 449 Glacial Unconformity, INU = Intra-Neogene Unconformity.

450 2.1.4 Central North Sea

451 Since Neogene times, up to 2 km of sediment accumulated in the Central Graben, of which up to ~1.2
 452 km is of Quaternary age in the central and southern North Sea (see also [Figure 6.4](#); [Ottesen et al. 2014](#);
 453 [Lamb et al. 2018](#); [Newton et al., 2024a](#); [Figure 2.7](#)). Basin-scale 3D-seismic data show that at ~2.6 Ma
 454 the North Sea formed an elongate depression with a narrow marine connection to the north ([Lamb et al.](#)
 455 [2018](#)). North-westward progradation of shelf deltaic systems in the southern North Sea and glaciogenic-
 456 linked progradation in the central/northern North Sea gradually infilled the Early Pleistocene basin with
 457 sediments from glacial erosion and deposition sourced from both the FIS and the BIIS, and the Baltic
 458 and Rhine-Meuse river systems ([Lamb et al. 2017, 2018](#); [Ottesen et al. 2018](#); [Newton et al. 2024a](#)).

459 Plio-Pleistocene intensification of Northern Hemisphere glaciation strengthened further during the
460 MPT and is captured within the North Sea Basin (Newton et al. 2024a). While direct glacial evidence
461 is scarce (e.g., Graham et al. 2011), 3D-seismic data reveal extensive Early Pleistocene glacial
462 landforms on clinoforms (e.g., Knutz 2010; Arfai et al. 2018; Rea et al. 2018; Newton et al. 2024a). In
463 the North Sea Basin scant direct evidence of Early Pleistocene glaciations are found in glacial
464 sediments recovered from below the Brunhes–Matuyama palaeomagnetic reversal (~780 ka BP): within
465 borehole 81/27 (Stoker et al. 1983); a buried sub-glacial till within borehole 81/26 (Sejrup et al. 1987;
466 Ekman and Scourse 1993; Sejrup et al. 2000); and a glacial diamicton from commercial well 22/07a-5
467 and 22/07a-6Z (Rea et al. 2018; Rose et al. 2018). Early studies suggested the subglacial Fedje Till
468 sampled within the Norwegian Channel was deposited ~1.1 Ma based on micropaleontology, Sr-
469 isotopes, paleomagnetism and amino acid geochronology (Sejrup et al. 1995; 2000). However, Løseth
470 et al. (2022) present evidence using 3D seismic data to suggest that the Norwegian Channel Ice Stream
471 initiated ~0.8 Ma and that sediments preserved at the base of the Norwegian Channel, such as the Fedje
472 Till, were instead deposited much later, about to or prior to 0.35 Ma. 3D seismic datasets have revealed
473 the presence of iceberg ploughmarks and mega-scale glacial lineations imaged on Early Pleistocene
474 clinoform horizons (Kuhlmann et al. 2006; Buckley 2017; Dowdeswell and Ottesen 2013; Rea et al.
475 2018). From ~2.53 Ma (MIS 100), Rea et al. (2018) provide the first evidence of large icebergs within
476 the central and northern North Sea sourced from non-confluent FIS and BIIS ice sheets to the east and
477 west. These icebergs were likely locally sourced as palaeo-bathymetric evidence reveals the presence
478 of a bathymetric sill north of 60° N preventing entry of icebergs from the northeast Atlantic Ocean
479 (Lamb et al., 2017; Rea et al., 2018). These studies suggest extensive glaciation within the North Sea
480 ~1.4 Myr earlier than previously accepted (Sejrup et al., 1995, 2000; Rea et al., 2018) although the FIS
481 and BIIS only coalesced in the centre of the North Sea from ~1.87 Ma, as indicated by ice flow
482 landforms (Rea et al. 2018). Furthermore, Rea et al. (2018) postulate that both the FIS and BIIS ice
483 sheets were significantly more extensive during the early Quaternary than previously thought
484 (Dowdeswell and Ottesen 2013; Ottesen et al. 2014), which is a matter of controversy at present due to
485 ambiguity in landform interpretation (Batchelor et al. 2021). A more detailed discussion on the
486 inconsistency in ice sheet reconstructions is presented in Newton et al. (2024a) and Ottesen et al. (2024).

487 Recent studies, imaging tunnel valleys in 3D seismic data (e.g. Ottesen et al., 2018, 2020; Kirkham et
488 al., 2024), show unequivocal evidence of grounded ice-sheet glaciations prior to the LGM as tunnel
489 valleys are considered to form subglacially. By separating the extensive networks of cross-cutting
490 tunnel valleys into generations, these studies suggest that there have been seven (or more) extensive
491 glaciations prior to MIS 2 (e.g. Stewart and Lonergan, 2011; Ottesen et al., 2020), indicating repeated
492 advance and growth of Pleistocene ice sheets in northwest Europe since the Brunhes–Matuyama
493 reversal (Figure 2.8).



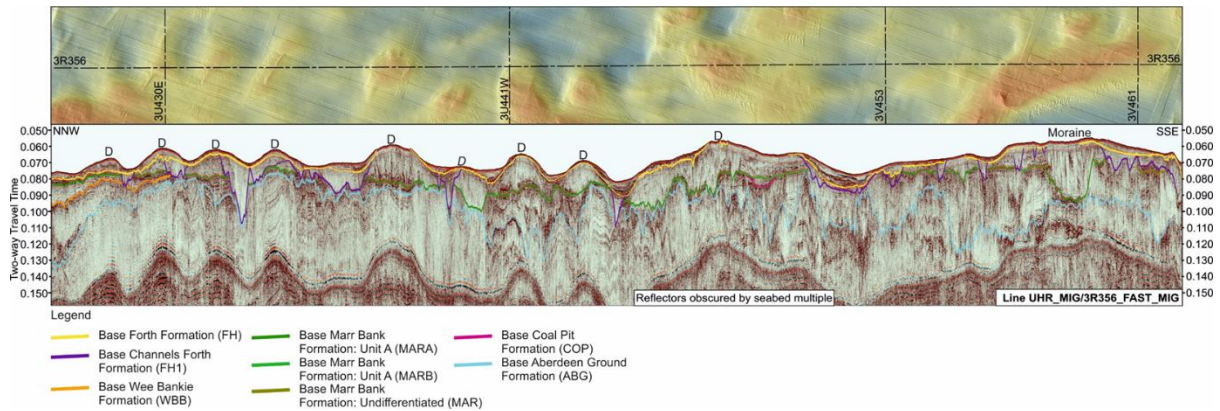
494

495 **Figure 2.8.** Regional 2D seismic line across the North Sea Basin (NW-SE) showing the distribution of
 496 tunnel valleys within the Quaternary stratigraphy, provided by TGS. Figure from Ottesen et al. (2020).
 497 URU: Upper Regional Unconformity. A velocity of 1800 m/s is used for depth conversion. See Figure
 498 2.10 for location.

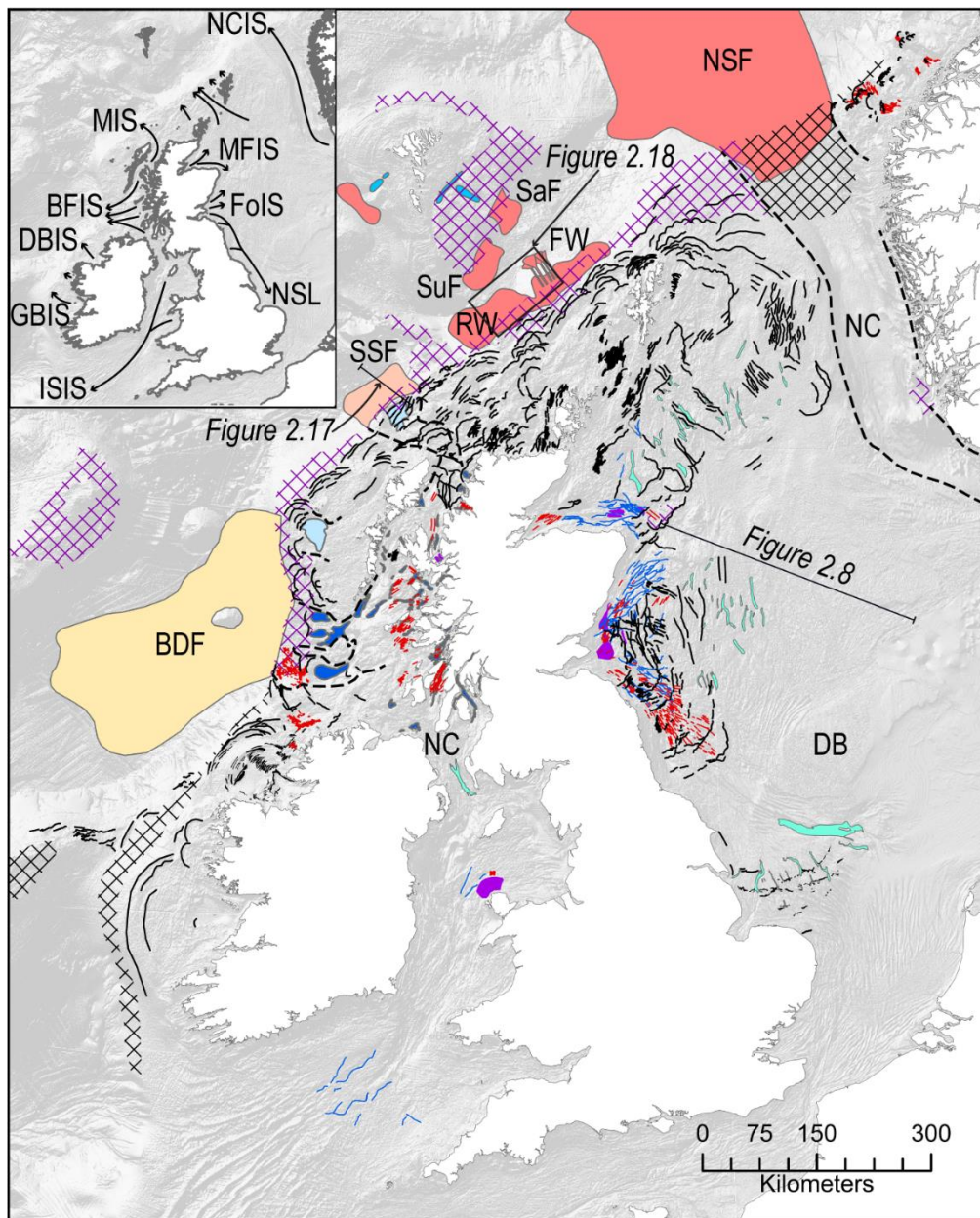
499 Numerous studies have presented and reviewed the evidence for ice-sheet glaciation of the North Sea
 500 Basin during the Late Pleistocene with good evidence for at least two phases of extensive ice-sheet
 501 development in the Early Weichselian (MIS 4; ~50–60 ka) and Late Weichselian (MIS 3/2) (e.g. Gatliff
 502 et al., 1994; Graham et al., 2011). High-resolution seismo-acoustic profiles, bathymetric elevation
 503 models and shallow marine cores have contributed to a relatively good understanding of the last glacial
 504 phase (MIS 2). During this time the BIIS expanded into the central and northern North Sea, extending
 505 to, or close to, the continental shelf edge from the Norwegian Channel to the NW of Ireland (e.g.
 506 Bradwell et al., 2008; Graham et al., 2009; Sejrup et al., 2016; Clark et al., 2017; Bradwell et al., 2019a;
 507 Roberts et al., 2019; Stewart et al., 2021, 2023; Evans et al., 2021). The last ice sheet reached its
 508 maximum extent ~30–24 ka, during or slightly after global Last Glacial Maximum (LGM; ~22–27 ka
 509 BP). Within the North Sea Basin the FIS and BIIS ice sheets coalesced on multiple occasions (Stoker
 510 and Bent, 1985; Cameron et al., 1987; Gatliff et al., 1994; Sejrup et al., 2000; Graham et al. 2011;
 511 Stoker et al., 2011; Sejrup et al., 2016; Newton et al., 2024a), with a number of scenarios presented for
 512 maximum extent of the LGM.

513 Much of the present-day topography of the seabed is directly related to the last glacial cycle (~32–11.5
 514 thousand years ago), which had a pronounced impact on the morphology and composition of the modern
 515 seabed. Mega-scale geomorphological features such as grounding zone wedges, channels, moraines,
 516 drumlins and deeply incised tunnel valleys formed beneath an ice sheet (e.g. the Devil’s Hole Deeps)
 517 (e.g. Bradwell et al. 2008; Clark et al. 2017; Stewart et al. 2021). In addition, previous glaciations within
 518 the Mid- and Early- Pleistocene may have influenced the materials underlying these Late Pleistocene
 519 deposits. These varying conditions will have had significant implications on the deposition,
 520 glaciotectonic disturbance (e.g., Figure 2.9), diagenesis and erosion of the soils together with the
 521 erosion, weathering and load history of the rocks. Meltwater channels, some with associated eskers (see
 522 Figure 2.14 in Section 2.1.7), are also present oriented roughly coast parallel extending from Arbroath
 523 in the south to Peterhead in the north incised into the Marr Bank and Aberdeen Bank, again related to

524 melting of the retreating ice sheet (Golledge and Stoker, 2006). Detailed seabed mapping of these glacial
 525 landforms has permitted reconstruction of the pattern of deglaciation following the LGM, at a time of
 526 rapidly rising sea levels (e.g. Bradwell et al., 2008; Dove et al., 2017; Clark et al., 2017; Stewart et al.,
 527 2021; Figure 2.10). Geomorphological evidence strongly suggests a dynamic switch in glacial styles,
 528 from terrestrial to strongly marine-influenced, ice-sheet retreat, resulting in rapid ice-mass losses at key
 529 time intervals (Bradwell et al. 2008, 2019a, 2019b; Clark et al. 2012; Sejrup et al. 2016; Evans et al.
 530 2021).



531
 532 **Figure 2.9.** Glaciotectonism observed coincident with smaller topographic features identified as
 533 drumlins and areas of ribbed moraine (also known as hummocky terrain) offshore eastern Scotland,
 534 central North Sea. The top panel displays corresponding Marine and Coastguard Agency multibeam
 535 bathymetry data gridded at 8 m resolution. Abbreviations: D = drumlin; D = buried drumlin. Data
 536 courtesy of SSE Renewables.



- | | |
|---|--|
| Moraine | Cross shelf trough edge |
| Meltwater channel thalweg | Subglacial streamlined landform |
| Glacially fed fan | Open tunnel valleys |
| Glacially fed fan (last active in MIS2) | Area of iceberg ploughmarks |
| Glacially fed fan (last active in MIS4?) | Area of iceberg ploughmarks (inferred) |
| Overdeepened glacial basin | Drumlin field |
| Overdeepened glacial basin (last active in MIS2) | |
| Overdeepened glacial basin (last active in MIS4?) | |

537

538 **Figure 2.10.** Selected large-scale glacial landforms including tunnel valleys and subglacial streamlined
 539 landforms, ice-marginal landforms represented by large moraines, glacial marine landforms such as
 540 trough-mouth fans and iceberg ploughmarks (adapted from Clark et al. (2017) and Stewart et al. (2021)).
 541 BDF = Barra-Donegal Fan, DB = Dogger Bank, FW = Foula Wedge, NC = North Channel, NSF =
 542 North Sea Fan, RW = Rona Wedge, SaF = Sandoy Fan, SSF = Sula Sgeir Fan, SuF = Suduroy Fan.

543 Inset map depicts generalised direction of offshore palaeo-ice streams. BFIS = Barra Fan Ice Stream
544 (also known as the Malin Sea Ice Stream and includes the unlabelled North Channel Ice Stream), DBIS
545 = Donegal Bay Ice Stream, FoIS = Forth Ice Stream (including the unlabelled Strathmore Ice Stream),
546 GBIS = Galway Bay Ice Stream, ISIS = Irish Sea Ice Stream, MFIS = Moray Firth Ice Stream, MIS =
547 Minch Ice Stream, NCIS = Norwegian Channel Ice Stream, NSL = North Sea Lobe (including the
548 unlabelled Tweed, Tyne Gap and Eden-Stainmore ice streams). Note that areas devoid of mapped
549 landforms are commonly areas of poor seafloor data rather than indicative of an absence of landform
550 assemblage. Regional Bathymetry from GEBCO Compilation Group (2024).

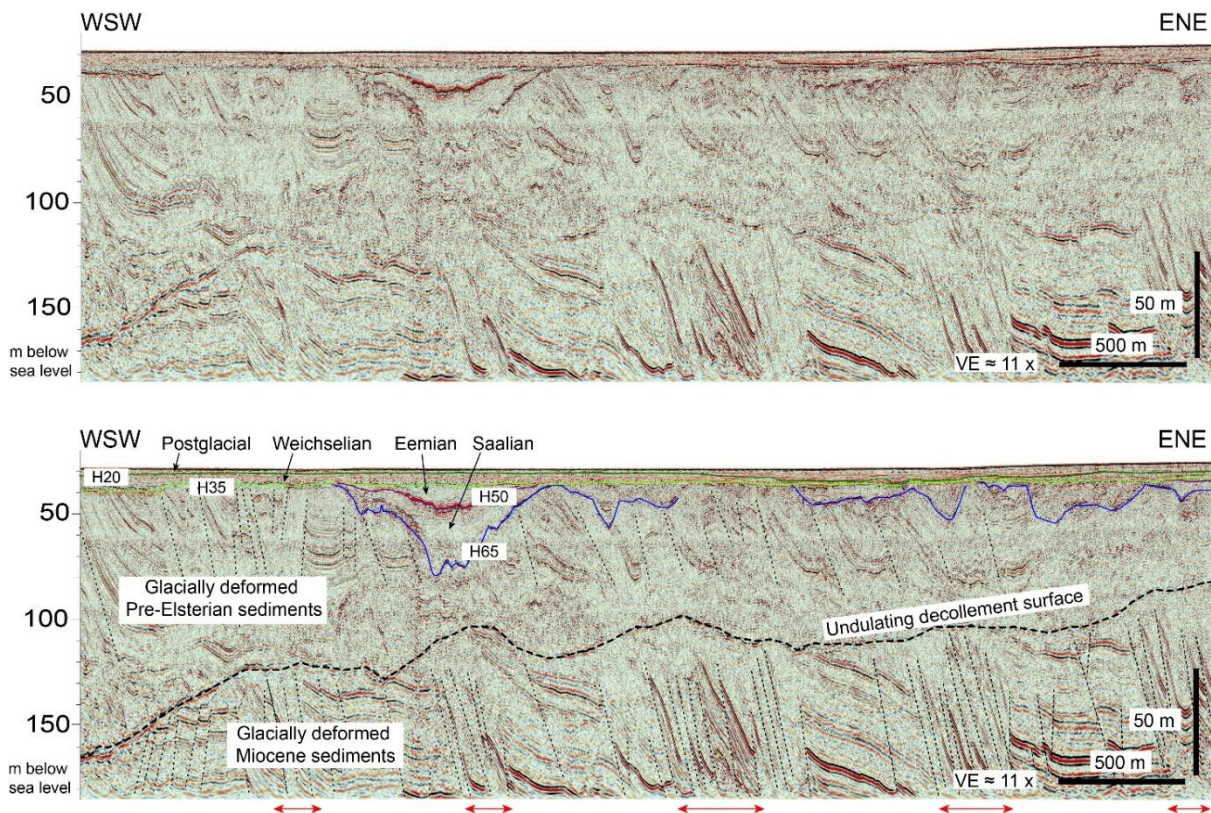
551 2.1.5 Southern North Sea

552 The Southern North Sea, defined in the context of this paper as the Danish, German, Dutch, Belgian
553 and British North Sea sectors south of Dogger Bank (Figure 2.1), comprises a wide (up to 300 km)
554 shallow water continental shelf. Water depths are generally less than 70 m except for the Norwegian
555 Channel where depths increase to over 600 m. During the Cenozoic, the epicontinental North Sea Basin
556 experienced very little subsidence, due to thermal relaxation from Jurassic rifting, however, significant
557 water depths within the basin enabled deposition of thick siliciclastic deltaic successions sourced mainly
558 from the Fennoscandian shield and the northwestern European continent (Huuse et al., 2001; Overeem
559 et al., 2001; Schiøler et al., 2007; Rasmussen et al., in press). As for the central and northern North Sea,
560 the southern North Sea was significantly influenced by the Pleistocene glaciations. While the Elsterian
561 and Saalian ice sheets advanced across the full area, the southern extent of the ice during the LGM
562 (MIS2) was close to the present day bathymetric high Dogger Bank (Figure 2.1; e.g. Hughes et al.,
563 2016). Evidence for potential earlier glaciations of the region is scarce making it extremely difficult to
564 reconstruct pre-mid Pleistocene ice sheet extents (Lee et al., 2012).

565 The Quaternary sedimentary record in the southern North Sea mainly comprises coarse-grained glacial
566 deposits including sand and gravels from the Elsterian and Saalian glaciations, while the Weichselian
567 deposits are dominated by sandy outwash (glacio-fluvial) deposits (Rijsdik et al., 2005; Coughlan et al.,
568 2018).

569 The pre-Elsterian Quaternary record is less well defined but also contains mainly sands originating from
570 Neogene delta topsets in the southeastern parts of the North Sea (Overeem et al., 2001; Thöle et al.,
571 2014) presumably reworked during early Quaternary sea-level cycles and compacted by subsequent
572 glacial loading (Coughlan et al., 2018; Fleischer et al., 2023). Neogene delta deposits below the
573 Quaternary strata are present westwards into the Dutch sector (Benvenuti et al., 2012; Moreau and
574 Huuse, 2014) while further westwards, older bedrock are encountered, e.g. Upper Cretaceous Chalk
575 (Mellett et al., 2019). The record furthermore holds local deposits of finer grained interglacial sediments
576 from the Holsteinian and Eemian interglacials, as well as highly heterogenic successions within buried
577 tunnel valley system (e.g., Hepp et al., 2012; Coughlan et al., 2018; Eaton et al., 2020; Fleischer et al.,

578 2023; Figure 2.9). The Late Weichselian (late glacial) and early Holocene record is particularly well
 579 preserved within younger buried valley systems, where there is often a continuous record from fluvial
 580 and estuarine to shallow and open marine conditions (Andresen et al., 2022; Prins and Andresen 2019,
 581 Özmaral et al., 2022; Hepp et al., 2019), reflecting the late Pleistocene to early Holocene flooding of
 582 the southern North Sea region. Peat and fine-grained siliciclastic are typically found within or in the
 583 proximity of such valleys, whereas the marine Holocene sedimentation has resulted in deposition of a
 584 fine-grained sand cover that is present in various thicknesses over most of the southern North Sea. These
 585 marine Holocene sand deposits show various degrees of mobility depending on the present-day
 586 oceanographic setting. The bottom current systems and tidal regimes in the southern North Sea were
 587 generally established after the opening of the English Channel (ca. 9 ka) and the submergence of Dogger
 588 Bank (ca. 7 ka) (Sturt et al., 2013). Ice marginal processes from all three glaciations are clearly
 589 evidenced by occurrence of tunnel valley systems, glacio-tectonic complexes and the extensive glacial
 590 outwash deposits (Andersen et al., 2004; Pedersen and Boldreel, 2016; Bendixen et al., 2017;
 591 Winsemann et al., 2019; Mellett et al., 2019; Cartelle et al., 2021; Andersen, 2004; Figures 2.8 and
 592 2.11). Several authors have furthermore suggested the occurrence of a large proglacial lake south of the
 593 Dogger Bank (Hjelstuen et al., 2018; Andresen et al., 2022), in part spatially coinciding with the Elbe
 594 Paleo Valley (Özmaral et al., 2022).

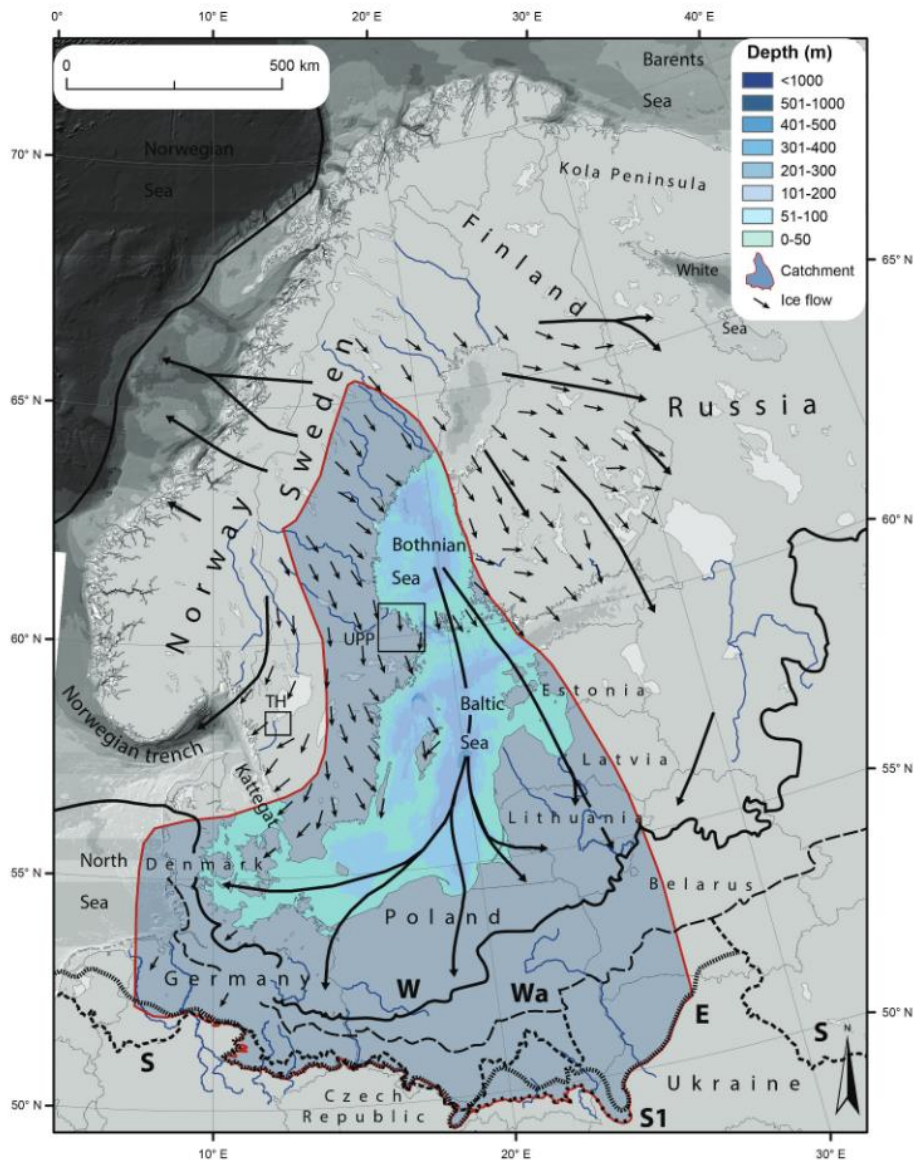


595
 596 **Figure 2.11.** Uninterpreted (top) and interpreted (base) 2D UHRS sparker profile from the North Sea 1
 597 offshore wind farm area in the Danish North Sea. The profile shows two sets of glaciotectonic thrust
 598 structures (black dashed lines) separated by an undulating decollement surface. Red arrows in the base

599 indicate areas with intense deformation in the lower thrust set. The upper deformed succession is incised
600 by Saalian valleys. Shown mapped surfaces are based on interpretations from Fugro (2024): H20 – base
601 Unit 20 (postglacial fresh water and marine sediments), H35 – base Unit 35 (Weichselian glacial
602 meltwater deposits), H50 – base Unit 50 (Eemian interglacial marine sediments), H65 – base Unit 65
603 (Saalian glacial deposits), H70 – base Unit 70 (Elsterian glacial deposits).

604 2.1.6 Baltic Sea

605 The Baltic Sea (Figure 2.1) is a shallow intracontinental sea extending between Scandinavia and Finland
606 in the North and Central and Eastern Europe to the South (Figure 2.12; Jakobsson et al., 2019; Rosentau
607 et al., 2017) with a very limited connection to the global ocean via the Danish straits and the North
608 Sea. The pre-Quaternary basement of the basin consists of crystalline and metamorphic bedrock of the
609 Baltic Shield in the north, which is often exposed at the seafloor and along the coast. Sedimentary rocks
610 of Palaeozoic and Mesozoic ages are subcropping further south or fill basins in the Gulf of Bothnia.
611 Towards the central and southern basin, the basement consists of various sedimentary rocks of
612 Palaeozoic and Mesozoic origin, including Cretaceous and Danian chalk, and even poorly consolidated
613 Paleogene/Neogene sediments underneath Quaternary deposits (Uścińowicz, 2014; Rosentau et al.,
614 2017).



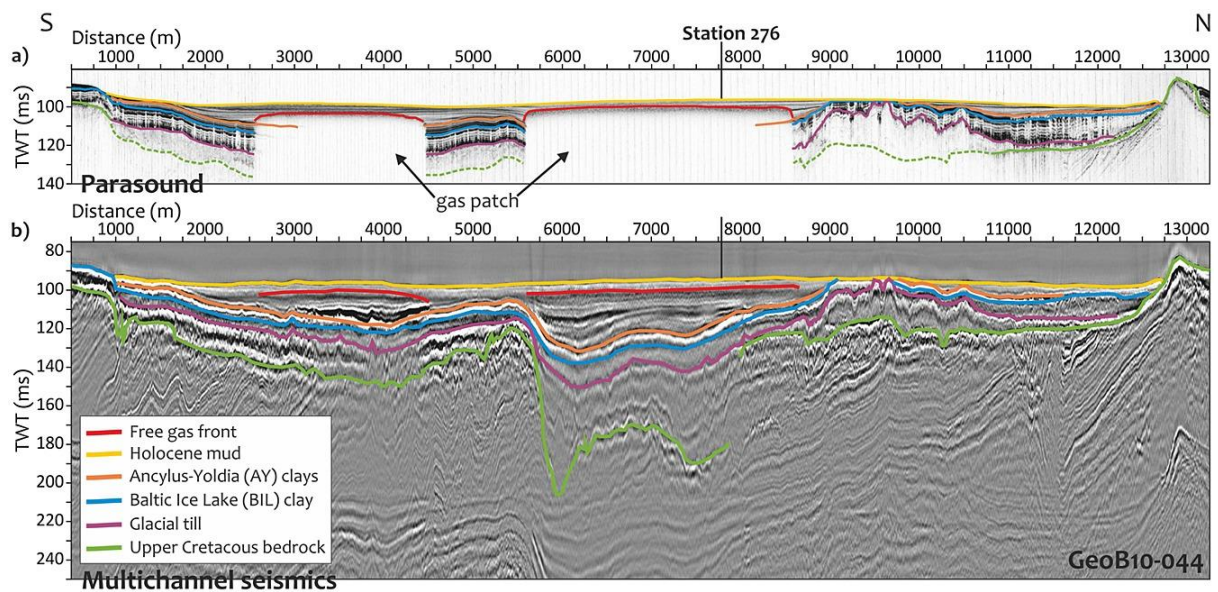
615

616 **Figure 2.12.** Bathymetry of the Baltic Sea basin with Pleistocene ice limits and flow lines. W Late
 617 Weichselian. Wa Warte. S1 Sanian 1, E Elsterian. S Saalian. Image from Hall and van Boeckel (2020).

618 In the Quaternary, the Baltic Sea area underwent multiple, repeated glaciations (Figure 2.12) and
 619 deglaciations that resulted in extensive erosion of pre-existing sediments and bedrock, leading to the
 620 formation of the basin (Overeem et al., 2001; Tuuling and Flodén, 2016; Hall and van Boeckel,
 621 2020). The Quaternary geologic record comprises Pleistocene glaciogenic and Holocene terrestrial,
 622 lacustrine and marine sediments, often distributed irregularly depending on erosion of bedrock and ice
 623 sheet dynamics (Obst et al., 2017; Hall and van Boeckel, 2020). Subglacial tunnel valleys (Figure 2.13)
 624 are present in many parts of the basin but do not reach the depths known from the neighbouring North
 625 Sea basin (Flóden et al., 1997).

626 The Baltic Sea basin was fully covered by the FIS for the last time during the LGM between 23 and 19
 627 cal kyr BP (Figure 2.12) followed by ice retreat from 17-16 cal kyr BP onwards (Hughes et al., 2016).

628 The retreat was punctuated by ice margin stabilisations and/or re-advances. Pro-glacial and
629 glaciomarine deposits that formed during this halting ice retreat can be observed in bathymetric data
630 throughout the basin (Jakobsson et al., 2019, Tylmann and Uścińowicz, 2022; Greenwood et al., 2017;
631 2024). Ice contact glaciofluvial deposit (ice contact fans and deltas) as well as recessional moraines
632 were formed at the margin of the retreating ice sheet and in front of it. Glaciotectonic deformations
633 (faulting and folding) are widespread in the southern Baltic. As a consequence, in the southern and
634 central Baltic, pre-Quaternary strata are blanketed with variable thicknesses of glaciogenic sediments
635 including tills deposited sub- and proglacially as well ice marginal and proglacial glaciofluvial deposits
636 (Obst et al., 2017). Glacial landforms and glacially sculpted bedrock surfaces become more prominent
637 in the north towards the coast of Sweden and Finland as well as into the Gulf of Bothnia. Subsequent
638 flooding of the basin initially formed isolated proglacial lakes and kettle holes formed in front of the
639 retreating ice margin around 15.5 cal kyr BP in the southern Baltic. Ice margin retreat in the northern
640 part, i.e. the Gulf of Bothnia, continued until significantly later and this part of the basin only became
641 ice free between 10-12 cal kyr BP. The freshwater Baltic Ice Lake (BIL) formed during the ice retreat
642 and covered large parts of the formerly glaciated landscape, itself isolated from the global ocean. The
643 lake drained during the Younger Dryas when two major BIL drainage events occurred though a
644 topographic low near Mount Billingen around 11.7 cal kyr BP with subsequent drainage events inferred
645 through Fehmarn Belt and Mecklenburgh Bight as the ice sheet margin was positioned across southern
646 Sweden and Finland, leading to ~25 m water level fall in a very short time. The geometry of the basin
647 combined with ice margin position during its retreat, global sea level fluctuations and glacial isostatic
648 adjustment of the region resulted in periodical isolation of the Baltic basin (Baltic Ice-Lake and Ancylus
649 Lake stages) and drainage and connection to the global oceans (Yoldia Sea, Mastogloia Sea and
650 Littorina/ Postlittorina Sea stages) (Uścińowicz, 2006; Andrén et al. 2011). During the Late Pleistocene
651 and Holocene, the postglacial fine grained organic-rich lacustrine and marine deposits can be found
652 mainly in deeper or isolated parts of the basin whereas shallower parts are often dominated by sandy
653 and gravelly deposits due to waves and currents reworking the glacial substrate. Boulders, as well as
654 shallow gas pockets, organic rich soils and laterally heterogeneous glaciogenic sediments and glacial
655 and mobile bedforms are common across the basin.



656

657 **Figure 2.13.** Interpreted sub-bottom profiler data (a) and seismic (b) profile in the Bornholm Basin
 658 showing typical basin filling geology. Above a Mesozoic basement lie glaciogenic till deposits followed
 659 by the typical late- and post-glacial sequence of limnic and marine sediments. Modern Holocene mud
 660 shows high organic content and shallow biogenic gas formation in the basins. Image from Tóth et al.
 661 (2014a).

662 2.1.7 Irish Sea and Celtic Sea

663 While the exact number of glacial periods to have directly influenced the Irish and Celtic Sea basins
 664 remains poorly constrained, it is generally accepted that the Elsterian, Saalian, and Weichselian ice
 665 sheets (the three most recent and largest glaciations in the Mid to Late Quaternary) were responsible
 666 for depositing the sedimentary packages that form the present-day Quaternary framework across this
 667 region (Figure 2.1; Jackson et al., 1995; Mellett et al., 2015). Naturally, there is a preservation bias as
 668 the BIIS of Weichselian age is likely to have reworked a significant portion of Elsterian and Saalian
 669 deposits and, as such, the majority of the Quaternary sequence across this region is associated with the
 670 Weichselian glaciation (Mellett et al., 2015).

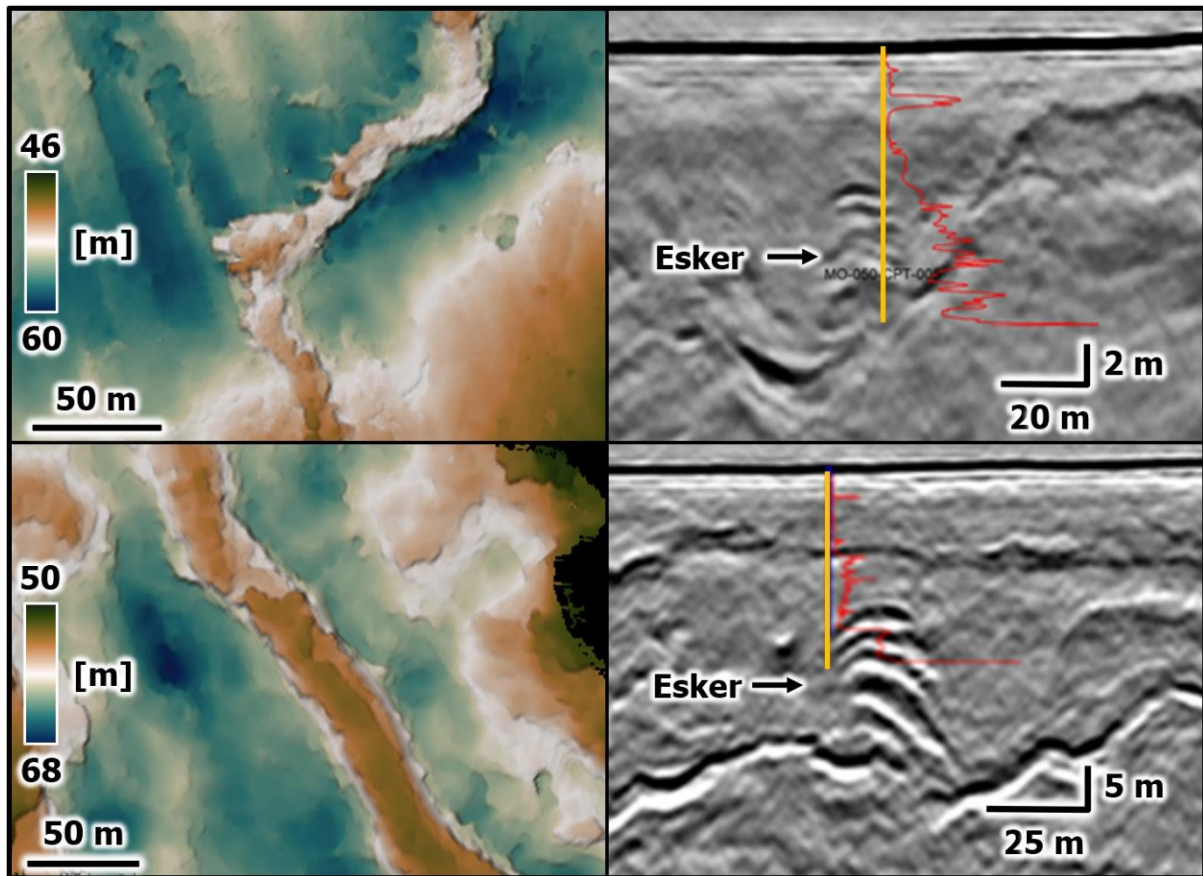
671 Fed by ice domes over Ireland, Scotland, the Lake District and Wales, fast moving ice started to develop
 672 sometime after 36 ka (Roberts et al., 2007), with Chiverrell et al. (2021) finding that ice build-up and
 673 expansion took place substantially between 30 ka through to ~26 ka. This area (i.e., Irish Sea sector) of
 674 the BIIS was unique in that it represented a bifurcating system with two distinct outlets; the Irish Sea
 675 Glacier (ISG), a non-streaming terrestrial terminus that extended over present-day Cheshire–Shropshire
 676 lowlands and into the English Midlands, and the Irish Sea Ice Stream (ISIS), a marine-terminating ice
 677 stream comprising fast flowing, generally grounded, ice which expanding south through the Irish Sea
 678 Basin and out across the Celtic Sea (Scourse et al., 2021). Ice sheet reconstruction work by Scourse et
 679 al. (2021) and Clark et al. (2022) showed that the maximum extent of the ISIS reached the shelf break

680 of the Celtic Margin, completely covering the Irish and Celtic Sea region, by around 26-25.5 ka (Praeg
681 et al. 2015; Scourse et al. 2019; Smedley et al., 2017). Across the Irish Sea and Celtic Sea sector, this
682 period of advance of the ISIS is recorded by the deposition of subglacial till, till deformation and
683 subglacial erosive features. In the north and central Irish Sea, tunnel valleys are understood to have been
684 initiated during this phase, with existing features often down-cut into bedrock (Whittington, 1977;
685 Jackson et al., 1995; Callaway et al., 2011; Coughlan et al., 2020a). Mega-scale glacial lineations
686 (MSGSL) initiated during this phase with examples noted in the north Irish Sea (Michel et al., 2023) and
687 offshore Anglesey (Van Landegehm and Chiverrell, 2020). Deposition of sub-glacial till and the
688 deformation and erosion of pre-Weichselian deposits are recorded off the southeast Irish coast (Tóth et
689 al., 2020), as well as southwest of Ireland (Giglio et al., 2022). Giglio et al. (2022) identified a drumlin
690 field more than 25 km offshore southwest Ireland signifying grounded ice in this area during the initial
691 ISIS advance. The legacy of this advance phase was to have a significant control over the deposition of
692 units and formation of other geomorphological features subsequently.

693 Scourse et al. (2021) conclude that this expansion of the ISIS would have been a relatively short-lived
694 but rapid event, resulting in thin ice forming a marine calving margin at the shelf break. Having reached
695 its maximum extent, rapid deglaciation followed as the ice margin collapsed and retreated 400 km
696 northwards across the Celtic Sea, where it stabilised in the region of St. George's Channel around 24.2
697 ka (Small et al., 2018). This period of retreat is recorded by a grounding zone wedge and recessional
698 moraines southwest of Ireland (Giglio et al., 2022), as well as the formation of an extensive subglacial
699 drainage system represented by tunnel valleys implying significant amounts of erosive meltwater
700 discharge (Giglio et al., 2021). Further evidence for subglacial drainage is recorded in the north Celtic
701 Sea through esker formation (Figure 2.14; Tóth et al., 2020). In this area, Tóth et al. (2020) infer the
702 deposition of ice-marginal, glacial outwash deposits, possibly in an ice-dammed lake that formed during
703 the retreat of the ISIS. The retreat of the ISIS margin in this nearshore area also un-impinged terrestrial
704 ice, allowing it to advance from inland centres reaching more than 15 km beyond the present coastline,
705 tectonising ISIS-related deposits (Tóth et al., 2020).

706 The subsequent ISIS withdrawal from the Irish Sea Basin was not a simple, continuous process.
707 Between St George's Channel (ca. 24 ka) and a line from Llŷn Peninsula – Wicklow approximately (ca.
708 21 ka), ISIS retreat slowed down with a series of stillstands, and oscillations recorded along the
709 coastlines of Ireland and Wales (Chiverrell et al., 2013, 2018; Smedley et al., 2017; Small et al., 2018).
710 This appears to be largely controlled by topographic pinning points and constrictions of the ice stream
711 (Scourse et al., 2021). This phase allowed for the further development of sub-glacial drainage in the
712 form of channel systems and tunnel valleys (Coughlan et al., 2020a; Michel et al, 2023) as well as mega-
713 scale glacial lineations (Van Landeghem and Chiverrell, 2020).

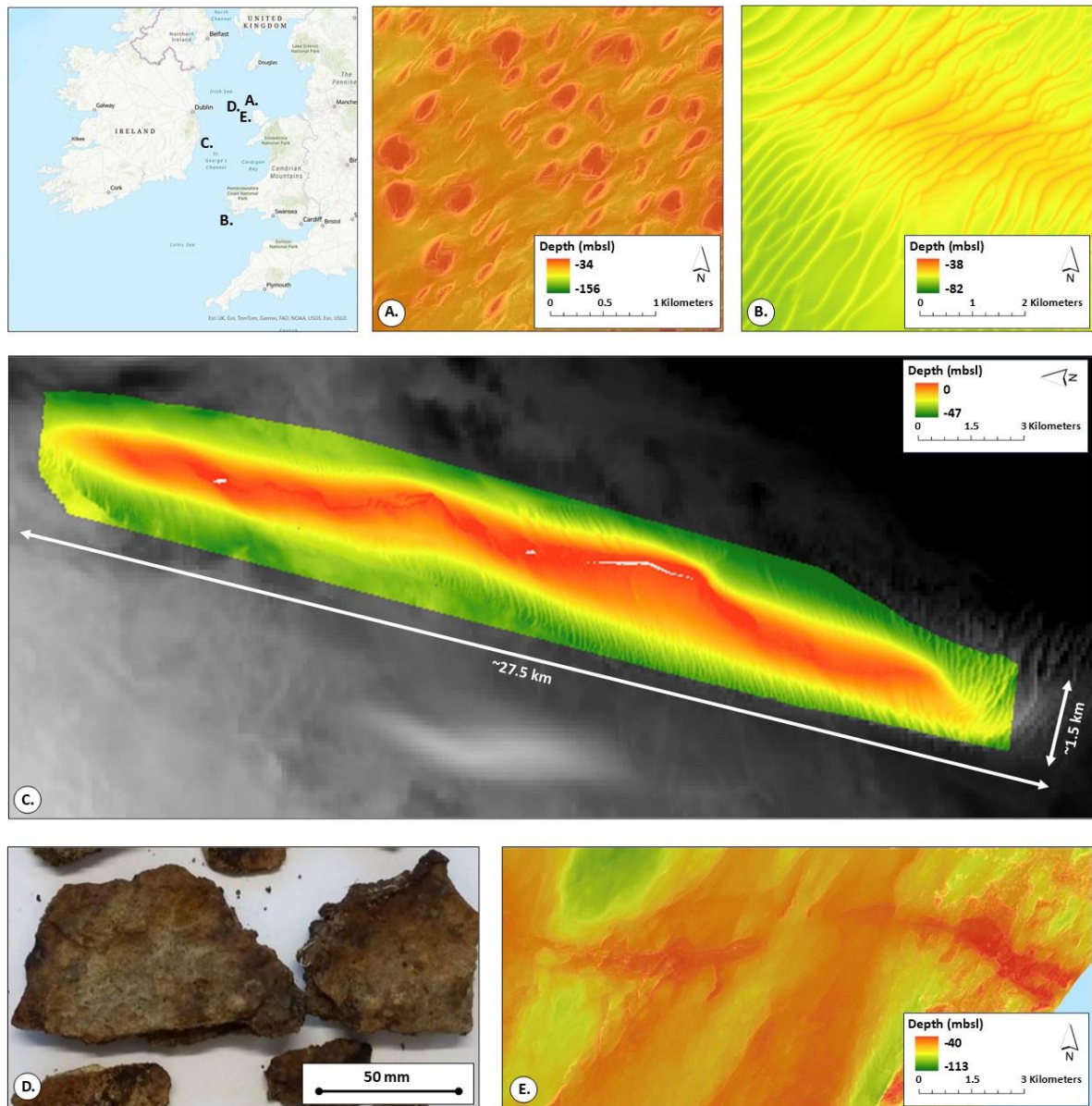
714



715

716 **Figure 2.14.** Examples of subsurface eskers related to the retreat of the BIIS circa 20 ka. Data courtesy
 717 of Mona Offshore Wind Limited.

718 The ISIS reached the north Irish Sea Basin by approximately 21.9 ka where, according to Scourse et al.
 719 (2021), it began to retreat rapidly again, primarily due to increased retreat space afforded by trough
 720 geometry, and deeper waters. Pronounced ice margins are recorded across the northern Isle of Man
 721 dated at 19.1 ka (Scourse et al., 2021; Clark et al., 2022). In the eastern Irish Sea, offshore Anglesey,
 722 evidence for this deglaciation of the Irish Sea Basin is well captured by seafloor and sub-seabed
 723 geomorphological assemblages, including substantial drumlin fields, ribbed and De Geer moraines,
 724 eskers, iceberg scour marks and flutes (Figure 2.15), and emphasising the continued oscillation of the
 725 ISIS margin during retreat, as well as the transition from old- to warm-based ice (Van Landeghem et
 726 al., 2009a; Van Landeghem and Chiverrell, 2020). To the north and northwest of the Irish Sea Basin,
 727 this glacial landscape has largely been buried by post glacial sedimentation, in particular by thick
 728 accumulations of marine sediment during the Holocene (Belderson, 1964, Pantin, 1978; Coughlan et
 729 al., 2019; Chiverrell et al., 2018).



730
 731 **Figure 2.15.** Examples of present-day seabed geomorphology across the Irish and Celtic Sea area. **a)**
 732 An extensive drumlin field offshore of Anglesey, with varying morphologies suggesting periods of both
 733 ice-streaming and slower-moving/static ice flow behaviour. **b)** A significant sand-wave field located on
 734 the margins of the Outer Bristol Channel. **c)** The Arklow Bank, a major N-S orientated linear, elongated
 735 sand bank, is located off the south-east coast of Ireland and measures approximately 27.5 km in length
 736 and 1-2 km in width (Creane et al., 2023a). **d)** The Croker Carbonate Slabs are methane derived
 737 authigenic carbonates deposited on the seabed through fluid escape. **e)** The remnants of a roughly E-W
 738 orientated moraine, located west of the island of Anglesey. Multibeam bathymetry sourced from the
 739 UK Hydrographic Office (UKHO) and Maritime & Coastguard Agency (MCA), EMODnet
 740 Bathymetry, and INFOMAR. MDAC photo is courtesy of The British Geological Survey (c) UKRI
 741 2025.

742 The ice margin eventually pulled back onto the terrestrial highs across the north of Ireland and SW
 743 Scotland at approximately 17 ka, which represented the final phase of retreat with complete deglaciation
 744 of the Irish Sea Basin being achieved in a fully marine setting (Scourse et al., 2021; Clark et al., 2022).
 745 This final deglaciation was punctuated by minor, local ice readvances during the Clogherhead Stadial
 746 (~18.4 ka BP) and Killard Point Stadial (~17.3 to 16.6 ka BP) which are well constrained onshore
 747 (McCabe et al., 2005, 2007; Chiverrell et al., 2018). Offshore, some evidence is found in the form of
 748 moraine development, for example in Dundalk Bay (Michel et al., 2023). Evidence of an unstable,
 749 calving ice front is also seen though the presence of buried iceberg scours (Michel et al., 2023).

750 The lithostratigraphical framework for Quaternary deposits in the Irish Sea and Celtic Sea sector is
 751 summarised in Table 2.1, according to Stoker et al. (2011), and Figure 2.16 shows a seismic section
 752 through the Quaternary sequence in the eastern Irish Sea.

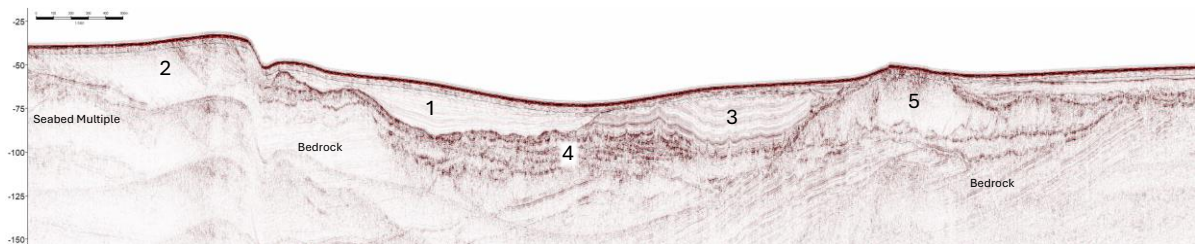
753

754 **Table 2.1.** Detailed formations of the Demetae Group and Brython Glacigenic Group as per Stoker et
 755 al. (2011).

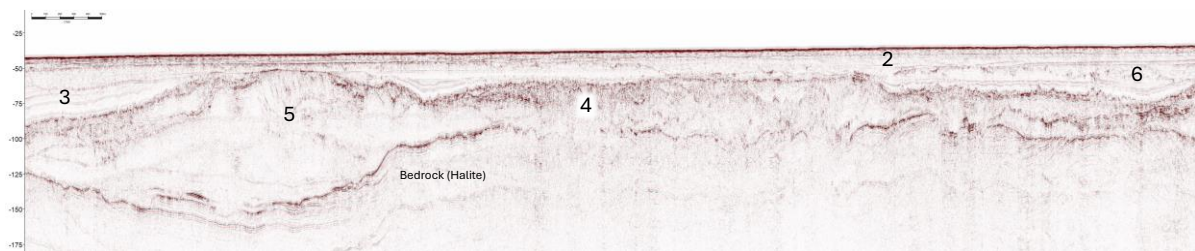
| Group | Formation | Member | Description | |
|--------------------------|---------------------|--|-------------|--|
| Brython Glacigenic Group | Surface Sands | Seabed Depression | | |
| | | Surface Layer 1 | | |
| | | Surface Layer 2 | | |
| | Western Irish Sea | Codling Bank Facies (offshore Wicklow only) | | A very clast-rich (cobble-boulder size) deposit possibly laid down as a diamicton through subaqueous ice-rafting and sediment gravity flows, or sandur deposits. |
| | | Mud facies | | Black to greenish grey, shelly silts, representing ice-distal glaciomarine deposits that pass upwards into fully marine deposits. |
| | | Prograded facies | | fine- to medium-grained sand representing prodeltaic and glaciomarine deposits |
| | | Chaotic facies* | | tabular-stratified deposits, likely to have been laid down under glaciolacustrine or glaciomarine ice-proximal settings. |
| | Cardigan Bay | Upper Till (late Weichselian) | | Stiff or very stiff diamicton of clay containing clasts up to boulder size (>1 m diameter). |
| | | Bedded and Infill member (late Saalian to early Weichselian) | | Sands with subordinate clay beds passing upward into fine-grained silty sands and sandy clays |
| | | Lower Till member (Saalian) | | Very stiff clay with abundant cobbles to a shelly sand with lithic gravels and occasional cobbles |
| | St George's Channel | | | Shelly glaciomarine muds |
| | Caernarfon Bay | Upper Unstratified member (early Saalian) | | Till or sandy to muddy diamicton with drops stones (probably an ice-sheet-proximal, glaciomarine deposit). |
| | | Incision Infill member (late Elsterian to Holsteinian) | | diamictons of stiff clay with lithic clasts, muds with clasts up to boulder size, sands, muds and clays |
| | | Bedded member (Elsterian) | | depositional environment unknown but consists of shelly sand with occasional clay beds and scattered cobbles. |
| | | Lower Unstratified member (Elsterian) | | Probable subglacial to proglacial olive-grey till |

| | | | |
|---|---------------|--|---|
| Demetae Group | Bardsley Loom | | heterogeneous mix of clay, sand, gravel and peat layers |
| Notes: * Geoscience data acquired for Offshore Wind Developments has allowed for a greater understanding of the depositional and glacial setting, but at the time of writing was yet to be publicised | | | |

756



757



758

759 **Figure 2.16.** Seismic section (west to east) through the Eastern Irish Sea Quaternary Sequence. 1. Mud
760 Facies [Glaciomarine], 2. Prograded Facies [Glaciomarine], 3. Chaotic Facies [Glaciolacustrine with
761 crevasse squeeze ridges], 4. Chaotic Facies [Pro-glacial outwash and lakes], 5. Upper Till [Glacio-
762 tectonised Moraine], 6. Chaotic Facies [Sandur Plain and Glaciofluvial]. Walney Wind Farm, publicly
763 available data.

764 Post-glacially, the Irish Sea and Celtic Sea seafloor has been heavily influenced by marine transgression
765 and contemporary hydrodynamics. As a result of glaciation, the seafloor sediment of this area largely
766 comprises reworked glacial or post-glacial material forming a mosaic of sediment types, that are often
767 reworked into bedforms (Figure 2.14). Linear sediment mega-ridges in the Celtic Sea have been
768 interpreted as tidal features, with a subglacial basement control, that formed under stronger current
769 conditions in the past (Lockhart et al., 2018; Praeg et al., 2015). In the Irish Sea, a series of linear, north-
770 south trending sandbanks are found close inshore and parallel to the Wexford, Wicklow and South
771 Dublin coast (Figure 2.14). These features form bathymetric highs relative to the surrounding seabed
772 and are understood to formed under more energetic tidal regimes in the geological past (Uehara et al.,
773 2006; Wheeler et al., 2001) or with a partly glacial origin (Whittington, 1977). They are currently
774 considered quasi-stable and in equilibrium with present hydrographic conditions, with some minor
775 morphological changes (Creane et al., 2023a; 2023b). These banks form sites for planned offshore wind
776 development. In general, the Irish Sea seafloor is dynamic with high levels of sediment erosion,
777 transport and deposition due to the energetic tidal regime (Coughlan et al., 2021a; Ward et al., 2015).
778 These conditions help maintain and drive bedform development and migration, including extensive
779 sediment wave fields (Creane et al., 2022; Van Landeghem et al., 2009b). This dynamic seafloor also
780 creates engineering issues such as scour, which has impacted on offshore wind turbine stability

781 previously (Whitehouse et al., 2011). The present-day seafloor in the Irish Sea also shows evidence of
782 fluid escape. Pockmarks and sub-surface gas accumulations in the Quaternary sequence has been
783 documented in the north Irish Sea (Coughlan et al., 2021b; Yuan et al., 1992) with methane derived
784 authigenic carbonates (MDAC; Figure 2.14) and mounds found in sandier deposits further south
785 (Croker et al., 2005; O'Reilly et al., 2014; Van Landeghem et al., 2015).

786 Despite the substantial sediment reworking and seafloor modification by post-glacial processes, the
787 present-day seabed captures this diverse and complex Quaternary history across this region. The growth
788 in national seabed mapping programmes, such as INFOMAR, has provided key large-scale datasets that
789 have allowed for the regional classification of glacial features (e.g. Arosio et al., 2023), and to identify
790 key geological constraints to the development of offshore infrastructure related to Quaternary processes
791 and deposits (Coughlan et al., 2020b; Guinan et al., 2020).

792 2.1.8 Outer Hebrides and Rockall

793 From Early Pliocene times onshore uplift of the northwest European Atlantic margin (west of Shetland,
794 Outer Hebrides, Rockall and west of Ireland) was accompanied with accelerated offshore subsidence,
795 coupled with seaward tilting of the continental margin that resulted in basinal progradation of the
796 northwest Atlantic Margin (Stoker and Varming, 2011; Stoker 2013). Progradation and development of
797 the Atlantic margin, of up to 50 km in the Hebridean region (Stoker 2013), was further enhanced by
798 multiple Late Pliocene to Pleistocene glaciations (Stoker and Varming, 2011; Stoker 2013) with much
799 of the sediment forming these wedges younger than around 2.5 Ma (Stoker, 2002; Stoker et al., 2005).

800 Across the Atlantic margin, regional mapping has shown that the Quaternary succession can be divided
801 into two separated by a widespread Mid-Pleistocene glacial erosion surface correlated with the Anglian
802 glacial stage (the Glacial Unconformity on Figure 2.17) dated to about 0.44 Ma on the continental
803 margin (Stoker et al., 2005). The glacial unconformity separates sediments of the Hebrides Margin
804 Group (below) from the Eilean Siar Glacigenic Group. Unlike the North Sea Basin, multiple glaciations
805 during the Mid and Late Pleistocene have removed much of the Early Pleistocene/Pre-Elsterian deposits
806 from the outer continental shelf (Stoker et al., 1993). Across the continental shelf the Quaternary
807 succession is comparatively thin, only attaining a thickness of up to around 200 m (Figure 6.4). At their
808 maximum extent, the BIIS delivered sediments directly to the continental slope generating large
809 glacigenic depocentres such as the Foula and Rona wedges in the Faroe Shetland Channel, and the Sula
810 Sgeir (Figure 2.18) and Barra–Donegal glacigenic fans in the Rockall Trough (Figure 2.10),
811 accumulating sequences up to around 800 m thick (Figure 6.4). The margin of the southern Rockall–
812 Porcupine area was largely sediment starved during Quaternary times (Stoker et al., 2005).

813 The Sula Sgeir and Barra–Donegal glacigenic fans are composed predominantly of stacked
814 accumulations of debris-flow diamictons interbedded with hemipelagic and contouritic
815 marine/glacimarine muds and thin-bedded turbidites (Stoker et al., 2005; Stoker, 2013). British

816 Geological Survey boreholes and a limited number of commercial wells located on the Hebridean
817 margin suggest that the regional Glacial Unconformity separates underlying sand-dominated strata of
818 the Hebrides Margin Group from overlying mud-dominated sediments of the Eilean Siar Glacigenic
819 Group (Stoker, 2013; Figure 2.17). Borehole 88/07,7A located on the Hebrides Slope proved ice-rafted
820 debris in the form of scattered dropstones at 86.0 m, more or less coincident with the Gauss–Matuyama
821 polarity transition (2.48 Ma) measured at 85.8 m (Stoker et al., 2005). This contrasts with
822 palaeontological evidence of warmer environmental conditions during deposition of the underlying
823 Pliocene section suggesting deterioration of climatic conditions from latest Pliocene to earliest
824 Pleistocene times (Stoker, 2013).

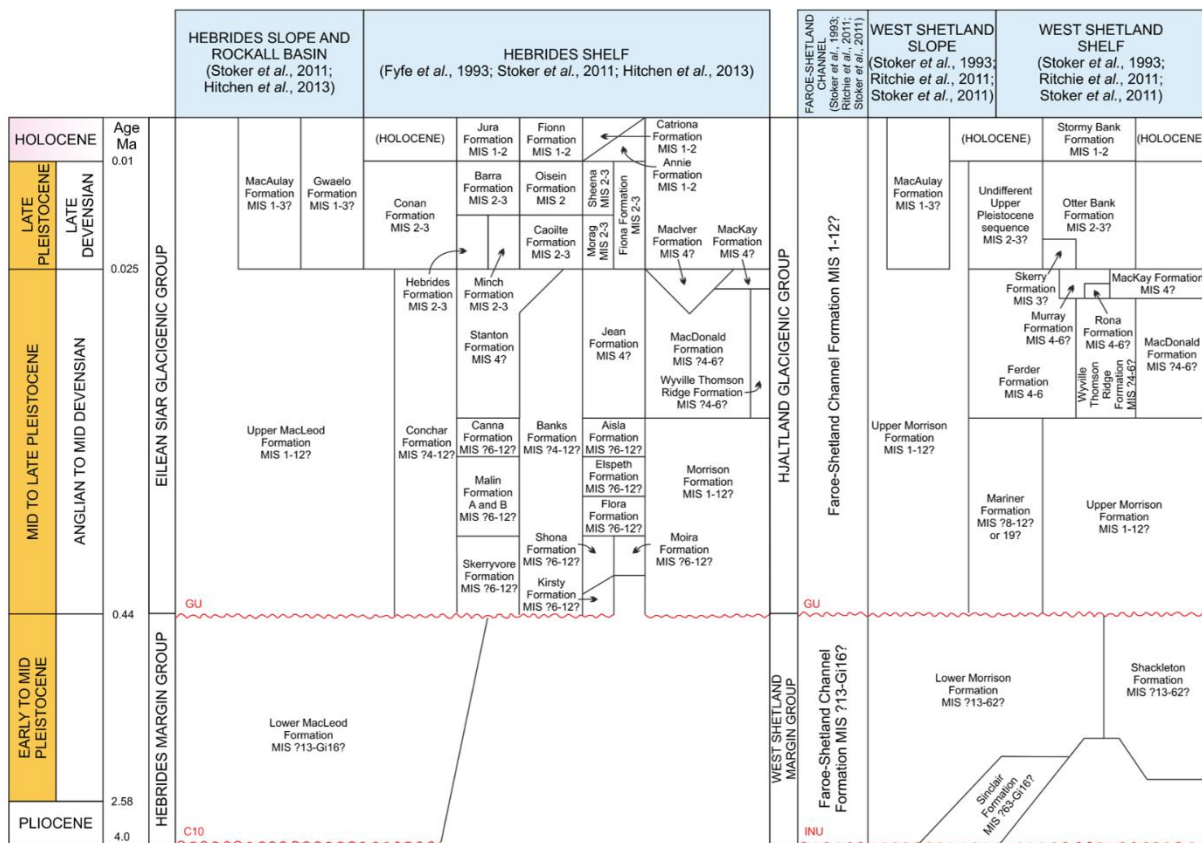
825 The planar to irregular, regional Glacial Unconformity typically truncates older Plio-Pleistocene
826 prograding strata, and is overlain by a flatter lying sequences that displays an aggrading geometry,
827 preserves glacial moraines on the continental shelf, and gives way to glacial-fed trough-mouth fans on
828 the slope (Figure 2.18; Stoker et al., 2005). This early Mid-Pleistocene stratigraphic expression marks
829 the switch from restricted (down to coastline) to expansive (shelf-wide) glaciations (Stoker, 2013).

830 Regional-scale geomorphology along the mid and outer shelves is dominated by a series of arcuate and
831 sometimes overlapping ice-marginal moraines (Figure 2.10). These ubiquitous bedforms relate to the
832 extent and retreat of grounded ice on the shelf. Large moraines show a clear geographic association to
833 glacially eroded troughs, and the depositional trough-mouth fans on the continental slope (Figure 2.10;
834 e.g. Sula Sgeir and Barra–Donegal fans), revealing the terminal positions of a number of palaeo-ice
835 streams extending out across the continental shelf to the shelf break. The excavated troughs and
836 depositional trough-mouth fans have been formed over successive glacial stages, while the moraines
837 are more likely associated with the most recent glaciation to impact the seabed as ice sheets tend to
838 remove surficial evidence from previous events. Some of the transverse ridges on the mid-shelf have
839 been interpreted as grounding-zone wedges (marking position between grounded ice and floating ice
840 shelf) rather than moraines, depending on the relative sea level at the time. These are particularly well
841 developed for the Minch Ice Stream (Bradwell et al., 2021), Barra–Donegal Ice Stream (Arosio et al.,
842 2018; Callard et al., 2018), Donegal Bay Ice Stream (Benetti et al., 2021), and Galway Bay Ice Stream
843 (Peters et al., 2015; Callard et al., 2020), suggesting punctuated or episodic retreat of the grounding line
844 from their maximum LGM extent.

845 As ice sheets retreat from the mid and outer shelf, proximal glacimarine sedimentation proceeded, and
846 these deposits still mantle the seabed in several places (e.g. near and beyond shelf break, North Lewis
847 and North Minch Basins). Acoustic gas-blanking is commonly reported within the sediments of the Jura
848 Formation, likely to be the result of very high rates of deposition and associated rapid burial of organic
849 matter (Fyfe et al., 1993). Where sheltered, low-energy coastal and estuarine conditions dominate,
850 accumulations of fine-grained sands and muds exhibit small areas of pockmarks on the seabed surface
851 (Audsley et al., 2021). Extensive basement platforms occur on the inner continental shelf in the vicinity

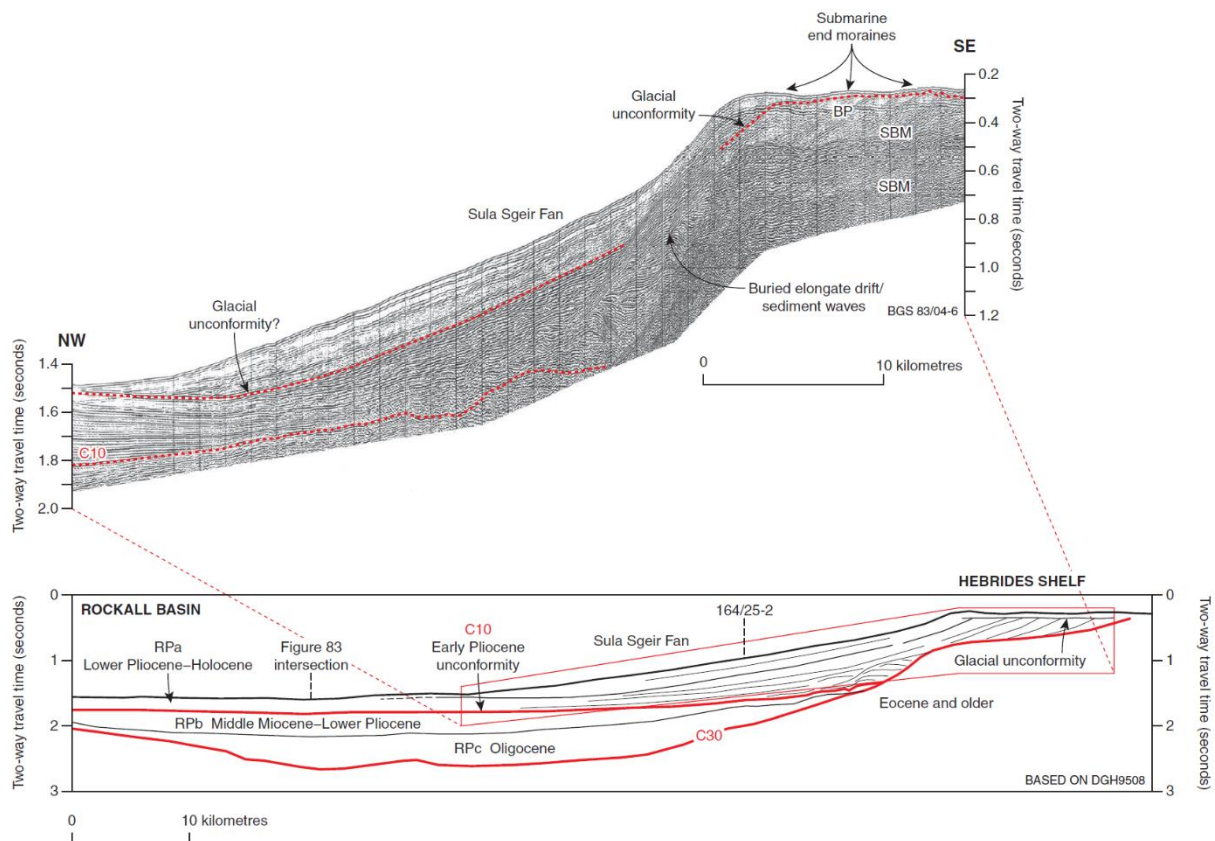
852 of the Outer Hebrides and Sea of the Hebrides. West of the Outer Hebrides these basement rocks
 853 comprise scoured Lewisian strata (>2500 million years old) cropping out at seabed across a large region,
 854 extending at least 150 km from north to south. Bedrock landforms produced by glacial erosion (e.g.
 855 bedrock crag-and-tails and streamlined rock drumlins), provide evidence of intense subglacial erosion
 856 by powerful fast-flowing ice, and key information regarding former ice-flow dynamics. Bedrock highs
 857 within the Minch and Sea of Hebrides, represent a marked increase in bed strength and a topographic
 858 pinning point that may provide vital stability of the marine-terminating margin during overall ice-stream
 859 retreat (Bradwell et al., 2019b, 2021; Stewart et al., 2022). Predisposed in places by the underlying
 860 structural geology, glacial troughs, up to ~100 m deeper than the surrounding seabed, are present in the
 861 North Channel and Inner Hebrides (Figure 2.10).

862



863

864 **Figure 2.17.** Summary of the Quaternary stratigraphy in the Hebridean, Rockall and West of Shetland
 865 regions. GU = Glacial Unconformity, INU = Intra-Neogene Unconformity, C10 = Early Pliocene
 866 unconformity.



867

868 **Figure 2.18.** British Geological Survey airgun profile 83/04-6 across the Hebridean margin showing
 869 the Lower Pliocene–Holocene slope apron of the prograding Sula Sgeir Fan overlying and partly
 870 interbedded with onlapping and upslope migrating contourite drift and sediment waves, which both
 871 comprise the RPa megasequence (sediments of both the Hebrides Margin and Eilean Siar Glacigenic
 872 groups). Submarine end moraines are preserved above the Mid Pleistocene glacial unconformity on the
 873 Outer Hebrides shelf. Modified after Stoker et al. (2005). For location see Figure 2.10. Image British
 874 Geological Survey © UKRI 2025.

875 2.1.9 West of Shetland

876 The Late Pliocene to Pleistocene history of the West of Shetland (WoS) margin, like the Outer Hebrides
 877 and Rockall margin, is also characterized by a dynamic interplay between glacial advances and retreats,
 878 fluctuating sea levels, and bottom current activity. This period witnessed significant progradation, with
 879 the margin extending seaward by up to 50 km since the early Pliocene (Stoker and Varming, 2011). The
 880 progradation can be broadly categorized into two distinct phases: a first phase as part of the Faroe
 881 Shetland Neogene 1 (FSN-1) mega-sequence followed by a second phase of the formation of the Glacial
 882 Unconformity, marking the onset of extensive shelf glaciation around 0.44 million years ago (Ma)
 883 (Stoker, 1995; Stoker and Varming, 2011; Clark et al., 2018).

884 Prior to the Mid Pleistocene glaciation, progradation was initially restricted to the outer shelf, gradually
 885 extending into deeper water over time (Stoker and Varming, 2011). Borehole data reveal a sand-
 886 dominated sequence underlying the Glacial Unconformity, attributed to the Sinclair and Morrison (unit

887 1) formations (Figure 2.17), which together comprise the older portion of the Rona and Foula wedges
888 (Stoker and Varming, 2011; Figure 2.10). These formations exceed 100 meters in thickness, with the
889 older Sinclair sequence occupying the innermost portion. Biostratigraphic dating suggests a Pliocene to
890 Early Pleistocene age for the Sinclair sequence.

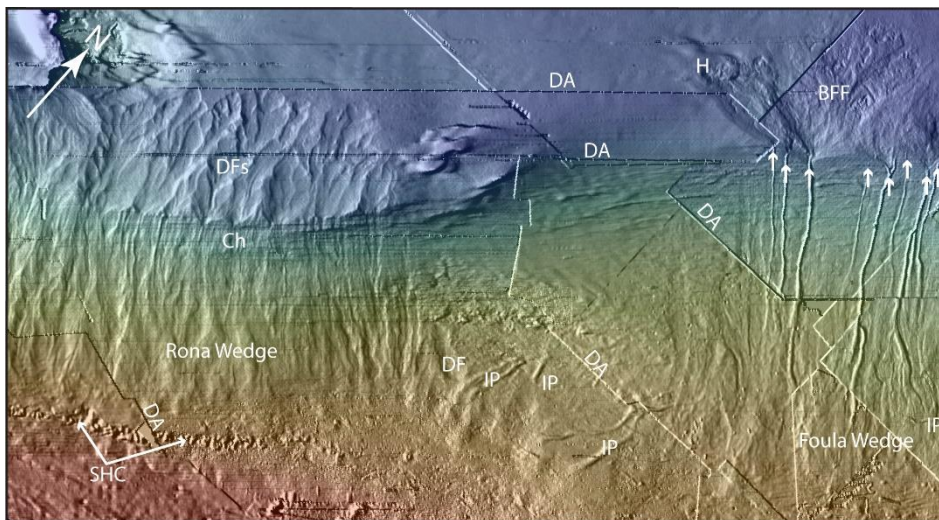
891 The Glacial Unconformity separates the underlying sand-rich strata (Morrison 1 Sequence) from the
892 overlying mud-dominated sediments (Morrison 2 Sequence; Stoker and Varming, 2011; Figure 2.17).
893 Mid-Pleistocene orbital shifts (100 ka cycles) drove extensive glaciation across the British continental
894 shelf, impacting sedimentation and margin development (Rea et al., 2018). Resulting glacial cycles led
895 to unconformities and prograding glacial wedge deposits on the shelf/slope. Since the Mid Pleistocene,
896 progradation has extended from the shelf to the Faroe-Shetland Basin (FSB) (Stoker and Varming,
897 2011). The uppermost sediments form, between 59.5°N and 61°N latitude, large, wedge-shaped deposits
898 (prograding wedges) and apron-like layers (slope aprons) as part of Trough Mouth Fan systems (Figures
899 2.10 and 2.19).

900 British Geological Survey borehole data indicate that many post-Glacial Unconformity units on the
901 outer shelf, such as, Foula and Rona sequences, are dominated by diamicton (glacigenic debris flow),
902 sand, and gravel (Stoker and Varming, 2011; Figure 2.17). These debris flow deposits are alternated to
903 contouritic clays and sands, alongside glacimarine clays and sands deposited by ice-rafted debris and
904 meltwater plumes (Davison, 2004; Knutz and Cartwright, 2003) with finer glaciomarine and contouritic
905 sediments. Further north, between 61°N and 62°N, these deposits transition into elongated, mounded
906 features, associated to bottom currents flowing along the continental slope. The latter represent the West
907 of Shetland Drifts (WSD) and are mirrored by sheeted contourite drifts across the Faroe-Shetland
908 Channel basin. These deposits are attributed to ice-marginal processes associated with the growth and
909 retreat of the BIIS (Stoker and Holmes, 1991) and successively by the combined BIIS and the FIS at,
910 or near, the WoS shelf break between 26-25 k yr BP (Stoker and Varming, 2011; Clark et al., 2018;
911 Hall et al., 2019; Ballantyne and Small, 2019; Bradwell et al., 2019). Notably, the Otter Bank sequence
912 displays mounded accumulations forming prominent seabed ridges (Stoker and Varming, 2011).

913 During glacial maxima, large ice sheets deposited thick sediment wedges (hundreds of meters) on the
914 continental slope. On the WoS slope, the prograding succession is primarily assigned to the Morrison
915 2 sequence, with a late to postglacial MacAulay sequence occupying the uppermost portion. Further
916 downslope from the Foula Wedge, the characteristic gully and basin floor fan systems imprinted in the
917 present-day seafloor suggests the lower slope experienced minimal sediment deposition, with most
918 material bypassing this area and accumulating across the basin area to form the triangular-shaped
919 complex glacigenic basin floor fan deposits, part of the distal Foula Wedge (Stewart and Long, 2012;
920 2016; Caruso et al., 2022).

921 Since the last glaciation and throughout the Holocene, the region has seen minimal terrestrial sediment
922 input. Seafloor sediments are linked to postglacial vertical rainout from meltwater plumes, including
923 ice-rafted debris and reworked Pleistocene sediments. Postglacial sedimentation is thought to be largely
924 controlled by ocean currents, with fully marine interglacial circulation established around 9,500 years
925 ago (Masson et al., 2004). Current sedimentation rates are typically less than 1 centimetre per thousand
926 years (Masson, 2001).

927 Notably, the southern WoS margin lacks significant head scarps or classic marine slides on the seafloor.
928 The large slides observed to the north and northeast of the Faroe Shetland basin are located within the
929 WSD slope body, with the Afen slide being a particularly well-studied example. Recent research
930 suggests that in low-angle, layered contourite drifts, specific sediment boundaries are more important
931 factors for slope failure than the overall slope geometry. The location of the Afen slide, free from
932 glaciogenic debris flows, suggests less influence from glacial activity on downslope sedimentation in
933 this region compared to the northern and southern ends of the FSC (Davison, 2004). This highlights the
934 contrasting depositional environments along the continental slope, resulting in distinct compositions of
935 the shallow sediments. In the Afen slide area the shallow sediments are dominated by bottom current-
936 related deposits which are considered a major preconditioning factor in past slope failures within the
937 region (Stoker and Varming, 2011; Gatter et al., 2020), similar to what has been observed on the
938 Norwegian margin (e.g., Storegga Slide; Bryn et al., 2005b;).



939
940 **Figure 2.19.** Seafloor image showing the glaciogenic debris flows the of Rona and Foula wedges adapted
941 from Stewart and Long (2016). Image derived from first returns from commercial 3D seismic surveys
942 (methodology in Bulat and Long 2001). Arrows indicate downslope slope gullies. BFF = Basin floor
943 fan, Ch = Channelised features, DA = Data artefact, DF = Debris fans, H = Hollow, IP = Iceberg
944 ploughmarks, SHC = Scour-hole complex. For location see Figure 2.10. Image British Geological
945 Survey © UKRI 2025.

3. Deglaciating continental margins: Processes

946
947
948
949
950
951
952
953
954
955
956
957
958

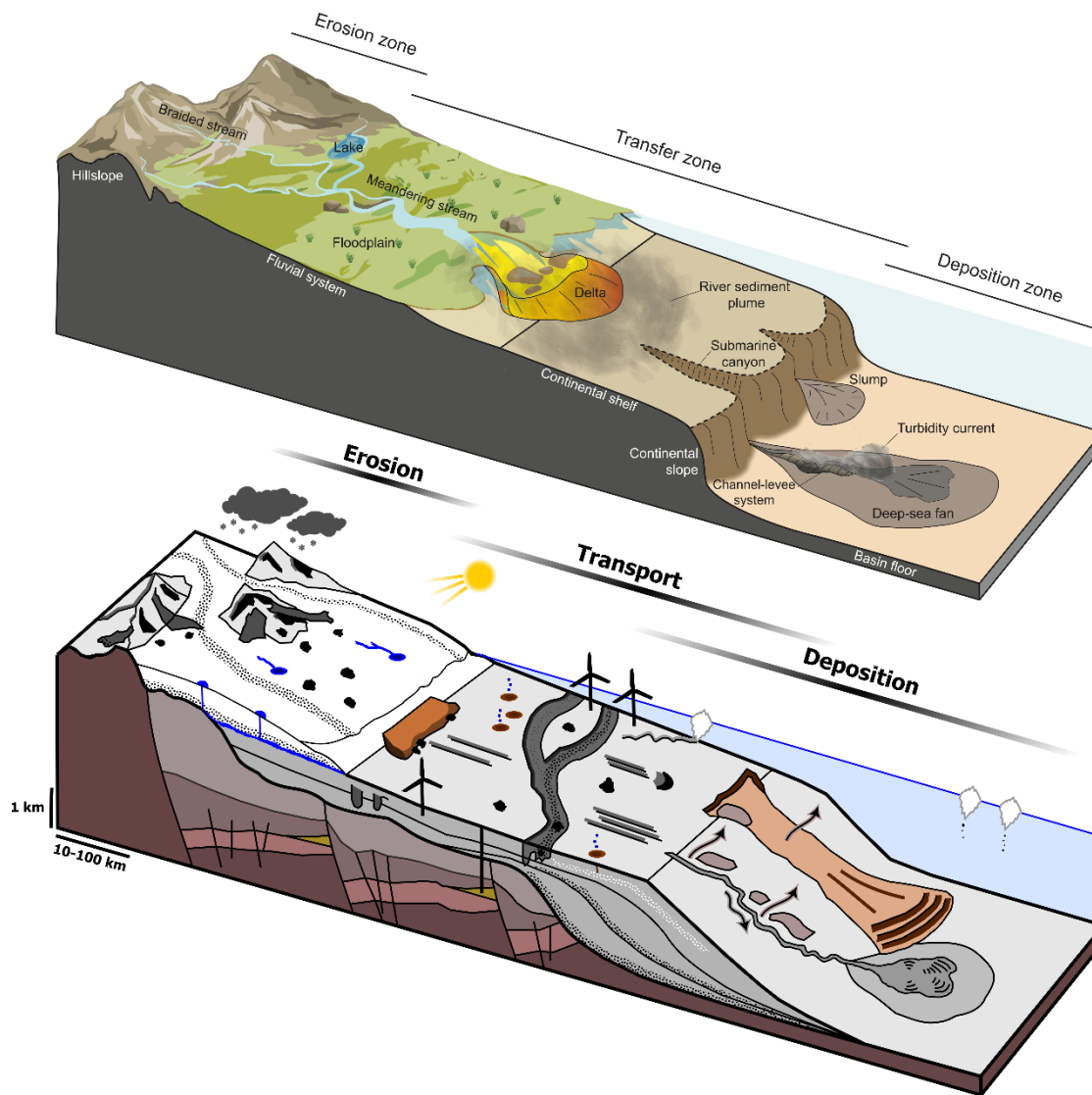
959
960
961
962
963
964
965
966
967
968
969
970

971
972
973
974

The glacial source-to-sink systems along the glaciating European margins are different compared to other sedimentary source-to-sink systems that do not account for glacial and ice-sheet processes as direct components of the system (Figure 3.1; Castelltort and Van Den Driessche, 2003; Vimpere et al., 2023). Sinks of the glacial source-to-sink system are diverse and time transgressive and include lakes, fjords, shelves, trough mouth fans, and ultimately the deep sea depending on the ice sheet or glacier catchment area and the concomitant ice margin position. (Figure 3.1). These sinks act as valuable archives for a variety of deposits during different parts of the glacial cycle (Figure 3.2; Sejrup et al., 1996). While lake and fjord basins record marine and glacio-marine sedimentation following ice retreat (Bellwald et al., 2016), they rarely preserve glacial tills recording subglacial conditions under the ice sheet. In contrast, ice-stream troughs on continental shelves, such as the Norwegian Channel in the North Sea or the Bear Island Trough in the Barents Sea comprise >70% glacial till, and are thus better archives for this type of glacial sediments (Figure 3.2; Sejrup et al., 1996).

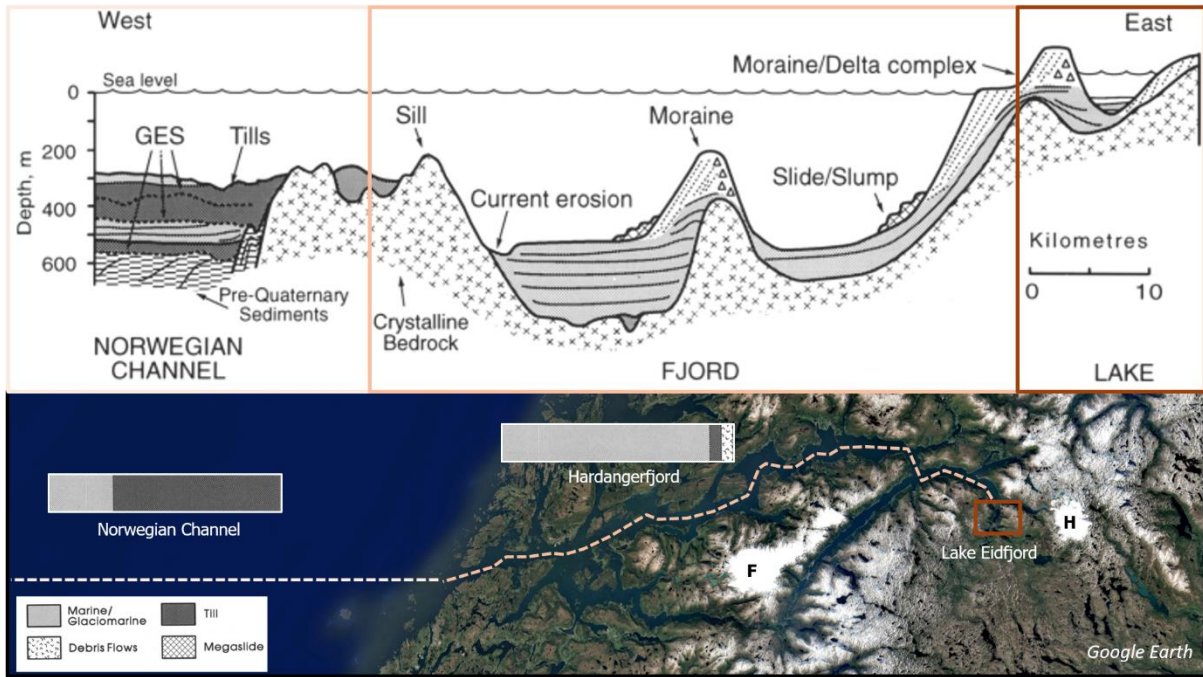
A wide variety of processes shaped the glaciating European margins, and in the following chapter, we discuss these processes throughout a glacial cycle, separated into glacial (incl. periglacial), deglacial, and interglacial time periods (Figure 3.3). Ice-sheet dynamics and hydrological evolution are crucial to define the interaction and (dis)connectivity of different systems. The ice-margin position of glaciers at a given time is an important location for the sedimentary activity as it can be used as an approximate location of a depocenter or a sink at a given time and which marks a boundary between lithological different sediments and landforms developed under and in front of the ice margin (Boulton, 1986, Kurjanski et al. 2020). For marine-terminating ice sheets, the location of the grounding line, defined as the transition from grounded into floating ice, is a key parameter for the study of processes and deposits. In glacial source-to-sink systems, significant changes in grain-size distribution, clast morphology, and mineral properties can occur on short lateral scales (<250 m; Kjær, 1999). The source-to-sink systems can further be modified during the engineering phase.

Bathymetric and side-scan sonar data allow for detailed reconstruction of processes shaping the seafloor, whereas conventional 2D/3D seismic, (ultra-)high-resolution 2D/3D seismic, and sub-bottom profiler data are commonly used to characterize landform assemblages buried by several meters of sediments (e.g., Dowdeswell et al., 2016; Hill et al., 2024).



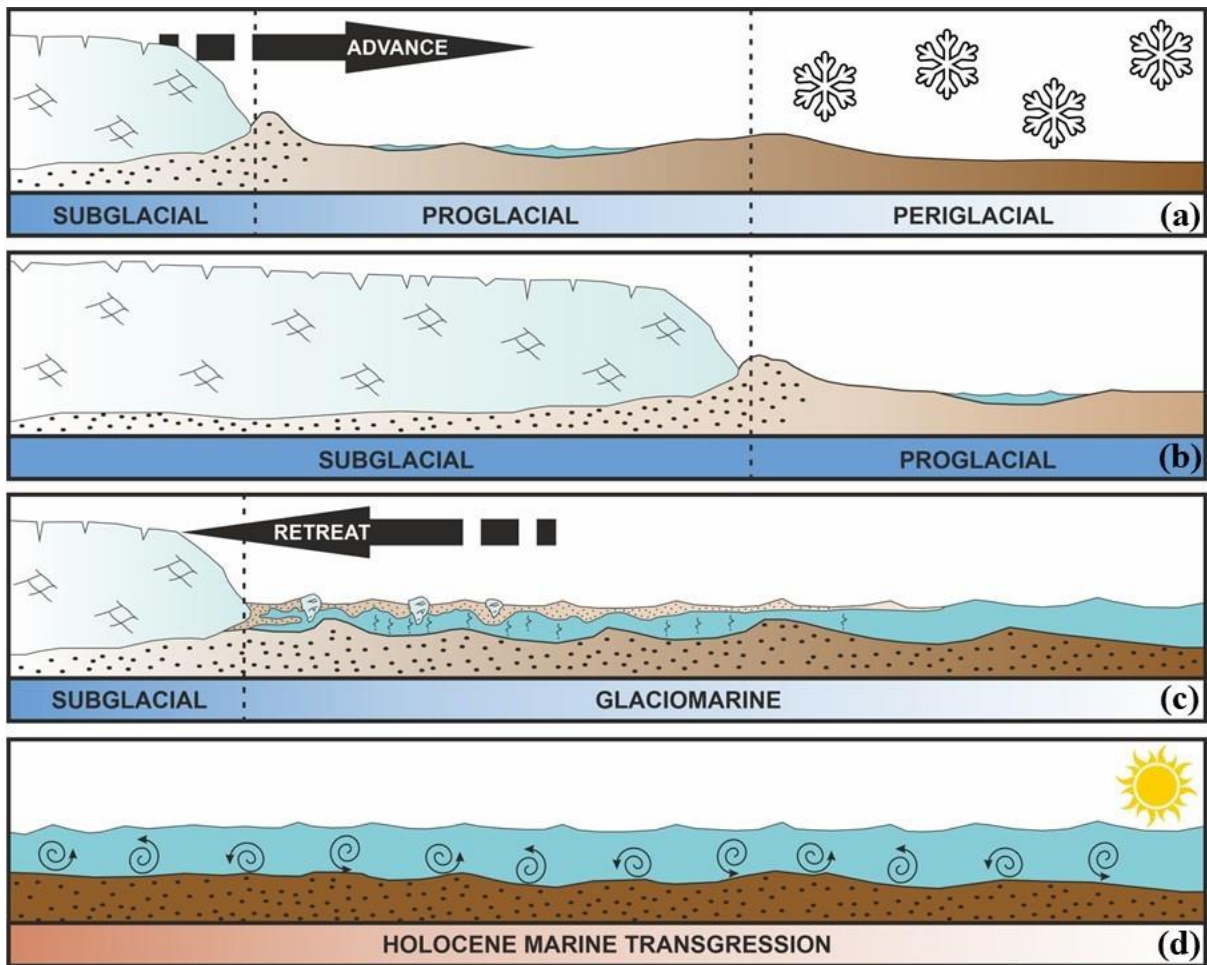
975

976 **Figure 3.1.** The concept of source-to-sink systems. Comparison of **a)** classical source-to-sink systems
 977 (from [Vimpere et al., 2023](#)) with **b)** glacial source-to-sink systems dominated by marine-terminating
 978 ice sheets (water depths >120 m).



979

980 **Figure 3.2.** The Hardanger fjord system in Western Norway and neighbouring Northern North Sea as
 981 a modern glacial source-to sink-system. Bars show the relative quantity of sediment types in different
 982 archives (after [Sejrup et al., 1996](#)). H: Hardanger Glacier, F: Folgefonna Glacier. Satellite image from
 983 GoogleEarth.



984

985 **Figure 3.3.** Processes and deposits during a glacial cycle. **a)** Periglacial. **b)** Glacial. **c)** Deglacial. **d)**
 986 Interglacial.

987 **3.1 Glacial**

988 At the onset of the cold climate, the ice sheets start to build-up and advance, and the sea-level drops,
 989 resulting in emerged platforms with occasional rivers forming proglacial fluvial channels (Prins and
 990 Andresen, 2019; Andresen et al., 2022). Large parts of presently submerged continental shelves of the
 991 study area were terrestrially exposed during the Pleistocene glaciations (Dimakis et al., 1998; Butt et
 992 al., 2002, Patton et al. 2017, Clark et al. 2022). During ice-sheet build-up, these platforms formed a
 993 periglacial environment dominated by the development of permafrost in the upper rock and soil units
 994 (Figure 3.3a). Climate was sufficiently cold to allow for freezing temperatures to propagate below the
 995 ground surface. Freeze-and-thaw processes often weakened the bedrock exposed to the atmosphere, and
 996 contribute to a bedrock weathering that commonly reaches depths of 5-10 m. However, in extreme cases
 997 where perennial freezing (scales of two yrs to hundreds of thousands of years or more) occurs,
 998 permafrost can propagate to subsurface depths of 1,500 m in temperatures of 0°C to ca. -24°C (Murton
 999 and Ballantyne, 2017).

1000 Erosion, transport and deposition of pre-existing sediments and bedrock occurred simultaneously during
1001 the build-up of these ice sheets (Figure 3.3b). The main subglacial processes are the accumulation of
1002 subglacial till and boulders as ice sheet grew and advanced as well as, glaciotectonic deformation at ice
1003 sheet margins, and reworking at the base of the ice streams. The interplay between subglacial erosion
1004 and deposition results in large vertical and lateral variability of soil properties through the glacial time
1005 period.

1006 During shelf-edge glaciations, ice streams rapidly deposited huge sediment quantities to the slopes
1007 (Hjelstuen and Sejrup, 2021). Sediment deposition on the slopes was dominated by submarine mass
1008 movements, such as glaciogenic debris flows downslope and contour currents alongslope (Nygård et al.,
1009 2005; Newton and Huuse, 2017). Contour currents are documented to be weakened during the glacial
1010 time period (Batchelor et al., 2021; Bellwald et al., 2024a). The tectonic stress field during glaciations
1011 was a different one compared to the modern stress field, with kilometers of ice covering the shelves (ice
1012 loading), and erosion and deposition resulting in a new sediment balance.

1013 Gas hydrates formed to subsurface depths of up to 200 m in regions with active hydrocarbon systems,
1014 such as the North Sea and the Barents Sea (Vadakkepuliambatta et al., 2017). Ice streams were locally
1015 frozen to the subsurface, and gas hydrates potentially acting as sticky spots (Winsborrow et al., 2016;
1016 Bellwald et al., 2023a).

1017 **3.2 Deglacial**

1018 Deglaciation is dominated by ice mass loss, either through iceberg calving (marine ice sheet margins)
1019 or ablation (marine and terrestrial ice sheets) (Figure 3.3c). Icebergs released from marine terminating
1020 ice sheets were often dragging their keels along the seabed forming a complex network of furrows
1021 known as iceberg ploughmarks. Subglacial meltwater discharge was enhanced during deglaciation and
1022 often resulted in erosion of tunnel valleys and meltwater channels subglacially on the continental
1023 shelves, as well as deposition meltwater turbidites on the continental slopes (Ó'Cofaigh et al., 2018,
1024 Bellwald et al., 2020; Garcia et al., 2024). The contour currents were still weakened during the deglacial
1025 time periods (Batchelor et al., 2021). As the ice margin stepped back from, the shelf edge during
1026 deglaciation the sediment sinks shifted from TMFs towards continental shelves, ice marginal and
1027 proglacial lakes, ponds, and kettle holes. Sediment distribution and sink areas were often constrained
1028 by previous glaciogenic landforms and pre-existing topography forming a series of backstepping mini
1029 basins constrained between the contemporaneous ice margin and former ice-marginal moraine. In some
1030 cases, catastrophic drainage of ice-dammed lakes formed outburst floods (Gupta et al., 2007; Høgaas
1031 and Longva, 2016). These outburst floods could transport boulders with diameters of up to 2 m and
1032 often produced erosive boundaries in the stratigraphic record. Otherwise in terrestrial setting, proglacial
1033 rivers acted as sediment conduits on these, then emergent, shelves (Bellwald et al., 2021). On the flat
1034 shelves, water was often not forced into one river channel, but formed braided river systems known also

1035 as sandar, which may have changed in time due to erosion of the riverbanks and variations in the amount
1036 of water.

1037 Glacio-isostatic rebound (see [Section 6.4](#)), and related seismic activity, started to increase, and likely
1038 reached its peak during deglaciation. In fjord systems, both terrestrial and marine slope instability was
1039 enhanced during at that time as the ice and permafrost support was removed. ([Bøe et al., 2004](#); [Böhme
1040 et al., 2015](#); [Hermanns et al., 2017](#); [Bellwald et al., 2019a](#)). Warmer waters resulted in the disintegration
1041 of gas hydrates, often documented by pockmarks and blow-out craters formed on deglacial surfaces
1042 ([Forsberg et al., 2007](#); [Andreassen et al., 2017](#); [Tasianas et al., 2018](#)).

1043 **3.3 Interglacial**

1044 During interglacials, the sea-level generally continued to rise, resulting in a marine transgression and
1045 full marine inundation of previously glaciated landscape but the sea relative sea level change was
1046 spatially variable as some areas experienced more isostatic rebound (cf. [Section 6.4](#)) ([Figure 3.3d](#); [Clark
1047 et al., 2022](#)). Postglacial channels are often found to be incised in regions with active discharge and
1048 shallow waters, resulting in an increase of terrestrial soil material especially during the interglacial
1049 transitions. As the Sea level was rising hydrodynamic forces acted on the unconsolidated, often
1050 terrestrially deposited, glacial substrate, remobilising and reworking the sediments in shallow marine
1051 environments. Sand banks, sand waves, and megaripples are common interglacial landforms on the
1052 shelf ([Bellec et al., 2019](#); see [Section 6.1](#)). The interglacial sedimentation of the slope is dominated by
1053 contourites, which are more active during interglacial time periods compared to their glacial
1054 counterparts ([Batchelor et al., 2021](#)). Several megaslides removed sediments from the upper slope into
1055 the deeper basins ([Solheim et al., 2005a](#); [Hjelstuen et al., 2007](#)). Tsunami deposits are reported for some
1056 of these megaslides ([Bondevik et al., 2005a](#); [2005b](#)). Most of the glacio-isostatic rebound and
1057 subsidence is completed in interglacial periods. However, rebound-related earthquakes are still reported
1058 as a potential trigger mechanism for submarine slides in interglacial times ([Bellwald et al., 2019a](#)) and
1059 slope instabilities in fjord systems ([Sørensen et al., 2023](#)).

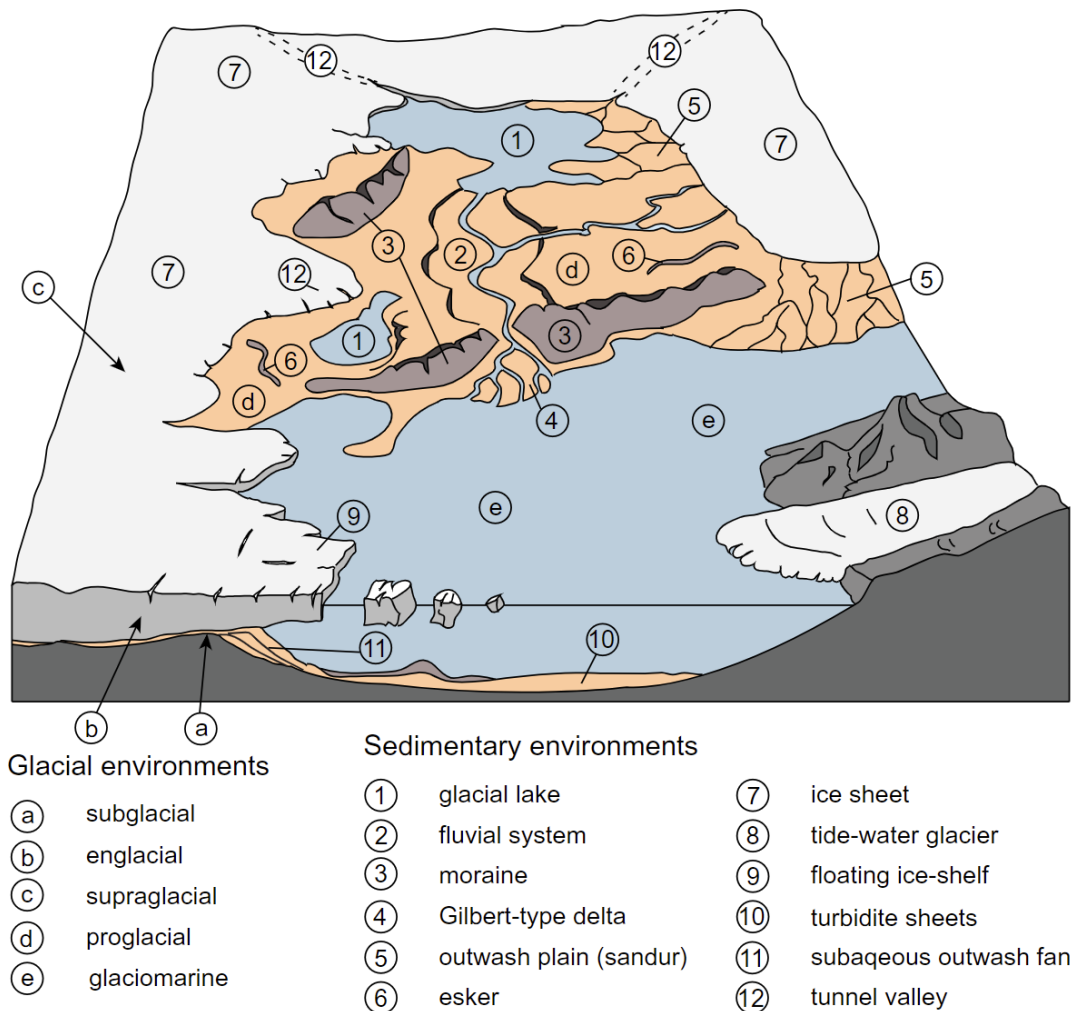
1060 **3.4 Land-sea correlations and modern analogues**

1061 The shelves within the study area have water depths of up to 400 meters. During the Pleistocene
1062 glaciations, most of these shelves represented a different sedimentary environment, with ice directly
1063 delivered into proglacial terrestrial and glaciomarine settings (e.g., [Walker et al., 2024](#)). A sketch
1064 summarizing glacial environments and sedimentary environments is shown in [Figure 3.4](#).

1065 The Barents Sea, with water depths of 200-400 m, was in the Early Pleistocene a subaerial platform
1066 ([Dimakis et al., 1998](#); [Butt et al., 2002](#)), most likely having similar sedimentary environments as the
1067 North Sea in the Late Pleistocene ([Bellwald et al., 2024a](#)). Environments similar to these paleo-shelves
1068 occur today in SE Iceland, Svalbard, Alaska, Greenland, Patagonia, and Antarctica ([Figure 3.5](#)). It is
1069 beneficial to use outcrops of such settings as modern analogues, and terrestrial outcrops allow

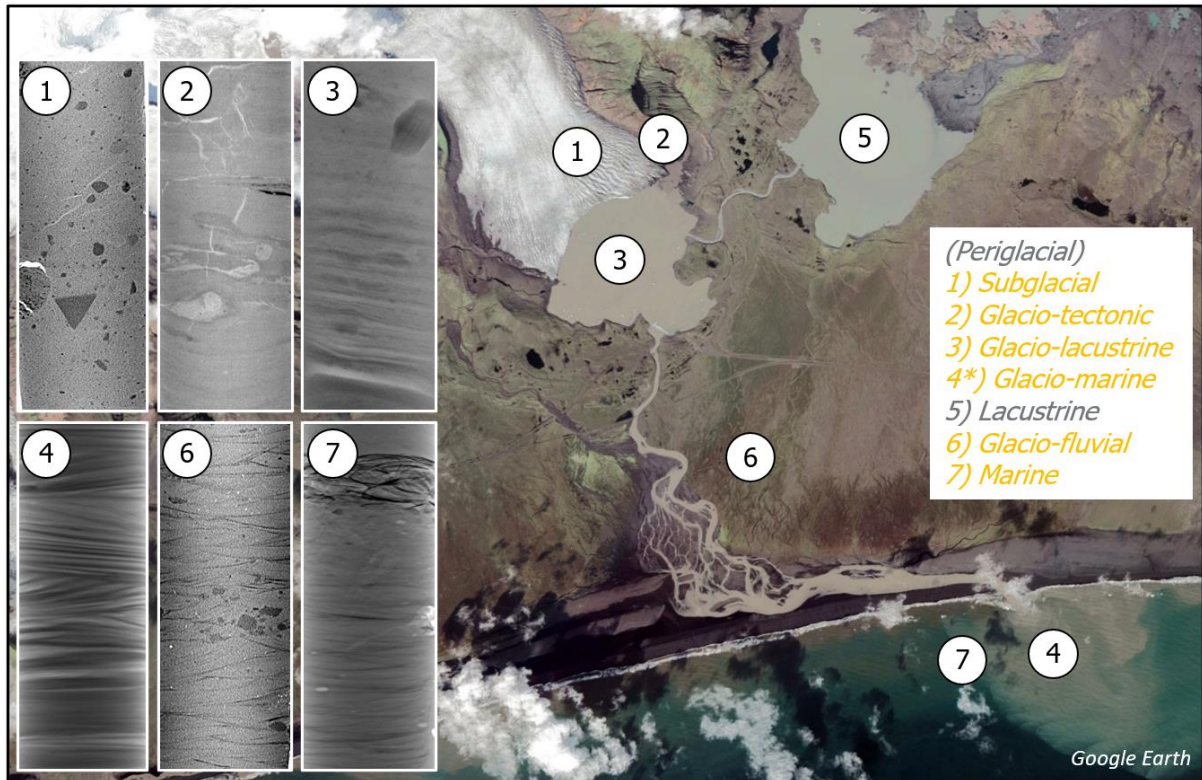
1070 correlations with less accessible submarine (and potentially buried) landscapes (Figure 3.6). Sediments
 1071 recovered from present-day submarine environments are valuable archives for the Quaternary evolution
 1072 of the area (Figures 3.6 and 3.7).

1073 Landforms, sediments and associated structures, as well as fossils are all proxies that allow conclusions
 1074 on time periods during which long-term observations are lacking. For instance, the well-preserved ice-
 1075 marginal geomorphology is beneficial in order to localize the development site in relation to the palaeo-
 1076 ice margin and predict possible depositional domains based on the understanding of processes unique
 1077 to areas under the ice, at the margin, and in front of it. Diatoms and mollusc can be used to provide
 1078 chronological correlation and ultimately help to define the paleogeographic environment and site
 1079 stratigraphy. Recovered sediments and glacial erratics originating from different provenances allows
 1080 the separation of river/ice-sheet systems and definitions of catchment areas.



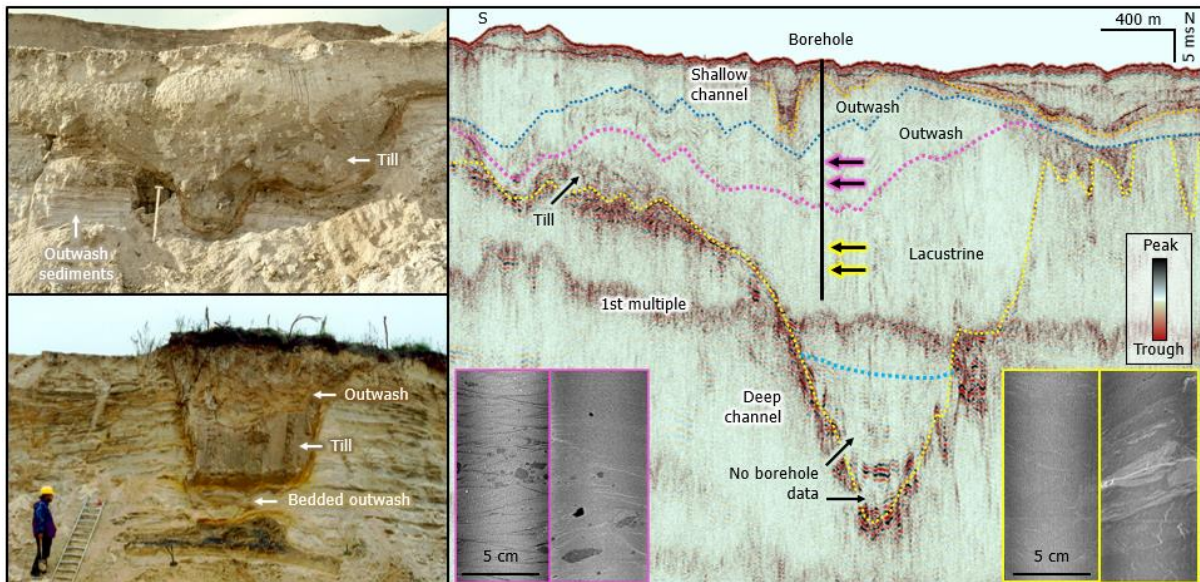
1081

1082 **Figure 3.4.** Glacial environments (from Huuse et al., 2012).



1083

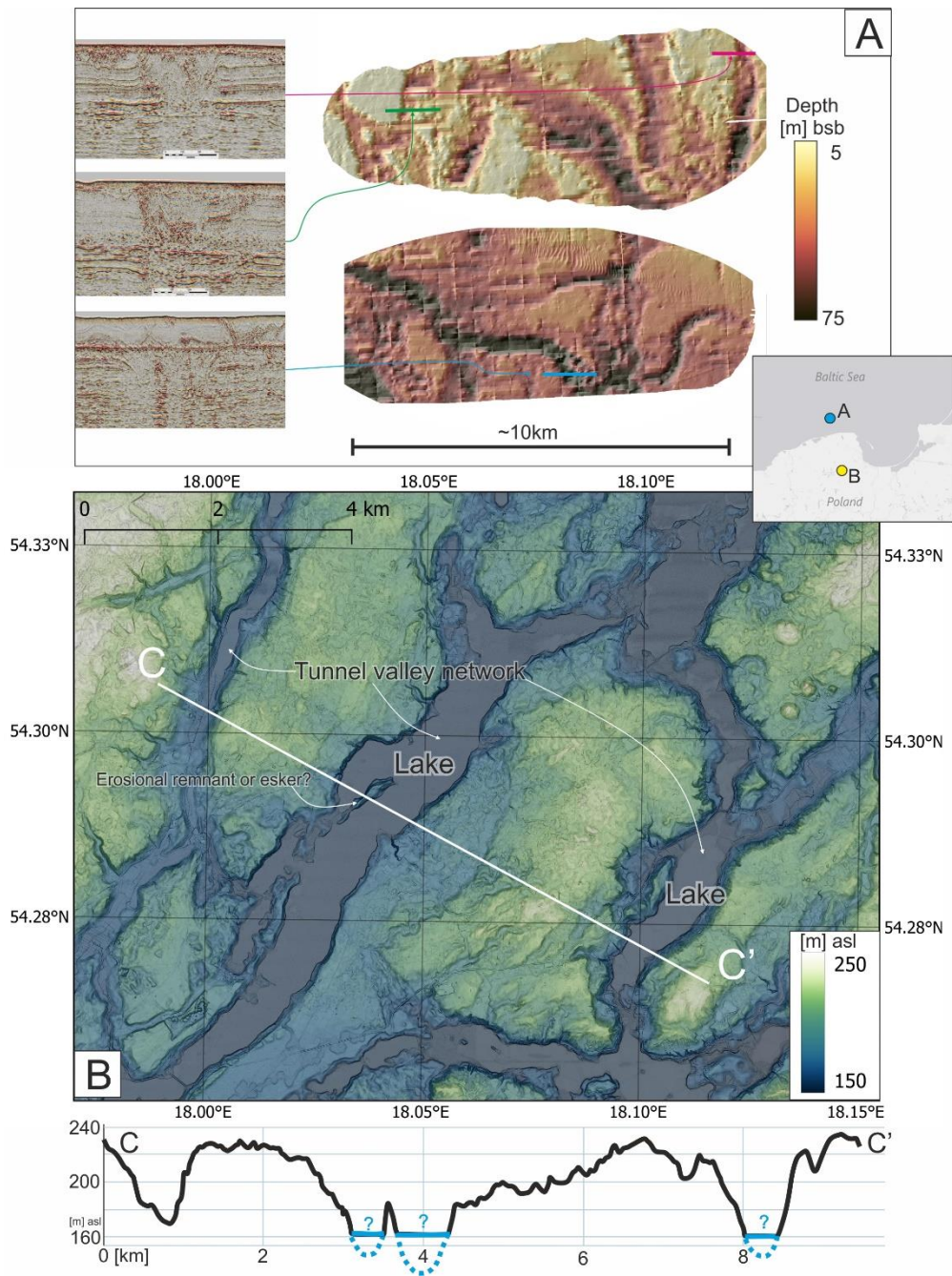
1084 **Figure 3.5.** Modern terrestrial environments as analogues for sedimentary units identified in subsurface
 1085 data from the marine domain of the glaciated European margins. Satellite image shows Fjallsárlón, SE
 1086 Iceland. Computer tomography imagery from different Offshore windfarm projects of the glaciated
 1087 European margins.



1088

1089 **Figure 3.6.** Integration with outcrops to further advance the geological understanding of offshore
 1090 windfarm sites (from Bellwald et al., 2023b). a) Infilled subglacial channel at Brügg (N Germany). b)
 1091 Infilled subglacial channel at Welzow South (E Germany). Both photos by Jan Piotrowski. c)
 1092 Expression of an infilled subglacial channel on UUHR seismic profile of the Southern Baltic Sea.

1093 Computer tomograph images show sedimentary structures of different glacial sequences (pink:
 1094 outwash, yellow: lacustrine).



1095

1096 **Figure 3.7. a)** Tunnel valleys mapped within the subsurface across an OWF site in the Southern Baltic
 1097 in the Slupsk Bank area. All valleys are fully filled with sediment leaving no expression at the seabed.
 1098 **b)** Underfilled tunnel valleys on land in Northern Poland shown in 1 m resolution lidar dataset. Lakes
 1099 are currently filling the overdeepened valleys. Both images are comparable in scale. Note the
 1100 similarities in dimensions and morphologies between tunnel valleys in both locations.

1101 **4. Deglaciaded continental margins: Deposits**

1102 Processes described in [Section 3](#) produced a diverse, and laterally and vertically heterogeneous,
1103 complex depositional record on formerly glaciated European continental margins as well as a rich
1104 variety of geomorphic features at the seabed and within the subsurface (e.g., [Newton et al., 2024a](#),
1105 [Kurjanski et al. 2020](#)). Typical sedimentological and geotechnical characteristics of the different glacial
1106 and interglacial facies observed along the glaciated European margins, and their potential engineering
1107 implications are presented in [Table 4.1](#). Note that that the description of ‘typical’ deposits for a given
1108 area or environment is a generalisation aiming to characterise most of the sedimentary package. Small-
1109 scale or local variations of grainsize, lithology or geometries within depositional environments are
1110 normal and should be expected.

1111 **4.1 Deposits of the shelves**

1112 The deposits of the shelves can range significantly in thickness ([Fjeldskaar and Amantov, 2018](#);
1113 [Hjelstuen and Sejrup, 2021](#); [Newton et al., 2024](#)). They can be absent or very thin when bedrock is
1114 close to the seabed but also can form basin fill often >100s of meters thick if accommodation is
1115 available. In such cases, for example in the North Sea, Quaternary sequences can be traced and
1116 correlated regionally for long distances ([Figure 4.1](#)). The deposits affected by ice loading and bulldozing
1117 can be overconsolidated and glacio-tectonically deformed, having high strengths. The sediments of the
1118 shelf are in general more coarse-grained, and boulders and gravel beds can frequently occur when
1119 compared to deposit accumulated along the slopes and within trough mouth fans. Although the glacial
1120 sediments of the shelf tend to be less sorted than deposits compared to sediments from other
1121 environments (e.g. shallow marine, fluvial, etc), in certain glacial environments, the sorting can be
1122 good: For example, the clean sands of an outwash fan deposited by the Norwegian Channel Ice Stream
1123 form the Peon discovery, one of the largest gas discoveries of the North Sea ([Bellwald et al., 2022b](#);
1124 [Figure 2.6](#)). The organic content is enhanced in shelf deposits compared to the deeper waters of the
1125 slopes, and decomposition of this material can often result in shallow, biogenic gas generation and
1126 accumulations frequently observed as acoustic blanking in shallow subsurface seismic data ([Arosio et
1127 al., 2018](#)).

1128 Lacustrine deposits form in closed basins isolated from the global ocean and saltwater input or within
1129 localised depressions within formerly terrestrially exposed shelves. These lacustrine deposits mainly
1130 consist of clays with dropstones delivered by icebergs, have a low to medium shear strength, and can
1131 be laminated or varved as a result of seasonal changes in sedimentation rates and energy within the
1132 environment. Glacio-fluvial channels frequently observed to be cut into the subsurface neighboring the
1133 lake environments. The channels cut by glacially-fed rivers are hotspots of complex infill, with multiple
1134 cut-and-fill sequences commonly preserved filling the incision. The channel infill can have all types of
1135 seismic facies, and shear strengths vary from low to very high.

1136 On formerly terrestrially exposed glaciated shelf's, large meltwater outflows with suspended sediment
1137 load and bedload of proglacial streams and rivers typically resulted in the deposition of extensive, gently
1138 sloping outwash plains known by the Icelandic term sandar (singular sandur). The deposits regionally
1139 are characterized by a general fining grainsize trend in a downstream direction which may not be evident
1140 locally as erosional nature of periodical/ seasonal high flows could result on removal of finer fractions
1141 and transport of coarser material further downflow. Fluvial deposits are often marked as a regional
1142 planar unconformity, with a prograding geometry and dipping reflections in all directions.

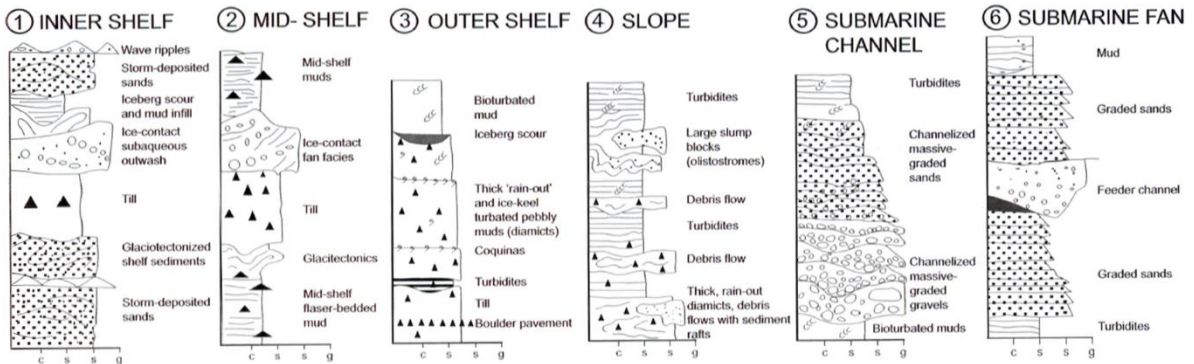
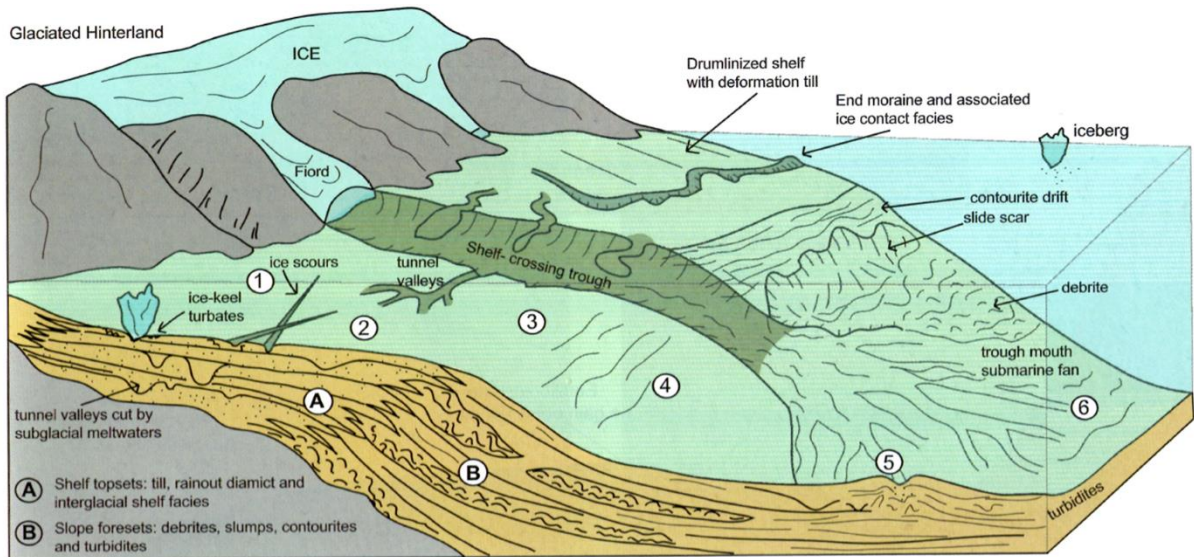
1143 **4.2 Deposits of the slopes**

1144 The deposits of the continental slopes are dominated by down-slope processes (turbidites, debris flows,
1145 landslides, and along-slope processes (contourites) that often are trackable for several 10s of kilometers
1146 (e.g., [Rydningen et al., 2020](#)). These deposits often form several kilometers-thick sequences ([Figure](#)
1147 [4.2](#); [Hjelstuen and Sejrup, 2021](#)) sediments better sorted and more fine-grained compared to the deposits
1148 of the shelf.

1149 Turbidites can bypass parts of the slope or deposit sediments, and form normally graded sediment
1150 sequences (vs. inverse grading of contourites). The turbidites consist of muddy sand ([Bellwald et al.,](#)
1151 [2024a](#)) up to sandy mud. Glacigenic debris flows have often a lens-shaped, homogenous facies in cross
1152 sections and lobate shapes in planar view ([Laberg and Vorren, 2000](#); [Nygård et al., 2005](#); [Løseth et al.,](#)
1153 [2020](#)). These debris flows are mud-dominated ([Baeten et al., 2014](#); [Bellwald et al., 2024a](#)). Landslides
1154 mainly consist of removed material of previously deposited debris flows and turbidites ([Barrett et al.,](#)
1155 [2021](#)). Contourites are enriched in mud, and have occasional sands ([Baeten et al., 2014](#); [Batchelor et](#)
1156 [al., 2021](#); [Bellwald et al., 2022b](#); [2024a](#)). Turbidites and debris flows are sudden and quick processes,
1157 remobilizing sediment downslope including sharp erosive contacts. Contourites are rather inversely-
1158 graded, compared to the normally graded turbidites. Contourites can have classical mounded geometry
1159 ([Rydningen et al., 2020](#)), but can also be more sheeted (e.g., sand sheets in Bear Island Fan) and filling
1160 megaslide escarpments (e.g., North Sea Fan; [Garcia et al., 2024](#)). Contourites are formed by continuous
1161 and slow processes (compared to turbidites and debris flows) and accumulate as sediment mounds or
1162 drifts along-slope in a rather continuous trend with gradational internal grainsize changes ([Rydningen](#)
1163 [et al., 2020](#); [Batchelor et al., 2021](#); [Bellwald et al., 2024a](#)).

1164 Boulders, cobbles and gravels dropped by meltout from icebergs (often referred to as ice rafted debris;
1165 IRD) are more commonly identified on the paleo-shelves but can also be deposited along the slopes of
1166 the NE Atlantic Ocean. Boulders are very few to absent on the slopes.

1167



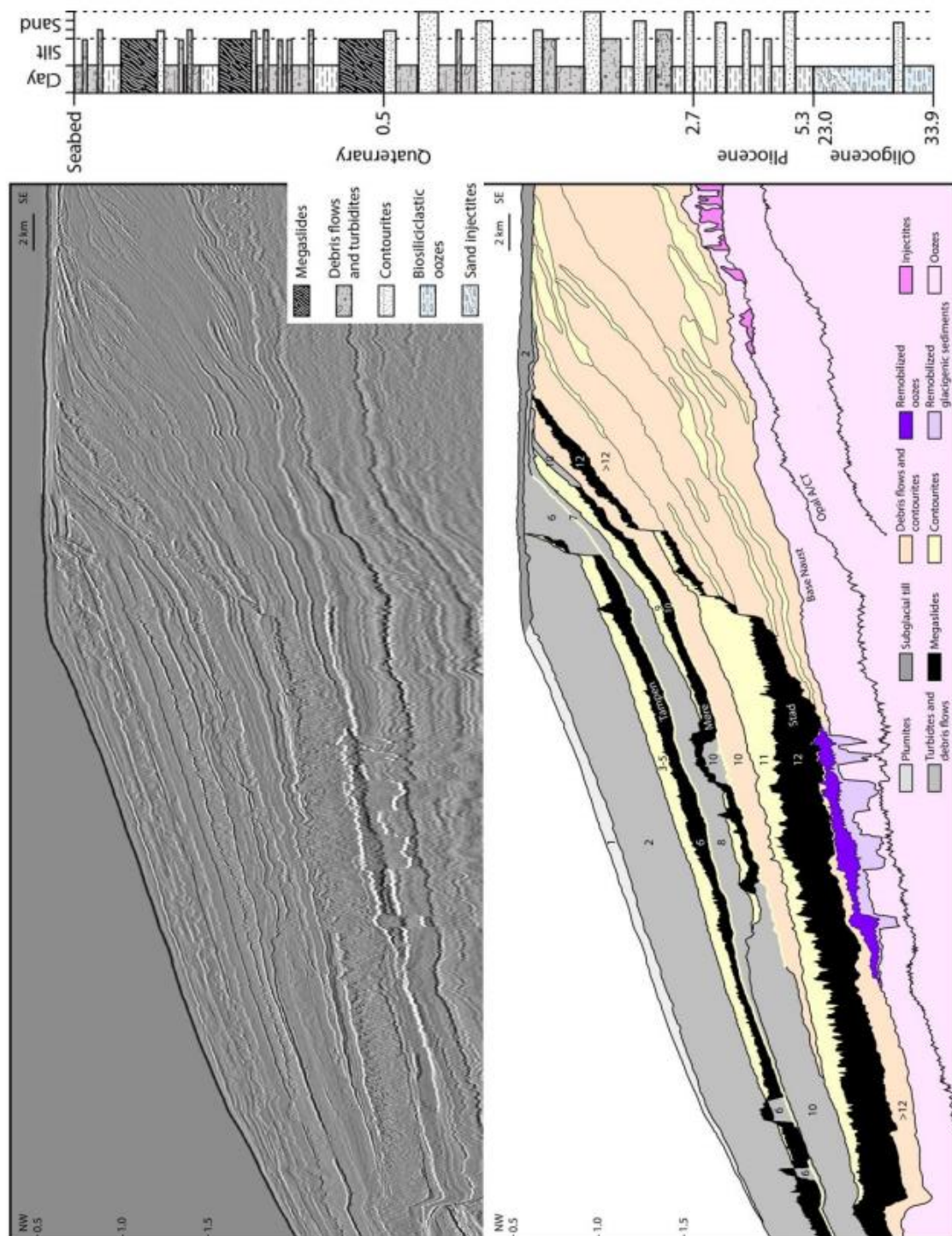
1168

1169

1170

1171

Figure 4.1. Cartoon showing the typical sedimentological characteristics associated with different proximities and relationships with the retreating ice sheet margin. Figure modified from Eyles and Eyles (2010).



1172

1173 **Figure 4.2.** Stratigraphy and lithology of the North Sea Fan. Seismic profile across the fan with
 1174 representative well log. Numbers indicate marine isotope stages (MIS) for different sedimentary units
 1175 (updated from [Nygård et al., 2005](#)). Data courtesy of TGS.

1176 **Table 4.1.** Typical sedimentological and geotechnical characteristics of the different glacial, deglacial, and interglacial facies observed along the glaciated
1177 European margins, and their potential engineering implications. Stage indication based on likelihood of formation during an ice advance (*Glacial*), retreat
1178 (*Deglacial*) or *Interglacial* conditions. Facies description ordered based on their prevailing stage of formation (from glacial to interglacial). Wording in bold
1179 indicates main stage of formation, whereas wording in parentheses as potential stage when such facies can be formed but are less prevalent. *Oversteepening,
1180 sediment delivery, and location within source-to-sink system are key.

| Facies Type | Stage | Sedimentology and Structure | Geotechnical Characteristics | Engineering Implications |
|---|------------------------------------|---|--|--|
| Till (e.g., traction, lodgement, and deformation) | Glacial (Deglacial) | <ul style="list-style-type: none"> Contains a wide range of particle sizes, including clay, silt, sand, gravel, and boulders (often gravely, matrix-supported clay). Often unstratified and unsorted to poorly sorted. Can show large variations over short distances. May contain large boulders (erratics) and incorporated rafts of pre-existing sediments or bedrock New and overridden sediments may contain faults and folds from cm- to km-scale. | <ul style="list-style-type: none"> Generally, very low permeability, high density, variable strength (often very high to extremely high shear strengths). Variable compressibility but often highly overconsolidated. Can be highly heterogenous. Traction till can be much softer compared to lodgement till. Deformed tills have heterogenous properties. | <ul style="list-style-type: none"> Challenging for construction due to potential inconsistency due to variable composition. Difficult to excavate. Requires thorough site investigation and may require ground improvement techniques. Often challenging to map transition from till into weathered or competent bedrock. Potential for boulders. Lithology within tills can vary significantly. |
| Ice-contact (e.g., against ice margins) | Glacial Deglacial | <ul style="list-style-type: none"> Range from till (e.g., potentially boulder-rich) to sorted sands, gravels, cobbles and even boulder beds/units. Heterogeneous due to direct ice contact. Show often evidence of deformation and compaction due to ice push. Dimensions: Typically, more continuous parallel to the palaeo-ice margin and forming sets of distinctive discrete sediment belts or ridges. From 1m in height and width (for example small push moraines) up to 100s-1000m wide and 10s m high complex ice marginal systems deposited when ice oscillated/stagnated in one location for a longer time. | <ul style="list-style-type: none"> Variable permeability. Compressibility and strength dependent upon level of overconsolidation. | <ul style="list-style-type: none"> Can provide excellent foundations, but variable strength requires thorough site investigation and potential ground improvement. Challenging due to variable material properties and potential for encountering deformed layers. |
| Glacioaeolian | Glacial (Deglacial) | <ul style="list-style-type: none"> Well sorted fine sands and silts, which can be homogeneous in extensive deposits. Can show regular stratification and layering. Shows often extensive sorting and rounding. Loess covers: Mixed quarts and feldspar silt grade deposits | <ul style="list-style-type: none"> Variable permeability. Variable compressibility. Strength can vary significantly. | <ul style="list-style-type: none"> Poor foundation material due to potential for erosion, low strength and high compressibility. Requires additional considerations for techniques and monitoring during construction. |
| Supraglacial | Deglacial (Glacial) | <ul style="list-style-type: none"> Primarily coarse debris composed of a mix of poorly sorted particle sizes from clay to boulders. Poorly stratified, chaotic; may have melt features. | <ul style="list-style-type: none"> Low to moderate permeability. Variable compressibility. Variable strength due to heterogeneity. | <ul style="list-style-type: none"> Often unstable, difficult to excavate and may require further considerations during site development. |

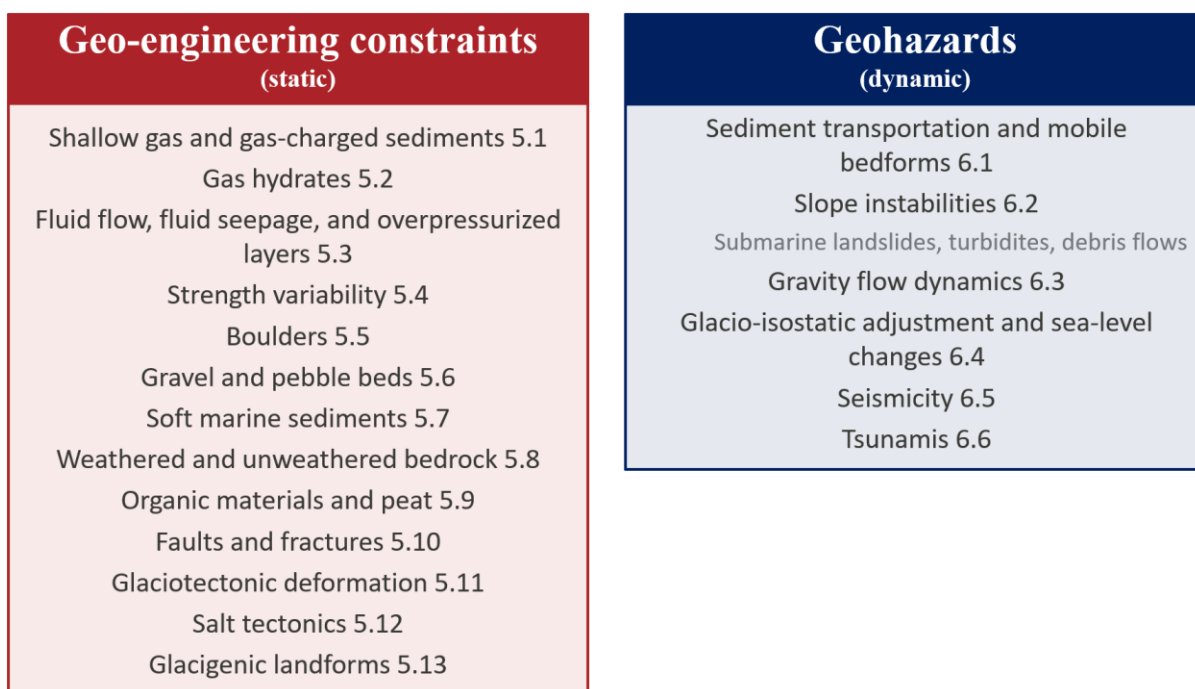
| | | | | |
|--|---|---|--|---|
| | | <ul style="list-style-type: none"> Shows often evidence of debris flows. | | <ul style="list-style-type: none"> Requires extensive site investigation due to heterogeneity and potential instability. |
| Glaciofluvial | Deglacial (Glacial) | <ul style="list-style-type: none"> Composed primarily of sands and gravels with minor silts and clays. Stratified, cross-bedding, ripples and foresets. Can show evidence of high-energy water flow. Multiple, clear erosive surfaces. Esker: Subglacial/englacial channel fill consisting of (sometimes sheeted) gravel, cobble and boulder-sized sediments and sands | <ul style="list-style-type: none"> High permeability, good bearing capacity. Low compressibility, high (low to very high) shear strength. Has typically good drainage properties. Eskers: Presence of boulders. | <ul style="list-style-type: none"> Generally good foundation material due to good bearing capacity. Requires assessment of stratification and compaction / degree of consolidation. Stacked sequences of cut-and-fill is a challenge for ground models. Eskers: Steep slopes, discrete, lateral variability, curvilinear and irregular zones of coarse sediment in ridges with steep slopes; cable trenching and pile driving may be difficult. |
| Glaciomarine | Deglacial (Glacial) | <ul style="list-style-type: none"> Often composed of silts and clays with interbedded sands and gravels. Can be laminated and may contain dropstones and ice-rafted debris. May show evidence of tidal influences. Can contain marine fossils and organic material. | <ul style="list-style-type: none"> Variable permeability. High compressibility and shear strength. May have elevated pore water pressures. Potential for gas hydrate presence. | <ul style="list-style-type: none"> Variable properties requiring site investigation. Potential instability from dropstones or gas hydrates. Intercalation with impermeable layers can weaken shear strength if overpressured. |
| Glaciolacustrine and lacustrine | Deglacial (Glacial) (Interglacial) | <ul style="list-style-type: none"> Sands, silts and clays, may contain dropstones. Laminations or varves create regular stratification. Organically enriched sediments and peats are likely to be associated with glaciolacustrine deposits | <ul style="list-style-type: none"> Low permeability, low to medium strength if fresh, high or very high strength when dried out or overconsolidated. High compressibility due to clay content. Low shear strength and low densities. Very high compressibility of organic rich sediments and peats when present within the sequence. | <ul style="list-style-type: none"> Poor foundation material due to high compressibility and low shear strength. Requires significant ground improvement. Requires careful drilling and monitoring. Variable strengths: From very soft/weak (soil-profile inversion in geotechnical terms) in their primary form to extremely hard and over-consolidated after being subject to subaerial exposure and drying or subsequent loading depending on site evaluation. Possible issues with slope instability or unstable trench sides Thermal properties of clays and organic rich strata may negatively impact installation process and power cable heat dissipation (high thermal resistivity) |
| Turbidites | Deglacial (Glacial) (Interglacial) | <ul style="list-style-type: none"> Well sorted, normal grading; consist of sand, silt, and mainly clay. May have sharp basal contacts, rip-up clasts, and flame structures. | <ul style="list-style-type: none"> High to moderate permeability. Shear strength and compressibility varies depending upon the dominant grain size. | <ul style="list-style-type: none"> Grading can impact load-bearing properties of the sediments. Potential for reactivation of turbidity currents and further erosion and/or deposition. |

| | | | | |
|-------------------------------------|--|---|--|---|
| Debris flows and slides | Deglacial* (Glacial*) (Interglacial*) | <ul style="list-style-type: none"> • Poorly sorted, deformed, and consist of sand, silt, and mainly clay, with occasional boulders. • Slide deposits often consist of reworked debris flows, including glaciogenic debris flows. • Can occur at a wide range of scales, including megaslides (e.g., Storegga). | <ul style="list-style-type: none"> • Low to very low permeability. • Chaotic structure, with random clast orientations leads to highly heterogeneous properties. • May contain variable levels of pore water content. • Low shear strengths and high compressibility. | <ul style="list-style-type: none"> • High water content may promote further mobility and flow behaviour of deposited sediments. • Potential for further debris flows or slides in the source area need to be considered. • Deposited materials may prevent fluid migration and elevate subsurface pore water pressure. |
| Fluvial and deltaic | Deglacial Interglacial | <ul style="list-style-type: none"> • Well-sorted sands and gravels with interbedded silts and clays. • Structures may include cross-bedding, channel fills, and point bars. | <ul style="list-style-type: none"> • Permeability and compressibility depend on dominant grain size and sorting. • Moderate to high shear strength in coarser deposits. | <ul style="list-style-type: none"> • Generally good foundation material but surveying is required to map heterogeneity of deposits. • Potential for subsidence of finer grained overbanks. |
| Contourite | Interglacial (Deglacial) | <ul style="list-style-type: none"> • Typically consist of well-sorted clays, silts and fine sands. • Commonly exhibit lamination and bioturbation. • May show features such as graded or inversely graded bedding, indicative of fluctuating current velocities. | <ul style="list-style-type: none"> • Moderate permeability due to the well-sorted nature of the sediments. • Shear strength can vary depending on sediment composition and degree of consolidation. | <ul style="list-style-type: none"> • Structures built in areas with active contour currents need to account for erosion and sediment reworking. • Fine-grained layers within contourites can pose issues for slope stability and consolidation (forming weak layers). |
| Marine | Interglacial | <ul style="list-style-type: none"> • Typically consists of well-sorted fine-grained materials, dependent on distance from the coast. • Often display laminated bedding. • May contain bioturbation. | <ul style="list-style-type: none"> • Compressibility and permeability are grain size dependent. • Often show low degree of overconsolidation • Typically, homogenous clay/silt but may grade to sands closer to the coast. • High pore water content. • Low density | <ul style="list-style-type: none"> • Can have well known geotechnical properties that lowers site investigation requirements, but still requires study. • Structures may need to consider potential winnowing/erosion of marine sediments. • Can be issues with slope instability / unstable trench sides |
| Organic-rich sediments /Peat | Interglacial | <ul style="list-style-type: none"> • Decomposed plant material and organic matter. • Often displays a fibrous structure with visible plant remains, arranged in layers. • May contain inorganic/lithic materials. | <ul style="list-style-type: none"> • Generally, very low shear strength due to high levels of organic content. • Geotechnical properties vary depending on the magnitude of peat decomposition and compression. | <ul style="list-style-type: none"> • Potential for stored gases. • Possible settlement over time and unsuitable for heavy structures without ground improvement. • Low thermal conductivity (overheating of cables). • Low load bearing capacity (implications for cable trenching and installation process) |
| Periglacial | Interglacial | <ul style="list-style-type: none"> • Primary sediments altered by freeze-thaw cycles and permafrost processes. • Ice wedge casts filled downwards with sediments from overlying strata forming thermal contraction polygons | <ul style="list-style-type: none"> • Laterally heterogeneous sediment properties • Weakened primary rock/ sediment strength due to frost weathering • Overconsolidation due to drying of sediments in cold conditions | <ul style="list-style-type: none"> • Poorly predictable sediment properties and load bearing capacity. • Discrete zones of different engineering sediment properties within ice-wedge casts. • Base of frost-weathered zone may be difficult to identify from boreholes and geophysical data |

1182 **5. Geo-engineering constraints**

1183 A geo-engineering constraint is here defined as an existing, static ground feature that poses an
1184 engineering challenge and that is addressed by routine geo-engineering solutions (see also ISO 19901-
1185 10). Geo-engineering constraints are dominated by static features, landforms, and deposits, whereas
1186 geohazards are more dynamic processes that can affect these static features (Figure 5.1). Glacial
1187 deposits are thus geo-engineering constraints, but can develop into a geohazard when triggered and
1188 affected. However, if these constraints are identified, mitigation is in general feasible. For instance,
1189 shallow gas is a geo-engineering constraint as it is static.

1190 This chapter reviews geo-engineering constraints characteristic for deglaciated continental margins. It
1191 is separated into sections related to fluids in the subsurface (Sections 5.1-5.3), effects of changes in
1192 grainsize distribution and lithology (Sections 5.4-5.7), the effect of weathering and presence of bedrock
1193 (Section 5.8), the presence of organic materials and peat (Section 5.9), subsurface features formed by
1194 tectonic processes (Sections 5.10-5.12), and glacial landforms (Section 5.13).



1195
1196 **Figure 5.1.** Geo-engineering constraints and geohazards along the glaciated European margins included
1197 in this review.

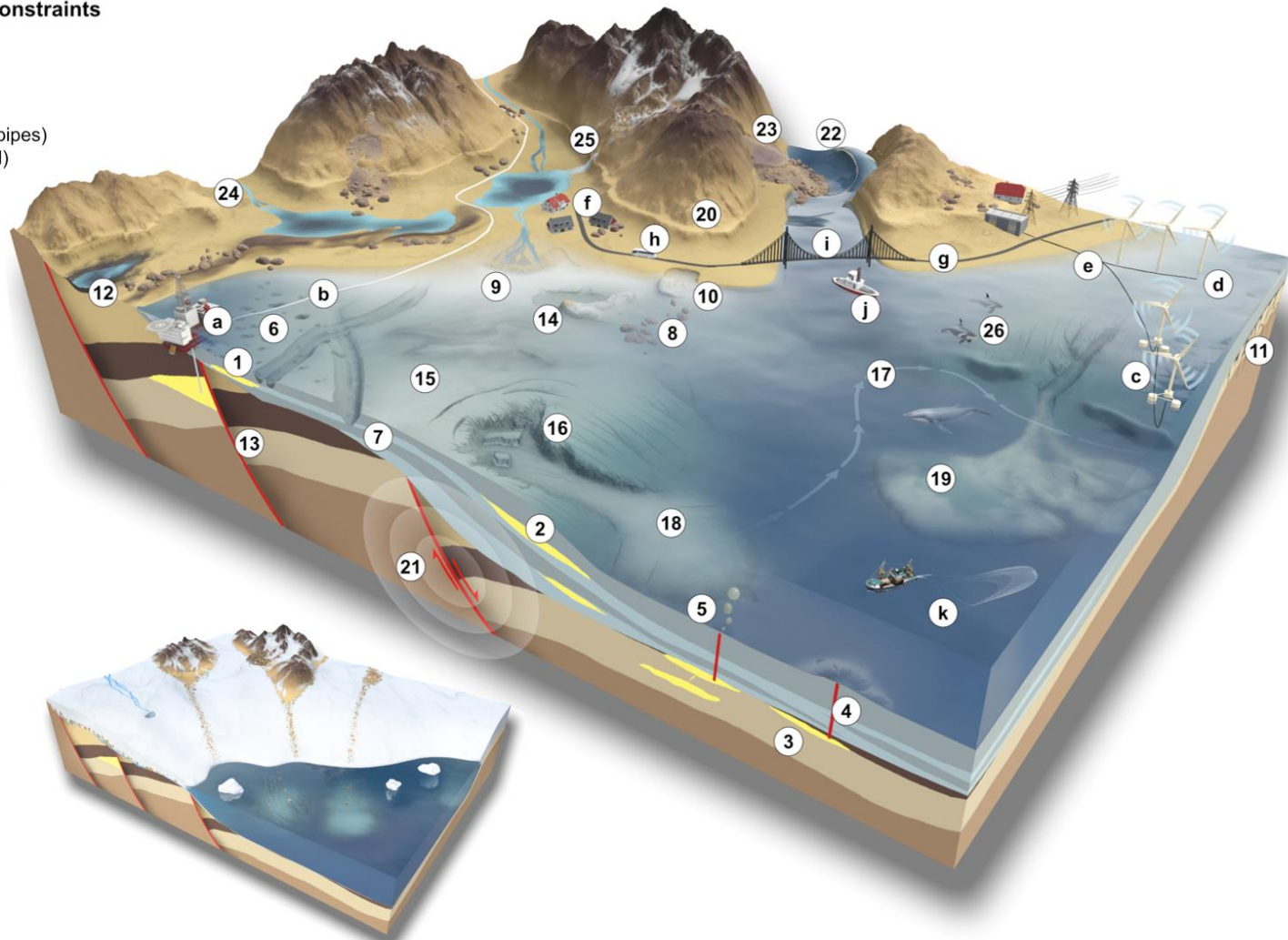
1198

Geohazards/Geo-engineering constraints

- 1 Shallow gas
- 2 Gas hydrates
- 3 Overpressurized layers
- 4 Fluid flow
- 5 Fluid seepage (faults, vents and pipes)
- 6 Seafloor seepage (pockmark field)
- 7 Strength variability
- 8 Boulders
- 9 Gravel and pebble beds
- 10 Soft clays and weak layers
- 11 Weathered bedrock
- 12 Organic materials and peat
- 13 Faults and fractures
- 14 Glaciotectonic deformation
- 15 Glacigenic landforms
- 16 Steep slope gradient
- 17 Bottom currents and seafloor sediment mobilisation
- 18 Slope instability (landslide)
- 19 Slope instability (turbidity current)
- 20 GIA and sea-level changes
- 21 Seismicity
- 22 Tsunami
- 23 Rock avalanche
- 24 Flood
- 25 Glacial outbursts
- 26 Marine life

Anthropogenic

- a Hydrocarbon and CCS platforms
- b Pipeline
- c Floating wind
- d Bottom-fixed wind
- e Power cable
- f Population center
- g Roads
- h Tourism
- i Bridge
- j Shipping
- k Fishing



1199

1200 **Figure 5.2.** Conceptual sketch of geohazards and geo-engineering constraints along the deglaciated European margins. Shown are the deglaciated margin (modern
 1201 setting) in large, and the ice-covered margin during glacial maxima in small. CCS: Carbon Capture and Storage, GIA: Glacio-isostatic adjustment.

1202 **5.1 Shallow gas and gas-charged sediments**

1203 The presence of gas in the subsurface can have major implications for engineering behaviour of
1204 sediments and is considered a major constraint and, when triggered, hazard to offshore engineering
1205 projects, particularly in drilling operations (Davis, 1992, and papers therein). The term “Shallow Gas”
1206 is loosely defined as ‘gas pockets or entrapped gas below impermeable layers at shallow depth’ by the
1207 Norm ISO 19905-1:202, and is alternatively defined as ‘gas-charged sediment occurring within the
1208 upper 1000 m of the seafloor’ (Judd and Hovland, 2009). Gas observed on seismic data is frequently
1209 used to define various forms of gas presence. Notably, even low concentrations ranging from 0.5% to
1210 2 % can result in significant seismic responses, such as acoustic blanking and turbidity (e.g., Schroot
1211 and Schüttenhelm 2003 and references therein; Morgan et al., 2012). However, in terms of risk to an
1212 offshore installation, not all gas poses the same level of threat. Therefore, to differentiate between gas
1213 that poses the largest threat in terms of safety, from other forms of gas presence, the following
1214 definitions are suggested in Table 5.1.

1215 **Table 5.1.** Proposed definitions of shallow gas.

| | |
|-----------------------------|--|
| Low permeability gas | Defined as gas in low porosity and permeability sediments/ rock that does not have sufficient concentration to cause an amplitude response on seismic data but may appear as areas of acoustic blanking (turbidity) on sub-bottom profiler data (frequency of c. 3000 Hz and above). |
| Solution gas | Solution gas (sometimes referred to a “fizz gas”) is defined as gas dissolved in water and hence not in the free gas phase and therefore undetectable on seismic data. |
| Shallow gas | Over-pressured free gas within a trap (structural or stratigraphic), which results in a significant increase in amplitude on seismic data. This type of gas is a serious threat to drilling operations if encountered when the well is in underbalance conditions. |

1216

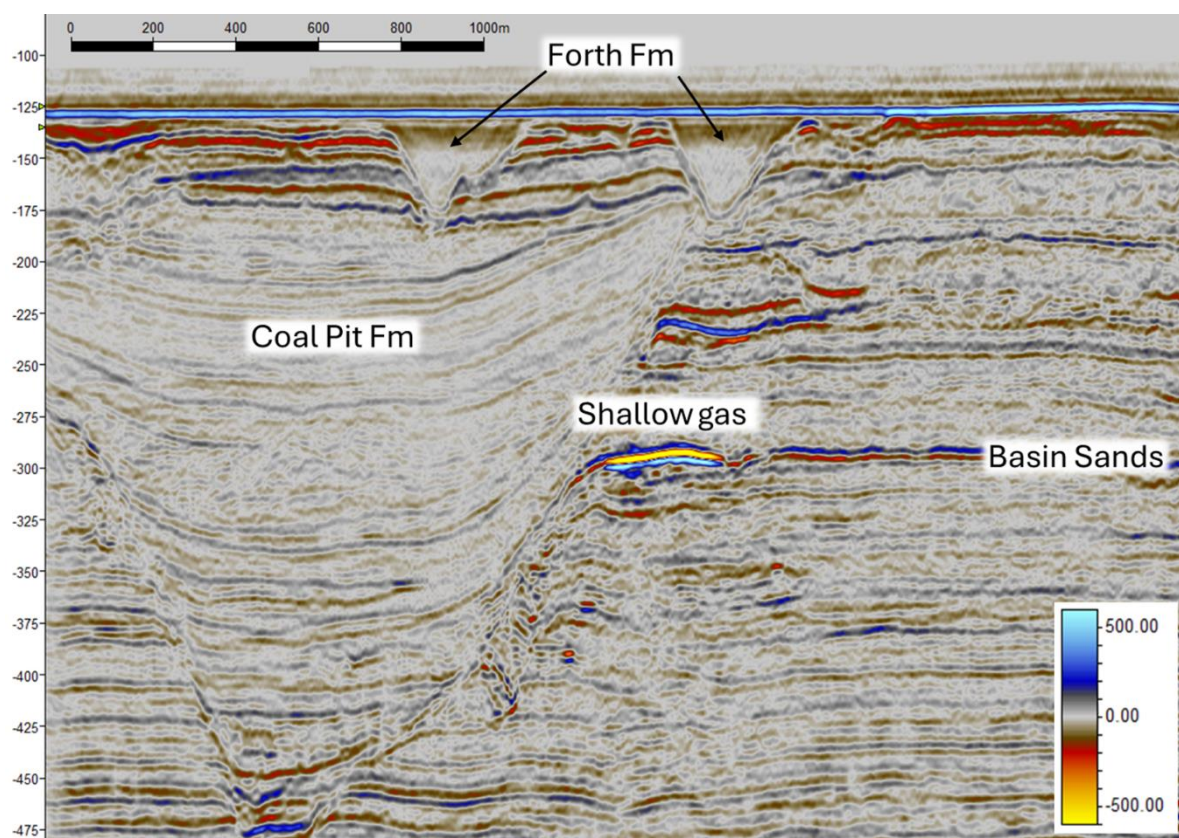
1217 **Engineering Considerations**

1218 The primary risk, in terms of offshore drilling, is posed by significant accumulations of free gas that are
1219 over-pressured, but of insufficient pressure to fracture the overburden (shallow gas - Table 5.1). Hence,
1220 once drilled into, the overpressure causes a rapid influx of gas into the wellbore if the retaining pressure
1221 inside the wellbore is not maintained in equilibrium, or slightly overbalanced. This is generally not an
1222 issue when drilling at depth (beyond surface casing depth), as pressure within the well is maintained by
1223 drilling mud and secondly, mechanical methods for controlling pressure within the well can be
1224 employed if a sudden increase in pressure were to occur, e.g. the blowout preventor, which “shuts the
1225 well in”.

1226 However, in the shallow overburden (Top-hole), where Quaternary soils are encountered (e.g., Figure
1227 5.3), the soils are too weak for the well to be “shut in” as the pressure within the wellbore would fracture
1228 the surrounding formation, and any chance of controlling the flow would be lost. Therefore, the internal

1229 wellbore pressure must be controlled using drilling fluid to maintain pressure equilibrium. This can be
1230 achieved with sea water if subsurface pressures permit, but often drilling muds of higher specific gravity
1231 are required, which increase the cost of a drilling operation. The SINTEF Offshore Blowout Database
1232 (2011) provides a full history on Industry events from the 1950's through to the present day, many of
1233 which incurred tragic loss of life (e.g., West Vanguard platform blowout in 1985, Figures 1.1c and 1.2)

1234 The use of high-resolution (HR) seismic data to identify shallow gas has been the Industry Standard
1235 since the early 1980's. Shallow gas is readily identifiable on seismic data as an anomalously high-
1236 amplitude, phase-reverse reflection (bright spot in clastic soils, see Figure 5.3). Other seismic indicators
1237 of the presence of shallow gas include velocity pull-down, polarity reversal, high-frequency attenuation,
1238 amplitude blanking (Figure 5.4) and a Class 3 AVO (amplitude-versus-offset) response. HR and EHR
1239 seismic provides the industry with a tool with which to evaluate risk and avoid or mitigate gas presence
1240 through well design and procedure, whereby 3D seismic gives better results for shallow-gas
1241 identification compared with 2D seismic (Figure 5.5). Shallow gas is still generally best avoided
1242 wherever possible.



1243

1244 **Figure 5.3.** Example of a shallow gas accumulation trapped against a tunnel valley infilled by the Coal
1245 Pit Formation, Central North Sea. Courtesy of bp Plc. Shallow gas is here indicated as an anomalously
1246 high-amplitude, phase-reverse reflection. Scale indicates the strength (amplitude) of the reflection.

1247 However, gas can exist in other states within the soil (see [Table 5.1](#)), and while not an immediate threat
1248 to a facility or its personnel, can influence long term integrity of structures.

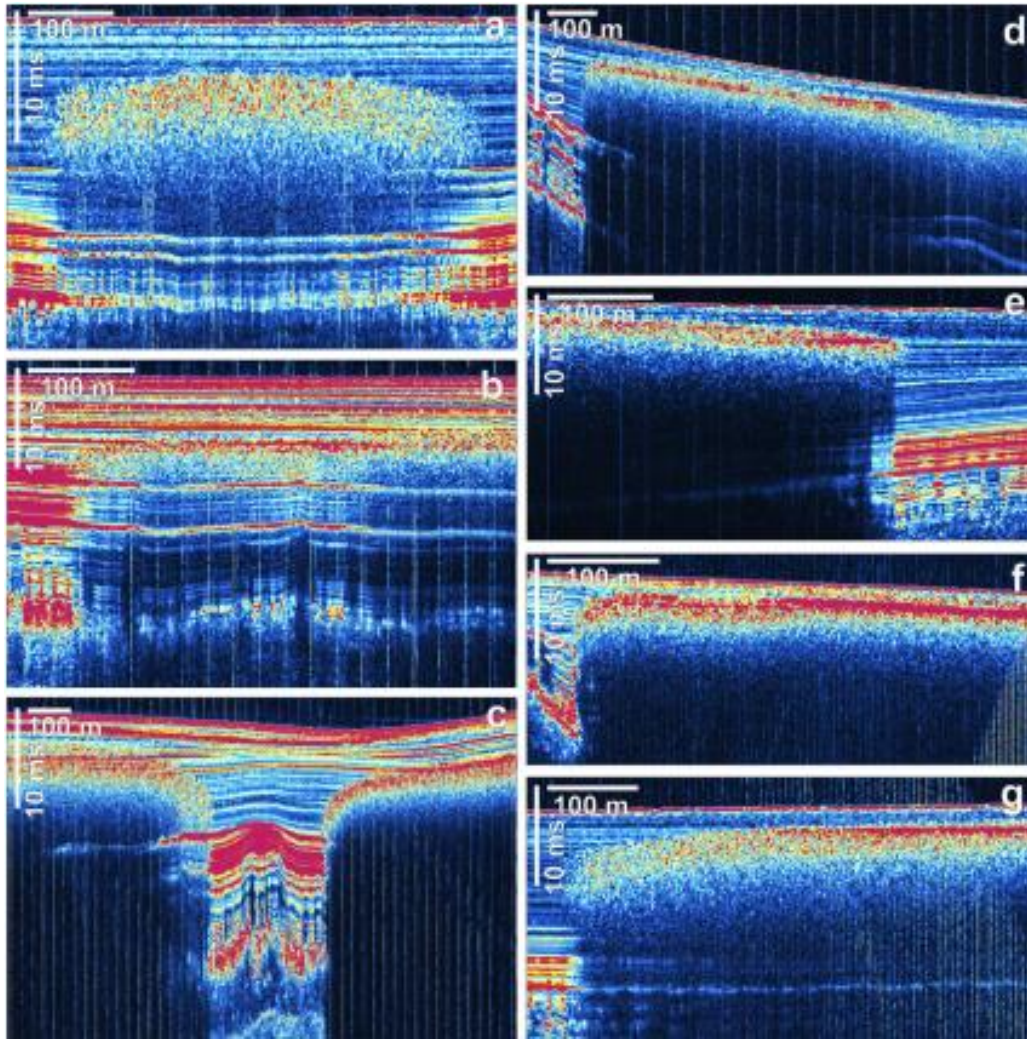
1249 Depending on the configuration of seismic data acquisition, low permeability gas may cause zones of
1250 acoustic blanking on sub-bottom profiler data ([Figure 5.4](#)) and while not a significant threat to Oil and
1251 Gas well drilling, can be an issue for geotechnical borehole drilling. There have been recorded incidents
1252 where gas has been brought to the drill floor through swabbing caused by temporary and local
1253 reductions in the borehole fluid and a disruption of the in-situ gas-fluid-soil equilibrium ([Kortekaas et
1254 al, 2008](#)). This can be challenging to mitigate for, especially in large offshore wind park projects, as
1255 this occurrence of gas can be widespread and unavoidable (e.g., in the Baltic Sea).

1256 Not only is low permeability gas an issue for geotechnical drilling, but also for detailed mapping of the
1257 subsurface, and identification of other hazards, as the acoustic scattering and attenuation create areas of
1258 blanking, below which, all acoustic energy is lost, and no reflections are recorded ([Figure 5.4](#)).

1259 Long-term exposure to low permeability gas, and gas in solution may be the cause of low state bubbling
1260 observed around Oil and Gas wells through channelling around the cemented casings and conductors.
1261 In extreme cases, this could lead to cratering around the conductor, loss of bearing capacity and well
1262 integrity. The same threat is posed to long term foundations such as deep piled structures, monopiles,
1263 and suction caissons/buckets.

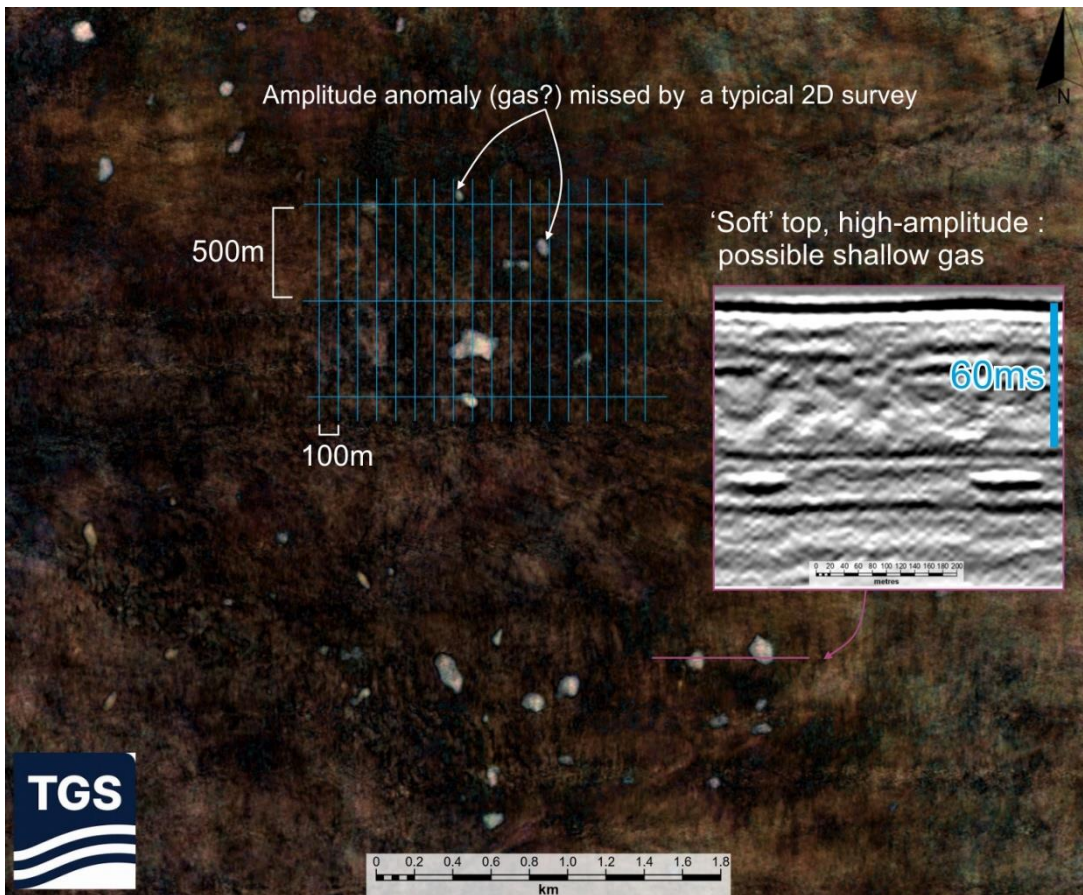
1264 So far, this section has dealt with the presence of biogenic methane gas. However, hydrogen sulphide
1265 (H_2S) is also a significant threat in certain environments and indications of H_2S have been noted in
1266 offshore wind sites around monopile foundations ([Soraghan, 2016; Blumenberg et al., 2022](#)). H_2S is
1267 colourless gas with the characteristic smell of rotten eggs in small concentration and becomes odourless
1268 in concentrations increase above 100 ppm. The gas is poisonous, corrosive, flammable and explosive
1269 in certain concentrations, and represents a significant risk to personnel, and long-term integrity of steel
1270 structures.

1271 In the southern North Sea, soils with high-organic content typically led to increased sulphate reduction
1272 rates and higher concentrations of sulphide (e.g., [Blumenberg et al., 2022](#)). Under anaerobic conditions,
1273 such as in submerged peat (see [Section 5.9](#)), sulphate reduction produces hydrogen sulphide (H_2S),
1274 contributing to the anaerobic decomposition of organic matter. If there is evidence of H_2S and a concern
1275 of risk, H_2S concentrations in shallow marine sediments should be understood. As samples for H_2S
1276 concentration are not easy to obtain, a better understanding can be achieved by analysing sediment and
1277 pore-water chemistry. Such analysis helps assess anoxic conditions and the sediment's scrubbing
1278 potential. Generally, the presence of minerals like pyrite in sediments indicates H_2S generation and
1279 reaction with iron, while abundant iron-oxide-bearing minerals suggest low H_2S levels.



1280

1281 **Figure 5.4.** Shallow gas imaged with the Parasound sediment echosounder (SLF 4.3 kHz, envelope
 1282 display). Gas bubbles in the Holocene mud appear as a patch or layer of point scatterers with highly
 1283 variable amplitudes, and they cause acoustic blanking as the scattering in the gassy layer disrupts the
 1284 sediment layering. From [Tóth et al., 2014a](#).



1285

1286 **Figure 5.5.** 3D high spectral decomposition time slice showing small high-amplitude, soft-topped
 1287 seismic anomalies interpreted as shallow gas accumulations. Note small size of gas ‘speckles’ making
 1288 them challenging to image by conventional 2D UHRS/ EHRS survey. Data courtesy of TGS

1289

1290 5.2 Gas hydrates

1291 Gas hydrates are solid compounds of water molecules encaging molecules of natural gas (example in
 1292 [Figure 5.6](#)). Although methane hydrates are the most widespread type of hydrate in continental margins,
 1293 any gas derived from chemical and biochemical processes within the sedimentary column (i.e.,
 1294 hydrocarbons and non-hydrocarbons, organic and inorganic) can form hydrates. Depending on the size
 1295 of the molecular cages and their crystalline structure, natural gas hydrates have been classified into:
 1296 type I, can trap methane, ethane and molecules with comparable diameter such as CO₂ and hydrogen
 1297 sulphide; type II, in addition to methane and ethane can trap larger-order hydrocarbons, e.g., propane;
 1298 and type H, the least commonly observed in nature (and perhaps the least understood) can have cages
 1299 even larger than type II ([Sloan, 1998a; 1998b](#)). Natural gas hydrates are found in continental margin
 1300 settings at combined low temperatures and high-pressure conditions, with factors such as salinity and
 1301 gas saturation and composition also controlling their stability ([Kvenvolden, 2000](#)).

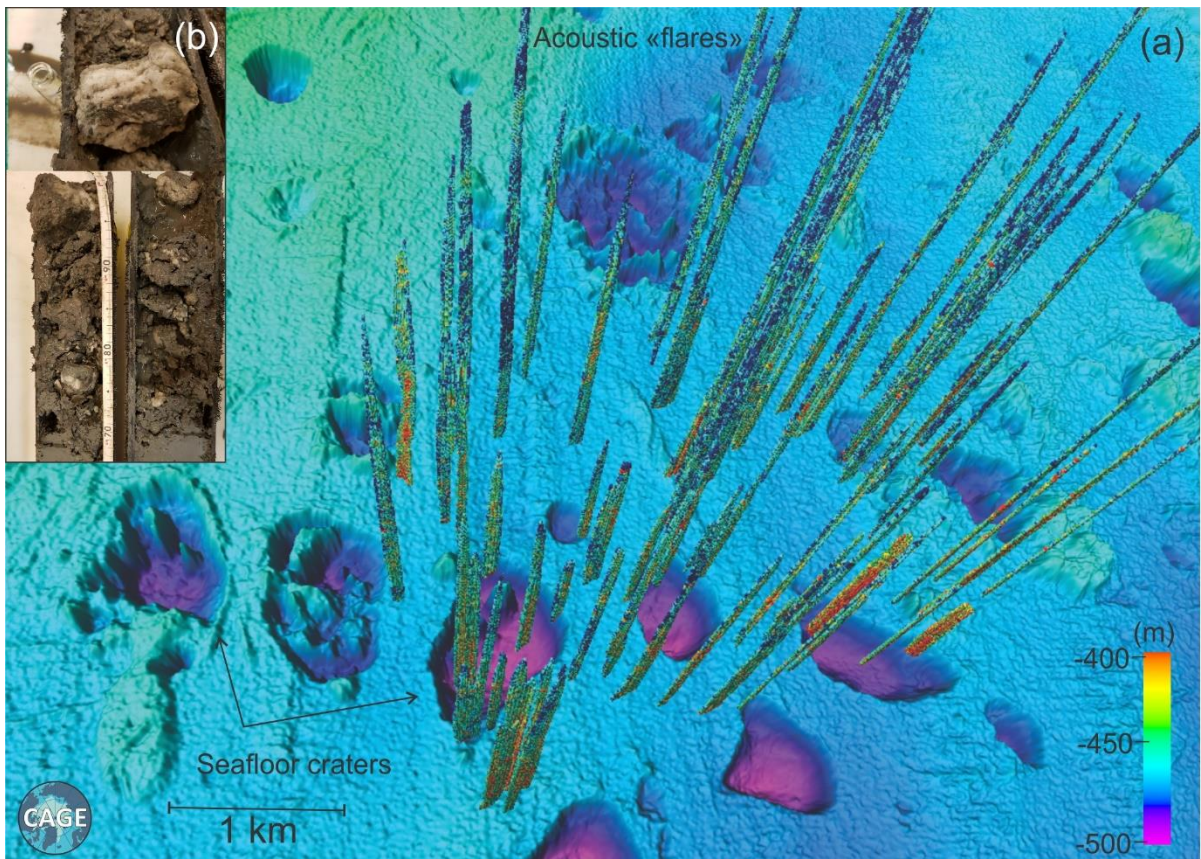
1302 The theoretical stability of gas hydrates can be estimated using relationships between geothermal
1303 gradient, bottom water temperatures and pore pressures at specific depths for given salinities and gas
1304 compositions (e.g., [Sloan and Koh, 2007](#)). In nature the presence of hydrates can be confirmed by
1305 sampling in sedimentary cores ([Figure 5.6b](#)) but also based on various geophysical and geochemical
1306 observations (e.g., [Minshull et al., 2020](#)):

- 1307 1) One of the most straightforward indications of gas hydrate in the sediment is the presence of
1308 bottom simulating reflections (BSR) in seismic data at the approximate depth of the theoretical
1309 base of the gas hydrate stability zone (e.g., [Hyndman and Spence, 1992](#); [Figures 5.7a and 5.7b](#)).
1310 Provided suitable seismic resolutions and survey orientations, a BSR is typically a high-
1311 amplitude reflection, characterized by a reverse polarity, with respect to the seafloor reflection,
1312 and in dipping layer settings it appears as a cross-cutting reflection ([Figures 5.7a and 5.7b](#)).
1313 Gas hydrate may be present even if a BSR is not observed in seismic data (i.e., the strength of
1314 the BSR reflection is mainly controlled by the accumulation of small amounts of free gas under
1315 lower permeability gas-hydrate bearing layers; [Figure 5.7a](#)). However, the presence of a BSR
1316 implies that hydrates are present and acting as a seal for upward migrating fluids. A free gas
1317 zone (often reaching tens of meters) develops under the BSR in settings with substantial gas
1318 generation or migration (e.g., [Hornbach et al., 2004](#); [Figure 5.7c](#));
- 1319 2) Observation of vertical fluid migration pathways and associated seafloor pockmarks and
1320 authigenic carbonate mounds, can often indicate gas hydrate related past methane seepage
1321 events ([Figure 5.7a](#); see also [Figure 5.11](#) in following section). When the gas hydrate stability
1322 zone is known, high interval P- and S-wave velocities (measured from multi-channel seismic
1323 data and/or ocean bottom seismometer experiments) and high resistivities (measured using
1324 controlled source electromagnetic methods), can be used as indicators of gas hydrates and
1325 methane-derived authigenic carbonate accumulations within vertical fluid pathways and sub-
1326 seabed faults and fractures (e.g., [Goswami et al., 2015](#); [Singhroha et al., 2020](#));
- 1327 3) Cone penetration tests (CPTU) integrated with seismic velocity analyses allow identifying gas
1328 hydrate bearing layers (i.e., often characterized by low density and high excess pore pressures
1329 upon penetration). The presence of authigenic carbonates commonly associated with focused
1330 fluid flow, seepage and gas hydrate dynamics may be also identified as anomalously low pore
1331 pressures, (i.e., in cases where fluids dissipate easier through higher permeability areas in the
1332 sediment surrounding the carbonates (e.g., [Sultan et al., 2007](#)).
- 1333 4) Often, the presence of a clear methane-sulphate transition zone (MSTZ), indicates how much
1334 methane reaches the seafloor. A several meters deep MSTZ indicates that low amounts of
1335 methane reach the seafloor and therefore limited gas hydrate accumulations can form.
1336 Similarly, high salinity inhibits gas hydrate formation and anomalously low salinities in the
1337 pore water may indicate gas hydrate dissociation (e.g., [Paull et al., 2005](#)).

1338 In glaciated continental margins, the stability of gas hydrates has been significantly affected by both
1339 temperature and pressure relevant processes associated with ice-sheet dynamics (e.g., the advance and
1340 retreat of large ice-masses, significant erosion of pre-glacial strata, increased sedimentation rates in
1341 catchment zones, crustal uplift and subsidence, fracturing, fault reactivation, among others). For
1342 example, large craters (< 1 km wide) in the Bjørnøyrenna trough in the Barents Sea (Figure 5.6b), have
1343 been suggested to be an expression of massive blow outs triggered by abrupt pressure changes following
1344 ice-sheet retreat after the LGM (Andreassen et al., 2017). Both microbial and thermogenic gas tend to
1345 migrate to the shallow subsurface and accumulate beneath gas-hydrate bearing sediments over millions
1346 of years, forming what is known as the free gas zone (e.g., Plaza-Faverola et al., 2012). Ice sheets keep
1347 the stability of these systems. However, upon ice-sheet retreat, gas hydrate may dissociate and the
1348 interactions with the associated free gas may lead to sediment deformation, fracturing, vertical fluid
1349 migration and seafloor expulsion (e.g., Forsberg et al., 2007). In addition, intervals of increased
1350 sedimentation along the continental slopes (e.g., glacial debris flows along the mid-Norwegian
1351 margin) can lead to basal gas hydrate dissociation events via a relative shift of gas hydrate bearing strata
1352 out of the base of the GHSZ that sustain fast vertical fluid migration (i.e., leading to pipe formation and
1353 seafloor pockmarks (Karstens et al., 2018; Plaza-Faverola et al., 2012). Post-glacial subsidence and
1354 uplift is another mechanism that leads to sub-seabed deformation and destabilization of gas hydrates
1355 and associated free-gas accumulations (e.g., Wallmann et al., 2018).

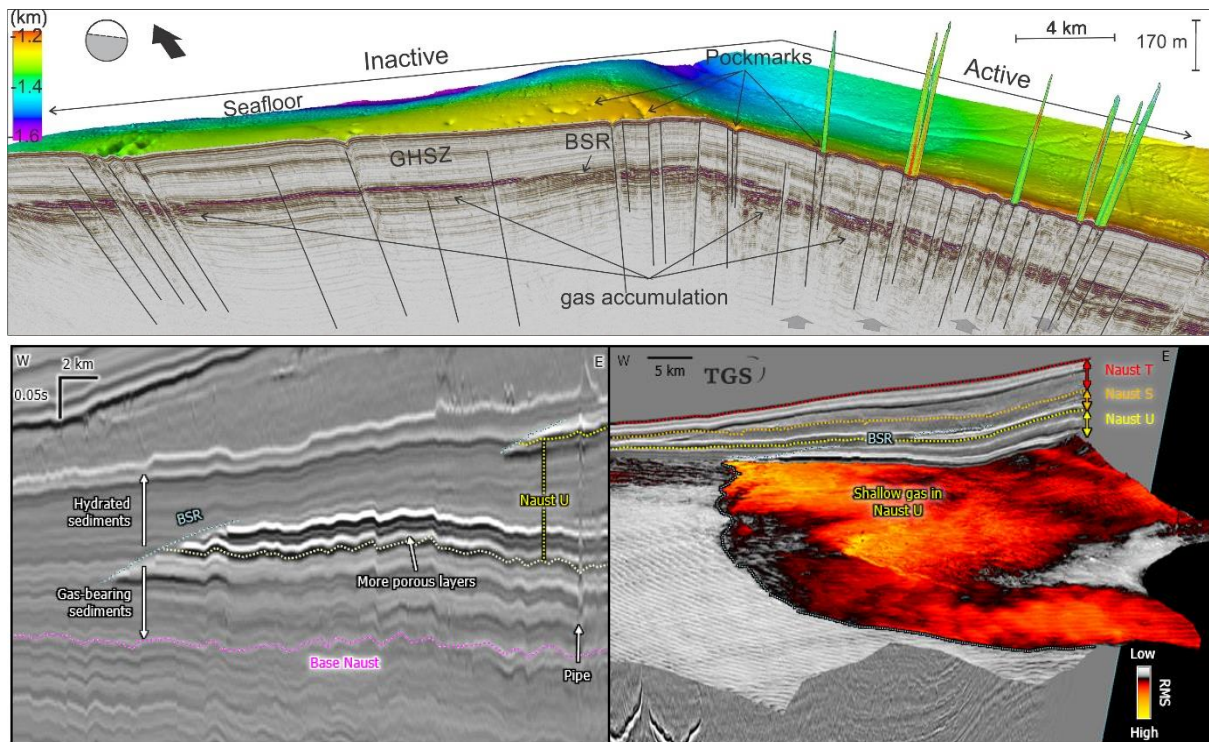
1356 On the upper continental slopes, the GHSZ pinches out at the seafloor (landwards) and forms the feather
1357 edge. The spatial location of this zone varies but it lays at water depths usually around the shelf break.
1358 The extent of the GHSZ is particularly sensitive to ocean warming, both locally and regionally, and at
1359 various scales (i.e., seasonal and diurnal as well as long term changes). Whilst relative sea-level changes
1360 typical of glacial-interglacial transitions has a more regional impact on gas hydrate stability. Multiphase
1361 fluid flow models from the west-Svalbard margin show that present day gas seepage at the feather edge
1362 can be sustained by temperature-controlled gas-hydrate dissociation in the recent past (Trivedi et al.,
1363 2023). These episodes of recent gas hydrate dissociation have an impact on the pore water salinity and
1364 likely on the sediment hydromechanical properties.

1365 The Norwegian Channel running from Skagerrak along the Norwegian coastline into the North Atlantic
1366 Ocean contains numerous pockmark fields (e.g., Troll field; see Chapter 5.3). Investigations of the
1367 pockmarks around the Troll hydrocarbon field have not revealed presently active pockmarks. However,
1368 these pockmarks have formation ages corresponding to the climatic amelioration at the end of the last
1369 ice age and are believed to have formed by gas from decomposing gas hydrates (Mazzini et al., 2017;
1370 Mazzini et al., 2016; Forsberg et al., 2007).



1371

1372 **Figure 5.6.** Gas hydrates related fluid dynamics on the shelves of the Arctic. **a)** Bathymetry data from
 1373 Bjørnøyrenna/Barents Sea collected with ship mounted multibeam on board R/V Helmer Hanssen. The
 1374 data show kilometer scale seafloor craters suggested to be caused by abrupt collapse of gas hydrate
 1375 charged sediment upon ice-sheet retreat during the Last Glacial Maximum (Andreassen et al., 2017).
 1376 Gas bubbles in the water column are indicated as vertical anomalies in hydroacoustic data and referred
 1377 to as acoustic “flares” in the literature; **b)** Inset showing an example of gas hydrate accumulations
 1378 retrieved within the upper 2 meters of sediment in a sediment core collected off the west-Svalbard coast.
 1379 The presence of sub-seabed gas hydrates and methane accumulations in fine-grained sediment have
 1380 been documented as direct sampling and as pressure and temperature pulses in piezometer data (Sultan
 1381 et al., 2020).



1382

1383

1384 **Figure 5.7.** Gas hydrates, shallow gas, and fluid flow as expressed in seismic data. **a)** Composite 3D
 1385 image of a deep marine gas hydrate system offshore west-Svalbard, the Vestnesa Ridge (from Plaza-
 1386 Faverola et al., 2017). The gas hydrate stability zone (GHSZ) in this area is 160-200 m thick and its
 1387 base is characterized by a well-defined bottom simulating reflection (BSR) in seismic data. A free gas
 1388 zone (tens of meters thick) has developed over geological time through accumulation of upward
 1389 migrating thermogenic gas as well as in-situ generated microbial gas. Widespread seafloor pockmarks
 1390 and associated authigenic carbonate indicate gas release over geological time scales. Today only a few
 1391 pockmarks are still releasing gas via advection through open cracks possibly regulated by changes in
 1392 the glacial stress regime (e.g., Vachon et al., 2022). **b)** Example of a typical BSR cross-cutting the
 1393 stratigraphic layers (here contourites within Naust Unit U), and associated free gas accumulation from
 1394 conventional 3D seismic data from the mid-Norwegian margin, north of the Storegga Slide (modified
 1395 from Bellwald et al., 2022b). Strong seismic amplitudes represent stratigraphically-bound, gas-charged
 1396 layers. **c)** The Naust Formation and its units are characterized by glacimarine sediments. The surface
 1397 shows the RMS amplitude within the Naust U sub-unit. The BSR limits the western extent of the gas-
 1398 charged layers (modified from Bellwald et al., 2022b).

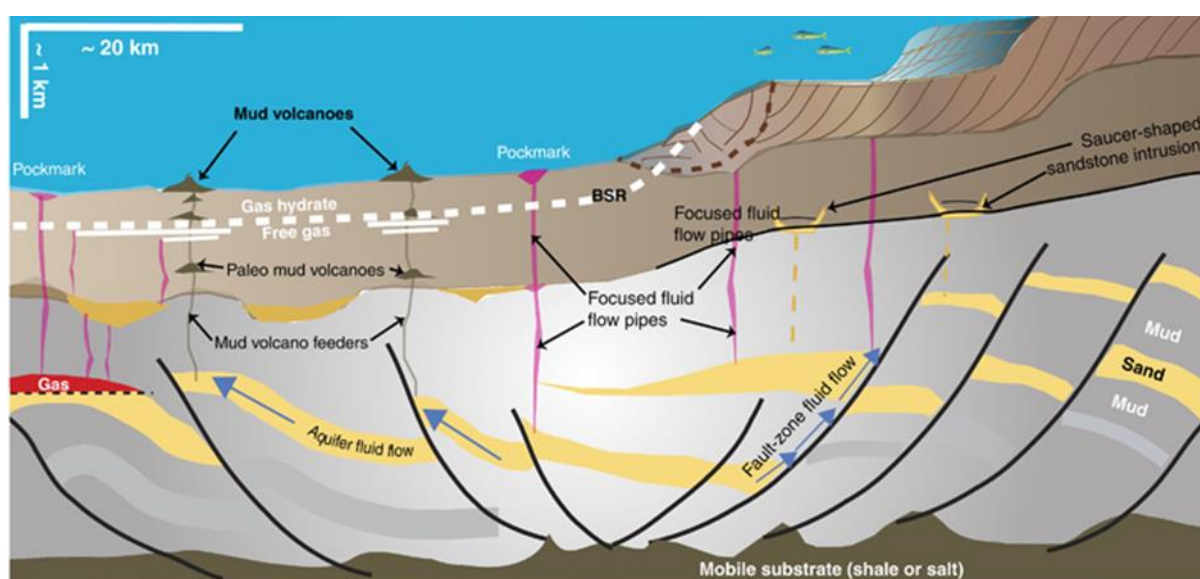
1399 5.3 Fluid flow, fluid seepage, and overpressurized layers

1400 Overpressure in sedimentary basins is caused by disequilibrium between compaction and
 1401 sedimentation. In different settings, overpressure can be attributed to sedimentation outpacing the
 1402 ability of low-permeability strata to evacuate physical and chemical compaction-derived fluids, and/or
 1403 from hydrocarbon generation or rapid tectonic or glacial loading and unloading (Figure 5.8).

1404 Overpressure can thus happen at numerous time- and spatial scales, from bed-scale to the scale of multi-
1405 km of overburden deposited over tens of millions of years.

1406 In the context of the glaciated European margins and the North Sea Basin, all of these factors are
1407 significant and sediment wedge deposition during the Quaternary (e.g., Lamb et al., 2018) is particularly
1408 important in providing a permanent load, tilting of the basins by very localised and (geologically-
1409 speaking) very quick sedimentation (>1km accumulated at >1mm/yr), on top of sequences characterised
1410 by much slower sedimentation (<0.1mm/yr; e.g., Bellwald et al., 2024b). The presence of petroleum
1411 systems, reservoirs and effective seals has resulted in a prominent pressure cell in the central North Sea
1412 and locally along the Norwegian margin (e.g. Evans et al. 2003; Morency et al. 2007; Vejbæk 2008;
1413 Lamb et al. 2018; Løseth et al. 2022).

1414 The presence of pressure disequilibrium leads to flow in cases where the system is open and may lead
1415 to catastrophic seal-breach where a system is effectively closed, and the fracture gradient is exceeded
1416 (Figures 5.8 and 5.9). Seal-breach may manifest itself as seepage or catastrophic depending on the depth
1417 of the pressure compartment and the rheologies involved in the sealing and the pressurised layers
1418 (Figure 5.10). Some of the most spectacular geology in the world results from catastrophic seal breach,
1419 including mud volcanoes, sandstone intrusions, blow-out pipes and pockmarks, which can range from
1420 metric to kilometric scales (Figures 5.8, 5.9, 5.10, and 5.11; Van Rensbergen et al., 2003; Judd and
1421 Hovland, 2007; Huuse et al., 2010). Smaller-scale pockmarks are often widespread and seen in
1422 abundance in fine grained units, suggesting they may be related to de-watering and/or very shallow de-
1423 gassing triggered by sea-level changes whilst larger pockmarks may represent cross stratal fluid
1424 conduits, evacuating fluids, often gas, from deeper levels (Judd and Hovland (eds) 2007; Böttner et al.
1425 2019; Figures 5.10 and 5.11).

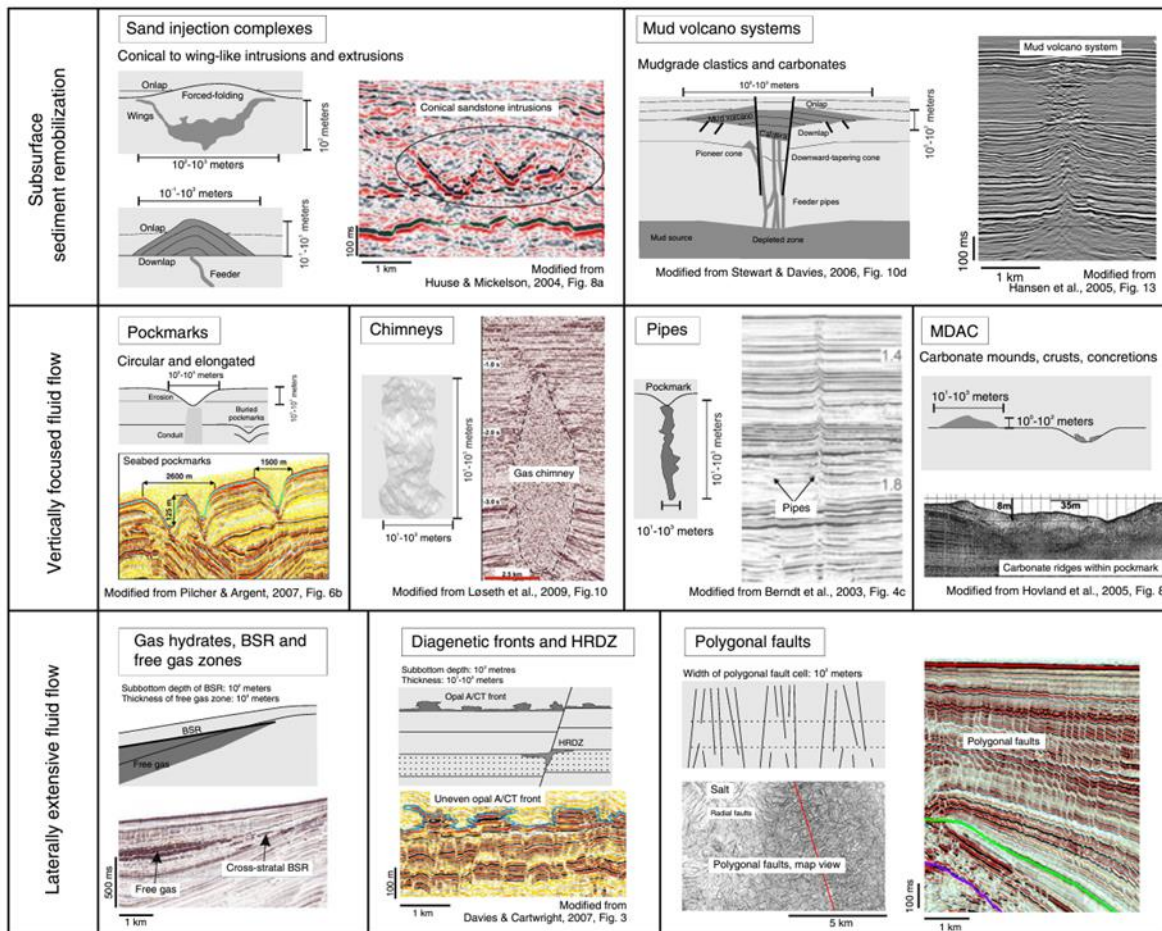


1426 **Figure 5.8.** Fluid flow in basins can take many forms and are a function of tectono-stratigraphy, rates
1427 of subsidence, nature of sedimentation, sediment porosity and permeability through time and modified
1428

1429 during burial, diagenetic processes and triggered by external factors such as glacial loading and
1430 unloading, earthquakes, tilting, and human interventions such as drilling (Huuse et al. 2010).

1431 Processes involved in fluid flow and blowouts can be subdivided into primers and triggers, many of
1432 which can happen on different magnitudes and time scales and thus can sometimes be considered both
1433 primer and trigger. Primers include deposition, erosion, compaction whereas triggers may include
1434 tectonics, diagenesis including oil and gas generation, silica diagenesis at shallow burial and smectite-
1435 illite transformation and quartz cementation at few km burial. These processes release significant
1436 volumes of water from the sedimentary column and are thus implicated in overpressure generation at
1437 depth whenever the fluids encounter barriers to fluid flow.

1438 In the Quaternary stratigraphy of the European margin, the most common features related to fluid flow,
1439 fluid seepage, and overpressurized layers are: i) gas flares in the water column (Plaza-Faverola et al.,
1440 2017; Serov et al., 2023; Figures 5.6 and 5.7), ii) pockmarks at the seafloor and within the buried
1441 stratigraphy (e.g., Judd and Hovland, 2007; Böttner et al. 2019; Tasianas et al., 2018; Figures 5.10 and
1442 5.11), iii) chimneys vertically crossing to modern and paleo-seafloors (e.g., Hustoft et al., 2009; Figure
1443 5.10); and iv) remobilized ooze mounds at multiple Quaternary stratigraphic levels with associated
1444 evacuation craters at the Base Quaternary (e.g., Riis et al., 2005; Bellwald et al., 2024b). A summary
1445 of fluid-flow phenomena is shown in Figure 5.9 (Andresen, 2012). The identification of fluid-flow
1446 related landforms increases the understanding of shallow fluid migration paths and mechanisms, which
1447 ultimately contributes to reduce risks associated to blowouts and changes in soil strength (Prins et al.,
1448 2025).



1449

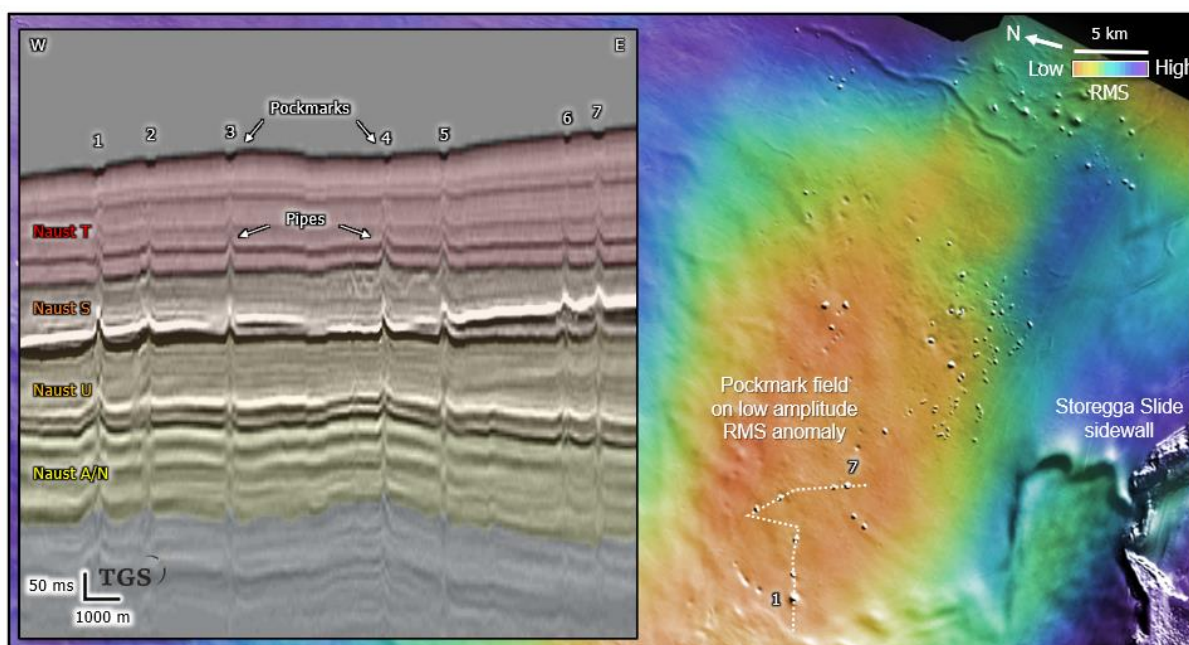
1450 **Figure 5.9.** Fluid flow phenomena in seismic data (Andresen, 2012).

1451 Fluid flow and human activity

1452 The drilling of a borehole for geotechnical testing, insertion of monopiles for wind turbines or wells
 1453 exploring explore for petroleum, geothermal or storage space would be considered a triggering process
 1454 due to their highly invasive nature, perforating sealing units and connecting reservoirs/aquifers at
 1455 different levels and to the surface. This connection between reservoirs at various stages of overpressure
 1456 and with different degrees of lateral transfer of pressure due to reservoir dip and any ongoing diagenetic
 1457 processes can cause internal and external blowout and fluidisation of unconsolidated aquifers,
 1458 potentially leading to the eruption of sediments (e.g. Davies et al. 2007). Evacuation of excess fluids
 1459 can lead to rapid compaction and seafloor subsidence (as seen on top of some producing North Sea
 1460 fields) whilst evacuation of sediments can lead to subsurface cavity formation and collapse as seen
 1461 around active mud volcanoes (Stewart and Davies 2006) and in association with deep-seated submarine
 1462 landslides (Bull et al. 2009).

1463 Pressure connections notwithstanding drilling can also cause release of non-aqueous fluids, dissociation
 1464 of gas hydrates, and drilling associated events can lead to knock-on effects including landslides and
 1465 blowouts.

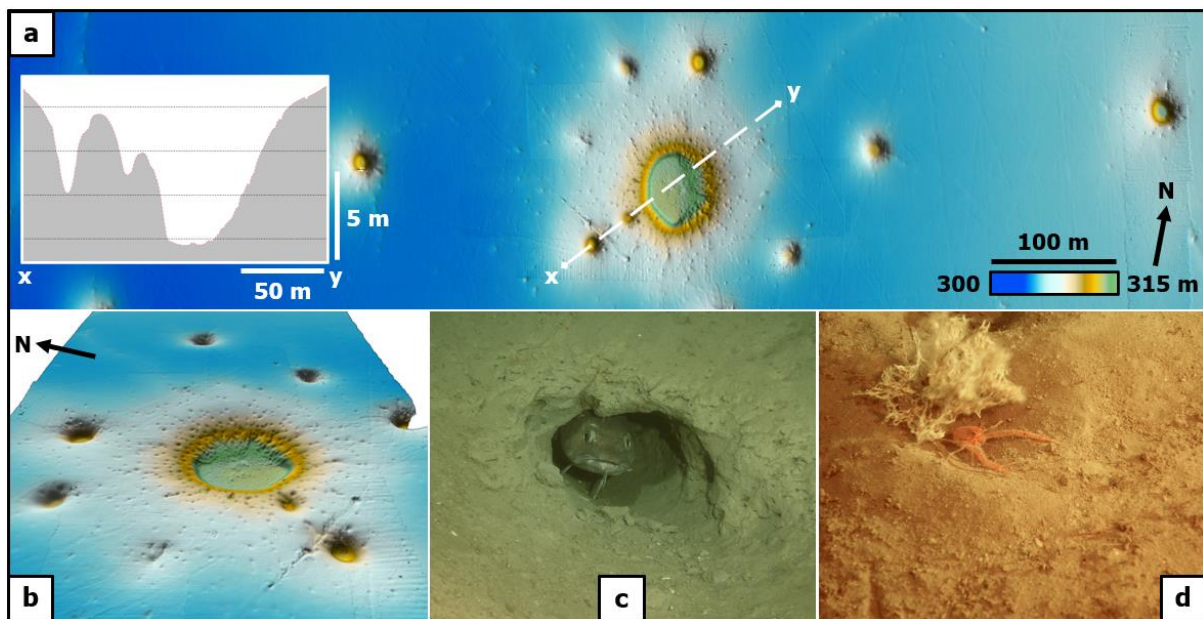
1466 The hazards associated with fluid flow and triggering by human intervention are undergoing a
 1467 significant change from petroleum fluid extraction and produced water injection towards widespread
 1468 installation of wind turbines, affecting the top 100-200 m of the seabed and large-scale injection of CO₂
 1469 which in some cases will cause pressure waves in aquifers and in the case of depleted fields, may cause
 1470 whole-scale uplift of the overburden. The latter effects may open new connections and could also
 1471 destabilise legacy boreholes and cause cross-stratal fluid flow in ways not experienced previously.
 1472 There is a strong need for monitoring to detect and action any evidence for such fluid flow and much
 1473 of the associated equipment will be deployed in near-surface environments. Any interventions would
 1474 need to be quick and effective and could lead to unexpected fluid flow phenomena (see also [Figure 1.3](#)).



1475 **Figure 5.10.** Fluid flow along the mid-Norwegian margin. **a)** Association between indications of fluid
 1476 escape features in the Quaternary and the seabed, and gas hydrates in the subsurface. Seismic profile
 1477 showing the subunits of the Quaternary Naust Formation and pipe structures crossing a BSR (black
 1478 arrow). **b)** Structure map of the seabed blended with RMS amplitude of the Naust S subunit. Pockmarks
 1479 at the seabed correlate with low RMS amplitudes of Naust S sub-unit and pipes in the subsurface data.
 1480 Data courtesy of TGS.

1482 The formation of pockmarks is often concluded to be triggered by fluid release, i.e. gas hydrate
 1483 dissociation ([Hovland et al., 2002](#); [Forsberg et al., 2007](#); [Mazzini et al., 2017](#); [Tasianas et al., 2018](#)).
 1484 High-resolution bathymetric examples from the Troll field in the Northern North Sea ([Mazzini et al.,](#)
 1485 [2017](#); [Figure 5.11](#)) and high-resolution 3D seismic interpretation of the seafloor of the Snøhvit field in
 1486 the Southwestern Barents Sea ([Tasianas et al., 2018](#)) show different types of pockmarks: i) Larger, but
 1487 fewer “normal pockmarks” c. 100 m wide and c. 10 m deep (e.g., Septagram on [Figure 5.11](#)), and ii)
 1488 smaller, but more numerous “unit pockmarks” ([Hovland et al., 2002](#)) some 10s of meter wide and c. 1
 1489 m deep (e.g., numerous points on [Figure 5.11](#)). Pockmark fields as locations of focused fluid seepage

1490 are often associated to habitats formed by chemosynthetic organisms using methane and precipitating
 1491 authigenic carbonate, and may thus present issues due to marine habitat protection (e.g., Noble-James
 1492 et al., 2020; Prins et al., 2025). ROV footage shows that pockmarks are refuges for marine benthic
 1493 biodiversity (Figure 5.11c; d; Webb et al., 2009). Although mentioned as the most common trigger
 1494 mechanism for pockmark formation, processes causing these depressions may not always relate to fluid
 1495 release (Krämer et al., 2017), and remain unclear in some cases (Böttner et al., 2024).



1496 **Figure 5.11.** Pockmarks on the seafloor of the Troll hydrocarbon field. **a)** Example of high-resolution
 1497 bathymetry (0.2 m resolution) of the Septagram pockmarks with profile across different types of
 1498 pockmarks. **b)** 3D view into the Septagram pockmarks. Note the numerous smaller dots referred to as
 1499 unit pockmarks. **c+d)** Marine life identified in the Troll pockmark field. Data courtesy: Equinor.

1501 5.4 Strength variability

1502 Soil strength can be defined as how much shear stress a soil can withstand without deformation or
 1503 failure. In the simplest description, low strength soils are easily deformable, whereas high strength soils
 1504 are more resistant to deformation. Strength variability is a product of multiple factors; the physical
 1505 makeup of soil particles (in terms of grain size, grain shape, and proportions of different grain sizes,
 1506 and type of grains), and the stress history of the soil (what the soil has gone through, since it was
 1507 deposited). Soils in glaciated environments can have a very complex stress history, and as such can be
 1508 extremely laterally and vertically variable (see Chapter 5.13).

1509 Consolidation specifically refers to the volume of water and physical particles within a soil and how
 1510 these change over time. Soils that are experiencing the same loads in the past as they are currently
 1511 experiencing, for example, recently deposited soils, are normally consolidated. Soils which have
 1512 previously experienced loading which has subsequently been removed are over-consolidated (e.g.,

1513 subglacial traction tills). Under-consolidated soils can be described as soils which have had a load
1514 applied, but there has yet been insufficient time for pore water pressures to equilibrate. Depending on
1515 the type of soil, consolidation can take a very long time, sometimes hundreds of years to fully
1516 equilibrate, assuming no other changes to the load applied on the soil.

1517 The three main stages of consolidation are: immediate settlement, where a soil fills a space without any
1518 change to the volume of water; primary consolidation where water in voids and pore spaces is expelled;
1519 and secondary consolidation where the physical grains undergo deformation. Whether or not a soil will
1520 behave in a plastic or brittle manner lies beyond the scope of this paper.

1521 Soils deposited or modified in glacial or periglacial environments have both a complex depositional
1522 setting, sometimes over very short time periods, with variations in grain size, type and water content,
1523 and complex post-depositional stress history. Much of north-west Europe has experienced repeated
1524 glacial and interglacial cycling and therefore over short lateral and vertical distances, soils can have
1525 very different geotechnical properties (Figures 5.12 and 5.13). These soils are often over-consolidated
1526 but under-consolidated soils also exist.

1527 Over-consolidated soils can occur in formerly glacially effected environments in three key settings: i)
1528 Soils that have been loaded directly by ice cover from above, such as subglacial tills; ii) soils that have
1529 been loaded regionally by nearby ice (indirect ice contact), such as on the margins of ice sheets or
1530 glaciers but not directly covered, as is exhibited in late-glacial glaciolacustrine sediments on the Dogger
1531 Bank, or soils which are immediately adjacent glacial systems, for example push moraines; and iii)
1532 permafrost environments where the expansion and freezing water can cause over-consolidation on the
1533 soil fabric scale.

1534 Due to the variability in stress history that can occur even to the same depositional unit over short
1535 distances, it can be difficult to predict how soils will behave under new loading for example the
1536 installation of offshore infrastructure (Figure 5.13).

1537 **Measuring soil variability**

1538 Measuring the shear strength of soils in such a variable stratigraphic setting can be challenging. The
1539 correct tooling for geotechnical sampling and testing should be considered based on the expected
1540 ground conditions that includes the number of locations, location selection, sampling and testing
1541 methodology, and appropriate twinning of locations. Some units will have a high proportion of granular
1542 material and care should be taken not to wash these out during borehole drilling. Similarly, very high
1543 strength, overconsolidated units or very dense sands can cause early refusal in Cone Penetration Tests
1544 (CPTs). As many of these soils are boulder-prone, early refusals can be a concern unless they are well
1545 tied into the geophysics and geological model.

1546 Subsequent parameter derivation of these soils can also be difficult. The lateral and vertical variability
1547 will often result in wide-ranging lower-bound and higher-bound estimates, which can lead to
1548 conservatism in any design for offshore infrastructure.

1549 **Seismic characteristics**

1550 Geophysics works best when the subsurface comprises layers with increasing strength with depth;
1551 usually, erosive surfaces result in an impedance contrast between the eroded surface, which is often
1552 over-consolidated, and the overlying units. However, in regions that have undergone multiple phases
1553 of glacial advance and retreat, lower strength or less consolidated layers can occur beneath higher
1554 strength/more consolidated layers. This leads to a difficulty interpreting boundaries for the top of the
1555 underlying units, and subsequently challenges mapping separate seismostratigraphic units across sites;
1556 particularly where different parts of a single seismostratigraphic unit may have undergone different
1557 levels of consolidation under subtly different circumstances, i.e., tills deposited as moraine at the front
1558 of a glacier versus the same till unit, which might have no obvious lateral boundary, but deposited
1559 directly beneath the glacier (for lateral variability in the same packages, see [Figure 5.13](#)).

1560 High levels of vertical and lateral variability also make velocity modelling across these regions
1561 challenging, resulting in inaccurate depth conversion and difficulty tying in geotechnical data correctly.
1562 It is important to integrate available geophysical, geotechnical and geological data to understand likely
1563 depositional environments to have the best chance of maximising the use of all datasets in these areas
1564 of high variability ([Figure 5.13](#)).

1565 **Engineering implications and considerations**

1566 High levels of lateral and vertical soil variability often result in a need for more detailed site
1567 investigations to reduce uncertainties in design parameters. Wide scatter in results will lead to larger
1568 uncertainties in design profiles and un-optimised design, and increased difficulties predicting how soil
1569 bodies will behave under new loads.

1570 For piles, incorrect assessment of required foundation weights and lengths lead to different scenarios,
1571 and can result in both over- and under-conservatism in design: i) Where soils are lower strength than
1572 characterised and designed for, the installation method may not be appropriate and over-heavy piles can
1573 experience excessive or rapid pile run beyond the expected settlement; ii) Where soils are higher
1574 strength than anticipated, this can result in excessive installation times when driving or pile refusal.

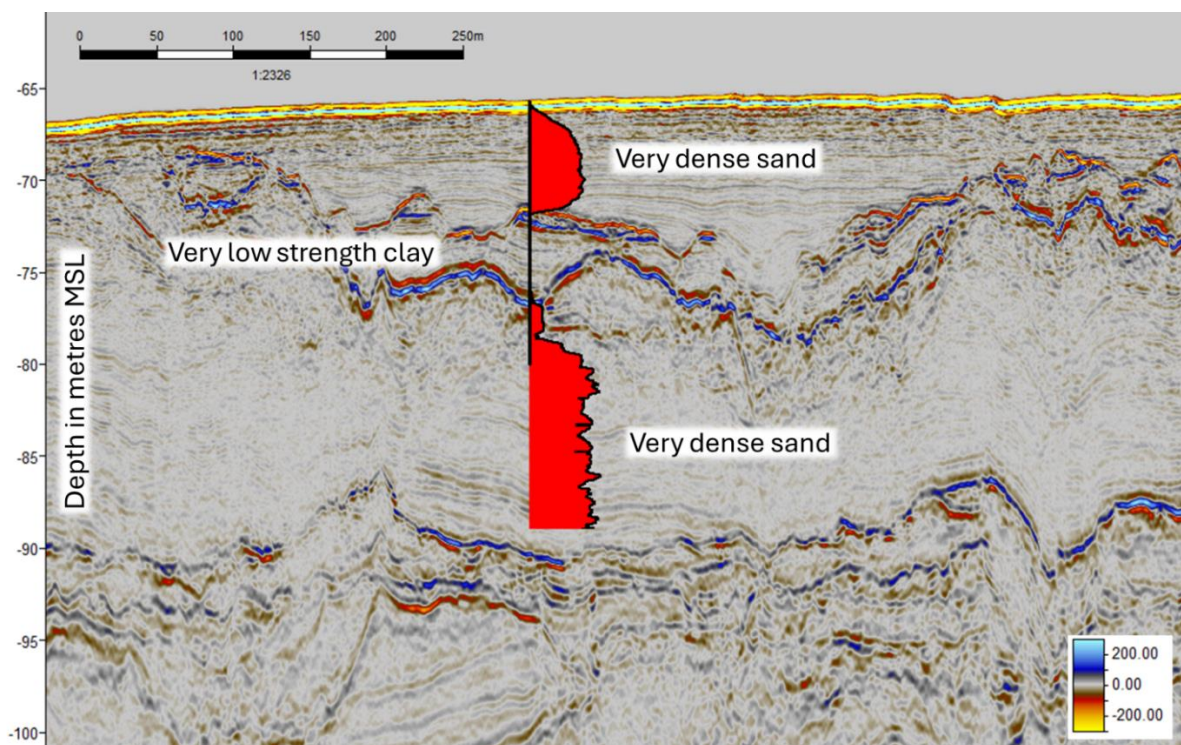
1575 During installation, issues may arise across the footprint of the foundation if soil strength variability is
1576 high. In some regions with high levels of glaciotectonism, such variability may be within the metre
1577 scale, and geotechnical response can be significantly different only few meters apart (e.g., at bump-over
1578 locations can be significantly different). To mitigate this, some larger structures may benefit from

1579 multiple CPT locations or extremely high-resolution 3D seismic data if lateral variability is expected to
1580 be high (Hill et al., 2024).

1581 For cables and pipelines, geospatial variability in soil conditions requires careful consideration of tool
1582 selection to prevent issues with achieving the desired depth of burial in over-consolidated soils, but also
1583 the risk of equipment loss in unexpectedly low-strength soils.

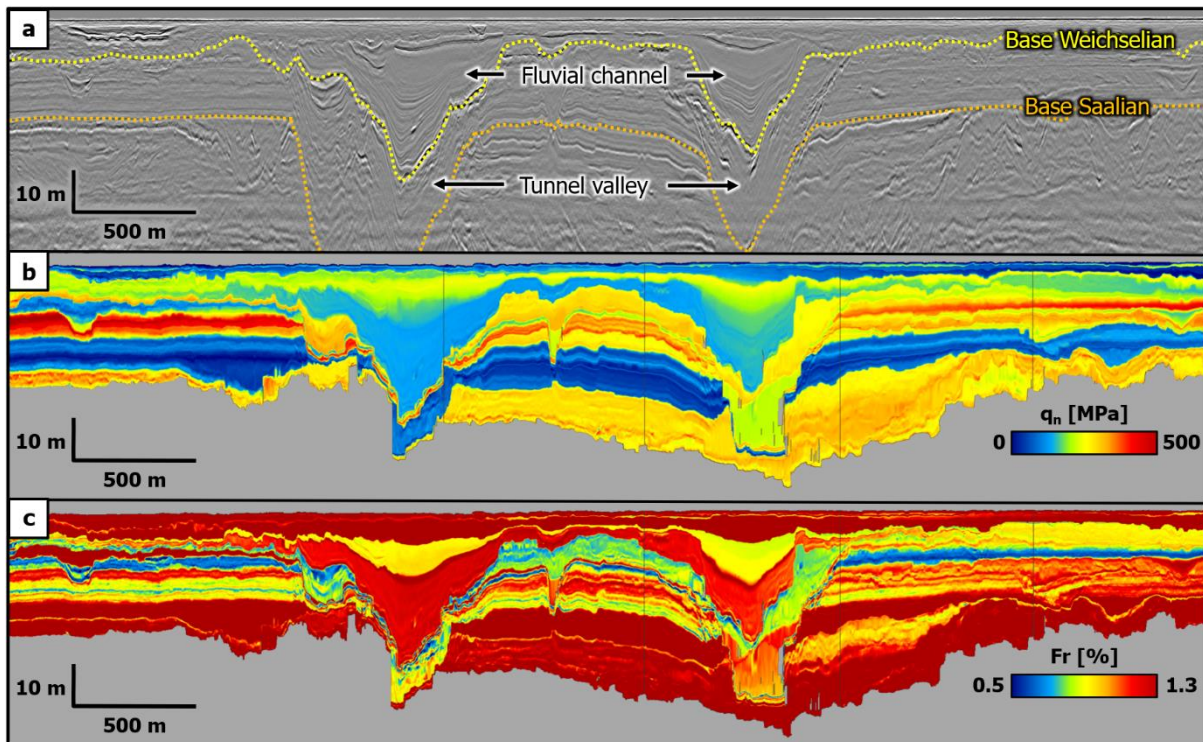
1584 The presence of strength variations within the very shallow foundation depths can pose a significant
1585 threat to mobile bottom-founded rigs and barges. Temporary works including jacking-up next to a jacket
1586 structure or installing a wind turbine may experience rapid leg penetration, or punch-through if there
1587 are stronger layers located over lower strength materials. This is especially important in glacialfluvial or
1588 glaciolacustrine sedimentary environments processes. Figure 5.12 shows a CPT profile depicting 3 m
1589 of dense sand over approximately 3 m of low strength clay in relatively shallow water. This profile
1590 represents a high chance of a punch-through incident occurring if not carefully assessed and managed.
1591 Procedures such as pre-loading and spud can foot design can help mitigate the risk.

1592 In order to mitigate the risks associated with soil strength variability, any project should make effective
1593 use of ground modelling to understand the soil depositional and post-depositional stress history (Figure
1594 5.13). Such an approach requires full and proper integration of geophysical, geotechnical and geological
1595 data; if one of these data sets has not been fully considered, knowledge gaps can provide results which
1596 may be open to misinterpretation. Therefore, a careful planning of all geophysical and geotechnical site
1597 investigations is required to ensure good coverage of expected soil units and seismostratigraphic units
1598 present across the site.



1599

1600 **Figure 5.12.** CPT profile showing near surface strength inversion from dense sand over low strength
 1601 clay. UK Central North Sea. Source: Anonymous.



1602
 1603 **Figure 5.13.** CPT-response models of the shallow subsurface offshore the Netherlands highlighting
 1604 distinct variations, both horizontally and vertically. **a)** Seismic profile showing the base of the last two
 1605 glaciations. The area has only been covered by the ice of the FIS during the Saalian glaciation. **b)**
 1606 Normalised cone resistance. Blue values indicate soft sediments, red values are hard sediments. **c)**
 1607 Normalized friction ratio. Blue indicates sandy sediments or desiccated clays. Red indicates clayey
 1608 sediments. CPT-response models generated by Eliis. Data courtesy of RVO.

1609 **5.5 Boulders**

1610 Boulders can be defined as “A smooth rounded mass or rock ... that has been shaped by erosion and
 1611 transported by ice or water from its original position” (collinsdictionary.com), although a boulder may
 1612 also be moved from its original position by human action or under the effect of gravity. There are several
 1613 definitions of the size of boulders, but most standards indicate a boulder is a rock that will not pass
 1614 through a 0.3 m square opening ([Table 5.2](#)). This implies that there is often some overlap in the size
 1615 spectrum between cobbles and boulders.

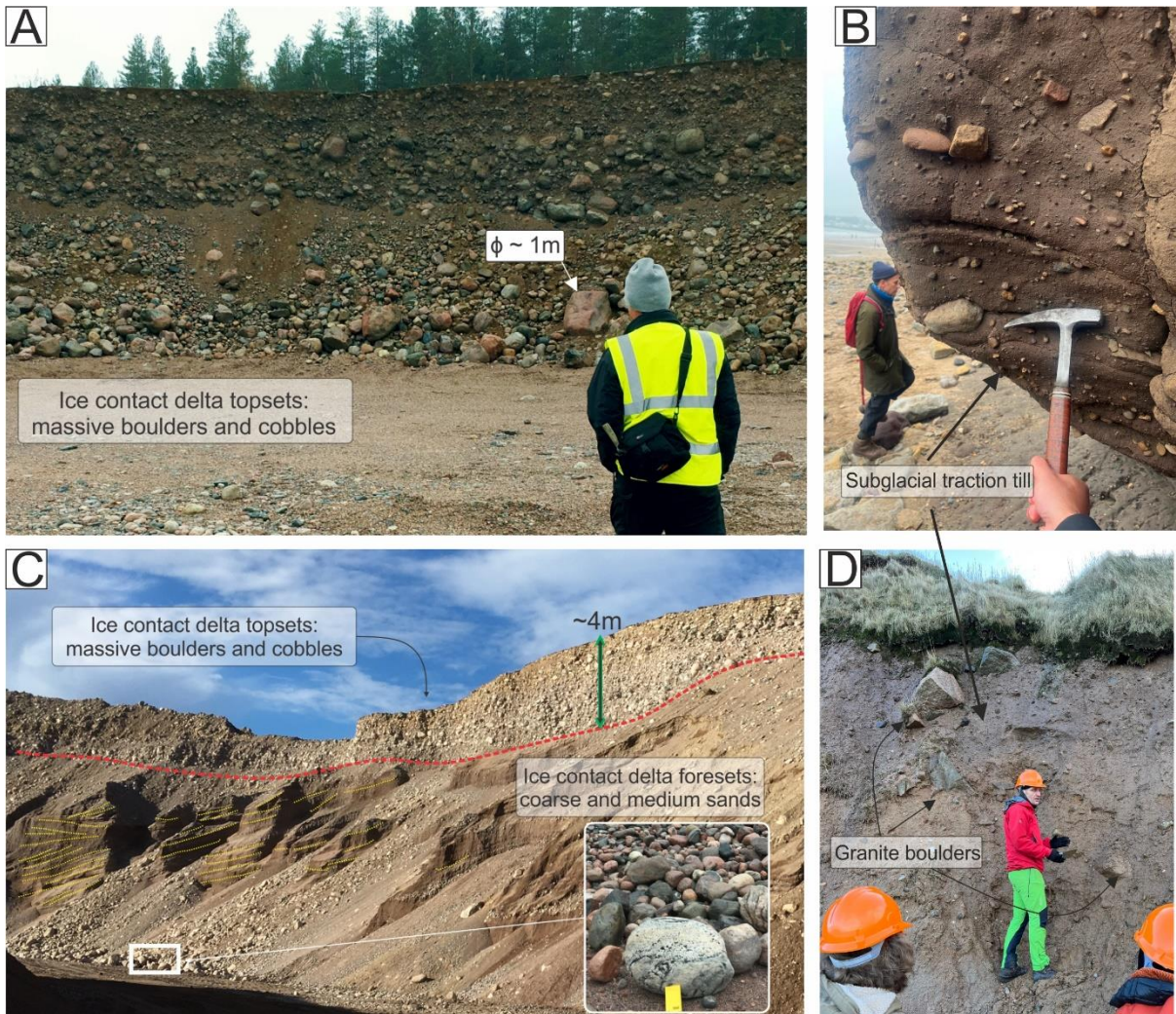
1616 **Table 5.2.** Different definitions of boulders according to object size.

| Reference | Boulder Size |
|-------------------|--------------|
| EN ISO 14689:2017 | >0.2 m |
| BS 5930:2015 | >0.2 m |
| Wentworth | >0.25 m |

| | |
|------|--------|
| ASTM | >0.3 m |
|------|--------|

1617

1618 Boulders represent the largest grain sizes that are deposited in glacial environments, being transported
 1619 on (supraglacial), within (englacial), and under (subglacial) the ice, bulldozed in front of it, and
 1620 transported by high-energy meltwater flows. Due to the range of depositional mechanisms associated
 1621 with glacial processes, single, as well as concentrations of boulders (boulder fields), may occur
 1622 anywhere within glacial deposits, and especially glacial tills. Boulders are ubiquitous along the
 1623 coastlines of previously glaciated margins, documenting their abundance within glacial deposits (Figure
 1624 5.14). Concentrations of boulders, known as boulder lag or palimpsest lag, may be expected at the base
 1625 of till deposits due to the very high level of energy involved with the deposition (e.g. Obst et al., 2017),
 1626 in positions of subsequent winnowing of finer material (e.g. channel bases, or the top of glacial deposits
 1627 effected by subsequent erosion) or within outwash plain deposits (Griffiths and Martin, 2017) (Figure
 1628 5.14)



1629

1630

1631 **Figure 5.14. a)** Massive boulder and cobble deposit forming the proximal part of an ice contact-delta
1632 within Salpausselka moraine near Lahti, Finland. **b)** Cobble and gravel clast-rich till from Filey Bay,
1633 Yorkshire, UK. **c)** last supported boulders and cobble-rich conglomerates forming topsets and sandy,
1634 steeply dipping forests of an ice contact delta near Lahti, Finland. The delta formed when the FIS margin
1635 was grounded in the Palaeo Baltic Ice Lake ~11.5 ka. Similar, but older, deposits can be expected from
1636 Slupsk Bank, Southern Middle Bank, and Northern Middle Bank offshore in the Baltic Sea. **d)** Boulder-
1637 rich sandy till from Sandford Bay near Peterhead, Scotland. Pictures: Bartosz Kurjanski

1638 Other sources of boulders that occasionally need to be considered include ice rafted boulders,
1639 commonly called “drop stones” (Griffiths and Martin, 2017; Donovan and Pickerill, 1997). These are
1640 often present in glaciomarine or glaciolacustrine deposits and can occur anywhere in the sequence of
1641 generally much finer-grained materials. However, it is important to note that ice rafted material can
1642 potentially be transported for a considerable distance from the glacial source.

1643 Boulders affected by glacial processes are representative of the rocks present in the path of glacial
1644 movement (provenance area), for example ice streams originating in Scandinavia will transport rocks
1645 from the crystalline and metamorphic basement; glacial deposits in the North Sea can contain rocks
1646 from the UK and/or Scandinavia. By assessing the lithology of these glacial erratics, it is possible to
1647 relatively reconstruct glaciations and ice flow pathways within specific ice-related deposits (e.g., Obst
1648 et al., 2017). Depending on the rock catchment of an ice sheet, boulders might be preserved to a lesser
1649 degree during the transport and erosion processes; igneous rocks might have a higher preservation
1650 potential than sedimentary rocks.

1651 *Geotechnical relevance*

1652 Boulders can be detrimental to several stages in offshore project development, depending on their size
1653 and distribution at and below seafloor within the area of interest. The prediction of boulder occurrence
1654 in previously glaciated margins is difficult and a holistic site appraisal is needed to understand its
1655 geologic development and to utilize available and suitable geophysical and geotechnical data. By
1656 understanding potential depositional environments, potentially boulder prone geological units such as
1657 glacial tills, channels, fans, or glaciomarine deposits can be investigated appropriately.

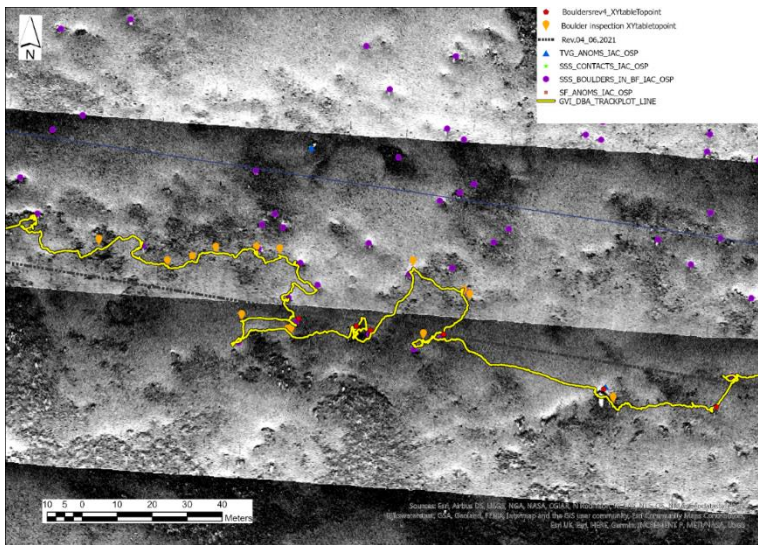
1658 During site investigation, boulders can cause early refusal during cone penetration testing (CPT), and
1659 numerous boulders can cause acoustic scattering during geophysical surveys. It is therefore important
1660 to consider how best to investigate areas known or expected to be boulder prone; even early site
1661 investigation “failures”, such as refusals and acoustic scattering, is information that can help inform
1662 future site investigation in these areas.

1663 Subsurface boulders may hinder the installation of piled foundations or damage piles during installation
1664 (Holeyman et al., 2015). Near-surface or surface boulders may damage jackup spud cans during

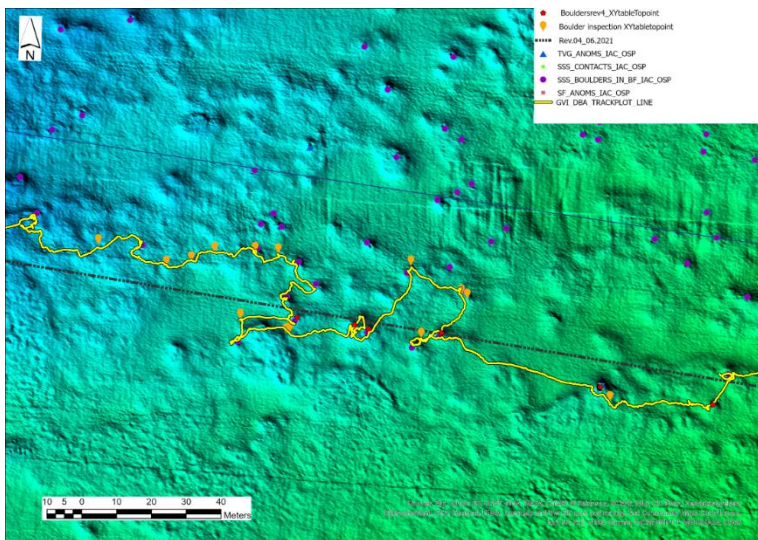
1665 installation or maintenance as well as hinder cable installation and burial. Engineering mitigation for
1666 the presence of boulders may include a review of the location of cable routes or pile installations to
1667 avoid local boulder presence (Figure 5.15). This may include the avoidance of areas of high boulder-
1668 probability (e.g. bases of tunnel valleys) or limited micro-siting to avoid identified individual objects.
1669 At the seafloor, boulders that are small enough to be lifted and still pose a risk may be removed to clear
1670 installation corridors, but larger boulders or those identified sub-seafloor need to be avoided or the
1671 installations hardened against them (e.g. pile tip reinforcements). For subsurface boulders, the strength
1672 of the surrounding matrix should be considered against the size of object considered a risk, as large
1673 infrastructure may effectively push objects aside in softer material. A 1 m boulder at depth in a low-
1674 strength clay will likely be pushed aside during monopile installation and not present an installation
1675 problem.

1676 *Boulder mapping and risk assessment*

1677 Boulders on the seafloor can generally be mapped out reliably using standard seismo-acoustic methods
1678 such as multibeam echosounders and side-scan sonars (SUT OSIG, 2022; IHO, 2020; Figure 5.15) and
1679 recent advances in technology mean other techniques, such as synthetic aperture sonar, can also be used,
1680 as they usually provide cm-scale horizontal resolution. Therefore, it is important to specify the
1681 minimum size of object that will pose an obstruction to engineering activities. Mapping all boulders on
1682 a site may be neither necessary nor cost-efficient and the focus should be on boulders of a critical size
1683 that is considered a risk (e.g. >0.5 m). Advances in automated data interpretation aid in dealing with
1684 large data volumes and target counts, however, these still require significant effort for quality control.
1685 It should be noted that seafloor imaging may only detect the surface expressions of buried boulders and
1686 further inspection, e.g. using remotely operated vehicles, may be needed to investigate complex areas
1687 (Figure 5.15).



1688



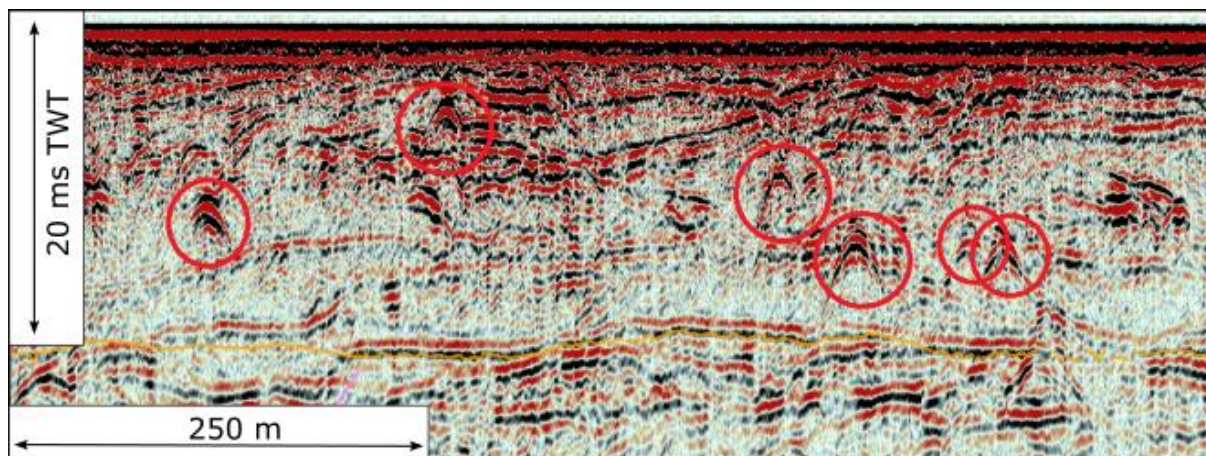
1689

1690 **Figure 5.15.** Boulders identified in different datasets. ROV track (yellow) and additional boulders
 1691 identified in ROV data (orange tags) compared to the side-scan-sonar targets (top) and multi-beam echo
 1692 identified in ROV data (orange tags) compared to the side-scan-sonar targets (top) and multi-beam echo
 1692 sounder targets (bottom). Data courtesy of SSE Renewables.

1693 Depending on the site geology, the subsurface may also contain significant boulder content that is not
 1694 as easily mapped. Boulders pose a significant challenge for geophysical methods due to their small size
 1695 and their characteristic as acoustic scatterers (Figures 5.16 and 5.17). Seismic methods are the
 1696 predominant means of subsurface boulder mapping, relying on the identification of diffraction energy
 1697 to pinpoint boulders. Due to the point-nature of the objects, such measurements need to be carried out
 1698 in 3D for accurate mapping (Figure 5.17), thus require a high effort in data acquisition, processing and
 1699 interpretation. The object size requires an extremely high resolution (EHR) seismic setup (see ISO
 1700 19901-10; Hill et al., 2024) to image objects in the relevant size range (e.g., Monrigal et al., 2017). It is
 1701 important to note that even for advanced 3D EHRS setups, the mapping of boulders within complex
 1702 glacial geology with a background of high impedance contrasts and spatially heterogenous unit
 1703 distribution is a challenging task. It is also important to consider that many EHRS setups will also be

1704 capable of detecting much smaller objects (<20 cm diameter), especially close to the seafloor, which
1705 might in reality be below the size threshold considered a risk for engineering. This could lead to
1706 alarming numbers of subsurface contacts and the potential for unnecessary engineering mitigations.
1707 However, determining exact object sizes at depth from seismic diffraction signals remains difficult and
1708 often leads to ambiguity during interpretation (e.g. Römer-Stange et al., 2022). The use of 3D EHRS
1709 techniques to map subsurface targets should therefore be proportionally balanced with the potential risk
1710 to projects, taking into consideration the limitations of the seismic equipment and the determined risk
1711 to engineering works.

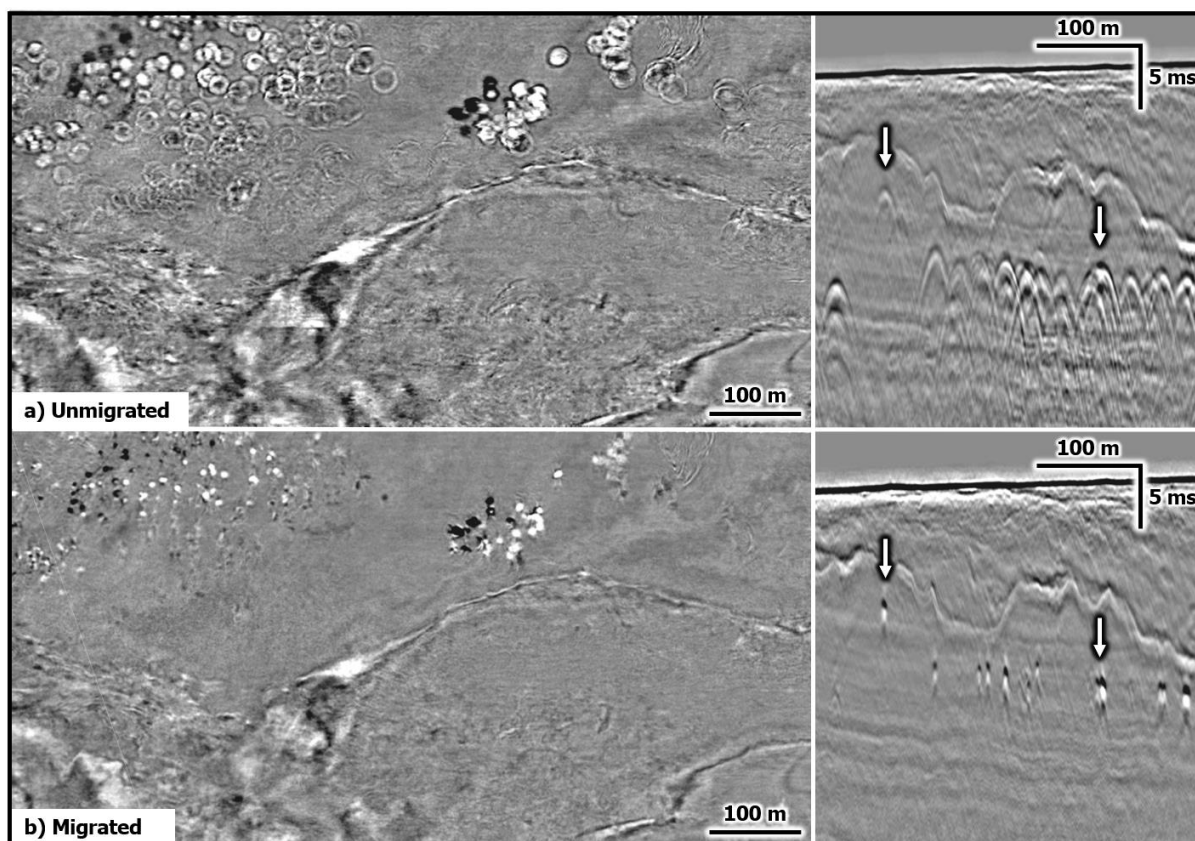
1712 Boulders (or discontinuities) may also stand out on 2D UHRS (Figure 5.16), however, due to the
1713 localization ambiguity for out-of-plane events, 3D EHRS is required for detailed subsurface contact
1714 mapping (Figure 5.17). 2D UHRS from site characterization surveys should be used for initial risk
1715 assessment and a precursor to dedicated boulder mapping activities where needed.



1716 **Figure 5.16.** Multichannel UHRS line in the southern North Sea showing diffractions visible in
1717 unmigrated data within the upper ~30 ms TWT. These diffractions in 2D UHRS data are interpreted as
1718 potential boulders and used as a risk indication for the area. Source: BSH, 2023.

1720 At different phases of a development, the risk posed by the presence of boulders should be revisited and
1721 survey equipment choice should be optimized to achieve the desired level of accuracy and detection,
1722 both for surface and sub-surface boulder presence. A phased approach may include (OWA, 2020):

- 1723 - Detection phase: Boulder-prone areas are identified and, at best, avoided during development
- 1724 - Zonal phase: If an area cannot be avoided, a perimeter with a defined boulder density
1725 classification is established
- 1726 - Locate and Measure phase: A targeted survey aims at determining the size and position of
1727 boulders in a defined area that require consideration and intervention
- 1728 - Mitigation phase: Micro-siting of cable, installation footprint, or foundation to avoid boulders



1729

1730 **Figure 5.17.** Boulder identification using diffractions in ultra-high-resolution 3D seismic data of the
 1731 Southern North Sea. **a)** Unmigrated data showing clear hyperboles. **b)** Migrated data showing point
 1732 anomalies. Hard kicks in black. Data courtesy of Vattenfall.

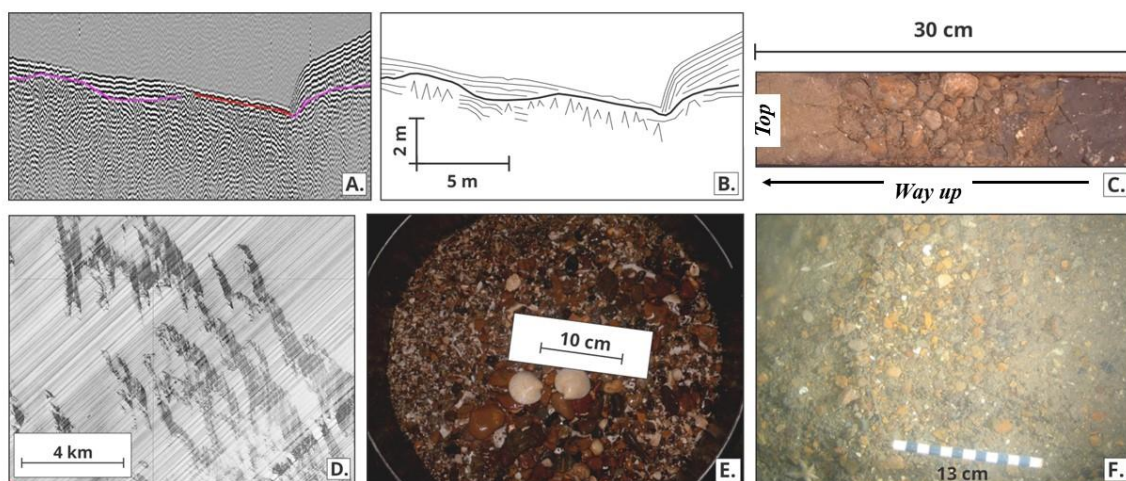
1733 **5.6 Gravel and cobble beds**

1734 Gravel lag deposits have been reported at various locations across the North Sea and North-East Atlantic
 1735 Margin in variable water depths (e.g., Carr, 1999; Howe et al., 2001; Diesing et al., 2009). Lag deposits
 1736 are often formed when bottom currents achieve adequate velocities to enable the winnowing of finer
 1737 particles (e.g., clay and silt) from the seabed soil unit, leaving behind a blanket of coarser materials.
 1738 Alternatively, high-energy depositional environments can also lead to the accumulation of thick gravel
 1739 and cobble deposits.

1740 The Dogger Bank and Bolders Bank Formations comprise soils deposited under glacial conditions,
 1741 often being lain down under and immediately in front of ice sheets that extended across the North Sea
 1742 during the Last Glacial Maximum (LGM). They occur extensively across the Central and Southern
 1743 North Sea and are often found within the uppermost 50 m of stratigraphy, occasionally outcropping at
 1744 seabed. Diesing et al. (2009) noted gravel lag deposits within bathymetric lows across the Dogger Bank
 1745 area, and attributed these soil units to the reworking of underlying glacial deposits. Clasts contained
 1746 within the Dogger Bank and Bolders Bank Formations comprise a wide variety of lithologies, however
 1747 clasts derived from weaker bedrock units (e.g., chalk, sandstone and mudstone) can become

1748 disaggregated through erosion which typically results in a gravel lag dominated by stronger lithologies
 1749 (e.g., igneous and metamorphic origins, and flint clasts from chalk units), which reflects the relative
 1750 high strength of these clasts within a high-energy setting. Studies of these gravel clasts have shown that
 1751 they originate from bedrock sources typically in Scotland and Northern England (Carr, 1999; Diesing
 1752 et al., 2009). In addition to the lithic fragments, biogenic gravels comprising shell debris and tests were
 1753 noted to have accumulated at various locations across the Dogger Bank site; these deposits are Holocene
 1754 in age and have built up over the past 7.5 ka following the complete inundation of Dogger Bank during
 1755 the Holocene marine transgression (Diesing et al., 2009).

1756 Gravel lag deposits have previously been identified in boreholes, cores, seabed samples and shallow
 1757 geophysics from across the wider Central and Southern North Sea, typically overlying glacial deposits
 1758 and blanketed by Holocene sands. Figure 5.18 illustrates examples of such surface and near-surface
 1759 gravel lag deposits from the Dogger Bank area, including a section of core comprising 45 cm of dark
 1760 greyish brown sand (Holocene sands) overlying 17 cm of gravel and cobbles, which in turn is underlain
 1761 by dark greyish brown slightly sandy clay containing chalk clasts (glacial diamicton; Figure 5.18c).

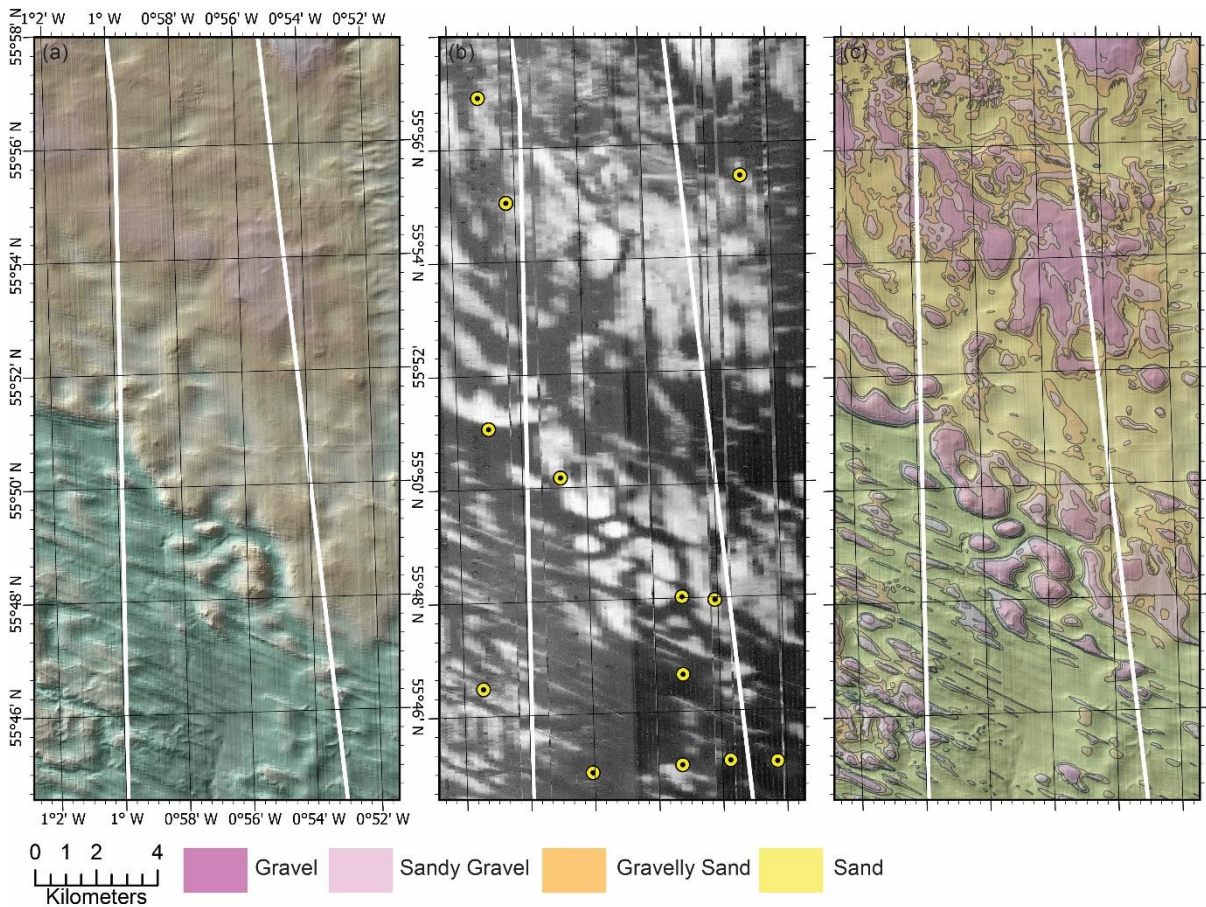


1762
 1763 **Figure 5.18.** Examples of seabed and shallow subsurface gravel lag deposits from the Dogger Bank
 1764 area of the North Sea. **a+b)** Multiple hyperbolae along a discrete horizon of high-resolution shallow
 1765 geophysics (pinger data), corresponding with surface and near-surface gravels. **c)** Sediment core
 1766 illustrating a gravel lag preserved between an underlying glacial diamicton and overlying Holocene
 1767 sand deposits. **d)** Sidescan Sonar (SSS) with darker grey representing surface gravels and cobbles in
 1768 NNW-SSE orientated troughs. **e)** Surface gravels recovered in grab samples. **f)** Evidence of gravel beds
 1769 preserved on the seafloor in sledge camera footage. Data examples courtesy of the British Geological
 1770 Survey and Dogger Bank Offshore Wind Farm (SSE and Equinor), modified from Carter et al. (2025).

1771 **Engineering considerations**

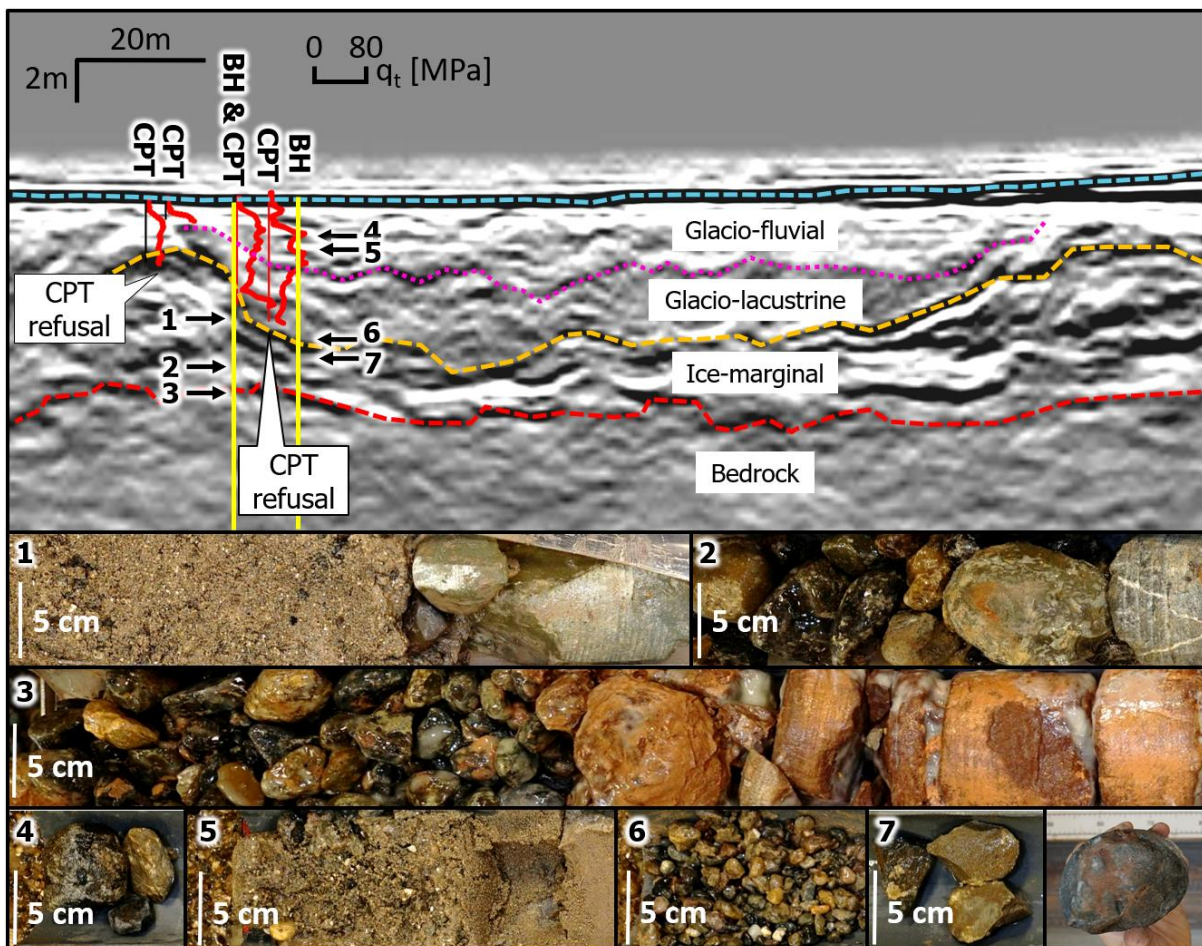
1772 In all stages of site and route selection, the presence of gravel beds can cause issues. Gravel beds on the
1773 seafloor are generally detected by the use of high-frequency side-scan sonar and multi-beam echo
1774 sounder (often using a by-product that measures the intensity of the reflection termed backscatter, to
1775 classify the seafloor composition). Gravel beds are used by several important commercial and protected
1776 fish species as spawning and nursery grounds (Ellis et al., 2012; Stewart et al., 2022) and as such can
1777 be a protected habitat that needs to, at least, be considered as part of any consenting requirements for a
1778 project and may be critical in cable routing, foundation location selection and installation planning
1779 (Figure 5.19).

1780

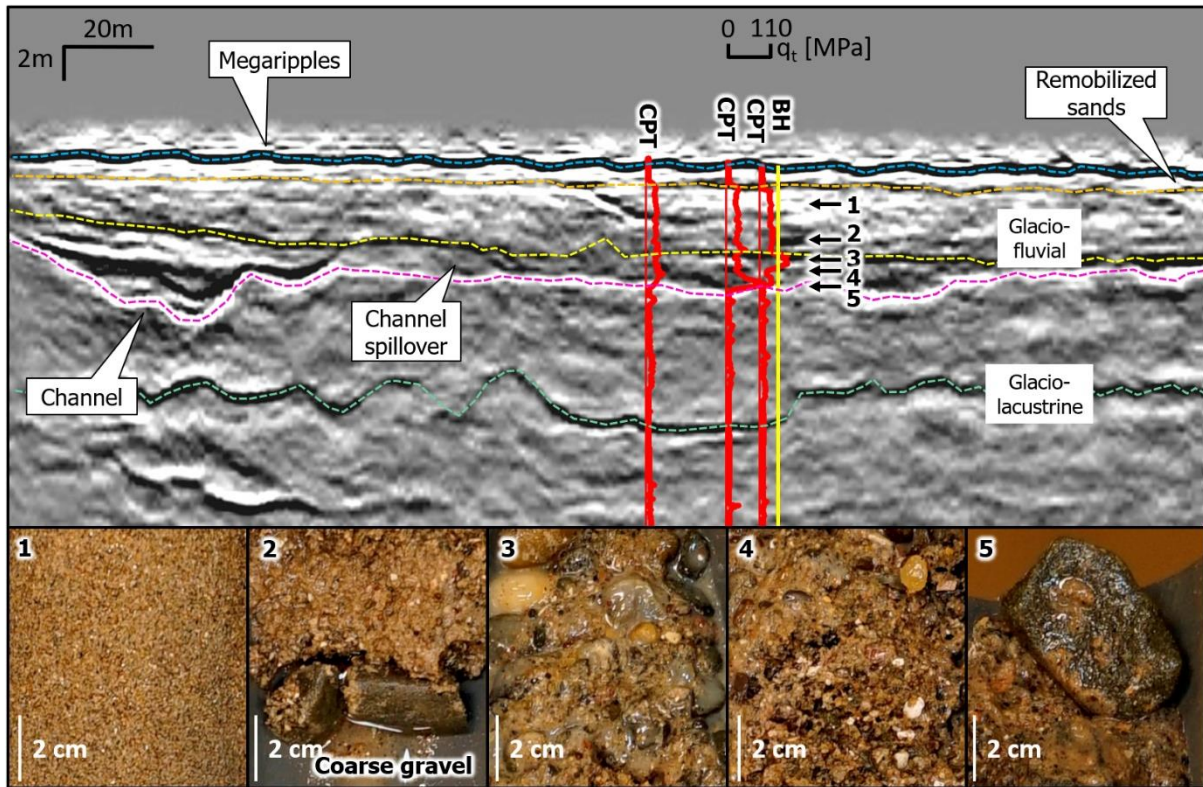


1782 **Figure 5.19.** Example of Benthic Habitat mapping related to gravel distribution along a proposed cable
1783 route (white outline) as part of the consent requirements for route selection. Example from the offshore
1784 expression of the North Sea Lobe palaeo-ice stream, an area of glacial ice streaming and deposition of
1785 moraines and grounding zone wedges. Multibeam bathymetry (a) and backscatter intensity (b) data
1786 acquired as part of the Civil Hydrography Programme (CHP) on behalf of the Maritime and Coastguard
1787 Agency (MCA) from survey HI1083. Ground-truthing data (yellow dots (b)) and seafloor substrate
1788 interpretation (c) by H.A. Stewart available online via the British Geological Survey Offshore GeoIndex
1789 (www.bgs.ac.uk/map-viewers/geoindex-offshore/ British Geological Survey © UKRI 2025).

1790 At the site investigation stage, gravel beds can cause early refusal during cone penetration (CPT),
 1791 vibrocore, or borehole testing, by acting as a physical barrier to effective penetration of the tool (Figure
 1792 5.20). However, if well sorted and more fine-grained, CPTs might get pushed through these beds (Figure
 1793 5.21). Gravel beds, either on the seabed or subsurface can also cause acoustic scattering during
 1794 geophysical surveys and therefore mask underlying structure, this property though, is also important in
 1795 being able to detect the depth and areal extent of buried gravel beds so they can be avoided or planned
 1796 for (Figure 5.20). Figures 5.20 and 5.21 highlight that understanding the paleo-geographic environment
 1797 (see Section 3.4), and the establishment of solid ground models, are crucial for the planning and success
 1798 of geotechnical site investigations: The gravels and cobbles deposited in subglacial environments are a
 1799 larger engineering constraint (Figure 5.20) compared to the gravels deposited on an outwash fan (Figure
 1800 5.21).
 1801



1802
 1803 **Figure 5.20.** Gravels, cobbles, and boulders in the shallow subsurface of the Irish Sea, with CPTs
 1804 refusing. Samples 1-3 and 7 are part of a subglacial/glaciotectionic unit, whereas samples 4-6 were
 1805 deposited in glacio-fluvial and glacio-lacustrine environments. Data courtesy of Morgan Offshore Wind
 1806 Limited.
 1807



1808

1809 **Figure 5.21.** Sand and gravels in the shallow subsurface of the Irish Sea, with CPTs penetrating.
 1810 Samples 1-5 are all taken from an outwash fan. Data courtesy of Morgan Offshore Wind Limited.

1811

1812 Gravel lag deposits can also be of interest to site developers as they have the potential to influence cable
 1813 trenching activities and parameters; certain trenching methods may have more difficulty with
 1814 excavating dense gravels when compared with finer-grained, looser sands and silts, resulting in trench
 1815 instability, high tow forces and/or planned Depth of Lowering (DoL) not being achieved in a single
 1816 vessel pass. Whilst not only being unsuitable for jetting methods of trench excavation, gravel lags may
 1817 also result in greater resistance and potential deviation of seabed ploughs leading to unexpected poor
 1818 performance (Dyer, 2011). This may result in the need to use larger and more costly devices. In addition
 1819 to impeding cable burial operations, gravel-rich soils can also prove problematic for certain foundation
 1820 types such as suction caisson, especially when interbedded with other soil units of different grain size,
 1821 providing a high degree of soil heterogeneity within the foundation zone of interest.

1822 **5.7 Soft marine sediments**

1823 Across the glaciated European margin, normally consolidated or (sometimes) underconsolidated (i.e.
 1824 incomplete consolidation) soft to very soft marine sediments, typically muds (clays and silts), occur at
 1825 or near the seafloor. The definition of “soft” refers to the relationship of undrained shear strengths, with
 1826 ISO standards designating Extremely low (< 10 kPa), Very low (10 to 20 kPa) and Low (20 to 40 kPa)
 1827 categories (ISO 14688-2). Common values of between 5 and 20 kPa have been reported for such units
 1828 in the Irish Sea for example (Coughlan et al., 2023; Mellet et al., 2015). The British Standards also

1829 describe a set of standardised field tests for soil strength, which can be used to identify “soft” material
 1830 (Table 5.3).

1831 **Table 5.3.** Standardised field tests for soil strength to describe soft sediments.

| | |
|--------------|--|
| BS 5930:2015 | |
| Very Soft | Finger easily pushed in up to 25 mm. Exudes between fingers |
| Soft | Finger pushed in up to 10 mm. Moulded by light finger pressure |
| BS 5930:1999 | |
| Very Soft | Finger easily pushed in up to 25 mm. Exudes between fingers |
| Soft | Finger pushed in up to 10 mm; moulded by light finger pressure |
| BS 5930:1981 | |
| Very Soft | Exudes between fingers when squeezed in hand |
| Soft | Moulded by light finger pressure |

1832

1833 During the Quaternary, the oscillation between glacial and interglacial periods has created a number of
 1834 low-energy environments across the glaciated European margin, allowing for the deposition of these
 1835 sediments, including glaciomarine to marine, glaciolacustrine and estuarine settings. Presently,
 1836 accumulations of these sediments on the continental shelf generally form under low bed-stress, or
 1837 depositional, conditions and are usually late-glacial to Holocene in age (e.g. [Ward et al., 2015](#); [Coughlan
 1838 et al., 2021a](#)). They can form thick deposits in depocenters in a variety of settings under differing
 1839 environmental conditions and processes ([Hanebuth et al., 2015](#); [Porz et al., 2021](#)). Well studied
 1840 examples of these deposits include the Witch Ground Formation in the North Sea ([Paul and Jobson,
 1841 1991](#)), the Mud Facies of the Western Irish Sea Formation ([Coughlan et al., 2023](#)), and the contouritic
 1842 infill in the northern Storegga escarpment ([Bryn et al., 2005a](#)). In the north Irish Sea, up to 40 m of soft
 1843 marine sediments were recorded in the British Geological Survey borehole 89/15 forming a valuable
 1844 palaeoenvironmental archive ([Woods et al., 2019](#)). A thick succession of weakly consolidated
 1845 glaciomarine clays have been identified in a recent desktop study in the Danish North Sea ([Jensen and
 1846 Benniken, 2022](#)). Extensive areas of surface soft marine sediments typically exhibit an overall flat
 1847 seabed, and these areas are typically targeted by bottom trawling activity as they form habitats for many
 1848 burrowing invertebrates ([Eigaard et al., 2017](#)) in addition to forming reservoirs of organic carbon
 1849 ([Diesing et al., 2017](#)). Deposits of silty to clay sediments can be found having been deposited under
 1850 conditions associated with palaeo-proglacial lakes ([Andresen et al., 2022](#); [Hjelstuen et al., 2018](#)).
 1851 Depending on the subsequent geological history of the area they were formed in, they can be soft. Their
 1852 extent in terms of vertical thickness and lateral continuity can be difficult to constrain.

1853 **Identification Criteria**

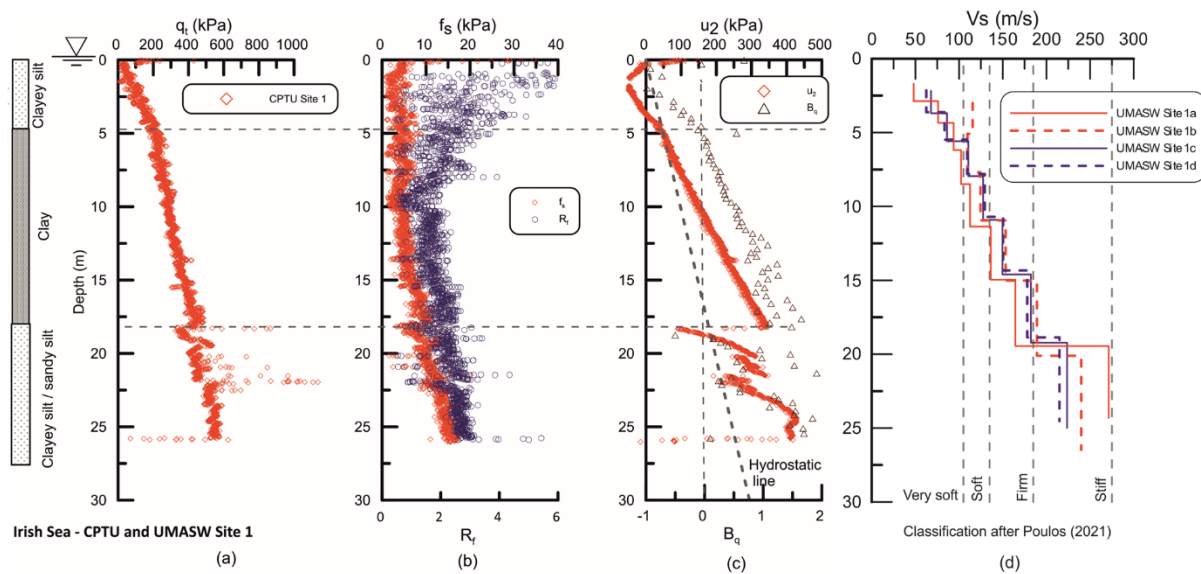
1854 At the site investigation stage soft marine sediments can be identified by multibeam echosounder
 1855 backscatter data at the surface. Where thick deposits occur, these deposits typically exhibit a laminated
 1856 or transparent character in reflection seismic profiles. Efforts have been made to characterise soft marine

1857 sediments using shear wave velocity (V_s) values with promising results (e.g. [Coughlan et al., 2023](#);
1858 [Trafford et al., 2022](#); [Figure 5.22d](#)), however this is not carried out normally as part of the site
1859 investigation process.

1860 Retrieving good quality borehole and core samples of these deposits can be difficult. Box corers can
1861 provide relatively intact and good quality samples but typically have shallow penetration and recovery
1862 depths of 20–60 cm below the seafloor. Vibrocores and gravity corers can recover deeper cores,
1863 reaching up to 15 m below the seafloor, although sediment disturbance and profile shortening can be
1864 significant issues (e.g. [Düick et al., 2019](#)). Piston corers provide higher sample quality, and to greater
1865 depths, but are expensive and more difficult to operate ([Lunne and Long, 2006](#); [Tommasi et al., 2019](#)).

1866 As a result, in-situ testing using cone penetration testing (CPT) with selected boreholes with piston
1867 sampling remains the tool of choice when characterising these sediments as it can deliver reliable, high-
1868 resolution, geotechnical profiling to depths of up to 50 m to International Standards Organisation (ISO)
1869 standards ([ISO 22476-1:2022](#); [Andersen et al., 2008](#); [Lunne et al., 2011](#); [Figure 5.22a-c](#)). The accuracy
1870 and applicability of CPTs in soft marine sediments can be improved through the use of “add on” devices
1871 such as the T-bar, ball, and plate penetrometers ([Qiao et al., 2023](#)). Data acquired through CPTs can be
1872 used to estimate sediments based on their soil behaviour type (SBT) according to certain parameter
1873 ranges, including normalized cone resistance (Q_t) and the pore pressure parameter B_q or normalized
1874 friction ratio (F_r) ([Robertson et al., 1986](#)). It has been reported that the use of the sleeve friction (f_s) data
1875 acquired by CPTs in soft marine sediments in some cases are unreliable ([Lunne et al., 2018](#)). Similarly,
1876 [Robertson \(1990\)](#) demonstrated that for soft soils normalised SBT charts are not overly sensitive to
1877 variations in f_s . Furthermore, these charts rely on the corrected cone resistance (q_t), requiring accurate
1878 pore pressure measurements to make the correction. In soft fine-grained sediments, the difference
1879 between uncorrected (q_c) and corrected cone resistance (q_t) can be significant where q_c is less than 1
1880 MPa. The application of a soil behaviour type index (I_c) to the [Robertson \(1990\)](#) $Q_t - F_r$ showed a
1881 simplification in characterisation ([Robertson, 2016](#)). However, the applicability of these charts depends
1882 on the accurate measurement of parameters, and obtaining reliable in-situ pore water pressure
1883 measurements in soft sediments remains a challenge and the similarity to the soils the diagrams were
1884 calibrated to ([Peuchan and Terwindt, 2014](#)). Data acquired through CPTs can be used to estimate other
1885 soil properties, such as undrained shear strength (s_u), stiffness, unit weight and pre-consolidation stress
1886 ([Lunne et al., 1997](#)).

1887 Aside from CPT data, V_s values can be used to estimate undrained shear strength ([L’Heureux and Long,](#)
1888 [2017](#); [Oh et al., 2017](#)), although such approaches heavily depend on locally derived correlations with
1889 good quality samples. Therefore, despite the applicability of CPT approaches to characterising soft
1890 marine sediments for engineering design, these data are often used in tandem with an extensive
1891 programme of laboratory-based testing (e.g. [Andersen et al., 2023](#)).



1893

1894 **Figure 5.22.** Typical CPTU and UMASW profile from the north Irish Sea consisting of soft marine
 1895 clays from 0 - ~17.5 mbsf, overlying coarser glacial outwash sediments. CPTU data versus depth for
 1896 Site 1. **a)** CPTU q_t . **b)** CPTU f_s and R_f . **c)** CPTU u_2 , u_0 and B_q . **d)** V_s derived from UMASW at the same
 1897 site superimposed limits for material classification from Poulos (2022). CPTU: In-situ cone penetration
 1898 testing with pore pressure measurement. UMASW: Underwater multichannel analysis of surface waves.

1899 Engineering Considerations

1900 Soft marine surficial sediments of typically <2 m thickness may pose problems for shallow foundations
 1901 as for example GBS or suction caissons but do not pose an issue for piled foundations. However, these
 1902 soft sediments have the potential to allow for much deeper anchor penetrations than expected, which
 1903 has implications for floating wind anchor systems (Petrie et al., 2022). With regard to cables, the low
 1904 bearing capacity of soft marine sediments poses a potential geo-constrain in terms of sinking as well as
 1905 trenching of the cable (DNV, 2014). When these deposits occur in thick packages, foundation sizes
 1906 increase significantly. Aside from low shear strength, other geotechnical characteristics associated with
 1907 soft marine sediments are high water content, high compressibility and low permeability. As a result,
 1908 these sediments can be challenging for foundations due their low bearing capacity, excessive settlement
 1909 and susceptibility to stiffness degradation. The presence of more resistant, stiffer underlying units (e.g.
 1910 glacial till) creates a strong mechanical contrast of sub-surface geological, increasing vertical
 1911 heterogeneity, and offering complex ground conditions. Furthermore, where significant accumulations
 1912 of soft marine sediments occur, they have been reported as being gas-bearing, as documented in the
 1913 Irish Sea (Coughlan et al., 2021b; Yuan et al., 1992), North Sea (Böttner et al., 2019) and the Baltic Sea
 1914 (Tóth et al., 2014b), which forms another constraint (see Section 5.1).

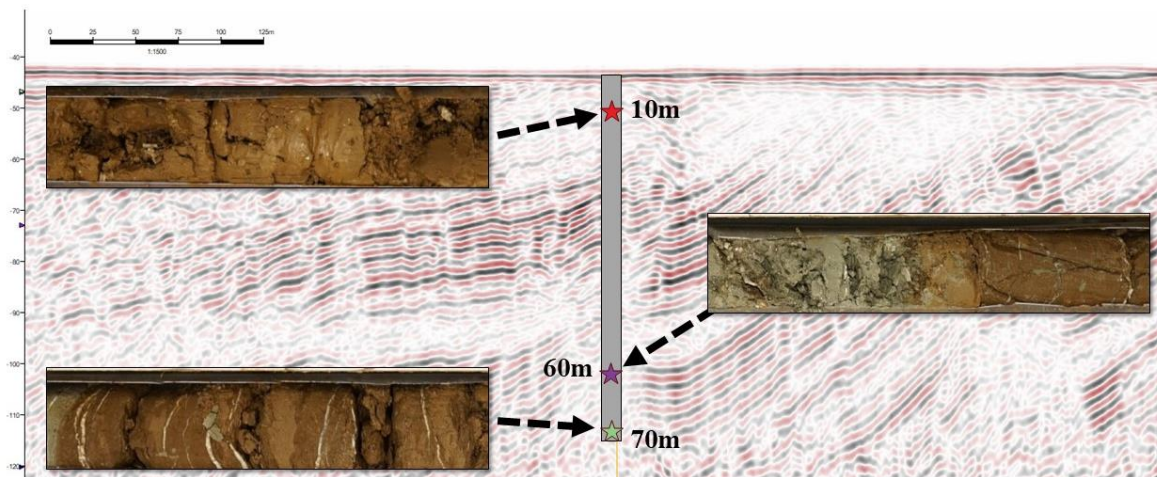
1915 Soft marine sediments are also prone to scouring. Whilst typically occurring in accretionary settings
1916 where they form a flat, featureless seabed topography, the introduction of obstacles can induce vortex
1917 shedding and enhanced current flow causing erosion and transport of sediment from around the base of
1918 the structure (e.g. [Callaway et al., 2009](#)). The extent of this phenomena in muds (i.e. silts and clay)
1919 depends on the degree of compaction ([Whitehouse et al., 2011](#)), whilst they are also prone to
1920 liquefaction ([Sumer and Kirca, 2022](#)). Dewatering in soft marine clays has also been reported in the
1921 Horns Rev III windfarm site ([Vattenfall, 2019](#); [Figure 1.3](#)). Scour is both an issue for foundation
1922 stability, as well as free-spanning in cables.

1923 The presence of soft sediment layers at depth below the seafloor are also known to play a significant
1924 role in controlling submarine landslide formation ([Gatter et al., 2021](#)). On the slopes offshore Norway,
1925 the glide planes and infill of mega-slide escarpments is often correlated to soft, contouritic clays
1926 ([Haflidason et al., 2003](#); [Bellwald et al., 2022a](#)), which show strain-softening behaviour which is very
1927 different from the glacial clays (e.g., [Bryn et al., 2005a](#); [2005b](#); [Kvalstad et al., 2005b](#)). In near-shore
1928 environments, quick clays pose a significant threat as well for engineering ([L'Heureux et al., 2018](#)).
1929 Quick clays are sensitive marine clays with unique behaviour when disturbed (e.g., vibrations, changes
1930 in stress state), rapidly losing their strength and becoming fluid. They form from normal clays deposited
1931 in marine environments, which become uplifted in response to glacio-isostatic rebound, and over time,
1932 the salt in the pore water is leached by freshwater leading to a change in the clay's structure and
1933 properties ([Thakur et al., 2017](#)). Quick clay failures are some of the most devastating hazards in
1934 formerly glaciated margins (e.g., Finneidfjord, Rissa, Kråknes, and Gjerdrum landslides in Norway;
1935 e.g., [L'Heureux et al., 2013b](#); [Giles, 2022b](#)).

1936 **5.8 Weathered and unweathered bedrock**

1937 If bedrock is within the depth of interest for the installation of foundations, pipelines, or cables,
1938 understanding its character, depth and distribution is critical to avoiding damage to the assets and costly
1939 delays to projects due to unforeseen ground conditions. Within the glaciated European margins,
1940 generally the likelihood of encountering bedrock within the depth of interest can be established early
1941 on in a project during the initial desk-top study phase by conducting a review of the various Nation
1942 States published geological information such as the British Geological Survey in the UK (e.g. the [British
1943 Geological Survey](#)). It is important to anticipate the presence and the type of bedrock as early in site
1944 development as possible, as the weathering profiles of rocks can vary significantly, which in turn can
1945 impact upon individual wind turbine generator (WTG) foundation selection right from the Front-End
1946 Engineering Design (FEED) phase of a project. Early work should also include careful consideration of
1947 relative sea level curves and wider geo-evolutionary history, to understand the likelihood of sites being
1948 subaerially exposed or affected by other processes such as periglacial frost shattering or desiccation.

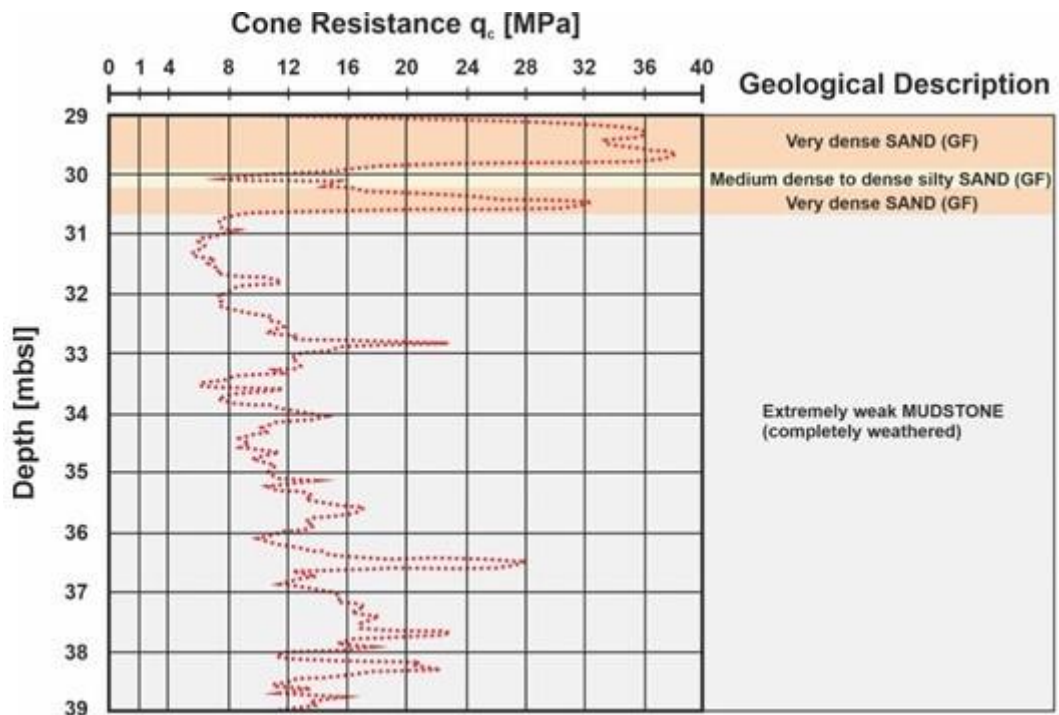
1949 If the presence of bedrock at the depth of interest at a site or along a cable or pipeline route is shown to
 1950 be a potential issue for foundation selection, cable installation and design, then it becomes a primary
 1951 objective of the geophysical survey and subsequent geotechnical survey to investigate the nature of that
 1952 bedrock. The primary concern is the potential for encountering unexpectedly strong to extremely strong
 1953 rockhead within the depth of interest resulting in early pile refusal or cable burial not achieving the
 1954 required depth. Conversely, the situation can be further complicated when the interface between
 1955 Quaternary sediments and the underlying bedrock is not clearly defined due to subglacial and periglacial
 1956 processes having acted upon the bedrock, creating a weathering zone (e.g., Dudgeon Offshore Wind
 1957 Farm, Mellett et al., 2020). This can result in the overlying Quaternary deposits having higher densities
 1958 (granular sediments) or shear strengths (cohesive sediments) than the underlying bedrock unit(s),
 1959 especially where the Quaternary sedimentary sequence has been overconsolidated through ice loading
 1960 (e.g., subglacial lodgement tills). In many cases, this can lead to the weathered ‘bedrock’ zone acting
 1961 more like an unlithified sedimentary deposit (e.g., a firm to stiff clay consistency) in terms of its
 1962 associated geotechnical properties and geomechanical behaviour (Figure 5.23).



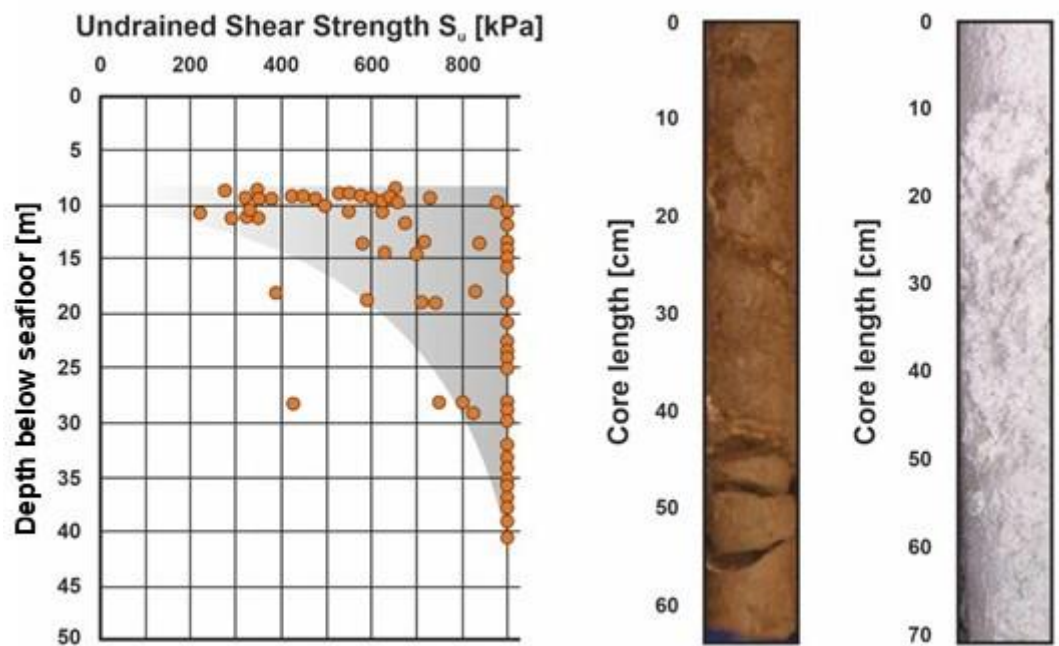
1963
 1964 **Figure 5.23.** Weathering of Mercia Mudstone in the East Irish Sea, evident in the upper 60 m below
 1965 seafloor where the unit acts geomechanically as a very to extremely high strength clay, as opposed to a
 1966 lithified rock. Data courtesy of Mona Offshore Wind Limited.

1967 An example of this scenario of inverse geotechnical properties at the sediment-rock interface can be
 1968 seen in the Irish Sea, between the mainland UK and Ireland, where the overlying tills and glaci-fluvial
 1969 deposits associated with the Cardigan Bay Formation are often observed to have much higher cone
 1970 resistance (q_c) values from Cone Penetration Tests (CPTs) than the underlying Triassic rocks of the
 1971 Mercia Mudstone Group (Figure 5.24). Similar inverse profiles have been observed at many locations
 1972 where rockhead is within foundation depths across the NW European Margin (e.g., the Chalk Group
 1973 and Smith Bank Formation of the Central-Southern North Sea), with weathering being particularly

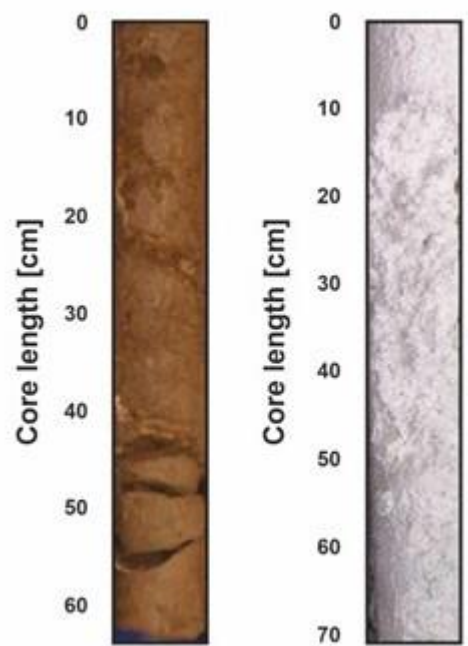
1974 amplified when the underlying bedrock is composed of fine-grained sedimentary strata (e.g., mudstones
 1975 and various carbonates; Figure 5.24).



A.



B.



C.

D.

1976

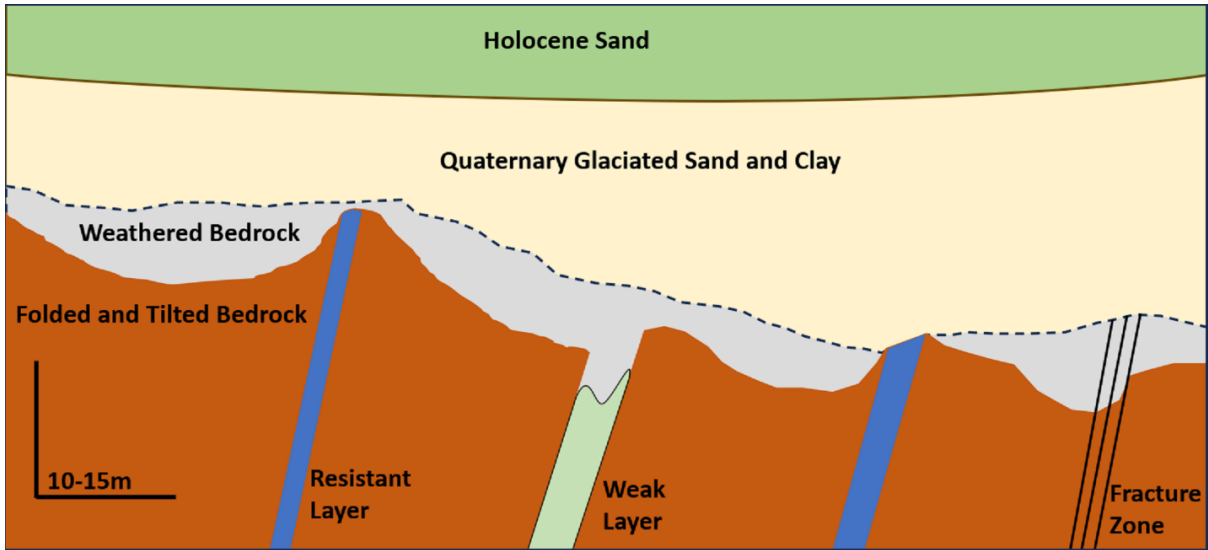
1977 **Figure 5.24.** Examples of engineering properties and core images from weathered bedrock units. **a)**
 1978 Example CPT plot demonstrating reduction in cone resistance (q_c) when penetrating down through
 1979 dense to very dense glaci-fluvial (GF) sands and into less resistant completely weathered Mercia
 1980 Mudstone. Plot adapted from southern Irish Sea location (Fugro, 2013). **b)** Shear Strength (S_u) plot
 1981 demonstrating a weathered surface in Mercia Mudstone, Irish Sea, with low (200-300 kPa) strength

1982 properties, increasing in strength with depth (grey shading to demonstrate increase curve). Plot adapted
1983 from Mellett et al. (2015). **e)** Core image showing completely weathered Mercia Mudstone Group from
1984 the southern Irish Sea (Fugro, 2013). **d)** Core image showing completely weathered Chalk Group with
1985 ‘putty’ consistency from the southern North Sea (Johnson et al., 2023).

1986 A further challenge lies in the structural framework of the bedrock unit(s) underlying the Quaternary
1987 sediments, whereby the orientation of individual subunits/beds within the overall bedrock formation
1988 can be steeply dipping with differing weathering profiles (Figure 5.23). An example of this would be
1989 the Chalk Group of the southern North Sea, where moderately to steeply dipping strata have given rise
1990 to differential weathering profiles on a metre-scale between beds of completely to moderately
1991 weathered chalk and more weathering-resistant flint bands. This Quaternary/bedrock interface will
1992 typically vary greatly, in terms of physical properties, over very short distances which can be in the
1993 order of <10 m and well within the average radius of modern pile foundation design; the problem is
1994 exacerbated when considering potential for difference across jacketed foundations or mooring/anchor
1995 solutions for floating offshore structures, which can have a much wider footprint.

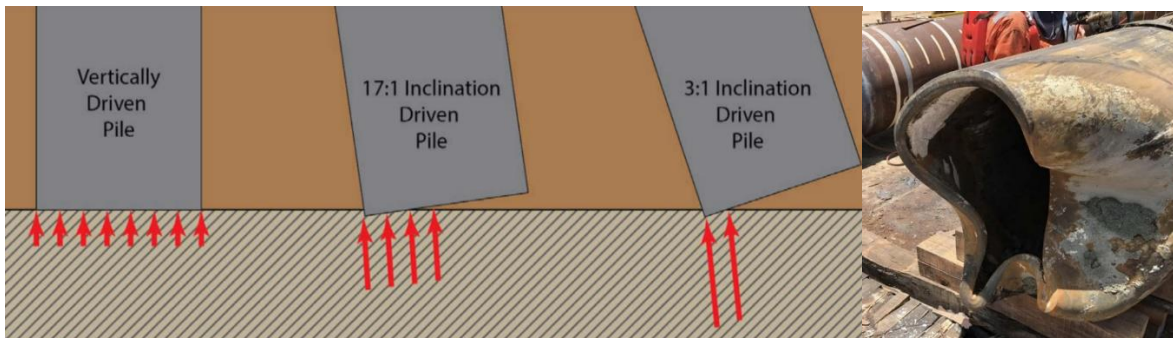
1996 While all bedrock types will have unique challenges regarding weathering profiles, particular attention
1997 must be paid in areas that have been subaerially exposed (or affected by subglacial water) and may also
1998 contain dissolution features, such as voids, infilled pipes, and sinkholes. All of these in turn present
1999 their own specific engineering considerations. These are commonly associated with calcium carbonate
2000 rocks, such as chalk or limestone, but can also occur in areas with other water-soluble minerals such as
2001 halite or gypsum. Considering this further, there are many sub-units of these rocks which will have
2002 individual weathering profiles, and it is important to appraise which specific units are present on site,
2003 for example as outlined in Mortimore (2014).

2004 When seen in geological profile, within the footprint of a typical monopile, the potential for a pile to
2005 encounter an irregular surface of varying localized properties within a short distance is high, as
2006 illustrated in Figure 5.25.



2007
 2008 **Figure 5.25.** Variation in rock properties occurring over very short distances. This variation is further
 2009 complicated by the presence of a weathered layer above that can affect the clear understanding of where
 2010 the interface occurs between Quaternary sediments and the underlying bedrock.

2011 This presents a problem in dealing with the types of open-ended piles typically favoured for WTG
 2012 foundations. The likelihood of encountering bedrock uniformly over the full cross-section of the pile is
 2013 low ([Pile Buck, 2022](#)) within an area of high variability in the local depth of the (weathered) rockhead.
 2014 This can generate significant risks to safe pile driving operations, when the forces required to drive the
 2015 pile are distributed unevenly across its base, creating the potential for pile buckling and penetration
 2016 failure to occur ([Figure 5.26](#)).



2017
 2018 **Figure 5.26.** Engineering implications of resistant layers. **a)** Illustrates how a change in the orientation
 2019 of the resistant layer can lead to buckling of a pile ([Pile Buck, 2022](#)). **b)** Illustrates the results of a 1070
 2020 mm (OD) pile that has been extracted having encountered a calcarenite (hard) layer within a weaker
 2021 limestone unit on one side of the pile ([Pile Buck, 2022](#)).

2022 The aforementioned issues can be exacerbated when there is not a clear understanding of the local
 2023 variation that may be encountered due to the nature of the datasets that are typically gathered for
 2024 offshore renewable projects. Well-developed ground models can anticipate the likelihood of specific
 2025 bedrock units and in some cases, when geophysical and geotechnical data are properly integrated with

2026 geological understanding, the likely behaviour of those rocks can be anticipated. For example, properly
2027 integrating all available geotechnical data can in some cases help determine the weathered layer from
2028 the non-weathered surface, indicated by subtle changes in P-S wave velocities and other records such
2029 as Natural Gamma and even calliper logs. However, the combination of using CPT and/or borehole
2030 information alongside 2D ultra-high-resolution seismic data can only hint at local variability. A CPT or
2031 borehole will be <120 mm in diameter and is probably not located directly on a corresponding seismic
2032 line, even an offset of 10 m can make all the difference (see also [Chapter 7.2.1](#)). Any mismatch between
2033 geotechnical and geophysical data can result in additional conservatism in design, and may not
2034 sufficiently de-risk sites from installation-related issues. The pile itself is sometimes sited off traditional
2035 2D-seismic lines, and a great deal of uncertainty exists as to the actual depth to (weathered) rockhead
2036 in the immediate vicinity of the pile footing.

2037 A solution to this problem can be the use of advanced techniques using 3D ultra-high-resolution or 3D
2038 extremely high-resolution seismic data ([Hill et al., 2024](#)) and processing techniques such as inversion
2039 and studies of basic geotechnical properties such as porosity ([Vardy et al, 2017](#)). These should be used
2040 in areas where the depth to the (weathered) rockhead is anticipated within the depth of interest and is
2041 capable of giving a much more accurate and informed picture of the distribution and character of the
2042 (weathered) rockhead ([Sauvin et al, 2019](#)).

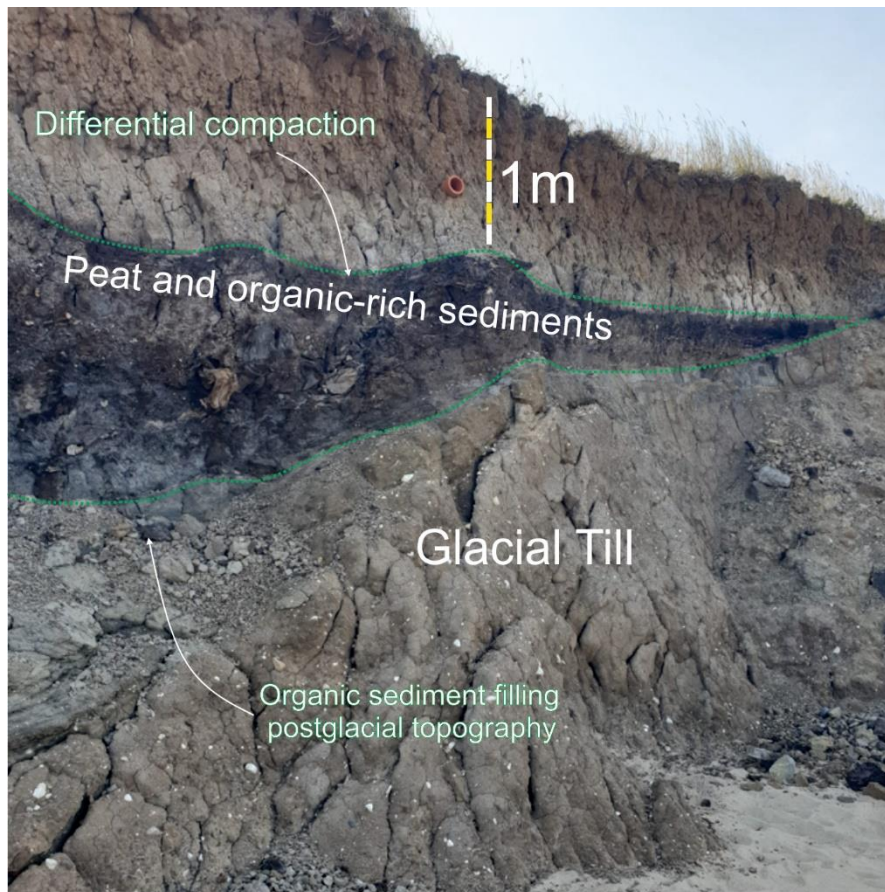
2043 **5.9 Organic materials and peat**

2044 The organic matter in soils originates from living plants, animals and organisms, forming
2045 biogenic matter in contrast to mineral matter. Organic soils are formed by the decomposition of the
2046 organic substances, a process which takes place mainly by bacterial activity, but which is intensified by
2047 a warm climate, humidity, and access to oxygen ([Larsson, 1990](#)). However, too much oxygen in the
2048 environment will result in complete organic matter decomposition therefore no organic rich soil or peat
2049 will be preserved. Generally speaking, peat is an organic soil with a very high organic content, whereas
2050 “organic soils” contain some fine-grained material of non-organic, mineral origin.

2051 Different countries have used various organic content thresholds which allow a soil to be termed a
2052 “peat” from an engineering point of view. For example, in the US an organic content limit of 75% is
2053 used to permit soil to be classified as “peat” ([ASTM, 2010](#)). In contrast, the Dutch National Annex to
2054 Eurocode 7 suggests that a soil can be classified as “peat” if the organic content exceeds 30% ([ASTM,](#)
2055 [2010; Lengkeek and Brinkgreve, 2022](#)). Peat is generally associated with high latitudes, and most
2056 existing peatlands globally were formed since the end of the last glacial period ([Minasny et al., 2019](#)).

2057 Across Europe, fluctuations of Quaternary sea level due to growing and shrinking ice sheets, combined
2058 with the effect of glacial isostatic adjustment and other complex factors resulted in periodic emergence
2059 and subsequent submergence of vast land areas that, at present, are inundated and form part of the
2060 European continental shelves.

2061 Relatively cold and wet climate following deglaciation combined with low-laying ground and
2062 undulating topography close to the water table formed favourable conditions for the formation of
2063 organic rich soils and peat (Figure 5.27 and 5.28). Conditions were favourable for early colonizing
2064 plants and the colder climate conditions hindered decomposition of organic matter and allowed for
2065 accumulation of organic-rich sediments (soils) and peats. The subsequent inundation of those areas as
2066 the sea level rose resulted in the burial and preservation of such sediments under shallow marine strata.
2067 Quaternary peats and organic-rich soils are typically associated with interglacial and post-glacial
2068 conditions and, if encountered at or under the seabed, are an important consideration for offshore
2069 engineering projects due to their varied physical properties, particularly their property as a thermal
2070 insulator. Well known examples of submerged organic rich sediments and peat were described from the
2071 southern North Sea and dated to 9.5-9 ka BP when large areas of present day-seabed were emergent
2072 (Brown et al., 2018; Hazell, 2008; Tappin et al., 2011; Hepp et al., 2019; Waller and Kirby, 2021;
2073 Özmaral et al., 2022; Eaton et al., 2024).



2074
2075 **Figure 5.27.** Coastal outcrop from Holderness coast near Skipsea, UK, showing peat and organic-rich
2076 sediments filling undulating topography of the top of glacial till. Peat accumulated in water-logged low
2077 ground areas following the ice retreat from the region. Note wood fragments within the peat. Unique
2078 finding of Beaver hair, suggesting a possible beaver dam and lodge, allowed to date the top of nearby

2079 peat succession at Withow Mere to ~4ka (<http://www.hullgeolsoc.co.uk/beaver.htm>). Photograph
2080 source: Leah Arlott.

2081 **Types of organic sediments and their depositional environments**

2082 Soils are generally considered to be slightly organic, or low content when the organic matter content in
2083 the sediment is greater than 2%, organic or medium content when above 6% and very organic or high
2084 content when above 20% (ISO 14688-1, 2017; ISO 14688-2, 2017). There are several subdivisions of
2085 organic soil types, including but not limited to peat, gyttja, dy, and sapropels, all varying in chemistry,
2086 source material and typical environment and conditions in which they form. Such deposits are referred
2087 to here as organic rich sediments as their detailed description and differentiation is beyond the scope of
2088 this paper.

2089 Definitions of peats vary between regions and standards but in general they are characterised as poorly
2090 consolidated sediments with organic matter content greater than 30-75% (ASTM, 2010; Huat et al.,
2091 2014; ISO 14688-1, 2017; ISO 14688-2, 2017; Larsson, 1990; Lengkeek and Brinkgreve, 2022). They
2092 are formed from partially decomposed plant matter deposited in waterlogged hypoxic or anoxic
2093 conditions, which allows for accumulation and preservation of organic material. Present day peats and
2094 peatlands can be found in most climates but are most prevalent in wetter and colder settings, particularly
2095 in high latitudes, where decomposition of organic matter is slower (Huat et al., 2014; Stolt and Lindbo,
2096 2010).

2097 In coastal settings, peats and organic-rich deposits can typically be associated with estuaries, or lagoonal
2098 environments behind which salt marshes or fringe peat deposits form. Peats and organic rich sediments
2099 can also be found in lacustrine, and fluvial settings where organic-rich deposits firstly accumulate in
2100 lakes, ponds and overgrown river channels (e.g. oxbow lake or abandoned channels after avulsions) or
2101 in vegetated deltaic and floodplain settings where gradual rise of water table due to transgression allows
2102 for preservation of organic detritus and eventual flooding of terrestrial vegetation (Waller and Kirby,
2103 2021).

2104 **Physical Properties of Peat and Organic Sediments**

2105 The texture of organic soils can vary significantly, depending on both the environment of deposition
2106 and the level of decomposition. The type and quantity of organic material can vary substantially ranging
2107 from barely discernible organic matter to large fibrous clasts, such as tree roots or other pieces of wood
2108 of substantial size.

2109 Offshore, due to the fibrous and/or unconsolidated nature of some peat and organic-rich sediments,
2110 these samples may be difficult to collect in vibrocore samples, push tubes or rotary cored samples,
2111 particularly if they are only partly decomposed peats with large woody pieces.

2112 Peat and organic-rich soils can be difficult to identify from cone penetration tests (CPTs), as they can
2113 sometimes be associated with an increase in tip resistance, or a drop in resistance in other cases.
2114 Research has shown that organic rich soils are often associated with high CPTU friction ratio values
2115 (f_s/q_t), e.g. in excess of 6% (Long et al., 2024). Organic-rich soils also show much lower shear wave
2116 velocity than purely mineral soils and this factor could also be potentially used to help in their
2117 characterisation (Trafford and Long, 2020).

2118 In settings where the presence of peat or organic-rich sediments is probable offshore, the use of thermal
2119 conductivity cones is essential to be able to aid determination of peat and should be employed as
2120 standard on any cable projects in areas where peat may be present.

2121 When logging cores, organic soils often have a distinctive odour due to their anaerobic decomposition;
2122 this can be “eggy” or sulphurous. They are also often dark in colour; black, dark brown, and dark
2123 greenish shades are most common, but they may be yellow or grey in some circumstances. The ISO
2124 14688-1 standards offer a specific guidance on sediment/soil colour to aid organic content identification
2125 within samples and cores.

2126 Geotechnically, peats and organic soils are generally characterised by low bulk density and high water
2127 content between particle density (PD) can range between 1.3 g/cm³ to 1.6 g/cm³ (average: ~1.4 g/cm³)
2128 depending on the level of decomposition (typical mineral soil PD 2.4-2.7g/cm³). The bulk density of
2129 peats and organic-rich soils depends on the level of compaction, water content and porosity which can
2130 reach up to 96% and typically ranges between 20 and 70%. This implies that peat in the subsurface can
2131 be characterised by bulk densities between 1.0 and 1.4 g/cm³ (typically around 1.05 g/cm³; M. Long -
2132 pers. comm.) depending on the level of compaction, decomposition, mineral content and pore water
2133 volume. (Huat et al., 2014). Physical properties of peats and their geotechnical parameters also differ
2134 between regions (e.g., Carsten, 2020; Den Haan and Kruse, 2007; Landva, 2006; Mesri and Ajlouni,
2135 2007).

2136 Peats and organic-rich soils are prone to shrinkage and cracking if exposed to atmospheric conditions.
2137 Cracks start to develop when moisture content is reduced by 50% and are prominently visible when
2138 moisture reaches 30%

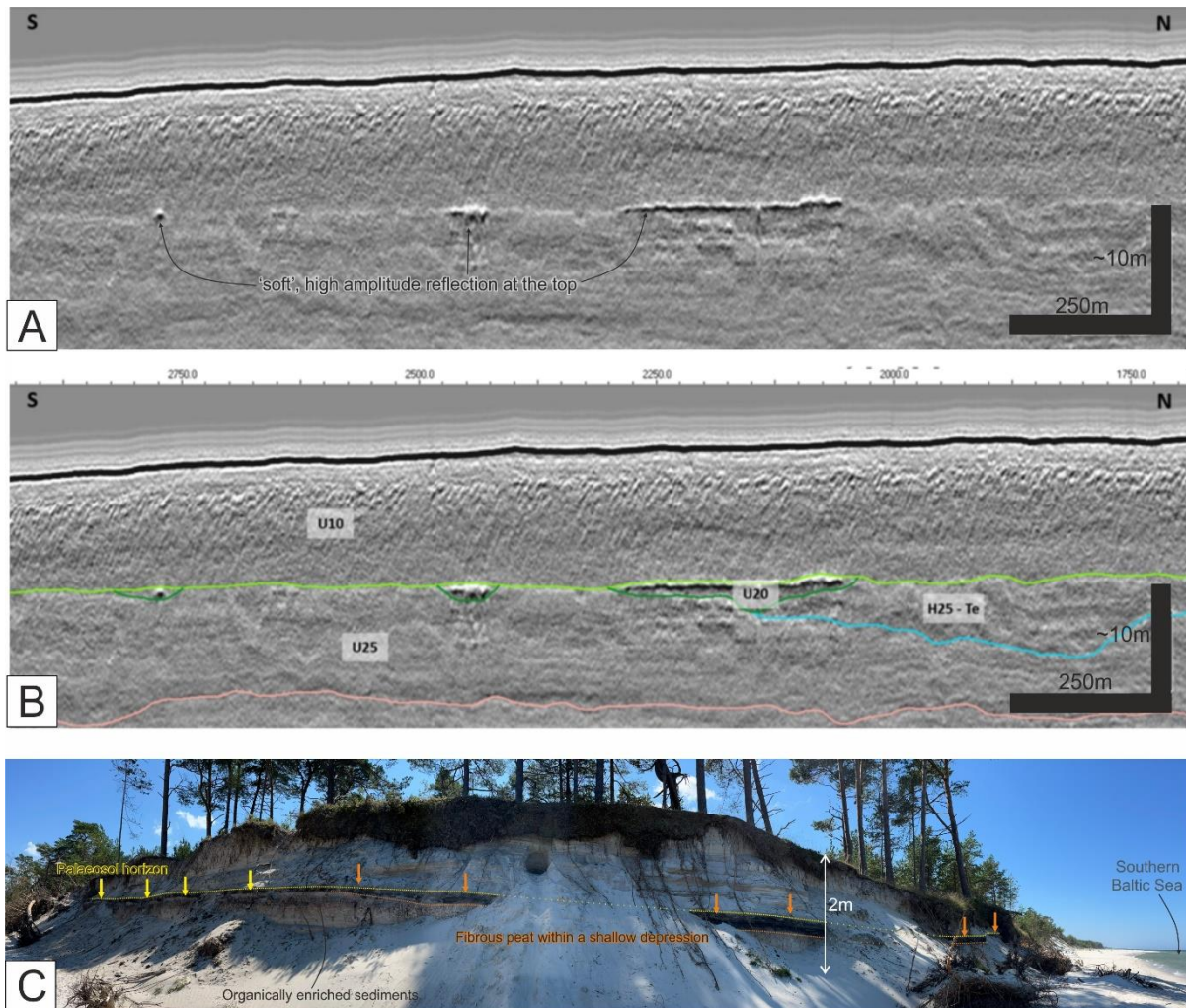
2139 **Geophysical/Seismic characteristics**

2140 Because of the varying nature of the physical properties of organic-rich soils and the range of
2141 depositional environments in which they occur, geophysical signatures of peat or other organic material
2142 can vary significantly. Peats and organic-rich soils can be complex to characterise using geophysical
2143 data and care must be taken to ensure a suitable geotechnical campaign to confirm the type of soil
2144 identified.

2145 Peats and terrestrial organic-rich soils were confirmed by boreholes from present-day offshore settings
2146 extensively across northwest Europe, particularly in the central and southern North Sea and shallow
2147 settings within the Irish Sea ([Figures 5.28 and 5.29](#)). Where identified in seismic data, peats and organic-
2148 rich sediments are sometimes characterised by high-amplitude, negative-polarity reflections ([Figure](#)
2149 [5.28](#)). The amplitude of these reflectors can vary significantly and in some cases be indiscernible from
2150 reflections representing different geological boundaries, which makes the lateral distribution of peat in
2151 some locations difficult to quantify (e.g. [Plets et al. 2007](#)).

2152 Terrestrial peats can form continuous or semi-continuous reflectors on top of other tabular units or may
2153 be confined to a specific bed or layer within a filled channel or depression ([Figure 5.28](#)). They may be
2154 preserved as a land surface below modern bedforms such as sandbanks, which is common off the
2155 Norfolk coast beneath the Norfolk Banks.

2156 Presence of biogenic gas associated with decomposition of organic matter often is shown as dim-out or
2157 acoustic blanking directly at or beneath suspected peat or organic-rich horizons but may also form a
2158 dissociated front in areas where organic-rich materials, such as those formed in eutrophic lake
2159 environments, fill deep incisions. These soils may also have low strength values (see [Chapter 5.7](#) on
2160 low-strength clays.)



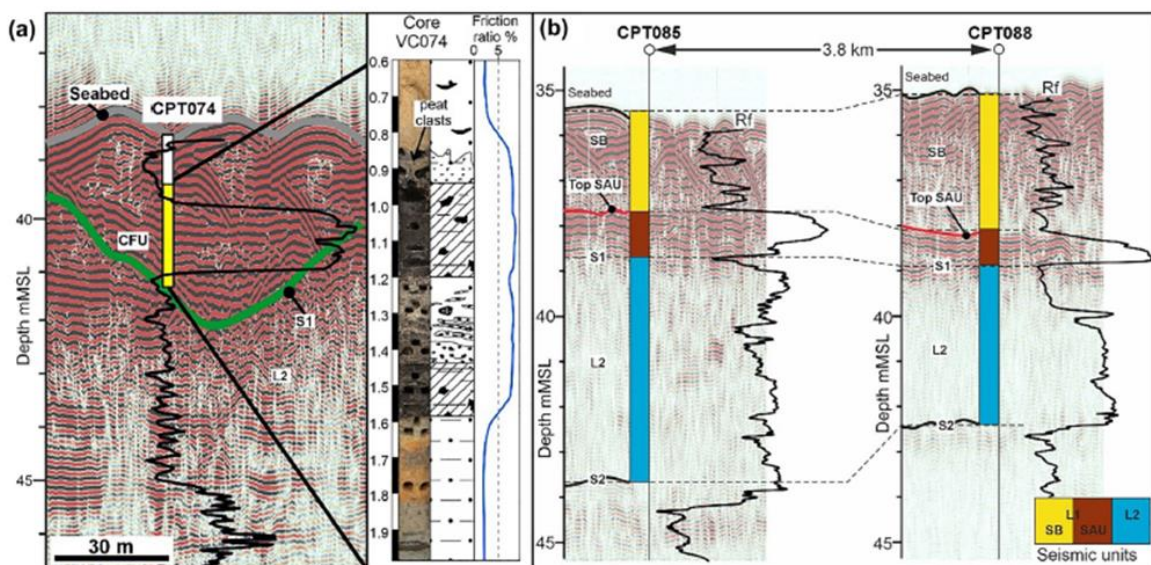
2161

2162 **Figure 5.28.** Peat beds in seismic profiles and outcrop. **a)** Uninterpreted and **b)** interpreted UHR seismic
 2163 profile showing high-amplitude ‘soft’ topped reflection linked to the presence of organic-rich sediments
 2164 along a palaeosol (green horizon) and confined to local depressions and channels. U10: Marine
 2165 Holocene sand deposits. U20: Infills of small basins and channels, likely in a restricted marine-tidal
 2166 setting, partially associated to a subaerial fluvial system. U25: Fine sediments: fine sands-silts (?)
 2167 deposited in a relatively low-energetic setting, possibly a glacial lake or a transgressive estuary.
 2168 Subdivided into subunits U25-Te and U25. Danish Energy Agency (2023). **c)** Example of laterally
 2169 continuous palaeosol horizon buried by coastal dunes on the coast of Southern Baltic Sea in Poland.
 2170 Note that ~30 cm beds of fibrous peat are only locally present along the surface and confined to a
 2171 shallow depression. The bed in the picture extends for ~300 m. Laminae and beds of organic rich sands
 2172 are present below the paleosol horizon. Photo: B. Kurjanski – private archive.

2173 Important contributions to the topic have been made for the Elbe Paleovalley (Hepp et al., 2019;
 2174 Özmaral et al., 2022) and for a windfarm site 50 km offshore of East Anglia (Figure 5.29; Eaton et al.,
 2175 2024). The origin of the organic rich deposits in both areas are described in detail. The Elbe Paleovalley
 2176 deposits are aged as being deposited between 8250 and 9900 years before present (Özmaral et al., 2022).

2177 This study was also able to outline some details on the early stages of the Paleovalley formation. Cuts
2178 were infilled with estuarine muds, peat and silty clay in freshwater marshes or in brackish/lagoonal
2179 environment. The peat is described as “very dark brown”, but no index testing results are given to help
2180 assess whether the material is truly peat or an organic-rich soil.

2181 The East Anglia work (Eaton et al., 2024) is of particular value as it also includes the results of some in
2182 situ CPTU tests (Figure 5.29). A seismic anomaly unit (SAU) was identified and found to comprise
2183 peat, organic-rich sands and silts and clays. The peat is described as a “dark brown, humified and
2184 amorphous with wood fragments” but again no engineering index parameters are given. The peat was
2185 formed between approximately 13,900 and 9,500 years before present in both laterally extensive sheets,
2186 which are now discontinuous, and along the margins of channels. Occasionally peat clasts were found
2187 in the overlying sandy soils providing evidence of erosion of the upper organic rich layer. It was found
2188 that a high friction ratio ($R_f > 5\%$) and a low cone resistance ($q_c < 1\text{MPa}$) corresponded well with the
2189 SAU (Figure 5.29).

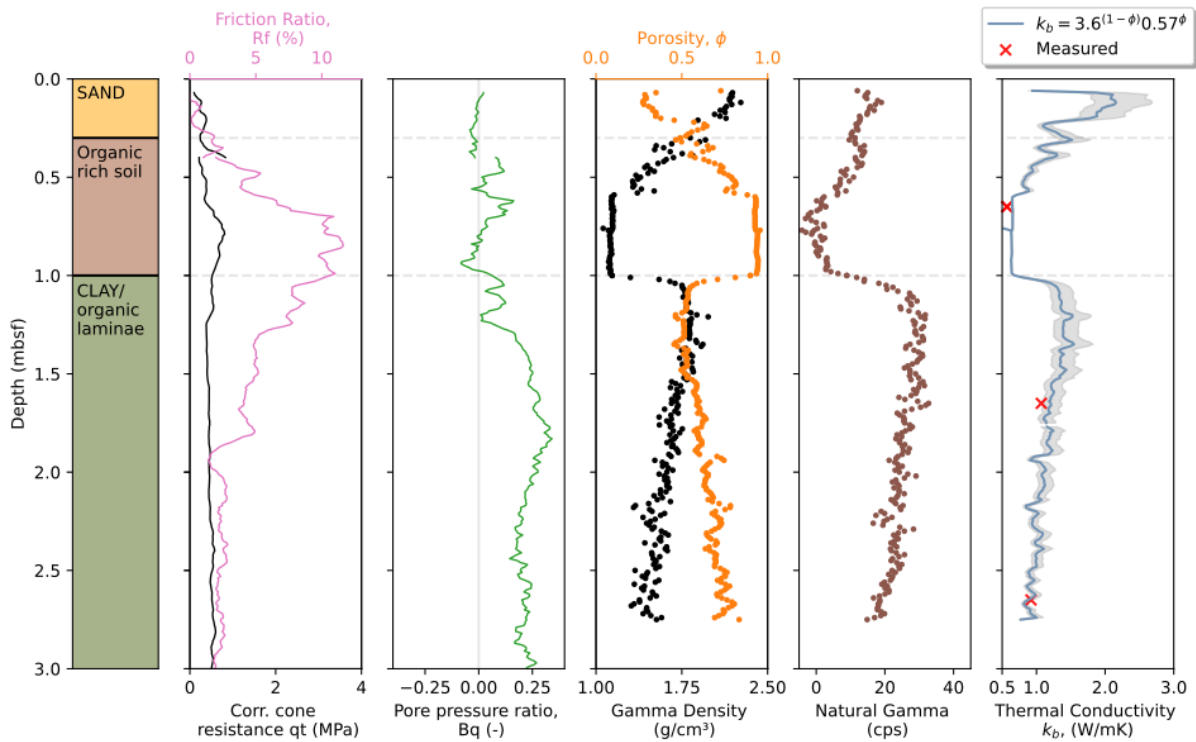


2190

2191 **Figure 5.29.** Peat identified in seismic, core, and CPT data in a windfarm project offshore East Anglia.
2192 CPT parameter (R_f : friction ratio) overlain in black. **a)** VC/CPT 074, with vibrocore path overlain on
2193 the seismic data. Yellow indicated the cored unit with the organic-rich interval, including peat within
2194 the channel-fill unit (CFU). Note the peat clasts in the overlying sand. **b)** CPT 085 and 088 to show the
2195 clear response in R_f of the seismic amplitude unit (SAU). SB: Seabed bedforms unit, S1: Surface 1, L1:
2196 Seismic unit 1, L2: Seismic unit 2. From Eaton et al. (2024).

2197 Some CPTU and MSCL data for a site in the Central North Sea are shown on Figure 5.30 (Smith et al.,
2198 2024). The lower density and higher porosity of the organic-rich sediments, as clearly delineated by the
2199 MSCL measurements, are consistent with the high R_f values from the CPTU. The organic rich and low

2200 organic content material have similar cone resistance (q_c) values thus confirming the usefulness of the
 2201 Rf data.



2202
 2203 **Figure 5.30.** Organic rich sediments in multi-sensor core logging (MSCL) data. Soil type, CPTu,
 2204 selected MSCL data and thermal conductivity profiles from the Central North Sea. The grey zone
 2205 indicates low and high estimates at 15 and 85% confidence. The distance between adjacent Vibrocores
 2206 and CPTu profiles is approximately 0.8 m. From Smith et al. (2024).

2207 **Engineering implications and associated geohazards**

2208 Peats and organic-rich soils are characterised by high compressibility and water (moisture) content of
 2209 up to 1500% (examples of up to 2000% are known; [M. Long – pers. comm.](#)), low shear strength
 2210 ($S_u = 5 - 20$ kPa), and can also be more laterally heterogeneous and more permeable than clays ([Huat et](#)
 2211 [al., 2014](#)). These characteristics can pose problems for infrastructure design and installation. Foundation
 2212 design may need to account for very high compressibility, where these soils occur in sufficient
 2213 thicknesses, but also for extremely low strength, fine-grained material where other organic rich soils
 2214 are present. The installation or maintenance of offshore structures must also take this into account, and
 2215 jacking operations need to consider the risk of punch through or hanging legs where peat “rafts” overlie
 2216 lower strength materials. For the installation of pipelines or cables in the marine environment, but also
 2217 in the nearshore and coastal environment, heavy plant such as trucks, horizontal drilling rigs, and
 2218 trenching equipment may get stuck if not appropriately specified.

2219 Organic- rich sediments are thermally insulating when compared to mineral deposits, with low thermal
2220 conductivity and high thermal resistivity. This means that design of thermally sensitive infrastructure,
2221 such as pipelines and cables, must properly consider the effects even small sections of peat or organic
2222 rich sediments may have on heat dissipation and thermal expansion during operation. As these soils do
2223 not allow for dissipation of heat generated by HVDC/AC cables, cables may encounter lower cable
2224 performance or, in extreme cases, in overheating and compromising an offshore transmission cable.

2225 Due to being deposited in anoxic environment organic soils have the potential for further degradation
2226 if exposed to oxygen- rich environment and may undergo substantial change in their physical properties
2227 (Clare et al., 2023; Zhao et al., 2019; Zhao and Si, 2019). This could happen during installation of cables
2228 or pipelines, when peat beds may be disturbed in addition, the decomposition of organic matter results
2229 in highly acidic environments (Zhao et al., 2019; Zhao and Si, 2019; Blumenberg et al., 2022). This can
2230 cause issues with corrosion which may reduce the operational life of offshore infrastructure, particularly
2231 for foundations (e.g., Fugro, 2017).

2232 The degradation of peat can also result in the modification of the overlying seabed, coastline or
2233 subsurface and release large amounts of inert, stored carbon to the ecosystem. Biogenic gas pockets
2234 associated with organic deposits can be a potential cause for blowouts, if disturbed, and pose a direct
2235 risk to life, health, and equipment.

2236 During cable or pipeline installation process using a trenching plough presence of fibrous and woody
2237 elements above 1% were reported to cause issues requiring several re-runs of plough to achieve the
2238 desired depth of lowering (Brown et al., 2015).

2239 Considering the potential issues associated with these soils, peats and organic soils are highly
2240 unfavourable from an engineering perspective. It is therefore important to utilise effective, fully
2241 integrated ground modelling techniques to identify locations and situations in which these soils might
2242 occur, and effective geophysical and geotechnical site investigation to ensure they are mapped and
2243 constrained appropriately.

2244 **5.10 Faults and fractures**

2245 The continental margins of Northern Europe are so called “passive margins” although the margins have
2246 been subjected to reiterative deformation since the opening of the North Atlantic Ocean ca. 55 Ma.
2247 Since then, the tectonic stress regime across the margins has evolved in time and space involving
2248 compression, transform faulting, extension, and even inversion (Gregersen et al., 1989; Mosar, 2003;
2249 Roberts and Yielding, 1991, Faleide et al., 2025). Fracturing and faulting is widespread in the shallow
2250 subsurface along these continental margins. Large-scale Mesozoic faults can extend to the Quaternary
2251 strata and have a connection with the present-day seafloor as observed broadly in the Barents Sea (e.g.,
2252 Faleide et al., 2019; Serov et al., 2023) and the Danish Basin in the North Sea (e.g., Ahlrichs et al.,
2253 2023). Polygonal faults, believed to be caused by dewatering of fine-grained saturated sediment, are

2254 also commonly observed along the continental margin since Miocene time (e.g., [Berndt et al., 2003](#);
2255 [Wrona et al., 2017](#)). The Quaternary sequence is particularly prone to tensile fracturing in places where
2256 the crust is subjected to doming. In general, any discontinuity and weakness zone have the potential to
2257 accumulate stress leading to local alterations of the regional stress field. These stress concentrations can
2258 lead to fault reactivation and to the development of new fractures ([Gudmundsson, 1999](#)).

2259 Stress changes associated with the advance and retreat of the large Quaternary ice sheets lead to the
2260 generation of glacially-induced seismicity and fracturing and deformation along continental margins at
2261 scales that are not easily identifiable due to their aseismic nature. In addition, periglacial areas (i.e.,
2262 areas adjacent to contemporary or past ice-sheets) along continental margins have been exposed to
2263 reiterative ground freezing and thawing through glacial cycles (see also [Section 5.8](#)). These processes
2264 lead to a very specific type of deformation in near-surface poorly consolidated strata, referred to as
2265 involution ([van Vliet-Lanoë et al., 2004](#)). Tectonic (including glaciotectonics; see [Section 5.12](#)) and
2266 periglacial deformation are two different styles of deformation affecting the stability of Quaternary
2267 sediments at glaciated margins, but they interact and interfere with each other. For example, frost and
2268 ice wedges will exploit preexisting fractures and mechanical discontinuities in the sediment. Similarly,
2269 fresh water will circulate preferentially through dilated faults leading to pingo formation. In active
2270 hydrocarbon systems, fluid migration and associated gas-hydrate formation may lead to enhanced
2271 glacio-tectonism along faults (e.g., [Bellwald et al., 2023a](#)). Overall, the continental margins of northern
2272 Europe have been affected by faulting and fracturing associated with the following mechanisms: 1)
2273 lithospheric plate movements due to mid-ocean ridge spreading along the mid and north Atlantic mid-
2274 ocean ridges (ridge push); 2) glacial isostatic adjustments; 3) local neotectonics; 4) gravitational forcing
2275 due to large scale erosion and sedimentation; 4) salt and sill intrusion tectonics; and 5) periglacial
2276 deformation.

2277 In compressional stress regimes on land (i.e., with reverse faults), high vertical stresses associated with
2278 the thick ice sheets (when present) tends to compensate the maximum, compressive horizontal
2279 background stress. This suppresses seismic activity (i.e., seismicity under Greenland and Antarctica is
2280 very low and the earthquakes that occur are relatively weak) (e.g., [Johnston, 1987](#)). However, crustal
2281 unloading following decay of the ice (i.e., reduction of the vertical stress) together with crustal strain
2282 accumulated under the ice sheets can lead to fault destabilization and strong seismicity occurring over
2283 a concentrated period of thousands of years (i.e., during deglaciation) (e.g., [Brooks and Adams, 2020](#);
2284 [Johnston, 1987](#)).

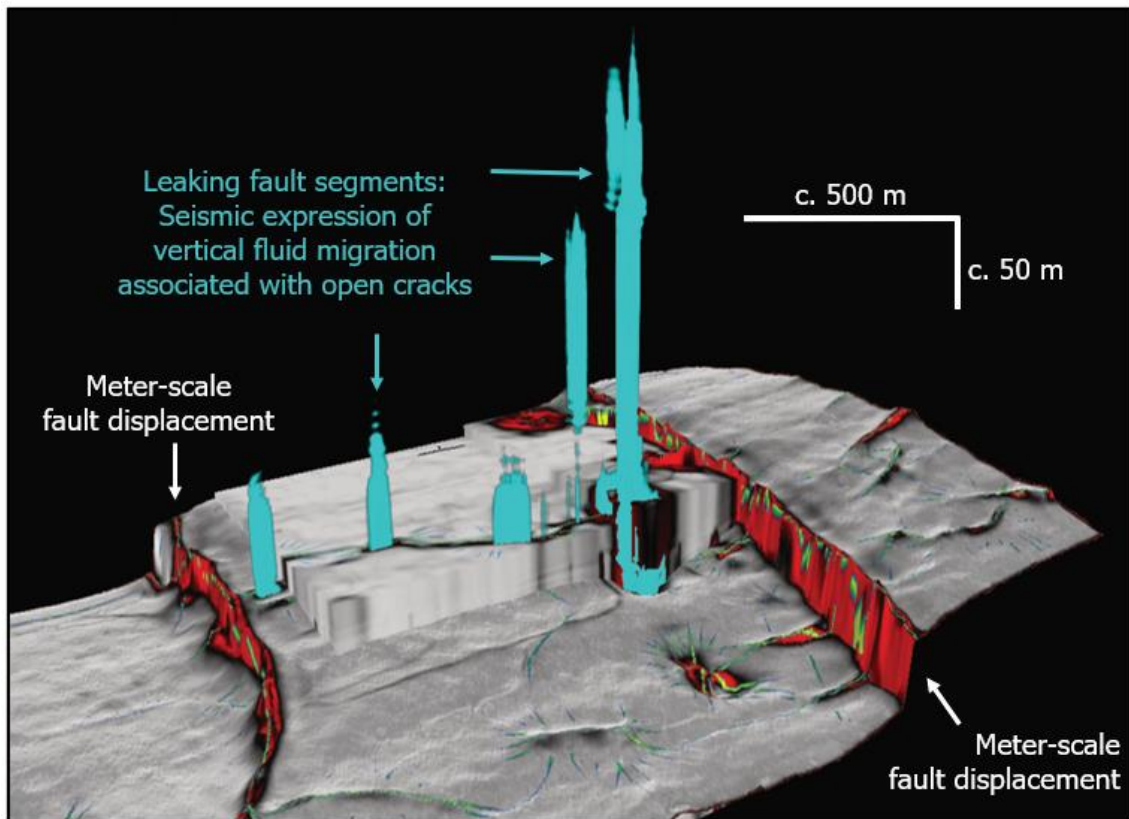
2285 Glacially induced seismicity accounts for most of the neotectonic phenomena at glaciated continental
2286 margins. It is a phenomenon that has been proved with numerous observations on land ([Brooks and
2287 Adams, 2020](#); [Olesen et al., 2004](#); [Olesen et al., 2013](#); [Brandes et al., 2015](#)). Glacially-induced faulting
2288 and earthquakes activity in Fennoscandia is widely demonstrated (e.g., [Olesen et al., 2004](#)). In Norway

2289 there have been many claims and reports of neotectonic activity on land and offshore. Liquefaction,
2290 rock failure events, and submarine landslides have been associated with large magnitude recent as well
2291 as paleo-earthquakes and sub-seabed deformation (Olesen et al., 2004; Bellwald et al., 2019a; Eldholm
2292 and Bungum, 2021; Sørensen et al., 2023).

2293 However, offshore evidence of glacially induced faulting and fracturing is less abundant. This could be
2294 due to 1) the fact that the stress regimes change significantly from the ice-sheet depocenter region to
2295 the forebulge regions. Glacially induced stress modelling for Fennoscandia shows that crust under a
2296 vanished ice sheet is currently experiencing uplift while the crust at the forebulge is experiencing
2297 present-day subsidence. These models also show that stress magnitude and orientations change more
2298 abruptly at the ice-sheet depocenters (Lund et al., 2009; Vachon et al., 2022); and/or 2) identifying fault
2299 propagation and near-surface seismicity is challenging due to thick Quaternary sediments covering
2300 relatively recent post-glacial faults and fractures. Nonetheless, theory shows that crustal doming
2301 associated with post-glacial uplift generates tensile stresses that are sufficiently large to generate tension
2302 fractures (e.g., Gudmundsson, 1999). Indeed, recent studies based on attribute analyses of high-
2303 resolution P-Cable 3D seismic data (3-5 m vertical resolution) off west-Svalbard reveal that certain
2304 chronological intervals are more severely fractured than others (Cooke et al., 2023; Figure 5.31).

2305 Large-scale faults (i.e., planar features with detectable vertical throw in seismic data) are generally easy
2306 to identify even in 2D seismic lines given a favourable orientation of the surveys with respect to the
2307 fault strikes. The detection of small-scale fracture networks, however, is dependent on the availability
2308 of ultra-high-resolution 3D seismic data (Figure 5.31). In general, faults and fractures are commonly
2309 identified thanks to advanced multi-attribute analyses in 3D seismic data, often involving neural
2310 networks training. The quality of the data, data resolution and the methodology implemented, all impact
2311 the accuracy of fine-scale faults and fracture interpretation (e.g., Cunningham et al., 2020; Ligtenberg,
2312 2005; Cooke et al., 2025).

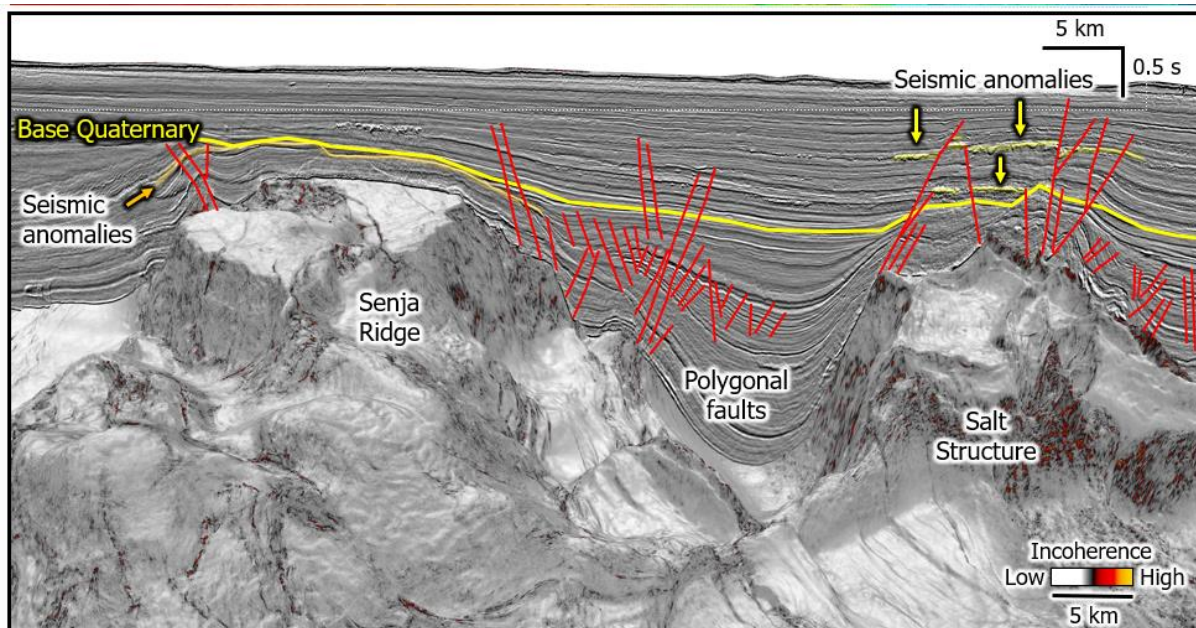
2313 The properties of faults and fractures in the shallow subsurface modulate the transport of fluids from
2314 deep to shallow sediments, and – in cases – into the ocean. Local changes in the stress field (i.e., given
2315 by stress focusing on small-scale features like fractures, fault segments, diagenetic depositions) can
2316 either enhance or hamper fluid migration, depending on whether permeability is increased (e.g., under
2317 tensile stress) or decreased (e.g., under compressive stresses) (e.g., Sibson, 1994) (Figure 5.31).



2318

2319 **Figure 5.31.** Example of vertical fluid migration (chimneys or pipes) through highly deformed strata
 2320 offshore west-Svalbard imaged with high-resolution P-Cable 3D seismic data. The figure shows seismic
 2321 variance extracted along a surface correlated with a ca. 1.2 Ma marker (close to the mid-Pleistocene
 2322 transition (Cooke et al., 2023). The restricted location of gas chimneys (blue) indicates that leakage
 2323 occurs exclusively through open segments along given deformation planes (Cooke et al., 2025). The
 2324 figure was kindly provided by Frances Cooke.

2325 Salt tectonics and polygonal faulting of dehydrated fine-grained sedimentary successions are geological
 2326 mechanisms that promote fault-controlled fluid migration and leakage into Quaternary strata (Figure
 2327 5.32). The hydro-mechanical properties (e.g., porosity and permeability) of Quaternary strata (i.e.,
 2328 within the upper ~2 km below the seafloor) are mostly controlled by compaction processes and to some
 2329 extent by diagenetic processes that contribute to volume changes (e.g., deposition of authigenic
 2330 carbonate or gas hydrates). The vertical stress exerted on the shallow subsurface at continental margins
 2331 is carried partly by the sediment matrix and partly by the fluid phase (e.g., Bjørlykke et al., 2015). Pore
 2332 pressure measurements are therefore critical for constraining the effective stress (the vertical stress
 2333 minus the fluid pressure) and assessing whether an area is critically pressured and is within the fracture
 2334 failure/reactivation point or whether it is stable. Detailed studies on the orientation of pre-existing
 2335 fractures in the shallow subsurface together with constraints on the regional stress regime are critical
 2336 for predicting the fracturing behaviour of fluid saturated sediments (e.g., Zoback and Lund Snee, 2018).



2337

2338 **Figure 5.32.** Chair view into Senja Ridge (basement high) and neighbouring salt structure with
 2339 overlying stratigraphy, Southwestern Barents Sea. Shown are different types of faulting, and their
 2340 implications on the Quaternary stratigraphy. Polygonal faulting mainly limited to the basin infill of
 2341 Paleogene and Neogene age, while faulting related to basement and salt structures affecting the
 2342 Quaternary stratigraphy. Example from SW Barents Sea. Data courtesy of TGS and VBER.

2343 **5.11 Glaciotectonic deformation**

2344 Glaciotectonic deformation refers to any kind of deformation within unconsolidated sediments and/or
 2345 bedrock that is caused by the motion of glaciers and ice sheets or by differential loading caused by the
 2346 ice mass. This includes faulting, folding, disturbance to pre-existing structure, or state of the sediments,
 2347 but also quarrying and re-location of intact fragments of pre-existing strata i.e. glaciotectonic rafts
 2348 (Aber, 1989, Aber and Ber 2011)

2349 Glaciotectonic deformations can occur at multiple scales from ice sheet-scale glaciotectonic thrust
 2350 sheets extending along the former ice margins for 10s of kilometres distorting 10s-100s of meters of
 2351 strata, to outcrop-scale deformation where individual beds are folded or offset by small-scale reverse
 2352 and normal faults on metre or cm scale (Figures 5.33 and 5.34) . The vast majority of glaciotectonic
 2353 deformation occurs close to the ice margin either in the subglacial zone or a distance up to several km
 2354 in front of it as the advancing ice mass loads, bulldozes and overrides sediments in front of it. On a
 2355 regional scale, large glaciotectonic complexes are often related to major ice-sheet advances, re-
 2356 advances, or stillstands of the ice sheet. Smaller glaciotectonic deformations are often present on more
 2357 local scale (i.e. annual oscillations of the ice margin overriding and thrusting a recessional moraine),
 2358 and are relatively common in former ice-marginal settings.

2359 Some of the larger glaciotectonic thrust complexes offshore formed during or after the LGM can be
2360 observed as major shallow banks detached from land and are preferentially targeted for offshore wind
2361 farm development as they are suitable for fixed offshore wind turbine foundation design and offer a
2362 higher wind yield due to their distal location. Examples include Dogger Bank wind developments in
2363 the Southern North Sea (Phillips et al., 2018; Emery et al., 2019) or Słupsk Bank and potentially
2364 Southern Middle Bank in the Baltic Sea (Figure 5.33). Despite being favourable from a bathymetric
2365 and wind yield point of view they are also associated with one of the most complex and variable
2366 glaciogenic deposits. It is also worth noting that not all glaciotectonic deformations, especially
2367 predating the LGM, are identifiable on bathymetric data (Figure 5.33). Evidence of former ice
2368 bulldozing and glaciotectonics is often only provided by seismic and borehole data (Figures 5.33 and
2369 5.34).

2370 **Types of glaciotectonic deformations**

2371 The basic type of large-scale glaciotectonic deformation was readily described by Aber (1989) as ‘Ice-
2372 scooped basin and ice-shoved hill’ otherwise known as a glacial over deepening followed by thrust
2373 complex sometimes combined with a marginal push moraine or sediment / bedrock raft. Following ice
2374 retreat the ‘hole’ often accommodates a proglacial lake where fine-grained cohesive sediments are
2375 likely to be deposited. It is worth noting that glaciotectonic deformation or complexes do not form
2376 universally at all ice margins (Bennett, 2001).

2377 Common characteristic of all glaciotectonic deformations is the presence of a detachment or
2378 decollement surface at the base of the glaciotectonically deformed zone (Lee and Phillips, 2013;
2379 Pedersen, 2014; Pedersen and Boldreel, 2015; Phillips et al., 2018; Vaughan-Hirsch and Phillips, 2017;
2380 Winsemann et al., 2020) (Figure 5.33). This surface typically forms along a strength anisotropy contrast
2381 within an undeformed sediment or rock package. The contrast may exist due to lithological differences
2382 (soft, weak clay under strong/stiff sand package), contrast between bedrock and unconsolidated
2383 sediments, fluid pore pressure gradient (e.g., permeable sands with high pore pressure under
2384 impermeable cohesive sediments) or the presence of permafrost horizon, or shallow gas and gas
2385 hydrates in the subsurface (Bellwald et al., 2023a; Huuse and Lykke-Andersen, 2000; Piotrowski et al.,
2386 2004; Winsemann et al., 2020 and references therein).

2387 Glaciotectonic deformation is typically most severe close to the paleo-ice margin position and decreases
2388 in magnitude distally (radially) away from it (Figure 5.34). In many cases sediments in the most
2389 proximal, ice-contact zone are almost completely distorted and homogenized making it impossible to,
2390 for example, correlate them to their host unit or quantify the degree of shortening (Emery et al., 2019;
2391 Phillips et al., 2018; Vaughan-Hirsch and Phillips, 2017). In seismic data such sediments often appear
2392 acoustically chaotic without any coherent, traceable internal reflectors. The ice contact surface on top
2393 of the package will likely be a strong, positive kick due to compaction by ice. In borehole or outcrop

2394 studies, the term ‘glaciotectonite’ is often used to describe sheared rocks or sediments with
 2395 unrecognisable or highly distorted primary structures and widespread shear structures (Bayliss et al,
 2396 2015).

2397 More distally to the ice margin, thrust faults form at +/-30° angle dipping towards the ice margin. These
 2398 thrusts are often subsequently over-steepened if the ice margin continues to push the sediment pile in
 2399 front of it and can ultimately be vertical to sub-vertical (for example Gehrmann, 2020). Subsurface
 2400 examples from seismic data offshore indicate that the final thrust block moraine is often a product of
 2401 multiple phases of ice advance and bulldozing (Emery et al., 2019b; Phillips et al., 2018). The resulting
 2402 glaciotectonic deformation is often complex with multiple stacked thrust sheets, back thrusts and
 2403 piggyback thrusts driven on top or cutting across the pre-existing deformed package. Imbricate stacks
 2404 can be imaged and recognised from seismic data, but it can be very challenging to correlate the thrusts
 2405 laterally and understand the orientation of thrust sheets unless 3D seismic data is available (Figure 5.34).
 2406 Further away distally (radially) from the ice mass, the deformation of sediment/rock pile is transitioning
 2407 from thrusting (due to breaching of the shear strength of sediments) to folding with decreasing
 2408 amplitude and increasing wavelength until all of contraction is accommodated (Figure 5.34). It is worth
 2409 mentioning that some glaciotectonic deformation can be caused by the loading by the ice mass alone
 2410 and does not rely only on the ‘push’ component (Andersen et al., 2005).

2411 Glaciotectonic deformation can be observed at all scales from outcrop and cm-scale reverse faults and
 2412 folds, through medium-scale thrusting on the scale of 10s and 100s of meters to extensive regional
 2413 thrust sheet complexes extending laterally and radially for 10s to 100s of kilometers (Figure 5.33 and
 2414 5.34; Cotterill et al., 2017; Emery et al., 2019b; Huuse and Lykke-Andersen, 2000; Phillips et al., 2018;
 2415 Vaughan-Hirsch and Phillips, 2017). Glaciotectonic deformation has been demonstrated to extend for
 2416 several to 10 km beyond the corresponding paleo ice extent (Andresen et al., 2005). The degree of
 2417 shortening within glaciotectonic complexes is variable and often difficult to quantify. Examples of
 2418 minimum shortenings of up to 50% are known from the North Sea.

2419 **Table 5.4.** Types of glaciotectonic deformation.

| Type | Variety | Description/ definition | Comment/dimensions |
|--|-----------------------|---|--|
| Large-scale glaciotectonic deformations | Thrust-block moraines | Formed proglacially by bulldozing of pre-existing sediments/rocks by advancing ice margin or by gravitational spreading under load | Also known as composite ridges. Imbricated stacks can be vertical or in the ice-proximal part. Multiple cross-cutting sets of thrusts could be present at the same margin. Individual thrust planes can be spaced very densely, even every 50-100 m. Laterally, thrust planes as short as 100 m were observed from seismic data. |
| | Cupola hills | A thrust-block moraine that was overridden by the ice resulting in partial erosion/scalping of the top of the thrust sheet and deposition of a till carapace on top | Many thrust block moraines have been at least partially overridden by the ice. They do not form a cupola hill <i>sensu stricto</i> , but their overridden parts can |

| | | | |
|--|---|--|---|
| | | | exhibit a very similar stratigraphic succession. |
| | Large-scale fold and thrust belts formed due to ice loading | Proglacial deformation driven by vertical load exerted by an ice mass on an unconsolidated sediment package | Thrusts will likely form at angles close to 30°. This deformation could affect large areas. |
| | Large push moraines | Push moraines are formed by a combination of ice push of unconsolidated loose material and melt out and plastering of basal sediments. Thrusts may be present but cannot be easily recognised due to the quasi-homogeneous nature of push moraine material. | Internal structure can be very chaotic and resemble glaciotectonite. Subglacial material, including boulders and till, could be incorporated in a push moraine. Slope failure and debris-flow sediments can often be expected with and on the flanks. |
| Small- and medium-scale glaciotectonic deformations | Recessional and de-Geer moraines. | Recessional moraines are formed by seasonal/ periodical re-advances of the ice margin during an overall retreat. Small volumes of sediments are bulldozed and deposited in linear mounds delineating the ice-margin position | De-Geer moraines are similar in their formation process but are characteristically formed when the ice margin is grounded in water. They are often very regular and evenly spaced. In general, recessional moraines can be composed of material similar to push moraines but their dimensions (meters high and 10s of meters wide) makes them difficult to observe in 2D seismic data) |
| | Ice-contact deformation of other landforms | In some cases, relatively minor ice-margin oscillations can cause glaciotectonic deformation of ice-contact parts of pre-existing sediments and landforms. Small, metre- to centimetre-scale faulting and folding can be readily observed in onshore outcrops. | This deformation may be too small to be imaged by UHRS data and difficult to identify from offshore sites. In such settings, it is crucial to understand whether the strength of the ground is reduced due to ice-contact deformation. |
| Glaciotectonic rafts | Sediment rafts | Sediment rafts form when portions of frozen but unconsolidated sediments are frozen onto the base of the moving ice or pushed in front of it without much disturbance to the primary internal structure. | Dimensions of glaciotectonic rafts can vary greatly from <10m ² to >10km ² . Rafts are typically much thinner than their horizontal dimensions. They can be transported subglacially for a long distance away from their source area. Undeformed rafts can form a part of a thrust-block moraines or be isolated and form a flat-topped hill. Large rafts of chalk embedded in glacial tills are know from onshore exposures and offshore borehole and seismic data in the North Sea Basin. |

| | | |
|---------------|---|---|
| Bedrock rafts | Bedrock rafts are similar sediment rafts but composed pre-glacial, often fully consolidated strata. Bedrock rafts are typically detached along a zone/ plane of weakness within the rock (bedding plane, joint set, foliation fault, etc.). | Dimensions of glaciotectonic rafts can vary greatly from <10m ² to >10km ² . Rafts are typically much thinner than their horizontal dimensions. They can be transported subglacially for a long distance away from their source area. Undeformed rafts can form a part of a thrust-block moraines or be isolated and form a flat-topped hill. Large rafts of chalk embedded in glacial tills are know from onshore exposures and offshore borehole and seismic data in the North Sea Basin. |
|---------------|---|---|

2420

2421

2422 **Geohazards and offshore engineering implications:**

2423 Geohazard and geoengineering constrains linked to glaciotectonically deformed sediments and

2424 bedrock are described in [Table 5.5](#).

2425 **Table 5.5.** Summary of geohazards and geo-engineering constraints related to glaciotectonics.

| | Description | Comment |
|--|--|--|
| Weakened ground properties | Presence of pre-existing shear planes will likely change/weaken the geotechnical properties of the unit when compared to the undeformed state. | Representative and dense borehole sampling and subsequent laboratory tests |
| Sharp lithological changes over 10s-100s of metres | Variable and poorly predictable ground properties over short distances, repeated sequences of strata due to thrusting and varying degree of deformation | Design approach assuming the ‘worst case ground conditions scenario’ for foundations and anchors may be required |
| Variable thrust/shear plane density and orientation | Orientation of deformation planes can vary greatly (up to 120°) with respect to the regional ice-flow direction. Deformation density is non uniform along the ice margin, resulting in heterogeneities of geotechnical properties. | Lateral shear bands within glaciotectonic complexes can be orientated quasi parallel to the ice flow direction making them very difficult to image on 2D seismic data |
| Changing degree of deformation | In general, the degree of deformation is likely to decrease radially away from the ice margin, and gradually changing from thrusting to folding. This will affect the geotechnical properties. | Grouping all strata affected by glaciotectonic deformation into one soil unit may not be a suitable approach and could result in oversimplification of ground conditions if deformation affects differing lithological units with variable intensity |
| Presence of boulders | Boulders in highest density are likely to be present in the ice-contact part of glaciotectonic complexes where ice-marginal and subglacial lithologies are deposited directly from the ice. | Boulders (and till) can be present on top a glaciotectonic complex if it was overridden by ice, or within it if a pre-existing boulder-rich lithology was deformed by glaciotectonics. |
| Potential fluid migration pathways | Thrust planes can provide preferential fluid (including shallow gas) migration pathways. | Small shallow gas accumulation can be difficult to detect due to often chaotic internal seismic reflection facies within glaciotectonic complexes |

High uncertainty in seismic imaging

Steep thrust planes and a high degree of deformation often result in poor subsurface imaging, thereby increasing the uncertainty in the ground model.

Some glaciotectonic features can be easily missed or misinterpreted due to their complex nature. This is more likely to occur if 2D seismic lines are not orientated and processed optimally or widely spaced. 3D seismic data are required for a more confident interpretation.

Presence of isolated sediment accumulations

Topography generated by glaciotectonics often results in accumulations of isolated sediments within ponds and kettle holes, or development of local drainage networks. Such soil units are often very local and can be difficult to identify, yet they will likely represent distinctively different ground properties.

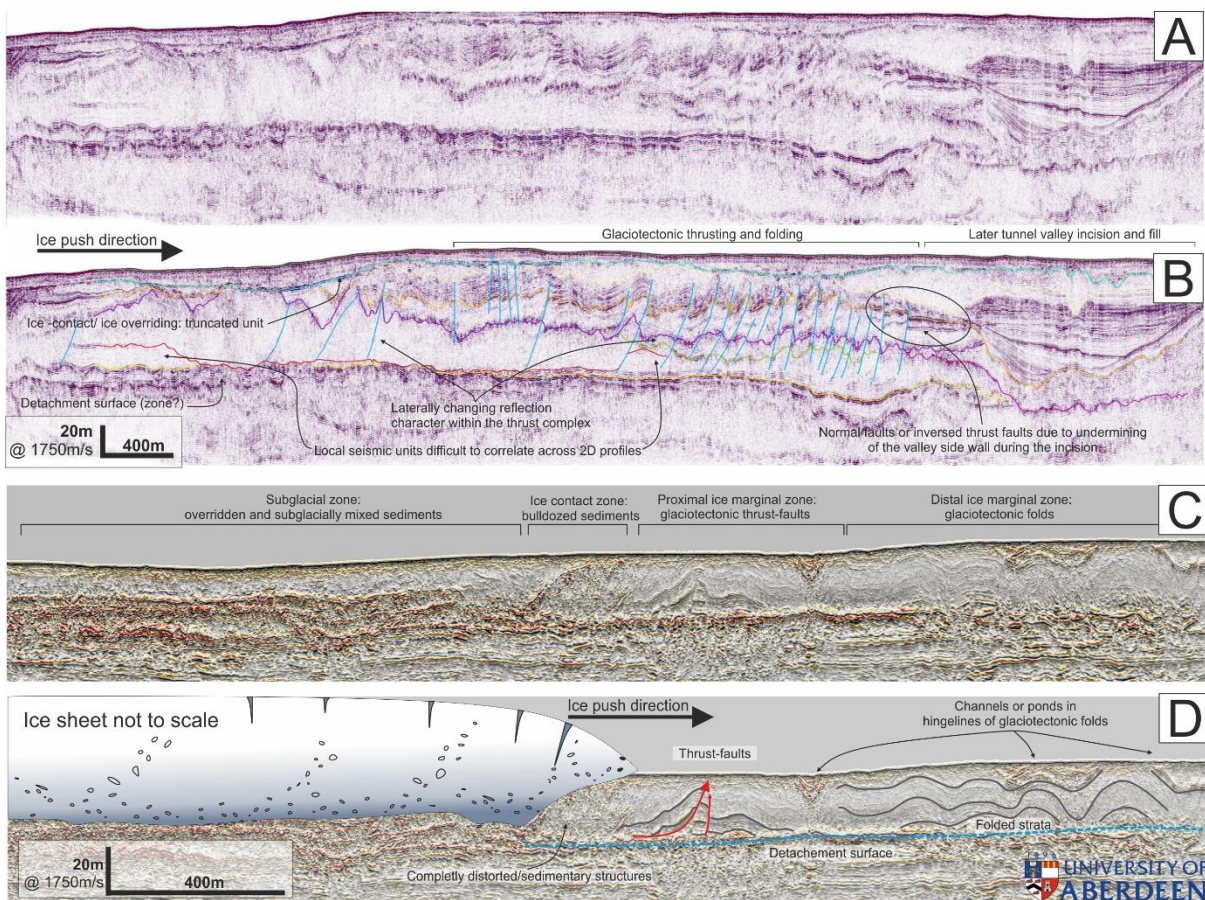
Fine-grained and organic-rich sediments formed in kettle-hole like depressions can often be found in similar settings onshore and are now being more frequently found offshore.

Presence of unexpected lithological units

Glaciotectonic rafts can be transported for long distances. In consequence, unexpected lithological units (i.e. rocks or sediment otherwise absent on the site) can be introduced.

Such units may not have the same geotechnical properties as their parent lithology due to a degree of deformation during quarrying and transport by ice sheets.

2426



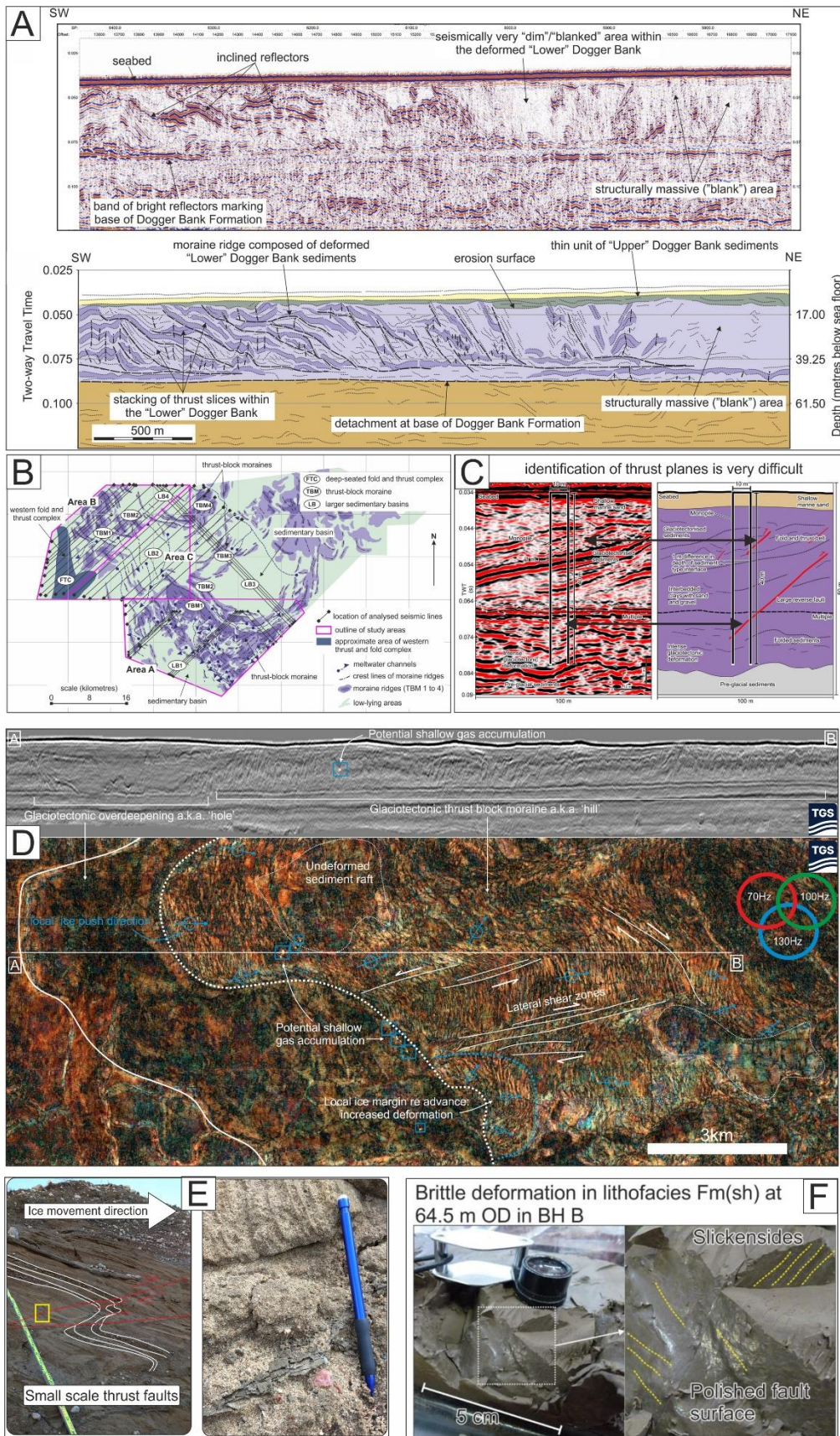
2427

2428 **Figure 5.33.** Complexes of glaciotectonic deformation. a) 2D UHR seismic profile from the North Sea.

2429 b) Interpreted seismic profile shown in Figure 5.33a. c) Seismic profile from the southern Baltic Sea.

2430 **d)** Explaining sketch and interpreted seismic profile shown in [Figure 5.33c](#). Note differences in
2431 thickness, style, complexity, and distribution of deformation between the examples that can be linked
2432 to differences in the ice-margin dynamics and position along the deformation front.

2433



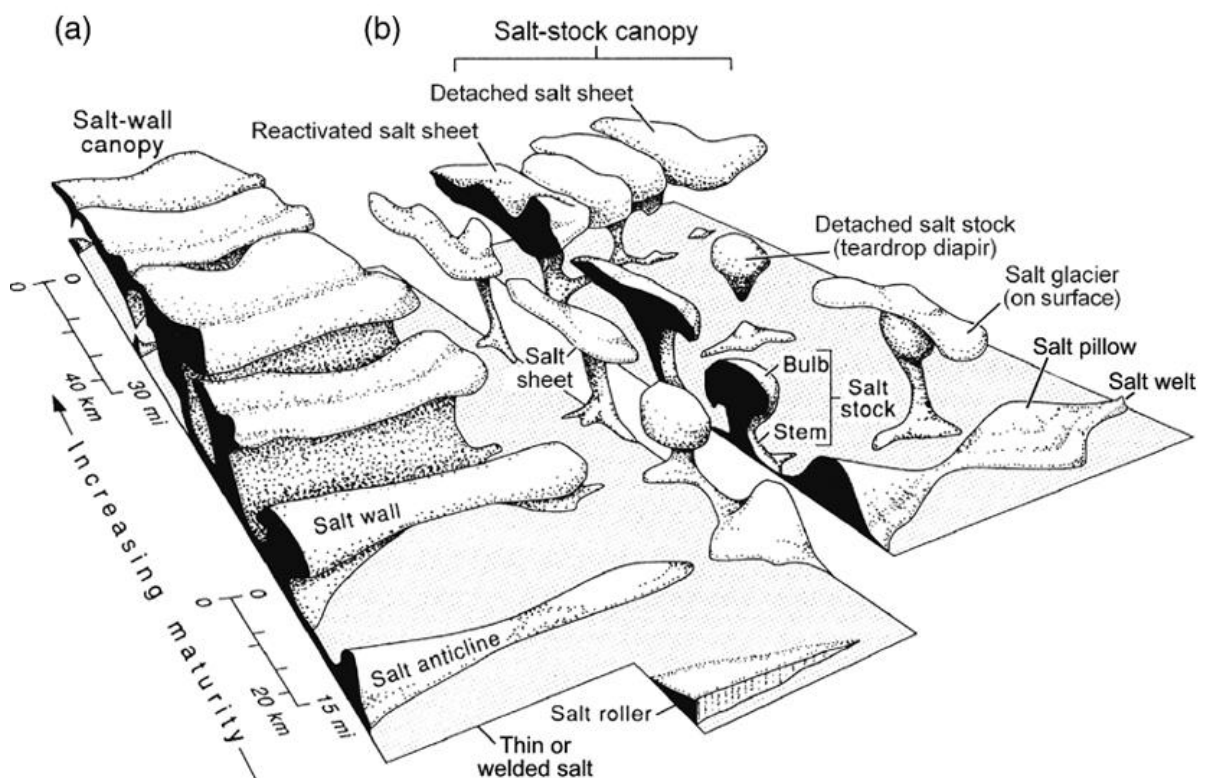
2434

2435 **Figure 5.34.** a) Uninterpreted and interpreted seismic cross section through a glaciotectonic complex
 2436 of Dogger Bank from Phillips et al. (2018). b) Plan view example of an interpreter glaciotectonic

2437 complex of Dogger Bank (Phillips et al., 2018). **c**): Example of a projected monopile foundation
 2438 penetrating glaciotectionised strata. Note several thrust planes intercepted by the foundation (modified
 2439 from Velenturf et al. (2021). **d**) Regional cross section and corresponding spectral decomposition slice
 2440 through a hill-hole pair. Note extensive thrusting with multiple lateral shear zones and variable local
 2441 thrusting vector (blue circle with arrow) despite the general eastward palaeo ice push. Small gas
 2442 accumulation can be observed as very bright spots (blue squares). HR data courtesy of TGS. **e**) Small
 2443 scale thrusts in ice-contact setting in granular sediments. Note the presence of clay along the thrust
 2444 plane possibly pointing to the role of pressurised water in the thrust formation (Kurjański et al., 2021).
 2445 **f**) Polished fault surfaces in cohesive sediments sampled from the Dogger Bank thrust complex (Emery
 2446 et al., 2019b)

2447 **5.12 Salt tectonics**

2448 Salt of Late Palaeozoic age is present throughout much of the North Sea Basin whilst salt of Triassic,
 2449 Jurassic and Cretaceous age is present along the Atlantic margins (Hudec and Jackson 2007). Salt
 2450 tectonics refers to any kind of deformation caused by the movement of salt, typically halite, from early-
 2451 stage deformation at surface, if deposited on a slope, to deformation during burial and tectonic re-
 2452 activation. Salt is largely incompressible and weak on geological time scales, causing it to flow under
 2453 differential loads (Hudec and Jackson 2007). Because of its incompressibility and low strength, salt,
 2454 unlike other Earth materials, can remain unstable for hundreds of millions of years, often resulting in
 2455 superimposed styles of deformation involving salt (Figure 5.35).



2456
 2457 **Figure 5.35.** Schematic representation of salt structures. NW European examples (North Sea Basin and

2458 Barents Sea) mainly comprise the low to middle maturity varieties, with the most mature structures
2459 mainly developing in continental margin or contractional basins with a strong slope (from [Hudec and](#)
2460 [Jackson 2007: fig 6](#))

2461 On a salt-tectonic timescale, the life span of an offshore installation (< 100 years) is relatively short,
2462 but salt structures can still affect offshore installation for a variety of reasons; a) Active deformation of
2463 the seabed; b) Triggering and reactivation by glacial loading; c) Providing juxtapositions of materials
2464 of different properties near the surface; d) Seismicity associated with salt tectonics adjusting to glacial
2465 loading/unloading; and e) by their strong control over subsurface fluid flow, often resulting in
2466 hydrocarbon seeps being located around the flanks or over the crests of salt bodies (e.g. [Serie et al.](#)
2467 [2017; Römer et al., 2021](#)).

2468 In the literature it has been suggested that salt structures may have controlled the location of glacial
2469 meltwater valleys (tunnel valleys). However, the evidence for this is sparse (see [Huuse and Lykke-](#)
2470 [Andersen, 2000](#)), and more recent compilations on regional and yet detailed scales using 3D seismic
2471 data show that any local controls are largely coincidental or second order with respect to regional ice-
2472 sheet hydrological controls (e.g. [Kristensen et al. 2007; Ottesen et al. 2023](#)). In terms of glaciotectonics,
2473 a similar second-order control is in place as the ice sheet is the primary driver imparting its load on
2474 substrate geo-mechanical properties, which can be affected by salt pushing up deeper layers or causing
2475 faults to propagate to the free land or sea-bed surface.

2476 Given the often continuous deformation in a relatively low-stress, near-surface environment, the
2477 seismicity associated with salt tectonics is expected to be relatively low. Hence the main impacts to
2478 near-surface installations (upper 200 m) are expected to be faults propagating to the sediment surface
2479 and any lateral changes in the substrate conditions and fluid flow associated with salt-associated
2480 deformation of aquifers, seals and rupture by faulting ([Figures 5.36, 5.37, and 5.38](#)). Faulting can be
2481 due to salt rise and collapse as seen in the UK ([Stewart, 2007](#)), the Dutch North Sea ([Harding and Huuse](#)
2482 [2005](#)), and elsewhere in the North Sea. Gravity sliding off buried highs, such as the Ringkobing-Fyn
2483 High, can lead to relatively long and linear faults ([Huuse, 1999](#)), but usually with small offsets and
2484 relatively little across-fault change in sediment properties, although across-fault changes in bathymetry
2485 could lead to peat accumulating in fault-controlled lows, with implications for high-voltage cable
2486 performance.

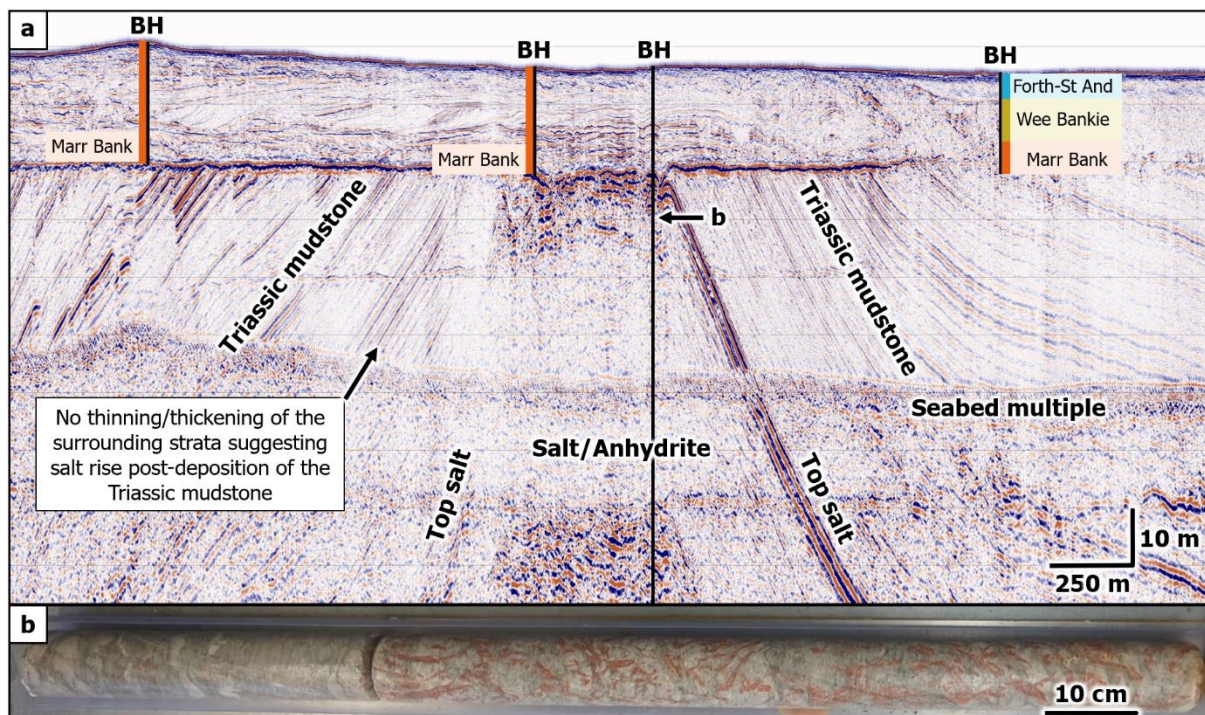
2487 Types/scales of deformation and constraints affecting the geotechnical realm, also shown in [Figure](#)
2488 [5.37](#), are:

- 2489 • Several km diameter of the diapir itself
- 2490 • Several km radius around salt domes

- Tens to hundreds km long fault systems along buried highs and basin flanks (Figures 5.37 and 5.38)
- Vertical deformation can be several km in the case of diapirs, bringing salt or indurated bedrock into the geotechnical realm (Figures 5.36, 5.37, and 5.38)
- Vertical deformation along buried highs and basin flanks often limited to less than a few tens of metres offset in the upper few hundred metres (Figures 5.37 and 5.38)
- Fluid flow from overpressured strata or hydrocarbon reservoirs can connect over lateral scales of tens of km and vertical scales exceeding several km causing significant geotechnical constraints around any salt domes or deep salt-detached fault systems (Figure 5.38).

2500 **Identification criteria (e.g., in geophysics):**

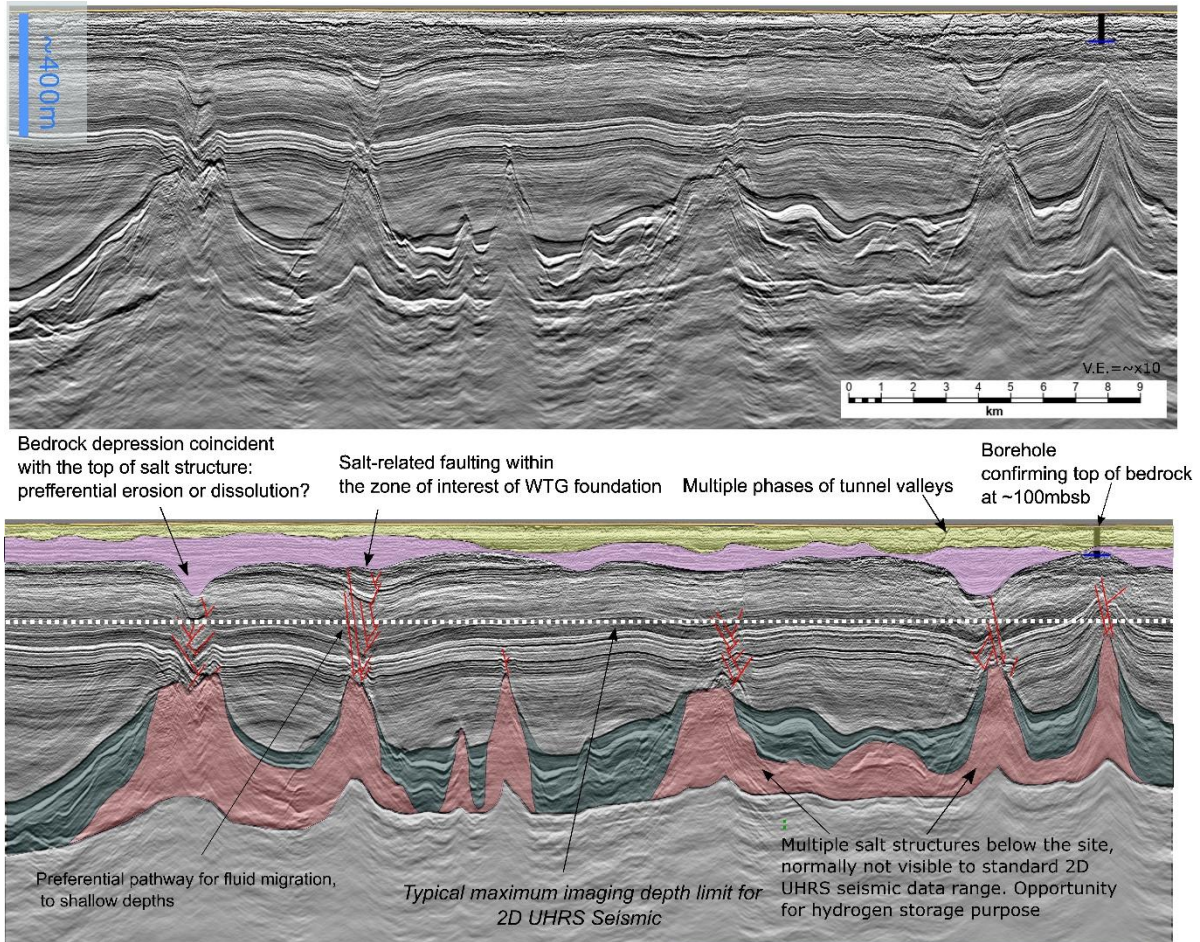
2501 Salt domes are usually easily recognised by their concentric deformed layering (in case of preserved
 2502 sedimentary overburden) or by near-surface chaotic facies characterised by an extremely high positive
 2503 reflection coefficient in case of salt extending to the near-seabed environment. Figure 5.36 shows a
 2504 hybrid case where the deformed sedimentary packages are seen dipping outward from a central diapir
 2505 core where the exposure to circulating groundwater and perhaps glacial flushing has dissolved some of
 2506 the evaporitic minerals leaving the anhydrite as a caprock with extreme acoustic impedance contrast
 2507 and thus high-amplitude seismic reflection.



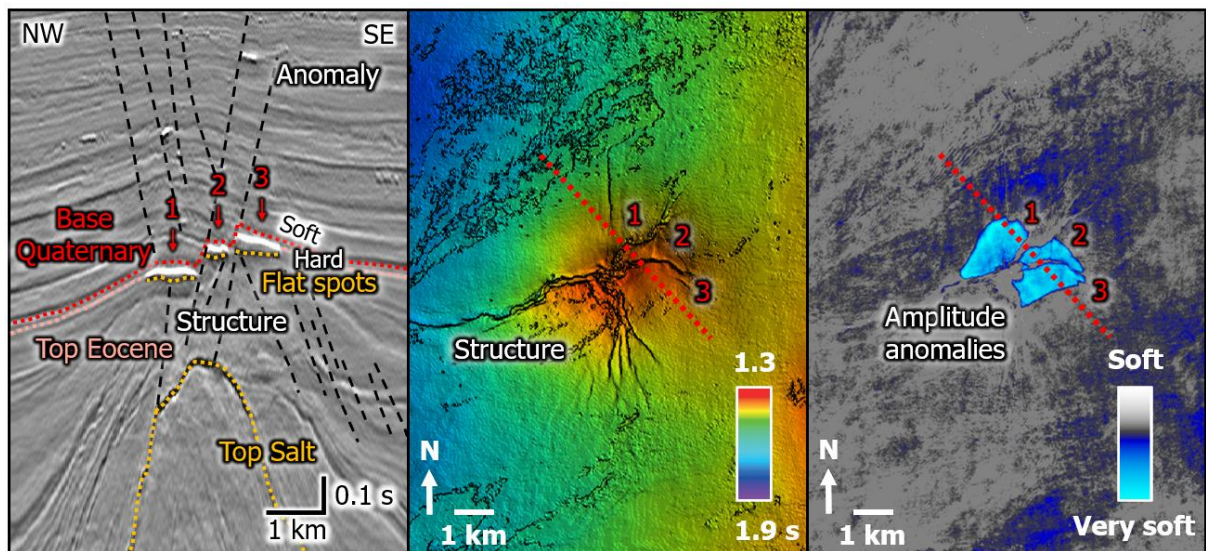
2508
 2509 **Figure 5.36.** Salt dome example from the Berwick Bank wind farm development area in the Firth of
 2510 Forth, UK North Sea. The seismic reflection character suggested possible salt dissolution and anhydrite

2511 presence at a candidate wind turbine location (Figure 5.36a), which was confirmed by drilling (Figure
2512 5.36b), causing the location to be moved. Data courtesy of SSE Renewables.

2513



2515 **Figure 5.37.** Repurposed 2D seismic line across the Mid North Sea High. The data was used for
2516 preliminary assessment of ground conditions across an OWF site prior to any commissioned site-
2517 specific survey. Note numerous salt structures and focused areas of salt- related faulting within the
2518 shallow subsurface within the dept of interest for WTG foundations. Thickened Quaternary sediments
2519 are present atop some of the salt structures potentially indicating salt dissolution or preferential erosion
2520 along the crests of structures. Figure modified from Tam (2023). Data courtesy of SSE Renewables.



2521

2522 **Figure 5.38.** Salt tectonic deformation in Quaternary sediments above salt structure in the SW Barents
 2523 Sea. **a)** Seismic profile indicating salt structure, Cenozoic overburden, and shallow gas trapped at the
 2524 Quaternary-Neogene interface. Faults are associated with the salt structure, and still identified within
 2525 the Quaternary stratigraphy. **b)** Structure map showing seismic geomorphology of the Base Quaternary
 2526 reflection. **c)** Minimum amplitude map of the Base Quaternary surface, highlighting the distribution of
 2527 the negative-amplitude anomalies along the fault segments of the salt structure. Potential shallow-gas
 2528 accumulations in the lower Quaternary show as very soft ‘bright spot’ anomalies and flat spots in the
 2529 faulted carapace to the salt dome. A 3D view into a salt structure is shown in [Figure 5.32](#). Data courtesy
 2530 of TGS and VBER.

2531 5.13 Glacigenic landforms

2532 A variety of glacigenic landforms shape the seafloor and shallow subsurface of glaciated margins
 2533 ([Figure 5.39](#); [Dowdeswell et al., 2016](#)). Along the glaciated European margins, these landforms are
 2534 mainly formed by processes related to the dynamics of the Eurasian ice sheets, in particular subglacial,
 2535 ice-marginal and proglacial deposition, reworking and erosion. Glacigenic landforms are often subject
 2536 to later periglacial modification of reworking in marine environments by waves, tides and currents on
 2537 continental shelves ([Section 6.1](#)), and submarine mass movements along the continental slopes ([Section](#)
 2538 [6.2](#)). The morphology of the present-day European margins is mainly caused by processes related to the
 2539 ice-sheet activity during the Pleistocene glaciations. The presence of these glacigenic landforms and the
 2540 deposits associated to the landforms have implications for geohazard assessments and marine
 2541 engineering, which are summarized in [Table 5.6](#).

2542 Bathymetric, side-scan sonar and seismic data combined with sediment cores and boreholes are
 2543 commonly used to study landforms located in the marine realm ([Bryn et al., 2005a](#); [Dowdeswell et al.,](#)
 2544 [2016](#); [Bellwald et al., 2019c](#); [Newton et al., 2024](#)). Over the last decade, developments of acquisition
 2545 and interpretation of (ultra-)high-resolution 3D reflection seismic data and application of seismic

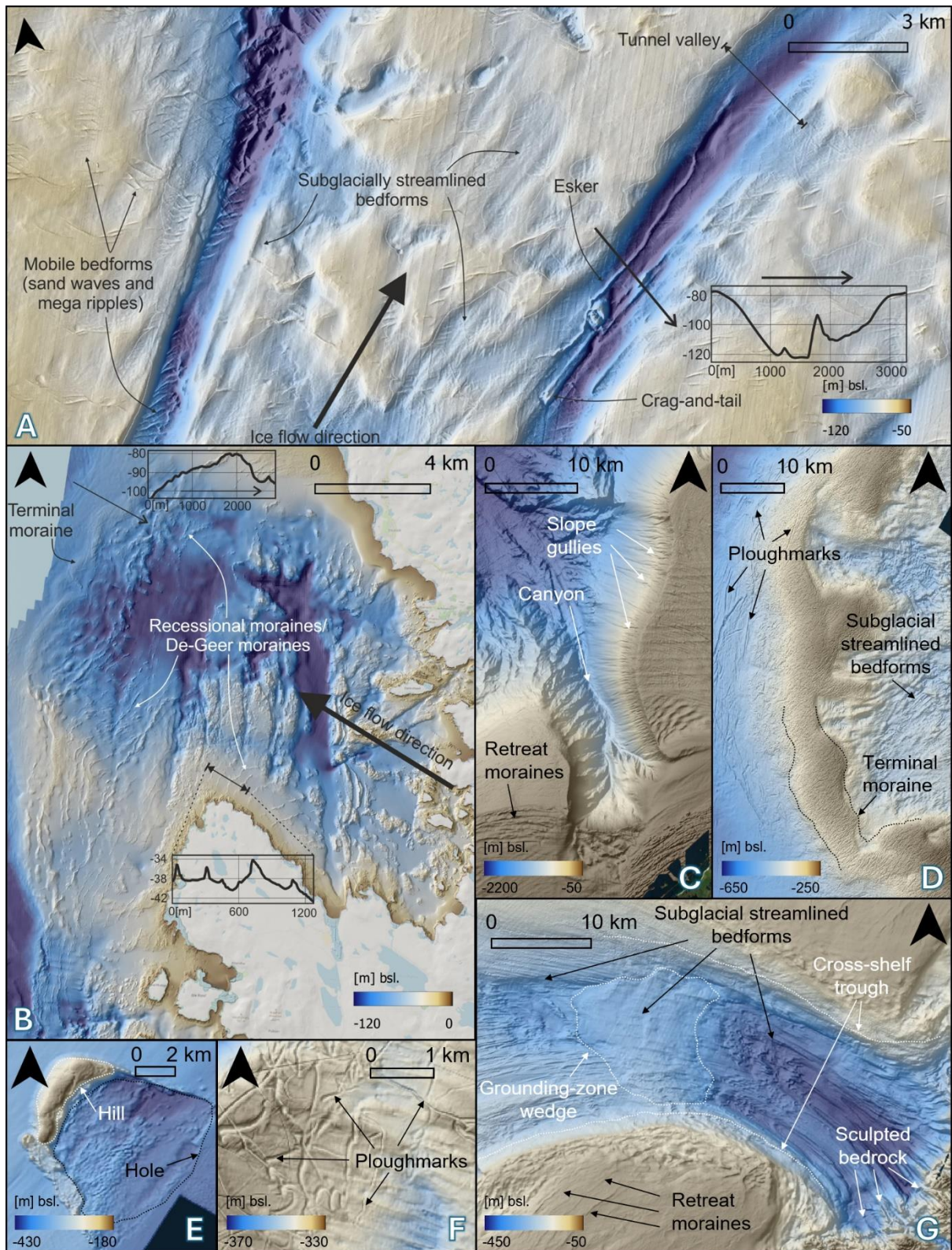
2546 geomorphology allowed to image glacial landforms below the present seafloor on a meter-scale,
2547 establishing strong links between subsurface structures (e.g., faults, topographic highs) and landforms
2548 (Bellwald et al., 2023a).

2549 *Types of glacial landforms and deposits*

2550 Glacial landforms vary significantly depending on whether they were formed under the ice
2551 (subglacial landforms), at the margin of a glacier or an ice sheet (ice-marginal landforms), or formed
2552 distally to the ice margin lacking any glacial contact (proglacial landforms; Figure 5.40; Kurjanski et
2553 al., 2020). All of these types of glacial landforms have been documented along the glaciated
2554 European margin (Dowdeswell et al., 2016; Newton et al., 2024a).

2555 Subglacial landforms can either be erosional (i.e. sliding of debris-rich basal ice abraded and eroded
2556 existing substratum), depositional (i.e. sediments were deposited from ice at the base of the ice sheet),
2557 or a combination of both. The resulting landforms also depend on their formation by a fast-flowing ice
2558 stream (i.e., mega-scale glacial lineations or drumlins), or a more slow-moving part of the ice sheet.
2559 Finally, the thermal regime at the base of the ice (i.e. whether the ice sheet is frozen to the ground or
2560 sliding at the interface) as well as presence and abundance of water at the ice-bed interface have an
2561 effect both on sliding velocities and types of landforms and sediments that are generated (Kurjanski et
2562 al., 2020; Bellwald et al., 2023a).

2563 In the ice-marginal and proglacial zones, the landforms and sediments depend mainly on the
2564 environment in which the ice terminated. Different landforms are observed when ice sheets terminate
2565 in water (sea or lake, for example grounding zone wedge) to the ones associated with a land-terminating
2566 ice sheet (for example glaciofluvial fans and outwash plains; Figure 5.40). Landforms will also vary
2567 depending on the mode of their formation. Ice push and bulldozing in the ice marginal zone will result
2568 in the formation of frontal moraines, thrust block moraines, and morainal banks, whereas deposition
2569 from meltwater fill form ice contact fans or deltas in marine environment and vast outwash plains (or
2570 sandar) in terrestrial conditions (Figure 5.40; Kurjanski et al., 2020).



2571

2572

2573

2574

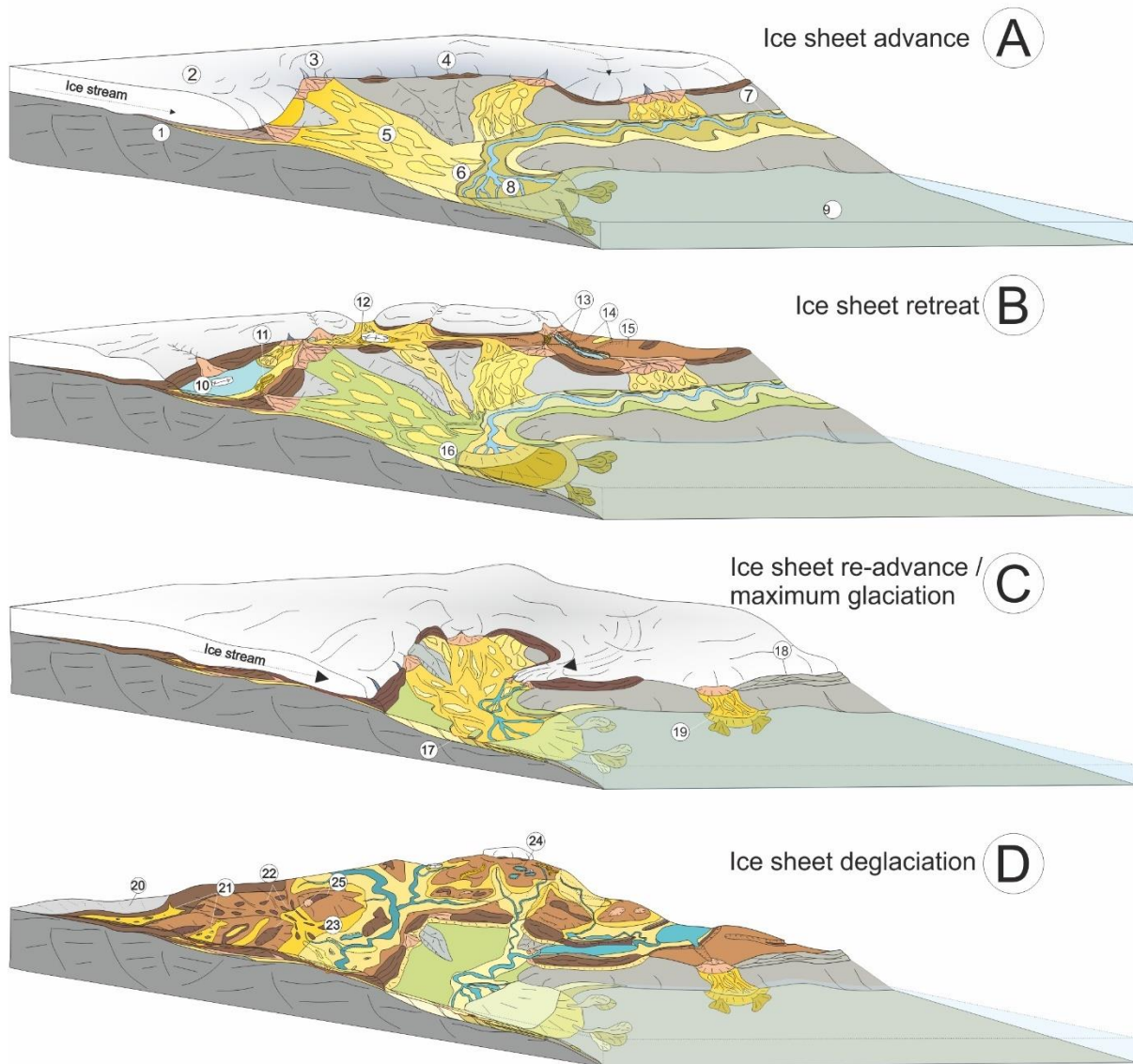
2575

2576

Figure 5.39. Examples of submarine glacial landforms observed along the European margin seafloor. Note that many of these same landforms can be observed buried in the shallow subsurface (see [Newton et al., 2024a](#)). **a)** Streamlined and glaciofluvial landforms, along with contemporary sediment waves observed offshore UK. **b)** Moraine features offshore UK showing former ice-margin positions. **c)** Retreat moraines, gullies, and a submarine canyon offshore Troms, northern Norway. **d)** The

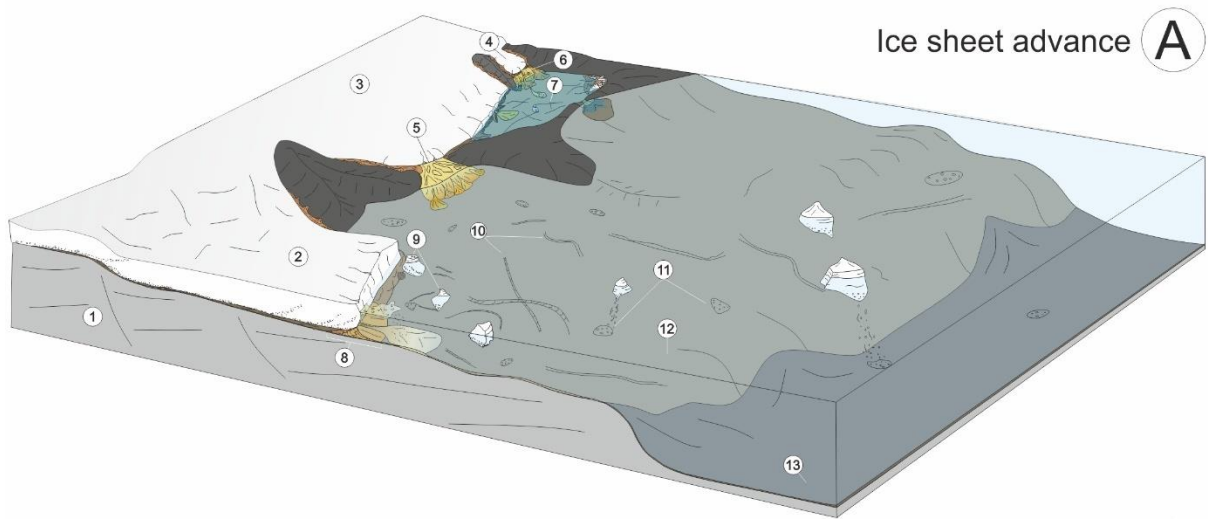
2577 Skjoldryggen terminal moraine on the outer mid-Norwegian shelf. **e)** A hill-hole pair observed on the
2578 mid-Norwegian shelf. **f)** Examples of iceberg ploughmarks. These landforms are observed extensively
2579 on the seafloor and within the subsurface. **g)** The Malangsdjupet cross-shelf trough offshore northern
2580 Norway with typical landforms associated in ice-stream and ice-stream proximal areas, such as
2581 moraines, streamlined bedforms, and a grounding-zone wedge. Data for the UK have been retrieved
2582 from the UK Hydrographic Office and data from Norway were provided by the MAREANO
2583 programme.

Land terminating ice sheet landsystem

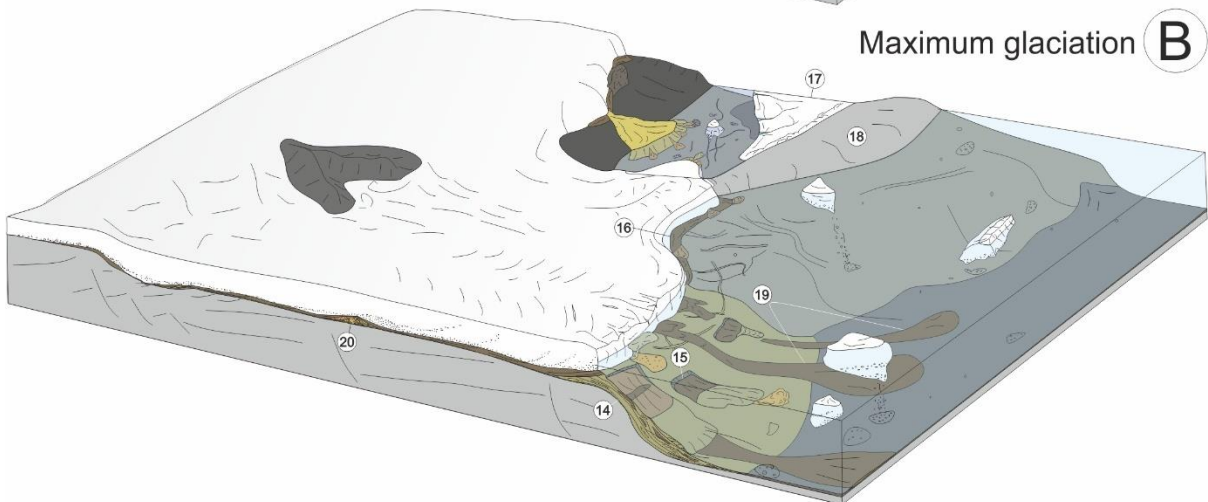


- | | | | | |
|--------------------------------|-------------------------------|--------------------------------|--------------------------------|--|
| ① Bedrock/preglacial sediments | ⑥ Sandur (distal) | ⑪ Esker | ⑯ Vegetated (abandoned) sandur | ⑳ Pitted sandur/ isolated subbasin |
| ② Ice sheet | ⑦ Valley train/spillway | ⑫ Kame | ⑰ Fluvial incision/erosion | ㉑ Streamlined subglacial bedforms (ribbed moraine/drumlins/MSGL) |
| ③ Ice-contact fan | ⑧ Delta | ⑬ Tunnel valley (under filled) | ⑱ Thrust-block moraine | ㉒ Tunnel valley (filled) |
| ④ Composite ridges | ⑨ Lake/Sea | ⑭ Recessional moraines | ⑲ Glacier-fed delta | ㉓ Kettle hole lakes |
| ⑤ Sandur (proximal) | ⑩ Proglacial/ice contact lake | ⑮ Traction till | ㉔ Striated pavement/bedrock | ㉕ Overridden moraines |

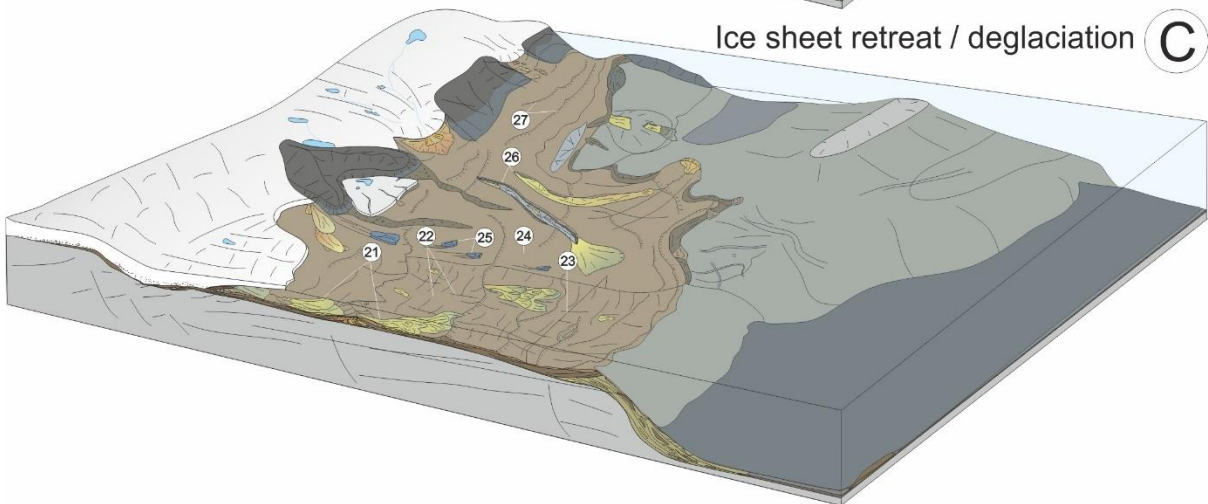
Marine/lacustrine terminating ice sheet landsystem



Ice sheet advance **(A)**



Maximum glaciation **(B)**



Ice sheet retreat / deglaciation **(C)**

- | | | | | |
|--------------------------------|------------------------------|----------------------------|----------------------------|--|
| ① Bedrock/preglacial sediments | ⑥ Glacier-fed delta | ⑪ Ice-rafted debris | ⑯ Composite ridge | ⑳ Streamlined subglacial bedforms (ribbed moraine/drumlins/MSGL) |
| ② Ice stream | ⑦ Ice-contact lake | ⑫ Glaciomarine diamicton | ⑰ Sea/lake ice | ㉓ Ice stream trough |
| ③ Ice dome | ⑧ Grounding zone wedge (GZW) | ⑬ Marine muds | ⑱ Emerged seabed | ㉔ Traction till |
| ④ Outlet glacier (Isbrae) | ⑨ Icebergs | ⑭ Trough mouth fan (TMF) | ㉑ Glaciogenic debris flows | ㉕ Bedrock rafts |
| ⑤ Ice-contact delta | ⑩ Iceberg ploughmarks | ⑮ Subaqueous slope failure | ㉒ Overridden GZW | ㉖ Tunnel valley |
| | | | ㉔ Subaqueous outwash fan | ㉗ Recessional moraines |

2586 **Figure 5.40.** Conceptual block diagrams showing the evolution of land terminating and marine
2587 terminating ice sheet ice landsystems over a glacial cycle. Vast areas of continental shelves in the
2588 Northern hemisphere that are currently submerged were hosting ice sheets that could be considered
2589 land-terminating due to the fact that the sea level was much lower than at present and parts of the
2590 present-day seabed were emergent. Note that multiple glacial cycles separated by warmer, interglacial
2591 conditions are likely to occur within an icehouse period. Landforms and sediments deposited during a
2592 glacial cycle are frequently eroded, transported and re-deposited during a subsequent ice-sheet advance
2593 leaving a mosaic-like patchy and highly discontinuous stratigraphic record. Nature of glacial deposition
2594 and erosion is responsible for the subsurface complexity of sediments on glaciated continental shelves.
2595 Figure modified from Kurjanski et al. (2020).

2596 *Implications*

2597 The deposits of the various glacial landforms can be very heterogenous vertically and laterally on
2598 10s to 100s meter scales, and their grain size varies from large boulders in glacial moraines and
2599 subglacial tills to fine clay in glacial lakes and kettle holes (e.g., [Figure 3.5](#)). Due to these
2600 heterogeneities, glacial landforms always express strength variations ([Section 5.4](#)), and lateral
2601 variability on a meter-scale. Thus, the identification of glacial landforms allows prediction of
2602 geotechnical properties even before CPT or borehole sampling. In addition, these landforms can define
2603 fluid flow pathways (e.g., [Mazzini et al., 2016](#); [Tasianas et al., 2018](#); [Bellwald et al., 2023a](#)). The
2604 implications of the landforms are summarized in [Table 5.6](#).

2605 Subglacial landforms, typically composed of subglacial lodgement till, are often characterized by high
2606 undrained shear strength values (>400 MPa), heterogenous deposits (including boulders), sediment
2607 deformation, and overconsolidation due to ice loading ([Clarke, 2018](#)). Matrix of subglacial tills is
2608 variable and depends largely on the substratum that is cannibalised by overriding ice sheets. Clay-rich
2609 tills can be expected if fine-grained lithologies were present at the base whereas sandy tills could be
2610 anticipated if fresh bedrock or coarse-grained sediments were locally present under the ice. Some glacial
2611 tills are known to be highly reactive to HCl as the ice overrode and abraded carbonate lithologies
2612 (limestones, or chalk) incorporating them into till matrix. Such tills, depending on the carbonate content,
2613 can be prone to partial dissolution and volume loss if exposed to unfavourable geochemical conditions.

2614 On formerly terrestrially exposed shelves, landforms and sediment formed by and deposited from
2615 glacial meltwaters, such as sandar, ice-contact deltas, tunnel valleys, eskers, and glaci-fluvial channels,
2616 are typically composed of better sorted, more permeable granular material. Eskers and topsets of ice-
2617 contact deltas are typically associated with boulder and cobble-sized deposits ([Figure 2.14](#)). The
2618 erosional nature of high-magnitude glacial meltwater flow, especially during deglaciation, implies that
2619 not all sediments are preserved, and erosional landforms or landscapes are formed. These landforms
2620 (i.e. tunnel valleys, meltwater corridors) are associated with steep slopes and a presence of very coarse

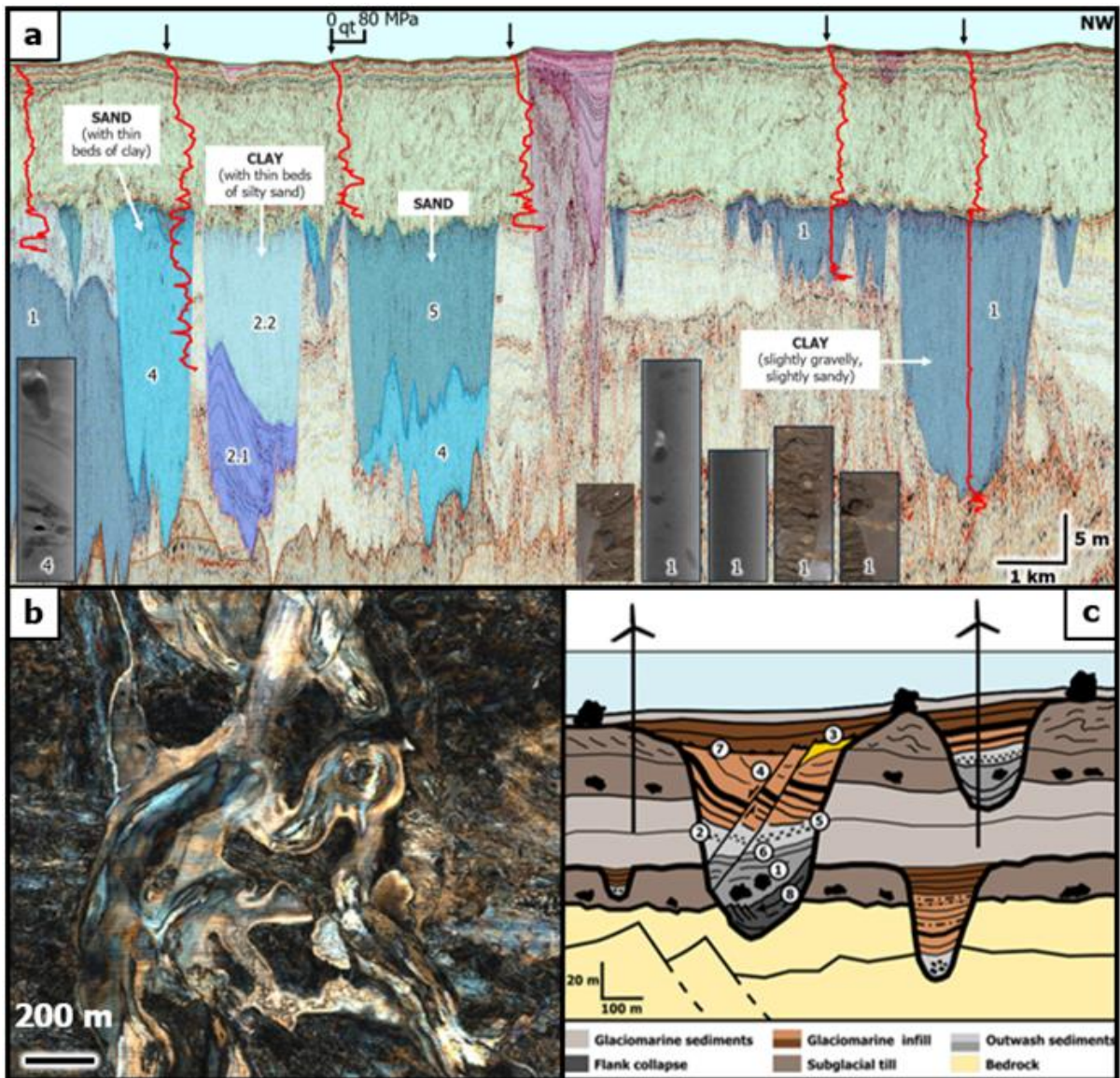
2621 fractions (up to boulder size) towards the base of such features (channel lag; [Figure 5.41](#)). The channel
2622 infill can consist of well-sorted sand and gravel layers that can act as fluid reservoirs, resulting in
2623 shallow gas accumulations in the channel and valley infill ([Bellwald et al., 2024c](#)). In contrast, if shear
2624 strength of the valley infill is enhanced compared to the surroundings (e.g., subglacial till infilling
2625 valley), then those valleys might actually act as a seal for fluid migration ([Figure 5.12](#)). In terrestrial
2626 settings, proglacial lakes and kettle holes (depressions formed by meltout of buried dead ice blocks) are
2627 characterized as lower-energy sedimentary environments, and often dominated by interbedded
2628 sediments ranging from soft clays and till with subordinate coarser fractions. Downslope processes such
2629 as turbidites and debris flows, however, might contribute to more coarse-grained layers in these
2630 depocenters. Organic-rich sediments and peats have been previously reported from kettle hole settings
2631 offshore. Although the layering of lacustrine sediments is often indicating a homogenous infill, units
2632 within lake systems might still undergo gradual lateral changes (e.g., lateral fining within the same unit
2633 from delta to deep basin).

2634 Pockmarks evidence shallow gas and gas hydrates in the subsurface, and occur in high densities in
2635 active hydrocarbon systems, such as the North Sea and Barents Sea ([Figure 5.11](#); [Forsberg et al., 2007](#);
2636 [Mazzini et al., 2017](#); [Tasianas et al., 2018](#)). Pingos and hill-hole pairs might indicate shallow gas
2637 ([Bellwald et al., 2023a](#)), but are less common compared with pockmarks. Megaripples, sand waves,
2638 sand banks, and sediment scouring are distinct landforms that indicate a mobile seafloor ([Passchier and](#)
2639 [Kleinhans, 2005](#); [Stow et al., 2009](#); [Bellec et al., 2019](#); [Figure 6.3](#)). Certain landforms, such as
2640 pockmarks, are important marine habitats ([Figure 5.11](#)). Interestingly, the Silver Pit Formation in the
2641 UK North Sea forming a prominent tunnel-valley infill unit, received its name due to its nature as good
2642 fishing ground.

2643 The shelf break is the transition from shallow (<500 m, with deepest depths in the mouths of cross-shelf
2644 troughs) to deeper waters (>2 km) and associated with an increase of slope gradient. Signatures related
2645 to downslope and along slope sedimentation shape the slopes of these regions ([Solheim et al., 2005a](#);
2646 [Bryn et al., 2005a](#); [Newton and Huuse, 2017](#); [Barrett et al., 2021](#)). Their deposits vary from boulders to
2647 sandy channel deposits to fine-grained contourite deposition ([Bellwald et al., 2024a](#)). The slope
2648 gradients of slide escarpments, fjord flanks, and canyons often incorporates slope instabilities (different
2649 types of mass movements) as an engineering constraint, and ultimately as a geohazard ([Sections 6.2](#)
2650 [and 6.3](#)).

2651 Identification of small landforms might be very relevant for offshore engineering: Pockmarks, for
2652 example, can generate problems for anchoring of seafloor infrastructure due to the soft-sediment infill
2653 during the Holocene ([Bellwald et al., 2018](#)), their correlation with sensitive benthic habitats ([Revelas et](#)
2654 [al., 2020](#); [Henkel et al., 2022](#); [Webb et al., 2009](#); [Mazzini et al., 2016](#); [2017](#)), unconfined sediment
2655 gravity flows ([Lundsten et al., 2024](#)), and their link to the fluid release ([Forsberg et al., 2007](#)). The

2656 identification of meter-scale pockmarks (also called unit pockmarks) is crucial, as they can reduce the
 2657 foundation capacity, and are in consequence avoided for foundations.



2658
 2659 **Figure. 5.41.** Implications of tunnel valleys and their infill. **a)** Signatures of tunnel-valley infill in the
 2660 Central North Sea. Ultra-high-resolution 2D seismic profile with cone penetration tests (black arrows
 2661 and red lines). Although all tunnel valleys are formed during the Saalian glaciation, their infill is
 2662 heterogeneous on short lateral distances. Different types of infill are labelled as 1-5, and shaded in
 2663 different types of blue. X-ray scans and (black and white images) and core photography (images in
 2664 brown) of the different infill are shown. Data courtesy of bp and EnBW. **b)** Geomorphologies within
 2665 the tunnel valley infill identified in ultra-high-resolution 3D seismic data, Offshore Netherlands. Data
 2666 courtesy of RVO. **c)** Sketch summarizing geo-engineering constraints and geohazards of tunnel valleys
 2667 and their infill. 1: Boulders, 2: Gravel and pebble beds, 3: Shallow gas, 4: Faults and deformation
 2668 structures, 5: Heterogeneities on small vertical and lateral scales, 6: Paleo-gas hydrates, 7: Low-strength

2669 clays, 8: Peat and high-organic sediments, 9: Slope instability. Figures compiled from Bellwald et al.
 2670 (2024c).

2671 **Table 5.6.** Landforms shaping the seafloor of the glaciated European margins and their implications for
 2672 offshore geohazard and geo-engineering.

| Landform | <i>Boulders</i> | <i>Gravels and cobbles</i> | <i>Sands</i> | <i>Soft clay</i> | <i>Peat</i> | <i>Shallow gas</i> | <i>Gas hydrates</i> | <i>Mobile sediments</i> | <i>Steep slopes (>5°)</i> | <i>Slope instability</i> | <i>High-strength sediments</i> | <i>Overconsolidation</i> | <i>Deformation</i> | <i>Hotspot for marine life</i> |
|--------------------------------------|-----------------|----------------------------|--------------|------------------|-------------|--------------------|---------------------|-------------------------|------------------------------|--------------------------|--------------------------------|--------------------------|--------------------|--------------------------------|
| Mega-scale glacial lineations | X | | | | | | | | | | X | X | X | |
| Iceberg ploughmarks | | | X | | | | | | X | | | | X | |
| Hill-hole pairs | | | | | | X | X | | X | | X | | X | |
| Glaciotectonic complexes | X | X | X | X | | | | | X | | X | X | X | |
| Glacial moraines | X | X | X | | | | | | X | | X | X | X | |
| Grounding zone wedges | X | X | X | | | | | | | | X | X | | |
| Esker | | X | X | | | | | | X | | | | | |
| Drumlin | X | X | X | | | | | | | | | | | |
| Tunnel valleys and infill | ? | X | X | X | X | X | | | X | X | X | X | X | |
| Fluvial channels and infill | X | X | X | X | X | X | | | X | X | | | | |
| Ice-contact deltas/fans | ? | X | X | | | ? | | | X | ? | | | ? | |
| Glacial lakes | | X | X | X | X | X | | | X | X | ? | | | |
| Kettle holes | | X | X | X | X | ? | | | X | | | | | |
| Slide escarpment | | | | X | | | ? | | X | X | | | X | |
| (Mega)slide | | X | X | X | | X | | | X | X | X | | X | |
| Rock avalanche | X | X | X | | | | | | X | X | | | X | |
| Turbidite channels | ? | X | X | X | | ? | | | | X | | | | |
| Debris lobes | X | X | X | X | | | | | | X | | | | |
| Contourite sheets and mounds | | | X | X | | X | X | X | | | | | | |
| Pockmarks | | | X | X | | X | X | X | | | | | | X |
| Pingos | | | | ? | | X | X | | X | | | | | |
| Sandwaves | | X | X | | | | | X | | | | | | ? |
| Megaripples | | X | X | | | | | X | | | | | | |
| Scouring marks | X | X | | X | | | | X | | | | | | |

2673

2674 6. Geohazards

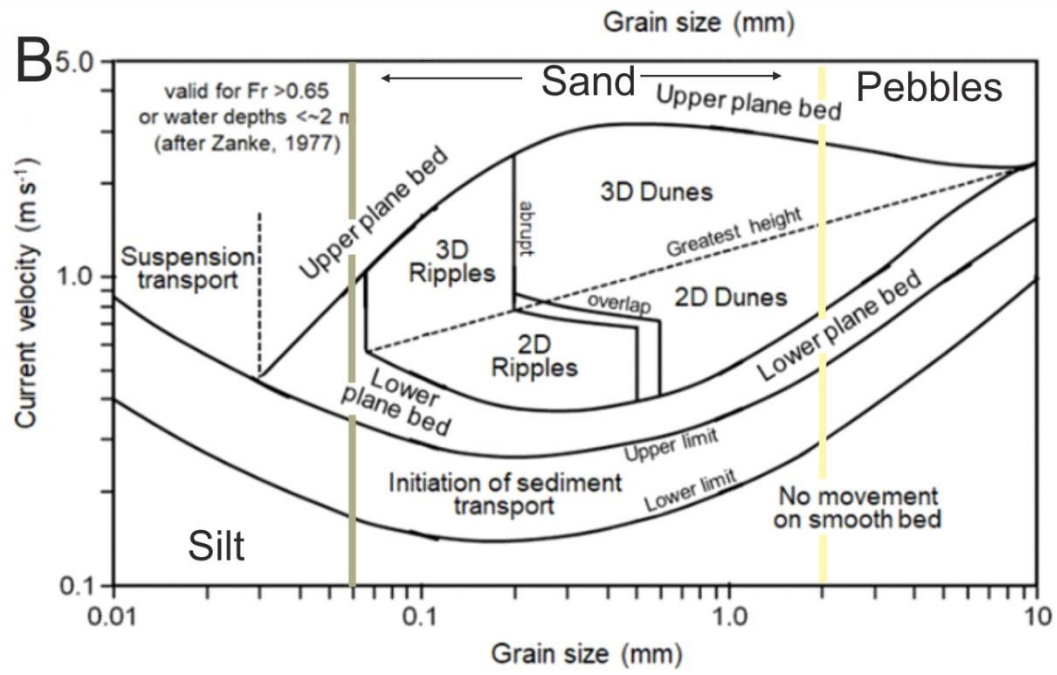
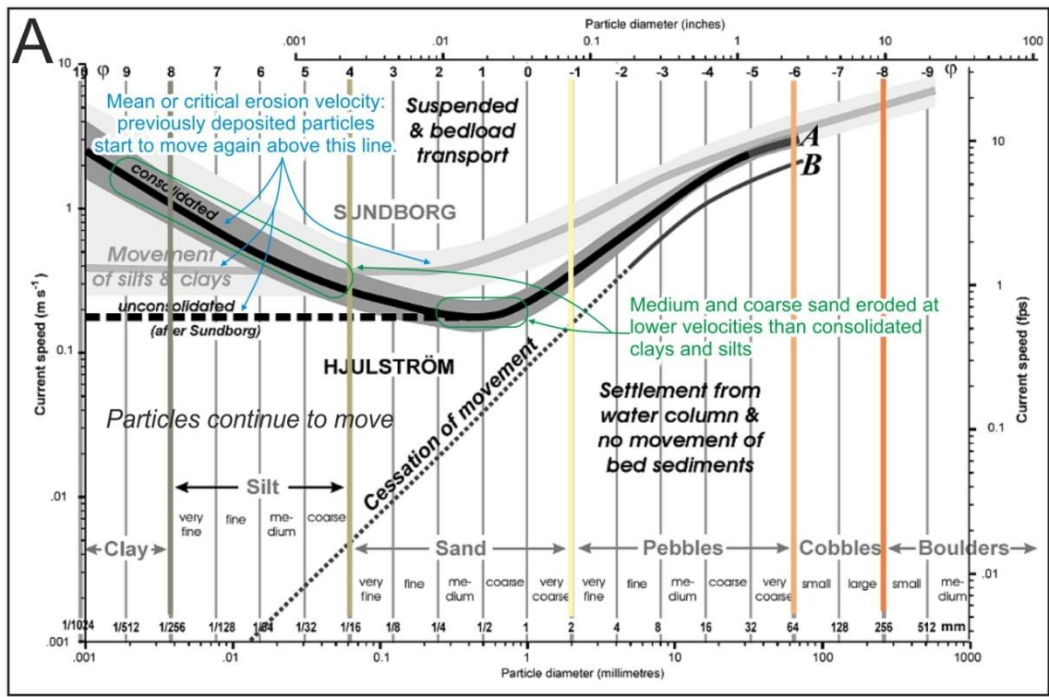
2675 This chapter is separated into geohazards characteristic for deglaciated continental margins related to
 2676 sediment mobility (Section 6.1), slope instabilities and mass flow dynamics (Sections 6.2-6.3), glacio-
 2677 isostatic rebound and sea-level changes (Section 6.4), seismicity (Section 6.5), and tsunamis (Section
 2678 6.6). A geohazard is here defined as a dynamic geo-event or process that is a risk to industry and/or
 2679 society and/or marine life, and is addressed by project management frameworks. Geohazards can affect

2680 the more static features, landforms, and deposits forming geo-engineering constraints (Figure 5.1; see
2681 also ISO 19901-10).

2682 **6.1 Sediment transportation and mobile bedforms**

2683 Sediment transport is broadly defined as the movement of particles by a fluid, which can be air or water
2684 (Collinson, 2005). The mechanism for transport depends principally on the grain size, the velocity, and
2685 viscosity of the fluid, together with gravity, but is also affected by grain angularity and grain-to-grain
2686 cohesion. Generally, the higher the velocity of the fluid and smaller the grain size, the more readily the
2687 particles are mobilized.

2688 The Hjulström curve (Figure 6.1a) was initially developed in the early 20th century to predict the
2689 relationship between the size of sediment grains and the velocity required to erode (remove from the
2690 deposited state), transport (move, either in suspension or as bed load), and deposit (below the settling
2691 velocity) mineral grains in rivers (Ward, 2021). The Hjulström curve is a useful proxy for understanding
2692 expected sediment transport in any given system that is affected by constant directional current (e.g.,
2693 ocean current circulation) or periodical changes in flow velocity (e.g., low and high tide flow).
2694 Generally, as grain size decreases, less energy is required to mobilize grains; however, in clay and silt-
2695 rich, cohesive soils, a larger flow speed is required to erode material due to grain-to-grain cohesion. As
2696 sediments are mobilised, they tend to self-organise into ridges, bands and furrows of different
2697 dimensions ranging from the i) small- cm-scale ripple marks through ii) sand dunes and sand waves
2698 that can reach several meters in height to iii) sand banks which can cover vast areas of seabed and be
2699 up to 10s of meters high. It is noteworthy that such bedforms are expressions within a relatively narrow
2700 spectrum of flow velocity and are dependent of the grain-size availability (Figure 6.1b; Boguchwal and
2701 Southard, 1989).



2702

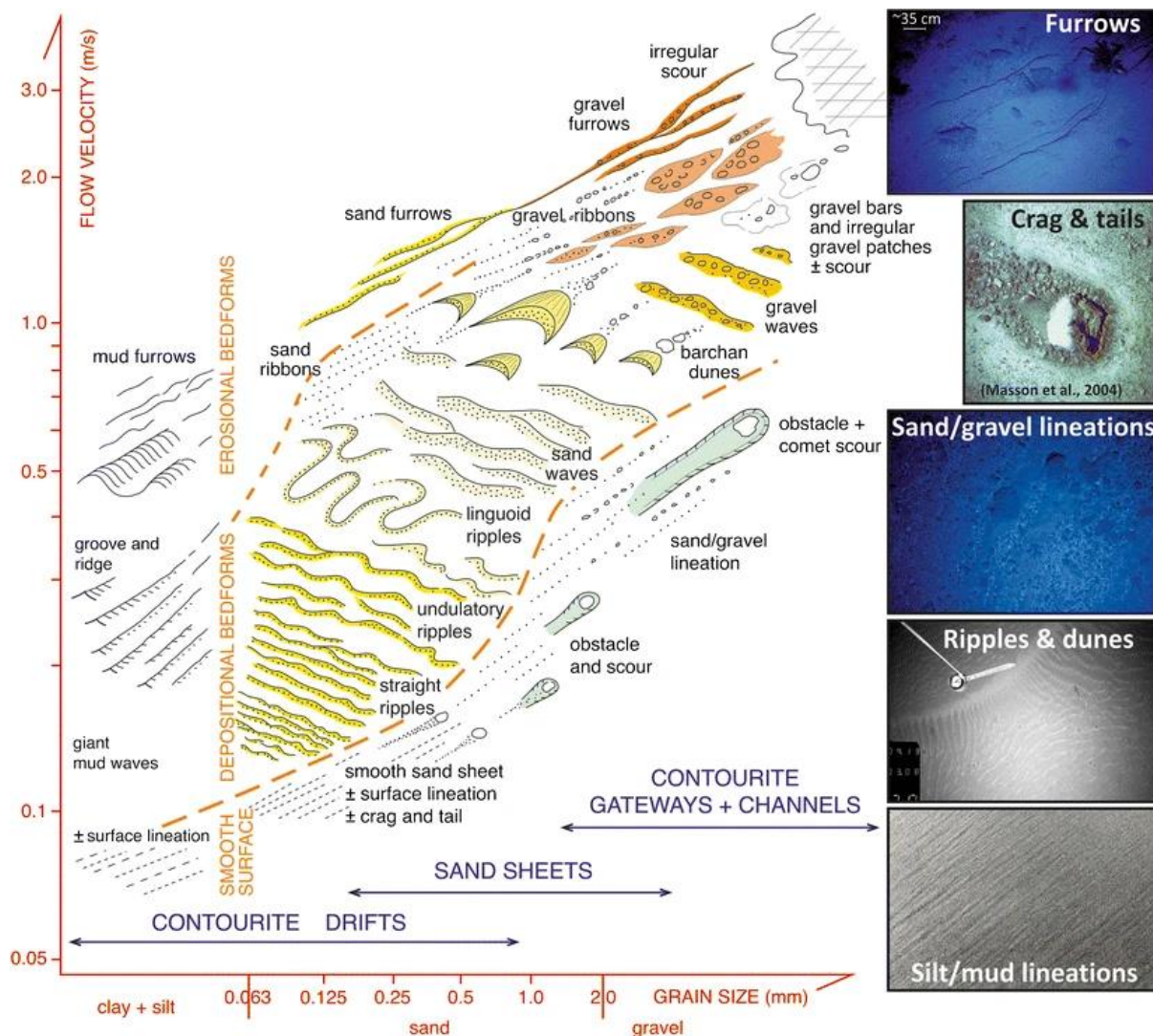
2703 **Figure 6.1. a)** Hjulström-Sundborg diagram with Wentworth-Krumbein grade scale, showing sediment
 2704 movement in flowing water as function of particle size and vertical-mean current (modified from Ward,
 2705 2021). **b)** Bedform phase diagram of North American researchers (modified from Boguchwal and
 2706 Southard, 1989). Note that the biggest variety of bedforms forms within sand grain-size range but that
 2707 does not exclude the possibility of sediment being mobile across a wider grain-size spectrum.

2708 The Northwest European continental shelf is a dynamic and complex marine system where the interplay
 2709 of waves, tides, and currents is having a substantial impact on the present-day seafloor landscape. With
 2710 a large quantity of loose, glacially supplied clastic material on the seafloor and further input of material

2711 from fluvial systems around the basin, conditions were and are optimal for the formation of a variety of
2712 mobile bedforms. The resulting seabed morphology can indicate both the processes active at present
2713 day, but also a record of relict seafloor processes during the marine transgression in the Late Pleistocene
2714 and Holocene. Key geological formations associated with mobile bedforms include the Naaldwijk
2715 Formation (offshore the Netherlands); the Bligh Bank Formation (offshore the UKS North Sea), and
2716 the Surface Sands Formation (offshore UKS Irish Sea), but there are many other and these are often
2717 locally subdivided or too small to be named.

2718 **Types of Bedforms**

2719 Features generated by sediment mobility vary greatly and these organised sediment accumulations are
2720 known collectively as bedforms (Figures 6.1b and 6.2). These bedforms vary in size, shape, formation
2721 processes and composition reflecting complex interactions between hydrodynamic conditions and
2722 seabed or coast topography. Any changes within the hydrodynamic conditions are likely going to be
2723 reflected as changes within seabed topography, including the effect of changes to flow and circulation
2724 introduced by offshore engineering projects. Figure 6.2 indicates a bedform velocity matrix, outlined
2725 by Stow et al. (2009), linking grain size and fluid velocity. It should be noted that Figure 6.2 was
2726 constructed with deepwater circulation in mind (i.e. beyond the shelf edge) and is only partially
2727 applicable to shallow continental margins.



2728
 2729 **Figure 6.2** Bedform velocity matrix. From Hernandez-Molina et al. (2011) and modified from Stow et
 2730 al. (2009).

2731 On the continental shelves, mobile bedforms can be classified based on their orientation with respect to
 2732 current direction, dimensions, and morphology as well as governing formation process (erosion,
 2733 transport or accumulation). There are a number of bedform classification schemes, which attempt to
 2734 categorize bedforms based on their wavelength and amplitude (e.g., Ashley, 1990). The truth is not so
 2735 readily defined, and in complex marine environments, the local metocean regime of any given site can
 2736 lead to a range of bedforms produced. An overview of some broad bedform types is included below.

2737 *Flow Transverse Bedforms*

2738 The crests of flow-transverse bedforms are perpendicular or quasi-perpendicular to the prevailing
 2739 current direction. These types of bedforms can readily be subdivided by their amplitude (height) and
 2740 wavelength (crest to crest distance).

2741 Ripples are the smallest mobile bedforms with amplitudes of several centimetres and wavelengths not
2742 exceeding tens of centimetres. Ripples can be symmetrical when formed by oscillatory flows (wave
2743 action) or asymmetrical when directional current component is involved (Amos et al., 2017). They can
2744 migrate downstream or alongshore and are often observed superimposed on larger bedforms, such as
2745 sandwaves. The presence of ripples has no direct bearing and poses no threat to seabed or coastal
2746 infrastructure.

2747 Megaripples are similar in shape to ripples but are significantly larger (tens of centimetres in height)
2748 and formed with longer wavelengths, with a crest-to-crest distance typically in the order of meters to
2749 tens of meters (Passchier and Kleinhans, 2005). Megaripples can also be symmetrical or asymmetrical.
2750 Their presence and migration across the site are unlikely to have a significant effect on seabed
2751 infrastructure.

2752 Sediment waves (or sand waves, where material is confirmed) are morphologically similar to
2753 megaripples but have a much larger heights (metres to some >10m), and longer wavelength (crest-to-
2754 crest spacing) between them, in the order of tens to hundreds of metres (Bellec et al., 2019; Creane et
2755 al., 2022; Németh et al., 2002; van Dijk et al., 2021). They are large-scale rhythmic transverse bedforms
2756 composed chiefly of sand, although gravel waves may also form in very high current areas. Their
2757 formation is typically related to a predominant directional flow, but wave action (oscillatory flows) can
2758 also affect their morphology. The heights of sand waves can grow up to 30% of the average water depth
2759 and may migrate with speeds of up to several metres per year (Adnyani et al., 2024). Distinction
2760 between megaripples and sand waves is often arbitrary and based on site specific size
2761 (height/wavelength) criterium rather than a difference in physical process of their formation. Sand
2762 waves have been extensively studied in the North Sea, as they are a navigational hazard and can be
2763 considered a constraint and geohazard for offshore infrastructure due to their migration across the shelf
2764 in shallow seas (Schmitt et al., 2007). While they are often formed in groups or sets, single, isolated,
2765 large scale sediment waves are also known to occur.

2766 *Flow-Parallel Bedforms*

2767 Flow-parallel bedforms such as sediment streaks, linear sediment banks, sediment ribbons, banner/
2768 headland banks are elongated parallel to the prevailing current direction, especially in tidally influenced
2769 waters and close to river mouth (Dyer and Huntley, 1999). Flow-parallel bedforms are often indicative
2770 of high current velocities associated with large tidal ranges; in macro- and mega-scale tidal
2771 environments, such banks can be re-shaped and migrate laterally during diurnal tidal cycles (Li et al.,
2772 2014). In extreme cases, when the current energy is high, the bedforms can be separated by erosional
2773 furrows. The banks are often quasi-stable and commonly have an anticlockwise migration of smaller
2774 bedforms on their flanks. In many cases, modern sand banks are anchored on older banks or glacial
2775 features.

2776 These large banks can pose a substantial constraint to development as a result of the strong tidal currents
2777 that form and maintain them and shallow waters along bank crests. Site characterisation of these areas
2778 can be challenging with vessel crabbing and potential collision issues while towing equipment near to
2779 seabed. Additionally, varying water depths due to the presence of mobile bedforms can also cause
2780 difficulties with seismic data acquisition due to source energy scattering, as well as problems with
2781 streamer positioning. Therefore, the site investigation must be carefully planned in these areas to capture
2782 site conditions appropriately. Similarly, design and installation of infrastructure will be constrained by
2783 current velocities and water depths, so developers in these areas need to work effectively across
2784 technical disciplines to ensure all infrastructure can be designed and installed appropriately for the site
2785 conditions.

2786 Sand banks, particularly where they occur within 20 m water depth, are often considered by Annex 1
2787 habitat under the JNCC Designated Special Areas of Conservation due to the range of invertebrate
2788 species they support, including Sabellaria spinulosa (Ross worm). They are therefore important to
2789 characterise correctly to ensure that the impact of offshore projects on these habitats is minimised during
2790 and following construction.

2791 *Non-Directional and Sorted Bedforms*

2792 Currents and waves can move sediment without organizing it into well-defined bedforms. Sand patches,
2793 sheets or drifts are frequently described from bathymetric data (Fenster, 2018; Dyer and Huntley, 1999).
2794 Their formation and mechanisms of mobility are poorly constrained, yet they can be significant in extent
2795 and thickness. The largest accumulations of unconsolidated sediments that are mobilised by currents
2796 and waves are often described as sand banks, which differs from the flow-parallel sand-bank definition.
2797 Although these non-directional sand banks are generally large, their migration rates are low, which
2798 allows for siting that limits the potential effect of sand bank migration on offshore infrastructure.

2799 Sand sheets and banks in this form are often associated with the nearshore area and thought to be a
2800 result of seasonal removal of beach material during winter storms (Fenster, 2018). These features
2801 require consideration for engineering such as horizontal directional drilling, as they may cover exit pits
2802 if their movement has not been accounted for.

2803 Discrete accumulations of isolated, often rippled or patchy coarser sediments on otherwise fine-grained
2804 substrate are referred to as sorted bedforms (Coco et al., 2007a; 2007b; Murray and Thielert, 2004).
2805 Such bedforms are typically re-generated as a consequence of interaction of waves and currents with
2806 poorly sorted bed material. These features are characterised by slight depressions (often <1m)
2807 composed of sequences of coarse-to-very coarse sand, gravel and/or shell debris, that is arranged into
2808 large wave-generated ripples, with wavelengths in the order of a metre (Murray and Thielert, 2004).

2809 Two scales of sorted bedforms are noted – Very large runnels 100s-1000s m wide and many kilometres
2810 in length (known as runnels) and smaller 10s-500s m more regular or circular depressions known as
2811 rippled scoured depression with relief <1.5m ((Dix et al., 2023.; Riera et al., 2023). Although individual
2812 features are relatively small, they can cover large areas with many 10s or 100s of such features close
2813 by.

2814 *Bedforms in Equilibrium*

2815 Bedforms are mobile and dynamically change morphology in response to hydrodynamic conditions
2816 until they achieve a hydraulically stable state when changes become more subtle. Such bedforms are
2817 considered in equilibrium and may not migrate or be modified by waves and or currents despite their
2818 appearance. Bedform equilibrium state is transient and specific to hydrodynamic conditions at a given
2819 time. Any changes to current direction or velocity, sediment supply, or topography and water depth,
2820 may disturb that equilibrium upon which sediments will re-organise to achieve a different hydraulically
2821 stable morphology. An example of such a disturbance is the formation of scour around a seafloor object
2822 or feature, which does not scour infinitely but becomes stable based on the size of the object after a
2823 period or duration of tidal cycling.

2824 Similarly, understanding the effects of sea level change is an important factor for assessing how climate
2825 change may impact the mobility of a site throughout the life of offshore assets.

2826 *Sediment availability, erosion and by-pass*

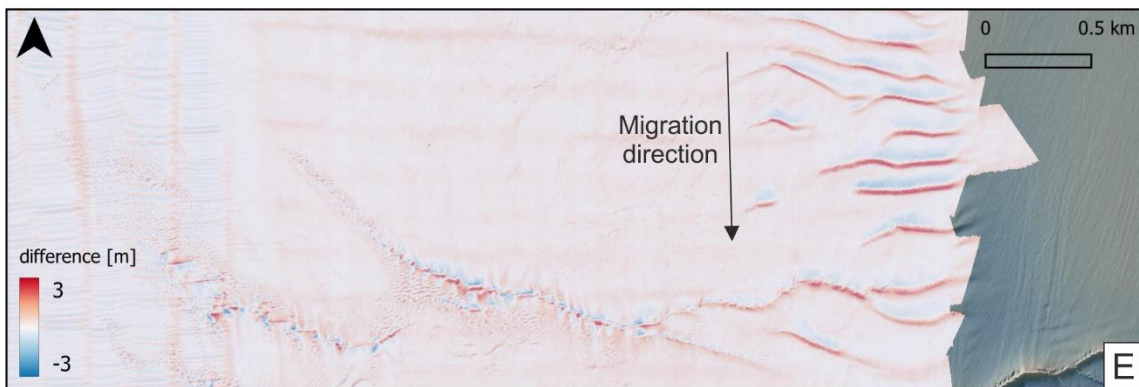
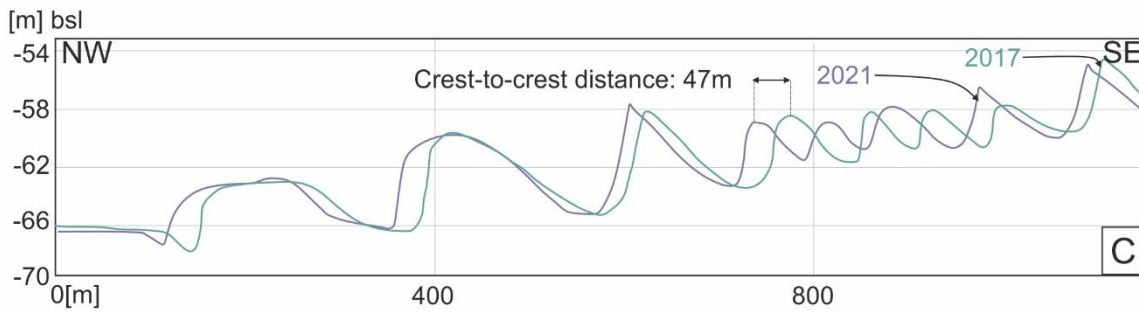
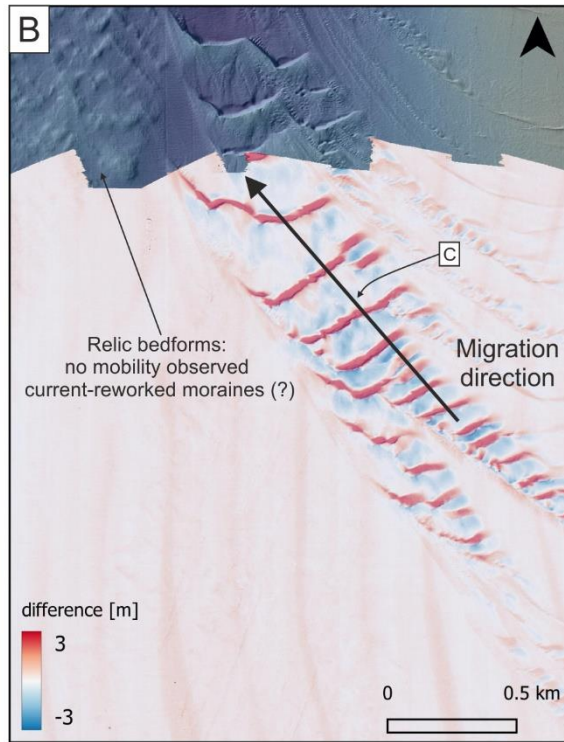
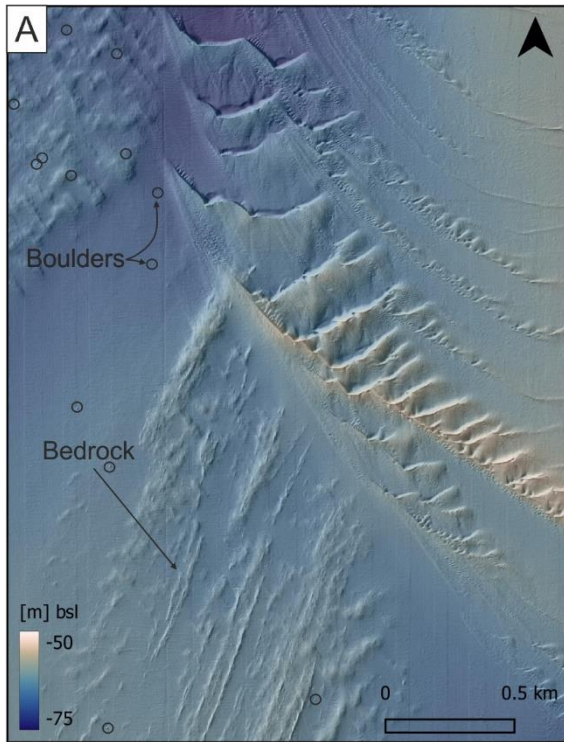
2827 Sediment mobility is prevailing where granular material is available, typically in nearshore areas where
2828 sediment supply by rivers is continuous, and areas where the substrate contains sufficient granular
2829 material, such as glaciated areas. In areas where sediment supply is scarce, mobile bedforms may be
2830 absent, despite sufficient current or wave energy, or may exist as ‘starved’ bedforms that bypass the
2831 seabed with minimal interaction and exchange of material with substrate. It is worth noting that the
2832 availability and distribution of granular material is broader on glaciated continental shelves that
2833 underwent dynamic changes in sediment supply and sea level. In consequence, (1) mobile bedforms
2834 may form further offshore and away from modern-day sediment input sources, (2) relict mobile
2835 bedforms active in the past due to different palaeoceanographic conditions not mobile at present, may
2836 be preserved at seabed, (3) the presence of steep glacial topography and reworking of glacial landforms
2837 at the seabed (moraines, lineations and iceberg ploughmarks) can result in complex seabed morphology
2838 and, consequently, challenges in identifying and quantifying sediment mobility.

2839 **Characterising and Monitoring Bedforms and Seabed Mobility**

2840 Several methods and approaches can be utilised to understand and quantify sediment mobility across
2841 an area of interest. These methods have been detailed in the [Table 6.1](#) below:

2842 **Table 6.1.** Methods used for sediment mobility assessment.

| Approach or method | Data and information obtained | Application to sediment mobility analysis |
|--|--|--|
| Met-ocean data acquisition – site specific | Wave, wind and current data Seabed shear stress Suspended sediment concentration | <ul style="list-style-type: none"> • To identify sediment mobility threshold based on oceanographic conditions and seabed sediment information • To provide input for hydrodynamic modelling of sediment mobility (for example computational fluid dynamics) |
| Bathymetric surveys (MBES) including repeated bathymetric surveys | Bathymetry and geomorphology of the seabed Multi-beam bathymetric surveys conducted at appropriate time intervals allow to trace the changes in seabed morphology | <ul style="list-style-type: none"> • To identify and map mobile bedforms • To map other geomorphic features (glacial landforms, submerged coastlines etc.) • To distinguish between relict and active bedforms • To model seabed changes and compute difference over time, evaluate bedform migration speed and direction, • To identify areas of sediment erosion and accumulation |
| Seabed lithology mapping | Sidescan sonar or acoustic backscatter data combined with sediment sampling (grab samples or box coring) | <ul style="list-style-type: none"> • To distinguish between mobile bedforms active at present and relict ones. • To identify and map the distribution of sediment types and grain size across the AoI. • To delineate areas of sediments likely to be remobilised. • To identify changes in acoustic response and texture of the seabed due to sediment mobility (repeated surveys required) |
| Sub-bottom profiler/ single channel seismic surveys | Imaging of the shallow subsurface in extremely high vertical resolution (2D) | <ul style="list-style-type: none"> • To identify the internal structure of mobile bedforms and confirm their formation process • To delineate a ‘base level’ defined as the base of a mobile sediment unit beyond which the seabed is unlikely to be lowered/eroded. |
| LiDAR surveys | High resolution topography in coastal areas. | <ul style="list-style-type: none"> • To identify areas of material loss and movement due to erosion, deposition and transport in the coastal environment. |



2844 **Figure 6.3** Mobile bedforms offshore on the seabed near Wick (NE Scotland). **a)** Bedforms at the
 2845 seabed as imaged in 2017. **b)** Difference map showing the migration of bedforms between 2017 and
 2846 2021. Note that bedforms in the northwestern corner of the map did not move and are likely relic glacial
 2847 features (moraines or crevasse-squeeze ridges). **c)** Bathymetric profile showing the morphological
 2848 change along the profile in [Figure 6.3b](#). Note the difference between smaller and bigger bedforms. **d+e)**
 2849 Morphological expression of linear dunes in 2017 and the difference map showing the bedform
 2850 migration between 2017 and 2021. Note that the migration direction is now to the South despite “site
 2851 d” being ~ 4 km away from site “site a”. All bedforms are in water depths exceeding 50 m and there is
 2852 no active terrestrial sediment supply. The bedforms are likely composed of current-reworked glacial
 2853 material and migrate on top of a glacial substratum as evidenced by the presence of boulders at the
 2854 seabed.

2855 **Implications and Considerations for Engineering**

2856 Sediment mobility has several engineering implications, depending on sediment erosion or sediment
 2857 accumulation. It is therefore important to understand sediment mobility and bedform migration rates
 2858 effectively to ensure continued integrity of the asset through their design life ([Table 6.2](#)).

2859 **Table 6.2.** Types of sediment mobility and implications for offshore assets.

| Type of sediment mobility | Description | Engineering implication |
|---|--|--|
| Scouring around a foundation/ anchor | Removal of material around foundations due to localised flow acceleration and development of turbulent eddies | <ul style="list-style-type: none"> Uncovering of buried parts of piles can affect their lateral stiffness, load bearing capacity and resonance frequency. In worst case scenario this can lead to inclination and failure of the structure Removal of material around the anchor or chai may reduce overall mooring holding strength. In extreme cases this may lead to mooring failure. |
| Accumulation of sediment around a foundation | Buildup of sediment around a structure | <ul style="list-style-type: none"> Considerations for the operation and maintenance stages of design life, restricting access to the structure by vessels and jack-ups Changes of resonance frequency and lateral stiffness |
| Burial of linear assets (cables and pipelines) | Migration of mobile bedforms across a section of a cable/pipeline or accumulation of a continuous sand bank/sand sheet | <ul style="list-style-type: none"> Negative effect on high-voltage direct current (HVDC) and high voltage alternating current cables (HVAC) as thicker sediments reduce dissipation of heat generated during transmission. This can result in reduced power transmission capacity or, in extreme cases, cable ‘cooking’ and breakage. Burial can exert excessive loading of an asset which can cause structural damage. Over-burial may prevent an asset from moving as it should under thermal expansion and contraction during operation, which could cause fatigue and stress points elsewhere in the structure. |
| Uncovering of linear assets (cables and pipelines) | Winnowing of sand sheets, migration of sand waves and sand banks away from | <ul style="list-style-type: none"> Uncovering buried linear assets leading to free spanning, where pipelines or cables can ‘hang’ in water column. Uncovered cables and pipelines are more susceptible to anchor striking and snagging by, for example fishing vessels. |

| | | |
|--|--|---|
| | the asset. Scouring around a linear asset | <ul style="list-style-type: none"> • Alternating burial and free spanning (for example by migrating sand waves) may cause sections of cables and pipelines to become over stiffened which in turn may lead to breakage as the asset thermally expands and contracts. |
| Nearshore and coastal sediment mobility | Accumulation or removal of coastal material and migration of coastline-attached sand banks | <ul style="list-style-type: none"> • Short migration timescales need to be accounted for while designing HDD solution or trenching as the seabed level may change by several meters on seasonal/annual basis due to migration. • Erosion of coast can put structural integrity of asset landfall at risk. Transition joint Bays (TJBs) need to be located sufficiently inland to mitigate the eventual erosion. |

2860

2861 There are also several additional aspects related to sediment mobility that are important to mention: (1)
2862 During decommissioning, substantial increase in material may be a significant consideration; it is
2863 commonly required to remove all trace of a turbine foundation to prevent future hazards to shipping
2864 once turbines are removed. (2) Landfalls for cables and pipelines are some of the most challenging areas
2865 of any offshore development and most sensitive to the effects of future climate change. A robust
2866 understanding of sediment mobility under different climate scenarios is needed to ensure suitability of
2867 the landfall throughout the design life of the offshore assets. (3) An important secondary consideration
2868 is the burial and emergence of potential unexploded ordnance on the seafloor where sediments are
2869 mobile. In such settings, magnetometric surveys provide only a snapshot of a site, and items may be
2870 buried or move depending on seafloor mobility levels. This means that data acquired has a “shelf life”
2871 which must be aligned with project development timelines and on-site activities to ensure maximum
2872 efficiency in data acquisition, analysis, and safe removal where required.

2873 **6.2 Slope instabilities**

2874 During the repetitive Quaternary EIS glaciations an up to 4500 m thick sedimentary package,
2875 comprising trough mouth fans (TMFs) and prograding wedges, was deposited along the Western
2876 European continental margin, from Ireland to Svalbard (Figure 6.4; Hjelstuen and Sejrup, 2021).
2877 Various types of mass movements, from large submarine landslides remobilizing sediment volumes in
2878 the order of 10^6 km^3 , to turbidity currents resulting in deposition of cm-to-meter-scale thick turbidite
2879 layers, were important sedimentary processes during the Western European margin development (e.g.,
2880 Nygård et al., 2005).

2881 **6.2.1 Submarine landslides**

2882 Around 20 larger-sized Quaternary submarine landslides have been mapped along the Western
2883 European margin (Table 6.3; Figure 6.4) (e.g., Berg et al., 2005; Evans et al., 2005). These landslides
2884 have, commonly, been identified by using 2D and 3D seismic data (Figure 6.5a) or bathymetric surveys.
2885 Indicators of mass movement events include vertical slide scars, acoustically chaotic seismic facies and
2886 the deep erosion of sediment layers stratigraphically beneath the interpreted landslide debrites (e.g.,
2887 Bryn et al., 2005a; Barrett et al., 2021).

2888 Along the Western European continental margin, the largest submarine landslides are located in the
2889 TMF systems (Figure 6.4). Furthermore, it seems that submarine landslides along this margin segment
2890 tend to occur recurrently at the same locations (Nygård et al., 2005). It has been estimated that the
2891 largest landslides remobilized a sediment volume of $25 \times 10^3 \text{ km}^3$ and affected an area of up to $120 \times$
2892 10^3 km^2 (Hjelstuen et al., 2007). However, more commonly, such failure events involved sediment
2893 volumes of $2\text{-}5 \times 10^3 \text{ km}^3$, where the sediment remobilization areas are around $10\text{-}15 \times 10^3 \text{ km}^2$ in size.

2894 The slope failures along the Western European continental margin seem to be restricted to the
2895 Quaternary time period (Figure 6.6). This restriction might partly be related to enhanced sedimentation
2896 rates associated with the Pleistocene glaciations (Bellwald et al., 2019b). Even though the chronological
2897 constraints in the region still are rather poor, it seems that most of the landslides occurred in the Middle
2898 and Late Pleistocene, i.e. over the last 0.78 million years (Figure 6.6; Solheim et al., 2005a; Nygård et
2899 al., 2005; Hjelstuen et al., 2007). Preconditioning factors and trigger mechanisms have been thoroughly
2900 studied within the region (e.g., Kvalstad et al., 2005a), and it is commonly accepted that high
2901 sedimentation rates, weak layers, abrupt lithological changes, and excess pore pressure are needed
2902 precondition factors for the slides to fail and that earthquakes resulting from isostatic uplift are the main
2903 trigger mechanism (e.g., Leynaud et al., 2009; Bellwald et al., 2019b; Llopart et al., 2019; Gatter et al.,
2904 2020).

2905 6.2.2 Turbidity currents

2906 Turbidity currents are commonly initiated in association with the larger-sized submarine landslides, as
2907 for instance the 8200 ka BP Storegga Slide event (e.g., Haflidason et al., 2005). Such mass movements
2908 are frequently occurring in fjord systems along the Western European continental margin, and it is also
2909 in such depositional environments that data, such as high-resolution seismic profiles and sediment
2910 cores, exist that allow for detailed studies of this mass movement process (Bøe et al., 2004; Bellwald et
2911 al., 2019a).

2912 In Norwegian fjord systems, turbidity currents have resulted in up to nearly 15 m thick turbidite layers
2913 (e.g., Bellwald et al., 2019a), which commonly are identified as acoustic transparent units in high
2914 resolution seismic data (Figure 6.5b). These turbidite layers have an erosive base and can be divided
2915 into two sub-units (Bellwald et al., 2016). Commonly, the lower sub-unit is fining upward, from fine
2916 sand to clay, having a shear strength of 10-55 kPa, whereas the upper sub-unit, representing the tail of
2917 the turbidity current, consists of homogeneous clay with a shear strength of 7-10 kPa. The potential
2918 trigger mechanisms considered for turbidity currents include climatic changes, variations in
2919 sedimentation rates, ocean and tsunami currents (such as the Storegga Slide tsunami), and earthquakes.

2920 6.2.3 Glacigenic debris flows

2921 Glacigenic Debris Flows (GDFs) (Figure 6.5c) are important building blocks of the TMF systems along
2922 the Western European continental margin (Laberg and Vorren, 1996; Dimakis et al., 2000; Nygård et

2923 al., 2002; Elverhøi et al., 2010; Beaten et al., 2014) and are also considered to represent an important
2924 precondition factor for landslide failures. In seismic data, GDFs are identified as hundreds of kilometres
2925 long lobate-shaped features, that are lensoid in cross section, 2–40 km wide and 15–60 m thick (Nygård
2926 et al., 2005; Garcia et al., 2024) (Figure 6.5c). The GDFs are only deposited when ice streams that
2927 occupied cross-shelf troughs during maximum glaciations transported huge amounts of sediments to
2928 the shelf edges (King et al., 1996). Shallow cores, penetrating into such flows, show that they are
2929 characterised by a complete lack of structure and that they are fine grained (1% gravel, 29% sand, 36%
2930 silt, and 34% clay) (King et al., 1998). GDFs are commonly stacked on top of each other, defining thick
2931 sedimentary units. During one shelf edge glaciation GDF units as thick as 400 m can be deposited, as
2932 evidenced from the North Sea TMF (Nygård et al., 2005). As the GDF units may be rapidly deposited
2933 stratigraphically above fine-grained thin deglacial and/or interglacial sediment layers (so-called “weak”
2934 layers) the TMFs complexes are prone to fail if a trigger mechanism such as e.g., an earthquake
2935 (Bellwald et al., 2019b), occurs.

2936 6.2.4 Slope instability as a modern geohazard: Spatio-temporal patterns

2937 Submarine landslides remobilized large sediment volumes along the Western European continental
2938 margin (e.g., Hjelstuen et al., 2007), and are commonly associated to major Mid- and Late Pleistocene
2939 glaciations (e.g., Nygård et al., 2005; Figure 6.6). However, studies along the Møre and Northern North
2940 Sea margins have concluded that another shelf-edge glaciation (with stratified sedimentation
2941 introducing weak layers exposed to earthquakes resulting from the glacio-isostatic uplift) is needed for
2942 large-scale submarine landslides to be initiated (Bryn et al., 2005a). As there is a lack of direct
2943 observations of megaslides occurring in historic times, the development and hazard potential for future
2944 events is mainly based on the study of the morphology of paleo-slide deposits (e.g., Barrett et al., 2021).
2945 Given thoughtful placement of infrastructure, seafloor stability in the form of a megaslide is not a big
2946 issue over the timeframe of the life of a producing oil and gas field (10-40 years; Shipp, 2017). However,
2947 the relief shaping the top surface of a megaslide still expressed on the seafloor might be a big challenge
2948 for seafloor infrastructure (e.g., pipelines or cable routes).

2949 Ocean and wave currents as well as extratropical cyclones and storm surges may affect seabed stability.
2950 Hence, one should expect that global warming affecting the patterns (likelihood/frequency, intensity)
2951 of the environmental impacts will also influence slope stability. Global warming may further be
2952 followed by increased seismicity around the present-day ice sheets (in particular Greenland), sea-level
2953 rise, hydrate melting, and ice loading alterations, thus triggering slope instability (Berndt et al., 2009;
2954 British Geological Survey, 2009; Huhn et al., 2020). However, Urlaub et al. (2013) show that there is
2955 no strong global correlation of landslide frequency with sea-level changes or increases in local
2956 sedimentation rate. A recent study on the Afen Slide suggests that lithological interfaces, particularly a
2957 sandy contourite layer overlying silty clay, can significantly influence slope instability in contourite

2958 drifts, and climate change may further precondition these failures, emphasising the need for multi-scale
 2959 analysis to understand submarine landslide hazards (Gatter et al, 2020; 2021).

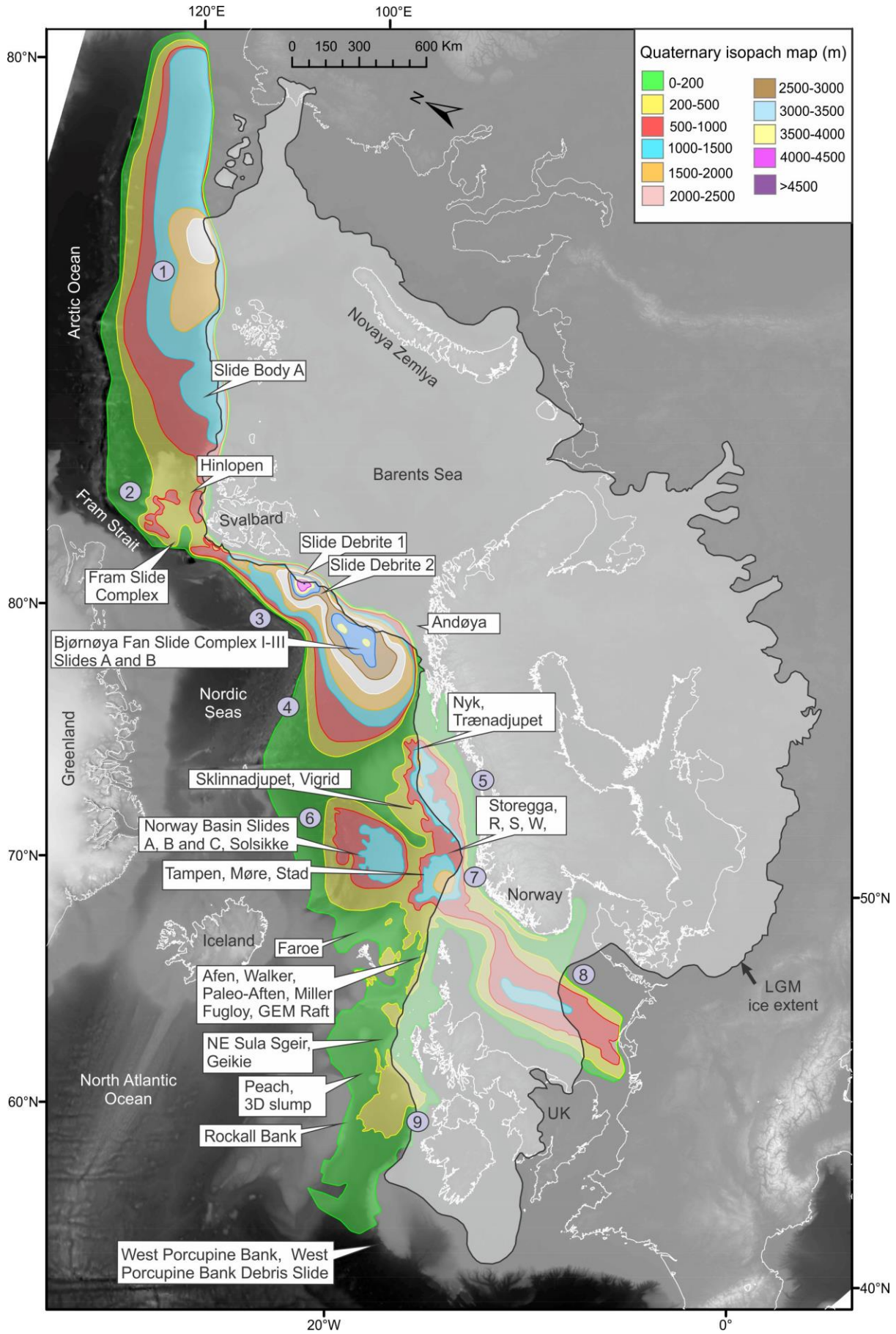
2960 Turbidite layers are commonly identified in deglacial and interglacial sequences in fjord environment,
 2961 and for Norwegian fjord systems it has been indicated that mass movements related to turbidity currents
 2962 may have been in the order of one event every 80 years, even for the Late Holocene (Bellwald et al.,
 2963 2019a). Turbidity currents and smaller sub-marine landslides in fjords should thus be evaluated
 2964 carefully in geohazard assessments (Carlton et al., 2019b), as they are a major threat for submarine
 2965 infrastructure and coastal societies.

2966 **Table 6.3.** Major submarine landslides in the study area, listed from north to south. References to those
 2967 papers that identified the submarine landslides first.

| Slide | Age | Area | Reference |
|-----------------------------------|-------------|----------------------------|-------------------------------|
| Slide Body A | Ca. 2.7 Ma | Northern Svalbard Margin | Lasabuda et al., 2018 |
| Hinlopen/Yermak | MIS3 | Northern Svalbard Margin | Winkelmann et al., 2007 |
| Fram Slide Complex | 5-0.068 Ma | Western Svalbard Margin | Elger et al., 2017 |
| Slide B | 0.5–0.6 | Western Barents Sea margin | Laberg and Vorren, 1996 |
| Slide A | 0.5–0.6 Ma | Western Barents Sea margin | Laberg and Vorren, 1996 |
| Bear Island Fan Slide Complex III | 0.2–0.5 Ma | Western Barents Sea margin | Hjelstuen et al., 2007 |
| Bear Island Fan Slide Complex II | 0.5–0.78 Ma | Western Barents Sea margin | Hjelstuen et al., 2007 |
| Bear Island Fan Slide Complex I | 0.78–1.0 Ma | Western Barents Sea margin | Hjelstuen et al., 2007 |
| Bjørnøya Slide | 0.2–0.3 Ma | Western Barents Sea margin | Laberg and Vorren, 1993; 1996 |
| Andøya Slide | Holocene | Lofoten-Vesterålen margin | Laberg et al., 2000 |
| Trænadjupet Slide | 4 ka | Mid-Norwegian margin | Laberg et al., 2002 |
| Nyk Slide | 16.3 ka | Mid-Norwegian margin | Lindberg et al., 2004 |
| Vigrid Slide | > 0.2 Ma | Mid-Norwegian margin | Solheim et al., 2005a |
| Sklinnadjupet Slide | 0.3 Ma | Mid-Norwegian margin | Solheim et al., 2005a |
| Slide R | 0.3 Ma | Mid-Norwegian margin | Solheim et al., 2005a |
| Slide W | > 1.7 Ma | Mid-Norwegian margin | Solheim et al., 2005a |
| Storegga Slide | 8.2 ka | Norwegian Sea | Haflidason et al., 2005 |

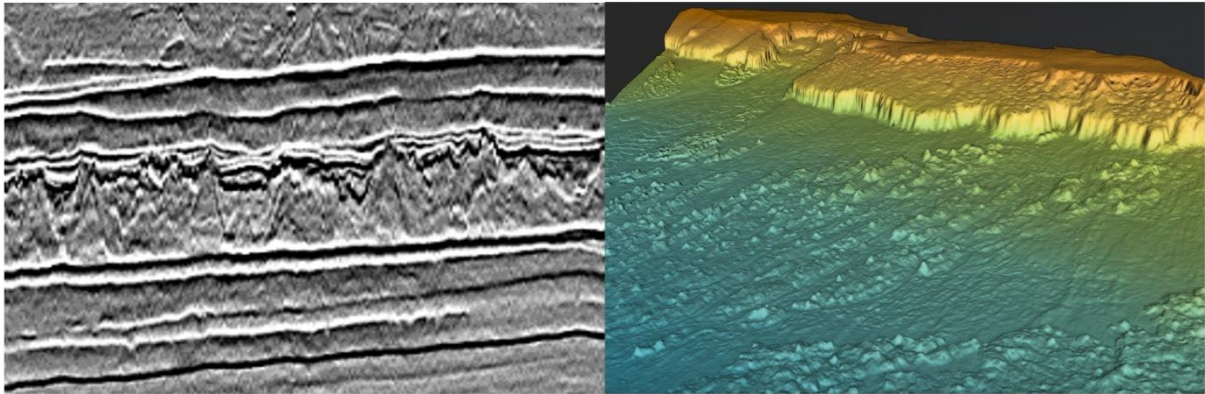
| | | | |
|---|---------------------------|------------------------|--|
| Slide S | 0.5 Ma | Mid-Norwegian margin | Solheim et al., 2005a |
| Tampen Slide | 0.13 Ma | Mid-Norwegian margin | Nygård et al, 2005 |
| Møre Slide | 0.38–0.4 Ma | Mid-Norwegian margin | Nygård et al, 2005 |
| Stad Slide | MIS12 | Mid-Norwegian margin | Hjelstuen and Grinde, 2016 |
| Solsikke Slide | MIS3 | Mid-Norwegian margin | Barrett et al., 2025 |
| Norway Basin Slide A | 2.7-1.7 Ma | Norway Basin | Hjelstuen and Andreassen, 2015 |
| Norway Basin Slide B | 1.7-1.1 Ma | Norway Basin | Hjelstuen and Andreassen, 2015 |
| Norway Basin Slide C | Ca. 0.5 Ma | Norway Basin | Hjelstuen and Andreassen, 2015 |
| Miller Slide | pre-MIS7 | | Long et al., 2011 |
| Faroe | 9.9 ka | Faroe slope | Lee, 2009 (and refs therein) |
| Afen Slide | 58 ka <2.9 ka | Faroe—Shetland Channel | Wilson et al., 2004; Long et al., 2011 |
| Palaeo-Afen Slide | Mid-Pleistocene | Faroe—Shetland Channel | Long et al., 2003 (and refs therein) |
| Walker Slide | ? | Faroe—Shetland Channel | Long et al., 2003 (and refs therein) |
| Fugloy Slide | ? | Faroe—Shetland Channel | Long et al., 2011 |
| GEM Raft | Late Pleistocene-Holocene | Faroe—Shetland Channel | Long et al., 2011 |
| NE Sula Sgeir Slide | Early Weichselian | Hebrides Slope | Baltzer et al., 1998 (and refs therein) |
| Geikie Slide | Early Weichselian | Hebrides Slope | Evans et al., 2005 (and refs therein) |
| 3B Slump, offshore Ireland | ? | Rockall Trough | EMODnet Map Viewer ("X Monteys (GSI) pers. comm (2011)") |
| Peach Slide | 10.5 ka | Rockall Trough | Lee, 2009 (and refs therein) |
| Rockall Bank Slide | 15-16 ka | | Lee, 2009 (and refs therein) |
| West Porcupine Bank | Pliocene-Pleistocene | Porcupine Bank | Unnithan et al., 2001 (and refs therein) |
| West Porcupine Bank Debris Slide | ? | Porcupine Bank | Weaver et al., 2000 (and refs therein) |

2968

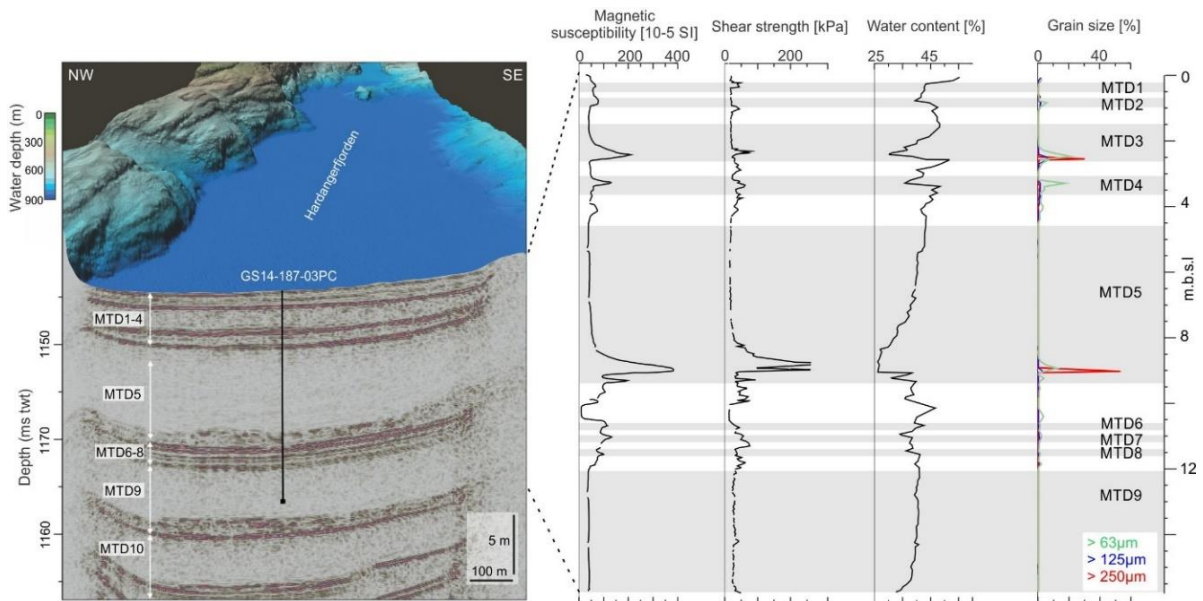


2971
2972

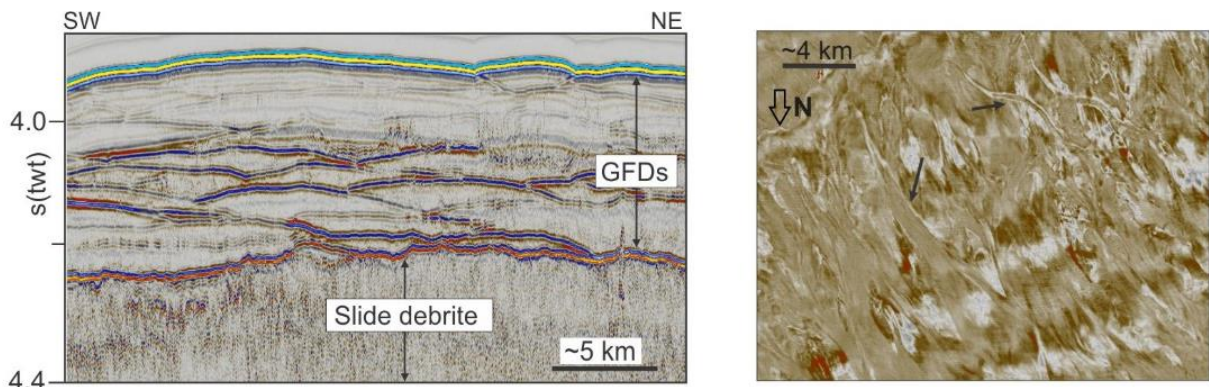
2973 **Figure 6.4.** Location of major landslides along the NE Atlantic margin (based on Lasabuda et al. (2018),
2974 Vanneste et al. (2006), Winkelmann et al. (2008), Elger et al. (2017), Safronova et al. (2015), Laberg
2975 and Vorren (1993; 1996), Knutsen et al. (1993), Hjelstuen et al. (2007), Hjelstuen and Andreassen
2976 (2015), Laberg et al. (2000; 2002), Lindberg et al. (2004), Rise et al. (2006), Nygård et al. (2005),
2977 Haflidason et al. (2005), Solheim et al. (2005a)). The Quaternary thickness map is from Hjelstuen and
2978 Sejrup (2021) and is clearly delineating the main sedimentary depocenters, i.e., trough mouth fans
2979 (TMFs) and prograding wedge systems, that have developed along the margin. (1) Nansen Basin, (2)
2980 Yermak Plateau, (3) Storfjorden TMF, (4) Bjørnøya TMF, (5) Mid-Norwegian Margin, (6) Norway
2981 Basin, (7) North Sea TMF, (8) North Sea, (9) Donegal Fan. LGM: Last Glacial Maximum (based on
2982 Patton et al., 2017).



2983

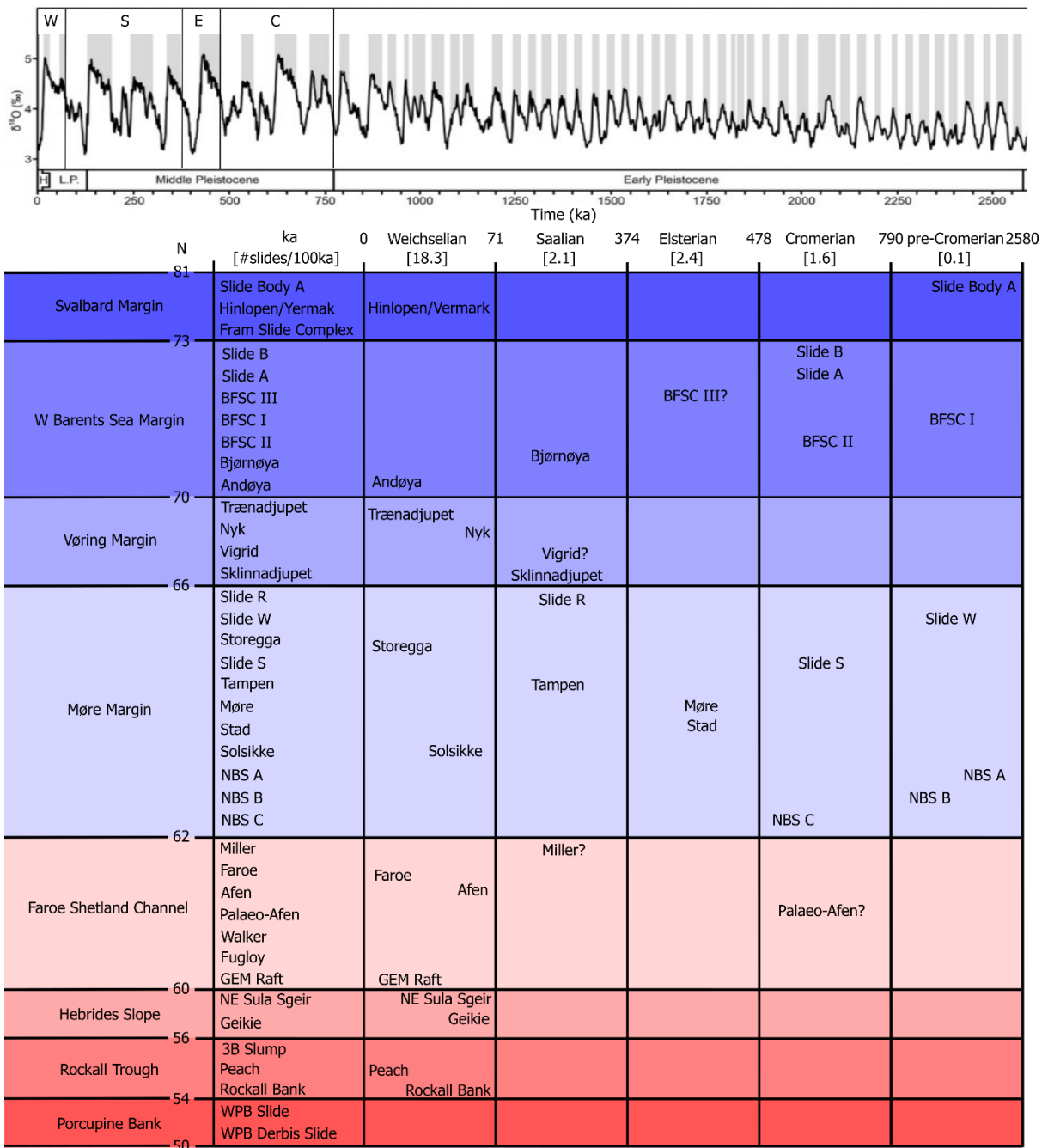


2984



2985
2986

2987 **Figure 6.5.** Expressions of different types of submarine mass movements. **a) Left panel:** Seismic
2988 expression of the buried Tampen Slide. **Right panel:** Top surface of the buried Tampen Slide on the
2989 North Sea Fan (modified after Barrett et al. (2021)). **b) Left panel:** High resolution TOPAS profile from
2990 Hardangerfjorden, western Norway, showing typical acoustic character of mass transport deposits
2991 (MTD 1-9), mostly interpreted as turbidite layers. **Right panel:** Analyze results from a c. 15-m-long
2992 sediment core showing typical lithological and geotechnical character of the identified MTDs. Modified
2993 from Bellwald et al. (2016). **c) Left panel:** 2D Multichannel seismic profile from the distal part of the
2994 North Sea TMF, showing the characteristic lensoid shape of Glacigenic Debris Flows (GDFs). Figure
2995 modified from Hjelstuen and Andreassen (2015). **Right panel:** Time slice, at approximately 300 metres
2996 below the seabed, from a 3D seismic cube located at the uppermost part of the North Sea TMF. Some
2997 of the GDFs observed are indicated by arrows. Figure modified from Hjelstuen and Grinde (2016).



2998

2999 **Figure 6.6.** Spatio-temporal distribution of major submarine landslides along the NE European margin.

3000 See [Table 6.3](#) for details. BFSC: Bear Island Fan Slide Complex, WPG: West Porcupine Bank. Ages of

3001 landslides indicated with ? are weakly constrained; Ages for Fugloy and Fram Slides are excluded due

3002 to lacking (precise) age suggestions. Global oxygen isotope curve after Lisiecki and Raymo (2005). W:

3003 Weichselian (MIS4-2), S: Saalian and Eemian (MIS10-5), E: Elsterian and Holsteinian (MIS12-11), C:

3004 Cromerian (MIS19-11).

3005 6.3 Gravity mass flow dynamics

3006 Understanding the dynamics of gravity mass flows (GMFs) both on land and in the water is a fascinating

3007 scientific problem that has attracted the attention of many researchers over more than a century. At the

3008 same time, it is of eminent practical importance in hazard mitigation. From a risk perspective, one needs

3009 to estimate the occurrence probability of such events (i.e., the probabilities of release – discussed in the
3010 preceding section – and of reaching specific points of interest), their intensity (typically characterized
3011 by the depth, velocity, density and possibly particle hardness and size), and their effect on living beings
3012 and material assets.

3013 Along the passive glaciated margins, two circumstances must be kept in mind: First, GMFs can originate
3014 not only in the sea but also on land, which means that their dynamics must be studied in both
3015 environments, with the transition from air to water posing specific challenges in connection with
3016 tsunamigenesis (see [Section 6.6](#)). Second, the moving particulate mass can range from huge rock
3017 fragments to highly sensitive clay, spanning an extremely wide range of rheological properties that
3018 translate into many different flow regimes. This section cannot cover them all but tries to highlight the
3019 physical phenomena that are most important in practical matters of hazard assessment and mitigation.
3020 One consequence of this variety of GMFs is that substantial events can originate in steep mountainous
3021 terrain (rock avalanches in fjords or flank collapses of volcanoes on islands) or gentle slopes on land
3022 (quick-clay landslides) or in almost flat areas of the continental shelf (submarine debris flows or
3023 landslides).

3024 6.3.1 Rheology

3025 A central step in assessing the dynamics of both submarine and onshore GMFs is to estimate the mass
3026 involved as well as to understand the physical properties of the sliding or flowing mass, the substrate,
3027 and the ambient fluid. These properties are decisive for the flow regime, run-out distance, velocity, and
3028 interaction of GMFs with obstacles.

3029 The ambient fluid plays a subordinate role in many GMFs on land because of the large density
3030 difference between air ($1\text{--}1.3\text{ kg m}^{-3}$) and soil (typically $1500\text{--}2500\text{ kg m}^{-3}$), but the turbulent
3031 entrainment of ambient air is the major resistive force in suspension flows like powder snow avalanches
3032 and pyroclastic suspension flows (nuées ardentes) with typical densities below 50 kg m^{-3} . In the marine
3033 environment, the ambient fluid density is much closer to the density of the mass flow so that ambient-
3034 water entrainment into turbidity currents as well as viscous drag (pressure drag and skin friction) and
3035 added mass are important, especially at high velocities or accelerations. The rheology of the ambient
3036 fluid is simple – it is a Newtonian fluid; however, near a GMF, the Reynolds number is very high, the
3037 fluid is in the turbulent regime and viscous drag typically grows as the square of velocity.

3038 Many numerical models of dense GMFs describe the shear stress, τ (Pa), inside the flow and at the bed-
3039 flow interface with the Coulomb failure criterion,

$$3040 \tau = \sigma_n \tan \phi = \mu \sigma_n. \quad (1)$$

3041 Here, σ_n (Pa) is the normal stress on the shear plane, ϕ is the friction angle (which may be different
3042 inside the flow and at its bottom); $\mu = \tan \phi$ (–) denotes the friction coefficient. In very rapid flows
3043

3044 like rock or snow avalanches, where the shear rates at the bottom of the flow are very high, the bed
 3045 shear stress is sometimes formulated as the Voellmy friction law (Voellmy, 1955),

$$3046 \quad \tau = \mu\sigma_n + k\rho_f u^2, \quad (2)$$

3047 with ρ_f (kg m^{-3}) the flow density, u (m s^{-1}) the mean flow velocity, and k a dimensionless drag
 3048 coefficient (often expressed as g/ξ in the literature, where ξ has the dimensions of the gravitational
 3049 acceleration g). The Coulomb law expresses the experimental observation that the shear strength of a
 3050 granular material is proportional to the overburden under quasi-static deformation. The Voellmy friction
 3051 law, inspired by open-channel hydraulics, accounts for the increase in shear stress at increasing shear
 3052 rates.

3053 A great many laboratory experiments (e.g., Pouliquen, 1999; GdR MiDi, 2004; Forterre and Pouliquen,
 3054 2009) have shown that the $\mu(I)$ rheology (Jop et al., 2006) provides a much better approximation of the
 3055 behaviour of granular matter than the Coulomb or Voellmy friction laws that are used in most models
 3056 in practical use. If the soil consists of dry sand or coarser grains, the shear stress can be expressed as

$$3057 \quad \tau = \mu_{\text{eff}}(I)\sigma_e = \left(\mu_1 + \frac{\mu_2 - \mu_1}{I_0/I + 1} \right) \sigma_e, \quad (3)$$

3058 where the so-called inertial number, I , is the non-dimensionalized shear rate (s^{-1}) and defined as

$$3059 \quad I = \frac{\dot{\gamma}d}{\sqrt{\sigma_n/\rho_f}}, \quad (4)$$

3060 with $\dot{\gamma} = \partial_z u$ the dimensional shear rate and d (m) the mean particle diameter. The effective friction
 3061 coefficient $\mu_{\text{eff}}(I)$ grows from a minimum value μ_1 at $I = 0$ to a maximum value μ_2 as $I \rightarrow \infty$, the
 3062 parameters $\mu_{1,2}$ and I_0 depending mainly on the shape and size distribution of the granular material. At
 3063 very low and high values of I , deviations from this behaviour have been found and parameterized
 3064 (Barker et al., 2017). GdR MiDi (2004) in addition showed that the volumetric concentration ($-$) in
 3065 steady flow also changes with I , according to

$$3066 \quad c(I) = c_0 - \beta I, \quad (5)$$

3067 at least up to moderate values of $I \ll c_0/\beta$.

3068 An important discovery was that the $\mu(I)$ -rheology also describes water-saturated or submerged
 3069 granular materials quite well, where fluid pore pressure is intimately coupled with granular dynamics.
 3070 This requires, however, redefining I in a way that accounts for the modified time scales of intergranular
 3071 processes due to the pore fluid (Cassar et al., 2005; Boyer et al., 2011; Guazzelli and Pouliquen, 2018).
 3072 In steady flows, the excess pore pressure is also controlled by this modified I . Perhaps not surprisingly,
 3073 the modified form of I depends on the fluid viscosity, the particle concentration and the ratio of particle

3074 to fluid density; moreover, it distinguishes between the viscous and inertial regime of particle motion
 3075 in the fluid. Further generalizations consider transition from geotechnical plasticity formulations (soil
 3076 behavior) to granular flow behavior, unifying cohesive and granular suspended fluids (Si et al., 2018;
 3077 Rauter et al., 2021). Most of the submarine landslides along the glaciated margins involve clayey
 3078 material, which shows rather different rheological behaviour from sandy materials. Clays are shear-
 3079 thinning visco-plastic fluids with a yield strength, τ_y (Pa), and are well described by the Herschel–
 3080 Bulkley rheology or flow rule,

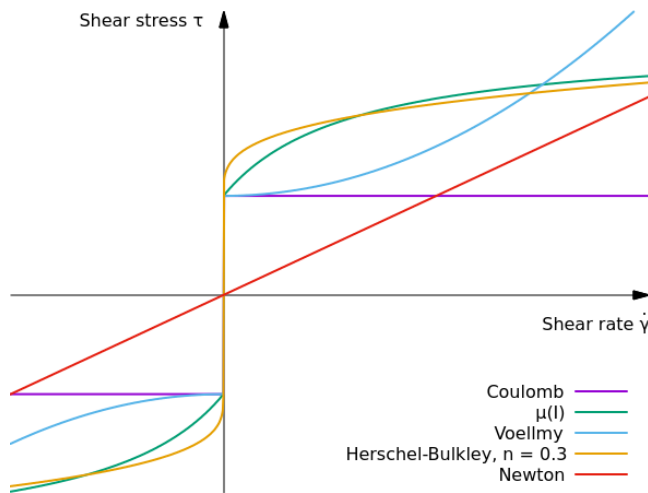
$$3081 \quad \tau = \tau_y + \eta \dot{\gamma}^n, \quad (6)$$

3082 where n (–) is the flow exponent (typically in the range 0.1–0.5 for clays) and η the generalized viscosity
 3083 (units Pa·s ^{n}). τ_y , η and, to some degree, n depend on the water content (or liquidity index) of the
 3084 material. This is of particular significance in the submarine realm, where ambient water can easily be
 3085 mixed into sandy flows but not into clay-rich flows because of their very low permeability.

3086 The amount and the type of clay is especially important for the cohesive (high clay-content) landslide
 3087 dynamics (Ilstad et al. 2004a,b,c; Elverhøi et al. 2005, 2010; Breien et al. 2007, 2010), from a modelling
 3088 perspective approximated by the Herschel–Bulkley rheology (e.g., Huang and Garcia 1998; Elverhøi et
 3089 al. 2005, Kim et al. 2019).

3090 Figure 6.7 compares the flow rules, i.e., the dependence of the shear stress on the shear rate,
 3091 schematically for these rheologies. For the Coulomb yield criterion, the $\mu(I)$ -rheology and the Voellmy
 3092 friction law, the offset of the curves at $\dot{\gamma} = 0$ is proportional to the effective normal stress. Here, it was
 3093 drawn equal to the one of the Herschel–Bulkley fluid to highlight the differences in the flow rules as
 3094 $\dot{\gamma} \rightarrow 0$ and $\dot{\gamma} \rightarrow \infty$.

3095 Yet another highly relevant property of clays is that they can lose a fraction of their original yield
 3096 strength and viscosity as a function of accumulated shear, which destroys the bonds between clay
 3097 platelets and frees the large amount of water that was trapped between them. This remoulding effect is
 3098 quantified by the sensitivity S (–) of the clay, which is the ratio of non-remoulded to fully remoulded
 3099 yield strength. In the case of quick clays, values of S up to 400 have been measured, i.e., the yield
 3100 strength may disappear almost completely. The development of a slide in sensitive clay depends
 3101 critically on how quickly the remoulding takes place. Some dynamical slide models attempt to capture
 3102 this by assuming τ_y and η to be empirical functions of the accumulated shear $\Gamma(t) = \int_0^t \dot{\gamma}(x(t'), t') dt'$,
 3103 e.g., $\tau_y(\Gamma) = \tau_{y,0} - (\tau_{y,0} - \tau_{y,\infty}) \exp(-\lambda\Gamma)$, $\tau_{y,0}$ the non-remoulded and $\tau_{y,\infty}$ the fully remoulded
 3104 yield strength (De Blasio et al., 2003). Toorman (1997) showed that a physical and accurate constitutive
 3105 equation for clayey muds as thixotropic fluids can be derived from structural kinetics theory, which
 3106 describes the competition between the formation (flocculation) and break-up of inter-particle bonds
 3107 under shear. This process-based approach deserves to be explored further.



3108

3109 **Figure 6.7.** Schematic representation of the flow rules mentioned in [Section 6.3.1 Rheology](#)

3110 6.3.2 Flow Regimes

3111 Like GMFs on land, submarine GMFs exhibit a wide variety of flow regimes; they may pass through
 3112 different regimes along their path, and the flow regime may vary spatially at a given instant. In dry
 3113 granular materials without cohesion, the flow regime is determined by the shear rate and the density. It
 3114 is crucial that subaerial GMFs are free-surface flows, i.e., they can adjust their density to the flow
 3115 conditions. At high density and very low shear rates, in the quasi-static regime, persistent contacts
 3116 between grains dominate and the concepts of critical-state soil mechanics can be applied: depending on
 3117 the initial volumetric particle concentration, the soil contracts or dilates until it reaches the critical-state
 3118 density. If one increases the shear rate, the density decreases and the contacts between particles become
 3119 more collisional than frictional. At high shear rates, the concentration diminishes to the point where
 3120 grains interact with each other only through collisions and the flow is fully fluidized. If the shear rate
 3121 is increased further, the mean free path of a particle between collisions exceeds a few particle diameters;
 3122 this is the inertial regime of a granular gas.

3123 In the submarine environment, the incompressibility and large mass of the water above do not allow the
 3124 flow to expand easily. Instead, the particle concentration can decrease only if ambient water penetrates
 3125 the soil. In sandy, non-cohesive flows, the stagnation pressure at the flow front leads to seepage and
 3126 dilution of the head ([Figure 6.8b](#)); this intermediate-density flow regime appears to be similar to the
 3127 fluidized or intermittency regime of dry-snow avalanches ([Sovilla et al., 2015](#)) and may be what is often
 3128 called a high-density turbidity current in the literature ([Shanmugam, 1996](#)). In rapid non-cohesive flows,
 3129 Kelvin–Helmholtz instabilities tend to develop along the upper surface of the flow, leading to intensive
 3130 mixing with ambient water and turbulent suspension of the soil particles. This is a different, much more
 3131 dilute flow regime, in which particle collisions are infrequent; it corresponds to the macro-viscous
 3132 regime in suspensions ([Bagnold, 1954](#)) except for the dominant role of turbulence.

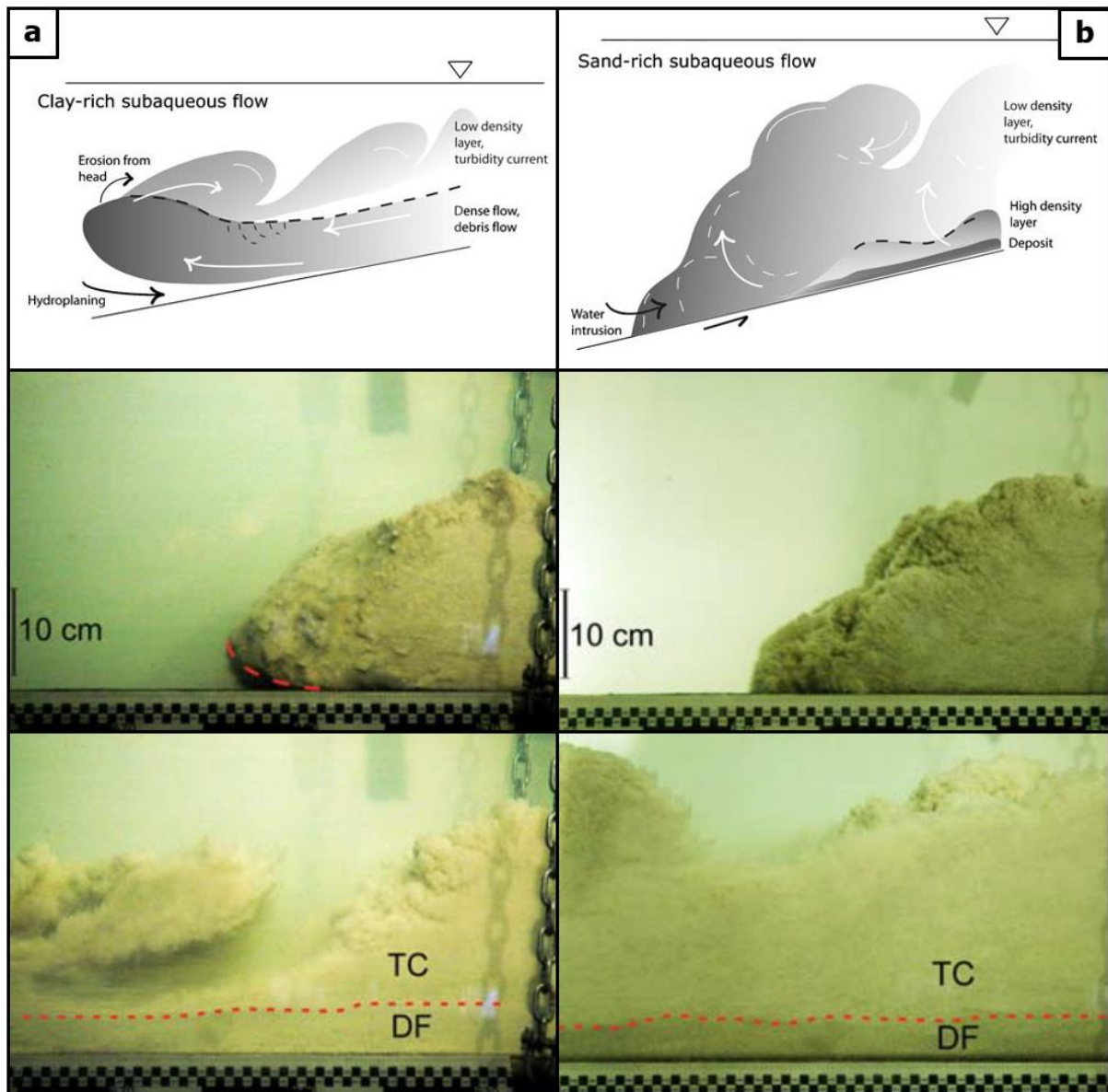
3133 In the late 1990s, laboratory experiments comparing clay-rich and sandy mixtures showed that the flow
3134 behaviour of these mixtures depends critically on the sand–clay ratio besides the water content. These
3135 flows could be described quite well with a visco-plastic rheology of the Bingham or the more general
3136 Herschel–Bulkley type (Imran et al., 2001). Mixtures with relatively high water and/or sand content
3137 had higher velocity and longer run-out in air than in water, as expected. In contrast, clay-rich mixtures
3138 ran out much farther and faster under water than in air. The reason is hydroplaning, i.e., ambient water
3139 penetrating underneath the front of clay-rich flows is trapped and lubricates the flow when the velocity
3140 becomes sufficiently high (Figures 6.8a and 6.9). The onset of hydroplaning is controlled by the
3141 densimetric Froude number $Fr = u_f / \sqrt{g' h_f}$, with u_f and h_f the front velocity and depth of the flow
3142 and $g' = (1 - \rho_w / \rho_f)g$ the gravitational acceleration (m s^{-2}) reduced for buoyancy. The critical value
3143 of Fr is of the order of 0.4 (Harbitz et al., 2003). This result is confirmed by numerical simulations
3144 (Gauer, 2006).

3145 As it is almost impossible to observe submarine debris flows when they occur, there is only
3146 circumstantial evidence for this phenomenon occurring in Nature. One indication could be the absence
3147 of bed erosion because the thin water layer underneath the flow reduces the bed shear stress dramatically
3148 (Mohrig et al., 1999), as illustrated in Figure 6.8a and demonstrated in the laboratory (Figure 6.9).
3149 However, hydroplaning occurs typically only in the head of the flow and the flow body may erode the
3150 bed. Outrunner blocks that travelled much farther than the main body—observed in many medium-size
3151 to very large events—can be explained by frontal hydroplaning leading to block detachment and
3152 enhanced run-out (Ilstad et al., 2004c). A particularly intriguing example is the relatively small 1996
3153 Finneidfjord landslide in northern Norway, where the distal-most outrunner block is of substantial size
3154 and was stopped by a mound more than 1 km beyond the deposits of the main body. Along its path,
3155 there are no signs of erosion on the fjord bottom except for a very shallow depression.

3156 In suspension flows, turbulent eddies can maintain particles in suspension, with the concentration
3157 gradient in the quasi-steady state directly coupled to the difference between mean eddy velocity and
3158 mean particle settling velocity. Along the upper surface of the suspension layer, entrained ambient fluid
3159 is imparted not only momentum from the flow body but also turbulent kinetic energy (TKE); moreover,
3160 lifting particles against gravity throughout the flow also dissipates TKE (Figure 6.11). This implies that
3161 the balance between creation and dissipation of TKE is of prime importance for the evolution of the
3162 flow (Parker et al., 1986).

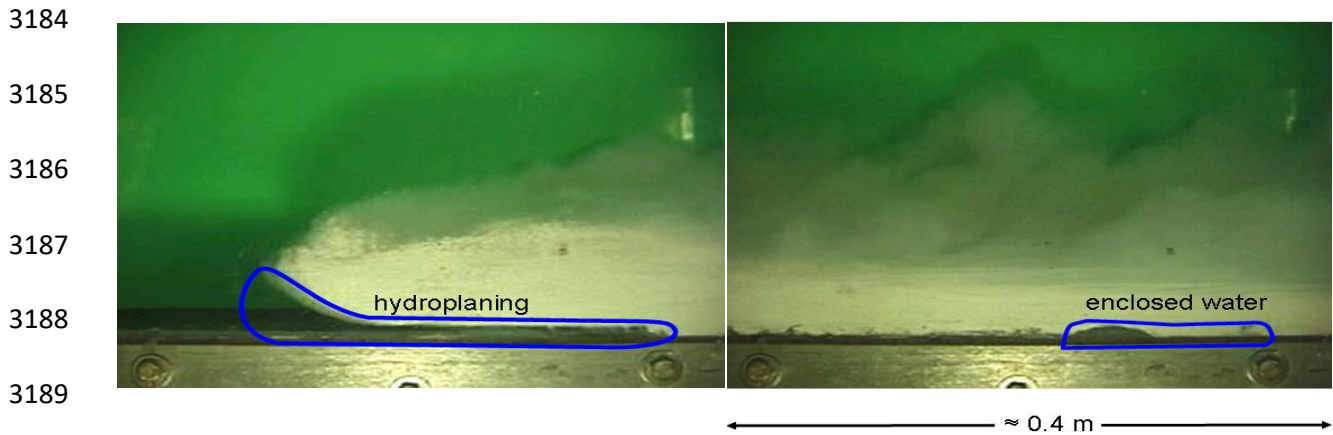
3163 Laboratory experiments including particle tracking and pressure measurements indicate that the
3164 dynamics of the body of sandy debris flows is complex (Ilstad et al., 2004a,b,c; Breien et al., 2010).
3165 The cohesive clay creates a matrix supporting the sand particles to some degree, but it is progressively
3166 elutriated from the top of the dense flow. Water progressively penetrates the sand and fluidizes it, but
3167 as the matrix strength diminishes, they settle progressively and form a deposit. Figure 6.11 illustrates

3168 these processes schematically. The velocity and runout of the flow body depend sensitively on the clay
 3169 type and content, the grain size distribution of the sand, the depth of the flow and the slope angle. These
 3170 effects are only partially analysed and mathematically modelled at present.



3171
 3172 **Figure 6.8.** Illustration of the difference between the flow regimes of (a) clay-rich and (b) sand-rich
 3173 sub-aqueous debris flows. The high cohesion of clay-rich flows prevents ambient water from
 3174 penetrating the head; instead, the stagnation pressure exceeds the weight of the snout above a critical
 3175 velocity (corresponding to a Froude number of approximately 0.4) and lifts it from the bed, leading to
 3176 hydroplaning. In clay-rich flows, the turbidity current consists mainly of elutriated clay and is usually
 3177 less developed. Clay and sand are more easily suspended from sand-rich flows, but keeping the sand in
 3178 suspension requires a strong and sustained production of turbulence. Figure from Elverhøi et al. (2010).
 3179 Photographs show comparison of the fronts and bodies of sand-rich (5% clay, upper images) and clay-
 3180 rich (20% clay, lower images) debris flows in the laboratory. In the sand-rich flow, the head is

3181 progressively diluted by water penetrating it while in the clay-rich, cohesive flow the head is lifted from
3182 the bed by the water that is pressed underneath. TC: Turbidity current; DF: Debris flow. From Breien
3183 et al. (2007).



3190 **Figure 6.9.** Side view of a highly cohesive laboratory flow at the St. Anthony Falls Laboratory. Except
3191 on the flow surface, there is very little internal shear in the flow. One can clearly see that a water layer
3192 lifts the front of the bed, dramatically reducing the bed friction of the head. In some experiments, auto-
3193 acephalation occurred, i.e., the velocity difference between the head and the body stretched and thinned
3194 the “neck” of the flow to the point where it broke. In sufficiently cohesive and thin flows, the head
3195 could be flipped back over the non-hydroplaning body. As the right image shows, a turbulent
3196 suspension layer is formed, but its density remains low, and it moves more slowly than the dense
3197 underflow. Figure from Gauer et al. (2006).

3198 This brief discussion of the flow behaviour of sub-aqueous GMFs shows that, if one wishes to model
3199 them in some detail, accounting for flow-regime transitions is crucial. The most pressing knowledge
3200 gaps, given their practical consequences, are (i) the question whether hydroplaning indeed occurs in
3201 full-size debris or mud flows, (ii) how quickly water can be mixed into the shear layer of dense flows,
3202 and (iii) how quickly the suspension layer is formed.

3203 6.3.3 Erosion and Deposition

3204 The very existence of submarine canyons of enormous dimensions testifies to the erosive power of
3205 GMFs in water. Entrainment of bed material can play a decisive role in the development of turbidity
3206 currents (TCs), as pointed out and modelled by Parker et al. (1986): To maintain their speed despite
3207 continuously mixing in ambient water, turbidity currents must be able to entrain the right amount of
3208 bed material. Various possible erosion mechanisms have been observed or hypothesized (Gauer and
3209 Issler, 2004). In the context of TCs, scour along the base of the flow is presumably dominant, but in
3210 non-cohesive beds, eruption currents at the front of large TCs, where the excess pore pressure in the
3211 bed generated by the approaching GMF may overcome soil cohesion and eject mass, might contribute
3212 significantly (Louge et al., 2011).

3213 Several experiments have studied the dependence of the entrainment rate, q_e , on the bed particle size
 3214 and the flow parameters for TCs over sandy beds, e.g., (Parker et al., 1987). Despite significant
 3215 differences between experiments and theoretical analyses, the general trends appear to be established.
 3216 For cohesive beds, the functional form of q_e does not appear to be well established; many analyses are
 3217 inconsistent with certain mechanical principles or are empirical to a degree that makes them highly
 3218 questionable outside the specific context in which they were developed. It is generally recognized that
 3219 pore pressure in the bed plays an important role in erosion, but the mechanisms of pore pressure
 3220 generation in rapid GMFs are still a topic of active research.

3221 Modelling erosion and entrainment in a mathematical model that resolves the structure of the bed and
 3222 flow in the bed-normal direction is, in principle, fairly straightforward: the response of the bed to the
 3223 extra normal load and shear stress of the approaching or overriding flow can be calculated in detail and
 3224 the assumed failure criterion can be applied to decide whether and how a portion of the bed is eroded
 3225 and entrained. However, in the frequently used, much more efficient depth-averaged flow models
 3226 (Section 6.3.4), this detailed information is not available and additional modelling assumptions must be
 3227 made to determine the entrainment rate. For non-cohesive granular beds, detailed theoretical analyses
 3228 (e.g. Gray, 2001) have elucidated much of the phenomenon and yielded erosion rate formulas that
 3229 appear to describe experiments well. If the bed material can be characterized as brittle with a clear yield
 3230 strength, a simple formula of the type

$$3231 \quad q_e \approx \Theta(\tau_b - \tau_c) \frac{\tau_b(h, u) - \tau_c}{u}, \quad (7)$$

3232 has been proposed (Fraccarollo and Capart, 2002; Issler, 2014). The step function $\Theta(x)$, which is 0 if
 3233 $x \leq 0$ and 1 otherwise, imposes a threshold τ_c on the bed shear stress τ_b for the onset of entrainment;
 3234 the fraction limits the entrainment rate so that the excess shear stress $\tau_b - \tau_c$ suffices to accelerate the
 3235 eroded mass to the flow velocity u . It remains to test this simple concept against carefully designed
 3236 laboratory experiments and evidence from field observations of different types of GMFs. Incidentally,
 3237 a similar approach can be applied at the interface between a dense flow and the suspension layer
 3238 developing above it. Observations on wet-snow avalanches, laboratory experiments on granular flows
 3239 (Barbolini et al., 2005) and numerical simulations (Li et al., 2022; Ligneau et al., 2024) point to the
 3240 importance of frontal entrainment by ploughing in relatively slow, dense flows. This mechanism was
 3241 already included in the first “modern” numerical model for snow avalanches in the 1960s (see Eglit et
 3242 al. (2020) for a summary and references).

3243 Many authors have assumed that deposition is simply the opposite process of entrainment; one could
 3244 then simply omit the step function in Eq. (7) and interpret negative q_e as the deposition rate. Up to
 3245 hysteresis effects, this works for dry, non-cohesive granular materials, but in general there is an
 3246 asymmetry between entrainment and deposition: Entropy increases in the transition from a solid to a

3247 (granular) fluid, but it must decrease during deposition. Entropy having the tendency to increase in a
 3248 closed system, deposition cannot simply be time-mirrored entrainment. Rauter and Köhler (2020)
 3249 analysed the velocity profiles of decelerating flows and found pronounced differences near the bed,
 3250 which led them to suggest the following expression for the deposition rate:

$$3251 \quad q_d = \Theta(u_{\text{dep}} - \|\mathbf{u}\|) \cdot \Theta(-\mathbf{u} \cdot (\mathbf{F}_g - \mathbf{F}_b - \mathbf{F}_p)) \cdot \left(1 - \frac{\|\mathbf{u}\|}{u_{\text{dep}}}\right) \cdot \frac{\|\mathbf{F}_g - \mathbf{F}_b - \mathbf{F}_p\|}{\|\mathbf{u}\|}. \quad (8)$$

3252 It captures that deposition only occurs (i) below some (material-dependent) maximum velocity u_{dep}
 3253 and (ii) if the flow decelerates, i.e., if the resultant of the gravitational force \mathbf{F}_g , the shear force \mathbf{F}_b at
 3254 the bed and the pressure-gradient force \mathbf{F}_p opposes the velocity \mathbf{u} . Moreover, (iii) q_d is assumed to
 3255 increase linearly with the difference between u_{dep} and $\|\mathbf{u}\|$. This assumption is theoretically less well
 3256 founded than the rest of Eq. (8), but it is simple and can be tested.

3257 6.3.4 Physical and Numerical Modelling

3258 Laboratory experiments on sub-aqueous GMFs have been carried out for more than 70 years (Kuenen,
 3259 1937) and have yielded many important insights about flow regimes, run-out distance, velocity, erosion
 3260 and deposition. There have been a few attempts to use physical modelling in a water tank to estimate
 3261 the path and run-out of full-scale debris flows or even the pressure distribution from powder-snow
 3262 avalanches, but the effort of constructing a scale model of the terrain, running the experiments and
 3263 analysing the data is too large in most practical problems. In addition, fulfilling all relevant scaling
 3264 requirements may be difficult or even impossible.

3265 Another approach—at least for estimating the run-out length of a potential future slide—makes use of
 3266 data aggregated from the entire world or, more specifically, from multiple events in a specific setting.
 3267 The run-out angle or the effective friction coefficient of sub-aerial landslides diminishes with increasing
 3268 volume, V ; Scheidegger (1973) found the relation

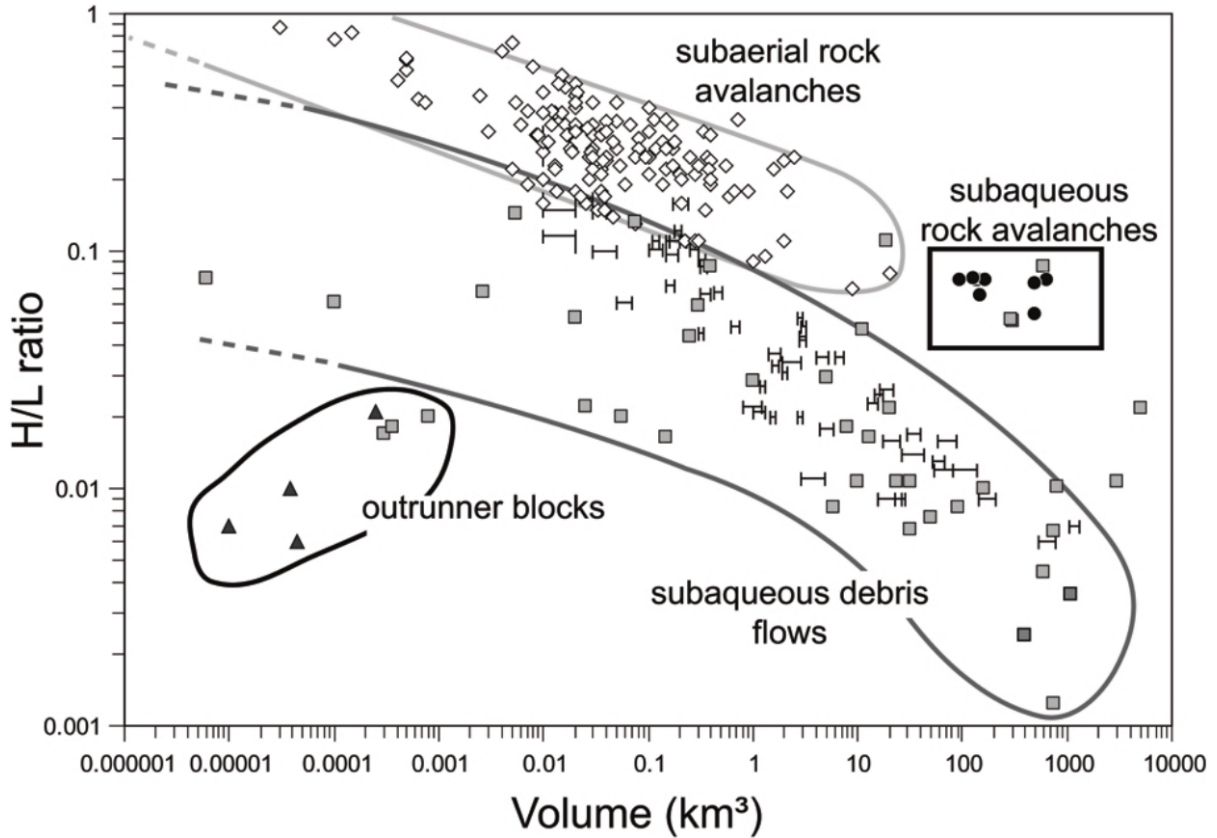
$$3269 \quad \mu_{\text{eff}} = 4.2 \cdot (V/1 \text{ m}^3)^{-0.16} \quad (9)$$

3270 for rock avalanches, which corresponds to run-out angles of 35° for $V = 10^5 \text{ m}^3$ and 9° for $V = 10^9 \text{ m}^3$.
 3271 (This does not apply to quick-clay slides, which typically have much higher mobility.) Landslides and
 3272 debris flows in the marine environment seem to obey a similar correlation up to volumes of about 10^9
 3273 m^3 . Beyond that threshold, events dominated by very large rock fragments appear to follow the same
 3274 trend, but the effective friction of large debris and mud flows decreases with a power close to $-1/3$
 3275 instead of $-1/6$, indicating the emergence of a different flow regime (Figure 6.10; Elverhøi et al., 2002;
 3276 De Blasio et al., 2006). The wide scatter in the global data set is not surprising, given the wide range of
 3277 geotechnical conditions. The single slide events identified in the extremely large Storegga slide complex

3278 ([Haflidason et al., 2005](#)) follow the same trend over the volume range 10^7 – 10^{11} m³ but have considerably
3279 lower scatter due to their highly similar soil compositions ([Issler et al., 2005](#)).

3280 These empirical scaling relations can be used to test theoretical concepts on GMF dynamics ([Issler et](#)
3281 [al., 2005](#)), but they are only useful in practical problems if one may assume that the exponent is about
3282 $-1/6$ for smaller slides and near $-1/3$ for large, clay-rich debris flows, and they do not give information
3283 about velocity, scour and impact pressure. Developing analogous correlations for these quantities—
3284 with traditional statistical methods or with machine learning—is hardly possible because measurements
3285 are too scarce.

3286 At this point, dynamical models based on the principle of conservation of mass, momentum and total
3287 energy come to the rescue. However, developing accurate yet practically useful models is a highly non-
3288 trivial task. There is a bewildering range of modelling approaches that can be useful under specific
3289 conditions with regard to the questions that must be answered, the required level of accuracy, the
3290 available computational resources, the size of the study area, the seascape, and the soil composition. At
3291 one end of this spectrum are extensions of the concept of mass-point models. At the other extreme,
3292 discrete element models (DEM) simulate the movement and interaction of large numbers of “particles”
3293 in 3D and may require weeks on a super-computer for a single simulation. The middle ground consists
3294 mostly of continuum models, which are solved numerically by discretizing the space–time continuum
3295 as finite time intervals and spatial cells; this turns the partial differential equations into algebraic ones.
3296 The models solve an appropriately simplified set of balance equations for mass, momentum and,
3297 possibly, different forms of energy, employing model-specific constitutive equations (describing
3298 material properties) for closure. In the following, only a few remarks on the merits and problems of a
3299 few selected modelling approaches can be given. Interested readers are referred to review papers (e.g.,
3300 [Trujillo-Vela et al., 2022](#), and [references contained therein](#)).



3301
 3302 **Figure 6.10.** Diagram showing the distribution of runout ratios H/L of subaqueous and subaerial
 3303 landslide deposits as a function of deposit volume. The plot is reproduced from De Blasio et al. (2006),
 3304 where the sources of the different data points are reported.

3305 Mass-point models solve the equation of motion of the centre of mass of the slide,

3306
$$\frac{dv}{dt} = g' \sin \theta(s) - \frac{F_r}{M} - \frac{Q_{e/d}v}{M}, \quad (10)$$

3307 together with the mass balance equation,

3308
$$\frac{dM}{dt} = Q_{e/d}. \quad (11)$$

3309 Here, t is the time, s the distance along the slope, $\theta(s)$ the spatially varying slope angle, $v = ds/dt$ the
 3310 velocity, $g' = g(1 - \rho_f/\rho_s)$ the effective gravitational acceleration accounting for buoyancy, with ρ_f
 3311 and ρ_s the densities of the ambient water and the flowing mass, respectively. F_r is the resistive force,
 3312 M the total mass of the slide, and $Q_{e/d}$ the net mass gain or loss per unit time interval.

3313 Huppert and co-workers chose a slightly different concept, modelling turbidity currents as elongating
 3314 and widening boxes or pie slices and obtained analytical solutions for the run-out distance and the
 3315 asymptotic behaviour of velocity and deposition depth on a plane, which correspond well with observed
 3316 turbidites (Dade and Huppert, 1994). These models are simplified to the most essential features yet
 3317 capture a surprising wealth of phenomena with very few adjustable parameters, and there are additional

3318 processes that could be built into them to describe more specific properties of these flows with modest
3319 computational effort—albeit at the cost of introducing additional parameters that must be calibrated.

3320 However, if one requires more detailed modelling and better spatio-temporal resolution, one may
3321 idealize the GMF as a continuum at a scale between the typical particle sizes and the typical flow depth
3322 and describe the relevant fluid properties (density, velocity, etc.) in terms of fields $\rho(\mathbf{x}, t)$, $\mathbf{u}(\mathbf{x}, t)$, etc.
3323 These fields must obey the mass conservation equation for a single-component fluid,

$$3324 \quad \partial_t \rho + \nabla \cdot (\rho \mathbf{u}) = 0, \quad (12)$$

3325 and the Navier–Stokes (momentum balance) equation,

$$3326 \quad \partial_t (\rho \mathbf{u}) + \nabla \cdot (\rho \mathbf{u} \mathbf{u}) = \mathbf{f} - \nabla p + \nabla \cdot \boldsymbol{\sigma}. \quad (13)$$

3327 $\mathbf{f} = \rho \mathbf{g}'$ is the body force per unit volume, i.e., the buoyant gravity in GMFs, while p is the pressure
3328 and $\boldsymbol{\sigma}$ the deviator of the stress tensor. As indicated in [Section 6.3.1](#) on rheology, the constitutive
3329 equations expressing p and $\boldsymbol{\sigma}$ in terms of ρ and \mathbf{u} (and other fields if additional variables are included)
3330 are much more complex than those for ideal fluids or gases. If they are formulated in a sufficiently
3331 general way, they can encompass both solid and fluid phases so that the transition between these phases
3332 during the release and stopping of a slide as well as erosion and deposition during the flow can be
3333 modelled, as demonstrated, e.g., by Gaume et al. (2019). However, if the constitutive relations are not
3334 smooth, as in the case of a yield-strength fluid, there can be significant numerical challenges.

3335 At any rate, solving these equations in 3D in a large area typical of submarine landslides requires an
3336 enormous computational effort. It can be reduced by some three orders of magnitude if one simulates
3337 only a longitudinal section of the flow (i.e., two dimensions in a vertical plane or 2DV), but essential
3338 information about the sideways spreading of the slide is lost. An alternative simplification is to formally
3339 integrate the Eqs. (12) and (13) over the flow depth to reduce them to two-dimensional (2DH) equations
3340 for $h\rho$ (or h if the density is constant) and $h\rho\mathbf{u}$ (or $h\mathbf{u}$). One thereby loses information about the
3341 variation of the fields in the bed-normal or vertical dimension but can reduce the computational effort
3342 typically by six orders of magnitude or more, which makes simulation practical in many cases. If the
3343 sideways spreading is not essential (e.g. when scanning the parameter space for a specific flow), a
3344 speed-up by another two orders of magnitude can be achieved by also integrating the equations over
3345 the flow width. Many variants of 1D or 2D depth-averaged continuum models for all types of GMFs
3346 have been developed over the past 60 years ([Eglit et al., 2020](#)) and have become indispensable tools in
3347 research as well as practical hazard management.

3348 In contrast to the Saint-Venant or shallow-water equations, depth-averaged models of GMFs necessarily
3349 include several source terms to describe the down-slope gravitational force, bed friction, and
3350 erosion/deposition. Extra conservation or constitutive equations are needed if the flow density is
3351 variable, if segregation must be accounted for, or if two or more different layers are present. Examples

3352 of the latter are turbidity currents with a dense underflow, coupled landslide–tsunami models and flows
 3353 of visco-plastic materials like clay with a plug layer riding on a basal shear layer, both of which have
 3354 variable thickness. We illustrate the complexity and wealth of options of such models with a minimal
 3355 two-layer formulation for (non-hydroplaning) debris flows developing a turbidity current, as
 3356 schematically depicted in [Figure 6.11](#). It comprises three mass-conservation equations for the bed
 3357 (index 0), the dense underflow (index 1) and the suspension flow layer (index 2) layers but not the
 3358 ambient water layer (index 3),

$$\partial_t b = -q_{01} + q_{10} - q_{02} + q_{20}, \quad (1)$$

$$\partial_t(h_1\rho_1) + \nabla \cdot (h_1\rho_1\mathbf{u}_1) = q_{01} - q_{10} - q_{12} + q_{21}, \quad (2)$$

$$\partial_t(h_2\rho_2) + \nabla \cdot (h_2\rho_2\mathbf{u}_2) = q_{02} - q_{20} + q_{12} - q_{21} + q_{32}, \quad (3)$$

3359 two volume-conservation equations for layers 1 and 2 because the particle concentration in these layers
 3360 can change,

$$\partial_t h_1 + \nabla \cdot (h_1\mathbf{u}_1) = \frac{q_{01} - q_{10} - q_{12} + q_{21}}{\rho_1} \quad (4)$$

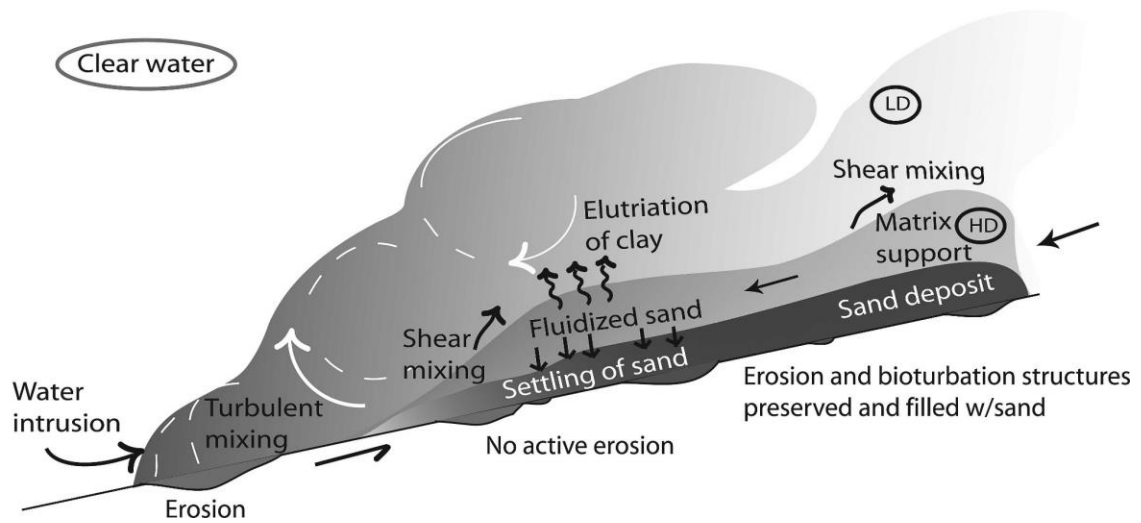
$$\partial_t h_2 + \nabla \cdot (h_2\mathbf{u}_2) = \frac{q_{02} - q_{20} + q_{12} - q_{21} + q_{32}}{\rho_2} \quad (5)$$

3361 and two vectorial momentum-balance equations,

$$\begin{aligned} \partial_t(h_1\rho_1\mathbf{u}_1) + \nabla \cdot (k_{1u}h_1\rho_1\mathbf{u}_1\mathbf{u}_1) \\ = \mathbf{f}_1 + \nabla \cdot (h_1\bar{\boldsymbol{\sigma}}_1) - \boldsymbol{\tau}_{10} + \boldsymbol{\tau}_{21} - (q_{10} + q_{12})\mathbf{u}_1 + q_{21}\mathbf{u}_2, \end{aligned} \quad (6)$$

$$\begin{aligned} \partial_t(h_2\rho_2\mathbf{u}_2) + \nabla \cdot (k_{2u}h_2\rho_2\mathbf{u}_2\mathbf{u}_2) \\ = \mathbf{f}_2 + \nabla \cdot (h_2\bar{\boldsymbol{\sigma}}_2) - \boldsymbol{\tau}_{20} - \boldsymbol{\tau}_{21} - \boldsymbol{\tau}_{23} - (q_{10} + q_{21})\mathbf{u}_2 + q_{12}\mathbf{u}_1. \end{aligned} \quad (7)$$

3362 These nine partial differential equations must be supplemented by closure relations for the six mass
 3363 exchange rates $q_{ij}, i, j = 0, 1, 2, i \neq j$, between layers and with the ambient fluid (q_{32}), the interfacial
 3364 shear stresses $\boldsymbol{\tau}_{10}, \boldsymbol{\tau}_{20}, \boldsymbol{\tau}_{21}, \boldsymbol{\tau}_{23}$ as well as the depth-averaged stress tensors $\bar{\boldsymbol{\sigma}}_1, \bar{\boldsymbol{\sigma}}_2$ and the pressure in
 3365 the ambient fluid. There is considerable freedom in modelling these relations, and the simulation results
 3366 depend crucially on these choices.



3367

3368 **Figure 6.11.** Schematic illustration of the structure and mass fluxes in a sand-rich subaqueous debris flow. Through the front, water intrudes into the head and dilutes it, thus generating a sizeable turbidity
3369 current if the velocity and the shear rate are high enough to produce enough turbulence to keep the sand
3370 particles in suspension. On an easily erodible sea floor, entrainment can make up for the mass loss of
3371 the head due to shedding wakes and maintain the flow over very long distances. The dynamics of the
3372 main body of the debris flow is governed by the interplay of clay elutriation, sand supported by the
3373 matrix of residual clay, fluidization of the sand by penetrating water, and settling of sand particles
3374 leading to deposition. The balance of these processes depends dynamically on the sediment
3375 composition, flow size, and stage of the flow. LD: Low density; HD: High density. From Breien et al.
3376 (2010).
3377

3378 Simple one-layer models with constant density are described by hyperbolic equations; in contrast,
3379 depth-averaged variable-density and/or two-layer models may not be hyperbolic in their entire
3380 parameter ranges (Nazarov, 1991), which may pose challenges for numerical codes. The proposed
3381 mathematical models have been implemented with finite-difference, finite-volume, finite-element and
3382 meshless discretization techniques like Smoothed Particle Hydrodynamics (SPH), or with a
3383 combination thereof in the case of the Material Point Method (MPM). Choosing the most suitable
3384 method for a given situation is challenging because increased flexibility or accuracy usually comes with
3385 higher program complexity and lower speed. While Eulerian finite-volume codes have been dominant
3386 for some decades, SPH and MPM codes have caught centre-stage recently (e.g., Pastor et al., 2024;
3387 Guillet et al., 2023).

3388 Assuming a code correctly solves the model equations, one must verify that these equations describe
3389 the target phenomenon sufficiently well for the purpose at hand. In this process, laboratory experiments
3390 play an important role because one can control the initial and boundary conditions and measure the flow

3391 variables during the flow. One can test whether a model correctly simulates the dependence of velocity
3392 and run-out on the soil composition. However, detailed laboratory studies of bed entrainment ([Barbolini
3393 et al., 2005](#)) and turbidity-current formation ([Mohrig and Marr, 2003](#)) are scarce. It would be equally
3394 important to validate and calibrate models against real-scale GMFs, but there are almost no
3395 measurements of the dynamics of sub-aqueous GMFs besides the recent exceptional data sets on
3396 turbidity currents, e.g., ([Paull et al., 2018](#)). Moreover, comprehensive geotechnical data from actual
3397 subaqueous landslides and their surroundings are available only for a few sites, where detailed
3398 assessment of the GMF risk was crucial (e.g., [Solheim et al., 2005b](#); [Carlton et al., 2018](#)). Such
3399 geotechnical data have recently been used as input to an advanced 2DV model, which uses MPM for
3400 simulating the solid constituents and computational fluid dynamics (CFD) for the interstitial and
3401 ambient water ([Tran et al., 2024](#)). The good agreement with the observed longitudinal deposit section
3402 and erosion depth suggests that satisfactory Class-A predictions can indeed be achieved, albeit at a
3403 staggering computational cost. At present, therefore, one may use such advanced models primarily to
3404 improve the closure relations in depth-averaged models, which will continue to be the workhorse in
3405 practical applications in the foreseeable future.

3406 6.3.5 Implications and Considerations for Engineering

3407 In practice, GMF dynamics is mainly relevant for estimating the key parameters of the tsunami that a
3408 given mass flow will generate (see [Sections 6.6.2](#)) and for determining whether sub-sea installations
3409 are potentially endangered and, if so, how large the impact forces may be. The run-out distance can
3410 often be estimated with relatively simple empirical models if the latter can be calibrated from observed
3411 nearby landslides with the same soil conditions, as was done, e.g., for the Ormen Lange gas field within
3412 the Storegga slide area ([De Blasio et al., 2003](#)). If not enough data for calibrating is available, models
3413 that incorporate more of the relevant physics and have been validated against observed GMFs with
3414 similar characteristics should be used.

3415 The interaction of GMFs with man-made sub-sea structures depends not only on the impact velocity
3416 and depth of the mass flow but also on its composition (notably its content of clay and/or hard rocks),
3417 the erodibility of the sea floor in the immediate surrounding of the structure, as well as the shape and
3418 exposed surface of the structure. In simple configurations like those in laboratory experiments, 2DV
3419 simulations with computational fluid dynamics (CFD) software have been carried out with rather
3420 satisfactory results ([Zakeri et al., 2009](#)). It is often assumed that the interaction of a GMF with an
3421 obstacle can only be modelled with a 3D simulation, and this is certainly true when studying the impact
3422 of a debris flow or turbidity current on a pipeline, where scour underneath the pipe is a critical effect.
3423 To make this practically feasible, one may carry out a depth-integrated simulation (in two horizontal
3424 dimensions) of the slide from release to the vicinity of the object and use the depth-integrated values to
3425 initialize the 3D simulation some distance upstream of the object. However, experience has shown that
3426 depth-averaged GMF models for granular flows are unexpectedly adept at simulating the main features

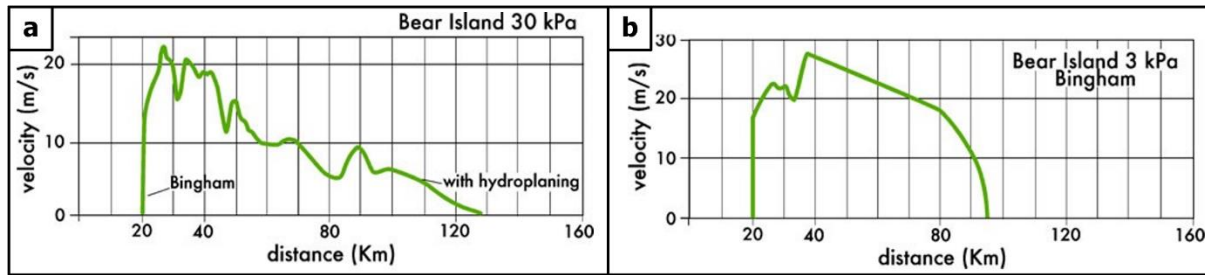
3427 of the flow interaction with obstacles like dams or mounds (Gray et al., 2003; Tregaskis, 2020). If the
3428 vertical velocity and density profiles can be estimated, one may obtain an approximate vertical
3429 distribution of the impact forces, which may be sufficient in many cases—especially for turbidity
3430 currents. However, the case of soil flows with considerable yield strength has not been extensively
3431 studied with such models so far, thus there is a large amount of uncertainty connected with clay-rich
3432 debris flows or mudflows and it is advisable to use a 3D model.

3433 Salmanidou et al. (2017) discussed uncertainty in landslide material parameter values by running
3434 multiple, simple granular (frictional-collisional) landslide-dynamics simulations for a statistical study.
3435 By comparing the results with observed landslide run-out distance for a large landslide at the Rockall
3436 Bank offshore Ireland, they found wide uncertainty distributions. However, this uncertainty can be
3437 reduced by also applying tsunami data (Løvholt et al., 2020) and measurements of geotechnical soil
3438 parameters, even though there is large epistemic uncertainty in the material behaviour that cannot be
3439 measured effectively in the laboratory (Vanneste et al., 2019).

3440 An additional complication arises for flows of sensitive clays because the yield strength varies from an
3441 initial to a final remoulded value as a function of the shear strain accumulated during the flow (De
3442 Blasio et al., 2005). The final yield strength normally has the strongest influence on the run-out distance
3443 (Marr et al., 2002; Løvholt et al., 2017, 2019; Kim et al., 2019; Vanneste et al., 2019). In hazard studies,
3444 yield strength parameter values are often tuned to match modelling results with observations of run-out
3445 distance and are typically found to be much lower than the corresponding values measured in the
3446 laboratory, as it to some extent represents different effects that reduce friction, such as hydroplaning,
3447 weak layers, pore overpressure, etc. Owing to consolidation, the yield strength measured today may
3448 also be higher than when the landslide took place. A combination of strain-softening clay with high
3449 sensitivity together with anisotropic strength properties also enables a retrogressive failure (Kvalstad et
3450 al. 2005b), which can take place as a fairly slow process mobilizing the blocks one-by-one or a much
3451 faster process involving several blocks at the same time (Gauer et al. 2005; Løvholt et al. 2016).

3452 In summary, numerical modelling of the release, propagation and impact of submarine GMFs still
3453 requires use of all available information on the geological setting of the area, the geotechnical properties
3454 of the soils, and the landslide history for calibration of the model(s). Based on this and the project
3455 requirements, the most suitable models must be chosen and their results critically appraised. Despite
3456 best efforts, the remaining uncertainty with regard to release probability, runout distance and impact on
3457 structures will often remain considerable. However, recent work (Tran et al., 2024) on highly
3458 sophisticated models holds promise of making numerical simulation of the entire process including
3459 slide release and impact possible, allowing so-called class-A predictions based on measured soil
3460 properties instead of calibrated empirical parameters. However, the computational cost for 3D
3461 simulations is prohibitive at present. As Figure 6.12 shows, even relatively simple models may be able

3462 to capture the main features of an event if they adequately capture the key flow mechanisms (in this
3463 case, hydroplaning)

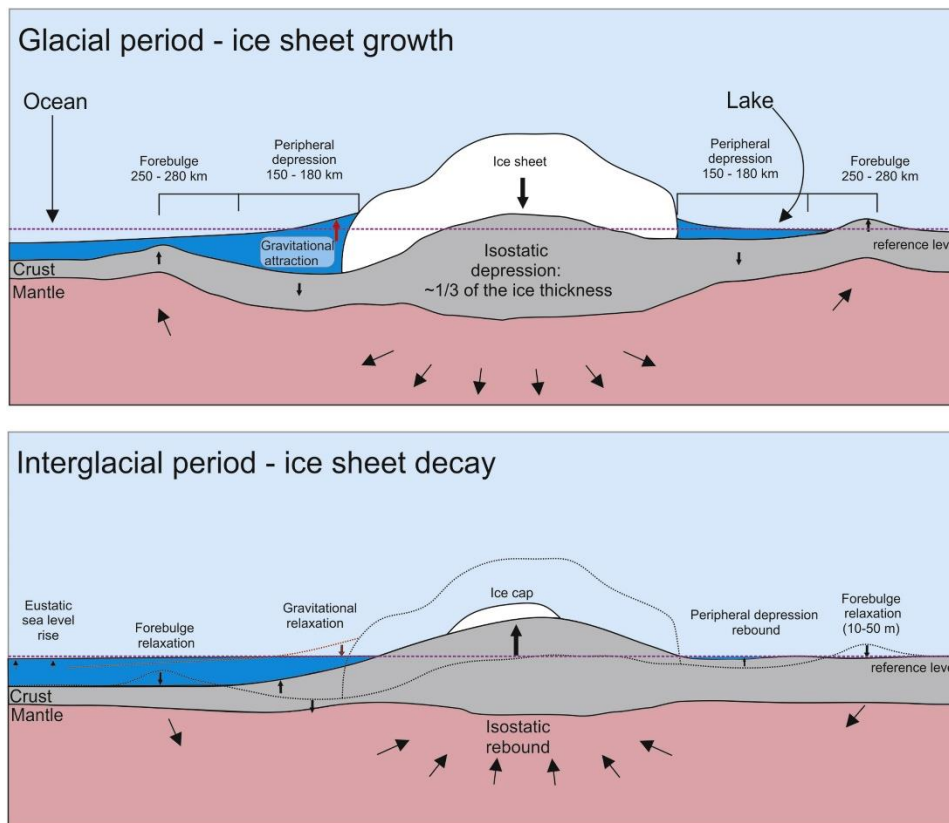


3464

3465 **Figure 6.12.** Illustrative example of numerical simulations of a subaqueous debris flow on the Bear
3466 Island Fan with the models BING (Imran et al., 2001) and W-BING (De Blasio et al., 2004). The
3467 observed runout exceeds 150 km, amounting to an effective friction coefficient of only 0.012. With the
3468 visco-plastic rheology implemented in BING, the observations cannot be reproduced even if the yield
3469 strength of the flowing material is set as low as 3 kPa. In contrast, W-BING includes hydroplaning at
3470 Froude numbers above 0.4 and almost reaches the observed runout with a yield strength of 30 kPa,
3471 which is realistic for over-consolidated clay deposits. Figure from Elverhøi et al. (2010).

3472 6.4 Glacio-isostatic adjustment and sea-level changes

3473 Generally, during the Pleistocene, global sea level varied from between approximately 10 m above
3474 present day to up to approximately 130 m below present levels (e.g., MIS2; Hansen et al, 2013;
3475 Lambeck et al., 2014). On glaciated continental margins the relative sea level is a combination of global
3476 sea level changes due to sequestration of water in ice sheets, and the viscos-elastic response of the crust
3477 and mantle to loading by growing and melting of continental-scale ice mass known as glacio-isostasy
3478 or glacio-isostatic adjustment (GIA; Shennan et al., 2011). Apart from the two primary mechanisms the
3479 relative sea level is also influenced by: (1) gravitational attraction of the water in the vicinity of the ice
3480 mass, (2) location and migration of a forebulge in front of the ice sheet as it grows and decays, and (3)
3481 thermal contraction and expansion of water due to changes in water temperature.

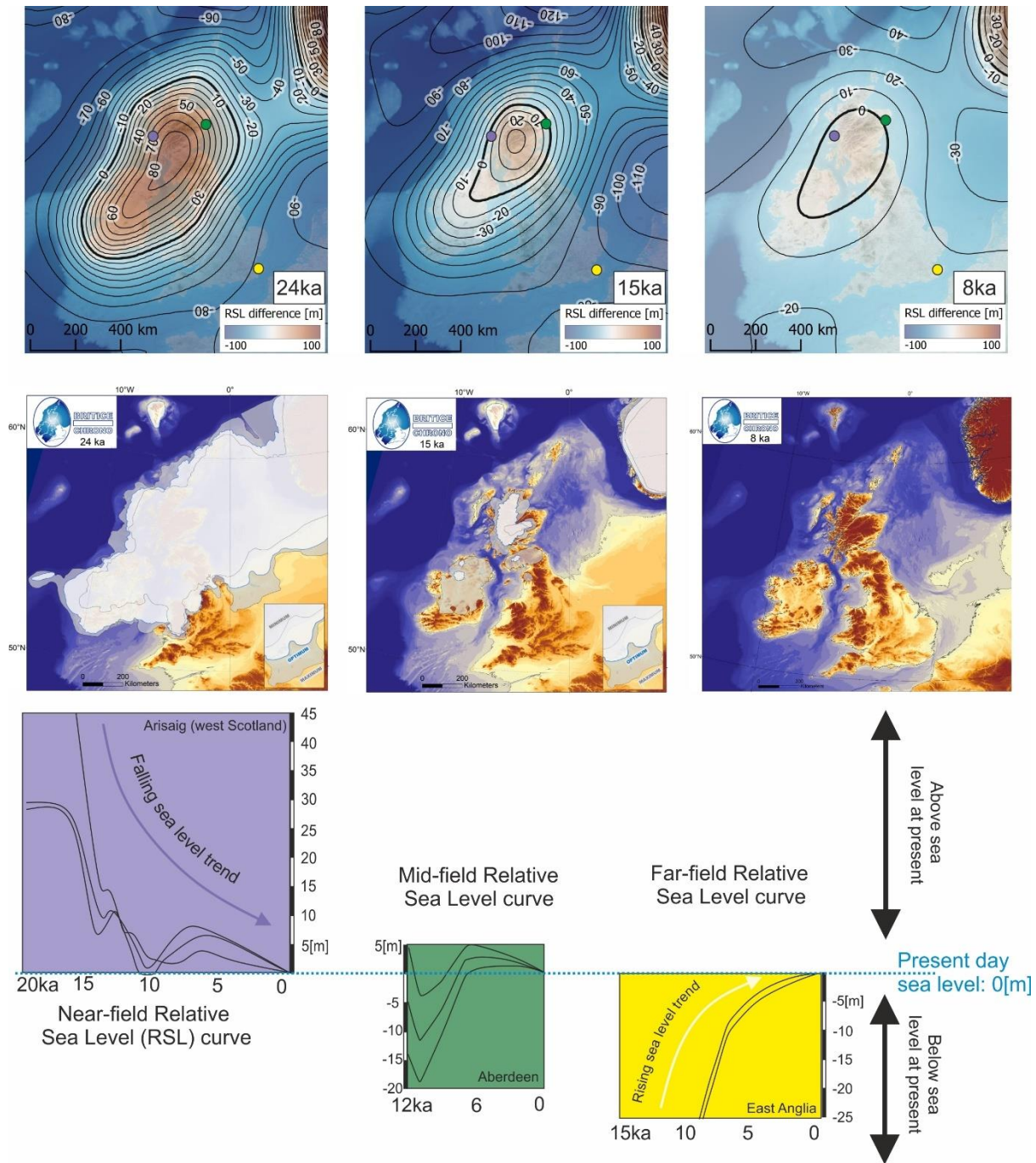


3482

3483 **Figure 6.13.** Behaviour of crust and mantle in response to loading by ice mass during ice-sheet growth
 3484 and subsequent ice-sheet decay. Note the changes of relative sea level between the vicinity of the ice
 3485 sheet (near field) and areas further afield (far field).

3486 The global sea level was generally lower during Pleistocene glaciations and rose following ice demise
 3487 (Figure 6.13). In the proximity of the ice sheet, the crustal rebound after deglaciation resulted in the
 3488 relative sea level fall (not rise) as the land uplift outpaced the rise in the global ocean (Figure 6.13).

3489 This can be described as a near-field relative sea-level trend where sea level generally is observed to
 3490 fall after deglaciation (Figure 6.14). The opposite trend is observed for sites further away from the
 3491 palaeo-ice sheet margins where only a sea-level rise is observed. Between the near-field and far-field
 3492 sites, there is a wide zone where the interplay of eustatic sea-level rise and isostatic rebound results on
 3493 a complex, undulating sea-level curve. This is referred to as a mid-field effect (Figure 6.14). This see-
 3494 saw behaviour repeated itself between glacial and interglacial periods and was further complicated by
 3495 spatiotemporal differences in ice extent, advance and decay rates (Figure 6.14).



3496

3497

3498 **Figure 6.14.** Top row: distribution of the relative sea level (RSL) difference between present day and
 3499 respective time in the past due to the combined effect of ice loading and changes in the global ocean
 3500 water volume due to sequestration within ice sheets and glaciers. Positive values indicate areas where
 3501 sea level was higher than at present whereas negative values show areas of lower sea level. Bold contour
 3502 indicates a ‘hinge line’ where sea level was the same as at present. Points on the map correspond to
 3503 colour-coded RSL curves at the bottom. Middle row: Paleogeographic reconstruction by Clark et al.,
 3504 (2022) showing the differences in the coastline position and ice-sheet coverage for respective time steps.

3505 Note for 24 ka that the land was still covered by thick ice sheets, and it was not submerged. Bottom:
3506 Relative sea-level (RSL) curves showing the difference of sea-level history depending on the
3507 region/distance in relation to the centre of the ice sheet. Purple curves are typical for regions close to
3508 the ice sheet where crustal rebound response dominates and RSL falls during and following
3509 deglaciation. Green curves show the mid-field response where the interplay of crustal response and
3510 changes of water volume in the global ocean interact dynamically resulting in a complex RSL curve.
3511 Yellow curves are typical for far-field where the effect of release of water from ice sheets dominates
3512 over the crustal rebound and the RSL rises.

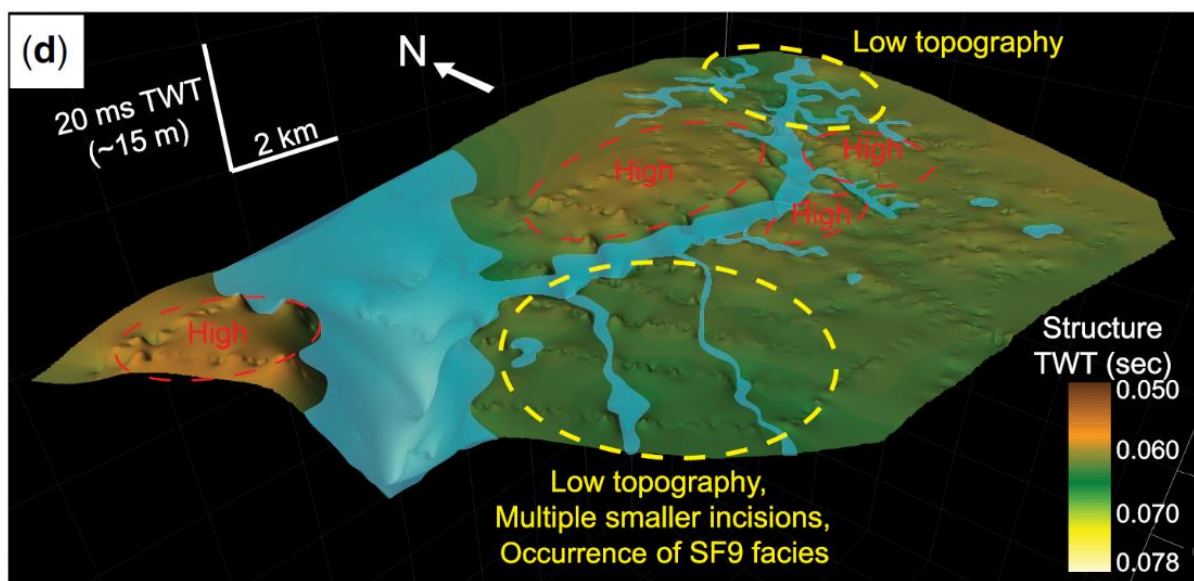
3513 Understanding the complex interplay between eustatic sea-level rise and GIA is important for the
3514 constraint of relative sea-level history, migration of coastlines and depositional environments, and
3515 associated geohazards and engineering constraints during ground modelling (Section 5.9), which in turn
3516 influence the design of offshore infrastructure. From a geohazard perspective, ongoing GIA is further
3517 relevant in terms of post-glacial faulting (Section 5.10). Glacio-isostatic uplift of former marine clays
3518 to elevations of >200 m asl (e.g., 220 m asl in SE Norway; NGU, 2025) resulted in pronounced marine
3519 limits in some fjord systems, below which quick clay (the formerly-deposited marine clay) can be
3520 located and acts as a serious geohazard for infrastructure projects and settlements (Figure 1.1; Section
3521 5.7; NGU, 2025) Calculated remaining uplift due to the melting of the Weichselian ice sheet is
3522 modelled to ~40 m in Central Fennoscandia (Fjeldskaar and Amantov, 2018).

3523 The load of large volumes of glacial sediments, in particular in trough mouth fans and thick progrades
3524 along the margins (Figure 6.4), resulted in local subsidence of neighboring regions, such as the North
3525 Sea Basin and the Northern North Sea (Sejrup et al., 2004). This subsidence, again, generates
3526 accommodation space for sediments on the shelves (e.g., North Sea; Lamb et al., 2018).

3527 Sea-level changes are additionally important when it comes to archaeology and assessment of
3528 submerged paleolandscape evolution (e.g. Andresen et al., 2022; Figure 6.15). For the southern North
3529 Sea, the exposed continental shelf constituted an attractive habitat for hunter-gatherer populations
3530 before it was flooded during the late glacial and early Holocene (Bailey et al., 2020). Findings of well-
3531 preserved archaeological artefacts in the shallow waters (< 10 m) of the inner Danish waters and
3532 southern Baltic Sea, document early human occupation in these areas (Bailey et al., 2020). In the
3533 southern North Sea and generally at deeper water depths, the archaeological potential remains uncertain.
3534 Cultural heritage and screening for marine archaeology (including wrecks and UXOs) are however in
3535 any cases, critical and costly elements of pre-investigation surveys for offshore windfarms and other
3536 offshore developments in areas such as the southern North Sea.

3537 Local GIA can vary considerably and in combination with global sea-level change can result in unique
3538 relative sea-level curves depending on location. For example, studies around the UK and Ireland show
3539 significantly different sea-level curves across a relatively short lateral distance (Shennan et al., 2018;

3540 [Figure 6.14](#)). The growth in offshore development size, including wind farms and large interconnector
 3541 projects, increasing amounts of pre-investigation data can mean that geo-evolutionary models and
 3542 relative sea-level curves can be varied across the breadth of a site area: some projects can have relative
 3543 sea-level curves that differ from one end of a route or site to the other. This needs to be appropriately
 3544 captured to fully appreciate geo-engineering constraints across a development area. Together with the
 3545 progression to deeper water settings, the current approach for archaeological screening requires revision
 3546 to better capture the archaeological potential. Machine learning approaches and automated
 3547 identification of geo-archaeological potential in prospect areas, need to be developed to ensure a fast
 3548 and efficient construction phase.



3549 **Figure 6.15.** 3D perspective view of a mapped former late glacial to early Holocene terrestrial surface
 3550 in the central North Sea, rivers and indications of topographical highs and lows added for visualization
 3551 purposes. Mapping based on sub-bottom profiles and sediment cores. From Andresen et al. (2022).
 3552

3553 6.5 Seismicity

3554 The seismic hazard in northern Europe is relatively low on a global scale. [Figure 6.16](#) shows the peak
 3555 ground acceleration (PGA) on bedrock ($V_{S30} = 800$ m/s) for a return period of 475 years estimated by
 3556 the SHARP storage project ([Carlton et al. 2024](#)). The values along the coasts of the UK, Norway,
 3557 Denmark and Germany are consistent with the corresponding values from the most recent onshore
 3558 national studies ([Mosca et al., 2024](#); [Lindholm et al., 2025](#); [Voss et al., 2015](#); [Grünthal et al, 2018](#),
 3559 respectively). The highest PGA values occur off the west coast of Norway in the Tampen Area (62°N,
 3560 4°E), between Norway and Denmark along the Tornquist Zone (57.5°N, 7.5°E), and at the Dover
 3561 Strait (51°N, 1.5°E). This follows roughly the same pattern as the observed seismicity ([Figure 6.17](#)).

3562 [Figure 6.17](#) displays seismicity in Northwestern Europe, Scandinavia, and the surrounding seas since
 3563 1900. The most seismic activity in the region is along the spreading mid-Atlantic ridge (e.g. [Engen et](#)
 3564 [al., 2003](#)), which is a divergent boundary formed by the separation of the North American Plate and the

3565 Eurasian Plate. Earthquakes along the ridge are frequent, moderate in size ($M < 6$), and mainly caused
3566 by the movement of the tectonic plates. The rest of the study area is a stable continental region
3567 characterised by lower seismicity. The three main hypotheses for the occurrence of earthquakes in this
3568 region are the release of stresses built up and propagated from the spreading of the mid-Atlantic ridge,
3569 stress adjustments caused by isostatic rebound related to deglaciation, and sediment loading/unloading
3570 (Fejerskov and Lindholm, 2000; Olesen et al., 2013). The completeness and accuracy of earthquake
3571 catalogues are continually advancing through improved instrumental coverage, better exploitation of
3572 historical data, and better location algorithms, with the current state of the art in regional seismic
3573 monitoring described by Ottemöller et al. (2021). The most recent update to the seismicity catalogue
3574 for the North Sea is provided by Kettlety et al. (2024) as part of the SHARP storage project.

3575 The largest earthquake onshore Norway in historical times was the 31. August 1819 Lurøy event (Muir
3576 Wood, 1989; Mäntyniemi et al., 2020), estimated at $M_{5.9}$, and the Nordland coastline is host to
3577 relatively frequent earthquake swarms with events up to $M_{4.5}$ (e.g. Bungum et al., 1979; Gibbons et
3578 al., 2007; Bungum et al., 2010). The earthquake of October 23, 1904, that caused significant damage in
3579 the city of Oslo, was attributed to a magnitude of 5.4 and located in the eastern Oslofjord by Bungum
3580 et al. (2009). There is evidence for paleoearthquakes of magnitude over 7 in Scandinavia (e.g.
3581 Arvidsson, 1996; Olesen et al., 2021), and Olesen et al. (2013) believe there is a possibility of magnitude
3582 6+ earthquakes along the coastal parts of western Norway, Nordland and the Oslo rift zone.

3583 Although the largest earthquakes are located along the mid-Atlantic ridge, there are notable exceptions
3584 such as the 1931 M_w 5.9 Dogger Bank earthquake off the east coast of England. More recent North Sea
3585 earthquakes, such as the 30 June 2017 (M_w 4.5, Jerkins et al., 2020) and 21 March 2022 (M_w 5.1,
3586 Jerkins et al., 2023) events, have been located and characterized with unprecedented accuracy with both
3587 global and regional seismic networks and using offshore permanent reservoir monitoring networks.

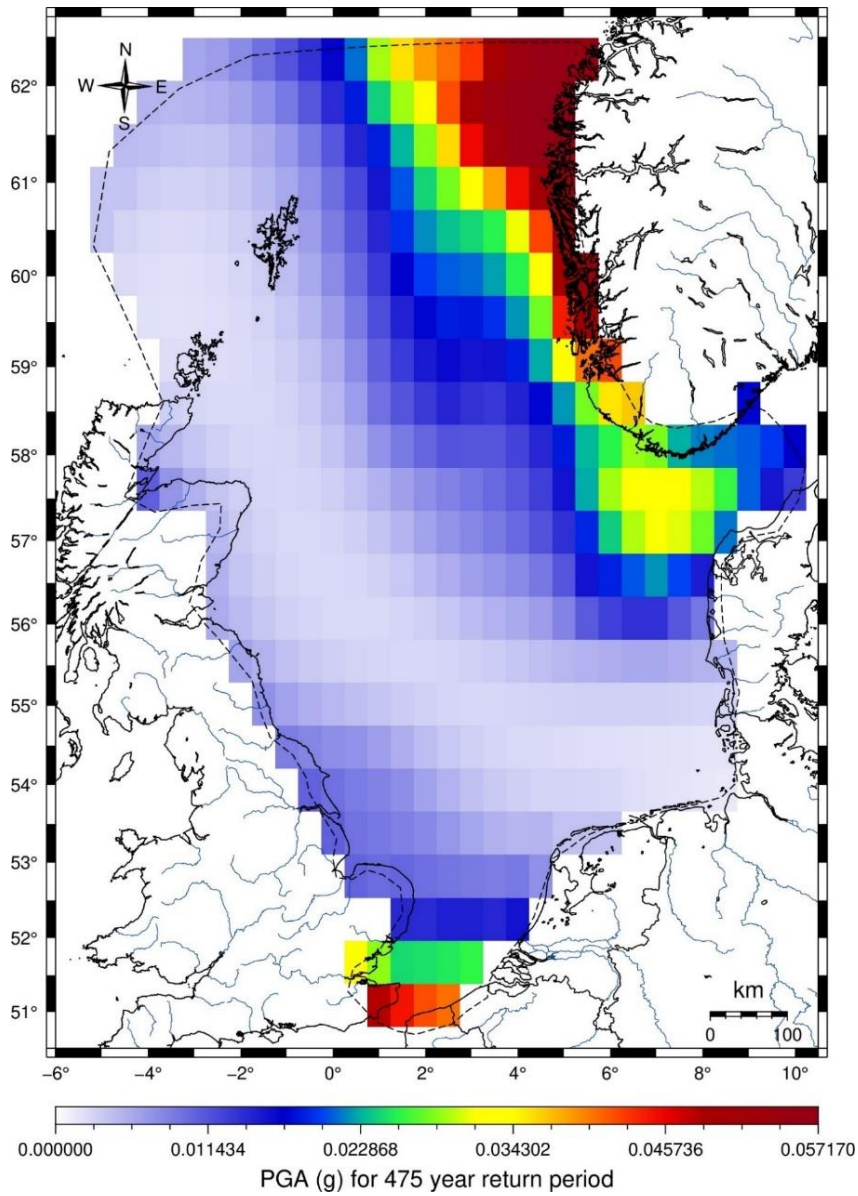
3588 Despite the relatively low seismic hazard, earthquakes can still pose a threat to offshore industries.
3589 Earthquake shaking in the horizontal direction is strongest between frequencies of 1-20 Hz. Offshore
3590 wind turbines (OWT) have low natural frequencies (0.25-0.5Hz), which means that they are generally
3591 not vulnerable to horizontal earthquake shaking in low-to-moderately seismic areas (Hovind et al.
3592 2014). However, OWTs are vulnerable to earthquake shaking in the vertical direction due to their low
3593 damping and similar natural frequencies in the vertical direction as earthquakes (Kjørlaug and Kaynia,
3594 2015). In addition, OWTs have strict performance requirements (e.g. less than one-degree allowable
3595 tilt), which means that even small deformations caused by earthquake shaking or liquefaction are not
3596 desired. Therefore, the seismic design of offshore wind turbines in low to moderately seismic areas is
3597 governed by performance-based considerations (Kaynia, 2019).

3598 CCS facilities are generally located shallower than most earthquakes. However, even small magnitude
3599 earthquakes, if they occur in the cap rock, could cause enough fault deformation to threaten the seal

3600 integrity (Zoback and Gorelick, 2012). This, along with the necessity to identify structural traps suitable
3601 for large-scale CO₂ storage in the North Sea (e.g. Osmond et al., 2022), has reinforced the need for
3602 robust monitoring of low-magnitude offshore seismicity (e.g. Zarifi et al., 2022). It is also important to
3603 remember that CCS and Oil and Gas activities may result in induced seismicity. For example, on May
3604 7, 2001, there was an Mw 4.3 vertical dip-slip seismic event in the Ekofisk field, resulting from an
3605 unintentional fluid injection (Selby et al., 2005; Ottemöller et al., 2005; Cesca et al., 2011; Dahm et al.,
3606 2015).

3607 The geological record is often used for the identification of paleoseismic events (e.g., Goldfinger, 2011;
3608 Kremer et al., 2017; Ojala et al., 2019), which commonly lacks historic documentation (Figure 6.18a).
3609 In passive continental margins such as our study area, this evidence is off-fault and considered as
3610 indirect evidence. Bellwald et al. (2019a) suggest based on marine sediments that over the last 11,000
3611 years, 33 earthquakes have simultaneously triggered submarine slides in different Norwegian fjords
3612 (Figure 6.18b), with a seismic activity highest during deglaciation, at around 8 ka, and in the past 4 ka
3613 (Figure 6.18c). The observations from the Norwegian sediment records match with the Swedish and
3614 Finish paleoseismic records (Figure 6.18c and 6.18d; Mörner, 2013; Bellwald et al., 2019a; Ojala et al.,
3615 2019). A higher seismic activity in the Late Holocene at around 4 ka is further supported by modelling
3616 of the reactivation potential of faults due to ice unloading in Northern Germany (Brandes et al., 2015),
3617 an area also affected by the Fennoscandian Ice Sheet. Sørensen et al. (2023) identified 22 landslides
3618 caused by eight earthquakes with M4.5-5.9 over the past 200 years in Norway, demonstrating that even
3619 in moderately seismic areas, earthquake induced landslides can occur with regularity. Along the
3620 glaciated European margins, several submarine mega-paleoslides have been identified (Table 6.1 and
3621 Figure 6.4). The most likely final trigger mechanism for these slides are earthquakes (Bellwald et al.,
3622 2019b; Eldholm and Bungum, 2021). For the Tampen Slide on the North Sea Fan, an earthquake of
3623 approximately Mw 6.9 or larger at a short distance from the headwall has been modelled to be the most
3624 likely triggering mechanism (Bellwald et al., 2019b).

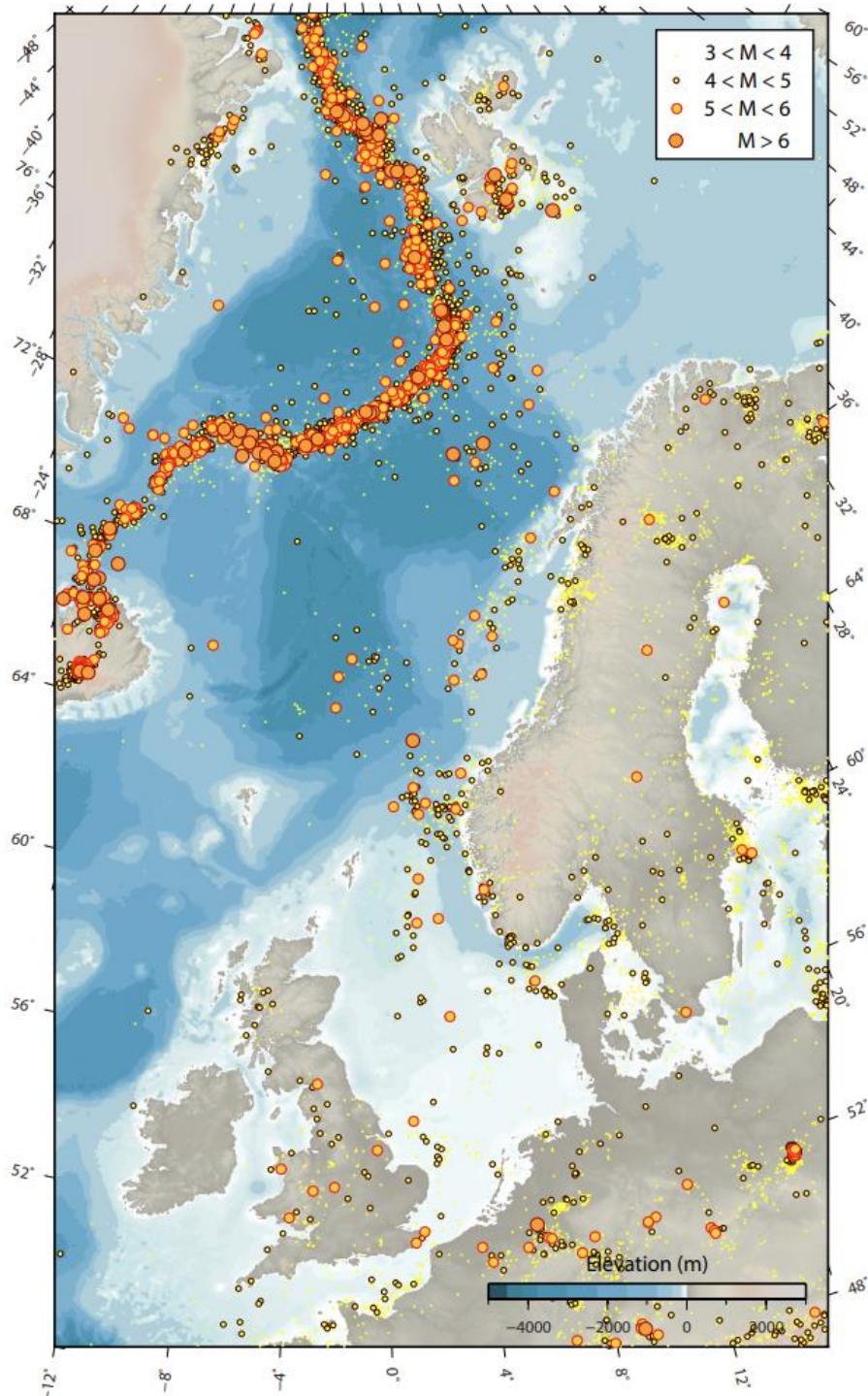
3625 The main geohazards related to earthquakes include primary effects such as shaking, fault displacement,
3626 and liquefaction, and secondary effects such as slope instabilities (Section 6.2), tsunami initiation
3627 (Section 6.6), and fluid release (Section 5.3) (Eldholm and Bungum, 2021), all of which can affect both
3628 society and infrastructure (e.g., Piper et al., 1988). Increased seismicity during deglaciation may have
3629 aided the escape of hydrocarbons from their source rocks through gas chimneys to produce pockmarks
3630 on the seafloor on the continental margins off Norway, the Barents Sea and Svalbard (Muir Wood and
3631 King, 1993; Olesen et al. 2004; Olesen et al., 2013, Eldholm and Bungum; 2021).



3632

3633 **Figure 6.16.** Peak ground acceleration (PGA) for $V_{S30} = 800$ m/s (soft rock) for a return period of 475
 3634 years from the SHARP project (Carlton et al. 2024).

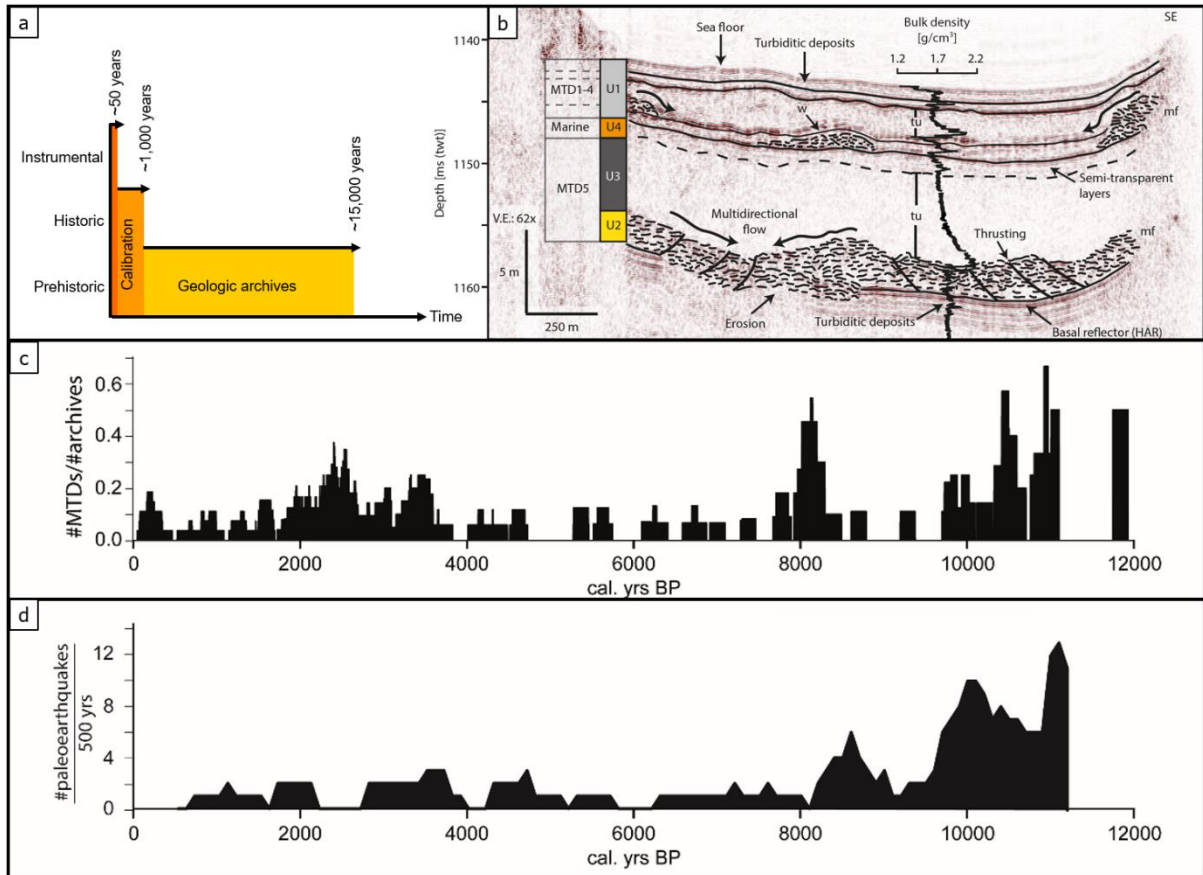
3635



3636

3637 **Figure 6.17.** Seismicity in Northwestern Europe, Scandinavia, and the surrounding seas from 1900 to
 3638 2022 as provided by the bulletin of the International Seismological Center (ISC, 2022). Events below
 3639 magnitude 3 are not displayed. Event clusters in Germany, the Netherlands, Poland, the Baltic Sea,
 3640 northern Sweden, and the Kola Peninsula are associated with mining and military operations and are
 3641 seldom natural earthquakes. The completeness of the underlying earthquake catalogue improves
 3642 dramatically in the most recent 30 years with the deployment and development of today's digital

3643 broadband seismic network (reference: [ISC, 2022. International Seismological Center Online Bulletin](https://doi.org/10.31905/D808B830)
3644 [[WWW Document](https://doi.org/10.31905/D808B830)]. <https://doi.org/10.31905/D808B830>)



3645

3646 **Figure 6.18.** Paleoseismic events in Fennoscandia. **a)** Geological archives as a tool for paleoseismic
3647 events. **b)** Multiple, coevally-triggered mass movements as proxy for paleoseismic event. Interpreted
3648 TOPAS seismic profile of the uppermost part of the infill of Hardangerfjorden. MTD5 indicates basin-
3649 wide, bi-directional mass flow (black arrows) and thrusting (black lines) of mass flow deposits, whereas
3650 multiple local wedges have been identified for MTD4, one wedge for MTD3, and no wedges for MTD1
3651 and MTD2 in this profile. Bulk density values shown are from the analyzed Calypso core. V.E.: Vertical
3652 exaggeration. Figure from Bellwald et al. (2016). **c)** Submarine mass movement activity in Norwegian
3653 fjords and lakes in the last 11,000 years (Bellwald et al., 2019a). **d)** Swedish paleoearthquake catalogue,
3654 with number of earthquakes within 500 years (from Mörner, 2013, and references therein).

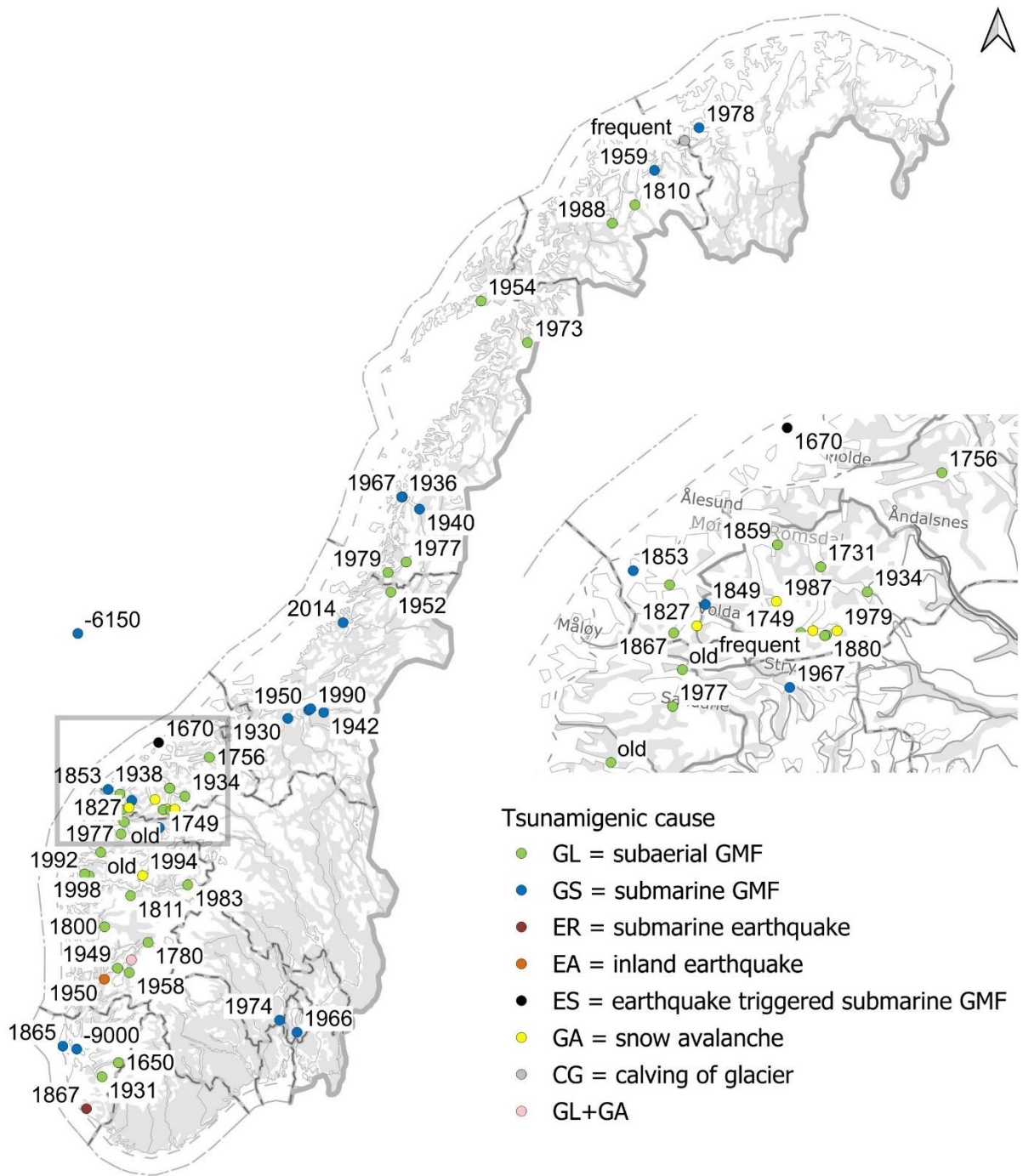
3655 6.6 Tsunamis

3656 6.6.1 Introduction

3657 Globally, earthquakes are the most frequent source of tsunamis. However, for the glaciated and
3658 currently passive European margin, gravity mass flows are the only significant source of tsunamis. For
3659 an extensive review of submarine landslide tsunamis, see Løvholt et al. (2022).

3660 Gravity mass-flow (GMF) tsunami sources in the glaciated European margin encompass submarine
3661 landslides (high-density flows like slides, slumps, debris flows, mud flows, and granular flows), and
3662 slides originating from onshore (or along the shoreline), including clay and quick-clay slides, debris
3663 flows, mud flows, rockslides, snow avalanches, and glacier calving. Depending on the material
3664 properties and speed of these mass flows, most of them (except rock, snow, and ice) can evolve into
3665 low-density turbidity currents of grains in turbulent suspension in the water (see [Chapter 6.3.2](#)).

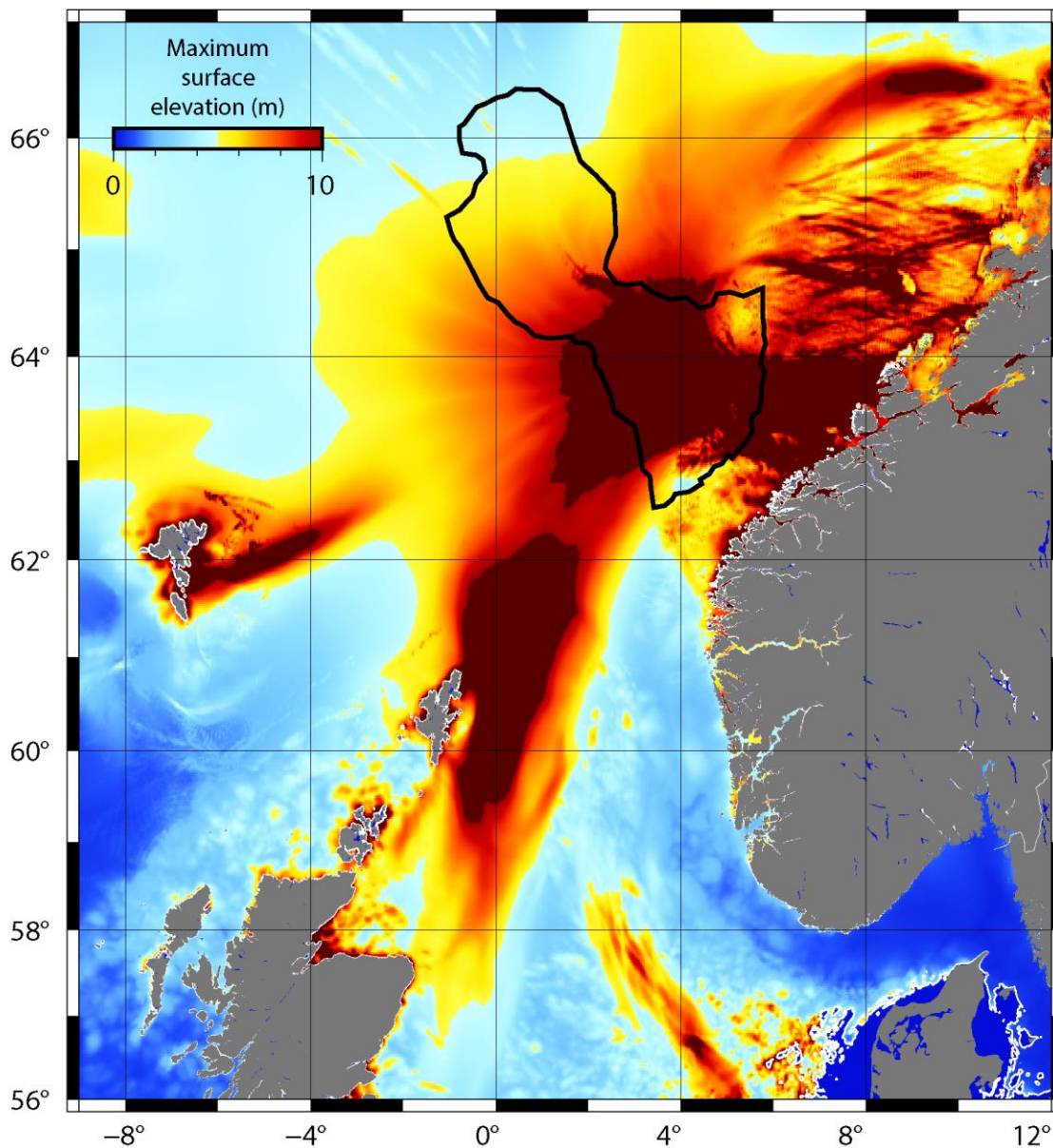
3666 The Euro-Mediterranean tsunami catalogue (EMTC, <https://doi.org/10.13127/tsunami/emtc.2.0>;
3667 [Maramai et al., 2019](#)) presently comprises 64 tsunami events in the Nordic Seas ([Figure 6.19](#)) spanning
3668 from an ancient 9000 BP Boknafjorden event inferred from archaeological interpretations ([Bøe et al.,](#)
3669 [2007](#)), via the well-documented 8150 BP Storegga slide and tsunami ([Figure 6.20](#); [Bryn et al., 2005a](#);
3670 [Bondevik et al., 2005a](#); [Kim et al., 2019](#)), to recent rockslide ([Harbitz et al., 2014](#); [Løvholt et al., 2020](#))
3671 and coastal (often quick-clay) landslide ([L'Heureux et al. 2011, 2013b, 2014, 2017](#); [Liu et al., 2021](#))
3672 tsunami events in the Norwegian fjords (events in lakes excluded). Out of these 64 events, we note that
3673 there are three small to moderately sized tsunami events caused by earthquakes in the region, four
3674 seiches events triggered by distant earthquakes, while the remaining 57 are caused by various kinds of
3675 mass flows. However, some tsunamigenic landslides may have been triggered by earthquakes, in
3676 particular during intensive periods of isostatic uplift following the final deglaciation. In this period,
3677 rockslide activity was also especially high ([Blikra et al., 2006](#); [NGU, 2009](#), [Bellwald et al., 2016](#);
3678 [Hermanns et al., 2017](#)), likely due to stronger isostatic uplift, more earthquakes, steeper reliefs, and
3679 permafrost melting ([Bøe et al., 2004](#); [Vorren et al., 2008](#); [Bellwald et al., 2019a](#)). The number of
3680 fatalities from fjord tsunamis is typically limited by the relatively local impact and sparsely populated
3681 settlements along the exposed coastlines; the event in historical times with the greatest number of
3682 fatalities (40) is the 1934 Tafjord rockslide tsunami (the 1905 and 1936 Lake Loen events with 61 and
3683 73 fatalities, respectively, are here excluded; [Harbitz et al., 2014](#)).



3684

3685

3686 **Figure 6.19.** Registered tsunami events in the Nordic Seas (with year of event). GMF = Gravity Mass
 3687 Flow. Seiche events triggered by distant earthquakes as well as all tsunami events in lakes are here
 3688 excluded.



3689

3690 **Figure 6.20.** “Wave directivity plot” showing maximum surface elevation in meters obtained during a
 3691 numerical simulation of the 8150 BP Storegga landslide and tsunami (using paleo-bathymetry). Surface
 3692 elevations greater than 10 m are shown in dark red. The thick black line indicates the outline of the
 3693 landslide runout area. Present-day land is shaded in grey, and the coastline of the paleo-bathymetry is
 3694 marked with a thin white line. Parameters for the numerical simulation are found in Bondevik et al.
 3695 (2024) and a new simulation of 20 hours following the slide was performed using the 8000 BP
 3696 bathymetric model of Clark et al. (2022).

3697 6.6.2 Basic mechanisms in tsunami generation

3698 Different types of GMFs have different tsunamigenic properties. The tsunamigenesis is primarily
 3699 controlled by the volume (length, height, width; for subaerial mass flows rather the frontal area) and
 3700 the dynamics of the mass flow (velocity u , acceleration a), as well as the water depth. The factors
 3701 controlling the landslide dynamics are primarily the slope angle, the volume and the rheological

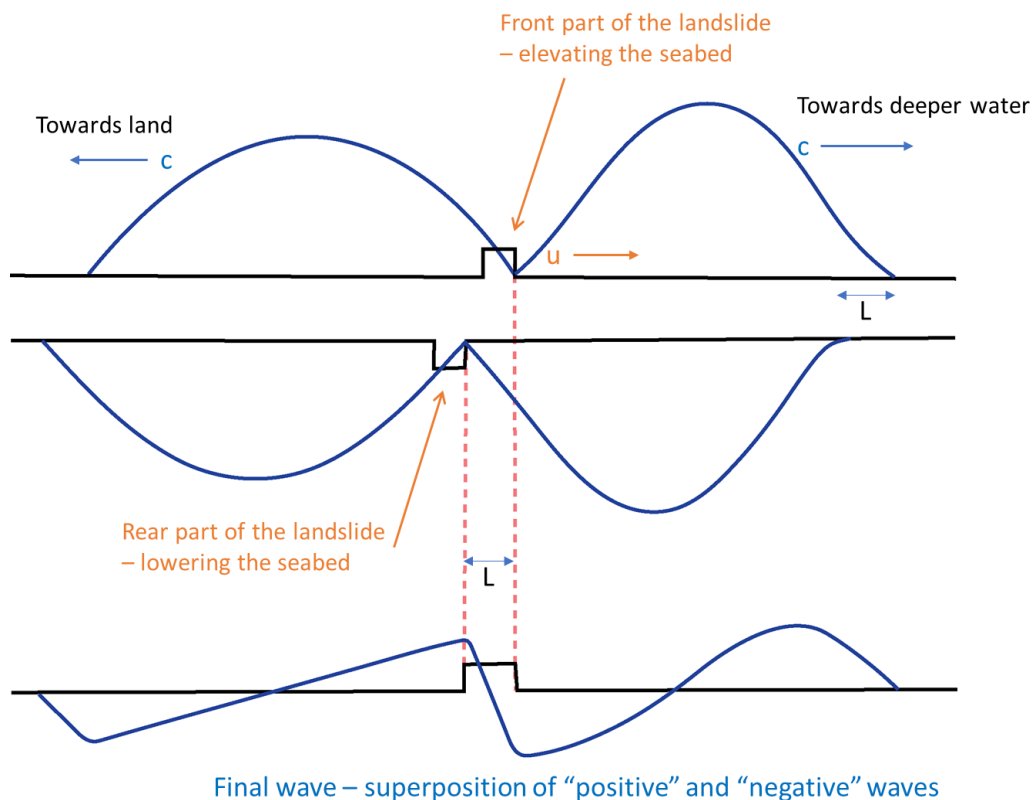
3702 properties of the landslide material (which in turn depend on the geological setting), as well as the
3703 external forces from the ambient water acting on the landslide. Submarine landslides with high clay
3704 content are more mobile than their subaerial counterparts and can reach high velocities (and long run-
3705 out distances) even on very gentle slopes. The mass flows go through various flow regimes from solid
3706 to fluid when evolving from failure to disintegration, remolding, erosion, and entrainment forming
3707 higher-density debris flows or lower-density suspension flows. The largest landslide volumes show the
3708 greatest mobility (De Blasio et al. 2006), while out-runner blocks being detached from the front of the
3709 slide due to hydroplaning can reach even longer run-out distances than the main body (Harbitz et al.
3710 2003; see also Section 6.3)

3711 Because of the strong influence of the complex topo-bathymetry on the dynamics, numerical models
3712 are needed to model the tsunami generation with sufficient accuracy (see e.g. Løvholt et al., 2015;
3713 Yavari-Ramshe and Ataie-Ashtiani, 2016; Behrens et al., 2021). Yet, simplified expressions relating
3714 either landslide geometry, friction, or ambient fluid resistance (e.g. Watts et al., 2005) or landslide
3715 kinematics (e.g. Zengaffinen et al., 2020) can offer hints regarding the parameter values governing
3716 tsunamigenesis.

3717 Submarine landslides are most often clearly sub-critical, implying that the Froude number (the ratio of
3718 the landslide velocity u to the linear shallow water wave celerity c), is much less than one. This implies
3719 that the tsunami will race away from the wave-generating landslide, limiting the build-up of the wave.
3720 Under such conditions, the maximum surface elevation increases with the landslide volume and
3721 acceleration but is inversely proportional to the wave speed (Løvholt et al. 2005; Figure 6.21). This
3722 scaling behaviour was explained through analytical models in simplified geometries by Haugen et al.
3723 (2005) but is also supported by earlier pioneering studies of Honda and Nakamura (1951) and Hammack
3724 (1973). This simplified analysis was performed assuming a very gentle slope and a non-deformable
3725 slide with a prescribed motion. With these assumptions it can be demonstrated that for debris flows, the
3726 related acceleration and deceleration phases may produce two sets of spatially and temporally shifted
3727 tsunami dipoles, each consisting of a positive and a negative surface elevation, that together form a
3728 quadrupole. For slumps, the surface elevation can be shown also to scale with the rotational dynamics
3729 (angular momentum; Zengaffinen et al., 2020). Slump acceleration processes may further happen so
3730 quickly that only one dipole is generated (see Løvholt et al., 2015). The tendency of submarine
3731 landslides to produce such an initial quadrupole-like tsunami shape, implies that landslide tsunamis are
3732 attenuated (radially) more efficiently compared with tsunamis from an earthquake dipole source that is
3733 distributed over a longer distance azimuthally along the fault. In addition, landslide tsunamis often
3734 produce shorter waves more subject to frequency dispersion, which may further reduce the potential for
3735 efficient far-field propagation (Glimsdal et al., 2013; Løvholt et al., 2015). However, landslides can
3736 generate larger vertical displacements than earthquakes and thus generate higher waves locally (e.g.,

3737 Okal and Synolakis, 2004). The commonly shorter waves are also more prone to amplification due to
 3738 shoaling (and possible wave breaking).

3739 For sensitive clay materials, the landslide can evolve like a series of blocks failing retrogressively
 3740 Kvalstad et al, 2005). A retrogressive failure normally reduces associated tsunami heights, but block-
 3741 wise retrogression might increase the height of the landward propagating wave for unfavourable time
 3742 lags between release of individual elements of the total landslide mass (e.g., Haugen et al., 2005;
 3743 Løvholt et al., 2016). Yet, Løvholt et al. (2017) showed that for large landslides a more rapid mass
 3744 mobilisation of a larger part of the slide body may follow even with a retrogressive failure initiating the
 3745 landslide, this may likely have been the case for the 8150 BP Storegga Slide. On the other hand, if the
 3746 retrogressive process is retained across the entire slide, or if there are major delays between the release
 3747 of individual slide blocks, the process is likely less tsunamigenic, which may have been the case for the
 3748 ~4000 BP Trænadjupet Slide.



3749
 3750 **Figure 6.21.** Illustration of how a landslide with length L and velocity u builds up a positive wave (with
 3751 celerity c) above its front where water is elevated (upper part of figure) until the build-up is cut off by
 3752 the negative wave formed above its rear end, where water is lowered and trailing a distance L behind
 3753 (mid part of figure). The two wave components combine to a dipole with a landward depression and a
 3754 seaward elevation (lower part of figure).

3755 Subaerial mass flows impacting the water body always give rise to super-critical wave generation in the
 3756 beginning, and they often produce an impact crater and ejection of the water body. Hence, the preceding

3757 tsunami propagation is therefore strongly affected by nonlinear effects in the initial stages. The
3758 generation, as studied in a high number of experimental analyses (see e.g. the analysis by Rauter et al.,
3759 (2021), or the review by Heller and Ruffini (2023)), is determined mainly by the frontal area, the impact
3760 velocity when plunging into the water body, and the water depth. As demonstrated by these studies,
3761 there is also a clear heterogeneity in the analytical expressions obtained from the experimental analysis.
3762 Hence, despite the large resources put into studies of gravity mass flow tsunamis in the laboratory, they
3763 have failed to produce predictive equations that are generally applicable. There has not been a similar
3764 number of numerical studies. This is partly due to the computational complexity needed to resolve the
3765 three-dimensional nature of the phenomenon, and partly due to the complex mechanics of rockslides.
3766 Yet, recent studies (e.g., Si et al., 2018; Macias et al., 2021; Esposti Ongaro et al., 2021; Rauter et al.,
3767 2022) show promise that improved predictive skills can be brought into numerical modelling of
3768 rockslide tsunamis, validated by both full-scale field observations and laboratory-scale studies. To this
3769 end, we note that also a set of benchmark studies for both submarine and subaerial landslides have been
3770 developed to improve model validation (Kirby et al., 2022).

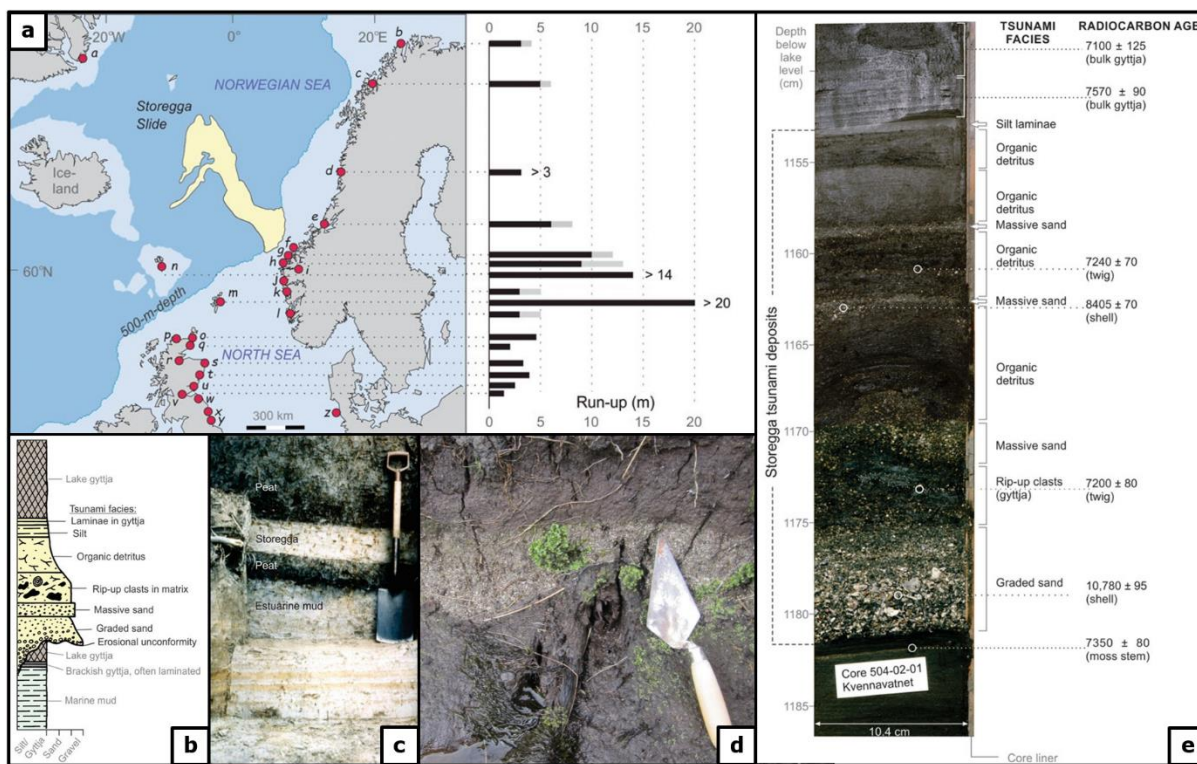
3771 6.6.3 Tsunami deposits

3772 When tsunamis flood the land, they may deposit sediments that over time may be well preserved, and
3773 along the coastlines of the North Atlantic these sediments are found along the coasts of Norway,
3774 Greenland, the Faroe Islands, and northern Britain (Figure 6.22; Bondevik and Svendsen, 1993;
3775 Bondevik et al., 1997a; Dawson et al., 1988; Dawson et al., 1993; Smith et al., 2004; Wagner et al.,
3776 2007; Bondevik, 2019). Failure of the most recent large-volume submarine landslides, the Storegga and
3777 Trænadjupet slides offshore Norway, would be expected to generate significant tsunamis, but the
3778 deposits identified so far have only been generated by the Storegga Slide, at 8150 BP, except for some,
3779 on the Shetland Islands, which are much younger, as they have been dated at 5,500 and 1,500 BP
3780 (Bondevik et al., 2005b). The origin of the younger deposits is unknown.

3781 The most prominent event deposits in the study area are the tsunami deposits triggered by the Storegga
3782 Slide (Figure 6.22): These deposits indicate that the runup height, of the tsunami varies between 10-11
3783 m along the Norwegian coast, 5 metres in eastern Scotland, to more than 20 m on the Shetland islands
3784 and in northern Britain (Figure 6.22a; Bondevik et al., 1998; 2019). The absence of sedimentary traces
3785 from the Trænadjupet Slide is supported by numerical modelling of the megaslide and its resulting
3786 (small) tsunami (Løvholt et al., 2017).

3787 Tsunamis are a large geohazard in modern fjord systems (Harbitz et al., 2014), but evidence on paleo-
3788 tsunamis is rather sparse, much due to a low preservation potential due to subsequent erosive processes
3789 and topography. In Boknafjorden, SW Norway, flint artefacts that are embedded in beach sediments are
3790 interpreted to be derived from near-shoreline sediments that were flooded and eroded by a slide-
3791 generated tsunami at approximately 10-9.7 ¹⁴C yr BP (Bøe et al., 2007).

3792 In 1580, an earthquake in the Dover Strait is proposed as triggering a cliff fall in the Chalk on the
 3793 southeast coast of England that triggered a tsunami that struck the coast of France with considerable
 3794 destruction to Calais and Boulogne (Neilson et al., 1984).



3795 **Figure 6.22.** Tsunami deposits of the Storegga Slide. **a)** Map of the Storegga Slide and tsunami deposits. Red dots show locations of Storegga tsunami deposits; Run-up estimates, inferred from deposits, are given to the right; black columns show minimum estimates, and gray columns give maximum estimates (from Bondevik, 2019). **b)** Description of the Storegga tsunami deposits (in yellow) presented as an idealized, complete facies sequence of tsunami deposits in nearshore lakes (from Bondevik, 2019). **c)** Outcrop at Maryton in the Montrose Basin, Eastern Scotland, shows the Storegga tsunami as a 25 cm thick silty sand deposit between peats. The estuarine mud is laminated silt and clay (Photo D. Smith, shown in Bondevik, 2019). **d)** Storegga tsunami sand, at Sullom Voe, Shetland. Note the underlying birch branch (trowel blade 12 cm long; Photo D.R. Tappin). **e)** Tsunami deposits in Kvennavatnet, Bjugn, Western Norway. Depth is cm below lake level. To the right is the description of deposits and radiocarbon ages (in ¹⁴C years BP). From Bondevik (2019).

3807 More broadly, tsunami deposits vary from laminated, graded to massive, depending on their sediment
 3808 composition and depositional mechanism (Figure 6.22b). The tsunami sediments in Norway are
 3809 preserved in coastal lakes located in uplifted basins, and deposited within marine or lacustrine gyttja
 3810 (peat) overlying an erosional unconformity surface (Figure 6.22e; Bondevik et al., 1998; Bondevik et
 3811 al., 1997b; Vasskog et al., 2013). In Scotland within subaerial peat layers, on which their dating is based,
 3812 and which allows their provenance to be ascertained by correlation with the source landslide (Figure

3813 6.22c). The lowermost sands are graded or massive and locally contain marine fossils. The sands thin
3814 and decrease in grain size in a landward direction. Overlying the sands is coarse organic detritus with
3815 rip-up clasts and finer organic detritus. The sands generally fine and thin upwards. In the higher basins
3816 (6-11 m above the 7000-year shoreline) there is one sand bed, whereas basins closer to the sea level
3817 7000 years ago, may show several sand beds separated by organic detritus. In basins that were some
3818 few metres below sea level at 7000 years BP, the tsunami deposit is more minerogenic and commonly
3819 present as graded sand beds. In some of these shallow marine basins, however, organic-rich facies occur
3820 between the sand beds. The total thickness of the tsunami deposit is 20-100 cm in most studied sites.
3821 Dating of organic matter in the tsunami deposits allowed their origin from the Storegga submarine
3822 landslide to be established (Figure 6.22e; Harbitz, 1992; Bondevik et al., 1998; Bondevik et al., 2005a).

3823 In Britain, the Storegga deposits extend from northeast England to the Shetland islands (Figure 6.22a).
3824 On Shetland, where they are best preserved, they are as follows (Smith et al., 2004). At the base, there
3825 is a sand and gravel surface, overlain to seaward by a grey silty clay which thins out landward and forms
3826 a gently sloping surface. Above the silty clay is a widespread layer of grey micaceous sand, up to 0.75
3827 m thick, containing fragments of vegetation (roots, stems and twigs) (Figure 6.22d).

3828 The Storegga tsunami deposits may contain fragments or intraclasts of organic material and intraclasts
3829 of silt (Figure 6.22b; 6.22e); there are rip-up clasts of peat. Above the sand, peat with horizons of
3830 organic silt and sand extends to the surface. The sand shows high values for corroded pollen and spores
3831 and the top, *Chenopodiaceae*. *Plantago maritima* in the sand layer, support a marine origin. No diatoms
3832 could be found in the fine sand, but the silty clay contains a few broken and eroded pennate forms,
3833 mainly *Pinnularia viridis*. The presence of *Pinnularia* fragments in the bottom silty clay is thought to
3834 indicate reworking of underlying freshwater (possibly peaty) sediments (Dawson et al., 1996). In
3835 eastern Scotland the tsunami deposits comprise a thin (centimetres) fine or fine-medium sand,
3836 sometimes with some silt and clay and very occasionally containing gravel or stones in the basal layers
3837 preserved within estuarine sediments or subaerial peats (Figure 6.22c; Smith et al., 2004). The high
3838 proportion of tythropelagic diatoms (i.e., those found living on bottom marine sediments), notably
3839 *Paralia sulcata* (Ehrenberg) Cleve, and some evidence of erosion of underlying sediments, originally
3840 led Smith et al. (1985) to interpret the sediments as deposits from a storm surge, but their continuous
3841 extent and height (15 metres) above sea level led to their reinterpretation as a tsunami deposit (Dawson
3842 et al., 1988).

3843 The evidence for the two younger tsunamis dated at 5,500 and 1,500 BP is from Shetland (Bondevik et
3844 al., 2005b). The sediment deposit of the 5,500 BP deposit is similar to that of the Storegga tsunami—
3845 rip-up clasts, sand layers, re-deposited material and marine diatoms. Runup was probably more than 10
3846 m. The 1,500 BP deposit is preserved in peat at two sites 40 km apart. The sand layer thins and fines
3847 inland and traced to ca 5–6 m above present high tide.

3848

3849 Evidence on the Dover Strait 1580 tsunami, triggered by a cliff fall, is limited. Effects on water were
3850 noticeable, especially since all accounts agree that at the time of the earthquake the weather was fine
3851 and calm. The agitation of the Thames is reported by Churchyard (1580) and others. In the English
3852 Channel, it was worse. At Sandwich, "the sea so foamed, that the ships tottered" (Stow, 1601). One
3853 contemporary account suggests that marine effects were more severe on the other side of the Channel.
3854 "In Calais ...there was such a horrible and fearful trembling that a great part of the houses collapsed and
3855 even the sea flooded into the town . . . In Boulogne there was a similar earthquake and flooding by the
3856 sea" (Coquerel, 1580). This may be a seismic sea-wave, but unfortunately there is some doubt about the
3857 time, and therefore about the actual relationship between earthquake and marine incursion. Elsewhere
3858 in the same document we find it stated that on the 7th of April between 4 and 5 a.m. (which
3859 coincidentally is the time of the third Kent aftershock) "there occurred in these places great signs of
3860 floods".

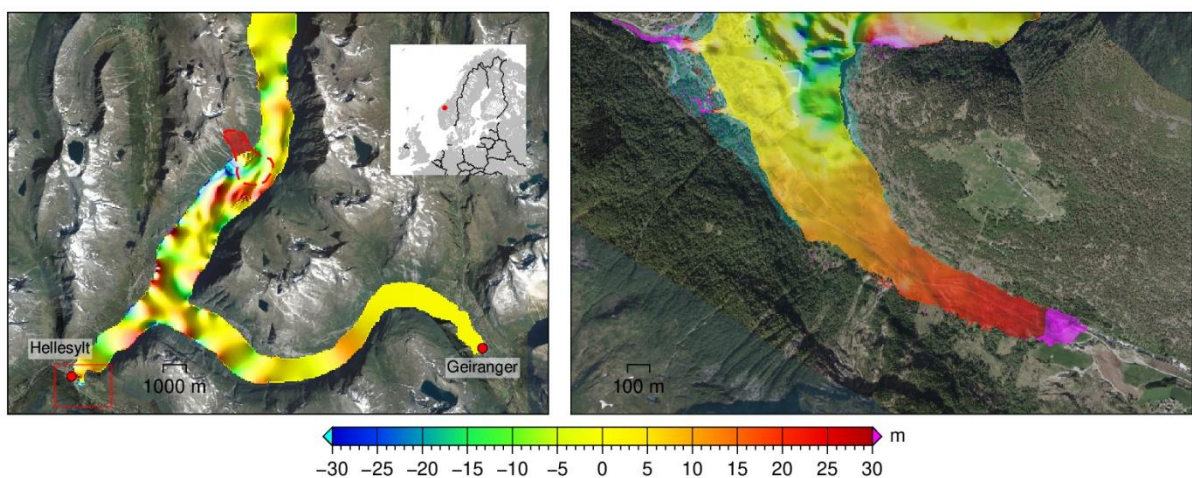
3861 6.6.4 Tsunamis as a geohazard on the glaciated European margins

3862 Both near-field and far-field potential tsunamigenic sources have been assessed for a first screening of
3863 regional tsunami hazard for the Northeast Atlantic (Harbitz et al., 2009). Trough mouth fans are
3864 locations with reoccurring megaslides (Nygård et al., 2005; Hjelstuen et al., 2007), and deserve specific
3865 attention (see Figure 6.3). Rapid sediment deposition on the North Sea Fan (location of the Storegga,
3866 Tampen, Møre, and Stad Slides) potentially builds up quite high pore pressures. However, preliminary
3867 studies of slope stability and the potential to develop new landslides concluded that the pore pressures
3868 in the North Sea Fan have been dissipating since the ice age (Bellwald et al., 2019b).

3869 Based on the present soil conditions and slope stability analysis, it is found that most of the unstable
3870 volumes are already released, and the stability of the offshore slopes is generally good. Hence, the
3871 present potential for large-scale tsunamigenic landslides in the Storegga/Ormen Lange area is also small
3872 (Kvalstad et al., 2005b; Nadim et al., 2005; Harbitz et al., 2009). It should be noted that global warming
3873 affecting the environmental impact might also influence slope stability (see Section 6.2.4).

3874 In conclusion, potential rockslides in the fjords of Norway and Greenland are considered the only high-
3875 risk tsunamigenic sources in the NE Atlantic (Harbitz et al., 2014). Figure 6.23 shows an example of a
3876 tsunami hazard analysis (based on long-wave equations) for the potential 54 Mm³ Åkerneset rockslide,
3877 western Norway. Future climate changes with global warming (implying more freezing–thawing
3878 situations and a potential role of permafrost melting) combined with more frequent and extreme
3879 situations of intense precipitation (leading to increased pore pressures) may increase the rockslide
3880 tsunami potential along the glaciated European margins (Hilger, 2019; Magnin et al. 2019). For
3881 Norway, the Norwegian Planning and Building Act has been altered to open for further development in
3882 exposed areas under given conditions. Probabilistic analyses of rockslide tsunamis are applied in hazard
3883 zoning and areal planning (Løvholt et al., 2020). Glacial debuttressing is the probable cause of a 25
3884 Mm³ rock-ice avalanche in a Greenland fjord in September 2023 that resulted in a tsunami with 200 m
3885 run-up (Svennevig et al., 2024).

3886 It should be noted that important segments of the continental margins surrounding the northern North
3887 Atlantic and Arctic Ocean are still not mapped in sufficient detail. Moreover, both submarine landslides
3888 and rockslides may cause potentially extreme tsunami run-up heights and dominate the (local) risk,
3889 which may be important for location and design of critical infrastructure often based on very long return
3890 periods (generally carrying the largest uncertainties).



3892 **Figure 6.23.** Example of tsunami hazard analysis; numerical tsunami simulation snapshots 400 s after
3893 a potential 54 Mm³ rockslide impacting the fjord at Åkerneset (area marked red), western Norway. Left
3894 panel: Tsunami propagation in Sunnlvsfjorden (linear dispersive equations). Right: High-resolution
3895 simulation of tsunami inundation at Hellesylt (nonlinear shallow-water equations). Figure based on
3896 simulations for the Åknes/Tafjord Beredskap IKS project.

3897 **7. Implications**

3898 Growth of near-shore population and increased scale of activities offshore due to energy transition and
3899 growth of blue economies, combined with the effects of climate change and geopolitical instabilities,
3900 mean that marine, especially continental shelf, areas are becoming more and more important. In the
3901 following chapter, we discuss the potential implications of geohazards and geo-engineering constraints
3902 on society and environment, offshore energy industries, and scientific drilling. We further summarize
3903 how the challenges vary in a regional context.

3904 **7.1 Society and environment**

3905 Marine geohazards and constraints related to marine geo-engineering can have a distinct societal
3906 impact:

- 3907 i) **Tsunami hazard:** Improved and advanced assessments – and particularly early warning
3908 systems – can save lives in urban centres along the coasts.
- 3909 ii) **Sites with cultural heritage:** The early identification of cultural heritage sites reduces the
3910 costs of the offshore infrastructure development.
- 3911 iii) **Environmental impact:** The environmental impact of anthropogenic actions can be
3912 reduced by detailed assessments. Keywords are shallow gas seepage, sediment
3913 remobilization, the presence of (cold-water) corals and benthic communities, but also
3914 anthropogenic features such as UXO (unexploded ordnance: mines, bombs, ammunition
3915 dumps).
- 3916 iv) **Geoscience mindset:** Specific skills are required for acquisition and interpretation of
3917 required datasets, in particular for the renewable energy transition. Working in a multi-
3918 disciplinary team, often consisting of geologists, geophysicists, geotechnical engineers,
3919 laboratory analysts, and numerical modellers (and as of late data scientists), is another
3920 requirement.

3921 **7.2 Offshore energy industry**

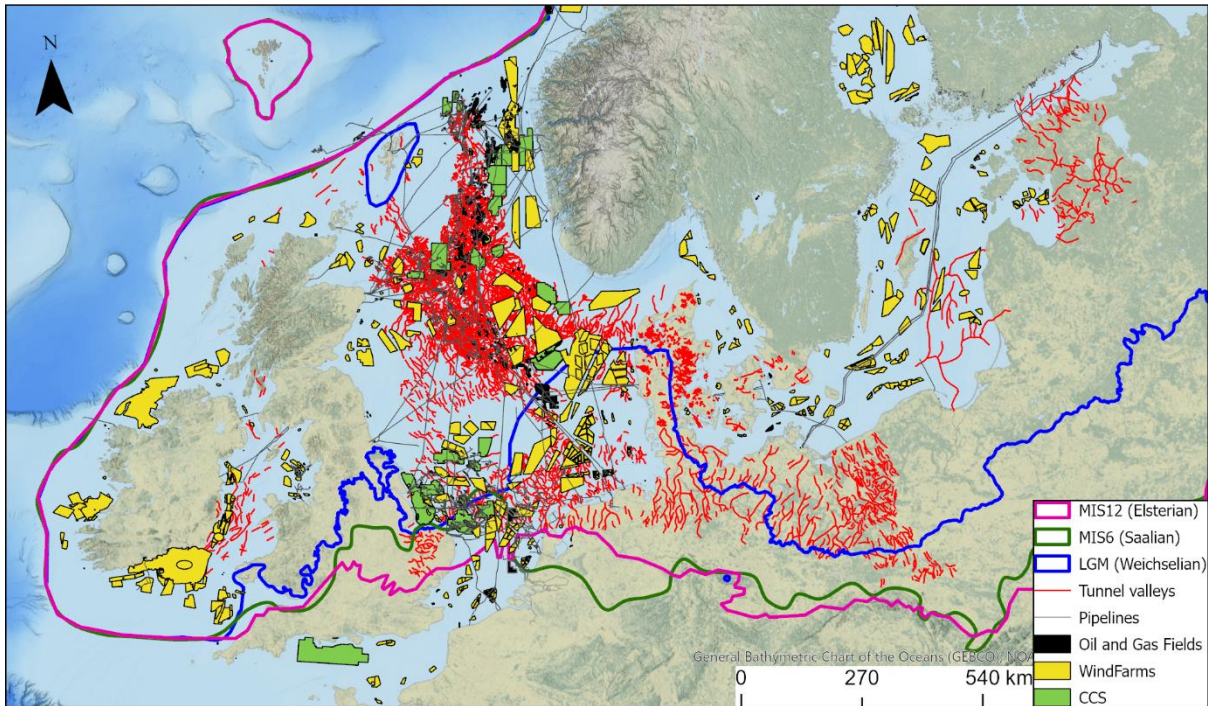
3922 The different sectors of the offshore energy industry have different needs ([Table 7.1](#)), and the ongoing
3923 energy transition may require a different focus on geohazard assessment and their importance (e.g.,
3924 [Velenturf et al., 2021](#)): The offshore wind industry typically targets much larger geographical areas and
3925 will require more densely spaced infrastructure compared to the infrastructure required by the
3926 hydrocarbon industry. Thus, certain hazards and particularly engineering constraints might be more
3927 frequent and not avoidable in offshore wind compared to the smaller acreage required for seafloor
3928 infrastructure in the hydrocarbon industry. However, the wells and deviated wells planned in the
3929 hydrocarbon industry require some planning and dedicated efforts too, covering several kilometers in
3930 depth.

3931 The different types of offshore energy technologies are affected by ecological, societal, and economic
 3932 factors: Although costs of offshore wind and other renewable technologies have rapidly decreased in
 3933 the last years (e.g., [Taylor et al., 2020](#)), these energy sources have currently very low profit margins
 3934 compared with oil and gas, and incorporate challenging financial conditions ([Table 7.1](#); [Virtanen et al.,](#)
 3935 [2022](#)). Despite the lower profitability, renewable energies have often a high societal acceptability
 3936 ([Karakosta et al., 2013](#); [Ahsan and Pedersen 2018](#)).

3937 **Table 7.1.** Comparison of different offshore-energy branches. HC: Hydrocarbon (oil and gas), CCS:
 3938 Carbon capture and storage. Conv: Conventional. MBES: Multi-beam echosounder, MSCL: Multi-
 3939 sensor core logger, SSS: Side-scan sonar. *seabed infrastructure, **exploration

| | HC and CCS | Offshore wind | Cable routes |
|---|--|--|--|
| Budget | High | Moderate | Low |
| Schedule | Wide | Tight (cycles are shorter) | Very tight |
| Profit margin/Profitability of project | High for HC; low for CCS | Moderate | Moderate |
| Areal extent (km²) | 1*-10,000** | 100-1000 | 10-100 |
| Subsurface depth of investigation (m) | 1000-6000 | <200 | <10 |
| Subsurface complexity | Moderate (as area of interest is smaller due to site investigations and often in deeper waters) | Very high (uppermost c. 100 m of large areas) | High (uppermost 6 m are of interest over very long distances, sometimes >100 km) |
| Geology | (Un-)Consolidated sediments*, bedrock** | Mobile sediments, (un-)consolidated sediments, bedrock | Mobile sediments, (un-)consolidated sediments, bedrock outcrops, soft sediments |
| Geophysical dataset | Conv3D (sometimes bottom nodes), HR2D/3D (reservoir and overburden); Foundation -> see offshore wind | 2DUHRS, 3DUHRS, SBP, SSS, MBES, magnetometer, metocean, seismic CPTs, MSCL | SBP, (Repeated) MBES, SSS, magnetometer |
| Geotechnical dataset | 10s of CPTs | 100s-1000s of CPTs; 10s-100s of BHs | Vibrocores (c. 1/km); Shallow CPTs (c. 1/km) |
| Resources for data interpretation | High | Moderate | Low |
| Amount of data | High | Very high | High |
| Data accessibility | Partly accessible after some years | Full access depending on national regulations | Full access depending on national regulations |

3940



3941

3942 **Figure 7.1.** The presence of tunnel valleys and their overlap with the different sectors of offshore energy
 3943 as shown for the southern part of the study area. Windfarms shapes include blocks defined as suitable
 3944 for future application rounds.

3945 7.2.1 Offshore wind

3946 By 2024, 37 GW of offshore wind have been installed in Europe (WindEurope, 2024). The global
 3947 demand for renewable energy is on the rise, and Europe could deploy up to 450 GW of offshore wind
 3948 by 2050 (Ramirez et al., 2020; WindEurope, 2024). Most of this energy is produced by windfarms
 3949 located on the formerly glaciated European margins, with the UK and Germany currently leading the
 3950 deployment.

3951 Depending on water depths and soil-rock conditions, a range of offshore foundations are used in
 3952 offshore wind. Most of the windfarms are located in regions with water depths of <40 m, some up to
 3953 80 m, with fixed foundations (e.g., monopiles, suction caisson jackets or piled jackets). These areas
 3954 with shallow water depths were terrestrially exposed platforms during the Quaternary glaciations and
 3955 sea level oscillations, and include a multitude of glacialigenic landforms.

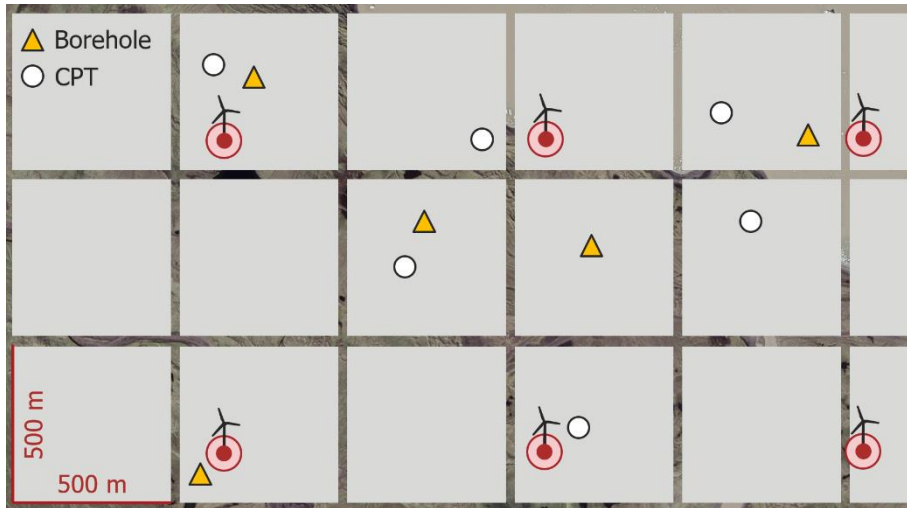
3956 Many glacialigenic landforms incorporate complexities (e.g., changing soil conditions); the best examples
 3957 for lateral variability are arguably glacial channels and tunnel valleys (Figure 5.41; Bellwald et al.,
 3958 2024c). The acreage defined for offshore wind (e.g., in the North Sea Basin) often coincides with
 3959 mapped tunnel valleys (Figure 7.1). These channels can have formed in several generations and be
 3960 located at multiple stratigraphic levels. Their infill, in addition, can be vertically changing on small
 3961 scales, thus requiring a proper subsurface characterization (Figure 5.41). This has implications for any
 3962 offshore energy business.

3963 Centimeter- to meter-scale lateral and vertical variability are important in offshore wind (Figure 7.2):
3964 The widths of existing monopiles vary from 4-15 m, and the footprint for certain foundation designs
3965 reaches 50 m with an engineering zone of influence around these considerably larger. Within such
3966 distances, the subsurface might change drastically (Figure 7.2).

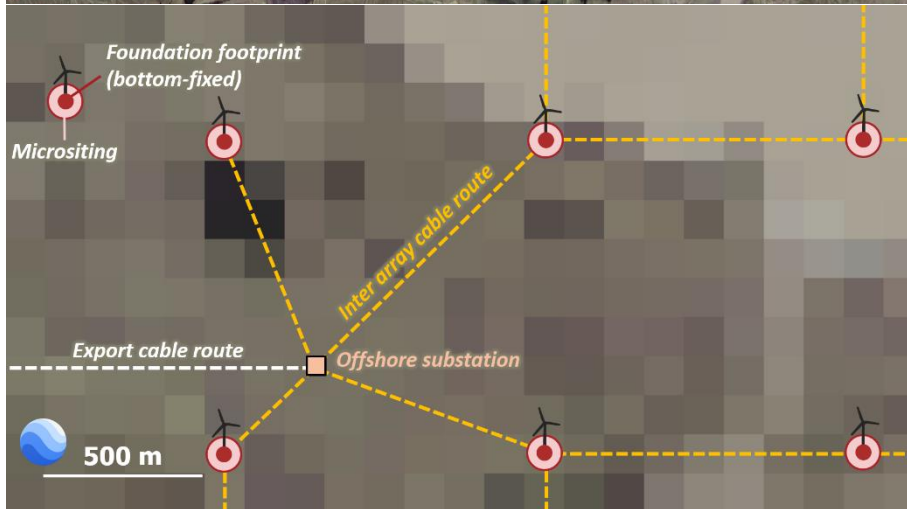
3967 It is also important to consider the operations and maintenance of offshore wind farms, particularly in
3968 shallower water where jack-up vessels are the vessel of choice for many operators. Jack-up activities
3969 are sensitive to a range of risks associated with vertical and lateral variability and a suitable footprint
3970 around foundation locations should also be considered to de-risk these activities.

3971 However, offshore wind turbines become larger and are gradually moving into deeper waters. Different
3972 foundation types are designed and installed in these deeper waters. Additional hazards or geo-
3973 constraints for floating wind (compared to fixed foundations) are deep-ocean currents, deepwater
3974 geohazards such as landslides and turbidity currents, gas hydrates (if occurring in foundation zone), and
3975 possible free gas trapped in the subsurface. Floating wind anchor solutions also have a wide footprint,
3976 and more contact points with the seabed than fixed bottom solutions, meaning characterising lateral
3977 variability is just as important for these sites.

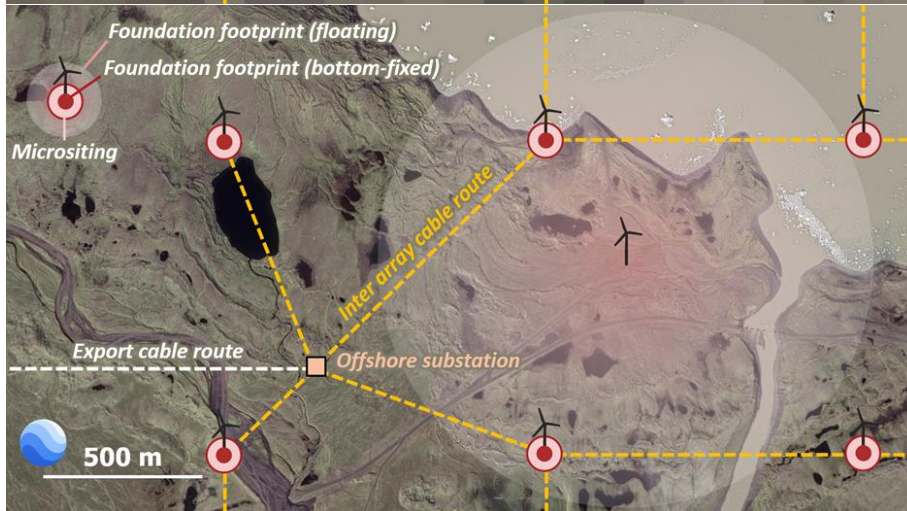
3978



3979



3980



3981 **Figure 7.2.** Glacial landscapes with extremely complex lateral changes (Fjallsárlón, SE Iceland).
 3982 Circles around WTGs have 25 m radius for foundation footprint and 50 m radius for micro-siting. Upper
 3983 panel: Early-phase offshore wind setup, with CPTs and boreholes away from the 2D seismic grid.
 3984 Central panel: Planar view of interpreting a densely-spaced 2D seismic grid (here 125 m bin size).
 3985 Lower panel: Planar view of interpreting a EHR3D seismic grid (here 1 m bin size). Satellite imagery
 3986 from 9/2019 CNES Airbus.

3987 7.2.2 Cable routes

3988 The transfer of energy from the offshore windfarm to the national power grids occurs via export cables.
3989 The export cable routes (ECR) are 10s to 100s of kilometres in length and may cross highly variable
3990 lithologies in commonly changing Quaternary terrains (Figures 7.2 and 5.19). Cable-route surveys are
3991 thus shaped as very long but narrow corridors, often limited to c. 100-400 m on either side of the cable
3992 allowing for flexibility in exact cable location within the corridor. The uppermost meters (e.g., 6 m) are
3993 usually of interest for cable burial risk assessment (Carbon Trust, 2016). In addition, inter-array cables
3994 (IAC) link individual wind turbines and deliver power to the offshore substation (OSS) or offshore
3995 converter platform (OCP). The OSS collects the power of the wind turbines and prepares it for
3996 transmission to shore. The OSS or OCP structures can be very large, with a footprint substantially
3997 exceeding that of the turbine foundation solutions. The goal of a cable-run setup is to define and derisk
3998 an effective route. Apart from cabling for offshore wind, submarine interconnector cables, supplying
3999 power between two land locations, or telecommunication cables, providing data links, are also
4000 frequently placed at and below the seabed on glaciated continental margins. Major challenges for most
4001 cable projects include:

- 4002 i) Complex geological settings: Physical material is commonly sampled in vibrocores
4003 combined with shallow CPTs, with an arbitrary spacing of c. 1 core per few hundreds of m
4004 to few kilometers (DNV, 2014). However, even within one kilometre, geospatial variability
4005 can be significant, and potentially affecting the operations (e.g., trenching, jetting).
4006 Sampling locations should be carefully considered in conjunction with ultra-high-
4007 resolution seismics (sub-bottom profiling) and geological data to optimize sampling in
4008 different soil types to ensure representative sampling.
- 4009 ii) Seafloor and sub-seafloor obstructions: The cable-route layouts are defined to avoid
4010 boulders or boulder fields, as moving or relocating boulders can be challenging, particularly
4011 if they are partially embedded in dense sand or high strength clay. Depending on the
4012 selected trenching technique, the critical boulder size can vary as well. Other obstructions
4013 could include environmentally sensitive habitats or archaeologically significant features.
- 4014 iii) Thermal conductivity: The transfer of electricity in cables causes the cables to heat up, and
4015 heat will dissipate into the surrounding soil or water medium. When heat dissipation is
4016 limited (e.g., cable in resistive materials), the transmission capacity reduces and can cause
4017 cable failure. Identification of thermally insulating materials within the ground from
4018 seismic data and geotechnical boreholes and testing (for example clays or organic-rich
4019 sediments and ashes), as well as in situ and laboratory thermal conductivity measurements
4020 are therefore crucial.
- 4021 iv) Steep slopes and high-angle gradients, associated with seabed morphology including
4022 mobile bedforms, outcropping geology or channel incisions, can present considerable

4023 challenges to installation vehicles and would normally be routed around. In areas of seabed
4024 mobility, pre-dredging may occur to create a suitable route through, with natural reburial.
4025 v) Rockhead or hard substrate present a considerable difficulty to cable installation, and it is
4026 often preferred to route to avoid having to install within those materials. However, closer
4027 to shore such conditions may be unavoidable, and a balance must be struck between costly
4028 installation methods and costly protection methods such as imported rock armour. It is
4029 therefore important to identify and map potential rock outcrop or subcrop along cable
4030 routes, and geotechnically characterise them sufficiently to understand the correct approach
4031 to take.
4032 vi) Also important is the potential for free-span, i.e., the cable becomes suspended between
4033 two points on the seafloor, which needs careful attention in the design. Free-span can be
4034 caused by uneven or undulating seafloor, current-induced erosion, scouring or seabed
4035 mobility, or hard seabed features. Free-span may result in fatigue, increased stress on the
4036 cable connections, higher likelihood of mechanical failures, and as indicated above,
4037 potential for overheating due to poor heat dissipation.

4038 7.2.3 CCS and hydrocarbon industry

4039 Capture and storage of CO₂ in geological formations represent an important measure with a large
4040 potential to reduce global greenhouse gas emissions (NPD, 2014). On the glaciated European margin,
4041 the CO₂ storage projects in operation are Sleipner, Greensand, Longship (all North Sea) as well as
4042 Snøhvit (Barents Sea). Approximately 1 Mt of CO₂ have per year been stored in Sleipner since 1996,
4043 and approximately 0.7 Mt of CO₂ have been safely injected and stored in the Snøhvit CCS project since
4044 2008 (NPD, 2014). 28 of the 43 European CCS projects are located within the glaciated European
4045 margins (IOGP, 2024; Figure 7.1). Until 2030, the annual CO₂ storage capacity of projects planned in
4046 Norway, the UK, Denmark, and the Netherlands account for approximately 87 MtCO₂/yr (compared to
4047 the approximately 4.7 MtCO₂/yr in operation in 2024; IOGP, 2024). This development shows that
4048 geohazard assessments and geo-engineering constraints in these glaciated settings will have to be
4049 analysed and monitored on larger scales in near future. Understanding the engineering properties of the
4050 Quaternary sediments are key to guarantee a safe and sustainable storage of CO₂.

4051 Several oil and gas fields are in operation from the mid-20 century onwards on the glaciated European
4052 margin, particularly on the UK Continental Shelf and the Norwegian Continental Shelf (Figure 7.1;
4053 5.41). Reservoir rocks commonly are of Paleozoic, Mesozoic, or Paleogene age. However,
4054 unconventional hydrocarbon models include Quaternary deposits for gas reservoirs (Huuse et al., 2012;
4055 Bellwald et al., 2022b). Structures and processes related to these deeper stratigraphic levels, such as salt
4056 tectonics and sill intrusions, can impact the Quaternary systems and deposits (see Figures 5.32 and
4057 5.38). The most prominent discoveries of Quaternary hydrocarbon reservoirs include the Peon field in
4058 the Northern North Sea (Figure 2.6) and the Aviat field in the Central North Sea.

4059 Quaternary sands might be charged with gas, as proven by the Peon discovery in the Northern North
4060 Sea. Despite proven as a gas discovery, the Peon field has not been developed yet. This might change
4061 with Norway's ambition to supply gas to Europe with the current geopolitical outlook, and it was stated
4062 that more wells are planned to be drilled around Peon ([Upstreamonline, 2025](#)).

4063 More commonly, Quaternary sediments act as the seal for the underlying pre-Quaternary reservoir
4064 rocks. Knowhow on the Quaternary (e.g., lateral heterogeneities) is important to properly image CCS
4065 and O&G reservoirs. Landforms identified in the overburden, such as tunnel valleys and their infill,
4066 might result in wrong conclusions when imaging the deeper reservoirs.

4067 The uppermost meters of the Quaternary stratigraphy are in addition very important for platform
4068 foundation, well placement, and well stability. Data collected for hydrocarbon exploration are
4069 commercially highly sensitive, compared to the less sensitive data collected for windfarm projects.

4070 Hydrocarbon exploration may extend into frontier areas, such as the Arctic waters of the Barents Sea,
4071 which is not yet seriously considered for offshore wind. However, there is serious public debate and
4072 concern over such developments. A safe assessment in these frontier areas, with additional geohazards
4073 and geo-engineering challenges, is key to convince society and stakeholders.

4074 7.2.4 Cable and pipeline landfalls

4075 The interface between land and sea is a complex juncture of physical processes (marine, terrestrial and
4076 atmospheric), anthropogenic use, and industry development. Bringing cables or pipelines ashore means
4077 crossing this boundary, and to do so conditions in all systems should be understood to engineer a
4078 suitable solution. Due to sea-level change and glacio-isostatic adjustment ([Section 6.4](#)), the coastline is
4079 dynamically evolving and, in some places, continues to respond to local and global changes. Therefore,
4080 consideration must be made not only to current conditions but past and future conditions as well when
4081 engineering the ocean-land interface.

4082 The geology and geomorphology of the landfall will often dictate the method of installation and
4083 subsequently how to investigate it. The two main options for landfalls are open cut and Horizontal
4084 Directional Drilling (HDD). The most common option for offshore wind is HDD, as it is less disruptive
4085 and obtrusive than an open cut. Drillers often prefer soils with good consistency, and so previously
4086 glaciated soils can present a particular challenge to HDD, which can encounter issues with:

- 4087 • Variable soils, which affect drilling pressures and progression if incorrectly characterised, for
4088 example beds of sand within stiff clays which can be washed out by drilling fluids;
- 4089 • Cemented layers, or beds of cobbles or boulders, which can alter the course of the drilling head
4090 away from the desired course;
- 4091 • Large individual very hard boulders, particularly stiff soils which cannot be drilled through or
4092 moved aside by the drill-head and directly obstruct or slow down drilling progression.

4093 It is therefore critical to correctly investigate the site to fully characterise ground conditions ahead of
4094 HDD works. However, the methods of geophysical, geotechnical and metocean investigation
4095 techniques in these areas can be variable and challenging. For example, restrictions on vessel size during
4096 geophysical surveys may restrict what equipment can be used compared to a “normal” offshore survey,
4097 and data types used in the nearshore zone need to be compatible with both onshore and deeper-water
4098 surveys.

4099 In addition to engineering for the current coastline, offshore energy developers need to be conscious
4100 of future changes to sea-levels, coastal position and erosion rates. Cable landfall HDD positions in
4101 areas with high erosion will need to be suitable for the future lifetime of the offshore project, so
4102 predictions of sea-level change and erosion rates/future positions need to be predicted for 30 to 50
4103 years into the future to be correctly designed. Previously glaciated soils, such as those on the East
4104 Riding of Yorkshire, are associated with some of the highest erosion rates in the world and also home
4105 to many of the North Sea wind farm cables coming into shore.

4106 **7.3 Scientific drilling**

4107 Drilling for scientific research is of crucial importance as it provides direct access to the geological
4108 records beneath the Earth’s surface in very-high (vertical) resolution, which sheds light on our
4109 understanding of the Earth systems, climate changes, oceanography and natural hazard assessments.
4110 The International Ocean Discovery Program (IODP), and its previous iterations, have been the main
4111 vehicle for this type of academic research, collecting up to ~500 km of core from across the globe since
4112 the late 1960s (IODP, 2024). From a drilling perspective, the documentation of geohazards, such as
4113 submarine landslides, methane hydrates, and fault zones, are all crucial for ensuring safe drilling
4114 operations and limiting the potential for wellbore collapse and the loss or damage of equipment. In
4115 order to drill through such features requires advanced geotechnical assessments and engineering
4116 protocols that are largely unaffordable outside of the energy industry. Thus, in such instances, scientific
4117 drilling, like that by IODP, must prioritise more cost-effective solutions. Often this will mean that drill-
4118 site planning deliberately avoids these strata entirely, requiring geohazard workflows for avoiding
4119 problematic features (Cox et al., 2020). The documentation of geohazards is not restricted to just drilling
4120 operations, but are themselves an area of scientific research. This is because of the potential to extract
4121 profound insights into Earth's dynamic processes, such as earthquakes, landslides, and tsunamis from
4122 the analyses of rock, sediment, and fluid samples that make up these hazards (IODP, 2020). These
4123 records can yield information on past climate changes and natural disasters, providing important
4124 information on the timing, the magnitude, and the nature of how these geohazards evolved in the first
4125 place, their initiation points, and the characteristics of potential preconditioning (IODP, 2020). All of
4126 this research is crucial for developing predictive models and risk mitigation strategies for natural
4127 hazards, as well as the development of engineering strategies for disaster preparedness and response.

4128 As outlined in this review paper, the northwest European margin has a wide range of geohazard features
4129 at a variety of different scales. Scientific drilling plays an important role in understanding the nature of
4130 these geohazards, while the geohazards and geo-engineering constraints themselves can provide a
4131 limiting factor on what can be drilled – i.e., it can be a bi-directional relationship. As such, there are
4132 several proposals currently under consideration that seek to target the Quaternary stratigraphy offshore
4133 northwest Europe and the potential insights that they may hold (e.g., Newton et al. (2024b) that seeks
4134 to drill in the North Sea). These proposals have required a detailed understanding of the nature and
4135 distribution of geohazards in the region. Knowledge on the geohazards on northwest Europe also have
4136 an increased relevance for the energy transition, where geohazards impact not just the initial drilling
4137 operations, but also the subsequent efficacy of potential sites to achieve their aims. For example, how
4138 subsurface geohazard features may have a positive or negative effect on the migration of greenhouse
4139 gases in potential sequestration aquifers (e.g., Lloyd et al., 2021). Documenting the distribution of
4140 geohazards on the northwest European margin is going to continue to be crucial for understanding
4141 climatic changes of the past and mitigating climate changes of the future.

4142

4143 **7.4 Implications for different regions of the glaciated European glaciated margin**

4144 The importance of geohazards and geo-engineering constraints depends on the region within the
4145 glaciated European margin. In the following table, we summarize the likelihood of the different
4146 geohazards and geo-engineering constraints depending on the location in the study area (see [Chapter](#)
4147 [2](#)).

4148 **Table 7.2.** Summary of geo-engineering constraints and geohazards in the different regions of the study
 4149 area. Traffic-light system is relative, with red: high potential of constraint/hazard, orange: moderate,
 4150 yellow: low.

| | | Barents Sea | Mid-Norway | Northern North Sea | Central North Sea | Southern North Sea | Baltic Sea and Gulf of Bothnia | Irish Sea and Celtic Sea | Outer Hebrides and Rockall | West of Shetland |
|------------------------------------|--|-------------|------------|--------------------|-------------------|--------------------|--------------------------------|--------------------------|----------------------------|------------------|
| Geo-engineering constraints | Shallow gas | Red | Orange | Red | Red | Red | Red | Yellow | Orange | Orange |
| | Gas hydrates | Red | Orange | Yellow | Yellow | Yellow | Yellow | Yellow | Yellow | Yellow |
| | Fluid flow | Red | Orange | Orange | Orange | Orange | Orange | Yellow | Orange | Orange |
| | Strength variability | Orange | Orange | Orange | Red | Red | Red | Red | Red | Red |
| | Boulders | Yellow | Yellow | Yellow | Red | Red | Orange | Yellow | Red | Red |
| | Gravel and pebble beds | Yellow | Yellow | Orange | Red | Orange | Orange | Red | Red | Red |
| | Soft marine sediments | Yellow | Yellow | Orange | Red | Orange | Orange | Orange | Red | Orange |
| | Weathered and unweathered bedrock (<200m) | Red | Yellow | Yellow | Orange | Red | Red | Red | Red | Yellow |
| | Organic materials and peat | Yellow | Yellow | Yellow | Yellow | Orange | Yellow | Yellow | Orange | Yellow |
| | Faults and fractures | Orange | Yellow | Yellow | Orange | Orange | Orange | Yellow | Red | Orange |
| | Glaciotectonic deformation | Red | Yellow | Yellow | Red | Red | Orange | Yellow | Orange | Orange |
| | Salt tectonics | Orange | Yellow | Orange | Orange | Orange | Orange | Yellow | Yellow | Yellow |
| | Glacigenic landforms | Orange | Orange | Orange | Red | Red | Orange | Orange | Red | Red |
| Geohazards | Sediment transportation and mobility | Orange | Yellow | Yellow | Orange | Orange | Yellow | Orange | Orange | Yellow |
| | Slope instabilities (at slopes; not fjords) | Orange | Orange | Orange | Yellow | Yellow | Yellow | Yellow | Orange | Yellow |
| | Glacio-isostatic adjustment; sea-level changes | Yellow | Orange | Orange | Orange | Orange | Yellow | Yellow | Yellow | Yellow |
| | Seismicity | Orange | Yellow | Yellow | Yellow | Yellow | Yellow | Yellow | Yellow | Yellow |
| | Tsunamis | Yellow | Yellow | Yellow | Yellow | Yellow | Yellow | Yellow | Yellow | Yellow |

4151

4152 **8. Summary**

4153 Processes related to glaciations and sea-level changes have defined sediment deposition in glaciated
 4154 regions over the last 2.58 million years, the time period called the Quaternary. The Quaternary
 4155 sediments along the glaciated European margin form a complex subsurface with thicknesses of some
 4156 10s to 100s of meters on the shelves, and 100s to 1000s of meters on the upper slopes and the central
 4157 North Sea. Changing sedimentary environments resulted in extreme geospatial variability, from basin
 4158 scale (e.g., instanced of large-scale instabilities) to local scale (e.g., specific glacial landforms like
 4159 moraines, eskers, etc.) as well as micro-scale (composition, porosity, permeability). As a consequence,
 4160 these deposits can host static geo-engineering constraints, which have different complexities: i) changes

4161 in grain sizes from fine clay to boulders, ii) accumulations of shallow gas, gas hydrates, and
4162 overpressured layers potentially resulting in fluid flow and fluid seepage, iii) composition and strength
4163 variability in particular related to glacigenic landforms, iv) faulted, fractured, and deformed packages,
4164 and v) high-organic-content sediments (e.g., presence of peat).

4165 Dynamic Earth processes affect and interfere with the Quaternary sediments, and form a variety of
4166 potential geohazards: i) seabed mobility, ii) slope instabilities, iii) earthquakes, iv) tsunamis, v) sea-
4167 level changes, and vi) glacio-isostatic adjustments. Some of these geohazards are challenging to identify
4168 and forecast (e.g., earthquakes, tsunamis); they affect large areas, and occur on short time scales. Other
4169 geohazards act on longer time scales, and have an easier predictability, such as glacio-isostasy and sea-
4170 level change. A proper identification and characterization of these geo-engineering constraints and
4171 geohazards, as well as understanding the processes and behaviour over time, allow a safe mitigation of
4172 the risks.

4173

4174 **Acknowledgements**

4175 We acknowledge the following companies for access of geophysical, geotechnical, and geological data:
4176 bp, Eliis, EnBW, Equinor, Fugro, GEO, Geo Marine Survey Systems, Mona Offshore Wind Limited,
4177 Morgan Offshore Wind Limited, RVO, SSE Renewables, TGS, Vattenfall, VBER, and Viridien.

4178 Lina Jakaite and Strike-dip.com are thanked for their artistic drawing of the sketch summarizing the
4179 geohazards and geo-engineering constraints. Sylfest Glimsdal is acknowledged for producing the figure
4180 on the tsunami model from Åknes/Tafjord, and Clement Tam for providing the figure on the salt in the
4181 North Sea. Elisabeth Hoffstad Reutz and Sigrid Esmeralda Arnestad are thanked for supporting GIS
4182 activities. Stein Bondevik is acknowledged for the fruitful feedback on the tsunami deposits.
4183 GeoSurveys is thanked for supporting our requests with figures on boulders and peat.

4184 Contributions to this paper were supported by the EU project “A Digital Twin for Geophysical
4185 Extremes” (DT-GEO) and has received funding from Horizon Europe under Grant Agreement No
4186 101058129. Documentation of landslide tsunami events was prepared under the “Geosphere
4187 INfrastructures for QUestions into Integrated REsearch” (Geo-INQUIRE) project, funded by the
4188 European Commission under project No. 101058518 within the HORIZON-INFRA-2021-SERV-01
4189 call. Both projects have also received funding from NGI’s internal R&D programme supported by the
4190 Research Council of Norway. David R. Tappin publishes with permission of the British Geological
4191 Survey, United Kingdom Research and Innovation.

4192 **References**

- 4193 Aber, J. S., & Ber, A. (2011). Glaciotectonic structures, landforms, and processes. Encyclopedia of
4194 Earth Sciences Series, Part 3, 444–458. [https://doi.org/10.1007/978-90-481-2642-](https://doi.org/10.1007/978-90-481-2642-2_217/FIGURES/7102)
4195 [2_217/FIGURES/7102](https://doi.org/10.1007/978-90-481-2642-2_217/FIGURES/7102)
- 4196 Aber, J. S., Croot, D. G., & Fenton, M. M. (1989). Nature of Glaciotectonism. In *Glaciotectonic*
4197 *Landforms and Structures* (pp. 1–12). https://doi.org/10.1007/978-94-015-6841-8_
- 4198 Adnyani, L. P., Draper, S., An, H. W., & Cheng, L. (2024). Modelling Sand Wave Evolution and
4199 Migration in North Sea Using ROMS. *Applied Mechanics and Materials*, 924, 139–152.
4200 <https://doi.org/10.4028/p-E52NOj>
- 4201 Ahlrichs, N., Hübscher, C., Andersen, T. R., Preine, J., Bogner, L., and Schäfer, W., 2023, The
4202 Langeland Fault System unravelled: Quaternary fault reactivation along an elevated basement block
4203 between the North German and Norwegian–Danish basins: *Boreas*, v. 52, no. 3, p. 381-401.
- 4204 Ahsan, D., & Pedersen, S. (2018). The influence of stakeholder groups in operation and maintenance
4205 services of offshore wind farms: Lesson from Denmark. *Renewable Energy*, 125, 819-828.
- 4206 Alexandropoulou, N., Winsborrow, M., Andreassen, K., Plaza-Faverola, A., Dessandier, P. A.,
4207 Mattingsdal, R., ... & Knies, J. (2021). A continuous seismostratigraphic framework for the Western
4208 Svalbard-Barents sea margin over the last 2.7 Ma: implications for the late Cenozoic glacial history of
4209 the Svalbard-Barents sea ice sheet. *Frontiers in Earth Science*, 9, 656732.
- 4210 Amos, C. L., Kassem, H., & Friend, P. L. (2017). Ripple Marks (pp. 1–8). [https://doi.org/10.1007/978-](https://doi.org/10.1007/978-3-319-48657-4_262-2)
4211 [3-319-48657-4_262-2](https://doi.org/10.1007/978-3-319-48657-4_262-2)
- 4212 Andersen, L. T., Hansen, D. L., & Huuse, M. (2005). Numerical modelling of thrust structures in
4213 unconsolidated sediments: Implications for glaciotectonic deformation. *Journal of Structural Geology*,
4214 27(4), 587–596. <https://doi.org/10.1016/J.JSG.2005.01.005>
- 4215 Andersen, K.H., Lunne, T., Kvalstad, T.J., Forsberg, C.F., 2008. Deep water geotechnical engineering,
4216 in: XXIV National Conference of the Mexican Society of Soil Mechanics. Norwegian Geotechnical
4217 Institute (NGI), Aguascalientes, Mexico, pp. 1–57.
- 4218 Andersen, K.H., Engin, H.K., D’Ignazio, M., Yang, S., 2023. Determination of cyclic soil parameters
4219 for offshore foundation design from an existing data base. *Ocean Eng.* 267, 113180.
4220 <https://doi.org/10.1016/j.oceaneng.2022.113180>
- 4221 Andreassen, K., Hubbard, A., Winsborrow, M., Patton, H., Vadakkepuliymbatta, S., Plaza-Faverola,
4222 A., Gudlaugsson, E., Serov, P., Deryabin, A., and Mattingsdal, R., 2017, Massive blow-out craters

- 4223 formed by hydrate-controlled methane expulsion from the Arctic seafloor: *Science*, v. 356, no. 6341, p.
4224 948-953.
- 4225 Andresen, K. J. (2012). Fluid flow features in hydrocarbon plumbing systems: What do they tell us
4226 about the basin evolution?. *Marine Geology*, 332, 89-108.
- 4227 Andersen, L. T., Hansen, D. L., & Huuse, M. (2005). Numerical modelling of thrust structures in
4228 unconsolidated sediments: implications for glaciotectonic deformation. *Journal of Structural Geology*,
4229 27(4), 587-596.
- 4230 Andresen, K.J., Hepp, D.A., Keil, H., Spiess, V. (2022): Seismic morphologies of submerged late
4231 glacial to early Holocene landscapes at the eastern Dogger Bank, central North Sea Basin - implications
4232 for geo-archaeological potential. *Geological Society London, Special Publication 525*.
4233 doi.org/10.1144/SP525-2021-155
- 4234 Andrews, I.J., Long, D., Richards, P.C., Thomson, A.R., Brown, S., Chesher, J.A., McCormac, M.
4235 (1990). United Kingdom offshore regional report: the geology of the Moray Firth. London: HMSO for
4236 the British Geological Survey.
- 4237 Arfai, J., Kuhlmann, G., Ladage, S., Lutz, R., Gaedicke, C. (2018). Iceberg scour marks in the Southern
4238 North Sea - Indications for iceberg transport at the beginning of Northern Hemisphere. 80th EAGE
4239 Conference and Exhibition 2018: Opportunities Presented by the Energy Transition, 2018, 1–5,
4240 <https://doi.org/10.3997/2214-4609.201801642>.
- 4241 Arosio, R., Dove, D., Ó Cofaigh, C., & Howe, J. A. (2018). Submarine deglacial sediment and
4242 geomorphological record of southwestern Scotland after the Last Glacial Maximum. *Marine Geology*,
4243 403, 62-79.
- 4244 Arosio, R., Wheeler, A.J., Sacchetti, F., Guinan, J., Benetti, S., O’Keeffe, E., van Landeghem, K.J.J.,
4245 Conti, L.A., Furey, T., Lim, A., 2023. The geomorphology of Ireland’s continental shelf. *J. Maps* 19.
4246 <https://doi.org/10.1080/17445647.2023.2283192>
- 4247 Arvidsson, R., 1996. Fennoscandian Earthquakes: Whole Crustal Rupturing Related to Postglacial
4248 Rebound. *Science* 274, 744–746. <https://doi.org/10.1126/science.274.5288.744>
- 4249 Ashley, G. (1990). Classification of Large-Scale Subaqueous Bedforms: A New Look at an Old
4250 Problem-SEPM Bedforms and Bedding Structures. *SEPM Journal of Sedimentary Research*. Vol. 60.
4251 10.1306/212F9138-2B24-11D7-8648000102C1865D.
- 4252 ASTM (2010). D2487: Standard practice for classification of soils for engineering purposes (unified
4253 soil classification system). In ASTM.

- 4254 Audsley, A., Bradwell, T., Howe, J., Baxter, J. (2021). Spatial Relationships between Pockmarks and
4255 Sub-Seabed Gas in Fjordic Settings: Evidence from Loch Linnhe, West Scotland. *Geosciences*, v. 11,
4256 283. <https://doi.org/10.3390/geosciences11070283>
- 4257 Baeten, N. J., Laberg, J. S., Vanneste, M., Forsberg, C. F., Kvalstad, T. J., Forwick, M., ... & Haflidason,
4258 H. (2014). Origin of shallow submarine mass movements and their glide planes—Sedimentological and
4259 geotechnical analyses from the continental slope off northern Norway. *Journal of Geophysical*
4260 *Research: Earth Surface*, 119(11), 2335-2360.
- 4261 Bagnold, R. A. (1954). Experiments on a gravity-free dispersion of large solid spheres in a Newtonian
4262 fluid under shear. *Philosophical Transactions of the Royal Society London, Series A* 225, 49–63, DOI
4263 10.1098/rspa.1954.0186.
- 4264 Baig, I., Faleide, J.I., Mondol, N.H., Jahren, J., 2019. Burial and exhumation history controls on shale
4265 compaction and thermal maturity along the Norwegian North Sea basin margin areas. *Mar. Petrol. Geol.*
4266 104, 61–85.
- 4267 Bailey, G., Galanidou, N., Peeters, H., Jöns, H. and Mennenga, M. (eds). 2020. *The Archaeology of*
4268 *Europe’s Drowned Landscapes*. Springer Open, Coastal Research Library, 35.
- 4269 Ballantyne, C.K., Small, D., 2019. The Last Scottish Ice Sheet. *Earth and Environmental Science*
4270 *Transactions of the Royal Society of Edinburgh*, 110, pp. 93–131.
- 4271 Baltzer, A., Holmes, R., & Evans, D. (1998). Debris flows on the Sula Sgeir Fan, NW of Scotland.
4272 *Geological Society, London, Special Publications*, 129(1), 105-115.
- 4273 Barbolini, M.; Biancardi, A.; Cappabianca, F.; Natale, L. and Pagliardi, M. (2005). Laboratory study of
4274 erosion processes in snow avalanches, *Cold Regions Science and Technology* 43: 1–9, DOI
4275 10.1016/j.coldregions.2005.01.007.
- 4276 Barker, T.; Schaeffer, D. G.; Shearer, M. and Gray, J. M. N. T. (2017). Well-posed continuum equations
4277 for granular flow with compressibility and $\mu(I)$ -rheology. *Proceedings of the Royal Society, London,*
4278 *Ser. A* 473: 20160846, DOI 10.1098/rspa.2016.0846.
- 4279 Barrett, R. S., Bellwald, B., Talling, P. J., Micallef, A., Gross, F., Berndt, C., ... & Krastel, S. (2021).
4280 Does retrogression always account for the large volume of submarine megaslides? Evidence to the
4281 contrary from the Tampen Slide, offshore Norway. *Journal of Geophysical Research: Solid Earth*,
4282 126(2), e2020JB020655.
- 4283 Barrett, R., Bellwald, B., Talling, P. J., Sokolkova, E., Grob, H., Lenz, K. F., ... & Krastel, S. (2025).
4284 Deep Secrets: Discovery of a giant mega-slide in the North Sea Fan, offshore Norway. *Marine Geology*,
4285 107554.

- 4286 Batchelor, C.L., Margold, M., Krapp, M., Murton, D.K., Dalton, A.S., Gibbard, P.L., Stokes, C.R.,
4287 Murton, J.B., Manica, A. 2019. The configuration of Northern Hemisphere ice sheets through the
4288 Quaternary. *Nature Communications*. 10:3713, 10pp.
- 4289 Batchelor, C. L., Bellwald, B., Planke, S., Ottesen, D., Henriksen, S., Myklebust, R., ... & Dowdeswell,
4290 J. A. (2021). Glacial, fluvial and contour-current-derived sedimentation along the northern North Sea
4291 margin through the Quaternary. *Earth and Planetary Science Letters*, 566, 116966.
- 4292 Batchelor, C.L., Christie, F.D.W., Ottesen, D. et al. Rapid, buoyancy-driven ice-sheet retreat of
4293 hundreds of metres per day. *Nature* 617, 105–110 (2023). <https://doi.org/10.1038/s41586-023-05876-1>
- 4294 Bayliss, A. I. (2015). Geotechnical characterization and performance of Glaciotectonites for earth
4295 structures and natural slopes.
- 4296 Behrens J, Løvholt F, Jalayer F, Lorito S, Salgado-Gálvez M, et al. (2021) Probabilistic tsunami hazard
4297 and risk analysis—A review of research gaps. *Frontiers in Earth Science* 9: 114.
4298 <https://doi.org/10.3389/feart.2021.628772>.
- 4299 Belderson, R.H., 1964. Holocene sedimentation in the western half of the Irish Sea. *Mar. Geol.* 2, 147–
4300 163.
- 4301 Bellec, V. K., Bøe, R., Bjarnadóttir, L. R., Albretsen, J., Dolan, M., Chand, S., Thorsnes, T., Jakobsen,
4302 F. W., Nixon, C., Plassen, L., Jensen, H., Baeten, N., Olsen, H., & Elvenes, S. (2019). Sandbanks,
4303 sandwaves and megaripples on Spitsbergenbanken, Barents Sea. *Marine Geology*, 416, 105998.
4304 <https://doi.org/10.1016/j.margeo.2019.105998>
- 4305 Bellwald, B., Hjelstuen, B.O., Sejrup, H.P., Haflidason, H., 2016. Postglacial mass movements and
4306 depositional environments in a high-latitude fjord system – Hardangerfjorden, Western Norway. *Marine*
4307 *Geology* 379, 157-175.
- 4308 Bellwald, B., Waage, M., Planke, S., Lebedeva-Ivanova, N., Polteau, S., Tasianias, A., ... & Myklebust,
4309 R. (2018, November). Monitoring Of CO2 Leakage Using High-Resolution 3D Seismic Data–
4310 Examples From Snøhvit, Vestnesa Ridge And The Western Barents Sea. In *Fifth CO2 Geological*
4311 *Storage Workshop* (Vol. 2018, No. 1, pp. 1-5). European Association of Geoscientists & Engineers.
- 4312 Bellwald, B., & Planke, S. (2019). Shear margin moraine, mass transport deposits and soft beds revealed
4313 by high-resolution P-Cable three-dimensional seismic data in the Hoop area, Barents Sea. *Geological*
4314 *Society, London, Special Publications*, 477(1), 537-548.
- 4315 Bellwald, B., Hjelstuen, B. O., Sejrup, H. P., Stokowy, T., & Kuvås, J. (2019a). Holocene mass
4316 movements in west and mid-Norwegian fjords and lakes. *Marine Geology*, 407, 192-212.

- 4317 Bellwald, B., Urlaub, M., Hjelstuen, B.O., Sejrup, H.P., Sørensen, M.B., Forsberg, C.F., and Vanneste,
4318 M., 2019b, NE Atlantic continental slope stability from a numerical modelling perspective: Quaternary
4319 Science Reviews, v. 203, p. 248-265, <https://doi.org/10.1016/j.quascirev.2018.11.019>.
- 4320 Bellwald, B., Planke, S., Lebedeva-Ivanova, N., Piasecka, E. D., & Andreassen, K. (2019c). High-
4321 resolution landform assemblage along a buried glacio-erosive surface in the SW Barents Sea revealed
4322 by P-Cable 3D seismic data. *Geomorphology*, 332, 33-50.2020
- 4323 Bellwald, B., Planke, S., Polteau, S., Lebedeva-Ivanova, N., Faleide, J. I., Morris, S. M., ... &
4324 Castellort, S. (2021). Characterization of a glacial paleo-outburst flood using high-resolution 3-D
4325 seismic data: Bjørnelva River Valley, SW Barents Sea. *Journal of Glaciology*, 67(263), 404-420.
- 4326 B. Bellwald, C. Batchelor, A. Garcia, R. Barrett, M. Rosenqvist, S. Planke, I. Midtkandal, R. Myklebust,
4327 B. Kjølhamar, 2022a. Contourites of the Northern North Sea, North Sea Fan, and Mid-Norwegian
4328 Margin. 83rd EAGE Annual Conference & Exhibition, Volume 2022, p.1 – 5 DOI:
4329 <https://doi.org/10.3997/2214-4609.202210247>
- 4330 Bellwald, B., Planke, S., Vadakkepuliambatta, S., Buenz, S., Batchelor, C., Manton, B., ... &
4331 Kjølhamar, B. (2022b). Quaternary and Neogene Reservoirs of the Norwegian continental shelf and the
4332 Faroe-Shetland basin. *First Break*, 40(6), 43-54.
- 4333 Bellwald, B., Stokke, H., Winsborrow, M., Planke, S., Sættem, J., Lebedeva-Ivanova, N., ... & Polteau,
4334 S. (2023a). Structural and fluid-migration control on hill-hole pair formation: Evidence from high-
4335 resolution 3D seismic data from the SW Barents Sea. *Geomorphology*, 420, 108502.
- 4336 Bellwald, B., Griffiths, L., Hansen, R. C., Dujardin, J., Forsberg, C., De Gail, M., ... & Piotrowski, J.
4337 A. (2023b, September). Multi-disciplinary Characterization of Sedimentary Environments on Glaciated
4338 Margins: Implications for Engineering of Offshore Windfarm Sites. In NSG2023 1st Conference on
4339 Sub-surface Characterisation for Offshore Wind (Vol. 2023, No. 1, pp. 1-5). European Association of
4340 Geoscientists & Engineers.
- 4341 Bellwald, B., Maharjan, D., Planke, S., Winsborrow, M., Rydningen, T.A., Alexandropoulou, N. and
4342 Myklebust, R., 2024a. Major tunnel valleys and sedimentation changes document extensive Early
4343 Pleistocene glaciations of the Barents Sea. *Communications Earth & Environment*, 5(1), p.551.
- 4344 Bellwald, B., Manton, B., Lebedeva-Ivanova, N., Zastrozhnov, D., Myklebust, R., Planke, S., ... &
4345 Locat, J. (2024b). Rapid glacial sedimentation and overpressure in oozes causing large craters on the
4346 mid-Norwegian margin: integrated interpretation of the Naust, Kai and Brygge formations.
- 4347 Bellwald, B., Kurjanski, B., Wood, G., Carter, G., Stokke, H. H., Planke, S., ... & Vanneste, M. (2024c,
4348 June). Resolution requirements for characterization of sedimentary environments in glaciated margins:
4349 a geomorphological perspective. In 85th EAGE Annual Conference & Exhibition (including the

4350 Workshop Programme) (Vol. 2024, No. 1, pp. 1-5). European Association of Geoscientists &
4351 Engineers.

4352 Benetti, S., Chiverrell, R.C., Cofaigh, C.Ó., Burke, M., Medialdea, A., Small, D., Ballantyne, C.,
4353 Bateman, M.D., Callard, S.L., Wilson, P., Fabel, D., Clark, C.D., Arosio, R., Bradley, S., Dunlop, P.,
4354 Ely, J.C., Gales, J., Livingstone, S.J., Moreton, S.G., Purcell, C., Saher, M., Schiele, K., Van
4355 Landeghem, K., Weilbach, K. (2021). Exploring controls of the early and stepped deglaciation on the
4356 western margin of the British Irish Ice Sheet. *Journal of Quaternary Science*, v. 36: 833-870.
4357 <https://doi.org/10.1002/jqs.3315>

4358 Bennett, M. R. (2001). The morphology, structural evolution and significance of push moraines. *Earth*
4359 *Science Reviews*, 53(3–4), 197–236. [https://doi.org/10.1016/S0012-8252\(00\)00039-8](https://doi.org/10.1016/S0012-8252(00)00039-8)

4360 Benvenuti, A., Kombrink, H., Veen, J.H. ten, Munsterman, D.K., Bardi, F., Benvenuti, M., 2012. Late
4361 Cenozoic shelf delta development and Mass Transport Deposits in the Dutch offshore area – results of
4362 3D seismic interpretation. *Netherlands Journal of Geosciences - Geologie en Mijnbouw* 91, 591–608.

4363 Berg, K., Solheim, A., and Bryn, P., 2005, The Pleistocene to recent geological development of the
4364 Ormen Lange area: Marine and Petroleum Geology, v. 22, p. 45-56,
4365 <https://doi.org/10.1016/j.marpetgeo.2004.10.009>.

4366 Berndt, C., Bünz, S., & Mienert, J. (2003). Polygonal fault systems on the mid-Norwegian margin: a
4367 long-term source for fluid flow.

4368 Berndt, C., Brune, S., Nisbet, E., Zschau, J., Sobolev, S.V., 2009. Tsunami modeling of a submarine
4369 landslide in the Fram Strait, *Geochem. Geophys. Geosyst.*, 10, Q04009, doi:10.1029/2008GC002292.

4370 Bienen, B., Qiu, G., & Pucker, T. (2015). CPT correlation developed from numerical analysis to predict
4371 jack-up foundation penetration into sand overlying clay. *Ocean Engineering*, 108, 216-226.

4372 Bjørlykke, K., Høeg, K., and Mondol, N. H., 2015, Introduction to Geomechanics: stress and strain in
4373 sedimentary basins: *Petroleum Geoscience: from sedimentary environments to rock physics*, p. 301-
4374 318.

4375 Blikra, L.H., Longva, O., Braathen, A., Anda, E., Dehls, J., and Stalsberg, K. (2006). Rock-slope
4376 failures in Norwegian fjord areas: examples, spatial distribution and temporal pattern. In: Evans, S.G.,
4377 Scarawcia Mugnozza, G., Strom, A.L., Hermanns, R.L. (Eds.), *Landslides from Massive Rock Slope*
4378 *Failure. Nato Science Series IV, Earth and Environmental Sciences*, 49, 475–496.

4379 Blumenberg, M., Schlömer, S., Reinhardt, L., Scheeder, G., Pape, T., & Römer, M. (2022). Biomarker
4380 insights into a methane-enriched Holocene peat-setting from “Doggerland”(central North Sea). *The*
4381 *Holocene*, 32(10), 1015-1025.

- 4382 Boguchwal, L. A., & Southard, J. B. (1990). Bed configurations in steady unidirectional water flows;
 4383 Part 1, Scale model study using fine sands. *Journal of Sedimentary Research*, 60(5), 649–657.
 4384 <https://doi.org/10.1306/212F923C-2B24-11D7-8648000102C1865D>
- 4385 Bondevik, S., Svendsen, J.I., 1993. Palaeotsunamis in the Norwegian Sea and the North Sea, in: Tinti,
 4386 S. (Ed.), *Genesis and Impact of Tsunamis on the European Coasts -- GITEC. Mid-Term Scientific*
 4387 *Report, Contract EV5F-CT92-0175, 7.2-7.27.*
- 4388 Bondevik, S., Svendsen, J.I., Johnsen, G., Mangerud, J.A.N., Kaland, P.E., 1997a. The Storegga
 4389 tsunami along the Norwegian coast, its age and run up. *Boreas* 26, 29-53.
- 4390 Bondevik, S., Svendsen, J.I., Mangerud, J.A.N., 1997b. Tsunami sedimentary facies deposited by the
 4391 Storegga tsunami in shallow marine basins and coastal lakes, western Norway. *Sedimentology* 44,
 4392 1115-1131.
- 4393 Bondevik, S., Svendsen, J.I., Mangerud, J., 1998. Distinction between the Storegga tsunami and the
 4394 holocene marine transgression in coastal basin deposits of western Norway. *Journal of Quaternary*
 4395 *Science* 13, 529-537.
- 4396 Bondevik, S., Løvholt, F., Harbitz, C., Mangerud, J., Dawson, A., and Svendsen, J. I. (2005a). The
 4397 Storegga Slide tsunami – comparing field observations with numerical simulations. In Ormen Lange –
 4398 *An integrated study for safe field development in the Storegga submarine area*, 195-208. Elsevier.
- 4399 Bondevik, S., Mangerud, J., Dawson, S., Dawson, A., Lohne, Ø., 2005b. Evidence for three North Sea
 4400 tsunamis at the Shetland Islands between 8000 and 1500 years ago. *Quaternary Science Reviews* 24,
 4401 1757-1775.
- 4402 Bondevik, S., Risebrobakken, B., Gibbons, S.J., Rasmussen, T.L., and Løvholt, F. (2024)
 4403 Contamination of 8.2 ka cold climate records by the Storegga tsunami in the Nordic Seas. *Nat. Comm.*
 4404 15, 2904.
- 4405 Boulton, G. S. (1986). Push-moraines and glacier-contact fans in marine and terrestrial environments.
 4406 *Sedimentology*, 33(5), 677-698.
- 4407 Boyer, F., Guazzelli, É. And Pouliquen, O. (2011). Dense suspensions in rotating-rod flows: normal
 4408 stresses and particle migration. *Journal of Fluid Mechanics* 686: 5–25, DOI 10.1017/jfm.2011.272.
- 4409 Braathen, A., Blikra, L.H., Berg, S.S. & Karlsen, F.: Rock-slope failures in Norway; type, geometry
 4410 and hazard. *Norwegian Journal of Geology*, Vol. 84, pp. 67-88. Trondheim 2004. ISSN 029-196X.
 4411 https://www.geologi.no/images/NJG_articles/NJG_84_67-88.pdf
- 4412 Bradwell, T., Fabel, D., Clark, C.D., Chiverrell, R.C., Small, D., Smedley, R.K., Saher, M.H., Moreton,
 4413 S.G., Dove, D., Callard, S.L., Duller, G.A.T., Madialdea, A., Bateman, D., Burke, M.J., McDonald, N.,

- 4414 Gilgannon, S., Morgan, S., Roberts, D.H., Ó Cofaigh, C. (2021) Pattern, style and timing of British–
4415 Irish Ice Sheet advance and retreat over the last 45,000 years: evidence from NW Scotland and the
4416 adjacent continental shelf. *Journal of Quaternary Science*. 1–63. DOI: 10.1002/jqs.3296
- 4417 Bradwell, T., Small, S., Fabel, D., Clark, C.D., Chiverrell, R.C., Saher, M.H., Dove, D., Callard, S.L.,
4418 Burke, M.J., Moreton, S.G., Madialdea, A., Bateman, D., Roberts, D.H., Golledge, N.R., Finlayson, A.,
4419 Morgan, S., Ó Cofaigh, C. (2019a). Pattern, style and timing of British–Irish Ice Sheet retreat: Shetland
4420 and northern North Sea sector. *Journal of Quaternary Science*. 1–42. <https://doi.org/10.1002/jqs.3163>.
- 4421 Bradwell, T., Small, S., Fabel, D., Smedley, R.K., Clark, C.D., Saher, M.H., Callard, S.L., Chiverrell,
4422 R.C., Dove, D., Moreton, S.G., Roberts, D.H., Duller, G.A.T., Ó Cofaigh, C. (2019b) Ice-stream demise
4423 dynamically conditioned by trough shape and bed strength. *Science Advances*, 5:eaau1380.
- 4424 Bradwell, T., Stoker, M.S., Golledge, N.R., Wilson, C.K., Merritt, J.W., Long, D., Everest, J. D.,
4425 Hestvik, O.B., Stevenson, A.G., Hubbard, A.L., Finlayson, A.G., Mathers, H.E. (2008). The northern
4426 sector of the last British Ice Sheet: Maximum extent and demise. *Earth-Science Reviews*, v. 88, 207–
4427 226.
- 4428 Brandes, C., Steffen, H., Steffen, R., Wu, P. (2015). Intraplate seismicity in northern Central Europe is
4429 induced by the last glaciation. *Geology*, 43(7), 611–614.
- 4430 Breien H, Pagliardi M, De Blasio FV, Issler D, and Elverhøi A (2007). Experimental studies of
4431 subaqueous vs. subaerial debris flows—velocity characteristics as a function of the ambient fluid. In:
4432 *Submarine Mass Movements and Their Consequences*, pp. 101–110. Dordrecht: Springer.
- 4433 Breien H, De Blasio FV, Elverhøi A, Nystuen JP, and Harbitz CB (2010). Transport mechanisms of
4434 sand in deep-marine environments—Insights based on laboratory experiments. *Journal of Sedimentary*
4435 *Research* 80(11): 975–990.
- 4436 British Geological Survey. (2009) TRANSFER project deliverable D3.1–D3.5: An examination of non-
4437 seismic sources of tsunamis and their impacts on European coastlines – WP3 of EU project TRANSFER
4438 <http://www.transferproject.eu>
- 4439 Brooks, G. R., Adams, J. (2020). A review of evidence of glacially-induced faulting and seismic shaking
4440 in eastern Canada: *Quaternary Science Reviews*, v. 228, p. 106070.
- 4441 Brown, M. J., Bransby, M. F., Knappett, J., Tovey, S., Lauder, K. D., & Pyrah, J. (2015). The effect of
4442 buried fibres on offshore pipeline plough performance. *Ocean Engineering*, 108, 760–768.
4443 <https://doi.org/10.1016/j.oceaneng.2015.08.022>

4444 Brown, A., Russell, J., Scaife, R. G., Tizzard, L., Whittaker, J., and Wyles, S. F. (2018). "Late glacial /
4445 early Holocene palaeoenvironments in the southern North Sea Basin: new data from the Dudgeon
4446 offshore wind farm." *Quaternary Science*, 33, 597 - 610.

4447 Bryn, P., Berg, K., Forsberg, C.F., Solheim, A., Kvalstad, T.J. (2005a). Explaining the Storegga Slide.
4448 *Marine and Petroleum Geology*, Volume 22, 11-19, <https://doi.org/10.1016/j.marpetgeo.2004.12.003>.

4449 Bryn, P., Berg, K., Stoker, M.S., Haflidason, H. Solheim, A. (2005b). Contourites and their relevance
4450 for mass wasting along the Mid-Norwegian Margin. *Marine and Petroleum Geology*, 22, 85–96,
4451 <https://doi.org/10.1016/j.marpetgeo.2004.10.012>

4452 BS 5930: 2015—The Code of Practice for Site Investigations. British Standards Institute, Milton
4453 Keynes.

4454 BS 5930:1981—The Code of Practice for Site Investigations. British Standards Institute, Milton
4455 Keynes.

4456 BS 5930:1981—The Code of Practice for Site Investigations. British Standards Institute, Milton
4457 Keynes.

4458 BSH. (2023). Geological Report of the Preliminary Investigation of FEP Site N-9.1 Investigation Area:
4459 N-09. Published by Bundesamt für Seeschifffahrt und Hydrographie, Hamburg, Germany.
4460 <https://pinta.bsh.de/N-9.1>

4461 Buckley, F.A. (2017). A glaciogenic sequence from the Early Pleistocene of the Central North Sea.
4462 *Journal of Quaternary Science*, 32(2), pp.145-168.

4463 Bulat, J., Long, D. (2001). Images of the seabed in the Faroe-Shetland Channel from commercial 3D
4464 seismic data. *Marine Geophysical Researches*, v. 22, 345–367.

4465 Bull, S., Cartwright, J., Huuse, M. (2009). A subsurface evacuation model for submarine slope failure.
4466 *Basin Research*, 21(4), 433-443.

4467 Bungum, H., Hokland, B.K., Husebye, E.S., Ringdal, F. (1979). An exceptional intraplate earthquake
4468 sequence in Meloy, Northern Norway. *Nature* 280, 32–35. <https://doi.org/10.1038/280032a0>

4469 Bungum, H., Alsaker, A., Kvamme, L.B., Hansen, R.A. (1991). Seismicity and seismotectonics of
4470 Norway and nearby continental shelf areas. *J Geophys Res* 96, 2249–2265.
4471 <https://doi.org/10.1029/90jb02010>

4472 Bungum, H., Lindholm, C.D., Dahle, A., Woo, G., Nadim, F., Holme, J.K., Gudmestad, O.T., Hagberg,
4473 T., Karthigeyan, K. (2000). New seismic zoning maps for Norway, the North Sea, and the United
4474 Kingdom. *Seismological research letters*, 71, 687-697.

- 4475 Bungum, H., Pettenati, F., Schweitzer, J., Sirovich, L., Faleide, J.I. (2009). The 23 October 1904 MS
4476 5.4 Oslofjord Earthquake: Reanalysis Based on Macroseismic and Instrumental Data. *Bull. Seismol.*
4477 *Soc. Am.* 99, 2836–2854. <https://doi.org/10.1785/0120080357>
- 4478 Bungum, H., Olesen, O., Pascal, C., Gibbons, S., Lindholm, C., VestØl, O. (2010). To what extent is
4479 the present seismicity of Norway driven by post-glacial rebound? *J. Geol. Soc.* 167, 373–384.
4480 <https://doi.org/10.1144/0016-76492009-009>
- 4481 Bunkholt, H. S., Oftedal, B. T., Hansen, J. A., Løseth, H., Kløvjan, O. S. (2024). Trøndelag Platform
4482 and Halten–Dønna Terraces Composite Tectono-Sedimentary Element, Norwegian Rifted Margin,
4483 Norwegian Sea. *Geological Society, London, Memoirs*, 57(1), M57-2017.
- 4484 Butt, F. A., Elverhøi, A., Solheim, A., & Forsberg, C. F. (2000). Deciphering Late Cenozoic
4485 development of the western Svalbard Margin from ODP Site 986 results. *Marine Geology*, 169(3-4),
4486 373-390.
- 4487 Butt, F. A., Drange, H., Elverhøi, A., Otterå, O. H., & Solheim, A. (2002). Modelling Late Cenozoic
4488 isostatic elevation changes in the Barents Sea and their implications for oceanic and climatic regimes:
4489 preliminary results. *Quaternary Science Reviews*, 21(14-15), 1643-1660.
- 4490 Böttner, C., Berndt, C., Reinardy, B.T.I., Geersen, J., Karstens, J., Bull, J.M., Callow, B.J., Lichtschlag,
4491 A., Schmidt, M., Elger, J., Schramm, B., Haeckel, M. (2019). Pockmarks in the Witch Ground Basin,
4492 Central North Sea. *Geochemistry, Geophys. Geosystems* 20, 1698–1719.
4493 <https://doi.org/https://doi.org/10.1029/2018GC008068>
- 4494 Böttner, C., Hoffmann, J. J., Unverricht, D., Schmidt, M., Spiegel, T., Geersen, J., ... & Schmidt, C.
4495 (2024). The enigmatic pockmarks of the sandy southeastern North Sea. *Geochemistry, Geophysics,*
4496 *Geosystems*, 25(11), e2024GC011837.
- 4497 Bøe, R., Longva, O., Lepland, A., Blikra, L.H., Sønstegaard, E., Haflidason, H., Bryn, P., Lien, R.
4498 (2004) Postglacial mass movements and their causes in fjords and lakes in western Norway. *Nor J Geol*
4499 84: 35-55.
- 4500 Bøe, R., Prøsch-Danielsen, L., Lepland, A., Harbitz, C.B., Gauer, P., Løvholt, F., and Høgestøl, M.
4501 (2007). An early Holocene submarine slide in Boknafjorden and the effect of a slide-triggered tsunami
4502 on the Stone Age settlement at Rennesøy, SW Norway. *Marine Geology*, Vol. 243, 157-168.
- 4503 Bünz, S., Mienert, J. (2004). Acoustic imaging of gas hydrate and free gas at the Storegga Slide, J.
4504 *Geophys. Res.*, 109, B04102, doi:10.1029/2003JB002863.
- 4505 Callard, S.L., Ó Cofaigh, C., Benetti, S., Chiverrell, R.C., Van Landeghem, K.J.J., Saher, M.H.,
4506 Livingstone, S.J., Clark, C.D., Small, D., Fabel, D., Moreton, S.G. (2020). Oscillating retreat of the last

- 4507 British-Irish Ice Sheet on the continental shelf offshore Galway Bay, western Ireland. *Marine Geology*,
4508 v. 420. <https://doi.org/10.1016/j.margeo.2019.106087>.
- 4509 Callard, S.L., Ó Cofaigh, C., Benetti, S., Chiverrell, R.C., Van Landeghem, K.J.J., Saher, M.H., Gales,
4510 J.A., Small, D., Clark, C.D., Livingstone, S.J., Fabel, D., Moreton, S.G. (2018). Extent and retreat
4511 history of the Barra Fan Ice Stream offshore western Scotland and northern Ireland during the last
4512 glaciation. *Quaternary Science Reviews*, v. 201, 280-302.
4513 <https://doi.org/10.1016/j.quascirev.2018.10.002>
- 4514 Callaway, A., Smyth, J., Brown, C.J., Quinn, R., Service, M., Long, D. (2009). The impact of scour
4515 processes on a smothered reef system in the Irish Sea. *Estuar. Coast. Shelf Sci.* 84, 409–418.
4516 <https://doi.org/http://dx.doi.org/10.1016/j.ecss.2009.07.011>
- 4517 Callaway, A., Quinn, R., Brown, C.J., Service, M., Long, D., Benetti, S. (2011). The formation and
4518 evolution of an isolated submarine valley in the North Channel, Irish Sea: an investigation of Beaufort's
4519 Dyke. *J. Quat. Sci.* 26, 362–373. <https://doi.org/10.1002/jqs.1460>
- 4520 Cameron, T.D.J., Stoker, M.S., Long, D. (1987) The history of Quaternary sedimentation in the UK
4521 sector of the North Sea Basin. *Journal of the Geological Society of London*, v. 144, 43–58.
- 4522 Carbon Trust. (2016). Application Guide for the specification of the Depth of Lowering using the Cable
4523 Burial Risk Assessment (CBRA) methodology. Report. 51pp.
- 4524 Carlsten, P. (2000). "Geotechnical properties of some Swedish peats." 13th Nordic Geotechnical
4525 Meeting (Nordiska Geoteknikermötet) NGM-2000, H. Rathmayer, ed., Finnish Geotechnical Society,
4526 Helsinki, Finland, Helsinki, Finland, 51-60.
- 4527 Carlton, B.D., Skurtveit, E., Atakan, K., Kaynia, A.M. (2019a). Probabilistic seismic hazard analysis
4528 of a CO2 storage prospect using the NGA East ground motion models. In Proceedings of the SECED
4529 2019 Conference, Greenwich, London, 9–10 September.
- 4530 Carlton, B., Vanneste, M., Forsberg, C. F., Knudsen, S., Løvholt, F., Kvalstad, T., ... & Haflidason, H.
4531 (2019b). Geohazard assessment related to submarine instabilities in Bjørnafjorden, Norway. *Geological*
4532 *Society, London, Special Publications*, 477(1), 549–566.
- 4533 Carlton, B., Shin, Y., Leoncino, V., Kaynia, A.M., (2021). Seismic Hazard Assessment for TNW Wind
4534 Farm Zone. NGI Report 20190798-03-TN. [https://offshorewind.rvo.nl/files/view/629c2998-6429-
4536 ent_rev0-f.pdf](https://offshorewind.rvo.nl/files/view/629c2998-6429-4f85-86d6-767c680e0ad0/1638781502tnw_20211202_gm_ngi_seismic%20hazard%20assessm
4535 ent_rev0-f.pdf).
- 4537 Carlton B., Barwise A., Kaynia A.M. (2022). Seismic Hazard Assessment for a Wind Farm Offshore
4538 England. *Geotechnics* 2(1):14-31. <https://doi.org/10.3390/geotechnics2010002>

- 4539 Carlton B., Huang, C., Kettlety, T., Larsen, T. (2024). Development of a ground motion model and
4540 probabilistic seismic hazard analysis for the North Sea. SHARP Storage project deliverable 5.5.
- 4541 Carr, S. (1999). The micromorphology of Last Glacial Maximum sediments in the Southern North Sea.
4542 *Catena*, Vol. 35, 123–145.
- 4543 Cartelle, V., Barlow, N.L.M., Hodgson, D.M., Busschers, F.S., Cohen, K.M., Meijninger, B.M.L., van
4544 Kesteren, W.P. (2021). Sedimentary architecture and landforms of the late Saalian (MIS 6) ice sheet
4545 margin offshore of the Netherlands. *Earth Surface Dynamics* 9, 1399–1421.
4546 <https://doi.org/10.5194/esurf-9-1399-2021>
- 4547 Carter, G.D.O., Birchall, R., Flint, A., Rose, M., Bellwald, B., Cotterill, C., Arlott, L., Wood, G. (2025).
4548 Formation and implications of glacially-derived gravel lag deposits; mapping a geo-constraint to
4549 shallow offshore infrastructure. 5th International Symposium on Frontiers in Offshore Geotechnics
4550 (ISFOG), Nantes, France.
- 4551 Caruso, S., Maselli V., Rea, B., Spagnolo, M. (2022). Deep-water sedimentation processes on a
4552 glaciated margin: The Foula Wedge trough mouth fan, West of Shetland. *Marine Geology* 446, 106769.
4553 <https://doi.org/10.1016/j.margeo.2022.106769>.
- 4554 Cassar, C.; Nicolas, M. Pouliquen, O. (2005). Submarine granular flows down inclined planes. *Physics*
4555 *of Fluids* 17: 103301, DOI 10.1063/1.2069864.
- 4556 Castellort, S., & Van Den Driessche, J. (2003). How plausible are high-frequency sediment supply-
4557 driven cycles in the stratigraphic record?. *Sedimentary Geology*, 157(1-2), 3-13.
- 4558 Cesca, S., Dahm, T., Juretzek, C., Kühn, D. (2011). Rupture process of the 2001 May 7 Mw 4.3 Ekofisk
4559 induced earthquake: The Ekofisk induced earthquake. *Geophys. J. Int.* 187, 407–413.
4560 <https://doi.org/10.1111/j.1365-246X.2011.05151.x>
- 4561 Chand, S., Mienert, J., Andreassen, K., Knies, J., Plassen, L., Fotland, B. (2008). Gas hydrate stability
4562 zone modelling in areas of salt tectonics and pockmarks of the Barents Sea suggests an active
4563 hydrocarbon venting system. *Marine and Petroleum Geology*, 25(7), 625-636.
- 4564 Chand, S., Rise, L., Knies, J., Haflidason, H., Hjelstuen, B.O., Bøe, L. (2011). Stratigraphic
4565 development of the south Vøring Margin (Mid-Norway) since early Cenozoic time and its influence on
4566 subsurface fluid flow. *Marine and Petroleum Geology*, 28(7), 1350-1363.
- 4567 Chiverrell, R.C., Thrasher, I.M., Thomas, G.S.P., Lang, A., Scourse, J.D., van Landeghem, K.J.J.,
4568 McCarroll, D., Clark, C.D., Ó Cofaigh, C., Evans, D.J.A., Ballantyne, C.K., 2013. Bayesian modelling
4569 the retreat of the Irish Sea Ice Stream. *J. Quat. Sci.* 28, 200–209. <https://doi.org/10.1002/jqs.2616>

4570 Chiverrell, R.C., Smedley, R.K., Small, D., Ballantyne, C.K., Burke, M.J., Callard, S.L., Clark, C.D.,
4571 Duller, G.A.T., Evans, D.J.A., Fabel, D., van Landeghem, K., Livingstone, S., Ó Cofaigh, C., Thomas,
4572 G.S.P., Roberts, D.H., Saher, M., Scourse, J.D., Wilson, P., 2018. Ice margin oscillations during
4573 deglaciation of the northern Irish Sea Basin. *J. Quat. Sci.* <https://doi.org/10.1002/jqs.3057>

4574 Chiverrell, R.C., Thomas, G.S.P., Burke, M., Medialdea, A., Smedley, R., Bateman, M., Clark, C.,
4575 Duller, G.A.T., Fabel, D., Jenkins, G., Ou, X., Roberts, H.M., Scourse, J., 2021. The evolution of the
4576 terrestrial-terminating Irish Sea glacier during the last glaciation. *J. Quat. Sci.* 36, 752–779.
4577 <https://doi.org/https://doi.org/10.1002/jqs.3229>

4578 Churchyard, T., 1580. *A warning for the wise*. J. Alde and N. Ling, London.

4579 Clare, M. A., Lichtschlag, A., Paradis, S., & Barlow, N. L. M. (2023). Assessing the impact of the
4580 global subsea telecommunications network on sedimentary organic carbon stocks. *Nature*
4581 *Communications*, 14(1), 2080. <https://doi.org/10.1038/s41467-023-37854-6>.

4582 Clark, C. D., Hughes, A. L. C., Greenwood, S. L., Jordan, C. J., and Sejrup, H.P. (2012) Pattern and
4583 timing of retreat of the last British–Irish Ice Sheet. *Quaternary Science Reviews*, v. 44, 112–149.

4584 Clark, C. D., Ely, J. C., Greenwood, S. L., Hughes, A. L. C., Meehan, R., Barr, I. D., Bateman, M. D.,
4585 Bradwell, T., Doole, J., Evans, D. J. A., Jordan, C. J., Monteys, X., Pellicer, X. M., Sheehy, M. (2017).
4586 BRITICE Glacial Map, version 2: a map and GIS database of glacial landforms of the last British–Irish
4587 Ice Sheet. *Boreas*, Vol. 47,11–27.

4588 Clark, C. D., Ely, J. C., Hindmarsh, R. C. A., Bradley, S., Ign'eczi, A., Fabel, D., Ó Cofaigh, C.,
4589 Chiverrell, R. C., Scourse, J., Benetti, S., Bradwell, T., Evans, D. J. A., Roberts, D. H., Burke, M.,
4590 Callard, S. L., Medialdea, A., Saher, M., Small, D., Smedley, R. K., Gasson, E., Gregoire, L., Gandy,
4591 N., Hughes, A. L. C., Ballantyne, C., Bateman, M. D., Bigg, G. R., Doole, J., Dove, D., Duller, G. A.
4592 T., Jenkins, G. T. H., Livingstone, S. L., McCarron, S., Moreton, S., Pollard, D., Praeg, D., Sejrup, H.
4593 P., van Landeghem, K. J. J. & Wilson, P. 2022 (October): Growth and retreat of the last British–Irish
4594 Ice Sheet, 31 000 to 15 000 years ago: the BRITICE-CHRONO reconstruction. *Boreas*, Vol. 51,
4595 pp.699–758. <https://doi.org/10.1111/bor.12594>. ISSN 0300-9483

4596 Clarke, B. G. (2018). The engineering properties of glacial tills. *Geotechnical Research*, 5(4), 262–277.
4597 <https://doi.org/10.1680/jgere.18.00020>

4598 Coco, G., Murray, A. B., & Green, M. O. (2007a). Sorted bed forms as self-organized patterns: 1. Model
4599 development. *Journal of Geophysical Research: Earth Surface*, 112(F3), 3015.
4600 <https://doi.org/10.1029/2006JF000665>

4601 Coco, G., Murray, A. B., Green, M. O., Thielert, E. R., & Hume, T. M. (2007b). Sorted bed forms as
4602 self-organized patterns: 2. Complex forcing scenarios. *Journal of Geophysical Research: Earth Surface*,
4603 112(F3). <https://doi.org/10.1029/2006JF000666>

4604 Collinson, J. (2005). SEDIMENTARY PROCESSES | Depositional Sedimentary Structures.
4605 *Encyclopedia of Geology*, 593–602. <https://doi.org/10.1016/B0-12-369396-9/00466-4>

4606 Cooke, F., Plaza-Faverola, A., Bünz, S., Sultan, N., Ramachandran, H., Bedle, H., ... & Knies, J. (2023).
4607 Sedimentary deformation relating to episodic seepage in the last 1.2 million years: a multi-scale seismic
4608 study from the Vestnesa Ridge, eastern Fram Strait. *Frontiers in Earth Science*, 11, 1188737.

4609 Cooke, F., Plaza-Faverola, A., Bünz, S., De Groot, P., & Peacock, D. C. (2025). Semiautomated
4610 analysis of faults with meter-scale displacements and networks of planar features using high-resolution
4611 3D seismic data to investigate gas leakage at the Vestnesa Ridge, Eastern Fram Strait. *Interpretation*,
4612 13(1), B1-B23.

4613 Coquerel, J., (1580). Discours d'une merveilleuse et veritable copie du grand deluge et debordemēt de
4614 la mer, avec le nom des lieux et places qui ont esté submergez et le nombre des navires qui ont esté
4615 peris entre Douvre&Calais,&autres lieux, le vi. et vii. jour d'Avril, 1580, Paris.

4616 Cotterill, C. J., Phillips, E., James, L., Forsberg, C. F., Tjelta, T. I., Carter, G., & Dove, D. (2017). The
4617 evolution of the Dogger Bank, North Sea: A complex history of terrestrial, glacial and marine
4618 environmental change. *Quaternary Science Reviews*, 171, 136–153.
4619 <https://doi.org/10.1016/j.quascirev.2017.07.006>

4620 Coughlan, M., Fleischer, M., Wheeler, A.J., Hepp, D.A., Hebbeln, D., Mörz, T., 2018. A revised
4621 stratigraphical framework for the Quaternary deposits of the German North Sea sector: a geological-
4622 geotechnical approach. *Boreas* 47. <https://doi.org/10.1111/bor.12253>

4623 Coughlan, M., Tóth, Z., Van Landeghem, K.J.J., McCarron, S., Wheeler, A.J., 2020a. Formational
4624 history of the Wicklow Trough: a marine-transgressed tunnel valley revealing ice flow velocity and
4625 retreat rates for the largest ice stream draining the late-Devensian British–Irish Ice Sheet. *J. Quat. Sci.*
4626 00, 1–13. <https://doi.org/10.1002/jqs.3234>

4627 Coughlan, M, Long, M., Doherty, P., 2020b. Geological and geotechnical constraints in the Irish Sea
4628 for offshore renewable energy. *Journal of Maps*, v. 16, 420–431.
4629 <https://doi.org/10.1080/17445647.2020.1758811>

4630 Coughlan, M, Guerrini, M., Creane, S., O’Shea, M., Ward, S.L., Van Landeghem, K.J.J., Murphy, J.,
4631 Doherty, P., 2021a. A new seabed mobility index for the Irish Sea: Modelling seabed shear stress and
4632 classifying sediment mobilisation to help predict erosion, deposition, and sediment distribution. *Cont.*
4633 *Shelf Res.* 229, 104574. <https://doi.org/10.1016/j.csr.2021.104574>

- 4634 Coughlan, M., Roy, S., O’Sullivan, C., Clements, A., O’Toole, R., Plets, R., 2021. Geological settings
4635 and controls of fluid migration and associated seafloor seepage features in the north Irish Sea. *Mar. Pet.*
4636 *Geol.* 123. <https://doi.org/10.1016/j.marpetgeo.2020.104762>
- 4637 Coughlan, M., Trafford, A., Corrales, S., Donohue, S., Wheeler, A.J., Long, M., 2023. Geological and
4638 geotechnical characterisation of soft Holocene marine sediments: A case study from the north Irish Sea.
4639 *Eng. Geol.* 313, 106980. <https://doi.org/10.1016/j.enggeo.2022.106980>
- 4640 Cox, D.R., Knutz, P.C., Campbell, D.C., Hopper, J.R., Newton, A.M.W, Huuse, M. and Gohl, K., 2020.
4641 Geohazard detection using 3D seismic data to enhance offshore scientific drilling site selection.
4642 *Scientific Drilling*, 28, pp.1-27.
- 4643 Creane, S., Coughlan, M., O’Shea, M., & Murphy, J. (2022). Development and Dynamics of Sediment
4644 Waves in a Complex Morphological and Tidal Dominant System: Southern Irish Sea. *Geosciences*,
4645 12(12), 431. <https://doi.org/10.3390/geosciences12120431>
- 4646 Creane, S., O’Shea, M., Coughlan, M., Murphy, J., 2023a. Hydrodynamic Processes Controlling Sand
4647 Bank Mobility and Long-Term Base Stability: A Case Study of Arklow Bank. *Geosci.* 13.
4648 <https://doi.org/10.3390/geosciences13020060>
- 4649 Creane, S., O’Shea, M., Coughlan, M., Murphy, J., 2023b. Morphological Modelling to Investigate the
4650 Role of External Sediment Sources and Wind and Wave-Induced Flow on Sand Bank Sustainability:
4651 An Arklow Bank Case Study. *J. Mar. Sci. Eng.* 11. <https://doi.org/10.3390/jmse11102027>
- 4652 Croker, P.F., Kozachenko, M., Wheeler, A.J., 2005. Gas-Related Seabed Structures in the Western Irish
4653 Sea (IRL-SEA6).
- 4654 Cunningham, J., Cardozo, N., Townsend, C., and Callow, R., 2020, The impact of seismic interpretation
4655 methods on the analysis of faults: a case study from the Snøhvit field, Barents Sea: *Solid Earth*
4656 *Discussions*, v. 2020, p. 1-48.
- 4657 Dade, W. B. and Huppert, H. E. (1994). Predicting the geometry of channelized deep-sea turbidites,
4658 *Geol.* 22: 645–648, DOI 10.1130/0091-7613(1994)022<0645:ptgocd>2.3.co;2.
- 4659 Dahm, T., Cesca, S., Hainzl, S., Braun, T., Krüger, F., 2015. Discrimination between induced, triggered,
4660 and natural earthquakes close to hydrocarbon reservoirs: A probabilistic approach based on the
4661 modeling of depletion-induced stress changes and seismological source parameters. *J. Geophys. Res.*
4662 *Solid Earth* 120, 2491–2509. <https://doi.org/10.1002/2014JB011778>
- 4663 Danish Maritime Authority (2023). Maritime spatial plan. [https://www.dma.dk/growth-and-](https://www.dma.dk/growth-and-framework-conditions/maritime-spatial-plan)
4664 [framework-conditions/maritime-spatial-plan](https://www.dma.dk/growth-and-framework-conditions/maritime-spatial-plan) . Accessed April 2025.

4665 Davies, R. J., Swarbrick, R. E., Evans, R. J. & Huuse, M., 2007. Birth of a mud volcano: East Java, 29
4666 May 2006. *GSA Today*: v. 17, no. 2, doi: 10.1130/GSAT01702A.1

4667 Davis, A. M. (1992). Shallow gas: an overview. *Continental shelf research*, 12(10), 1077-1079.

4668 Davison, S., 2004. Reconstructing the Last Pleistocene (Late Devensian) Glaciation on the Continental
4669 Margin of Northwest Britain. Ph.D. Thesis. The University of Edinburgh.

4670 Dawson, A.G., Long, D., Smith, D.E., 1988. The Storegga Slides: evidence from eastern Scotland for
4671 a possible tsunami. *Marine Geology* 82, 271–276.

4672 Dawson, A.G., Long, D., Smith, D.E., Shi, S., Foster, I.D.L., 1993. Tsunamis in the Norwegian Sca and
4673 North Sea caused by the Storegga submarine landslides, in: Tinti, S. (Ed.), *Tsunamis in the World*.
4674 Kluwer Academic Publishers, The Netherlands, pp. 31 -42.

4675 Dawson, S., Smith, D.E., Ruffman, A., Shi, S., 1996. The diatom biostratigraphy of tsunami sediments:
4676 Examples from recent and middle holocene events. *Physics and Chemistry of the Earth* 21, 87-92.

4677 De Blasio, F. V.; Issler, D.; Elverhøi, A.; Harbitz, C. B.; Ildstad, T.; Bryn, P.; Lien, R. and Løvholt, F.
4678 (2003). Dynamics, velocity and run-out of the giant Storegga slide. In: *Submarine Mass Movements
4679 and Their Consequences*, Locat, J. and Mienert, J. (eds.), *Adv. Natural Technol. Hazards Res.* 19 : 223–
4680 230, DOI 10.1007/978-94-010-0093-2_25.

4681 De Blasio, F. V., Engvik, L., Harbitz, C. B. and Elverhøi, A. (2004). Hydroplaning and submarine debris
4682 flows. *Journal of Geophysical Research* 109, C01002, DOI 10.1029/2002JC001714.

4683 De Blasio F. V., Elverhøi A., Issler D., Harbitz C. B., Bryn P., and Lien R. (2005) On the dynamics of
4684 subaqueous clay rich gravity mass flows—the giant Storegga slide, Norway. In: *Ormen Lange — an
4685 Integrated Study for Safe Field Development in the Storegga Submarine Area*, pp. 179–186. Elsevier.

4686 De Blasio, F.V., Elverhøi, A., Engvik, L., Issler, D., Gauer, P., and Harbitz, C. B. (2006). Understanding
4687 the high mobility of subaqueous debris flows. *Norwegian Journal of Geology* 86, 275–284.

4688 De Falco, G., Budillon, F., Conforti, A., Di Bitetto, M., Di Martino, G., Innangi, S., Simeone, S., &
4689 Tonielli, R. (2015). Sorted bedforms over transgressive deposits along the continental shelf of western
4690 Sardinia (Mediterranean Sea). *Marine Geology*, 359, 75–88.
4691 <https://doi.org/10.1016/j.margeo.2014.11.008>

4692 de Jonge-Anderson, I., & Underhill, J. R. (2022). Use of subsurface geology in assessing the optimal
4693 co-location of CO2 storage and wind energy sites. *Earth Science, Systems and Society*, 2(1), 10055.

4694 Den Haan, E. J., and Kruse, G. A. M. (2007). "Characterisation and engineering properties of Dutch
4695 peats." *Characterisation and Engineering Properties of Natural Soils*, T. S. Tan, K. K. Phoon, D. W.
4696 Hight, and S. Leroueil, eds., Taylor and Francis Group, London, Singapore, 2101-2133.

4697 Diesing, M., Ware, S., Foster-Smith, R., Stewart, H., Long, D., Vanstaen, K., Forster, R., & Morando,
4698 A. (2009). Understanding the marine environment – seabed habitat investigations of the Dogger Bank
4699 offshore draft SAC. Joint Nature Conservation Committee, Peterborough. JNCC Report No. 429, 89pp.,
4700 5 Appendices.

4701 Diesing, M., Kröger, S., Parker, R., Jenkins, C., Mason, C., Weston, K., 2017. Predicting the standing
4702 stock of organic carbon in surface sediments of the North–West European continental shelf.
4703 *Biogeochemistry* 135, 183–200. <https://doi.org/10.1007/s10533-017-0310-4>

4704 Dimakis, P., Braathen, B. I., Faleide, J. I., Elverhøi, A., & Gudlaugsson, S. T. (1998). Cenozoic erosion
4705 and the preglacial uplift of the Svalbard–Barents Sea region. *Tectonophysics*, 300(1-4), 311-327.

4706 Dimakis, P., Elverhøi, A., Høeg, K., Solheim, A., Harbitz, C.B., Laberg, J.S., Vorren, T., and Marr, J.
4707 (2000). Submarine slope stability on high-latitude glaciated Svalbard–Barents Sea margin. *Marine*
4708 *Geology*, Vol. 162, No. 2–4, 303–316.

4709 Dimmock, P. S., Riera, R., Tam, T. A., & Boylan, N. (2023, January). Geohazard or Geo-engineering
4710 constraint?. In *Offshore Site Investigation Geotechnics 9th International Conference Proceeding* (Vol.
4711 2067, No. 2071, pp. 2067-2071). Society for Underwater Technology.

4712 Dix, J. K., Riera, R., Dimmock, P., Barwise, A., & Arlott, L. (n.d.). Sorted bedforms implications for
4713 offshore renewable infrastructure. *9th International SUT Offshore Site Investigation Geotechnics*
4714 *Conference Proceedings “Innovative Geotechnologies for Energy Transition,”* 643–650.
4715 <https://doi.org/10.3723/MLPJ7639>

4716 DNV, D. N. V. (2014). DNV-RP-J301: Subsea power cables in shallow water renewable energy
4717 applications. Høvik, Oslo, Norway.

4718 Donovan, S.K., Pickerill, R.K., 1997. Dropstones: their origin and significance: a comment.
4719 *Palaeogeography, Palaeoclimatology, Palaeoecology* 131, 175–178. [https://doi.org/10.1016/S0031-](https://doi.org/10.1016/S0031-0182(96)00150-2)
4720 [0182\(96\)00150-2](https://doi.org/10.1016/S0031-0182(96)00150-2)

4721 Dove, D., Evans, D.J.A., Lee, J.R., Roberts, D.H., Tappin, D.R., Mellett, C.L., Long, D., Callard, S.L.
4722 (2017). Phased occupation and retreat of the last British–Irish Ice Sheet in the southern North Sea;
4723 geomorphic and seismostratigraphic evidence of a dynamic ice lobe. *Quaternary Science Reviews*, v.
4724 163, 114–134.

4725 Dowdeswell, J.A., Ottesen, D., and Rise, L., 2010, Rates of sediment delivery from the Fennoscandian
4726 Ice Sheet through an ice age: *Geology*, v. 38, p. 3–6, <https://doi.org/10.1130/G25523.1>.

- 4727 Dowdeswell, J. A., & Ottesen, D. (2013). Buried iceberg ploughmarks in the early Quaternary
4728 sediments of the central North Sea: a two-million year record of glacial influence from 3D seismic data.
4729 *Marine Geology*, 344, 1-9.
- 4730 Dowdeswell, J. A., Canals, M., Jakobsson, M., Todd, B. J., Dowdeswell, E. K., & Hogan, K. A. (2016).
4731 The variety and distribution of submarine glacial landforms and implications for ice-sheet
4732 reconstruction. *Geological Society, London, Memoirs*, 46(1), 519-552.
- 4733 Durán, R., Guillén, J., Muñoz, A., Durán, R., Guillén, Á. J., & Muñoz, A. (2017). Sorted Bedforms
4734 Developed on Sandy Deposits Derived from Small Ephemeral Streams (Catalan Continental Shelf).
4735 *Atlas of Bedforms in the Western Mediterranean*, 127–133. [https://doi.org/10.1007/978-3-319-33940-](https://doi.org/10.1007/978-3-319-33940-5_21)
4736 [5_21](https://doi.org/10.1007/978-3-319-33940-5_21)
- 4737 Dyer, K. R., & Huntley, D. A. (1999). The origin, classification and modelling of sand banks and ridges.
4738 *Continental Shelf Research*, 19(10), 1285–1330. [https://doi.org/10.1016/S0278-4343\(99\)00028-X](https://doi.org/10.1016/S0278-4343(99)00028-X)
- 4739 Dyer, J. M. (2011). Geohazard identification: the gap between the possible and reality in geophysical
4740 surveys for the engineering industry. *Marine Geophysical Researches*, Vol. 32, 37–47.
- 4741 Dück, Y., Lorke, A., Jokiel, C., Gierse, J., 2019. Laboratory and field investigations on freeze and
4742 gravity core sampling and assessment of coring disturbances with implications on gas bubble
4743 characterization. *Limnol. Oceanogr. Methods* 17, 585–606. <https://doi.org/10.1002/lom3.10335>
- 4744 Eaton, S.J., Hodgson, D.M., Barlow, N.L.M., Mortimer, E.E.J., Mellett, C.L., 2020. Palaeogeographical
4745 changes in response to glacial–interglacial cycles, as recorded in Middle and Late Pleistocene seismic
4746 stratigraphy, southern North Sea. *Journal of Quaternary Science* 35, 760–775.
4747 <https://doi.org/10.1002/jqs.3230>
- 4748 Eaton, S., N. L. M. Barlow, D. M. Hodgson, C. L. Mellet, and A. R. Emery (2024). Landscape evolution
4749 during Holocene transgression of a mid-latitude low-relief coastal plain: The southern North Sea, *Earth
4750 Surface Processes and Landforms*, 49, 3139–3157, doi:<https://doi.org/10.1002/esp.5880>.
- 4751 Eglit, M. E.; Yakubenko, A. and Zayko, J. (2020). A review of Russian snow avalanche models — from
4752 analytical solutions to novel 3D models, *Geosciences* 10: 77, DOI 10.3390/geosciences10020077.
- 4753 Eidvin, T., Bugge, T. & Smelror, M., 2007: The Molo Formation, deposited by coastal progradation on
4754 the inner Mid-Norwegian continental shelf, coeval with the Kai Formation to the west and the Utsira
4755 Formation in the North Sea. *Norwegian Journal of Geology* 87, 75–142.
- 4756 Eigaard, O.R., Bastardie, F., Hintzen, N.T., Buhl-Mortensen, L., Buhl-Mortensen, P., Catarino, R.,
4757 Dinesen, G.E., Egekvist, J., Fock, H.O., Geitner, K., Gerritsen, H.D., González, M.M., Jonsson, P.,
4758 Kavadas, S., Laffargue, P., Lundy, M., Gonzalez-Mirelis, G., Nielsen, J.R., Papadopoulou, N., Posen,

- 4759 P.E., Pulcinella, J., Russo, T., Sala, A., Silva, C., Smith, C.J., Vanelslander, B., Rijnsdorp, A.D., 2017.
4760 The footprint of bottom trawling in European waters: distribution, intensity, and seabed integrity. *ICES*
4761 *J. Mar. Sci.* 74, 847–865. <https://doi.org/10.1093/icesjms/fsw194>
- 4762 Ekman, S.R., Scourse, J.D. (1993) Early and Middle Pleistocene pollen stratigraphy from British
4763 Geological Survey Borehole 81/26, Fladen Ground, central North Sea. *Review of Palaeobotany and*
4764 *Palynology*, v. 79, 285–295.
- 4765 Eldholm, O., and Bungum, H. (2021). Potential secondary events caused by early Holocene
4766 paleoearthquakes in Fennoscandia – a climate-related review. *Norwegian Journal of Geology* 101,
4767 202108. <https://dx.doi.org/10.17850/njg101-2-3>
- 4768 Elger, J., Berndt, C., Krastel, S., Piper, D.J.W., Gross, F., Geissler, W.H., 2017. Chronology of the Fram
4769 Slide Complex offshore NW Svalbard and its implications for local and regional slope stability, *Marine*
4770 *Geology*, Volume 393, 141-155, <https://doi.org/10.1016/j.margeo.2016.11.003>.
- 4771 Ellis, J.R., Milligan, S.P., Readdy, L., Taylor, N. and Brown, M.J. 2012. Spawning and nursery grounds
4772 of selected fish species in UK waters. *Sci. Ser. Tech. Rep.*, Cefas Lowestoft, 147: 56pp
- 4773 Elverhøi, A., & Solheim, A. (1983). The Barents Sea ice sheet – a sedimentological discussion. *Polar*
4774 *Research*, 1(1), 23-42.
- 4775 Elverhøi, A.; De Blasio, F. V.; Butt, F. A.; Issler, D.; Harbitz, C. B.; Engvik, L.; Solheim A. and Marr,
4776 J. (2002). Submarine mass-wasting on glacially influenced continental slopes—processes and
4777 dynamics. In: *Glacier-Influenced Sedimentation on High-Latitude Continental Margins*, Dowdeswell,
4778 J. A. and Ó Cofaigh, C. (eds.), *Special Publications*, No. 203, Geological Society of London: London,
4779 U.K., pp. 73–87, DOI 10.1144/gsl.sp.2002.203.01.05.
- 4780 Elverhøi A, Issler D, De Blasio FV, Iltstad T, Harbitz CB, and Gauer P (2005). Emerging insights into
4781 the dynamics of submarine debris flows. *Natural Hazards and Earth System Sciences* 5(5): 633–648,
4782 DOI 10.5194/nhess-5-633-2005.
- 4783 Elverhøi, A., Breien, H., De Blasio, F.V., Harbitz, C.B., and Pagliardi, M. (2010). Submarine landslides
4784 and the importance of the initial sediment composition for run-out length and final deposit. 70th
4785 anniversary of Prof. B. N. Gjevik. *Ocean Dynamics Special Issue* 60(4): 1027–1046, DOI
4786 10.1007/s10236-010-0317-z.
- 4787 Emery, A. R., Hodgson, D. M., Barlow, N. L. M., Carrivick, J. L., Cotterill, C. J., Mellett, C. L., &
4788 Booth, A. D. (2019). Topographic and hydrodynamic controls on barrier retreat and preservation: An
4789 example from Dogger Bank, North Sea. *Marine Geology*, 416.
4790 <https://doi.org/10.1016/j.margeo.2019.105981>

- 4791 Engen, Ø., Eldholm, O., Bungum, H., 2003. The Arctic plate boundary. *J. Geophys. Res. - Solid Earth*
4792 108, 2075+. <https://doi.org/10.1029/2002jb001809>
- 4793 Esposti Ongaro, T., de'Michieli Vitturi, M., Cerminara, M., Fornaciai, A., Nannipieri, L., Favalli, M.,
4794 Calusi, B., Macías, J., Castro, M.J., Ortega, S., González-Vida, J.M., and Escalante, C. (2021).
4795 Modeling tsunamis generated by submarine landslides at Stromboli Volcano (Aeolian Islands, Italy): A
4796 numerical benchmark study. *Frontiers in Earth Science*, 9, 628652.
- 4797 Evans, D., Graham, C., Armour, A. & Bathurst, P. (editors) 2003. *The Millennium Atlas: Petroleum*
4798 *Geology of the Central and Northern North Sea*. 389 pp. London, Bath: Geological Society of London.
4799 ISBN 1 86239 119 X.
- 4800 Evans, D., Harrison, Z., Shannon, P.M., Laberg, J.S., Nielsen, T., Ayers, S., Holmes, R., Hoult, R.J.,
4801 Lindberg, B., Haflidason, H., Long, D., Kuijpers, A., Andersen, E.S., and Bryn, P., 2005, Palaeoslides
4802 and other mass failures of Pliocene to Pleistocene age along the Atlantic continental margin of NW
4803 Europe: Marine and Petroleum Geology, v. 22, p. 1131-1148.
4804 <https://doi.org/10.1016/j.marpetgeo.2005.01.010>.
- 4805 Evans, D.J.A., Roberts, D.H., Bateman, M.D., Clark, C.D., Medialdea, A., Callard, S.L., Grimoldi, E.,
4806 Chiverrell, R.C., Ely, J.C., Dove, D., O' Cofaigh, C., Saher, M., Bradwell, T., Moreton, S.G., Fabel, D.,
4807 Bradley S.L. (2021) Retreat dynamics of the eastern sector of the British–Irish Ice Sheet during the last
4808 glaciation. *Journal of Quaternary Science*, 1-29.
- 4809 Eyles, N. (Ed.). (2013). *Glacial geology: an introduction for engineers and earth scientists*. Elsevier.
- 4810 Eyles, C.H., Eyles, N., 2010. Glacial Deposits, in: *Facies Models 4*. The Geological Association of
4811 Canada, Ontario, pp. 73–104.
- 4812 Faleide, J. I., Solheim, A., Fiedler, A., Hjelstuen, B. O., Andersen, E. S., & Vanneste, K. (1996). Late
4813 Cenozoic evolution of the western Barents Sea-Svalbard continental margin. *Global and Planetary*
4814 *Change*, 12(1-4), 53-74.
- 4815 Faleide, J. I., P. W. Wong, M. Hassaan, R. H. Gabrielsen, M. M. Abdelmalak, S. Planke, F. Tsikalas,
4816 B. Manton, and R. Myklebust (2025), West Barents Sheared Margin Composite Tectono-Sedimentary
4817 Element, Norwegian–Greenland Sea and Fram Strait, Geological Society, London, *Memoirs*, 57(1),
4818 M57-2023-2019.
- 4819 Faleide, T. S., Midtkandal, I., Planke, S., Corseri, R., Faleide, J. I., Serck, C. S., and Nystuen, J. P.,
4820 2019, Characterisation and development of Early Cretaceous shelf platform deposition and faulting in
4821 the Hoop area, southwestern Barents Sea—constrained by high-resolution seismic data: Norwegian
4822 *Journal of Geology*, v. 99, no. 3, p. 1-20.

- 4823 Fejerskov, M., and Lindholm, C. (2000). Crustal stress in and around Norway: an evaluation of stress
4824 generating mechanisms. Geological Society, London, Special Publications, 167, 451–467.
- 4825 Fenster, M.S. (2018). Offshore Sand Sheets. In: Finkl, C., Makowski, C. (eds) Encyclopedia of Coastal
4826 Science . Encyclopedia of Earth Sciences Series. Springer, Cham. https://doi.org/10.1007/978-3-319-48657-4_236-2
4827
- 4828 Fjeldskaar, W., & Amantov, A. (2018). Effects of glaciations on sedimentary basins. Journal of
4829 Geodynamics, 118, 66-81.
- 4830 Fleischer, M., Abegunrin, A., Hepp, D.A., Kreiter, S., Coughlan, M., Mörz, T., 2023. Stratigraphic and
4831 geotechnical characterization of regionally extensive and highly competent shallow sand units in the
4832 southern North Sea. Boreas 52, 78–98. <https://doi.org/10.1111/bor.12595>
- 4833 Forterre, Y. and Pouliquen, O. (2009). Granular flows. Sémin. Poincaré XIII: 69–100, DOI
4834 10.1007/978-3-0348-0084-6_4.
- 4835 Forsberg, C. F., Plank, S., Tjelta, T. I., Svano, G., Strout, J. M., & Svensen, H. (2007, September).
4836 Formation of pockmarks in the Norwegian Channel. In SUT Offshore Site Investigation and
4837 Geotechnics (pp. SUT-OSIG). SUT.
- 4838 Forterre, Y. and Pouliquen, O., 2009. Granular flows. Séminaire Poincaré XIII: 69–100. DOI
4839 10.1007/978-3-0348-0084-6_4.
- 4840 Fraccarollo, L. and Capart, H. (2002). Riemann wave description of erosional dam-break flows. Journal
4841 of Fluid Mechanics 461: 183–228, DOI 10.1017/S0022112002008455.
- 4842 Fugro Engineering Services. (2013). Burbo Bank Extension Offshore Wind Farm; Geotechnical Site
4843 Investigation. C1516/G2667/N1220016U. 2078pp.
- 4844 Fugro, 2017. Microbial Influenced Corrosion. Hollandse Kust (zuid) Wind Farm Zone. Technical Note
4845 for Rijksdienst voor Ondernemend Nederland (RVO). 24 pp.
- 4846 Fugro, 2024. Report no 2, 2D UHRS Survey Geomodel Integrated with CPT Data, Full Site, Danish
4847 Offshore Wind 2030, North Sea 1, Denmark, F217715-REP-002 [03], 222 pp.
- 4848 Fyfe, J. A., Long, D., Evans, D. (1993). United Kingdom offshore regional report: the geology of the
4849 Malin-Hebrides sea area. London: HMSO for the British Geological Survey.
- 4850 Garcia, A. M., Bellwald, B., Planke, S., Anell, I., Myklebust, R., Sternai, P., & Midtkandal, I. (2024).
4851 Sedimentation record of a complete glacial-interglacial cycle: Down-slope deposits, contourites and
4852 plumites of the North Sea trough mouth fan. Quaternary Science Reviews, 339, 108839.

4853 Gatliff, R.W., Richards, P.C., Smith, K., Graham, C.C., McCormac, M., Smith, N.J.P., Long, D.,
4854 Cameron, T.D.J., Evans, D., Stevenson, A.G., Bulat, J., Ritchie, J.D. (1994) UK Offshore Regional
4855 Report: the Geology of the Central North Sea. London: HMSO for the British Geological Survey.

4856 Gatter, R., et al., 2020. A multi-disciplinary investigation of the AFEN Slide: the relationship between
4857 contourites and submarine landslides. From: Georgiopoulou, A., Amy, L. A., Benetti, S., Chaytor, J.
4858 D., Clare, M. A., Gamboa, D., Haughton, P. D. W., Moernaut, J. and Mountjoy, J. J. (eds) 2020.
4859 Subaqueous Mass Movements and their Consequences: Advances in Process Understanding,
4860 Monitoring and Hazard Assessments. Geological Society, London, Special Publications, 500,
4861 <https://doi.org/10.1144/SP500-2019-184>.

4862 Gatter, R., Clare, M. A., Kuhlmann, J., & Huhn, K. (2021). Characterisation of weak layers, physical
4863 controls on their global distribution and their role in submarine landslide formation. *Earth-Science*
4864 *Reviews*, 223, 103845.

4865 Gauer, P. and Issler, D. (2004). Possible erosion mechanisms in snow avalanches. *Annals of Glaciology*
4866 32: 384–392, DOI 10.3189/172756404781815068.

4867 Gauer P, Kvalstad TJ, Forsberg CF, Bryn P, and Berg K (2005). The last phase of the Storegga slide:
4868 Simulation of retrogressive slide dynamics and comparison with slide-scar morphology. *Marine and*
4869 *Petroleum Geology* 22(1–2): 171–178. DOI 10.1016/j.marpetgeo.2004.10.004.

4870 Gauer, P.; Elverhøi, A.; Issler, D. and De Blasio, F. V. (2006). On numerical simulations of subaqueous
4871 slides: Back-calculations of laboratory experiments of clay-rich slides. *Norwegian Journal of Geology*
4872 86(3): 295–300.

4873 Gaume, J.; van Herwijnen, A.; Gast, T.; Teranc, J. and Jiang, C. (2019). Investigating the release and
4874 flow of snow avalanches at the slope-scale using a unified model based on the material point method.
4875 *Cold Regions Science and Technology* 168: 102847, DOI 10.1016/j.coldregions.2019.102847.

4876 GdR MiDi (Groupement de Recherche Milieux Divisés), 2004. On dense granular flows. *The European*
4877 *Physical Journal E* 14:340–365. DOI 10.1140/epje/i2003-10153-0.

4878 GEBCO Compilation Group (2024) GEBCO 2024 Grid (doi:10.5285/1c44ce99-0a0d-5f4f-e063-
4879 7086abc0ea0f)

4880 Gibbons, S.J., Bøttger Sørensen, M., Harris, D.B., Ringdal, F., 2007. The detection and location of low
4881 magnitude earthquakes in northern Norway using multi-channel waveform correlation at regional
4882 distances. *Phys. Earth Planet. Inter.* 160, 285–309. <https://doi.org/10.1016/j.pepi.2006.11.008>

4883 Giglio, C., Benetti, S., Sacchetti, F., Lockhart, E., Hughes Clarke, J., Plets, R., Van Landeghem, K., Ó
4884 Cofaigh, C., Scourse, J., Dunlop, P., 2021. A Late Pleistocene channelized subglacial meltwater system

4885 on the Atlantic continental shelf south of Ireland. *Boreas* 51, 118–135.
4886 <https://doi.org/10.1111/bor.12536>

4887 Giglio, C., Benetti, S., Plets, R.M.K., Dunlop, P., Ó Cofaigh, C., Sacchetti, F., Salomon, E., 2022a.
4888 Character of advance and retreat of the southwest sector of the British-Irish Ice Sheet during the last
4889 glaciation. *Quat. Sci. Rev.* 291, 107655. <https://doi.org/10.1016/j.quascirev.2022.107655>

4890 Giles, D.P., (2020a). Introduction to Geological Hazards in the UK: Their Occurrence, Monitoring and
4891 Mitigation. Geological Society, London, Engineering Geology Special Publications, 29, 1-41.

4892 Giles, D. P. (2020b). Quick clay behaviour in sensitive Quaternary marine clays—a UK perspective.

4893 Glimsdal, S., Pedersen, G.K., Harbitz, C.B., and Løvholt, F. (2013). Dispersion of tsunamis: does it
4894 really matter? *Nat. Hazards Earth Syst. Sci.*, 13, 1507-1526, doi: 10.5194/nhess-13-1507-2013.

4895 Goldfinger, C. (2011). Submarine paleoseismology based on turbidite records. *Annual Review of*
4896 *Marine Science*, 3(1), 35-66.

4897 Goldstein, E. B., Murray, A. B., & Coco, G. (2011). Sorted bedform pattern evolution: Persistence,
4898 destruction and self-organized intermittency. *Geophysical Research Letters*, 38(24).
4899 <https://doi.org/10.1029/2011GL049732>

4900 Golledge, N.R., Stoker, M.S. (2006) A palaeo-ice stream of the British Ice Sheet in eastern Scotland.
4901 *Boreas*, v. 35, 231–243.

4902 Goswami, B. K., Weitemeyer, K. A., Minshull, T. A., Sinha, M. C., Westbrook, G. K., Chabert, A., ...
4903 & Ker, S. (2015). A joint electromagnetic and seismic study of an active pockmark within the hydrate
4904 stability field at the Vestnesa Ridge, West Svalbard margin. *Journal of Geophysical Research: Solid*
4905 *Earth*, 120(10), 6797-6822.

4906 Graham, A.G.C., Lonergan, L., Stoker, M.S. (2009) Seafloor glacial features reveal the extent and decay
4907 of the last British Ice Sheet, east of Scotland. *Journal of Quaternary Science*, v. 24, 117–138.

4908 Graham, A.G.C. Stoker, M.S., Lonergan, L., Bradwell, T. & Stewart, M.A., 2011. Chapter 21-
4909 The Pleistocene Glaciations of the North Sea Basin. *Developments of Quaternary Science*, Vol 15, 261-
4910 278.

4911 Gray, J. M. N. T. (2001). Granular flow in partially filled slowly rotating drums. *Journal of Fluid*
4912 *Mechanics* 441: 1–29, DOI 10.1017/S0022112001004736.

4913 Gray, J. M. N. T.; Tai, Y.-C. and Noelle, S. (2003). Shock waves, dead-zones and particle-free regions
4914 in rapid granular free surface flows. *Journal of Fluid Mechanics* 491: 161–181, DOI
4915 10.1017/s0022112003005317.

- 4916 Greenwood, S. L., Clason, C. C., Nyberg, J., Jakobsson, M., & Holmlund, P. (2017). The Bothnian Sea
4917 ice stream: early Holocene retreat dynamics of the south-central Fennoscandian Ice Sheet. *Boreas*,
4918 46(2), 346-362.
- 4919 Greenwood, S. L., Avery, R. S., Gyllencreutz, R., Regnéll, C., & Tylmann, K. (2024). Footprint of the
4920 Baltic Ice Stream: geomorphic evidence for shifting ice stream pathways. *Boreas*, 53(1), 4-26.
- 4921 Gregersen, S., Basham, P. W., and Wood, R. M., 1989, Fifty million years of ‘passive
4922 margin’ deformation in North West Europe: Earthquakes at North-Atlantic passive margins:
4923 neotectonics and postglacial rebound, p. 7-36.
- 4924 Griffiths, J. S., & Martin, C. J. (Eds.). 2017. *Engineering Geology and Geomorphology of Glaciated
4925 and Periglaciated Terrains*. London, UK: Geological Society of London.
- 4926 Grimstad E, Nesdal S (1990) The Loen rockslides—a historical review. In: Barton M, Stephanson W
4927 (eds) *Rock joints*. Balkema, Rotterdam, pp 1–6
- 4928 Groupement de Recherche Milieux Divisés (2004). On dense granular flows. *Eur. J. Phys. E* 14(4) :
4929 340–365, DOI 10.1140/epje/i2003-10153-0.
- 4930 Grünthal, G., Stromeyer, D., Bosse, C. Cotton, F. & Bindi, D. (2018). The probabilistic seismic hazard
4931 assessment of Germany — version 2016, considering the range of epistemic uncertainties and aleatory
4932 variability. *Bulletin of Earthquake Engineering*, 16, p. 4339-4395.
- 4933 Guazzelli, É. and Pouliquen, O. (2018). Rheology of dense granular suspensions. *Journal of Fluid
4934 Mechanics* 852: P1, DOI 10.1017/jfm.2018.548.
- 4935 Gudmundsson, A., 1999, Postglacial crustal doming, stresses and fracture formation with application
4936 to Norway: *Tectonophysics*, v. 307, no. 3-4, p. 407-419.
- 4937 Guillet, L.; Blatny, L.; Trottet, B.; Steffen, D. and Gaume, J. (2023). A depth-averaged Material Point
4938 Method for shallow landslides: Applications to snow slab avalanche release. *Journal of Geophysical
4939 Research – Earth Surface* 128: e2023JF007092, DOI 10.1029/2023JF007092.
- 4940 Guinan, J., McKeon, C., O’Keeffe, E., Monteys, X., Sacchetti, F., Coughlan, M., Nic Aonghusa, C.,
4941 2020. INFOMAR data supports offshore energy development and marine spatial planning in the Irish
4942 offshore via the EMODnet Geology portal. *Q. J. Eng. Geol. Hydrogeol.* 54, qjegh2020-033.
4943 <https://doi.org/10.1144/qjegh2020-033>
- 4944 Gupta, S., Collier, J. S., Palmer-Felgate, A., & Potter, G. (2007). Catastrophic flooding origin of shelf
4945 valley systems in the English Channel. *Nature*, 448(7151), 342-345.

4946 Haflidason, H., Sejrup, H. P., Berstad, I. M., Nygård, A., Richter, T., Bryn, P., ... & Berg, K. (2003). A
4947 weak layer feature on the Northern Storegga Slide escarpment. *European Margin Sediment Dynamics:*
4948 *side-scan sonar and seismic images*, 55-62.

4949 Haflidason, H., Lien, R., Sejrup, H.P., Forsberg, C.F., Bryn, P., 2005. The dating and morphometry of
4950 the Storegga Slide. *Marine and Petroleum Geology* 22, 123–136, DOI
4951 10.1016/j.marpetgeo.2004.10.008.

4952 Hall, A., & van Boeckel, M. (2020). Origin of the Baltic Sea basin by Pleistocene glacial erosion. *Gff*,
4953 142(3), 237-252.

4954 Hall, A. M., Merritt, J., W., Connel, E. R., Hubbard, A., 2019. Early and Middle Pleistocene
4955 environments, landforms and sediments in Scotland. *Earth and Environmental Science Transactions of*
4956 *the Royal Society of Edinburgh*, 110, 5–37, <https://doi.org/10.1017/S1755691018000713>.

4957 Hammack JL (1973) A note on tsunamis: Their generation and propagation in an ocean of uniform
4958 depth. *Journal of Fluid Mechanics* 60(4): 769–799.

4959 Hanebuth, T.J.J., Lantzsch, H., Nizou, J., 2015. Mud depocenters on continental shelves—appearance,
4960 initiation times, and growth dynamics. *Geo-Marine Lett.* 35, 487–503. [https://doi.org/10.1007/s00367-](https://doi.org/10.1007/s00367-015-0422-6)
4961 [015-0422-6](https://doi.org/10.1007/s00367-015-0422-6)

4962 Hansen, J., Sato, M., Russell, G., & Kharecha, P. (2013). Climate sensitivity, sea level and atmospheric
4963 carbon dioxide. *Philosophical Transactions of the Royal Society A: Mathematical, Physical and*
4964 *Engineering Sciences*, 371(2001), 20120294.

4965 Harbitz, C. (1992). Model Simulations of Tsunamis Generated by the Storegga Slides. *Marine Geology*,
4966 Vol. 104.

4967 Harbitz, C., Pedersen, G. and Gjevik, B. (1993). Numerical Simulations of Large Water Waves Due to
4968 Landslides. *Jour. of Hydr. Eng.*, Vol. 119, No. 12.

4969 Harbitz, C. B., Parker, G., Elverhøi, A., Marr, J.G., Mohrig, D., and Harff, P.A. (2003). Hydroplaning
4970 of subaqueous debris flows and glide blocks: Analytical solutions and discussion. *Journal of*
4971 *Geophysical Research* 108(B7), 2349–2366, DOI:10.1029/2001JB001454.

4972 Harbitz, C.B., Glimsdal, S., Løvholt, F., Pedersen, G.K., Vanneste, M., Eidsvig, U.M.K, and Bungum,
4973 H. (2009). Tsunami hazard assessment and early warning systems for the North East Atlantic.
4974 *Proceedings of the DEWS Midterm Conference 2009, Potsdam, Germany, 7-8 July 2009.*

4975 Harbitz, C. B., Glimsdal, S., Løvholt, F., Kveldsvik, V., Pedersen, G. K., and Jensen, A. (2014).
4976 Rockslide tsunamis in complex fjords: From an unstable rock slope at Åkerneset to tsunami risk in
4977 western Norway. *Coastal engineering*, 88, 101-122.

- 4978 Harding, R., & Huuse, M. (2015). Salt on the move: Multi stage evolution of salt diapirs in the
4979 Netherlands North Sea. *Marine and Petroleum Geology*, 61, 39-55.
- 4980 Haugen, K.B., Løvholt, F., and Harbitz, C.B. (2005). Fundamental mechanisms for tsunami generation
4981 by submarine mass flows in idealised geometries. Ormen Lange Special Issue, *Marine and Petroleum*
4982 *Geology* 22, 209-217, doi: 10.1016/j.marpetgeo.2004.10.016.
- 4983 Hazell, Z. J. (2008). Offshore and intertidal peat deposits, England—a resource assessment and
4984 development of a database. *Environmental Archaeology*, 13(2), 101-110.
- 4985 Heller, V. and Ruffini, G., 2023. A critical review about generic subaerial landslide-tsunami
4986 experiments and options for a needed step change *Earth-Science Reviews*.
- 4987 Henkel, S.K., Revelas, E.C., Wodzicki, S., and Chapman, J. 2022. Discovery of a large offshore
4988 population of the northeast Pacific burrowing shrimp *Neotrypaea* sp.(Decapoda: Axiidea). *Estuarine,*
4989 *Coastal and Shelf Science*. doi.org/10.1016/j.ecss.2022.107936
- 4990 Henriksen, S. & Weimer, P. 1996: High-frequency depositional sequences and stratal stacking patterns
4991 in lower Pliocene coastal deltas, mid-Norwegian continental shelf. *American Association of Petroleum*
4992 *Geologists Bulletin* 80, 1867–1895. [https://doi.org/10.1306/64EDA226-1724-11D7-](https://doi.org/10.1306/64EDA226-1724-11D7-8645000102C1865D)
4993 [8645000102C1865D](https://doi.org/10.1306/64EDA226-1724-11D7-8645000102C1865D)
- 4994 Hepp, D. A., Romero, O. E., Mörz, T., DE POL-HOLZ, R., & Hebbeln, D. (2019). How a river
4995 submerges into the sea: a geological record of changing a fluvial to a marine paleoenvironment during
4996 early Holocene sea level rise. *Journal of Quaternary Science*, 34(7), 581-592.
- 4997 Hermanns, R. L., Schleier, M., Böhme, M., Blikra, L. H., Gosse, J., Ivy-Ochs, S., & Hilger, P. (2017).
4998 Rock-avalanche activity in W and S Norway peaks after the retreat of the Scandinavian ice sheet. In
4999 *Advancing Culture of Living with Landslides: Volume 5 Landslides in Different Environments* (pp.
5000 331-338). Springer International Publishing.
- 5001 Hernández-Molina, F. J., Stow, D. A. V., Llave, E., Rebesco, M., Ercilla, G., van Rooij, D., Mena, A.,
5002 Vázquez, J. T., & Voelker, A. H. L. (2011). Deep-water Circulation: Processes & Products (16-18 June
5003 2010, Baiona): Introduction and future challenges. *Geo-Marine Letters*, 31(5–6), 285–300.
5004 <https://doi.org/10.1007/S00367-011-0261-Z/FIGURES/10>
- 5005 Hilger, P. (2019). Rock-slope failures in Norway - temporal development and climatic conditioning.
5006 Doctoral thesis University of Oslo, Dept. of Geosciences.
5007 <https://www.duo.uio.no/bitstream/handle/10852/70806/1/PhD-Hilger-2019.pdf>

5008 Hill, J., Collins, G. S., Avdis, A., Kramer, S. C., & Piggott, M. D. (2014). How does multiscale
5009 modelling and inclusion of realistic palaeobathymetry affect numerical simulation of the Storegga Slide
5010 tsunami?. *Ocean Modelling*, 83, 11-25.

5011 Hill, A. W., Nicol, G., & Cook, M. R. (2024). A Proposed Standard Seismic Frequency Nomenclature
5012 for Geophysical Site Investigation Surveys in the Offshore Energy Sector. *First Break*, 42(11), 37-41.

5013 Hitchen, K., Johnson, J., Gatliff, R.W. (2013). Geology of the Rockall Basin and adjacent areas. British
5014 Geological Survey Research Report, RR/12/03.

5015 Hjelstuen, B.O., Eldholm, O. & Faleide, J.I. 2007: Recurrent Pleistocene mega-failures on the SW
5016 Barents Sea Margin. *Earth and Planetary Science Letters* 258, 605–618.
5017 <https://doi.org/10.1016/j.epsl.2007.04.025>.

5018 Hjelstuen, B.O., and Andreassen, E.V., 2015, North Atlantic Ocean deep-water processes and
5019 depositional environments: A study of the Cenozoic Norway Basin: *Marine and Petroleum Geology*, v.
5020 59, p. 429-441, <https://doi.org/10.1016/j.marpetgeo.2014.09.011>.

5021 Hjelstuen, B.O., Grinde, S., 2016. 3D seismic investigation of Pleistocene Mass Transport Deposits and
5022 Glacigenic Debris Flows on the North Sea Fan, NE Atlantic Margin. In: Lamarche, G et al. (eds)
5023 Submarine Mass Movements and Their Consequences, *Advances in Natural and Technological Hazard*
5024 *Research*, pp 265-272.

5025 Hjelstuen, B. O., Sejrup, H. P., Valvik, E., & Becker, L. W. (2018). Evidence of an ice-dammed lake
5026 outburst in the North Sea during the last deglaciation. *Marine Geology*, 402, 118-130.

5027 Hjelstuen, B.O., Sejrup, H.P., 2021. Latitudinal variability in the Quaternary development of the
5028 Eurasian ice sheets—Evidence from the marine domain. *Geology* 49, 356-351.

5029 Hjelstuen B.O., Sejrup, H.P., 2023. The North Sea and Mid-Norwegian Continental Margin: glacial
5030 landforms during deglaciation, the Bølling-Allerød Interstadial and the Younger Dryas. In: Palacios et
5031 al. (eds) *European Glacial Landscapes: Last Deglaciation*. Elsevier. Part III, Section 1, Chapter14, pp
5032 119-127.

5033 Hjelstuen, B.O., Eldholm, O. and Skogseid, J., 1997. Vøring Plateau diapir fields and their structural
5034 and depositional settings. *Marine Geology* 144: 33-57.

5035 Holeyman, A., Peralta, P., Charue, N., 2015. Boulder-soil-pile dynamic interaction, in: Meyer, V. (Ed.),
5036 *Frontiers in Offshore Geotechnics III*. CRC Press, London, pp. 563–568.

5037 Honda, H. and Nakamura, K. (1951). The waves caused by one-dimensional deformation of the bottom
5038 of shallow sea of uniform depth, *Sci. Rep. Tohoku Univ. Ser., Geophysics*, 3, 133-137.

- 5039 Hornbach, M. J., Saffer, D. M., and Steven Holbrook, W., 2004, Critically pressured free-gas reservoirs
5040 below gas-hydrate provinces: *Nature*, v. 427, no. 6970, p. 142-144.
- 5041 Hovind E, Kaynia AM. Earthquake response of wind turbine with non-linear soil-structure interaction.
5042 In: Proceedings of the 9th international conference on structural dynamics EUROODYN2014. Porto;
5043 2014, p. 623–30.
- 5044 Hovland, M., Gardner, J.V. and Judd, A.G., 2002. The significance of pockmarks to understanding fluid
5045 flow processes and geohazards. *Geofluids*, 2(2), 127-136.
- 5046 Howe, J. A., Stoker, M. S., & Woolfe, K. J. (2001). Deep-marine seabed erosion, and gravel lags in the
5047 northwestern Rockall Trough, North Atlantic Ocean. *Journal of the Geological Society of London*, Vol.
5048 158, 427–438.
- 5049 Huang, X. and García, M. H. (1998). A Herschel–Bulkley model for mud flow down a slope. *Journal*
5050 *of Fluid Mechanics* 374: 305–333, DOI 10.1017/S0022112098002845.
- 5051 Huat, B. B. K., Prasad, A., Asadi, A., & Kazemian, S. (2014). *Geotechnics of Organic Soils and Peat*.
5052 CRC Press. <https://doi.org/10.1201/b15627>
- 5053 Hudec, M. R., & Jackson, M. P. (2007). Terra infirma: Understanding salt tectonics. *Earth-Science*
5054 *Reviews*, 82(1-2), 1-28.
- 5055 Hughes, A. L., Gyllencreutz, R., Lohne, Ø. S., Mangerud, J., & Svendsen, J. I. (2016). The last Eurasian
5056 ice sheets—a chronological database and time-slice reconstruction, DATED-1. *Boreas*, 45(1), 1-45.
- 5057 Huhn, K., Arroyo, M., Cattaneo, A., Clare, M.A., Gràcia, E., Harbitz, C.B., Krastel, S., Kopf, A.,
5058 Løvholt, F., Rovere, M., Strasser, M., Talling, P.J., and Urgeles, R. (2020). Modern Submarine
5059 Landslide Complexes: A Short Review. In: Ogata, K., Festa, A., and Pini, G.A. (eds.). *Submarine*
5060 *Landslides – Subaqueous Mass Transport Deposits from Outcrops to Seismic Profiles*. Geophysical
5061 *Monograph* 246. John Wiley & Sons, NJ 07030 and the American Geophysical Union, Washington,
5062 D.C. 20009.
- 5063 Hustoft, S., Büinz, S., Mienert, J., & Chand, S. (2009). Gas hydrate reservoir and active methane-venting
5064 province in sediments on < 20 Ma young oceanic crust in the Fram Strait, offshore NW-Svalbard. *Earth*
5065 *and Planetary Science Letters*, 284(1-2), 12-24.
- 5066 Huuse, M., Jackson, C.A.L., Van Rensbergen, P., Davies, R.J., Flemings, P.B. and Dixon, R.J., 2010.
5067 *Subsurface sediment remobilization and fluid flow in sedimentary basins: an overview*. *Basin Research*,
5068 22(4), 342-360.
- 5069 Huuse, M. (1999). Detailed morphology of the Top Chalk surface in the eastern Danish North Sea.
5070 *Petroleum Geoscience*, 5(3), 303-314.

5071 Huuse, M., & Lykke-Andersen, H. (2000). Large-scale glaciotectonic thrust structures in the eastern
5072 Danish North Sea. Geological Society, London, Special Publications, 176(1), 293–305.
5073 <https://doi.org/10.1144/GSL.SP.2000.176.01.22>Huuse, M., Lykke-Andersen, H. and Michelsen, O.,
5074 2001. Cenozoic evolution of the eastern Danish North Sea. Marine Geology, 177(3-4), pp.243-269.

5075 Huuse, M., Le Heron, D. P., Dixon, R., Redfern, J., Moscariello, A., & Craig, J. (2012). Glaciogenic
5076 reservoirs and hydrocarbon systems: an introduction.

5077 Hyndman, R., and Spence, G., 1992, A seismic study of methane hydrate marine bottom simulating
5078 reflectors: Journal of Geophysical Research: Solid Earth, v. 97, no. B5, p. 6683-6698.

5079 Høgaas, F., & Longva, O. (2016). Mega deposits and erosive features related to the glacial lake Nedre
5080 Glomsjø outburst flood, southeastern Norway. Quaternary Science Reviews, 151, 273-291.

5081 IHO (2020). IHO standards for hydrographic surveys 6th Edition special publication No.44

5082 Ilstad T, Elverhøi A, Issler D, and Marr JG (2004a). Subaqueous debris flow behaviour and its
5083 dependence on the sand/clay ratio: A laboratory study using particle tracking. Marine Geology 213(1–
5084 4): 415–438.

5085 Ilstad T, Marr JG, Elverhøi A, and Harbitz CB (2004b). Laboratory studies of subaqueous debris flows
5086 by measurements of pore-fluid pressure and total stress. Marine Geology 213(1–4): 403–414.

5087 Ilstad T, De Blasio FV, Elverhøi A, Harbitz CB, Engvik L, Longva O, and Marr JG (2004c). On the
5088 frontal dynamics and morphology of submarine debris flows. Marine Geology 213(1–4): 481–497.

5089 Imran, J.; Parker, G.; Locat, J. and Lee, H. (2001). 1D numerical model of muddy subaqueous and
5090 subaerial debris flows. J. Hydr. Eng. 127(11): 959–968, DOI 10.1061/(asce)0733-
5091 9429(2001)127:11(959).

5092 IODP, 2020. International Ocean Discovery Program (IODP), 2020. 2050 Science Framework:
5093 Exploring Earth by Scientific Ocean Drilling. Available at: [https://www.iodp.org/2050-science-
5094 framework](https://www.iodp.org/2050-science-framework)

5095 IODP, 2024. International Ocean Discovery Program (IODP), 2024. Core Repositories.
5096 <https://www.iodp.org/resources/core-repositories>

5097 IOGP, 2024. CO2 storage projects in Europe. International Association of Oil and Gas Producers.
5098 October 2024. [https://iogpeurope.org/wp-content/uploads/2024/10/CO2-Storage-Projects-in-Europe-
5099 map.pdf](https://iogpeurope.org/wp-content/uploads/2024/10/CO2-Storage-Projects-in-Europe-map.pdf). Accessed 05 May 2025.

5100 Ismail-Meyer, K., Stolt, M. H., & Lindbo, D. L. (2018). Soil Organic Matter. Interpretation of
5101 Micromorphological Features of Soils and Regoliths, 471–512. [https://doi.org/10.1016/B978-0-444-
5102 63522-8.00017-6](https://doi.org/10.1016/B978-0-444-63522-8.00017-6)

5103 ISO 14688-2:2018. Geotechnical investigation and testing. Identification and classification of soil.
5104 British Standard Institute.

5105 ISO 14688-1:2017. Geotechnical investigation and testing. Identification and classification of soil - Part
5106 1: Identification and description. .

5107 ISO 14688-2:2017. Geotechnical investigation and testing. Identification and classification of soil - Part
5108 2: Principles for a classification.

5109 ISO 19901-10: 2018(E), 2018. Petroleum and natural gas industries — Specific requirements for
5110 offshore structures — Part 8: Marine geophysical investigations. ISO/TC 67/SC 7/WG 10

5111 Issler, D.; De Blasio, F. V.; Elverhøi, A.; Bryn, P. and Lien, R. (2005). Scaling behaviour of clay-rich
5112 submarine debris flows. *Marine and Petroleum Geology* 22: 187–194, DOI
5113 10.1016/j.marpetgeo.2004.10.015.

5114 Issler, D. (2014). Dynamically consistent entrainment laws for depth-averaged avalanche models.
5115 *Journal of Fluid Mechanics* 759: 701–738, DOI 10.1017/jfm.2014.584.

5116 Jackson, D.I., Jackson, A.A., Evans, D., Wingfield, R.T.R., Barnes, R.P., Arthur, M.J., 1995. United
5117 Kingdom offshore regional report: the geology of the Irish Sea. British Geological Survey, London.

5118 Jakobsson, M., Stranne, C., O'Regan, M., Greenwood, S. L., Gustafsson, B., Humborg, C., & Weidner,
5119 E. (2019). Bathymetric properties of the Baltic Sea. *Ocean Science*, 15(4), 905-924.

5120 Jensen, J.B. and Bennike, O. (2022). Geological screening of Kattegat Area A and B. Geological seabed
5121 screening in relation to possible location of windfarm areas. Client Danish Energy Agency. GEUS,
5122 Copenhagen. Danmarks og Grønlands Geologiske Undersøgelse Rapport 2021(64).
5123 <https://doi.org/10.22008/gpub/34624>

5124 Jerkins, A.E., Shiddiqi, H.A., Kværna, T., Gibbons, S.J., Schweitzer, J., Ottemöller, L., Bungum, H.,
5125 2020. The 30 June 2017 North Sea Earthquake: Location, Characteristics, and Context. *Bull. Seismol.*
5126 *Soc. Am.* 110, 937–952. <https://doi.org/10.1785/0120190181>

5127 Jerkins, A.E., Oye, V., Alvizuri, C., Halpaap, F., Kværna, T., 2023. The 21 March 2022 Mw 5.1 Tampen
5128 Spur Earthquake, North Sea: Location, Moment Tensor, and Context. *Bull. Seismol. Soc. Am.*
5129 <https://doi.org/10.1785/0120230163>

5130 Johnson, H., Richards, P.C., Long, D., Graham, C.C. (1993). United Kingdom offshore regional report:
5131 the geology of the northern North Sea. London: HMSO for the British Geological Survey.

5132 Johnson, K. R., Dakin, N., Carter, G. D. O., Phillips, E. R. P. (2023). Geo-challenges for ground model
5133 development in previously glaciated and periglacial terrains. In 9th International SUT Offshore Site

- 5134 Investigation and Geotechnics Conference, Innovative Geotechnologies for Energy Transition. 12-14
5135 September 2023, London, UK
- 5136 Johnston, A. C. (1987). Suppression of earthquakes by large continental ice sheets: *Nature*, v. 330, no.
5137 6147, p. 467-469.
- 5138 Jop, P., Forterre, Y., Pouliquen, O. (2006) A constitutive law for dense granular flows. *Nature* 441
5139 (7094): 727–730. DOI 10.1038/nature04801.
- 5140 Judd, A., Hovland, M. (2007). Seabed fluid flow: the impact on geology, biology and the marine
5141 environment. Cambridge University Press. Online version 2009:
5142 <https://doi.org/10.1017/CBO9780511535918>.
- 5143 Karakosta, C., Pappas, C., Marinakis, V., & Psarras, J. (2013). Renewable energy and nuclear power
5144 towards sustainable development: Characteristics and prospects. *Renewable and Sustainable Energy*
5145 *Reviews*, 22, 187-197.
- 5146 Karstens, J., Haflidason, H., Becker, L. W., Berndt, C., Rüpke, L., Planke, S., Liebetrau, V., Schmidt,
5147 M., and Mienert, J., 2018, Glacigenic sedimentation pulses triggered post-glacial gas hydrate
5148 dissociation: *Nature communications*, v. 9, no. 1, p. 635.
- 5149 Kaynia, A.M. (2019). Seismic considerations in design of offshore wind turbines. *Soil Dynamics and*
5150 *Earthquake Engineering*, 124, 399–407.
- 5151 Kettlety, T., Martuganova, E., Kühn, D., Schweitzer, J., Weemstra, C., Baptie, B., Dahl-Jensen, T.,
5152 Jerkins, A., Voss, P. H., Michael, J., & Skurtveit, E. (2024). A Unified Earthquake Catalogue for the
5153 North Sea to Derisk European CCS Operations. *First Break*, 42(5), 31–36.
5154 <https://doi.org/10.3997/1365-2397.fb2024036>
- 5155 Kim, J., Løvholt, F., Issler, D., and Forsberg, C. F. (2019). Landslide material control on tsunami
5156 genesis—the Storegga Slide and tsunami (8,100 years BP). *Journal of Geophysical Research: Oceans*
5157 124(6): 3607–3627, DOI 10.1029/2018JC014893.
- 5158 King, E.L., Sejrup, H.P., Haflidason, H., Elverhøi, A., and Aarseth, I., 1996, Quaternary seismic
5159 stratigraphy of the North Sea Fan: glacially-fed gravity flow aprons, hemipelagic sediments and large
5160 submarine slides: *Marine Geology*, v. 130, p. 295-315, [https://doi.org/10.1016/0025-3227\(95\)00168-9](https://doi.org/10.1016/0025-3227(95)00168-9).
- 5161 King, E.L., Haflidason, H., Sejrup, H.P., and Løvlie, R., 1998, Glacigenic debris flow on the North Sea
5162 Trough Mouth Fan during ice stream maxima: *Marine Geology*, v. 152, p. 217-246,
5163 [https://doi.org/10.1016/S0025-3227\(98\)00072-3](https://doi.org/10.1016/S0025-3227(98)00072-3).
- 5164 Kirby, J. T., Grilli, S. T., Horrillo, J., Liu, P. L.-F., Nicolsky, D., Abadie, S., Ataie-Ashtiani, B., Castro,
5165 M.J., Clous, L., Escalante, C., Fine, I., González-Vida, J.M., Løvholt, F., Lynett, P., Ma, G., Macías, J.,

- 5166 Ortega, S., Shi, F., Yavari-Ramshe, S., and Zhang, C. (2022). Validation and inter-comparison of
5167 models for landslide tsunami generation. *Ocean Modelling*, 170, 101943.
- 5168 Kirkham, J.D, Hogan, K.A., Larter, R.D, Arnold, N.S., Ely, J.C., Clark, C>D>, Games, K, Huuse, M,
5169 Stewart, M.A., Ottesen, D, Dowdeswell, J.A. (2024). Tunnel valley formation beneath deglaciating
5170 mid-latitude ice sheets: Observations and modelling. *Quaternary Science Reviews*, v. 323, 2974–2981.
- 5171 Kishankov, A., Serov, P., Bünz, S., Patton, H., Hubbard, A., Mattingsdal, R., ... & Andreassen, K.
5172 (2022). Hydrocarbon leakage driven by Quaternary glaciations in the Barents Sea based on 2D basin
5173 and petroleum system modeling. *Marine and Petroleum Geology*, 138, 105557.
- 5174 Kjær, Kurt H. "Mode of subglacial transport deduced from till properties, Mýrdalsjökull, Iceland."
5175 *Sedimentary Geology* 128.3-4 (1999): 271-292.
- 5176 Kjølraug RA, Kaynia AM (2015). Vertical earthquake response of megawatt-sized wind turbine with
5177 soil-structure interaction effects. *Earthq Eng Struct Dyn*, 44:2341–58.
- 5178 Knies, J., Matthiessen, J., Vogt, C., Laberg, J. S., Hjelstuen, B. O., Smelror, M., ... & Vorren, T. O.
5179 (2009). The Plio-Pleistocene glaciation of the Barents Sea–Svalbard region: a new model based on
5180 revised chronostratigraphy. *Quaternary Science Reviews*, 28(9-10), 812-829.
- 5181 Knutsen, S.-M., Richardsen, G., Vorren, T.O. (1993) Late Miocene–Pleistocene sequence stratigraphy
5182 and mass-movements on the western Barents Sea margin, *Norwegian Petroleum Society Special*
5183 *Publications*, Volume 2, 573-606, <https://doi.org/10.1016/B978-0-444-88943-0.50038-1>.
- 5184 Knutz, P.C. and Cartwright, J.A. (2003) Seismic stratigraphy of the West Shetland Drift: Implications
5185 for late Neogene paleocirculation in the Faeroe-Shetland gateway. *Paleoceanography*. v. 18, No. 4,
5186 1093.
- 5187 Knutz, P.C. (2010) 3D seismic imaging of aggradational channels related to geostrophic currents
5188 through the Pliocene North Sea basin. *Geo-Temas*, 11, 89-90.
- 5189 Kortekaas, S., Peuchen, J, 2008. Measured Swabbing Pressures and Implications for Shallow Gas
5190 Blowout. OTC.08: Proceedings 2007 Offshore Technology Conference, Houston, Texas, USA, OTC
5191 Paper 19280.
- 5192 Kremer, K., Wirth, S. B., Reusch, A., Fäh, D., Bellwald, B., Anselmetti, F. S., ... & Strasser, M. (2017).
5193 Lake-sediment based paleoseismology: Limitations and perspectives from the Swiss Alps. *Quaternary*
5194 *Science Reviews*, 168, 1-18.
- 5195 Krämer, K., Holler, P., Herbst, G., Bratek, A., Ahmerkamp, S., Neumann, A., ... & Winter, C. (2017).
5196 Abrupt emergence of a large pockmark field in the German Bight, southeastern North Sea. *Scientific*
5197 *reports*, 7(1), 5150.

- 5198 Kristensen, T. B., Huuse, M., Piotrowski, J. A., & Clausen, O. R. (2007). A morphometric analysis of
5199 tunnel valleys in the eastern North Sea based on 3D seismic data. *Journal of Quaternary Science:*
5200 *Published for the Quaternary Research Association*, 22(8), 801-815.
- 5201 Kuenen, P. H. (1937). Experiments in connection with Daly's hypothesis on the formation of submarine
5202 canyons. *Leidse Geologische Mededelingen* 8: 327–335.
- 5203 Kuhlmann, G., Wong, T.E. 2008. Pliocene paleoenvironment evolution as interpreted from 3D-seismic
5204 data in the southern North Sea, Dutch offshore sector. *Marine and Petroleum Geology*, Volume 25,
5205 Issue 2, 173-189. <https://doi.org/10.1016/j.marpetgeo.2007.05.009>.
- 5206 Kuhlmann, G., Langereis, C., Munsterman, D., van Leeuwen, R.J., Verreussel, R., Meulenkamp, J. and
5207 Wong, T., 2006. Chronostratigraphy of Late Neogene sediments in the southern North Sea Basin and
5208 paleoenvironmental interpretations. *Palaeogeography, Palaeoclimatology, Palaeoecology*, 239(3-4),
5209 pp.426-455.
- 5210 Kurjanski, B., Rea, B. R., Spagnolo, M., Cornwell, D. G., Howell, J., & Archer, S. (2020). A conceptual
5211 model for glaciogenic reservoirs: From landsystems to reservoir architecture. *Marine and Petroleum*
5212 *Geology*, 115, 104205. <https://doi.org/10.1016/j.marpetgeo.2019.104205>.
- 5213 Kurjański, B., Rea, B. R., Spagnolo, M., Cornwell, D. G., Howell, J., Comte, J., Quirós, A. G., Palmu,
5214 J., Oien, R. P., & Gibbard, P. L. (2021). Cool deltas: Sedimentological, geomorphological and
5215 geophysical characterization of ice-contact deltas and implications for their reservoir properties
5216 (Salpausselkä, Finland). *Sedimentology*, sed.12884. <https://doi.org/10.1111/sed.12884>
- 5217 Kvalstad TJ, Andresen L, Forsberg CF, Berg K, Bryn P, Wangen M (2005a) The Storegga slide:
5218 evaluation of triggering sources and slide mechanics. *Mar Pet Geol* 22: 245-256.
- 5219 Kvalstad TJ, Nadim F, Kaynia AM, Mokkalbost KH, and Bryn P (2005b) Soil conditions and slope
5220 stability in the Ormen Lange area. *Marine and Petroleum Geology* 22: 299–310.
5221 <https://doi.org/10.1016/j.marpetgeo.2004.10.021>.
- 5222 Kvenvolden, K. A., 2000, Natural gas hydrate: Background and history of discovery, *Natural Gas*
5223 *Hydrate: In Oceanic and Permafrost Environments*, Springer, p. 9-16.
- 5224 Laberg, J.S., Vorren, T.O., 1993. A Late Pleistocene submarine slide on the Bear Island Trough Mouth
5225 Fan. *Geo-Mar. Lett.* 13, 227-234.
- 5226 Laberg, J.S., Vorren, T.O., 1996. The Middle and Late Pleistocene evolution of the Bear Island Trough
5227 Mouth Fan. *Global Planet. Change* 12, 309-330.

- 5228 Laberg, J.S., and Vorren, T.O., 2000, Flow behaviour of the submarine glacial debris flows on the
5229 Bear Island Trough Mouth Fan, western Barents Sea: *Sedimentology*, v. 47, p. 1105-1117,
5230 <https://doi.org/10.1046/j.1365-3091.2000.00343.x>.
- 5231 Laberg, J.S., Vorren, T.O., Dowdeswell, J.A., Kenyon, N.H., Taylor, J., 2000. The Andøya Slide and
5232 the Andøya Canyon, north-eastern Norwegian-Greenland Sea. *Mar. Geol.* 162, 259-275.
- 5233 Laberg, J.S., Vorren, T.O., Mienert, J., Bryn, P., Lien, R., 2002. The Trænadjupet Slide: a large slope
5234 failure affecting the continental margin of Norway 4,000 years ago. *Geo-Mar. Lett.* 22, 19-24.
- 5235 Laberg, J.S., Guidard, S., Mienert, J., Vorren, T.O., Haflidason, H., Nygård, A., 2007. Morphology and
5236 morphogenesis of a high-latitude canyon; the Andøya Canyon, Norwegian Sea, *Marine Geology*, 246,
5237 Pages 68-85, <https://doi.org/10.1016/j.margeo.2007.01.009>.
- 5238 Laberg, J.S., Eilertsen, R.S. & Vorren, T.O. 2009: The paleo-ice stream in Vestfjorden, north Norway,
5239 over the last 35 ky: Glacial erosion and sediment yield. *Geological Society of America Bulletin* 121,
5240 434–447. <https://doi.org/10.1130/B26277.1>
- 5241 Laberg, J. S., Andreassen, K., Knies, J., Vorren, T. O., & Winsborrow, M. (2010). Late Pliocene–
5242 Pleistocene development of the Barents Sea ice sheet. *Geology*, 38(2), 107-110.
- 5243 Laberg, J. S., Andreassen, K., & Vorren, T. O. (2012). Late Cenozoic erosion of the high-latitude
5244 southwestern Barents Sea shelf revisited. *Bulletin*, 124(1-2), 77-88.
- 5245 Laberg, J.S., Baeten, N.J., Vanneste, M., Forsberg, C.F., Forwick, M., Haflidason, H. (2016). Sediment
5246 Failure Affecting Muddy Contourites on the Continental Slope Offshore Northern Norway: Lessons
5247 Learned and Some Outstanding Issues. In: Lamarche, G., et al. *Submarine Mass Movements and their*
5248 *Consequences*. *Advances in Natural and Technological Hazards Research*, vol 41. Springer, Cham.
5249 https://doi.org/10.1007/978-3-319-20979-1_28
- 5250 Lacasse, S., L'Heureux, J.S., Liu, Z. 2022. Reducing landslide risk - Emerging challenges and novel
5251 technologies. *Geohazards VIII*.
- 5252 Lamb, R.M., Huuse, M., Stewart, M.A. (2017). Early Quaternary sedimentary processes and
5253 palaeoenvironments in the central North Sea. *Journal of Quaternary Science*, 32(2), 127-144.
- 5254 Lamb, R.M., Harding, R., Huuse, M., Stewart, M.A., Brocklehurst, S.H. (2018). The early quaternary
5255 North Sea basin. *Journal of the Geological Society*, 175(2), 275-290.
- 5256 Lambeck, K., Rouby, H., Purcell, A., Sun, Y. and Sambridge, M. 2014. Sea-level and global ice
5257 volumes from the Last Glacial Maximum to the Holocene. *PNAS*, 111, 15296–15303,
5258 <https://doi.org/10.1073/pnas.1411762111>

- 5259 Landva, A. O. (2006). "Characterisation of Escuminac peat and construction on peatland." Proc., Proc.
5260 of Characterisation and Engineering Properties of Natural Soils, 2135-2191.
- 5261 Larsson, R. (1990). Behaviour of organic clay and gyttja. Report No. 38.
- 5262 Lasabuda, A.P.E., Hanssen, A., Laberg, J.S. et al. Paleobathymetric reconstructions of the SW Barents
5263 Seaway and their implications for Atlantic–Arctic ocean circulation. *Commun Earth Environ* 4, 231
5264 (2023). <https://doi.org/10.1038/s43247-023-00899-y>
- 5265 Lasabuda, A., Geissler, W.H., Laberg, J.S., Knutsen, S.-M., Rydningen, T.A., and Berglar, K., 2018,
5266 Late Cenozoic erosion estimates for the Northern Barents Sea: Quantifying Glacial Sediment Input to
5267 the Arctic Ocean: *Geochemistry, Geophysics, Geosystems*, v. 19, p. 4876-4903,
5268 <https://doi.org/10.1029/2018GC007882>.
- 5269 Lee, J. R., Busschers, F. S., & Sejrup, H. P. (2012). Pre-Weichselian Quaternary glaciations of the
5270 British Isles, The Netherlands, Norway and adjacent marine areas south of 68 N: implications for long-
5271 term ice sheet development in northern Europe. *Quaternary Science Reviews*, 44, 213-228.
- 5272 Lee, J. R., & Phillips, E. (2013). Glacitectonics - a key approach to examining ice dynamics, substrate
5273 rheology and ice-bed coupling. *Proceedings of the Geologists' Association*, 124(5), 731–737.
5274 <https://doi.org/10.1016/j.pgeola.2013.07.006>
- 5275 Leifer, I., & Judd, A. (2015). The UK22/4b blowout 20 years on: Investigations of continuing methane
5276 emissions from sub-seabed to the atmosphere in a North Sea context. *Marine and Petroleum Geology*,
5277 68, 706–717. <https://doi.org/10.1016/j.marpetgeo.2015.11.012>
- 5278 Lengkeek, H. J., & Brinkgreve, R. B. J. (2022). CPT-based classification of soft organic clays and peat.
5279 In *Cone Penetration Testing 2022* (pp. 509–514). CRC Press. [https://doi.org/10.1201/9781003308829-](https://doi.org/10.1201/9781003308829-72)
5280 72.
- 5281 Leynaud, D., Mienert, J., Vanneste, M., 2009. Submarine mass movements on glaciated and non-
5282 glaciated European continental margins: a review of triggering mechanisms and preconditions to
5283 failure. *Mar. Petrol. Geol.* 26, 618-632.
- 5284 L'Heureux, J.-S., Glimsdal, S., Longva, O., Hansen, L., and Harbitz, C.B. (2011). The 1888 shoreline
5285 landslide and tsunami in Trondheimsfjorden, central Norway. *Marine Geophysical Research*, Vol. 32,
5286 Issue 1, 313-329. DOI 10.1007/s11001-010-9103-z.
- 5287 L'Heureux, J. S., Vanneste, M., Rise, L., Brendryen, J., Forsberg, C. F., Nadim, F., ... & Haflidason, H.
5288 (2013a). Stability, mobility and failure mechanism for landslides at the upper continental slope off
5289 Vesterålen, Norway. *Marine Geology*, 346, 192-207.

- 5290 L'Heureux, J.S., Hansen, L., Longva, O. Eilertsen, R.S. (2013b). Landslides along Norwegian fjords:
5291 causes and hazard assessment. *Landslide Science and Practice: Volume 5: Complex Environment*,
5292 pp.81-87.
- 5293 L'Heureux, J. S., Ø. A. Høydal, A. P. Paniagua Lopez, and S. Lacasse. (2018). Impact of climate change
5294 and human activity on quick clay landslide occurrence in Norway. Paper to the Second JTC1 Workshop
5295 on Triggering and Propagation of Rapid Flow-like Landslides, Hong Kong, pp. 3-5. 2018.
- 5296 L'Heureux, J.-S., Long, M. (2017). Relationship between Shear-Wave Velocity and Geotechnical
5297 Parameters for Norwegian Clays. *J. Geotech. Geoenvironmental Eng.* 143, 4017013.
5298 [https://doi.org/10.1061/\(ASCE\)GT.1943-5606.0001645](https://doi.org/10.1061/(ASCE)GT.1943-5606.0001645)
- 5299 L'Heureux, J.-S., Longva, O., Hansen, L., Vanneste, M. (2014). The 1930 Landslide in Orkdalsfjorden:
5300 Morphology and Failure Mechanism. In: Krastel, S., Behrmann, J.-H., Völker, D., Stipp, M., Berndt,
5301 C., Urgeles, R., Chaytor, J., Huhn, K., Strasser, M., and Harbitz, C.B. (Eds.), *Submarine Mass
5302 Movements and Their Consequences: Proceedings of the 6th International Symposium, Kiel, September
5303 2013. Advances in Natural and Technological Hazards Research*, vol. 37 (pp. 239-248). Cham: Springer
5304 International Publishing.
- 5305 L'Heureux, Jean-Sébastien, Steinar Nordal, and Synnøve W. Austefjord. (2017) "Revisiting the 1959
5306 quick clay landslide at Sokkelvik, Norway." *Landslides in sensitive clays: From research to
5307 implementation*: 395-405.
- 5308 Li, M. Z., Shaw, J., Todd, B. J., Kostylev, V. E., Wu, Y. (2014). Sediment transport and development
5309 of banner banks and sandwaves in an extreme tidal system: Upper Bay of Fundy, Canada. *Continental
5310 Shelf Research*, 83, 86–107. <https://doi.org/10.1016/j.csr.2013.08.007>
- 5311 Li, X.; Sovilla, B.; Ligneau, C.; Jiang, C. and Gaume, J. (2022). Different erosion and entrainment
5312 mechanisms in snow avalanches. *Mechanics Research Communications* 124: 103914, DOI
5313 10.1016/j.mechrescom.2022.103914.
- 5314 Lien, Ø. F., Hjelstuen, B. O., Zhang, X., Sejrup, H. P. (2022). Late Plio-Pleistocene evolution of the
5315 Eurasian Ice Sheets inferred from sediment input along the northeastern Atlantic continental margin.
5316 *Quaternary Science Reviews*, 282, 107433.
- 5317 Ligneau, C.; Sovilla, B. Gaume, J. (2024). Modelling erosion, entrainment and deposition in cohesive
5318 granular flows: Application to dense snow avalanches. *Cold Regions Science and Technology* 219:
5319 104103, DOI 10.1016/j.coldregions.2023.104103.
- 5320 Ligtenberg, J. (2005) Detection of fluid migration pathways in seismic data: implications for fault seal
5321 analysis: *Basin Research*, v. 17, no. 1, p. 141-153.

- 5322 Lindberg, B., Laberg, J.S., Vorren, T.O. (2004). The Nyk Slide – morphology, progression, and age of
5323 a partly buried submarine slide offshore northern Norway. *Mar. Geol.* 213, 277-289.
- 5324 Lindholm, C., Bungum, H., Ghione, F., Meslem, A., Huang, C., Oye, V. (2025). Earthquakes and
5325 seismic hazard for Norway and Svalbard. *Journal of Seismology*, [https://doi.org/10.1007/s10950-024-](https://doi.org/10.1007/s10950-024-10270-z)
5326 10270-z.
- 5327 Lisiecki, L. E., & Raymo, M. E. (2005). A Pliocene-Pleistocene stack of 57 globally distributed benthic
5328 $\delta^{18}\text{O}$ records. *Paleoceanography*, 20(1).
- 5329 Liu, Z., L'heureux, J. S., Glimsdal, S., and Lacasse, S. (2021). Modelling of mobility of Rissa landslide
5330 and following tsunamis. *Computers and Geotechnics*, 140, 104388.
- 5331 Llopart, J., Urgeles, R., Forsberg, C. F., Camerlenghi, A., Vanneste, M., Rebesco, M., ... & Lantzsch,
5332 H. (2019). Fluid flow and pore pressure development throughout the evolution of a trough mouth fan,
5333 western Barents Sea. *Basin Research*, 31(3), 487-513.
- 5334 Lloyd, C., Huuse, M., Barrett, B.J., Stewart, M.A. Newton, A.M.W. (2021a) regional CO₂ containment
5335 assessment of the northern Utsira Formation seal and overburden, northern North Sea. *Basin Research*,
5336 33(3), pp.1985-2017.
- 5337 Lockhart, E.A., Scourse, J.D., Praeg, D., Van Landeghem, K.J.J., Mellett, C., Saher, M., Callard, L.,
5338 Chiverrell, R.C., Benetti, S., Ó Cofaigh, C., Clark, C.D. (2018) A stratigraphic investigation of the
5339 Celtic Sea megaridges based on seismic and core data from the Irish-UK sectors. *Quat. Sci. Rev.* 198,
5340 156–170. <https://doi.org/10.1016/j.quascirev.2018.08.029>
- 5341 Long, D., Stevenson, A. G., Wilson, C. K., Bulat, J. (2003) Slope failures in the Faroe–Shetland
5342 Channel. 281–289 in *Submarine mass movements and their consequences*. Locat, J, and Mienert, J
5343 (editors). *Advances in Natural and Technological Hazards Research Series*. (Dordrecht: Kluwer
5344 Academic Publishers.)
- 5345 Long, D., Ziska, H., Musson, R. (2011) Geohazards. In: Ritchie, J.D., Ziska, H., Johnson, H. & Evans,
5346 D. (eds) *Geology of the Faroe–Shetland Basin and Adjacent Areas*. British Geological Survey Research
5347 Report, RR/11/01, Jarðfeingi Research Report, RR/11/01, HMSO for the British Geological Survey,
5348 London, pp 239-253.
- 5349 Long, M. L., Tucker, G. T., Leth, C. T. L. (2024). Experience of in situ geotechnical tests and their
5350 interpretation in organic soils and peat. 7th International Conference on Geotechnical and Geophysical
5351 Site Characterization (ISC 24). <https://doi.org/10.23967/ISC.2024.182>

- 5352 Louge, M. Y., Carroll, C. S., Turnbull, B. (2011). Role of pore pressure gradients in sustaining frontal
5353 particle entrainment in eruption currents: The case of powder snow avalanches. *Journal of Geophysical*
5354 *Research* 116: F04030, DOI 10.1029/2011JF002065.
- 5355 Lund, B., Schmidt, P., Hieronymus, C. (2009). Stress evolution and fault stability during the
5356 Weichselian glacial cycle. Swedish Nuclear Fuel and Waste Management Co., Stockholm (Sweden)
5357 Technical Report SKB-TR-09-15. <https://www.osti.gov/etdeweb/biblio/971759>
- 5358 Lundsten, E., Paull, C. K., Gwiazda, R., Dobbs, S., Caress, D. W., Kuhnz, L. A., ... & Addison, J.
5359 (2024). Pockmarks offshore Big Sur, California provide evidence for recurrent, regional, and
5360 unconfined sediment gravity flows. *Journal of Geophysical Research: Earth Surface*, 129(5),
5361 e2023JF007374.
- 5362 Lunne, T., Andersen, K.H., Low, H.E., Randolph, M.F., Sjursen, M. (2011). Guidelines for offshore in
5363 situ testing and interpretation in deepwater soft clays. *Can. Geotech. J.* 48, 543–556.
5364 <https://doi.org/10.1139/t10-088>
- 5365 Lunne, T., Long, M. (2006). Review of long seabed samplers and criteria for new sampler design. *Mar.*
5366 *Geol.* 226, 145–165. <https://doi.org/10.1016/j.margeo.2005.07.014>
- 5367 Lunne, T., Robertson, P.K., Powell, J.J.M. (1997). *Cone Penetration Testing in Geotechnical Practice*.
5368 Blackie Academic & Professional, London.
- 5369 Lunne, T., Strandvik, S., Kasin, K., L’Heureux, J.S., Haugen, E., Uruci, E., Veldhuijzen, A., Carlson,
5370 M., Kassner, M. (2018). Effect of cone penetrometer type on CPTU results at a soft clay test site in
5371 Norway, in: *Cone Penetration Testing 2018*. <https://doi.org/10.1088/1755-1315/710/1/012010>
- 5372 Løseth, H. (2021) Comment on ‘A Miocene age for the Molo Formation, Norwegian Sea shelf off
5373 Vestfjorden, based on marine palynology’. *Norwegian Journal of Geology* 101, 202102.
5374 <https://doi.org/10.17850/njg101-1-2>
- 5375 Løseth, H. (2023). The Norwegian strandflat reviewed and constrained in an offshore perspective.
5376 *Norwegian Journal of Geology*, 103.
- 5377 Løseth, H., Kyrkjebø, R., Hilde, E., Wild, R.J., Bunkholt, H. (2017) 500 m of rapid base level rise along
5378 an inner passive margin–Seismic observations from the Pliocene Molo Formation, mid Norway. *Marine*
5379 *and Petroleum Geology* 86, 268–287. <https://doi.org/10.1016/j.marpetgeo.2017.05.039>
- 5380 Løseth, H., Dowdeswell, J.A., Batchelor, C.L., Ottesen, D. (2020). 3D sedimentary architecture
5381 showing the inception of an Ice Age. *Nat. Commun.* <https://doi.org/10.1038/s41467-020-16776-7>.

- 5382 Løseth, H., Nygård, A., Batchelor, C. L., & Fayzullaev, T., 2022. A regionally consistent 3D seismic-
5383 stratigraphic framework and age model for the Quaternary sediments of the northern North Sea. *Marine*
5384 *and Petroleum Geology*, 142, 105766.
- 5385 Løseth, H., Nygård, A., Batchelor, C.L., Fayzullaev, T. (2022). A regionally consistent 3D seismic-
5386 stratigraphic framework and age model for the Quaternary sediments of the northern North Sea. *Marine*
5387 *and Petroleum Geology*, 142, p.105766.
- 5388 Løvholt, F., Harbitz, C.B., Haugen, K.B. (2005). A parametric study of tsunamis generated by
5389 submarine slides in the Ormen Lange/Storegga area off western Norway. *Ormen Lange Special Issue,*
5390 *Marine and Petroleum Geology* 22, 219-231; doi: 10.1016/j.marpetgeo.2004.10.0017.
- 5391 Løvholt, F., Pedersen, G., Harbitz, C.B., Glimsdal, S., Kim, J. (2015) On the characteristics of landslide
5392 tsunamis. *Philosophical Transactions of the Royal Society A: Mathematical, Physical and Engineering*
5393 *Sciences* 373(2053): 20140376.
- 5394 Løvholt, F., Pedersen, G., Harbitz, C.B. (2016) Tsunami-genesis due to retrogressive landslides on an
5395 inclined seabed. In: *Submarine Mass Movements and Their Consequences*, pp. 569–578. Cham:
5396 Springer.
- 5397 Løvholt, F., Bondevik, S., Laberg, J.S., Kim, J., Boylan, N. (2017) Some giant submarine landslides do
5398 not produce large tsunamis. *Geophysical Research Letters* 44(16): 8463–8472. DOI
5399 10.1002/2017gl074062.
- 5400 Løvholt, F., Schulten, I., Mosher, D., Harbitz, C., Krastel, S. (2019). Modelling the 1929 Grand Banks
5401 slump and landslide tsunami. *Geological Society, London, Special Publications* 477(1): 315–331.
- 5402 Løvholt, F., Glimsdal, S., and Harbitz, C. B. (2020). On the landslide tsunami uncertainty and hazard.
5403 *Landslides*, 17(10): 2301–2315.
- 5404 Løvholt, F., Urgeles, R.E., Harbitz, C.B., Vanneste, M., Carlton, B. (2022). Submarine Landslides. In
5405 *Treatise on Geomorphology (Second Edition)*, Vol. 8, 919-959. [https://doi.org/10.1016/B978-0-12-](https://doi.org/10.1016/B978-0-12-818234-5.00139-5)
5406 [818234-5.00139-5](https://doi.org/10.1016/B978-0-12-818234-5.00139-5).
- 5407 Macías, J., Escalante, C., Castro, M. J. (2021). Multilayer-HySEA model validation for landslide-
5408 generated tsunamis–Part 1: Rigid slides. *Natural Hazards and Earth System Sciences*, 21(2), 775-789.
- 5409 Magnin, F., Etzelmüller, B., Westermann, S., Isaksen, K., Hilger, P., Hermanns, R. L. (2019).
5410 Permafrost distribution in steep rock slopes in Norway: measurements, statistical modelling and
5411 implications for geomorphological processes, *Earth Surf. Dynam.*, 7, 1019–1040,
5412 <https://doi.org/10.5194/esurf-7-1019-2019>.

- 5413 Majcher, J., Quinn, R., Smyth, T., Plets, R., McGonigle, C., Westley, K., Sacchetti, F., & Coughlan, M.
5414 (2022). Using difference modelling and computational fluid dynamics to investigate the evolution of
5415 complex, tidally influenced shipwreck sites. *Ocean Engineering*, 246, 110625.
5416 <https://doi.org/10.1016/J.OCEANENG.2022.110625>
- 5417 Mangerud, J. A. N., Dokken, T., Hebbeln, D., Heggen, B., Ingólfsson, Ó., Landvik, J. Y., ... & Vorren,
5418 T. O. (1998). Fluctuations of the Svalbard–Barents Sea Ice Sheet during the last 150 000 years.
5419 *Quaternary Science Reviews*, 17(1-3), 11-42.
- 5420 Maramai A., Graziani L., Brizuela B. (2014). Euro-Mediterranean Tsunami Catalogue (EMTC)
5421 (Version 1.0). Istituto Nazionale di Geofisica e Vulcanologia (INGV).
5422 <https://doi.org/10.13127/tsunami/emtc.1.0>
- 5423 Marr JG, Elverhøi A, Harbitz CB, Imran J, Harff P (2002) Numerical simulation of mud-rich
5424 subaqueous debris flows on the glacially active margins of the Svalbard-Barents Sea. *Marine Geology*
5425 188: 351–364.
- 5426 Masson, D.G. (2001). Sedimentary processes shaping the eastern slope of the Faroe–Shetland Channel.
5427 *Continental Shelf Research* 21, 825-857. doi: 10.1016/S0278-4343(00)00115-1.
- 5428 Masson, D.G., Wynn, R.B., Bett, B.J. (2004). Sedimentary environment of the Faroe–Shetland and
5429 Faroe Bank Channels, north-east Atlantic, and the use of bedforms as indicators of bottom current
5430 velocity in the deep ocean. *Sedimentology* 51, 1207-1241. doi: 10.1111/j.1365-3091.2004.00668.x.
- 5431 Mazzini, A., Svensen, H. H., Planke, S., Forsberg, C. F., Tjelta, T. I. (2016). Pockmarks and
5432 methanogenic carbonates above the giant Troll gas field in the Norwegian North Sea. *Marine Geology*,
5433 373, 26-38.
- 5434 Mazzini, A., Svensen, H. H., Forsberg, C. F., Linge, H., Lauritzen, S. E., Haflidason, H., ... & Tjelta,
5435 T. I. (2017). A climatic trigger for the giant Troll pockmark field in the northern North Sea. *Earth and*
5436 *Planetary Science Letters*, 464, 24-34.
- 5437 McCabe, A.M., Clark, P.U., Clark, J. (2005). AMS C dating of deglacial events in the Irish Sea Basin
5438 and other sectors of the British – Irish ice sheet. *Quat. Sci. Rev.* 1673–1690.
5439 <https://doi.org/10.1016/j.quascirev.2004.06.019>
- 5440 McCabe, A.M., Clark, P.U., Clark, J., Dunlop, P. (2007). Radiocarbon constraints on readvances of the
5441 British – Irish Ice Sheet in the northern Irish Sea Basin during the last deglaciation. *Quat. Sci. Rev.* 26,
5442 1204–1211. <https://doi.org/10.1016/j.quascirev.2007.01.010>

- 5443 Meier, M., Schlindwein, V., Scholz, J. -R., Geils, J., Schmidt-Aursch, M.C., Krüger, F., Czuba, W.,
5444 Janik, T. (2021). Segment-scale seismicity of the ultraslow spreading Knipovich Ridge. *Geochem.*
5445 *Geophys. Geosystems* 1–21. <https://doi.org/10.1029/2020gc009375>
- 5446 Mellett, C. L., Long, D., Carter, G. D. O. (2015). *Geology of the seabed and shallow subsurface: The*
5447 *Irish Sea. British Geological Survey Commissioned Report, CR/15/057. 52pp.*
- 5448 Mellett, C. L., Phillips, E., Lee, J. R., Cotterill, C. J., Tjelta, T. I., James, L., & Duffy, C. (2020).
5449 Elsterian ice-sheet retreat in the southern North Sea: antecedent controls on large-scale glaciotectonics
5450 and subglacial bed conditions. *Boreas*, 49(1), 129-151.
- 5451 Mesri, G., Ajlouni, M. (2007). "Engineering properties of fibrous peats." *Journal of Geotechnical and*
5452 *Geoenvironmental Engineering, ASCE*, 133(7), 850-866.
- 5453 Michel, G., Coughlan, M., Arosio, R., Emery, A.R., Wheeler, A.J. (2023). Stratigraphic and palaeo-
5454 geomorphological evidence for the glacial-deglacial history of the last British-Irish Ice Sheet in the
5455 north-western Irish Sea. *Quat. Sci. Rev.* 300, 107909.
5456 <https://doi.org/https://doi.org/10.1016/j.quascirev.2022.107909>
- 5457 Mikalsen, H. (2015). *Reservoir Structure and Geological Setting of the Shallow PEON Gas Reservoir*
5458 *(Master's Thesis. UiT The Arctic University of Norway.*
- 5459 Minasny, B., Berglund, Ö., Connolly, J., Hedley, C., de Vries, F., Gimona, A., ... & Widyatmanti, W.
5460 (2019). Digital mapping of peatlands—A critical review. *Earth-Science Reviews*, 196, 102870.
- 5461 Minshull, T. A., Marín-Moreno, H., Betlem, P., Bialas, J., Bünz, S., Burwicz, E., Cameselle, A. L.,
5462 Cifci, G., Giustiniani, M., Hillman, J. I. (2020) Hydrate occurrence in Europe: A review of available
5463 evidence: *Marine and Petroleum Geology*, v. 111, p. 735-764.
- 5464 Mohrig, D., Marr, J. G. (2003). Constraining the efficiency of turbidity current generation from
5465 submarine debris flows and slides using laboratory experiments. *Marine and Petroleum Geology* 20:
5466 883–899, DOI 10.1016/j.marpetgeo.2003.03.002.
- 5467 Mohrig, D.; Elverhøi, A. Parker, G. (1999). Experiments on the relative mobility of muddy subaqueous
5468 and subaerial debris flows, and their capacity to remobilize antecedent deposits. *Marine Geology* 154:
5469 117–129, DOI 10.1016/s0025-3227(98)00107-8.
- 5470 Monrigal, O., de Jong, I., Duarte, H. (2017). An ultra-high-resolution 3D marine seismic system for
5471 detailed site investigation. *Near Surface Geophysics* 15, 335–345. [https://doi.org/10.3997/1873-](https://doi.org/10.3997/1873-0604.2017025)
5472 [0604.2017025](https://doi.org/10.3997/1873-0604.2017025)

- 5473 Montelli, J.A. Dowdeswell, D. Ottesen, S.E. Johansen, (2017). Ice-sheet dynamics through the
5474 Quaternary on the mid-Norwegian continental margin inferred from 3D seismic data, *Marine and*
5475 *Petroleum Geology*, Volume 80, Pages 228-242, <https://doi.org/10.1016/j.marpetgeo.2016.12.002>.
- 5476 Moreau, J., Huuse, M. (2014). Infill of tunnel valleys associated with landward-flowing ice sheets: The
5477 missing Middle Pleistocene record of the NW European rivers? *Geochemistry, Geophysics,*
5478 *Geosystems* 15, 1–9. <https://doi.org/10.1002/2013gc005007>.
- 5479 Morency, C., Huismans, R.S., Beaumont, C. Fullsack, P. (2007). A numerical model for coupled fluid
5480 flow and matrix deformation with applications to disequilibrium compaction and delta stability. *Journal*
5481 *of Geophysical Research: Solid Earth*, 112(B10).
- 5482 Morgan, E. C., Vanneste, M., Lecomte, I., Baise, L. G., Longva, O., McAdoo, B. (2012). Estimation of
5483 free gas saturation from seismic reflection surveys by the genetic algorithm inversion of a P-wave
5484 attenuation model. *Geophysics*, 77(4), R175-R187.
- 5485 Mortimore, R. N. (2014). *Logging the Chalk* (pp. 48-117). Dunbeath, Scotland: Whittles Publishing.
- 5486 Mosar, J., 2003, Scandinavia's North Atlantic passive margin: *Journal of Geophysical Research: Solid*
5487 *Earth*, v. 108, no. B8.
- 5488 Mosca, I., Baptie, B., Haslam, R., Gafeira, J., Jenkins, G. (2024). Seismic Hazard Assessment for the
5489 UK Offshore Exclusive Economic Zone. British Geological Survey Open Report, OR/24/012.
- 5490 Muir Wood, R. (1988). The Scandinavian Earthquakes of 22 December 1759 and 31 August 1819.
5491 *Disasters* 12, 223–236. <https://doi.org/10.1111/j.1467-7717.1988.tb00672.x>
- 5492 Muir-Wood, R., King, G. C. (1993). Hydrological signatures of earthquake strain. *Journal of*
5493 *Geophysical Research: Solid Earth*, 98(B12), 22035-22068. Murray, A. B., & Thielert, E. R. (2004). A
5494 new hypothesis and exploratory model for the formation of large-scale inner-shelf sediment sorting and
5495 “rippled scour depressions.” *Continental Shelf Research*, 24(3), 295–315.
5496 <https://doi.org/10.1016/J.CSR.2003.11.001>
- 5497 Murray, A. B., Thielert, E. R. (2004). A new hypothesis and exploratory model for the formation of
5498 large-scale inner-shelf sediment sorting and “rippled scour depressions.” *Continental Shelf Research*,
5499 24(3), 295–315. <https://doi.org/10.1016/J.CSR.2003.11.001>
- 5500 Murton, J. B., & Ballantyne, C. K. (2017). Periglacial and permafrost ground models for Great Britain.
5501 In J. S. Griffiths and C. J. Martin (Eds.), *Engineering Geology and Geomorphology of Glaciated and*
5502 *Periglaciated Terrains* (pp. 501-583). The Geological Society.

5503 Mäntyniemi, P., Sørensen, M.B., Tatevossian, R.E. (2020). Testing the Environmental Seismic
5504 Intensity Scale on Data Derived from the Earthquakes of 1626, 1759, 1819, and 1904 in Fennoscandia,
5505 Northern Europe. *Geosciences* 11, 14. <https://doi.org/10.3390/geosciences11010014>.

5506 Mörner, N. A. (2013). Patterns in seismology and palaeoseismology, and their application in long-term
5507 hazard assessments—the Swedish case in view of nuclear waste management. *Pattern Recognition in*
5508 *Physics*, 1(1), 75-89.

5509 Nadim, F., T.J. Kvalstad, and T. Guttormsen (2005): Quantification of risks associated with seabed
5510 instability at Ormen Lange. *Marine and Petroleum Geology*, 22, 311-318.

5511 Nazarov, A. N. (1991). Mathematical modelling of a snow-powder avalanche in the framework of the
5512 equations of two-layer shallow water. *Fluid Dynamics* 26: 70–75, DOI 10.1007/BF01050115.

5513 Neilson, G., Musson, R.M.W., Burton, P.W. (1984). The “London” earthquake of 1580, April 6
5514 *Engineering Geology*. 20 (1–2). 113-141.

5515 Németh, A. A., Hulscher, S. J. M. H., De Vriend, H. J. (2002). Modelling sand wave migration in
5516 shallow shelf seas. *Continental Shelf Research*, 22(18–19), 2795–2806. [https://doi.org/10.1016/S0278-](https://doi.org/10.1016/S0278-4343(02)00127-9)
5517 [4343\(02\)00127-9](https://doi.org/10.1016/S0278-4343(02)00127-9)

5518 Newton, A. M., & Huuse, M. (2017). Late Cenozoic environmental changes along the Norwegian
5519 margin. *Marine Geology*, 393, 216-244.

5520 Newton, A. M., Montelli, A., Batchelor, C. L., Bellwald, B., Harding, R., Huuse, M., ... & Planke, S.
5521 (2024a). Glacial seismic geomorphology and Plio-Pleistocene ice sheet history offshore NW Europe.

5522 Newton, A.M.W., et al., 2024b. Late Cenozoic Glaciers, Landscapes, Climates, and Ecosystems of the
5523 North Sea (GLACE-NS): 1236-1012-Full. Available at: [https://www.iodp.org/docs/proposals/1236-](https://www.iodp.org/docs/proposals/1236-1012-full-newton-cover/file)
5524 [1012-full-newton-cover/file](https://www.iodp.org/docs/proposals/1236-1012-full-newton-cover/file).

5525 NGU (2009). Rock avalanches — distribution and frequencies in the inner part of Storfjorden, Møre og
5526 Romsdal County, Norway. Geological Survey of Norway Report 2009.002.

5527 NGU (2025). Marine limits and the possibility for quick clay – Marine limits and formerly submerged
5528 areas. Geological Survey of Norway. https://geo.ngu.no/kart/losmasse_mobil/?lang=nor&map=9

5529 Noble-James, T., Bullimore, R., McBreen, F., O’Connor, J., Highfield, J., McCabe, C., Archer-Rand,
5530 S., Downie, A.L., Hawes, J. and Mitchell, P., 2023. Monitoring benthic habitats in English Marine
5531 Protected Areas: Lessons learned, challenges and future directions. *Marine Policy*, 157, p.105852.

5532 Noble-James, T., Judd, A., Diesing, M., Clare, D., Eggett, A., Silburn, B., & Duncan, G. (2020).
5533 Monitoring shallow methane-derived authigenic carbonate: Insights from a UK Marine Protected Area.
5534 *Aquatic Conservation: Marine and Freshwater Ecosystems*, 30(5), 959-976.

5535 NPD (2014). CO2 Storage Atlas Norwegian Continental Shelf. Norwegian Petroleum Directorate
5536 (NPD). Editors: Eva K. Halland, Jasminka Mujezinović, Fridtjof Riis. [https://www.sodir.no/en/whats-](https://www.sodir.no/en/whats-new/publications/co2-atlases/co2-atlas-for-the-norwegian-continental-shelf/)
5537 [new/publications/co2-atlases/co2-atlas-for-the-norwegian-continental-shelf/](https://www.sodir.no/en/whats-new/publications/co2-atlases/co2-atlas-for-the-norwegian-continental-shelf/). Accessed 05. May 2025.

5538 NVE (2021). Årsaksvurdering Kvikkleireskredet ved Kråkne i Alta 3. Juni 2020. External report Nr.
5539 4/2021. Norges vassdrags- og energidirektorat. 200 pp. 978-82-410-2113-8.

5540 Nygård, A., Sejrup, H.P., Haflidason, H., and King, E.L., 2002, Geometry and genesis of glacial
5541 debris flows on the North Sea Fan: TOBI imagery and deep-tow boomer evidence: *Marine Geology*, v.
5542 188, p. 15-33, [https://doi.org/10.1016/S0025-3227\(02\)00273-6](https://doi.org/10.1016/S0025-3227(02)00273-6).

5543 Nygård, A., Sejrup, H.P., Haflidason, H., Cecchi, M., Ottesen, D., 2004. Deglaciation history of the
5544 southwestern Fennoscandian Ice Sheet between 15 and 13 14C ka BP. *Boreas*, 33: 1-17.
5545 <https://doi.org/10.1111/j.1502-3885.2004.tb00992.x>

5546 Nygård, A., Sejrup, H.P., Haflidason, H., and Bryn, P., 2005, The glacial North Sea Fan, southern
5547 Norwegian Margin: architecture and evolution from the upper continental slope to the deep-sea basin:
5548 *Marine and Petroleum Geology*, v. 22, p. 71-84, <https://doi.org/10.1016/j.marpetgeo.2004.12.001>.

5549 Obst, K., Nachtweide, C., Müller, U., 2017. Late Saalian and Weichselian glaciations in the German
5550 Baltic Sea documented by Pleistocene successions at the southeastern margin of the Arkona Basin.
5551 *Boreas* 46, 18–33. <https://doi.org/10.1111/bor.12212>

5552 Ó Cofaigh, C., Hogan, K. A., Jennings, A. E., Callard, S. L., Dowdeswell, J. A., Noormets, R., Evans,
5553 J. (2018). The role of meltwater in high-latitude trough-mouth fan development: the Disko Trough-
5554 Mouth Fan, West Greenland. *Marine Geology*, 402, 17-32.

5555 Oh, T.-M., Bang, E.-S., Cho, G.-C., Park, E.-S., 2017. Estimation of undrained shear strength for
5556 saturated clay using shear wave velocity. *Mar. Georesources Geotechnol.* 35, 236–244.
5557 <https://doi.org/10.1080/1064119X.2016.1140855>

5558 Ojala, A. E., Mattila, J., Hämäläinen, J., & Sutinen, R. (2019). Lake sediment evidence of
5559 paleoseismicity: timing and spatial occurrence of late-and postglacial earthquakes in Finland.
5560 *Tectonophysics*, 771, 228227.

5561 Okal EA and Synolakis CE (2004). Source discriminants for near-field tsunamis. *Geophysical Journal*
5562 *International* 158(3): 899–912.

5563 Olesen, O., Blikra, L. H., Braathen, A., Dehls, J. F., Olsen, L., Rise, L., Roberts, D., Riis, F., Faleide,
5564 J. I., and Anda, E., 2004, Neotectonic deformation in Norway and its implications: a review: *Norwegian*
5565 *Journal of Geology/Norsk Geologisk Forening*, v. 84, no. 1.

- 5566 Olesen, O., Bungum, H., Dehls, J., Lindholm, C., Pascal, C. & Roberts, D. (2013). Neotectonics,
5567 seismicity and contemporary stress field in Norway - mechanisms and implications. Geological Survey
5568 of Norway, Special Publication 13, 145–174.
- 5569 Olesen, O., Olsen, L., Gibbons, S.J., Ruud, B.O., Høgaas, F., Johansen, T.A., Kværna, T., 2021.
5570 Postglacial Faulting in Norway, in: Steffen, H., Olesen, O., Sutinen, R. (Eds.), *Glacially-Triggered*
5571 *Faulting*. Cambridge University Press, pp. 198–217.
- 5572 O'Reilly, S.S., Hryniewicz, K., Little, C.T.S., Monteys, X., Szpak, M.T., Murphy, B.T., Jordan, S.F.,
5573 Allen, C.C.R., Kelleher, B.P., 2014. Shallow water methane-derived authigenic carbonate mounds at
5574 the Codling Fault Zone, western Irish Sea. *Mar. Geol.* 357, 139–150.
5575 <https://doi.org/10.1016/j.margeo.2014.08.007>
- 5576 OSIG (Offshore Site Investigation and Geotechnics Committee), 2022. Guidance for the Planning and
5577 execution of geophysical and geotechnical ground investigations for offshore renewable energy
5578 developments. Society Underwater Technology (SUT) ISBN 0 906940 59 1.
- 5579 Osmond, J.L., Mulrooney, M.J., Holden, N., Skurtveit, E., Faleide, J.I., Braathen, A., 2022. Structural
5580 traps and seals for expanding CO₂ storage in the northern Horda platform, North Sea. *AAPG Bull.* 106,
5581 1711–1752. <https://doi.org/10.1306/03222221110>
- 5582 Ottemöller, L., Nielsen, H.H., Atakan, K., Braunmiller, J., Havskov, J. (2005) The 7 May 2001 induced
5583 seismic event in the Ekofisk oil field, North Sea. *J. Geophys. Res.* 110, B10301+.
5584 <https://doi.org/10.1029/2004jb003374>
- 5585 Ottemöller, L., Michalek, J., Christensen, J., Baadshaug, U., Halpaap, F., Natvik, Ø., Kværna, T., Oye,
5586 V. (2021) UiB-NORSAR EIDA Node: Integration of Seismological Data in Norway. *Seismol. Res.*
5587 *Lett.* <https://doi.org/10.1785/0220200369>
- 5588 Ottesen, D., Rise, L., Knies, J., Olsen, L. and Henriksen, S. (2005b) The Vestfjorden-Trænadjupet
5589 palaeo-ice stream drainage system, mid-Norwegian continental shelf. *Marine Geology* 218, 175–189.
5590 <https://doi.org/10.1016/j.margeo.2005.03.001>
- 5591 Ottesen, D., Rise, L., Andersen, E.S., Bugge, T. & Eidvin, T. (2009) Geological evolution of the
5592 Norwegian continental shelf between 61°N and 68°N during the last 3 million years. *Norwegian Journal*
5593 *of Geology* Vol. 89, pp. 251-265. Trondheim 2009, ISSN 029-196x
- 5594 Ottesen, D., Dowdeswell, J.A., Rise, L., Bugge, T. (2012) Large-scale development of the mid-
5595 Norwegian shelf over the last three million years and potential for hydrocarbon reservoirs in glacial
5596 sediments. *Geol. Soc. Lond. Spec. Publ.* 368 (1), 53–73.

5597 Ottesen, D., Dowdeswell, J. A., Bugge, T. (2014). Morphology, sedimentary infill and depositional
5598 environments of the Early Quaternary North Sea Basin (56–62 N). *Marine and Petroleum Geology*, 56,
5599 123-146.

5600 Ottesen, D., Batchelor, C.L., Dowdeswell, J.A., Løseth, H. (2018) Morphology and pattern of
5601 Quaternary sedimentation in the North Sea Basin (52–62° N). *Mar. Petrol. Geol.* 98, 836–859.

5602 Ottesen, D., Stewart, M., Brønner, M., Batchelor, C. L. (2020) Tunnel valleys of the central and northern
5603 North Sea (56 N to 62 N): Distribution and characteristics. *Marine Geology*, 425, 106199.

5604 Ottesen, D., Batchelor, C., Bjarnadóttir, L.R., Wiberg, D.H., Dowdeswell, J.A., (2022) Glacial
5605 landforms reveal dynamic ice-sheet behaviour along the mid-Norwegian margin during the last glacial-
5606 deglacial cycle, *Quaternary Science Reviews*, Volume 285, 107462,
5607 <https://doi.org/10.1016/j.quascirev.2022.107462>.

5608 Ottesen, D., Batchelor, C. L., Løseth, H., & Brunstad, H. (2024). 3D seismic evidence for a single Early
5609 Pleistocene glaciation of the central North Sea. *Science Advances*, 10(50), eadq6089.

5610 Overeem, I., Weltje, G.J., Bishop-Kay, C., Kroonenberg, S.B. (2001) The Late Cenozoic Eridanos delta
5611 system in the Southern North Sea Basin: a climate signal in sediment supply? *Basin Research*, v. 13,
5612 293-312. 10.1046/j.1365-2117.2001.00151.x

5613 OWA (2020). Offshore Wind Accelerator. Guidance for Geophysical Surveying for UXO and Boulders
5614 Supporting Cable Installation. Report No. C862R04-3a. Carbon Trust.

5615 Özmaral, A., Abegunrin, H. Keil, D. A. Hepp, T. Schwenk, H. Lantzsch, T. Mörz, and V. Spiess
5616 (2022), The Elbe Palaeovalley: Evolution from an ice-marginal valley to a sedimentary trap (SE North
5617 Sea), *Quaternary Science Reviews* 282, 107453, doi:<https://doi.org/10.1016/j.quascirev.2022.107453>.

5618 Paolo, F., Kroodsmas, D., Raynor, J., Hochberg, T., Davis, P., Cleary, J., ... & Halpin, P. (2024). Satellite
5619 mapping reveals extensive industrial activity at sea. *Nature*, 625(7993), 85-91.

5620 Parker, G.; Fukushima, Y. and Pantin, H. M. (1986). Self-accelerating turbidity currents, *Journal of*
5621 *Fluid Mechanics* 171: 145–181, DOI 10.1017/S0022112086001404.

5622 Parker, G.; Garcia, M.; Fukushima, Y. and Yu, W. (1987). Experiments on turbidity currents over an
5623 erodible bed. *Journal of Hydraulic Research* 25(1): 123–147, DOI 10.1080/00221688709499292.

5624 Pantin, H.M. (1978). Quaternary sediments from the north-east Irish Sea: Isle of Man to Cumbria. *Bull.*
5625 *Geol. Surv. G. B.* 64.

5626 Passchier, S., & Kleinhans, M. G. (2005). Observations of sand waves, megaripples, and hummocks in
5627 the Dutch coastal area and their relation to currents and combined flow conditions. *Journal of*
5628 *Geophysical Research: Earth Surface*, 110(F4), n/a-n/a. <https://doi.org/10.1029/2004JF000215>

5629 Pastor, M.; Tayyebi, S. M.; Hernández, A.; Zheng, J.; Suárez, G. and Reyes, M. E. (2024). Modeling
5630 fast flows with variable water content: A depth-integrated SPH approach. *Computers and Geotechnics*
5631 174: 106581, DOI 10.1016/j.compgeo.2024.106581.

5632 Patton, H., Hubbard, A., Andreassen, K., Auriac, A., Whitehouse, P.L., Stroeven, A.P., Shackleton, C.,
5633 Winsborrow, M., Heyman, J., Hall, A.M. (2017) Deglaciation of the Eurasian ice sheet complex:
5634 *Quaternary Science Reviews*, v. 169, p. 148-172, <https://doi.org/10.1016/j.quascirev.2017.05.019>.

5635 Patton, H., Hubbard, A., Heyman, J. et al. The extreme yet transient nature of glacial erosion. *Nat*
5636 *Commun* 13, 7377 (2022). <https://doi.org/10.1038/s41467-022-35072-0>

5637 Paul, M.A., Jobson, L.M. (1991). Geotechnical properties of soft clays from the Witch Ground Basin,
5638 central North Sea. *Geol. Soc. Eng. Geol. Spec. Publ.* 7, 151–156.
5639 <https://doi.org/10.1144/GSL.ENG.1991.007.01.12>

5640 Paull, C., Ussler, W., Lorensen, T., Winters, W., Dougherty, J. (2005), Geochemical constraints on the
5641 distribution of gas hydrates in the Gulf of Mexico: *Geo-Marine Letters*, v. 25, p. 273-280.

5642 Paull, C. K.; Talling, P. J.; Maier, K. L.; Parsons, D.; Xu, J.; Caress, D. W.; Gwiazda, R.; Lundsten, E.
5643 M.; Anderson, K.; Barry, J. P.; Chaffey, M.; O’Reilly, T.; Rosenberger, K. J.; Gales, J. A.; Kieft, B.;
5644 McGann, M.; Simmons, S. M.; McCann, M.; Sumner, E. J.; Clare, M. A. and Cartigny, M. J. (2018).
5645 Powerful turbidity currents driven by dense basal layers. *Nature Communications* 9: 4114, DOI
5646 10.1038/s41467-018-06254-6.

5647 Pedersen, S. (2014). Architecture of Glaciotectonic Complexes. *Geosciences*, 4(4), 269–296.
5648 <https://doi.org/10.3390/geosciences4040269>

5649 Pedersen, S. A. S., & Boldreel, L. O. (2015). Thrust-fault architecture of glaciotectonic complexes in
5650 Denmark. *GEUS Bulletin*, 33(JUNE), 17–20. <https://doi.org/10.34194/GEUSB.V33.4479>

5651 Peters, J.L., Benetti, S., Dunlop, P., Ó Cofaigh, C. (2015). Maximum extent and dynamic behaviour of
5652 the last British–Irish Ice Sheet west of Ireland. *Quaternary Science Reviews*, v. 128, 48-68.
5653 <https://doi.org/10.1016/j.quascirev.2015.09.015>

5654 Peuchan, J., Terwindt, J. (2014). Introduction to CPT accuracy, in: 3rd International Symposium on
5655 Cone Penetration Testing CPT14: May 12-14, 2014. Las Vegas, Nevada, USA, p. 45 pp.

5656 Pile Buck International, Inc.(2022). *Pile Buck Magazine*, www.pilebuck.com.

5657 Piper, D. J., Shor, A. N., & Clarke, J. E. H. (1988). The 1929 “Grand Banks” earthquake, slump, and
5658 turbidity current.

5659 Plaza-Faverola, A., Bünz, S., Mienert, J. (2012) The free gas zone beneath gas hydrate bearing
5660 sediments and its link to fluid flow: 3-D seismic imaging offshore mid-Norway: *Marine Geology*, v.
5661 291, p. 211-226.

5662 Plaza-Faverola, A., Vadakkepuliambatta, S., Hong, W. L., Mienert, J., Bünz, S., Chand, S., & Greinert,
5663 J. (2017). Bottom-simulating reflector dynamics at Arctic thermogenic gas provinces: An example from
5664 Vestnesa Ridge, offshore west Svalbard. *Journal of Geophysical Research: Solid Earth*, 122(6), 4089-
5665 4105.

5666 Plets, R., Dix, J., Bastos, A., & Best, A. (2007). Characterization of buried inundated peat on seismic
5667 (Chirp) data, inferred from core information. *Archaeological Prospection*, 14(4), 261–272.
5668 <https://doi.org/10.1002/ARP.318>

5669 Porz, L., Zhang, W., Hanebuth, T.J.J., Schrum, C., 2021. Physical processes controlling mud depocenter
5670 development on continental shelves – Geological, oceanographic, and modeling concepts. *Mar. Geol.*
5671 432, 106402. <https://doi.org/https://doi.org/10.1016/j.margeo.2020.106402>

5672 Pouliquen, O., 1999. Scaling laws in granular flows down rough inclined planes. *Physics of Fluids*
5673 11(3): 542–548. DOI 10.1063/1.869928.

5674 Poulos, H.G., 2022. Use of shear wave velocity for foundation design. *Geotech. Geol. Eng.* 40, 1921–
5675 1938. <https://doi.org/10.1007/s10706-021-02000-w>.

5676 Praeg, D., McCarron, S., Dove, D., Ó Cofaigh, C., Scott, G., Monteys, X., ... & Coxon, P. (2015). Ice
5677 sheet extension to the Celtic Sea shelf edge at the Last Glacial Maximum. *Quaternary Science Reviews*,
5678 111, 107-112.

5679 Prins, L. T., & Andresen, K. J. (2019). Buried late Quaternary channel systems in the Danish North
5680 Sea–Genesis and geological evolution. *Quaternary Science Reviews*, 223, 105943.

5681 Prins, L. T., Andresen, K. J., Owen, M., and Knutz, P. C. (2025). A review of subsurface geosystems
5682 and de-risking offshore construction in the Danish North Sea. *GEUS Bulletin* 52. 8371.
5683 <https://geusbulletin.org/index.php/geusb/article/view/8371/14568>

5684 Qiao, H., Liu, L., He, H., Liu, Xiaoyan, Liu, Xuening, Peng, P., 2023. The Practice and Development
5685 of T-Bar Penetrometer Tests in Offshore Engineering Investigation: A Comprehensive Review. *J. Mar.*
5686 *Sci. Eng.* 11. <https://doi.org/10.3390/jmse11061160>

5687 Ramírez, L., Fraile, D., & Brindley, G. (2020). *Offshore wind in Europe: Key trends and statistics 2019*.

5688 Rasmussen, E.S., Dybkjær, K., Toft, J.C., Nielsen, O.B., Sheldon, E., Mørk, F (in press):
5689 Lithostratigraphy of the Neogene succession of the Danish North Sea. *GEUS Bulletin*

- 5690 Rauter, M. and Köhler, A. (2020). Constraints on entrainment and deposition models in avalanche
5691 simulations from high-resolution radar data. *Geosciences* 10(1): 9, DOI 10.3390/10010009.
- 5692 Rauter M, Hoße L, Mulligan RP, Take WA, and Løvholt F (2021) Numerical simulation of impulse
5693 wave generation by idealized landslides with OpenFOAM. *Coastal Engineering* 165: 103815.
- 5694 Rauter, M., Viroulet, S., Gylfadóttir, S. S., Fellin, W., and Løvholt, F. (2022). Granular porous landslide
5695 tsunami modelling – the 2014 Lake Askja flank collapse. *Nature Communications*, 13(1), 678.
- 5696 Raymo, M. E., Lisiecki, L. E., & Nisancioglu, K. H. (2006). Plio-Pleistocene ice volume, Antarctic
5697 climate, and the global $\delta^{18}\text{O}$ record. *Science*, 313(5786), 492–495.
- 5698 Rea, B. R., Newton, A. M., Lamb, R. M., Harding, R., Bigg, G. R., Rose, P., Spagnolo, M., Huuse, M.,
5699 Cater, J. M. L., Archer, S., Buckley, F., Halliyeva, M., Huuse, J., Cornwell, D. G., Brocklehurst, S. H.,
5700 Howell, J. A. (2018). Extensive marine-terminating ice sheets in Europe from 2.5 million years ago.
5701 *Science Advances*, 4(6), eaar8327.
- 5702 Revelas, E.C., Sackmann, B.S., Maher, N.M., Jones, C.A. (2020). Mapping of benthic habitats at marine
5703 renewable energy sites using multibeam echosounder and sediment profile imaging technologies.
5704 Offshore Technology Conference. Houston, Texas. May. doi.org/10.4043/30733-MS
- 5705 Riis, F., Berg, K., Cartwright, J., Eidvin, T., & Hansch, K. (2005). Formation of large, crater-like
5706 evacuation structures in ooze sediments in the Norwegian Sea. Possible implications for the
5707 development of the Storegga Slide. In Ormen Lange—an Integrated Study for Safe Field Development
5708 in the Storegga Submarine Area (pp. 257-273). Elsevier.
- 5709 Rijdsdijk, K.F., Passchier, S., Weerts, H.J.T., Laban, C., Van Leeuwen, R.J.W., Ebbing, J.H.J. (2005)
5710 Revised Upper Cenozoic stratigraphy of the Dutch sector of the North Sea Basin: towards and integrated
5711 lithostratigraphic, seismostratigraphic and allostratigraphic approach. *Netherlands Journal of*
5712 *Geosciences — Geologie en Mijnbouw*, Vol. 84, 129–146.
- 5713 Rise, K., Ottesen, D., Berg, K., Lundin, E. (2005). Large-scale development of the mid-Norwegian
5714 margin during the last 3 million years. *Marine and Petroleum Geology* 22(1–2), 33–44,
5715 <https://doi.org/10.1016/j.marpetgeo.2004.10.010>.
- 5716 Rise, L., Ottesen, D., Longva, O., Solheim, A., Andersen, E.S., Ayers, S. (2006). The Sklinnadjupet
5717 slide and its relation to the Elsterian glaciation on the mid-Norwegian margin: *Marine and Petroleum*
5718 *Geology*, v. 23, p. 569-583, <https://doi.org/10.1016/j.marpetgeo.2006.05.005>.
- 5719 Rise, L., Chand, S., Hjelstuen, B.O., Haflidason, H., Bøe, R. (2010). Late Cenozoic geological
5720 development of the south Vøring margin, mid-Norway. *Marine and Petroleum Geology* 27, 1789-1803.

- 5721 Rise, L., Bøe, R., Riis, F., Bellec, V. K., Laberg, J. S., Eidvin, T., ... & Thorsnes, T. (2013). The Lofoten-
5722 Vesterålen continental margin, North Norway: Canyons and mass-movement activity. *Marine and*
5723 *Petroleum Geology*, 45, 134-149.
- 5724 Ritchie, J.D., Ziska, H., Johnson, H., Evans, D. (2011) *Geology of the Faroe–Shetland Basin and*
5725 *Adjacent Areas*. British Geological Survey Research Report, RR/11/01, Jarðfeingi Research Report,
5726 RR/11/01, HMSO for the British Geological Survey, London.
- 5727 Roberts, A. M., Yielding, G. (1991). Deformation around basin-margin faults in the North Sea/mid-
5728 Norway rift. *Geological Society, London, Special Publications*, 56(1), 61-78.
- 5729 Roberts, D. H., Dackombe, R. V., Thomas, G. S. (2007). Palaeo-ice streaming in the central sector of
5730 the British—Irish Ice Sheet during the Last Glacial Maximum: evidence from the northern Irish Sea
5731 Basin. *Boreas*, 36(2), 115-129.
- 5732 Roberts, D.H., Grimoldi, E., Callard, S.L., Evans, D.J.A., Clark, C.D., Stewart, H.A., Dove, D., Saher,
5733 M., Ó Cofaigh, C., Chiverrell, R.C., Bateman, M.D., Moreton, S.G., Bradwell, T., Fabel, D., Medialdea,
5734 A. (2019) The mixed-bed glacial landform imprint of the North Sea Lobe in the western North Sea.
5735 *Earth Surface Processes and Landforms*, v. 44: 1233-1258.
- 5736 Robertson, P.K. (1990). Soil classification using the cone penetration test. *Can. Geotech. J.* 27, 151–
5737 158.
- 5738 Robertson, P.K., Campanella, R.G., Gillespie, D., Greig, J. (1986). Use of Piezometer Cone data, in:
5739 ASCE Speciality Conference In-Situ '86: Use of In-Situ Testing in Geotechnical Engineering.
5740 American Society of Engineers (ASCE). ASCE, Reston, Blacksburg, pp. 1263–1280.
- 5741 Rose P., Byerley, G., Vaughan, O., Cater, J., Rea, B. R., Spagnolo, M., Archer, S. (2018). Aviat: a
5742 Lower Pleistocene shallow gas hazard developed as a fuel gas supply for the Forties Field. From:
5743 Bowman, M. & Levell, B. (eds) 2018. *Petroleum Geology of NW Europe: 50 Years of Learning –*
5744 *Proceedings of the 8th Petroleum Geology Conference*, 485–505, <https://doi.org/10.1144/PGC8.16>
- 5745 Rosentau, A., Bennike, O., Uścińowicz, S., & Miotk-Szpiganowicz, G. (2017). The baltic sea basin.
5746 *Submerged landscapes of the European continental shelf: quaternary paleoenvironments*, 103-133.
- 5747 Rydningen, T.A., Laberg, J.S., Kolstad, V. (2015). Seabed morphology and sedimentary processes on
5748 high-gradient trough mouth fans offshore Troms, northern Norway, *Geomorphology*, 246, 205–219.
5749 <https://doi.org/10.1016/j.geomorph.2015.06.007>.
- 5750 Rydningen, T.A., Laberg, J.S., Kolstad, V. (2016). Late Cenozoic evolution of high-gradient trough
5751 mouth fans and canyons on the glaciated continental margin offshore Troms, northern Norway—

5752 Paleoclimatic implications and sediment yield. *GSA Bulletin*; 128 (3-4): 576–596. doi:
5753 <https://doi.org/10.1130/B31302.1>

5754 Rydningen, T. A., Høgseth, G. V., Lasabuda, A. P. E., Laberg, J. S., Safronova, P. A., Forwick, M.
5755 (2020). An early Neogene—Early Quaternary contourite drift system on the SW Barents Sea continental
5756 margin, Norwegian Arctic. *Geochemistry, Geophysics, Geosystems*, 21(11), e2020GC009142.

5757 Römer, M., Blumenberg, M., Heeschen, K., Schloemer, S., Müller, H., Müller, S., Hilgenfeldt, C.,
5758 Barckhausen, U., Schwalenberg, K. (2021). Seafloor methane seepage related to salt diapirism in the
5759 northwestern part of the German North Sea. *Frontiers in Earth Science* 9, 319.
5760 <https://doi.org/10.3389/feart.2021.556329>

5761 Römer-Stange, N., Wenau, S., Bihler, V., Keil, H., Ramos Córdova, C.A., Spiess, V. (2022). Boulder
5762 detection in the shallow sub-seafloor by diffraction imaging with beamforming on ultra-high resolution
5763 seismic data—a feasibility study. *Earth and Space Science* 9, e2021EA002156.
5764 <https://doi.org/10.1029/2021EA002156>

5765 Rütther, D. C., Mattingsdal, R., Andreassen, K., Forwick, M., Husum, K. (2011). Seismic architecture
5766 and sedimentology of a major grounding zone system deposited by the Bjørnøyrenna Ice Stream during
5767 Late Weichselian deglaciation. *Quaternary Science Reviews*, 30(19-20), 2776-2792.

5768 Safronova, P. A., Laberg, J. S., Andreassen, K., Shlykova, V., Vorren, T. O., Chernikov, S. (2015). Late
5769 Pliocene–early Pleistocene deep-sea basin sedimentation at high-latitudes: mega-scale submarine slides
5770 of the north-western Barents Sea margin prior to the shelf-edge glaciations. *Basin Research*, 29, 537-
5771 555, <https://doi.org/10.1111/bre.12161>

5772 Salmanidou, D.M., Guillas, S., Georgiopoulou, A., Dias, F. (2017). Statistical emulation of landslide-
5773 induced tsunamis at the Rockall Bank, NE Atlantic. *Proceedings of the Royal Society A: Mathematical,*
5774 *Physical and Engineering Sciences* 473(2200): 20170026.

5775 Sauvin, G., Vanneste, M., Vardy, M., Klinkvort, R., Forsberg, C.F. (2019) "Machine Learning and
5776 Quantitative Ground Models for Improving Offshore Wind Site Characterization." Paper presented at
5777 the Offshore Technology Conference, Houston, Texas, May 2019. doi: <https://doi.org/10.4043/29351->
5778 MS

5779 Scheidegger, A. E. (1973). On the prediction of the reach and velocity of catastrophic rockfalls. *Rock*
5780 *Mechanics* 5: 231–236.

5781 Schiøler, P., Andsbjerg, J., Clausen, O.R., Dam, G., Dybkjær, K., Hamberg, L., Heilmann-Clausen, C.,
5782 Johannessen, E.P., Kristensen, L.E., Prince, I., Rasmussen, J.A. (2007). Lithostratigraphy of the
5783 Palaeogene – Lower Neogene succession of the Danish North Sea. *GEUS Bulletin*, 12, 1–77.
5784 <https://doi.org/10.34194/geusb.v12.5249>

- 5785 Schmitt, T., Mitchell, N. C., Ramsay, T. S. (2007). Use of swath bathymetry in the investigation of sand
5786 dune geometry and migration around a near shore “banner” tidal sandbank. Geological Society Special
5787 Publication, 274, 53–64. <https://doi.org/10.1144/GSL.SP.2007.274.01.07>
- 5788 Schroot B. M., Schüttenhelm R.T.E. (2003). Expressions of shallow gas in the Netherlands North Sea.
5789 Netherlands Journal of Geosciences / Geologie en Mijnbouw 82 (1): 91-105.
- 5790 Scourse, J. D., Chiverrell, R. C., Smedley, R. K., Small, D., Burke, M. J., Saher, M., ... & Clark, C. D.
5791 (2021). Maximum extent and readvance dynamics of the Irish sea ice stream and Irish Sea Glacier since
5792 the last glacial maximum. Journal of Quaternary Science, 36(5), 780-804.
- 5793 Sejrup H. P., Aarseth I., Ellingsen K. L., Reither E., Jansen E. (1987) Quaternary stratigraphy of the
5794 Fladden area, central North Sea: a multidisciplinary study. Journal of Quaternary Science, v. 2, 35–58.
- 5795 Sejrup, H. P., Aarseth, I., Hafliðason, H., Løvlie, R., Bratten, Å., Tjøstheim, G., ... & Ellingsen, K. L.
5796 (1995). Quaternary of the Norwegian Channel: glaciation history and palaeoceanography. Norsk
5797 geologisk tidsskrift, 75(2-3), 65-87.
- 5798 Sejrup, H. P., Clark, C. D., Hjelstuen, B. O. (2016). Rapid ice sheet retreat triggered by ice stream
5799 debulking: Evidence from the North Sea. Geology, v. 44, 355–358.
- 5800 Sejrup, H. P., King, E. L., Aarseth, I., Hafliðason, H., & Elverhøi, A. (1996). Quaternary erosion and
5801 depositional processes: western Norwegian fjords, Norwegian Channel and North Sea Fan. Geological
5802 Society, London, Special Publications, 117(1), 187-202.
- 5803 Sejrup, H. P., Larsen, E., Landvik, J., King, E. L., Hafliðason, H., & Nesje, A. (2000). Quaternary
5804 glaciations in southern Fennoscandia: evidence from southwestern Norway and the northern North Sea
5805 region. Quaternary Science Reviews, 19(7), 667-685.
- 5806 Sejrup, H. P., Hjelstuen, B. O., Dahlgren, K. T., Hafliðason, H., Kuijpers, A., Nygård, A., ... & Vorren,
5807 T. O. (2005). Pleistocene glacial history of the NW European continental margin. Marine and Petroleum
5808 Geology, 22(9-10), 1111-1129.
- 5809 Sejrup, H. P., Hjelstuen, B. O., Patton, H., Esteves, M., Winsborrow, M., Rasmussen, T. L., ... &
5810 Hubbard, A. (2022). The role of ocean and atmospheric dynamics in the marine-based collapse of the
5811 last Eurasian Ice Sheet. Communications Earth & Environment, 3(1), 119.
- 5812 Selby, N.D., Eshun, E., Patton, H.J., Douglas, A. (2005). Unusual long-period Rayleigh wave radiation
5813 from a vertical dip-slip source: The 7 May 2001 North Sea earthquake. J. Geophys. Res. Solid Earth
5814 110, 2005JB003721. <https://doi.org/10.1029/2005JB003721>
- 5815 Serié, C., Huuse, M., Schødt, N. H., Brooks, J. M., & Williams, A. (2017). Subsurface fluid flow in the
5816 deep-water Kwanza Basin, offshore Angola. Basin Research, 29(2), 149-179.

5817 Serov, P., Mattingdal, R., Winsborrow, M., Patton, H., and Andreassen, K., 2023, Widespread natural
5818 methane and oil leakage from sub-marine Arctic reservoirs: *Nature Communications*, v. 14, no. 1, p.
5819 1782.

5820 Shanmugam, G. (1996). High-density turbidity currents: Are they sandy debris flows? *Journal of*
5821 *Sedimentary Research* 66(1), 2–10. DOI: 10.1306/D426828E-2B26-11D7-8648000102C1865D.

5822 Shennan, I., Bradley, S. L., & Edwards, R. (2018). Relative sea-level changes and crustal movements
5823 in Britain and Ireland since the Last Glacial Maximum. *Quaternary Science Reviews*, 188, 143-159.

5824 Shennan, I., Milne, G. and Bradley, S. (2012), Late Holocene vertical land motion and relative sea-level
5825 changes: lessons from the British Isles. *J. Quaternary Sci.*, 27: 64-70. <https://doi.org/10.1002/jqs.1532>

5826 Shipp, 2017. Marine Geohazards. Workshop handout. Submarine Mass Movements and Their
5827 Consequences. 4th International Symposium. Vancouver Island, Canada. November 2017.

5828 Si P, Shi H, and Yu X. (2018) A general numerical model for surface waves generated by granular
5829 material intruding into a water body. *Coastal Engineering* 142: 42–51.

5830 Sibson, R. H., 1994, Crustal stress, faulting and fluid flow: Geological Society, London, Special
5831 Publications, v. 78, no. 1, p. 69-84.

5832 Singhroha, S., Bünz, S., Plaza-Faverola, A., and Chand, S., 2020, Detection of gas hydrates in faults
5833 using azimuthal seismic velocity analysis, Vestnesa Ridge, W-Svalbard Margin: *Journal of Geophysical*
5834 *Research: Solid Earth*, v. 125, no. 2, p. e2019JB017949.

5835 SINTEF Offshore Blowout Database, [http://www.sintef.no/home/Technology-and-Society/Safety-](http://www.sintef.no/home/Technology-and-Society/Safety-Research/Projects/SINTEF-Offshore-Blowout-Database/)
5836 [Research/Projects/SINTEF-Offshore-Blowout-Database/](http://www.sintef.no/home/Technology-and-Society/Safety-Research/Projects/SINTEF-Offshore-Blowout-Database/) Trondheim, Norway, 2011

5837 Sloan, E. D. (1998a). Gas hydrates: review of physical/chemical properties. *Energy & fuels*, 12(2), 191-
5838 196.

5839 Sloan, E. D. (1998b). Physical/chemical properties of gas hydrates and application to world margin
5840 stability and climatic change. Geological society, London, special publications, 137(1), 31-50.

5841 Sloan, E. D., and Koh, C. A., 2007, Clathrate hydrates of natural gases, CRC press.

5842 Small, D., Smedley, R. K., Chiverrell, R. C., Scourse, J. D., Ó Cofaigh, C., Duller, G. A., ... & Clark,
5843 C. D. (2018). Trough geometry was a greater influence than climate-ocean forcing in regulating retreat
5844 of the marine-based Irish-Sea Ice Stream. *GSA Bulletin*, 130(11-12), 1981-1999.

5845 Smedley, R. K., Scourse, J. D., Small, D., Hiemstra, J. F., Duller, G. A. T., Bateman, M. D., ... & Xu,
5846 S. (2017). New age constraints for the limit of the British–Irish Ice Sheet on the Isles of Scilly. *Journal*
5847 *of Quaternary Science*, 32(1), 48-62.

- 5848 Smith, D. E., Cullingford, R. A., and Haggart, A., 1985. Major Coastal Flood During the Holocene in
5849 Eastern Scotland, *E&G Quaternary Sci. J.*, 35, 109–118
- 5850 Smith, D.E., Shi, S., Cullingford, R.A., Dawson, A.G., Dawson, S., Firth, C.R., Foster, I.D.L., Fretwell,
5851 P.T., Haggart, B.A., Holloway, L.K., Long, D., 2004. The Holocene Storegga Slide tsunami in the
5852 United Kingdom. *Quaternary Science Reviews* 23, 2291-2321.
- 5853 Smith, S. A., Vanneste, M., Faleide, T. S. and Bertrand, A., 2024. Multi-sensor core logging of marine
5854 sediments for continuous thermal conductivity profiles. In *Proceedings of the 7th International*
5855 *Conference on Geotechnical and Geophysical Site Characterization (Vol. 18, p. 21).*
- 5856 Solheim, A., Berg, K., Forsberg, C.F., Bryn, P., 2005a. The Storegga Slide complex: repetitive large
5857 scale sliding with similar cause and development. *Marine and Petroleum Geology*, 22, 97–107.
5858 <https://doi.org/10.1016/j.marpetgeo.2004.10.013>.
- 5859 Solheim, A., Bryn, P., Berg, K., Sejrup, H.P. & Mienert, J. 2005b: Ormen Lange: An integrated study
5860 for the safe development of a deep-water gas field within the Storegga Slide Complex, NE Atlantic
5861 continental margin. Thematic Volume. *Marine and Petroleum Geology* 22, 1–9.
5862 <https://doi.org/10.1016/j.marpetgeo.2004.10.001>.
- 5863 Soraghan, C., 2016. Management of Hydrogen Sulphide (H₂S) Gas in Wind Turbine Sub-Structures:
5864 identifying and managing H₂S. Case Study published by Catapult Offshore renewable Energy, TLI-
5865 CS-00006.
- 5866 Sovilla, B., McElwaine, J. N. and Louge, M. Y, (2015). The structure of powder snow avalanches.
5867 *Comptes Rendus Physique* 16(1), 97–104. DOI: 10.1016/j.crhy.2014.11.005.
- 5868 Standards Australia. (2001). AS/NZS 4801 Occupational health and safety management
5869 systems - Specification with guidance for use. Sydney: Standards Australia.
- 5870 Stewart, S. A. (2007). Salt tectonics in the North Sea Basin: a structural style template for seismic
5871 interpreters.
- 5872 Stewart, S.A., Davies, R.J. (2006). Structure and emplacement of mud volcano systems in the South
5873 Caspian Basin. *AAPG bulletin*, 90(5), pp.771-786.
- 5874 Stewart, H.A., Bradwell, T., Carter, G.D.O., Dove, D., Gafeira, J. (2021) Chapter 6: Geomorphology
5875 of the Offshore Continental Shelf. 117-134 in *World Geomorphological Landscapes: Landscapes and*
5876 *Landforms of Scotland (J. Gordon and C. Ballantyne Editors).* (London Springer) DOI: 10.1007/978-
5877 3-030-71246-4_6
- 5878 Stewart, H. A., Cooper, R. M., Lewis, W. D. (2022) Reprocessing of CHP datasets (HI1567 & HI1570)
5879 and Seafloor Substrate Interpretation for Selected Areas: Inner Sound off Skye on the West Coast of

5880 Scotland. British Geological Survey Commissioned Report, 44 pp. (CR/21/080).
5881 <https://nora.nerc.ac.uk/id/eprint/531840>

5882 Stewart, H.A., Hinxman, D., Dyer, N., Moore, J., Baker, A., Plenderleith, G., Terente, V., Holland, R.,
5883 Rose, M. (2023) Ice sheet and retreat dynamics of the eastern sector of the British–Irish Ice Sheet:
5884 implications for sustainable offshore wind development, Berwick Bank Wind Farm. Quaternary
5885 Research Association Annual Discussion Meeting, 5-6 January 2023, Geological Society of London.

5886 Stewart, H. A., Long, D. (2012) The timing and significance of gully incision on the eastern flank of
5887 the Faroe-Shetland channel and its impact on seafloor infrastructure. European Association of
5888 Geoscientists & Engineers. Near Surface Geophysics. V.10 n.4, 317-331.

5889 Stewart, H.A., Long, D. (2016). Glacigenic debris flows observed in 3D seismic high-resolution
5890 seafloor imagery, Faroe–Shetland Channel, NE Atlantic. From: Dowdeswell, J A, Canals, M,
5891 Jakobsson, M, Todd, B J, Dowdeswell, E K and Hogan, K A (eds). Atlas of Submarine Glacial
5892 Landforms: Modern, Quaternary and Ancient. Geological Society, London, Memoirs, v. 46, 361–362.

5893 Stewart, M. A., Lonergan, L. (2011) Seven glacial cycles in the middle-late Pleistocene of northwest
5894 Europe: geomorphic evidence from buried tunnel valleys. *Geology*, v. 39, 283–286.

5895 Stoker, M. S., 1995. The influence of glacigenic sedimentation on slope-apron development on the
5896 continental margin off Northwest Britain. In Scrutton, R. A., Stoker, M. S., Shimmield, G. B. &
5897 Tudhope, A. W. (eds), 1995. *The Tectonics, Sedimentation and Palaeoceanography of the North*
5898 *Atlantic Region*, Geological Society Special Publication No. 90, 159-177.

5899 Stoker M.S. (2002). Late Neogene development of the UK Atlantic mar-gin. In Doré A.G., Cartwright
5900 J.A., Stoker M.S., Turner J.P. and White N. (eds) *Exhumation of the North Atlantic Margin: Timing,*
5901 *Mechanisms and Implications for Petroleum Exploration*, Geological Society of London Special
5902 *Publication*, v. 196, 313-329.

5903 Stoker, M.S. (2013) Cenozoic sedimentary rocks. In: Hitchen, K., Johnson, H. & Gatliff, R. W. (eds)
5904 *Geology of the Rockall Basin and Adjacent Areas*. British Geological Survey Research Report,
5905 RR/12/03, HMSO for the British Geological Survey, London, pp 96-136.

5906 Stoker, M.S., Balson, P.S., Long, D., Tappin, D.R. (2011) An overview of the lithostratigraphical
5907 framework for the Quaternary deposits on the United Kingdom continental shelf. British Geological
5908 Survey Research Report, RR/11/03. 48pp. www.bgs.ac.uk/downloads/start.cfm?id=2084

5909 Stoker, M.S., Bent, A.J.A. (1985) Middle Pleistocene glacial and glaciomarine sedimentation in the
5910 west Central North Sea. *Boreas*, v. 14, 325–332.

- 5911 Stoker, M.S., Hitchen, K., Graham, C.C. (1993). United Kingdom offshore regional report: The geology
5912 of the Hebrides and West Shetland shelves, and adjacent deep-water areas. London: HMSO for the
5913 British Geological Survey.
- 5914 Stoker, M.S., Praeg, D., Hjelstuen, B.O., Laberg, J.S., Nielsen, T., Shannon, P. M. (2005). Neogene
5915 stratigraphy and the sedimentary and oceanographic development of the NW European Atlantic margin.
5916 *Marine and Petroleum Geology*, v. 22, 977–1005.
- 5917 Stoker, M.S., Varming, T. (2011) Cenozoic (sedimentary). In: Ritchie, J.D., Ziska, H., Johnson, H. &
5918 Evans, D. (eds) *Geology of the Faroe–Shetland Basin and Adjacent Areas*. British Geological Survey
5919 Research Report, RR/11/01, Jarðfeingi Research Report, RR/11/01, HMSO for the British Geological
5920 Survey, London, pp 151–208.
- 5921 Stolt, M. H., & Lindbo, D. L. (2010). Soil Organic Matter. Interpretation of Micromorphological
5922 Features of Soils and Regoliths, 369–396. <https://doi.org/10.1016/B978-0-444-53156-8.00017-9>
- 5923 Stow, J., 1601. *The Chronicles of England*, London.
- 5924 Stow, D.A.V., Hernandez-Molina, F.J., Llave, E., Sayago-Gil, M., Diaz del Rio, V., Branson, A. (2009).
5925 "Bedform-velocity matrix: The estimation of bottom current velocity from bedform observations".
5926 *Geology*. 37 (4): 327–330
- 5927 Sturt, F., Garrow, D., & Bradley, S. (2013). New models of North West European Holocene
5928 palaeogeography and inundation. *Journal of Archaeological Science*, 40(11), 3963-3976.
- 5929 Sultan, N., Voisset, M., Marsset, T., Vernant, A.-M., Cauquil, E., Colliat, J., and Curinier, V., 2007,
5930 Detection of free gas and gas hydrate based on 3D seismic data and cone penetration testing: An
5931 example from the Nigerian Continental Slope: *Marine Geology*, 240 (1–4), 235–255.
- 5932 Sultan, N., Plaza-Faverola, A., Vadakkepuliymbatta, S., Buenz, S., & Knies, J. (2020). Impact of tides
5933 and sea-level on deep-sea Arctic methane emissions. *Nature communications*, 11(1), 5087.
- 5934 Sumer, B.M., Kirca, V.S.O., 2022. Scour and liquefaction issues for anchors and other subsea structures
5935 in floating offshore wind farms: A review. *Water Sci. Eng.* 15, 3–14.
5936 <https://doi.org/10.1016/j.wse.2021.11.002>
- 5937 SUT (2022). *Guidance Notes for the Planning and Execution of Geophysical and Geotechnical Ground*
5938 *Investigations for Offshore Renewable Energy Developments*. Cook, M (Editor). (The Society for
5939 Underwater Technology: London) ISBN 0 906940 59 1. 71pp.
- 5940 Svennevig, K., Hicks, S.P., Forbriger, T., Lecocq, T., Widmer-Schmidrig, R., Mangeney, A., Hibert, C.,
5941 Korsgaard, N.J., Lucas, A., Satriano, C., Anthony, R.E., Mordret, A., Schippkus, S., Rysgaard, S.,
5942 Boone, W., Gibbons, S.J., Cook, K.L., Glimsdal, S., Løvholt, F., Van Noten, K., Assink, J.D.,

- 5943 Marboeuf, A., Lomax, A., Vanneste, K., Taira, T., Spagnolo, M., De Plaen, R.S.M., Koelemeijer, P.,
5944 Ebeling, C., Cannata, A., Harcourt, W.D., Cornwell, D.G., Caudron, C., Poli, P., Bernard, P., Larose,
5945 E., Stutzmann, E., Voss, P.H., Lund, B., Cannavo, F., Castro-Díaz, M.J., Chaves, E.J., Dahl-Jensen, T.,
5946 Pinho Dias, N. De, Déprez, A., Develter, R., Dreger, D., Evers, L.G., Fernández-Nieto, E.D., Ferreira,
5947 A.M.G., Funning, G.J., Gabriel, A.-A., Hendrickx, M.E., Kafka, A.L., Keiding, M., Kerby, J., Khan,
5948 S.A., Dideriksen, A.K., Lamb, O.D., Larsen, T.B., Lipovsky, B., Magdalena, I., Malet, J.-P., Myrup,
5949 M., Rivera, L., Ruiz-Castillo, E., Wetter, S.; Wirtz, B. (2024). A rockslide-generated tsunami in a
5950 Greenland fjord rang Earth for 9 days. *Science* 385 (6714), 1196–1205.
- 5951 Svendsen, J. I., Alexanderson, H., Astakhov, V. I., Demidov, I., Dowdeswell, J. A., Funder, S., ... &
5952 Stein, R. (2004). Late Quaternary ice sheet history of northern Eurasia. *Quaternary Science Reviews*,
5953 23(11-13), 1229-1271.
- 5954 Sørensen, M.B., Haga, T., Nesje, A. (2023). Earthquake-induced landslides in Norway. *Nat. Hazards*
5955 *Earth Syst. Sci.*, 23, 1577–1592.
- 5956 Tam, C. 2023. Leveraging the use of repurposed Oil and Gas 2D seismic data to de-risk offshore wind
5957 farm development projects. A case study from the Central North Sea. EGC1 Conference poster,
5958 Aberdeen
- 5959 Tappin, D. R., Chadwick, R. A., Jackson, A. A., Wingfield, R. T. R. and Smith, N. J. P., 1995. The
5960 geology of Cardigan Bay and the Bristol Channel, United Kingdom Offshore Regional Report. British
5961 Geological Survey. London: HMSO
- 5962 Tappin, D.R., Pearce, B., Fitch, S., Dove, D., Gearey, B., Hill, J.M., Chambers, C., Bates, R., Pinnion,
5963 J., Diaz Doce, D. and Green, M. (2011). The Humber regional environmental characterisation. Marine
5964 Aggregate Levy Sustainability Fund.
- 5965 Tasianias, A., Bünz, S., Bellwald, B., Hammer, Ø., Planke, S., Lebedeva-Ivanova, N., & Krassakis, P.
5966 (2018). High-resolution 3D seismic study of pockmarks and shallow fluid flow systems at the Snøhvit
5967 hydrocarbon field in the SW Barents Sea. *Marine Geology*, 403, 247-261.
- 5968 Taylor, M., Ralon, P., Anuta, H., & Al-Zoghoul, S. (2020). IRENA renewable power generation costs
5969 in 2019. International Renewable Energy Agency: Abu Dhabi, UAE.
- 5970 Thakur, V., L'Heureux, J. S., & Locat, A. (2017). Landslides in sensitive clays. *Advances in Natural*
5971 *and Technological Hazards Research*, 46, 593.
- 5972 Thöle, H., Gaedicke, C., Kuhlmann, G., Reinhardt, L., 2014. Late Cenozoic sedimentary evolution of
5973 the German North Sea – A seismic stratigraphic approach. *Newsletters on Stratigraphy* 299–329.
5974 <https://doi.org/10.1127/0078-0421/2014/0049>

5975 Tommasi, P., Avalle, A., Budillon, F., Romeo, R., Caburlotto, A., Conforti, A., Di Martino, G.,
5976 Pagliaroli, A., Magagnoli, M., Urgeles, R., Llopart, J., Camerlenghi, A., 2019. Evaluation of
5977 disturbance induced on soft offshore sediments by two types of gravity piston coring techniques. *Mar.*
5978 *Geol.* 417, 106005. <https://doi.org/10.1016/j.margeo.2019.106005>

5979 Toorman, E. A. (1997). Modelling the thixotropic behavior of dense cohesive sediment suspensions.
5980 *Rheologica Acta* 36: 56–65, DOI 10.1007/bf00366724.

5981 Tóth, Z., Spiess, V., Mogollón, J.M., Jensen, J.B., 2014a. Estimating the free gas content in Baltic Sea
5982 sediments using compressional wave velocity from marine seismic data. *Journal of Geophysical*
5983 *Research: Solid Earth* 119, 8577–8593. <https://doi.org/10.1002/2014JB010989>

5984 Tóth, Z., Spieß, V., Jensen, J., 2014b. Seismo-acoustic signatures of shallow free gas in the Bornholm
5985 Basin, Baltic Sea. *Cont. Shelf Res.* 88, 228–239.
5986 <https://doi.org/https://doi.org/10.1016/j.csr.2014.08.007>

5987 Tóth, Z., McCarron, S., Wheeler, A. J., Wenau, S., Davis, S., Lim, A., & Spiess, V. (2020).
5988 Geomorphological and seismostratigraphic evidence for multidirectional polyphase glaciation of the
5989 northern Celtic Sea. *Journal of Quaternary Science*, 35(3), 465-478.

5990 Trafford, A., & Long, M. (2020). Relationship between Shear-Wave Velocity and Undrained Shear
5991 Strength of Peat. *Journal of Geotechnical and Geoenvironmental Engineering*, 146(7), 04020057.
5992 [https://doi.org/10.1061/\(ASCE\)GT.1943-5606.0002298/ASSET/F2C1F035-9C2D-4E63-A96E-](https://doi.org/10.1061/(ASCE)GT.1943-5606.0002298/ASSET/F2C1F035-9C2D-4E63-A96E-E6C0F55BB547/ASSETS/IMAGES/LARGE/FIGURE9.JPG)
5993 [E6C0F55BB547/ASSETS/IMAGES/LARGE/FIGURE9.JPG](https://doi.org/10.1061/(ASCE)GT.1943-5606.0002298/ASSET/F2C1F035-9C2D-4E63-A96E-E6C0F55BB547/ASSETS/IMAGES/LARGE/FIGURE9.JPG)

5994 Trafford, A., Ellwood, R., Wacquier, L., Godfrey, A., Minto, C., Coughlan, M., Donohue, S., 2022.
5995 Distributed acoustic sensing for active offshore shear wave profiling. *Sci. Rep.* 12, 9691.
5996 <https://doi.org/10.1038/s41598-022-13962-z>

5997 Tran, Q. A.; Grimstad, G. and Ghoreishian Amiri, S. A. (2024). MPMICE: A hybrid MPM-CFD model
5998 for simulating coupled problems in porous media. Application to earthquake-induced submarine
5999 landslides. *Intl. J. Num. Meth. Eng.* 125(5) : e7383, DOI 10.1002/nme.7383. 10.1002/nme.7383.

6000 Tregaskis, C. (2020). Granular Avalanches Past Obstacles and Erosion and Deposition Processes in
6001 Shallow Granular Flows. PhD thesis, Dept. of Mathematics, University of Manchester, Manchester,
6002 UK. https://pure.manchester.ac.uk/ws/portalfiles/portal/213186161/FULL_TEXT.PDF.

6003 Trivedi, A., Sarkar, S., Ker, S., and Minshull, T. A., 2023, An improved Weichselian seismic
6004 stratigraphic framework of the Kongsfjorden-Isfjorden Interfan region off western Svalbard from high-
6005 frequency deep-towed seismic data and its implication on fluid migration and methane venting:
6006 Copernicus Meetings.

6007 Trujillo-Vela, M. G.; Ramos-Canón, A. M.; Escobar-Vargas, J. A. and Galindo-Torres, S. A. (2022).
6008 An overview of debris-flow mathematical modelling. *Earth-Science Reviews* 232: 104135, DOI
6009 10.1016/j.earscirev.2022.104135.

6010 Tuuling, I., & Flodén, T. (2016). The Baltic Klint beneath the central Baltic Sea and its comparison
6011 with the North Estonian Klint. *Geomorphology*, 263, 1-18.

6012 Tylmann, K., & Uścińowicz, S. (2022). Timing of the last deglaciation phases in the southern Baltic
6013 area inferred from Bayesian age modeling. *Quaternary Science Reviews*, 287, 107563.

6014 Uehara, K., Scourse, J. D., Horsburgh, K. J., Lambeck, K., & Purcell, A. P. (2006). Tidal evolution of
6015 the northwest European shelf seas from the Last Glacial Maximum to the present. *Journal of*
6016 *Geophysical Research: Oceans*, 111(C9).

6017 Unnithan, V., Shannon, P. M., McGrane, K., Readman, P. W., Jacob, A. W. B., Keary, R., & Kenyon,
6018 N. H. (2001). Slope instability and sediment redistribution in the Rockall Trough: constraints from
6019 GLORIA.

6020 Upstreamonline (2025). Equinor sharpens its exploration tools to bring gas to Europe.
6021 [https://www.upstreamonline.com/exclusive/equinor-sharpens-its-exploration-tools-to-bring-gas-to-](https://www.upstreamonline.com/exclusive/equinor-sharpens-its-exploration-tools-to-bring-gas-to-europe/2-1-1749879)
6022 [europe/2-1-1749879](https://www.upstreamonline.com/exclusive/equinor-sharpens-its-exploration-tools-to-bring-gas-to-europe/2-1-1749879). Accessed on 05 May 2025.

6023 Urlaub, M., Talling, P.J., Masson, D.G., 2013. Timing and frequency of large submarine landslides:
6024 implications for understanding triggers and future geohazard, *Quaternary Science Reviews* 72, 63-82,
6025 <https://doi.org/10.1016/j.quascirev.2013.04.020>.

6026 Uścińowicz, S. (2006). A relative sea-level curve for the Polish Southern Baltic Sea. *Quaternary*
6027 *International*, 145, 86-105.

6028 Uścińowicz, S. (2014). The baltic sea continental shelf.

6029 Vachon, R., Schmidt, P., Lund, B., Plaza-Faverola, A., Patton, H., and Hubbard, A., 2022, Glacially
6030 Induced Stress Across the Arctic From the Eemian Interglacial to the Present—Implications for Faulting
6031 and Methane Seepage: *Journal of Geophysical Research: Solid Earth*, v. 127, no. 7, p. e2022JB024272.

6032 Vadakkepuliymbatta, S., Chand, S., & Bünz, S. (2017). The history and future trends of ocean
6033 warming-induced gas hydrate dissociation in the SW Barents Sea. *Geophysical Research Letters*, 44(2),
6034 835-844.

6035 van Dijk, T. A. G. P., Best, J., & Baas, A. C. W. (2021). Subaqueous and Subaerial Depositional
6036 Bedforms. In *Encyclopedia of Geology* (pp. 771–786). Elsevier. [https://doi.org/10.1016/B978-0-08-](https://doi.org/10.1016/B978-0-08-102908-4.00187-9)
6037 [102908-4.00187-9](https://doi.org/10.1016/B978-0-08-102908-4.00187-9)

- 6038 Van Landeghem, K. J., Uehara, K., Wheeler, A. J., Mitchell, N. C., & Scourse, J. D. (2009a). Post-
6039 glacial sediment dynamics in the Irish Sea and sediment wave morphology: Data–model comparisons.
6040 *Continental Shelf Research*, 29(14), 1723-1736.
- 6041 Van Landeghem, K. J., Wheeler, A. J., Mitchell, N. C., & Sutton, G. (2009b). Variations in sediment
6042 wave dimensions across the tidally dominated Irish Sea, NW Europe. *Marine Geology*, 263(1-4), 108-
6043 119.
- 6044 Van Landeghem, K. J., Niemann, H., Steinle, L. I., O'Reilly, S. S., Huws, D. G., & Croker, P. F. (2015).
6045 Geological settings and seafloor morphodynamic evolution linked to methane seepage. *Geo-Marine*
6046 *Letters*, 35, 289-304.
- 6047 Van Landeghem, K. J., & Chiverrell, R. C. (2020). Bed erosion during fast ice streaming regulated the
6048 retreat dynamics of the Irish Sea Ice Stream. *Quaternary Science Reviews*, 245, 106526.
- 6049 Van Rensbergen, P., Hillis, R. R., Maltman, A. J. & Morely, C. K. (editors) 2003. Subsurface Sediment
6050 Remobilization. Geological Society, London, Special Publications 216;
6051 <https://doi.org/10.1144/GSL.SP.2003.216.01.34>
- 6052 Vanneste, M., Mienert, J., and Bünz, S., 2006, The Hinlopen Slide: A giant, submarine slope failure on
6053 the northern Svalbard margin, Arctic Ocean: *Earth and Planetary Science Letters*, v. 245, p. 373-388,
6054 <https://doi.org/10.1016/j.epsl.2006.02.045>.
- 6055 Vanneste, M., Sultan, N., Garziglia, S., Forsberg, C. F., & l'Heureux, J. S. (2014). Seafloor instabilities
6056 and sediment deformation processes: The need for integrated, multi-disciplinary investigations. *Marine*
6057 *Geology*, 352, 183-214.
- 6058 Vanneste M, Løvholt F, Issler D, Liu Z, Boylan N, and Kim J (2019) A novel quasi-3D landslide
6059 dynamics model: From theory to applications and risk assessment. In: *Proceedings of the Offshore*
6060 *Technology Conference 2019*, OTC-29363-MS. ISBN: 978-1-61399-641-6.
- 6061 van Vliet-Lanoë, B., Magyari, A., and Meilliez, F., 2004, Distinguishing between tectonic and
6062 periglacial deformations of quaternary continental deposits in Europe: *Global and Planetary Change*, v.
6063 43, no. 1-2, p. 103-127.
- 6064 Vardy, M.E., Vanneste, M., Henstock, T.J., Clare, M.A., Forsberg, C.F., and G. Provenzano, 2017.
6065 State-of-the-art remote characterization of shallow marine sediments: the road to a fully integrated
6066 solution. *Near Surface Geophysics*, 15, 387-402.
- 6067 Vasskog, K., Waldmann, N., Bondevik, S., Nesje, A., Chapron, E., & Ariztegui, D. (2013). Evidence
6068 for Storegga tsunami run-up at the head of Nordfjord, western Norway. *Journal of Quaternary Science*,
6069 28(4), 391-402.

6070 Vattenfall, 2019: Horns Rev III Wind Farm Zone, Location E03 Seabed and soils. Report, 102 pages

6071 Vaughan-Hirsch, D. P., & Phillips, E. R. (2017). Mid-Pleistocene thin-skinned glaciotectonic thrusting
6072 of the Aberdeen Ground Formation, Central Graben region, central North Sea. *Journal of Quaternary*
6073 *Science*, 32(2), 196–212. <https://doi.org/10.1002/JQS.2836>

6074 Vejbæk, O.V., 2008. Disequilibrium compaction as the cause for Cretaceous–Paleogene overpressures
6075 in the Danish North Sea. *AAPG bulletin*, 92(2), pp.165-180.

6076 Velenturf, A. P. M., Emery, A. R., Hodgson, D. M., Barlow, N. L. M., Mohtaj Khorasani, A. M., Van
6077 Alstine, J., ... & Thorp, M. (2021). Geoscience solutions for sustainable offshore wind development.
6078 *Earth Science, Systems and Society*, 1(1), 10042.

6079 Vimpere, L., Spangenberg, J. E., Roige, M., Adatte, T., De Kaenel, E., Fildani, A., ... & Castellort, S.
6080 (2023). Carbon isotope and biostratigraphic evidence for an expanded Paleocene–Eocene Thermal
6081 Maximum sedimentary record in the deep Gulf of Mexico. *Geology*, 51(4), 334–339.

6082 Viner, D. (1991). *Accident analysis and risk control*. Derek Viner Pty Ltd, Melbourne.

6083 Vinnem, JE., Røed, W. (2020). *Lessons from Major Accidents*. In: *Offshore Risk Assessment Vol. 1*.
6084 *Springer Series in Reliability Engineering*. Springer, London. [https://doi.org/10.1007/978-1-4471-](https://doi.org/10.1007/978-1-4471-7444-8_4)
6085 [7444-8_4](https://doi.org/10.1007/978-1-4471-7444-8_4)

6086 Virtanen, E. A., Lappalainen, J., Nurmi, M., Viitasalo, M., Tikanmäki, M., Heinonen, J., ... & Moilanen,
6087 A. (2022). Balancing profitability of energy production, societal impacts and biodiversity in offshore
6088 wind farm design. *Renewable and Sustainable Energy Reviews*, 158, 112087.

6089 Voellmy, A. (1955). Über die Zerstörungskraft von Lawinen [On the destructive power of avalanches]
6090 (in German). *Schweiz. Bauztg* 73(12, 15, 17, 19) : 159–165, 212–217, 246–249, 280–285.

6091 Vorren, T.O., and Laberg, J.S., 1997, Trough mouth fans – palaeoclimate and ice-sheet monitors:
6092 *Quaternary Science Reviews*, v. 16, p. 865-881, [https://doi.org/10.1016/S0277-3791\(97\)00003-6](https://doi.org/10.1016/S0277-3791(97)00003-6).

6093 Vorren, T. O., Laberg, J. S., Blaume, F., Dowdeswell, J. A., Kenyon, N. H., Mienert, J., ... & Werner,
6094 F. (1998). The Norwegian–Greenland Sea continental margins: morphology and late Quaternary
6095 sedimentary processes and environment. *Quaternary Science Reviews*, 17(1-3), 273-302.

6096 Vorren, T.O., Mangerud, J., Blikra, L.H., Nesje, A., and Sveian, H. (2008). The emergence of modern
6097 Norway. In: Ramberg, I.B., Bryhni, I., Nøttvedt, A., Rangnes, K. (Eds.) *The Making of a Land —*
6098 *Geology of Norway*. Norsk Geologisk Forening, Trondheim, 534–559.

6099 Voss, P., Dahl-Jensen, T. & Larsen, T. B. (2015) *Earthquake hazard in Denmark*, GEUS. Danmarks
6100 og Grønlands Geologiske Undersøgelse Rapport Vol. 2015 No. 24 <https://doi.org/10.22008/gpub/30674>

- 6101 Wagner, B., Bennike, O., Klug, M., Cremer, H., 2007. First indication of Storegga tsunami deposits
6102 from East Greenland. *Journal of Quaternary Science* 22, 321-325.
- 6103 Waldmann N, Vasskog K, Simpson G, Chapron E, Støren EWN, Hansen L, Loizeau J-L, Nesje A and
6104 Ariztegui D (2021) Anatomy of a Catastrophe: Reconstructing the 1936 Rock Fall and Tsunami Event
6105 in Lake Lovatnet, Western Norway. *Front. Earth Sci.* 9:671378. doi: 10.3389/feart.2021.671378
- 6106 Waller, M., & Kirby, J. (2021). Coastal peat-beds and peatlands of the southern North Sea: their past,
6107 present and future. *Biological Reviews*, 96(2), 408–432. <https://doi.org/10.1111/brv.12662>
- 6108 Wallmann, K., Riedel, M., Hong, W. L., Patton, H., Hubbard, A., Pape, T., ... & Bohrmann, G. (2018).
6109 Gas hydrate dissociation off Svalbard induced by isostatic rebound rather than global warming. *Nature*
6110 *communications*, 9(1), 83.
- 6111 Walker, J., Gaffney, V., Fitch, S., Muru, M., Fraser, A., Bates, M., & Bates, R. (2020). A great wave:
6112 the Storegga tsunami and the end of Doggerland?. *Antiquity*, 94(378), 1409-1425.
- 6113 Walker, J.D. and Geissman, J.W., compilers. (2022). *Geologic Time Scale v. 6.0*. Geological Society
6114 of America. <https://doi.org/10.1130/2022.CTS006C>.
- 6115 Walker, J., Gaffney, V., Harding, R., Fraser, A.I., Fitch, S., Boothby, V. (2024). Winds of Change:
6116 Urgent Challenges and Emerging Opportunities in Submerged Prehistory, a Perspective from the North
6117 Sea. *Heritage* 2024, 7, 1947–1968. <https://doi.org/10.3390/heritage7040093>
- 6118 Waller, M. and Kirby, J. (2021). Coastal peat-beds and peatlands of the southern North Sea: their past,
6119 present and future. *Biol. Rev.* (2021), 96, pp. 408–432. doi: 10.1111/brv.12662
- 6120 Ward, S.L., Neill, S.P., Van Landeghem, K.J.J., Scourse, J.D., 2015. Classifying seabed sediment type
6121 using simulated tidal-induced bed shear stress. *Mar. Geol.* 367, 94–104.
6122 <https://doi.org/10.1016/j.margeo.2015.05.010>
- 6123 Watts, P., Grilli, S. T., Tappin, D. R., and Fryer, G. J. (2005). Tsunami generation by submarine mass
6124 failure. II: Predictive equations and case studies. *Journal of waterway, port, coastal, and ocean*
6125 *engineering*, 131(6), 298-310.
- 6126 Watts, R., Lee, A., and Snieckus, D. (2021). Saipem woe as ‘soil and foundations’ issues hit work on
6127 North Sea wind farm installation. *UpStream*. [https://www.upstreamonline.com/energy-](https://www.upstreamonline.com/energy-transition/saipem-woe-as-soil-and-foundations-issues-hit-work-on-north-sea-wind-farm-installation/2-1-971065)
6128 [transition/saipem-woe-as-soil-and-foundations-issues-hit-work-on-north-sea-wind-farm-installation/2-](https://www.upstreamonline.com/energy-transition/saipem-woe-as-soil-and-foundations-issues-hit-work-on-north-sea-wind-farm-installation/2-1-971065)
6129 [1-971065](https://www.upstreamonline.com/energy-transition/saipem-woe-as-soil-and-foundations-issues-hit-work-on-north-sea-wind-farm-installation/2-1-971065) (accessed April 2025).
- 6130 Weaver, P. P., Wynn, R. B., Kenyon, N. H., & Evans, J. (2000). Continental margin sedimentation,
6131 with special reference to the north-east Atlantic margin. *Sedimentology*, 47, 239-256.

- 6132 Webb, K. E., Barnes, D. K., & Plankea, S. (2009). Pockmarks: Refuges for marine benthic biodiversity.
6133 *Limnology and Oceanography*, 54(5), 1776-1788.
- 6134 Wentworth, C.K., 1922. A scale of grade and class terms for clastic sediments. *The Journal of Geology*,
6135 30, pp. 377-392
- 6136 Westerhold, T., Marwan, N., Drury, A. J., Liebrand, D., Agnini, C., Anagnostou, E., ... & Zachos, J. C.
6137 (2020). An astronomically dated record of Earth's climate and its predictability over the last 66 million
6138 years. *science*, 369(6509), 1383-1387.
- 6139 Wheeler, A. J., Walshe, J., & Sutton, G. D. (2001). Seabed mapping and seafloor processes in the Kish,
6140 Burford, Bray and Fraser Banks area, South-Western Irish Sea. *Irish Geography*, 34(2), 194-211.
- 6141 Whitehouse, R.J.S., Harris, J.M., Sutherland, J., Rees, J., 2011. The nature of scour development and
6142 scour protection at offshore windfarm foundations. *Mar. Pollut. Bull.* 62, 73–88.
6143 <https://doi.org/10.1016/j.marpolbul.2010.09.007>
- 6144 Whittington, R.J. (1977). A late-glacial drainage pattern in the Kish Bank area and post-glacial
6145 sediments in the Central Irish Sea. In Kidson, C., Toolet, M.J. (Eds.), *The Quaternary History of the*
6146 *Irish Sea*. Seel House, Liverpool, pp. 55–68.
- 6147 WindEurope (2024). Wind energy in Europe. Statistics 2024 and the outlook for 2025-2030. 64 pp.
- 6148 Winkelmann, D., Geissler, W., Schneider, J., Stein, R., 2008. Dynamics and timing of the
6149 Hinlopen/Yermak Megaslide north of Spitsbergen, Arctic Ocean. *Marine Geology*, Volume 250, 34-
6150 50, <https://doi.org/10.1016/j.margeo.2007.11.013>.
- 6151 Winsborrow, M. C., Andreassen, K., Corner, G. D., & Laberg, J. S. (2010). Deglaciation of a marine-
6152 based ice sheet: Late Weichselian palaeo-ice dynamics and retreat in the southern Barents Sea
6153 reconstructed from onshore and offshore glacial geomorphology. *Quaternary Science Reviews*, 29(3-
6154 4), 424-442.
- 6155 Winsborrow, M., Andreassen, K., Hubbard, A., Plaza-Faverola, A., Gudlaugsson, E., & Patton, H.
6156 (2016). Regulation of ice stream flow through subglacial formation of gas hydrates. *Nature Geoscience*,
6157 9(5), 370-374. Woods, M.A., Wilkinson, I.P., Leng, M.J., Riding, J.B., Vane, C.H., Lopes dos Santos,
6158 R.A., Kender, S., De Schepper, S., Hennissen, J.A.I., Ward, S.L., Gowing, C.J.B., Wilby, P.R., Nichols,
6159 M.D., Rochelle, C.A., 2019. Tracking Holocene palaeostratification and productivity changes in the
6160 Western Irish Sea: A multi-proxy record. *Palaeogeogr. Palaeoclimatol. Palaeoecol.* 532, 109231.
6161 <https://doi.org/https://doi.org/10.1016/j.palaeo.2019.06.004>
- 6162 Winsemann, J., Koopmann, H., Tanner, D. C., Lutz, R., Lang, J., Brandes, C., & Gaedicke, C. (2020).
6163 Seismic interpretation and structural restoration of the Heligoland glaciotectionic thrust-fault complex:

6164 Implications for multiple deformation during (pre-)Elsterian to Warthian ice advances into the southern
6165 North Sea Basin. *Quaternary Science Reviews*, 227, 106068.
6166 <https://doi.org/10.1016/J.QUASCIREV.2019.106068>

6167 Wrona, T., Magee, C., Jackson, C. A., Huuse, M., & Taylor, K. G. (2017). Kinematics of polygonal
6168 fault systems: Observations from the northern North Sea. *Frontiers in Earth Science*, 5, 101.

6169 Yavari-Ramshe S and Ataie-Ashtiani B (2016) Numerical modeling of subaerial and submarine
6170 landslide-generated tsunami waves—Recent advances and future challenges. *Landslides* 13(6): 1325–
6171 1368.

6172 Yuan, F., Bennell, J.D., Davis, A.M., 1992. Acoustic and physical characteristics of gassy sediments in
6173 the western Irish Sea. *Cont. Shelf Res.* 12, 1121–1134.

6174 Zakeri, A.; Høeg, K. and Nadim, F. (2009). Submarine debris flow impact on pipelines – Part II:
6175 Numerical analysis. *Coastal Engineering* 56: 1–10, DOI 10.1016/j.coastaleng.2008.06.005.

6176 Zarifi, Z., Köhler, A., Ringrose, P., Ottemöller, L., Furre, A.-K., Hansteen, F., Jerkins, A., Oye, V.,
6177 Dehghan Niri, R., Bakke, R., 2022. Background Seismicity Monitoring to Prepare for Large-Scale CO2
6178 Storage Offshore Norway. *Seismol. Res. Lett.* <https://doi.org/10.1785/0220220178>

6179 Zengaffinen T, Løvholt F, Pedersen GK, and Harbitz CB (2020) Effects of rotational submarine slump
6180 dynamics on tsunami genesis: New insight from idealized models and the 1929 grand banks event.
6181 *Geological Society, London, Special Publications* 500(1): 41–61. Zhang C, Kirby JT, Shi F, Ma G, and
6182 Grilli ST (2021).

6183 Zhang C, Kirby JT, Shi F, Ma G, and Grilli ST (2021) A two-layer non-hydrostatic landslide model for
6184 tsunami generation on irregular bathymetry. 1. Theoretical basis. *Ocean Modelling* 159: 101749.

6185 Zhao, Y., & Si, B. (2019). Thermal properties of sandy and peat soils under unfrozen and frozen
6186 conditions. *Soil and Tillage Research*, 189, 64–72. <https://doi.org/10.1016/j.still.2018.12.026>

6187 Zhao, Y., Si, B., Zhang, Z., Li, M., He, H., & Hill, R. L. (2019). A new thermal conductivity model for
6188 sandy and peat soils. *Agricultural and Forest Meteorology*, 274, 95–105.
6189 <https://doi.org/10.1016/j.agrformet.2019.04.004>

6190 Zoback, M. D., & Gorelick, S. M. (2012). Earthquake triggering and large-scale geologic storage of
6191 carbon dioxide. *Proceedings of the National Academy of Sciences*, 109(26), 10164-10168.

6192 Zoback, M. D., and Lund Snee, J.-E., 2018, Predicted and observed shear on pre-existing faults during
6193 hydraulic fracture stimulation, SEG Technical Program Expanded Abstracts 2018, Society of
6194 Exploration Geophysicists, p. 3588-3592.